AD-A021 053

PROCEEDINGS OF THE TRISERVICE CORROSION OF MILITARY
EQUIPMENT CONFERENCE (1974), HELD AT DAYTON, OHIO
ON 29-31 OCTOBER 1974.   VOLUME I.   SESSIONS I THROUGH
III

Fred H. Meyer, Jr.

Air Force Materials Laboratory
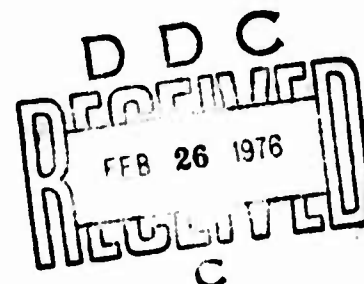Wright-Patterson Air Force Base, Ohio

September 1975

062150

AFML-TR-75-42
Volume I

PROCEEDINGS OF THE 1974 TRISERVICE CORROSION OF MILITARY EQUIPMENT CONFERENCE, 29-31 OCTOBER 1974
Volume I. Sessions I through III

AERONAUTICAL SYSTEMS BRANCH
SYSTEMS SUPPORT DIVISION

DDC

FEB 26 1976

SEPTEMBER 1975

TECHNICAL REPORT AFML-TR-75-42, Volume I
FINAL REPORT FOR PERIOD 31 OCTOBER 1974 — 1 FEBRUARY 1975

Approved for public release; distribution unlimited

AIR FORCE MATERIALS LABORATORY
AIR FORCE WRIGHT AERONAUTICAL LABORATORIES
Air Force Systems Command
Wright-Patterson Air Force Base, Ohio 45433

FRED H. MEYER Jr.
Project Engineer

FOR THE COMMANDER

T. D. COOPER, Chief
Aeronautical Systems Branch
Systems Support Division

SECURITY CLASSIFICATION OF THIS PAGE (When Data Entered)

REPORT DOCUMENTATION PAGE		READ INSTRUCTIONS BEFORE COMPLETING FORM
1. REPORT NUMBER AFML-TR-75-42, Volume I	2. GOVT ACCESSION NO.	3. RECIPIENT'S CATALOG NUMBER
4. TITLE (and Subtitle) PROCEEDINGS OF THE 1974 TRISERVICE CORROSION OF MILITARY EQUIPMENT CONFERENCE, 29-31 OCTOBER 1974		5. TYPE OF REPORT & PERIOD COVERED Final Technical Report 31 Oct 74 - 1 Feb 75
		6. PERFORMING ORG. REPORT NUMBER
7. AUTHOR(s) Fred H. Meyer, Jr. (Editor)		8. CONTRACT OR GRANT NUMBER(s)
9. PERFORMING ORGANIZATION NAME AND ADDRESS Aeronautical Systems Branch (MXA) Materials Laboratory Wright-Patterson AFB, Ohio 45433		10. PROGRAM ELEMENT, PROJECT, TASK AREA & WORK UNIT NUMBERS 73810701
11. CONTROLLING OFFICE NAME AND ADDRESS Systems Support Division (MX) Materials Laboratory Wright-Patterson AFB, Ohio 45433		12. REPORT DATE September 1975
		13. NUMBER OF PAGES 550
14. MONITORING AGENCY NAME & ADDRESS(if different from Controlling Office)		15. SECURITY CLASS. (of this report) UNCLASSIFIED
		15a. DECLASSIFICATION/DOWNGRADING SCHEDULE

16. DISTRIBUTION STATEMENT (of this Report)

Approved for public release; distribution unlimited.

17. DISTRIBUTION STATEMENT (of the abstract entered in Block 20, if different from Report)

18. SUPPLEMENTARY NOTES

19. KEY WORDS (Continue on reverse side if necessary and identify by block number)

Corrosion

20. ABSTRACT (Continue on reverse side if necessary and identify by block number)

This report is a compilation of papers presented at the 1974 Triservice Corrosion of Military Equipment Conference held in Dayton, Ohio, 29-31 October 1974.

DD FORM 1473 EDITION OF 1 NOV 65 IS OBSOLETE

SECURITY CLASSIFICATION OF THIS PAGE (When Data Entered)

FOREWORD

This report was compiled by the Aeronautical Systems Branch, Systems Support Division, Air Force Materials Laboratory, Wright-Patterson AFB, Ohio. It was initiated under Project 7381, "Materials Applications," Task 738107, "Corrosion Control and Failure Analysis," with Mr. Fred H. Meyer, Jr. as the Project Engineer. The 1974 Triservice Conference is a follow-up to three similar conferences held in 1967, 1968, and 1972.

The report includes all available papers from the 1974 Triservice Corrosion of Military Equipment Conference.

This technical report was submitted by the author in February 1975.

Proceedings of prior conferences are available in AFML Technical Report TR-67-329 (1967) and in Metals and Ceramics Information Center Report MCIC 73-19.

The purpose of the 1974 Conference was to continue interservice coordination in the areas of corrosion research and corrosion prevention and control. Specifically, the objectives were to make Department of Defense personnel, contractors and interested individuals aware of the important corrosion problems in military equipment, to present the status of significant corrosion research projects currently pursued by the military services and to provide a general forum for exchange of corrosion prevention and control information.

AFML-TR-75-42
Volume I

TABLE OF CONTENTS

Preceding page blank

TABLE OF CONTENTS (Cont'd)

TABLE OF CONTENTS (Cont'd)

TABLE OF CONTENTS (Cont'd)

TECHNICAL PROGRAM COMMITTEE

Murray M. Jacobson
Army Materials and Mechanics Research Center
Watertown, Massachusetts 02172

Anthony Gallaccio
Frankford Arsenal-Pittman Dunn Laboratories
Philadelphia, Pennsylvania 19137

George J. Danak
Naval Ship Research and Development Center
Annapolis, Maryland 21402

Samuel Goldberg
Naval Air Systems Command
Washington, D.C.   20361

William Thompson
Warner Robins Air Logistics Center
Robins AFB, Georgia   31098

Lt Col James Upp
Hq, United States Air Force
Washington, D.C.   20330

Fred H. Meyer, Jr.
Air Force Materials Laboratory
Wright-Patterson AFB, Ohio 45433

PROGRAM SPEAKERS

Opening Remarks

Mr. Fred H. Meyer, Jr.
Corrosion Specialist
Air Force Materials Laboratory
Conference Chairman

Welcoming Address

Mr. George Peterson
Director
Air Force Materials Laboratory

Introductory Remarks

Brig Gen Gerald Post
Air Force Logistics Command
Deputy Chief of Staff
Materiel Management

Keynote Speaker

Mr. W. J. Willoughby
Consultant/Chief
Naval Materials
Department of the Navy

Banquet Speaker

Mr. Dean Hannick
Allison Division
General Motors Corporation

Preceding page blank

LIST OF ATTENDEES

Dr. Philip A. Adler
Research Department, Plant 26
Grumman Aerospace Corporation
Bethpage, New York 11714

Capt Francis (Sid) W. A'Hearn
Hq AFSC/SDDE
Andrews AFB, Maryland 20334

John A. Alexander
6854 Harper Drive
Painesville, Ohio 44077

Earl R. Allen
11312 South Sheridan
Tacoma, Washington 98444

Jay M. Armstrong
Naval Weapons Station WQEC
Seal Beach, California 90740

Forrest H. Arnold, Jr.
Naval Air Systems Command
U.S. Naval Air Station, North Island
San Diego, California 92135

Chris Atnanasopoulos
1700 South Mt. Prospect Road
Des Plaines, Illinois

Hargrow D. Barber
2142 66th Avenue
Oakland, California 94621

M. S. Bartlett
Officers Mess, RAF High Wicombe Bucks
ME (Trans)
HQSTC RAF

Ben L. Bates
P. O. Box 748
Fort Worth, Texas 76101

J. R. Beard, Jr.
Lockheed Georgia Company
862 Cobb Drive
Marietta, Georgia 30060

LIST OF ATTENDEES (Cont'd)

Marvin S. Berger
1029 Monette
Corpus Christi, Texas 78412

Dr. Kirit J. Bhansali
AFML/LLN
Wright-Patterson AFB, Ohio 45433

G. C. Booth
C/O R. H. Warren
British Defence Staff, British Embassy
3100 Massachusetts Avenue, NW
Washington, D.C. 20008

W. K. Boyd
505 King Avenue
Columbus, Ohio 43201

Robert E. Brandenburg
ASD/SDM
Wright-Patterson AFB, Ohio 45433

Mrs. Marjorie E. Brown
707 Tomkin Street
Eau Gallie, Florida 32935

Joel Wayne Browning
P. O. Box 428
Fort Worth, Texas

Michael A. Buppert
36 Vivian Court
Howell, New Jersey 07731

Dr. Harris M. Burte
AFML/LL
Wright-Patterson AFB, Ohio 45433

Nick Caliendo
AFLC/MMEA
Wright-Patterson AFB, Ohio 45433

Roy Canon
4430 Director Drive
San Antonio, Texas 78219

Dale K. Carter
Warner Robins ALC
Robins AFB, Georgia 31090

LIST OF ATTENDEES (Cont'd)

Capt John F. Chambers
Hq ATC/LGMAT
Randolph AFB, Texas   78148

Sidney Childers
AFML/MXA
Wright-Patterson AFB, Ohio   45433

Tim Chin
Raytheon Company
Hartwell Road
Bedford, Massachusetts   01730

Mal Clancy
2700 Cantana
Fullerton, California   92635

Philip A. Clarkin
Office of Naval Research, Code 471
800 North Quincy Street
Arlington, Virginia   22217

David L. Clouse
5617 Hunters Ridge Road
Dayton, Ohio   45431

Bennie Cohen
AFML/MXA
Wright-Patterson AFB, Ohio   45433

Joe F. Collins
Code 341, Bldg 44, NARF
Naval Air Station
Alameda, California   94501

Capt William C. Connors
CCJ/MASDC
Davis Monthan AFB, Arizona   85707

Lester S. Constantine
6 Ingleside Court
Rockville, Maryland   20850

Thomas D. Cooper
AFML./MXA
Wright-Patterson AFB, Ohio   45433

William A. Cori
25 George Road
Glen Rock, New Jersey   07452

LIST OF ATTENDEES (Cont'd)

Calvin R. Cox
303 ARRSq/LGMF
March AFB, California   92508

Robert Crowe
U.S. Naval Surface Weapons Center
Code GWR
Dahlgren, Virginia   22401

Walter F. Czyrklis
Army Materials and Mechanics Research Center
Metals Research Division, AMMRC
Arsenal Street
Watertown, Massachusetts   02172

Donald E. Dadigan
3836 Santa Fe Way
North Highlands, California   95660

George J. Danek
Code 2813 Naval Ship R&D Center
Annapolis, Maryland   21402

Dr. Bhagwan K. Das
Orgn 2-5540, MS 73-09
The Boeing Company
Materials and Processes Group
P.O. Box 3707
Seattle, Washington   98124

Dr. H. M. Davis
U.S. Army Research Office
Box CM Duke Station
Durham, North Carolina   27706

John J. DeLuccia
U.S. Naval Air Development Center
Code 3022
Warminster, Pennsylvania   18974

Lt Peter F. Dexter
AFFDL/FEM
Wright-Patterson AFB, Ohio   45433

James L. Dobbs, Jr.
5136 Ginkgo Drive, SW
Tacoma, Washington   98438

LIST OF ATTENDEES (Cont'd)

Francis J. Dougherty, Jr.
C/O Frankford Arsenal
L3300 PDM-A
Bridge and Tacony
Philadelphia, Pennsylvania 19137

Fred W. Drosten
P. O. Box 209 AMSAV-EFS
St. Louis, Missouri 63166

Paul G. Dry
P. O. Box 274
Bandera, Texas 78003

Capt Steven R. Erickson
CINCPACAF/LGMW
APO San Francisco 96553

L. Frazier Fall
Army Materials and Mechanics Research Center
Engineering Standardization Branch
Watertown, Massachusetts 02172

Steven G. Fishman
U. S. Naval Surface Weapons Center
Code GWR
Dahlgren, Virginia 22401

Jerry G. Fuller
Hq ARRS/LOW
Scott AFB, Illinois 62225

Anthony Gallaccio
410 Covington Road
Havertown, Pennsylvania 19083

George A. Gehring, Jr.
Tennessee Avenue, S. Beach, Thoro.
Ocean City, New Jersey 08226

Raymond E. Geisert
18901 Euclid Avenue
Cleveland, Ohio 44117

Lt Edward R. Gilley, USN
COMLATWING One Code 43
NAS
Cecil Field, Florida 32215

LIST OF ATTENDEES (Cont'd)

Wing Commander G. B. Gilmore
New Zealand Embassy Defence Staff
1601 Connecticut Avenue
Washington, D.C. 20009

Herman L. Gilmore
EH22
Materials and Processing Laboratory
Marshall Space Flight Center
Huntsville, Alabama 35812

Lavon Glover, Jr.
P. O. Box 2774
Nellis AFB, Nevada 89191

Joseph A. Goebel
P. O. Box 611
Middletown, Connecticut 06457

Samuel Goldberg
Naval Air Systems Command
NAVAIR
Washington, D.C. 20361

Cdr Richard J. Green
USCG Liaison Office (MCLCG)
Wright-Patterson AFB, Ohio 45433

Dr. Michael Groves
TRW Inc., T/M 2988
23555 Euclid Avenue
Cleveland, Ohio 44117

Thomas G. Harvey
D1033
Naval Avionics Facility
6000 East 21st Street
Indianapolis, Indiana 46218

T. A. Higdon
Code 34300 Building 341
Naval Air Rework Facility
NAS North Island
San Diego, California 92135

T/Sgt Charles Q. Hill, Jr.
PCS#2 Box 18273
APO San Francisco, California 96311

LIST OF ATTENDEES (Cont'd)

Gilbert F. Hinkeldey
Route 3, Box 3783
Issaquah, Washington 98027

James A. Hoffner
Code Air-52031C
Naval Air Systems Command Hq
Washington, D.C. 20361

T/Sgt Ralph H. Houghton
9309 Victoria Lane
Tampa, Florida 33610

Dean K. Houink
Detroit Diesel Allison
Tibbs Avenue, Box 894
Indianapolis, Indiana 46220

Al Houman
Unit 2-52450
P. O. Box 5907
Dallas, Texas 75221

M/Sgt Donald Howard
4257 H FCN
McGuire AFB, New Jersey 08641

William H. Hudgins
Commanding Officer
Naval Air Rework Facility (Code 431)
NAS
Jacksonville, Florida 32212

Werner J. Iller
808 East Dorothy Lane
Kettering, Ohio 45440

Shin Inouye
AFML/LTM
Wright-Patterson AFB, Ohio 45433

A. L. Jackman
P. O. Box 98
Magna, Utah 84044

Elwin L. Jang
Sacramento ALC/MANCA
McClellan AFB, California 95652

LIST OF ATTENDEES (Cont'd)

Edward J. Jankowsky
890 Sycamore Drive
Southampton, Pennsylvania 18966

Clifton E. Janney
Naesudet Jax
P. O. Box 75
NAS
Jacksonville, Florida 32212

James F. Jenkins
Civil Engineering Laboratory
Port Hueuene, California 93043

Charles E. Johnson
Boeing Aerospace Company
M&P Staff, AWACS
P. O. Box 3999
Seattle, Washington 98124

Howard A. Johnson
Orgn 2-5540, MS 73-09
Boeing Aerospace Company
P. O. Box 3999
Seattle, Washington 98124

Jim Johnson
Code GC
Naval Surface Weapons Center
Dahlgren, Virginia 22401

K. T. Kamber
P. O. Box 92957
Los Angeles, California 90009

Major Daniel J. Kamish
Hq USAFE
Box 6154
Ramstein AB, Germany
APO New York 09012

Daniel R. Kelly
1419 Biddle Avenue
Wyandotte, Michigan 48192

Clifford Kelto
AFML/MXA
Wright-Patterson AFB, Ohio 45433

LIST OF ATTENDEES (Cont'd)

Sara J. Ketcham
Alden Park Manor
Philadelphia, Pennsylvania 19144

Thomas O. Knight
169 Tchefuncte Drive
Covington, Louisiana 70433

Charles S. Kortovich
1668 Empire Road
Wickcliffe, Ohio 44092

George Kostas
6243 Valley Forge
Houston, Texas 77027

Theodore G. Kozan
8600 Lockmoor Circle
Wichita, Kansas 67207

W. James Lane
Alcoa Tech Center
Alcoa Application Engineering Division
Alcoa Center, Pennsylvania 15069

Harold Langley
Hq SAC LGMS
Offutt AFB, Nebraska 68113

Charles P. Lascaro
AMSEL-TL-IR
ET&DL
USAECOM
Fort Monmouth, New Jersey 07703

Sylvester J. Lee
AFIT/ENB
Wright-Patterson AFB, Ohio 45433

Thomas J. Lennox, Jr.
Naval Research Laboratory
Code 6386
Washington, D.C. 20375

Irwin (Bud) Levine
Deft Chemical Coatings
612 Maple Avenue
Torrance, California 90503

LIST OF ATTENDEES (Cont'd)

Milton Levy
Army Materials and Mechanics Research Center
Watertown, Massachusetts 02172

R. I. Lindberg
Reynolds Metals Company
4th and Canal Streets
Richmond, Virginia 23218

M/Sgt John L. Lindsey
313 Air Division/LGMC
PSC Box 10836
APO San Francisco 96367

Dr. Charles T. Lynch
AFML/LLN
Wright-Patterson AFB, Ohio 45433

Elizabeth L. MacNamara
96 Woodlake Drive
Holland, Pennsylvania 18966

Dr. Florian Mansfeld
P. O. Box 1085
Thousand Oaks, California 91360

Brian Manty
712 Magnolia Drive
Lake Park, Florida

Kenneth Mathews
Warner Robins ALC
Robins AFB, Georgia 31098

Lt Col Everett C. McCormick
AFCS
6803 King Louis
San Antonio, Texas 78243

Thomas F. McGann
Owens-Corning Fiberglas Corporation
Granville, Ohio 43023

D. W. McKee
General Electric Company
R&D Center
P. O. Box 8
Schenectady, New York 12301

LIST OF ATTENDEES (Cont'd)

Lawrence H. McVittie
6431 South M Street
Tacoma, Washington 98439

Donald L. Mellem
Martin Marietta Aluminum
19200 South Western Avenue
Torrance, California 90509

M. D. Mendenhall
1500 Polco Street
Indianapolis, Indiana 46224

Charles A. Merritt
P. O. Box 9161
Corpus Christi, Texas 78408

Glenn W. Mettler
Products Research and Chemical Corporation
2328 Elliott Avenue
Seattle, Washington 98121

Fred H. Meyer, Jr.
AFML/MXA
Wright-Patterson AFB, Ohio 45433

Marjorie A. Meyer
AFML/MXA
Wright-Patterson AFB, Ohio 45433

Dr. Robert N. Miller
Lockheed-Georgia Company
Dept 72-62, Zone 319
Marietta, Georgia 30060

Cmdr J. R. Milligan
COMFITAEWWINGPAC STAFF
NAS
Miramar, California 92145

Robert E. Minear
Rohr Industries, Inc.
Foot of "H" Street
Chula Vista, California 92012

E. Scott Minner
General Dynamics, Convair Division
P. O. Box 80847
San Diego, California 92138

LIST OF ATTENDEES (Cont'd)

William J. Mongeau
P. O. Box 397
Chugiak, Alaska 99567

Major Thomas K. Moore
ASD/ENFSS
Wright-Patterson AFB, Ohio 45433

John F. Moran
U.S. Army Natick Labs
Kansas Street
Natick, Massachusetts 01760

Capt John H. Morilak
4310 Ridgeglen Road
Colorado Springs, Colorado 80907

A. W. Morris
McDonnell Douglas Corporation
P. O. Box 516
St. Louis, Missouri 63166

William M. Moscrip
Code GCM
U.S. Naval Surface Weapons Center
Dahlgren, Virginia 22448

Leonard Moskowitz
Naval Air Engineering Center
Code NE 34
Philadelphia, Pennsylvania 19112

R. E. Moulton
Northrop - Aircraft Division
3901 West Broadway
Hawthorne, California 90250

Paul M. Munafo
Chrysler Corporation Space Division
P. O. Box 29200
New Orleans, Louisiana 70189

Richard K. Munger
Naval Air Development Center
Warminster, Pennsylvania 18974

James E. Newhart
Naval Air Propulsion Test Center
1440 Parkway Avenue
Trenton, New Jersey 08628

LIST OF ATTENDEES (Cont'd)

Martin Nievelstein
Treuvogelweg 215
Amersfoort, Netherlands

Lt Col Paul L. Noll
SAMTEC/SUM
Vandenberg AFB, California 93437

Linus J. Novachi
Battelle Columbus Labs
505 King Avenue
Columbus, Ohio 43201

Carl B. Overall
AGMC/SNR
Newark AFS
Newark, Ohio 43055

Worth H. Owen
302nd S.O. Sq
Luke AFB
Phoenix, Arizona 85301

Vito Palombella
Grumman Aerospace Corporation
Bethpage, New York 11714

Don R. Payne
U.S. Army Bell Plant Activity - SAVBE-E
P. O. Box 1605
Fort Worth, Texas 76101

1Lt John N. Perin
SAC Aircraft Engine Division
CINCSAC/LGME
Offutt AFB, Nebraska

Squadron Leader P. J. Perry
Ministry of Defence
Whitehall
London SW1A 2EU, England

Kent R. Petersen
Ogden ALC/MMETM
Hill AFB, Utah 84406

Thomas E. Philipps
Owens Corning Fiberglas Corporation
Box 415
Granville, Ohio 43023

LIST OF ATTENDEES (Cont'd)

T/Sgt Richard L. Pogany
DSC #1
Box 727
APO San Francisco 96286

John Prati
P. O. Box 6971
Toledo, Ohio 43612

Oscar E. Richard
USAF Environmental Technical Applications Center (ETAC)
Building 159, Navy Yard Annex
Washington, D.C. 20333

William F. Roeckl
Grumman Aerospace
14342 San Down Court
Poway, California 92064

N. L. Rogers
Bell Helicopter Company
P. O. Box 482
Fort Worth, Texas 76101

Theodore Rosica
904 TAGP/LGME
Hamilton AFB, California 94934

Hilton A. Roth
United Aircraft Research Laboratory
East Hartford, Connecticut 06410

William P. Schemerman
Cleveland Pneumatic
3781 East 77th Street
Cleveland, Ohio 44105

David W. Seitz
Army Materials and Mechanics Research Center
Arsenal Street
Watertown, Massachusetts 02172

Henry J. Selfridge
Western AFRR/LGMV
Hamilton AFB, California 94934

M. Byron Shumaker
Alcoa Laboratories
Alcoa Technical Center
Alcoa Center, Pennsylvania 15069

LIST OF ATTENDEES (Cont'd)

T/Sgt James E. Slaughter
23rd Field Maintenance Squadron
England AFB, Louisiana   71301

R. Smeeton
MOD(PE)
MAP2 (B) 1
Ministry of Defence Procurement Executive
1-13 St. Giles High Street
London WC2H 8 LD

SMSgt Everett J. Smith
Hq MAC/LGMWB
Scott AFB, Illinois   62225

Pat E. Smith
Eldorado Chemical Company
P. O. Box 32101
San Antonio, Texas   78216

James O. Snider
AVSCOM Engineering Support Branch
Corpus Christi Army Depot
Corpus Christi, Texas   78419

Donald O. Sprowls
Alcoa Laboratories
Alcoa Center, Pennsylvania   15069

Kenneth E. Steube
6 San Camille
St. Charles, Missouri   63166

Harold Stevens
AF Civil Engineering Center
AFCEC/DL
Tyndall AFB, Florida   34201

Flight Lieutenant J. E. Stevens, RAF
Ministry of Defence - Air Force Department
Whitehall
London SW1 A2EU, England

Gary Stevenson
AFML/MXA
Wright-Patterson AFB, Ohio   45433

LIST OF ATTENDEES (Cont'd)

Emory L. Stewart
AF Logistics Command
Maintenance Technology Division (MAUT)
Wright-Patterson AFB, Ohio   45433

M/Sgt Ernest A. Stone
USAFSO/LGM
CMR Box 4047
APO New York   09020

LeRoy P. Streett
Rockwell International Corporation
4300 East Fifth Avenue
P. O. Box 1259
Columbus, Ohio   43216

T. J. Summerson
P. O. Box 870
Pleasanton, California   94566

Robert Summitt
AFML/LLN
Wright-Patterson AFB, Ohio   45433

Barry C. Syrett
Stanford Research Institute
Ravenswood Avenue
Menlo Park, California   94025

Edward Taylor
Standard Pressed Steel Company
Highland Avenue
Jenkintown, Pennsylvania   19046

Rod Teel
The International Nickel Company, Inc.
1 New York Plaza
New York, New York   10004

Claude S. Thompson
425 J Avenue
Coronado, California   92118

William A. Thompson
Warner Robins ALC/MMETC
P. O. Box 1041
Perry, Georgia   31069

LIST OF ATTENDEES (Cont'd)

John M. Thorp
U.S. Army Aviation Systems Command
12th and Spruck Streets
St. Louis, Missouri 63166

Walter C. Tripp
Systems Research Laboratories, Inc.
2800 Indian Ripple Road
Dayton, Ohio 45440

Burr L. Tucker, Jr.
305th ARRS
Selfridge ANG Base, Michigan 48045

Dr. R. C. Tucker, Jr.
1500 Polco Street
Indianapolis, Indiana 46224

Lt Col James R. Upp
Hq USAF/LGYE
Pentagon
Washington, D.C. 20330

Fred W. Vahldiek
AFML/LLN
Wright-Patterson AFB, Ohio 45433

Henri P. Van Leeuwen
National Aerospace Laboratory, NLR
2 Anthony Tokkerwer
Amsterdam, Netherlands

B. Cotter Vaughn
Naval Avionics Facility
6000 East 21st Street
Indianapolis, Indiana 46218

Major Gary R. Verfuss
AFML/MXA
Wright-Patterson AFB, Ohio 45433

Ishmael L. Villalva
Naval Aviation Engineering Service Unit
Naval Air Station, Cecil Field
Jacksonville, Florida 32215

Wing Commander R. N. Wade, MBE
Royal Australian Air Force
1601 Massachusetts Avenue, WWN
Washington, D.C. 20036

LIST OF ATTENDEES (Cont'd)

J. Bruce Wagner, Jr.
Director, MRC and Professor, Department of Materials Science
Northwestern University (Tech)
2145 Sheridan Road
Evanston, Illinois

John Wanamaker
Lockheed-California Company
P. O. 551
Burbank, California 91520

Thomas E. Warner
914th Maintenance Sq
Niagara Falls Municipal Airport
Niagara Falls, New York 14304

Tom J. Weidig
LTV Aerospace Corporation - Michigan Division
P. O. Box 909
Warren, Michigan 48090

Martin Weinstein
Turbine Support Division, Chromalloy American Corporation
4430 Director Drive
San Antonio, Texas 78219

Lawrence Weirick
Sandia
Box 969
Livermore, California 94550

Richard L. Weis
725-21st Avenue, E.
East Moline, Illinois 61244

Ladislav E. Wieser
AFML/MXA
Wright-Patterson AFB, Ohio 45433

W. J. Willoughby
NAVMAT CP-5
Washington, D.C.

John T. Winters
Andrews AFB, Maryland

S. R. Winters
Detroit Diesel Allison, Division GMC
P. O. Box 894
Indianapolis, Indiana 46206

LIST OF ATTENDEES (Cont'd)

Eric E. Wolber
4229 Bardstown Road
Suite 215-E
Louisville, Kentucky 40218

W. H. Womer
Naval Air Engineering Center
SE-624, GSED, Hangar 5
Lakehurst, New Jersey 08733

Robert F. Wrightman
3204 Unruh Street
Pittman-Dunn Laboratories
Frankford Arsenal
Bridge and Tacony Streets
Philadelphia, Pennsylvania 19137

Luke A. Yerkouich
Huntington Alloy Products Division
Guyan River Road
Huntington, West Virginia 25720

Robert J. Yinger
Carpenter Technology Corporation
Front and Bern Streets
Reading, Pennsylvania 19603

George C. Young
AFML/MXA
Wright-Patterson AFB, Ohio 45433

Howard W. Zoeller
AFML/MXA
Wright-Patterson AFB, Ohio 45433

AFML-TR-75-42
Volume I

SIXTH ANNUAL WORLD-WIDE AIR FORCE
CORROSION MANAGERS PRESENTATIONS

XXX

THE AIR FORCE CORROSION PREVENTION
AND CONTROL PROGRAM

PRESENTED BY
LT COL JAMES R. UPP
HEADQUARTERS USAF

TO THE

TRI-SERVICES AND AIR FORCE
WORLDWIDE CORROSION CONFERENCES

29 Oct 1974

1

THE AIR FORCE CORROSION AND PREVENTION AND CONTROL PROGRAM

SLIDE (1) Today, I will review the Air Forces Corrosion Prevention and Control program, which as I will explain a bit later, has been given the rather appropriate name "Rivet Bright". I would like to cover our program changes, efforts we have and are making now, and then where we are heading in the future. I would be the last to represent these endeavors as the ultimate answer to all ills. But they are a starting point from which we can improve and expand our efforts. None of us is singlely capable of providing a panacea to the many interactive relationships associated with the corrosion phenomenon. However, if each of us reason and work together, there is hope that the necessary solutions will be found.

SLIDE (2) Corrosion is one of the most insideous, costly, and most common destroyers of aerospace systems and equipment in the Air Force today. It is indiscriminate as to where and when it stikes and is highly detrimental to the operational capability of first line weapon systems and equipment. Corrosion prevention and control is never-ending and cannot be resolved solely by the periodic processing of aircraft and equipment through a depot facility. It must, of necessity, start at the lowest echelons and be routinely practiced on a regular daily basis. Failure to do so generally results in corrosion problems of major magnitude and a subsequent costly corrective program. Corrosion today is causing intolerable costs and maintenance problems in the field and at overhaul facilities. Effective corrosion prevention programs will contribute to stopping its progress before it affects the operational capability of a weapon system. Incorporation of preventive measures into the design and development of new systems or equipment before the equipment is exposed to severe environmental operating conditions will contribute significantly to reducing corrosion problems and costly maintenance actions.

SLIDE (3) These are all real nice words and they definitely relate to a very serious and costly problem in the Air Force today. To prevent these from becoming "buzz words", we want to have a program that dynamically addresses the problem from systems inception.

  Not to make light of the complexities, scope, or effort of our problems, the real thrust to minimizing the effects of corrosion must come in the "up-front" considerations of the design, development and acquisition processes. The Air Force must make every effort to reduce support costs in the coming years if we are to have the necessary dollars to develop and operate a viable Air Force. To reduce this cost of ownership, adequate considerations as to the corrosion prevention and control for a weapon system, equipment and subsystems will contribute significantly to reducing total life cycle costs. Withput intelligent and effective designed in corrosion prevention, no amount of field or depot level efforts will lick the problem. The philosophy and direction of todays AF corrosion program is now receiving ever increasing importance, and I can assure you, emphasis at all levels of command and management.

SLIDE (4) To illustrate the range and the magnitude of the corrosion problem, let me cite a few facts and figures.

2

- It has often been thought or assumed that our depot work, and costs, were caused by wear out or structural repair. This isn't the case anymore - Actually upwards of %60 of the FY 75 structural repair and replacement manhours was caused by, or related to, corrosion.

- To cite a few specific aircraft systems, the Air Force Logistics Command has spent

- 31 million dollars on corrosion rework of the C-130 during FY 73/74

- 12 million on the C-141 during the same period

- over 2 million on corrosion of the F-4 in FY 74

- another 2 million on the F-111 during FY73

- and now, 7 million dollars is being spent to repair corrosion damage on the B-52G force just to prevent major structural repair at the next PDM.

If I may stretch a speakers prerogative just a bit, let me highlight some examples that make up our corrosion losses:

SLIDE (5) In the area of electronics - this relay box was installed unprotected in the nose wheel-well of an older fighter aircraft. Similar installations are in our fleets of first line aircraft and still causing serious problems.

SLIDE (6) This antenna was installed on an ECM pod - it had been held in a readiness condition (but never been used) and I doubt very much that it would be very effective as a penetration aid for a fighter attack force.

SLIDE (7) Switching to Maintenance Structures-this is a C-130 longeron end fitting discovered during programmed depot maintenance.

SLIDE (8) This condition was found under a helicopter cabin floor - over and above the visual finding, it also relates to very poor maintenance and housekeeping.

SLIDE (9) This was a structural member of a transportable airborne battlefield command post. Rehabilitation costs are approaching initial costs.

SLIDE (10) I certainly would hate to be a downed flier depending on this hoist during a crunch type situation.

SLIDE (11) Storage is an often forgotten area.
- This outer wing spent three years in outside storage - this was found on the outside of the wing rendering it quite useless until repaired.

SLIDE (12) This diesel engine was used for about 6 hours then stored in sunny California for a year. You could have given it a good wash job with the quantity of water found inside.

SLIDE (13) This shows corrosion deterioration war reserve material. This is,

as you can surmise, but a small sampling. I only have dwelt on this with you to emphsis that occurances of this nature must be reduced and prevented now, not several years hence. We just don't have the resources available to us, either in the O/M, or acquisition pocketbooks to let it continue.

SLIDE (14) The Air Force Corrosion Prevention and Control program, has as its goal "The reduction of the deterioration by corrosion to aerospace systems, equipment and components". And as the design allowable criteria of our materials become more restrictive, corrosion prevention emphasis becomes more important. To increase awareness and the overall emphasis on the corrosion program, it was given the official nick-name, "Rivet Bright". Someone apparently felt that it symbolized a clean, sound weapon system that is corrosion free and operationally ready. Our intention is to use "Rivet Bright" to highlight and identify the impact corrosion has on the Air Force mission, what is is costing us, and what we can do to correct the situation.

SLIDE (15) Our corrosion program is still in the throes of re-vitalization, expansion and improvement. Summarizing briefly, these changes include:

    - redirecting a major portion of the program to a philosophy of prevention rather than control - remembering the old saying "an Ounce of Prevention".

    - clarifying program objectives so that we're all headed in the same direction.

    - expanding Air Staff involvement, responsibilities and response to insure that the program gets the visibility and support it requires.

    - directing the establishment of corrosion prevention advisory boards for all new major weapon systems, including prototype, before the design is finalized and full scale development begins.

    - identifying actions to insure corrosion prevention requirements are included in new system and modification programs.

    - enhancing the exchange of technical and management information to insure that the latest state-of-the-art corrosion technology is available and used.

    - expanding ATC training emphasis on corrosion prevention and control in all maintenance, logistics and supply curricula.

    Without detailing the policies and procedures of Rivet Bright,

SLIDE (16) it will suffice to say that all levels of management and command will become involved. We want to:

    - insure that operational units have weapons and equipment as corrosion free as we can give them.

    - minimize the impact of corrosion on our maintenance capabilities

4

- use our resources, both dollars and people power, in the most productive manner.

- have continuous communication with industry and with other services to promote technological advancements and to adopt such advancements to Air Force use.

- assure corrosion prevention technology is included throughout the design, development, fabrication, operation, and maintenance activities of a system life cycle.

SLIDE (17) As I said, particular emphasis must, and will be directed toward incorporating corrosion prevention into the acquisition process through what we refer to now as "Up-Front Logistics". This embodies the various programs and techniques utilized during acquisition of systems and equipments to consider and minimize the downstream costs of ownership. Of major importance in regards to corrosion is the feedback of design or material deficiencies uncovered in operational systems and equipments so that they can be minimized or eliminated in future designs.

We must insure that corrosion prevention and control is given adequate consideration from the start, even in protype development. Industury and Government cannot in the interest of minimizing prototype costs, delay the inclusion of corrosion protection in early design studies for it will heavily burden future operating costs of the system. The implementation of corrosion prevention advisory boards is one way to insure that such technical considerations are made.

While I feel that we now have "Rive Bright" headed in the right direction, and have optimistic hopes for its future, I didn't intend to leave you with the feeling that we're just beginning our efforts - To the contrary, a great many things have been and are going on - each of which has had a direct influence on changing the philosophy and attack of the program.

SLIDE (18) In addition to revising the regulation governing the corrosion program, which was published on 18 October;

- a HQ USAF OPR has been established to respond to the needs of the program and insert Front-end Logistics considerations.

- An AF standard for materials and processes for corrosion prevention and control has been drafted and will be going through coordination shortly,

- efforts have been underway to establish corrosion prevention advisory boards for the ACF and AMST and the ACF board is now being formed.

- an excellent training film for corrosion has been made and distributed

- joint AFLC/AFSC command corrosion surveys have been performed for most major commands

- PACER LIME, a corrosion severity classification project has been underway

5

since 1972.

    - productive meetings and exchanges of information have been held both
in this country and the United Kingdom with our friends in the RAF

    - a major effort has been launched by the commands, and fully supported
by the Air Staff, for acquisition of new/modernized corrosion control
facilities

    - a long term test and evaluation of dessert storage procedures has
been completed

    - the general series technical orders relating to corrosion were revised
and subsequently updated - CEM and Storage are in progress

    - extensive materials research and field test programs have been
initiated

    - initial efforts to develop a corrosion data prediction system has been
started

These are all highly productive and beneficial efforts, - But they are only
the beginning. I would like to reiterate, if we are to reduce those hundreds
of millions of dollars corrosion is costing the AF each year, a lot more has
to be done, and without much more delay.

SLIDE (19) Let me mention several areas where I feel we must take initiative
and start something moving. We must;

    - include the requirements for corrosion prevention considerations for a
weapon system in all primary acquisition regulations

    - identify and define critical areas in Rivet Bright, and establish the
priorities to obtain the necessary resources

    - develop adequate corrosion programs for systems and equipment other than
aircraft/missiles - eg avionics/electronics, vehicles, AGE

    - foster joint service coordination and interfacing in the methodologies
of corrosion program management and reduce any unnecessary duplication.

    - in addition to predictive efforts, develop a viable and productive
corrosion data system for the prevention, control and repair of corrosion
damage on all systems and equipment.

    - motivate industry to develop and use materials and techniques that
are productive in preventing and reducing corrosion

    - and lastly, establish a direct positive interface between those programs
and technologies that have such an important influence on each other - namely
corrosion, NDI and ASIP

SLIDE (20) In conclusion, I submit that these are the challenges of the present and the future. In the past we concerned ourselves with controlling corrosion just so we could keep our heads above water. To continue on such a path is cost prohibitive. Today the pendulum is moving toward emphasis on prevention as the best and most cost effective means of controlling corrosion. To accomplish our goals, it will require the development and implementation of techniques which will provide incentives to improve the corrosion protection of a weapon system; optimize resource management; and resolving the conflict between design-to-cost goals and the trade-off flexibility required to reduce the cost of ownership. The need and the task is there - Now all that is required is for us to get busy and get it done.

U
S
A
F

CORROSION PREVENTION
AND CONTROL PROGRAM

RIVET BRIGHT

Slide 1

8

ENVIROMENT
SYSTEMS DESIGN
OPERATIONAL CAPABILITIES
PREVENTION

CORROSION

FIELD LEVEL MAINTENANCE
INCREASING COSTS
DEPOT REPAIR

Slide 2

9
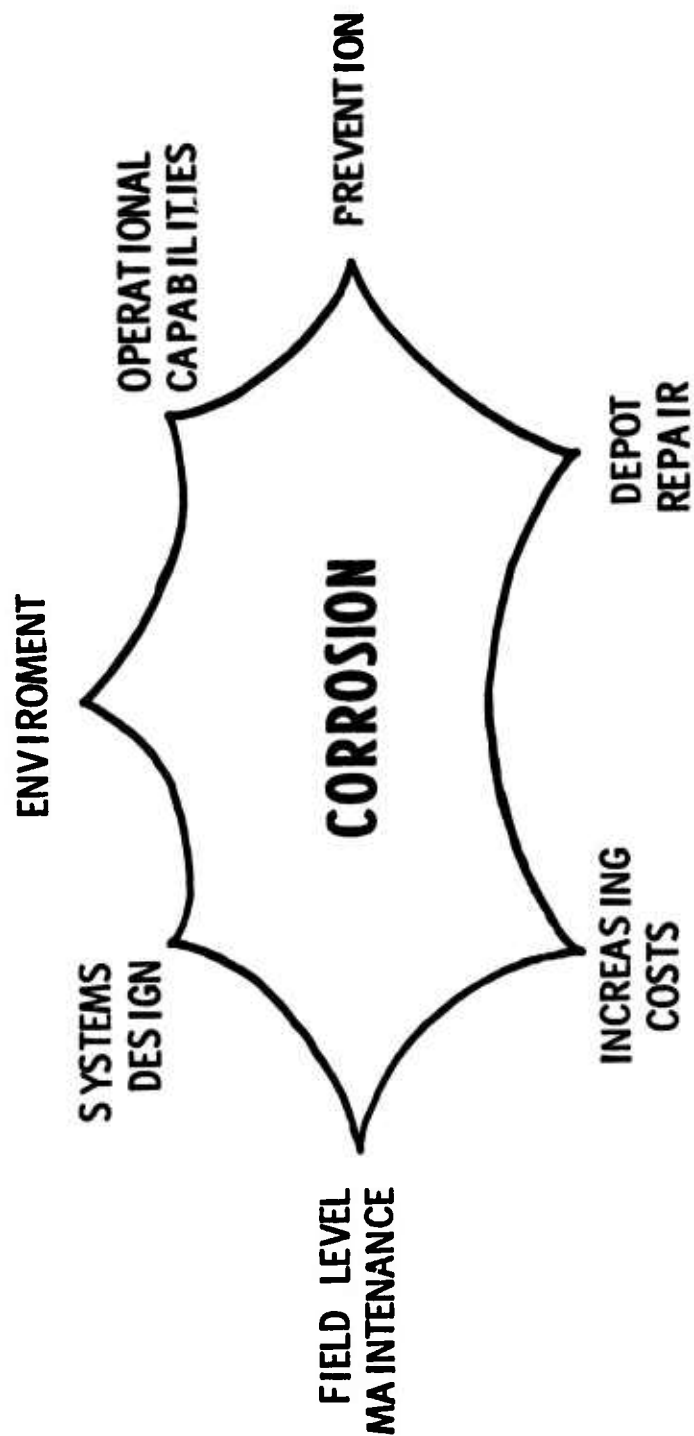
BUZZ WORDS REQUIRE

- UP - FRONT THINKING

- REDUCED COSTS

- TOTAL INVOLVEMENT

Slide 3
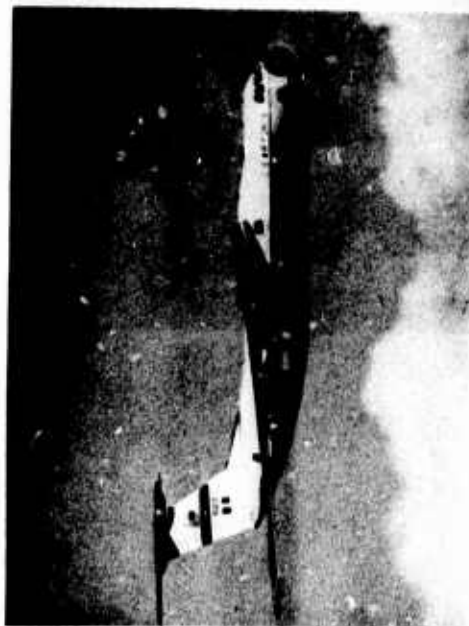
B 52 G

F-111

F-4

Slide 4

C 141

C 130

11

Slide 5

Slide 6

13

Slide 7

14

Slide 8

15

Slide 9

16

Slide 10

17

Slide 11

SLIDE 12

19
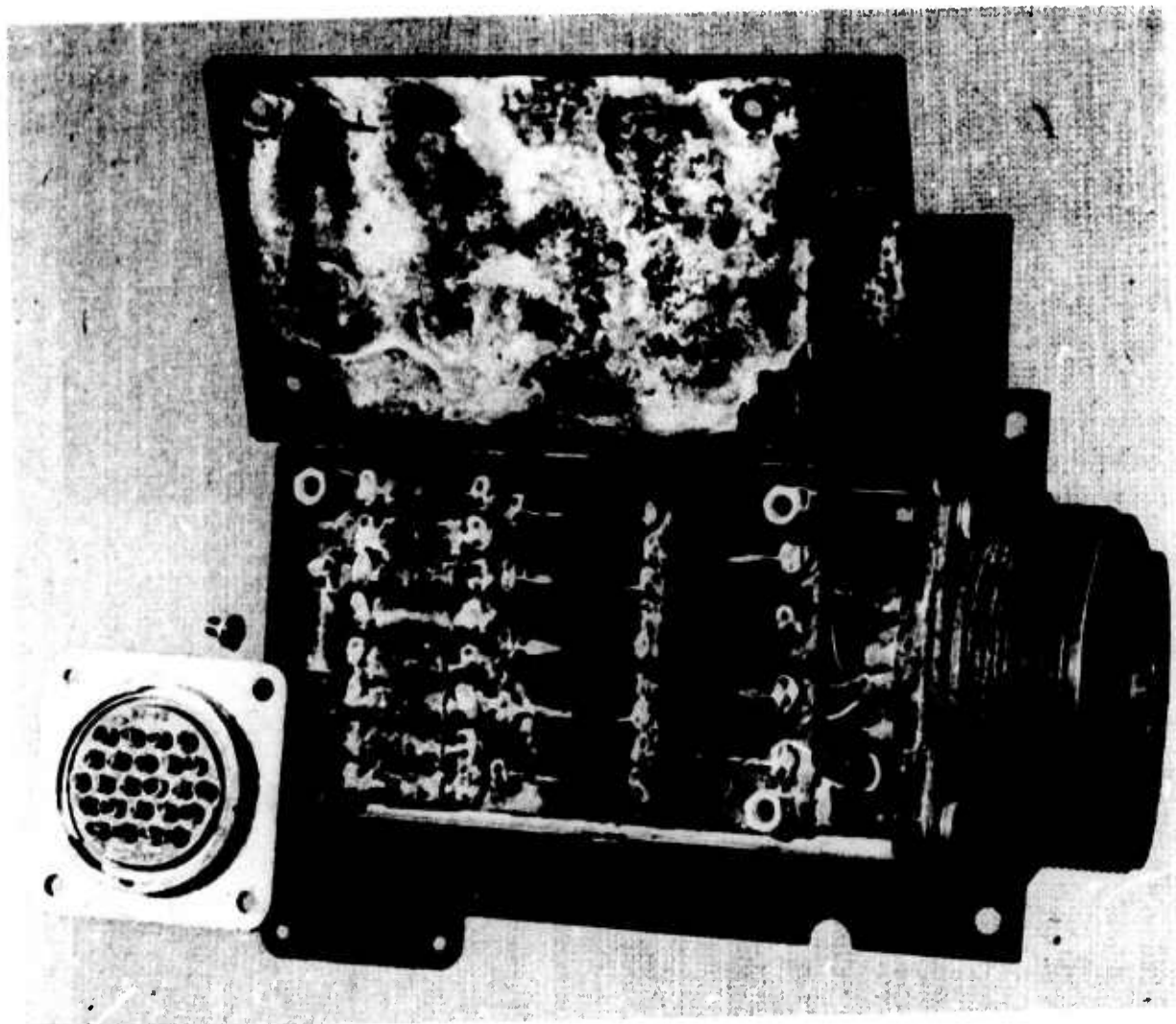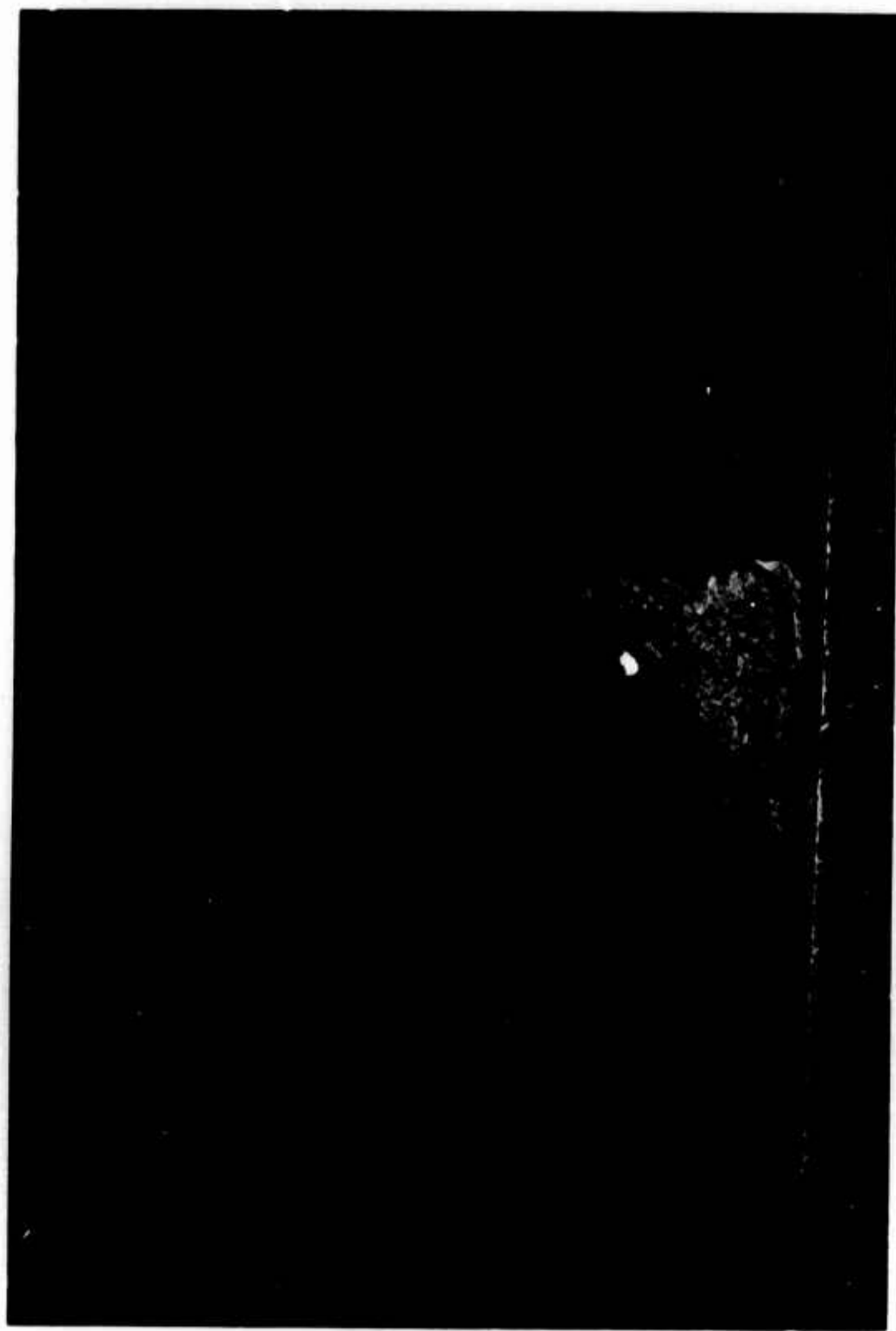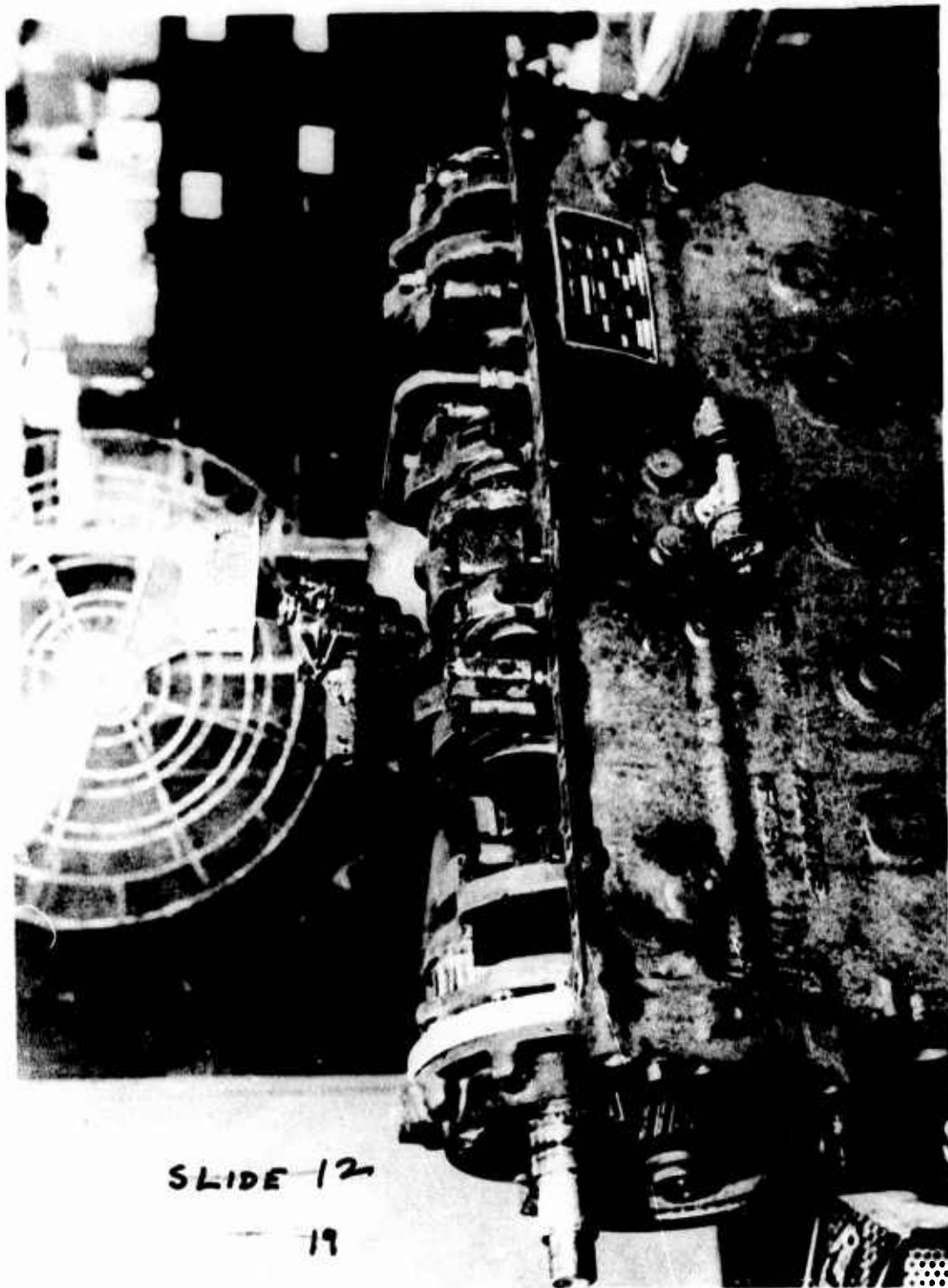
Slide 12

Slide 13

RIVET BRIGHT

- AWARENESS
- EMPHASIS
- PREVENTION

Slide 14

RE-VITALIZATION

- CHANGE PHILOSOPHY / POLICY

- TOTAL INVOLVEMENT

- PREVENTION

- COMMUNICATIONS

Slide 15

22
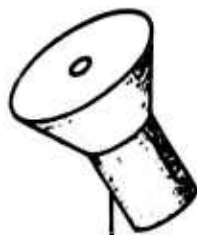
PROGRAM OBJECTIVES

- IMPACT ON WEAPONS / MAINTENANCE

- USE OF RESOURCES

- COMMUNICATIONS

- PREVENTION TECHNOLOGY

Slide 16

23

FRONT-END LOGISTICS

- FEEDBACK

- DEFERRED ITEMS

- CPABS

Slide 17

PROGRAM ACTIVITIES

- USAF INVOLVEMENT

- AF STANDARD / CPAB

- TECHNICAL INFORMATION

- COMMAND SURVEYS / PACER LIME

- INTERCHANGES

- FACILITIES

- FIELD TESTS / DATA SYSTEMS

Slide 18

INITIATIVES
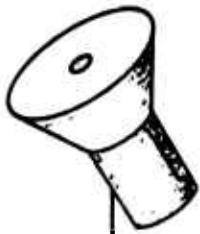
- ACQUISITION REGULATIONS

- IDENTIFY PROBLEMS

- EXPAND PROGRAMS

- ADVANCE COORDINATION

- DATA SYSTEMS

- MOTIVATE INDUSTRY

- INTERFACE

Slide 19

26

SUMMARY

- PREVENTION

- INCENTIVES

- RESOURCES

- RESOLUTION

Slide 20

ATC CORROSION CONTROL

TODAY I WANT TO GIVE YOU A GENERAL IDEA OF THE BASIS FOR THE ATC
CORROSION CONTROL EFFORT BY DESCRIBING OUR FLEET AND SOME OF ITS
CHARACTERISTICS AND FOLLOW THAT WITH A COUPLE OF PROBLEMS WHICH
HAVE BEEN ABSORBING OUR TIME AND EFFORT.

THE FLEET

WHEN SOMEONE MENTIONS A MAINTENANCE PROBLEM THAT AIR TRAINING COMMAND
IS HAVING, YOU MAY CHUCKLE TO YOURSELF AND WONDER -- NOW WHAT SORT OF
PROBLEM COULD ANYONE HAVE ON AIRCRAFT AS SMALL AND UNSOPHISTICATED AS
THE T-37 AND T-38? WELL, LET ME ASSURE YOU THAT WHAT WE MAY LACK IN
SIZE OF OUR AIRCRAFT IS MORE THAN OFFSET BY SHEER NUMBERS. THE
PARKING RAMPS AT OUR UPT BASES ARE LITTERED WITH TINY AIRPLANES --
EACH FLYING TRAINING WING OWNS FROM 165 TO 200 OF THE PRIMARY
TRAINERS; AND, AS YOU WELL KNOW, CORROSION IS NOT A PROBLEM THAT
DEPENDS ON THE COMPLEXITY OF A WEAPON SYSTEM.

THE T-38 IS BUILT FROM A VARIETY OF MATERIALS -- STEEL, MAGNESIUM,
TITANIUM, AND OVER 10 DIFFERENT ALUMINUM ALLOYS. WHILE THIS VARIETY
OF METALS IS NOT UNIQUE, THE FACT THAT IT IS PACKAGED IN SUCH A SMALL
AIRCRAFT WITH LIMITED ACCESSIBILITY MAKES CORROSION CONTROL ON THE
T-38 NO SMALL MATTER.

ALTHOUGH WE DO NOT OFFICIALLY PAINT AIRCRAFT FOR APPEARANCE, ONE LOOK
AT A "STRIPPED" '38 WOULD MAKE YOU THINK THAT IF AN EXCEPTION IS EVER
MADE TO THAT RULE, IT WILL BE FOR THE '38. SERIOUSLY, THOUGH, THE
CONSTRUCTION OF THE T-38, WHICH MAKES EXTENSIVE USE OF ALUMINUM
HONEYCOMB, HAS PRESENTED SPECIAL PROBLEMS WHICH WE HAVE JUST BEGUN TO
ADDRESS. MORE ON THAT LATER.

OUR OTHER PRIMARY TRAINER, THE T-37, WAS DELIVERED TO THE AIR FORCE
AS AN ALUMINUM AIRPLANE. THE MAJORITY OF EXTERIOR SURFACES ARE CLAD
ALUMINUM. THROUGHOUT THE LONG AND USEFUL LIFE OF THE T-37 (WHICH DATES
BACK TO 1956) WE EXPERIENCED LITTLE CORROSION TROUBLE. BUT ABOUT FOUR
YEARS AGO, WE COULD FORESEE MAJOR PROBLEMS DEVELOPING ON THE EXTERIOR
OF THE AIRCRAFT, PRIMARILY ON THE AFT SECTION AND EMPENNAGE IN THE
EXHAUST TRAIL. THE CLAD SURFACE WAS BEING ERODED AND PITTING CORROSION
WAS ATTACKING THE BASE METAL, QUITE SEVERELY IN SOME CASES. FOLLOWING
A JOINT AFLC/ATC FLEET SURVEY, THE DECISION WAS MADE TO PAINT THE T-37
TO HALT THE CORROSION AND ADD MORE YEARS OF USEFUL LIFE TO THE AIRFRAME.
THE CHOICE OF A PAINT SCHEME BECAME A CONTROVERSIAL MATTER, WITH ALL
CONCERNED AGENCIES MAKING RECOMMENDATIONS. FINALLY, A PLAIN WHITE PAINT
SCHEME WAS CHOSEN.

Preceding page blank

SO, NOW EACH WING OWNS AT LEAST 165 TINY AIRPLANES WHICH ARE PAINTED
AS A PRIMARY MEANS OF CORROSION PREVENTION. EACH WING HAS ONE
CORROSION FACILITY FOR STRIPPING, COMPLETE REPAINTING, AND MAJOR
TOUCHUP OF THESE AIRCRAFT.

THE COMPLETE STRIPPING, CORROSION TREATMENT, AND REPAINT OF A T-37
OR T-38 REQUIRES FIVE FULL WORKDAYS TO COMPLETE. ON A SMOOTH,
UNINTERRUPTED SCHEDULE, EACH AIRCRAFT CAN BE BROUGHT IN FOR A COMPLETE
GOING-OVER ONLY APPROXIMATELY ONCE EVERY FOUR YEARS. THAT REALLY
STRETCHES THE EFFECTIVE SERVICE LIFE OF ANY PAINT FILM, PARTICULARLY
ON A SUPERSONIC AIRCRAFT LIKE THE T-38. WE HAVE TO MAINTAIN TIGHT
SCHEDULES. EVEN SO, THE RANDOLPH SHOP MANAGED TO COMPLETE THE FIRST
T-38 TRANSFERRED TO THE THUNDERBIRDS.

THE PROBLEMS

WITH THAT BACKGROUND, YOU CAN IMAGINE THE IMPACT OF THE RECENT SHORTAGE
OF POLYURETHANE PAINT. SOME BASES WERE WITHOUT PAINT, WITH THE EXCEPTION
OF RESERVES FOR MINOR TOUCHUP, FOR SIX WEEKS. IN A SITUATION LIKE THIS,
NOT ONLY ARE THOSE AIRCRAFT CURRENTLY IN DIRE NEED OF TREATMENT DELAYED,
BUT ALL THOSE FURTHER DOWN THE LINE ARE POSTPONED AND SUFFER THE
CONSEQUENCES. WE FOUND THAT WHILE THE MIL SPEC PAINT WAS NOT AVAILABLE
AT GSA, IT WAS AVAILABLE FROM THE SAME COMMERCIAL SOURCES THAT SUPPLY
GSA, ALTHOUGH AT A HIGHER PRICE. WE FEEL THAT PROBLEMS OF THIS SORT
COULD BE AVOIDED OR TEMPERED BY A PROVISION FOR A LONG LEAD WARNING OF
IMPENDING SHORTAGES. EVEN THOUGH CORROSION PREVENTION IS MUCH CHEAPER
THAN CORROSION CORRECTION, IT IS GOING TO COST A GREAT DEAL MORE IN THE
FUTURE.

THE IMMEDIACY OF THE PAINT SHORTAGE IS, I FEEL, FAR OUTWEIGHED BY AN
INSIDIOUS PROBLEM WHICH HAS JUST BEGUN TO SURFACE. THIS PROBLEM IS
PECULIAR TO HONEYCOMB STRUCTURES; AND, IN THE T-38, THAT'S SERIOUS.

FOR A LONG TIME NOW, WE'VE HAD TO WATCH HONEYCOMB VERY CLOSELY. SKIN-
TO-CORE DISBOND OF HONEYCOMB HAS CAUSED THE FAILURE OF STRUCTURAL
COMPONENTS SUCH AS THE WING TIP. WHEN THE WING TIP FAILS AND LEAVES
THE AIRCRAFT, IT CAUSES FURTHER DAMAGE TO THE FUSELAGE AND RUDDER
IN ADDITION TO JEOPARDIZING THE AIRCRAFT AND CREW. THE WING TIP PROBLEM
INTRODUCED US TO THE SPECIAL PROBLEMS OF HONEYCOMB AND LED US INTO A
SEARCH FOR NDI METHODS TO DETECT DELAMINATION. THE RESULT WAS THAT WE
INTRODUCED TO THE AIR FORCE INVENTORY THE COMMERCIAL SONDICATOR FOR
HONEYCOMB INSPECTION. WE DIDN'T KNOW IT AT THE TIME, BUT DELAMINATION
IS A SYMPTOM OF OTHER PROBLEMS AND NOT NECESSARILY A PROBLEM BY ITSELF.

INCOMPLETE OR POOR BONDS BETWEEN THE SKIN AND CORE OF A HONEYCOMB PANEL
ALLOWS THE INTRODUCTION OF WATER VAPOR TO THE CORE. THE WATER VAPOR
CONDENSES AND OVER A PERIOD OF TIME, THE CORE FILLS WITH WATER AND A
VARIETY OF FAILURES RESULT:

A. THE MOISTURE CORRODES THE SKIN BETWEEN THE SKIN AND ADHESIVE
AND DEGRADES THE BOND OVER A LARGE ENOUGH AREA TO CAUSE STRUCTURAL
FAILURE.

B. THE MOISTURE CAN FREEZE AT ALTITUDE AND CRUSH THE CORE AND
DELAMINATE LARGE AREAS OF THE PANEL. THIS HAS HAPPENED ON THE RUDDERS
OF SEVERAL T-38'S AND CAUSED THE LOSS OF A NUMBER OF RUDDERS.

C. THE MOISTURE SETS UP CORROSION IN THE HONEYCOMB MATERIAL --
ONLY .0007 TO .001 GAGE ALUMINUM AND QUITE HANDILY EATS AWAY THE
STRENGTH OF THE PANEL WITH NO EVIDENCE OF DELAMINATION.

D. THE MOISTURE ENCOURAGES THE SKIN TO CORRODE TO THE POINT THAT
HOLES ARE EATEN THRU THE PANEL FROM THE INSIDE OUT -- REGARDLESS OF HOW
FINE A JOB CORROSION CONTROL SPECIALISTS DO.

WE'VE KNOWN FOR A LONG TIME THAT WE HAD SOME MOISTURE IN OUR HONEYCOMB,
BUT IN THE ABSENCE OF AN INEXPENSIVE, RELIABLE INSPECTION METHOD, WE
DIDN'T KNOW HOW MUCH OR WHERE. NOW THAT THE KODAK INDUSTREX RADIO-
GRAPHIC PAPER IS AVAILABLE, WE CAN INSPECT THE ENTIRE HONEYCOMB AREA
OF THE T-38 FOR MOISTURE FOR ABOUT 30 DOLLARS IN MATERIALS. HERE IS
AN EXAMPLE: WE JUST RECENTLY STARTED A SAMPLE INSPECTION OF THE T-38
FLEET USING THE RADIOGRAPHIC PAPER IN AN ATTEMPT TO DETERMINE THE
EXTENT AND SEVERITY OF THE MOISTURE PROBLEM. INITIAL RESULTS SEEM TO
INDICATE THAT IT IS NOT THE CLIMATE OF THE AREA WHERE THE AIRCRAFT IS
LOCATED OR THE CARE IN HANDLING AND TREATMENT IT GETS THAT AFFECTS THE
MOISTURE PROBLEM. WE SUSPECT THAT IT IS THE BASIC MANUFACTURING PROCESS
THAT PERMITS THE INTRODUCTION OF MOISTURE.

IN OUR EFFORTS TO SOLVE OR AT LEAST SOFTEN THIS CORROSION PROBLEM,
WE'VE DONE A LOT OF RESEARCH AND FOUND A DEARTH OF INFORMATION ON
HONEYCOMB AND ITS TREATMENT. ONLY ONE GROUP IS ACTIVELY PURSUING
THE PROBLEM AND THEY ARE HERE AT THE MATERIALS LAB WHERE A LONG RANGE
STUDY AND COMPILATION OF INFORMATION IS UNDERWAY. THEIR RESULTS WILL
BE PUBLISHED IN THE FORM OF A HANDBOOK, I UNDERSTAND, IN A COUPLE OF
YEARS.

IN AN AIRCRAFT WHERE SO MUCH OF THE STRUCTURE IS HONEYCOMB, A SERIOUS
PROBLEM WITH HONEYCOMB CAN CRIPPLE THE FLEET. WITH THE T-38 MARKED
FOR SERVICE 'TIL 1985, WE'VE GOT A REAL CHORE CUT OUT FOR OURSELVES
IN THE SEARCH FOR A SOLUTION TO THE MOISTURE PROBLEM.

I HOPE I'VE GIVEN YOU AN INSIGHT INTO SOME OF THE CORROSION CONTROL
WORK IN ATC. IF NOTHING ELSE, I HOPE YOU REALIZE NOW THAT THE SIZE
OF AN AIRCRAFT DOESN'T DICTATE THE SIZE OF ITS CORROSION PROBLEMS.

SESSION I

CORROSION IN AIRBORNE ELECTRONIC COUNTERMEASURES EQUIPMENT

by

Thomas K. Moore, Major, USAF, ASD/ENFSS

James R. Myers, Professor of Metallurgy, AFIT/DET

U. S. involvement in Southeast Asia and the recent Israeli-Arab War have clearly established the importance of airborne electronic countermeasures (ECM) equipment. Reliable ECM equipment must be available if tactical and strategic aircraft operations are to be conducted effectively with a minimum of losses. Unfortunately, electronic equipment is vulnerable to various forms of mechanical damage; it is also susceptible to deterioration by an electrochemical process called corrosion. Corrosion can occur any time the components within an ECM package are exposed to an aggressive environment, such as humid air and water. Corrosion damage can frequently be related to the dense packaging of components in ECM devices which often results in the intermetallic contact of dissimilar metals; it is compounded by a general lack of corrosion prevention during fabrication and maintenance. As a result, a wide variety of corrosion forms can occur. These include: (1) exfoliation (intergranular attack); (2) general corrosion; (3) concentration cell corrosion; (4) galvanic corrosion; and (5) pitting attack.

The purposes of this paper are: (1) to examine several typical examples of corrosion which have occurred in ECM equipment; (2) to identify the form(s) of corrosion associated with each case; and (3) to discuss methods of minimizing the problem. Basically, it will demonstrate that improved manufacturing processes must be used to insure that materials susceptible to corrosion will not come into contact with a corrosive environment.

Waveguides are a typical component of ECM systems; they are generally fabricated from 6061-T6 aluminum alloy. Because waveguides can be large structures, they are assembled from sections. This means that the uncoated waveguide interior can be exposed to an aggressive environment during shipment, when for example the packaging fails to provide adequate temporary protection. A typical example of poor packaging is the mere placement of the waveguide section in a polyethylene bag, secured with a rubber band. Poor packaging will allow moisture

to come into contact with the bare metal (which is required to obtain the correct electrical properties inside the waveguide) and corrosion will result.

The electrical requirement for a bare waveguide interior surface makes it impossible to coat the inside of the waveguide with an epoxy primer (Ref. 1) which would normally be required inside aluminum tubing in aircraft (Ref. 2).

Corrosion, as shown in Figure 1, inside waveguides creates an insulator (hydrated Al_2O_3) on the surface; this significantly decreases the efficiency of this electronic component in providing a propagation path for the microwave energy. Being a portion of the transmitter, the corroded waveguide results in less energy available for radiation and a decrease in the effectiveness of the countermeasures system.

Since in this application the use of paints or primers to provide protection from the environment would result in unacceptable electronic properties, other protection must be used. The aluminum waveguide must be isolated from the electrolyte (water). A close fitting, water-impervious, molded plastic cap to close off the end of the waveguide would provide such protection and make this uniform attack and pitting less probable. This low cost protection provides satisfactory isolation of the waveguide. As a result, the expense of replacing this complex-shape waveguide can be avoided.

An array of spiral antennae (Figure 2) is used as a part of the receiver section of certain electronic countermeasure devices. The spiral of copper is fabricated by chemically milling (or etching) in an acid bath. Material not needed to form the spiral is removed by this controlled corrosion process. After being etched in acid the spiral is encased in plastic. The plastic coating provides excellent environmental protection by effectively isolating the copper.

Failures of these antennae have been reported in the field after several months of service. The copper spiral, as shown in Figure 2, undergoes corrosive attack. Failure analysis established that the antenna manufacturer had not properly removed all of the etchant from the copper component's surface. Acid was therefore included along with the antenna during encapsulation. Replacement of more than one hundred antennae was necessary to remove the corroded ones from service.

This corrosion experience points out the need for careful process

FIGURE 1 - Pitting attack and general corrosion of 6061-T6 aluminum
alloy waveguide. White colored corrosion products on the
surface are a hydrated form of aluminum oxide.

FIGURE 2 - General corrosion of copper spiral antenna caused by acid trapped during encapsulation.

control during manufacture. Many large electronic firms buy critical components from small suppliers who have inadequate knowledge of the corrosion problems which can be introduced by manufacturing processes. Small manufacturers should be provided finish-system requirements; this may require considerable guidance in order to obtain components which meet specified requirements.

Crevice corrosion, which occurred in the structure of one electronic countermeasure pod designed for external carriage on fighter aircraft, is evident in Figure 3. Galvanic corrosion also occurred because of the dissimilar alloys which were in intimate contact. The ring structure of the pod, as indicated by arrow 1, is 17-4PH stainless steel; the shell structure pointed out by arrow 2 is 2024 aluminum alloy; and the mechanical fasteners in the shell, as indicated by arrow 3, are AISI 8740 steel.

Corrosion products are visible in the crevice between the corrosion resistant steel ring and the aluminum sheet structure. The aluminum alloy shell also shows evidence of some pitting while the steel fasteners are covered with hydrated ferric hydroxide (FeOOH).

This structural assembly received very little corrosion protection. Only the aluminum alloy was protected; this was only given a chromate conversion coating (Ref. 3) even though dissimilar metals, as defined by MIL-STD-889 (Ref. 4), are present.

Had the aluminum, and preferably also the 17-4PH stainless steel, been primed in detail before assembly, and if the alloy steel fasteners had been installed with wet primer, the corrosion probably would not have occurred. Electrical isolation of dissimilar metals is generally required to prevent galvanic corrosion. Currently-used coating systems provide considerable resistance to electrochemical attack by isolating the dissimilar metals and preventing the penetration of the electrolyte to the corrosion cell.

Numerous failures of soldered connections have been found during field inspection and repair of printed circuits and other electronic components. In many instances the failed joints have shown visible evidence of solder flux residues. This was confirmed by chemical analysis. In corroded solder connections, traces of rosin and of chloride compounds have been found. While rosin is less corrosive than zinc or ammonium chlorides, which are commonly used soldering fluxes, even mild rosin fluxes contain components which when combined with other electrolytes promote corrosion.

FIGURE 3 - Crevice corrosion, pitting attack, general corrosion, and galvanic corrosion of inside ECM pod structure.

Corrosion of soldered connections can be prevented by removing all flux after soldering. This process control is essential if corrosion is to be avoided. Methods of removing corrosive solder flux include vapor degreasing (Ref. 5). Solvents, such as alcohol or ether, may also be used to remove fluxes from soldered components. Denison (Ref. 6) has described the problem of improperly cleaned printed circuit boards and provides information on both the need and methods of cleaning them.

Another example of corrosion in electronic countermeasure equipment involves bare coaxial connectors. A partially disassembled hard coaxial connector showing corrosion both inside the connector and on the aluminum alloy structure adjacent to the connector is shown in Figure 4. The materials involved here are Type 303S austenitic stainless steel (the connector nut), 6061-T6 aluminum alloy (the aluminum frame), and silverplated, copper-coated steel (the central element in the coaxial cable).

The corrosion inside the connector occurred because water seeped into the area. Water will penetrate to the central conductor, when the connector nut is not properly torqued during manufacture or routine maintenance. When properly torqued the nut will prevent water from penetrating the connector and providing the electrolyte necessary for corrosion. Reliability of this ECM system improved after the institution of stringent quality control measures in manufacturing, including the checking of each threaded connector for proper torque values.

It should also be noted in Figure 4 that exfoliation of the aluminum alloy, indicated by arrow 2, occurred near the connector nut. The connector nut was so close to the aluminum frame that a drop of water could bridge the gap between the two components. The presence of this electrolyte in an area where the chromate coating had been partially removed from the aluminum alloy frame by mechanical action during nut installation, served to complete the corrosion cell.

To demonstrate more clearly the nature of the attack which occurs when a galvanic couple of 6061 aluminum alloy and Type 303S corrosion resistant steel, metallically-connected specimens of these materials were exposed by the authors to aqueous environments for extended times. These 6000 hour tests included exposure to both oxygen-saturated water and to an oxygen-saturated 3.5% NaCl solution. It is known, but not widely appreciated, that 6061-T6 aluminum alloy can exfoliate. An example of exfoliation in this alloy is shown in Figure 5.
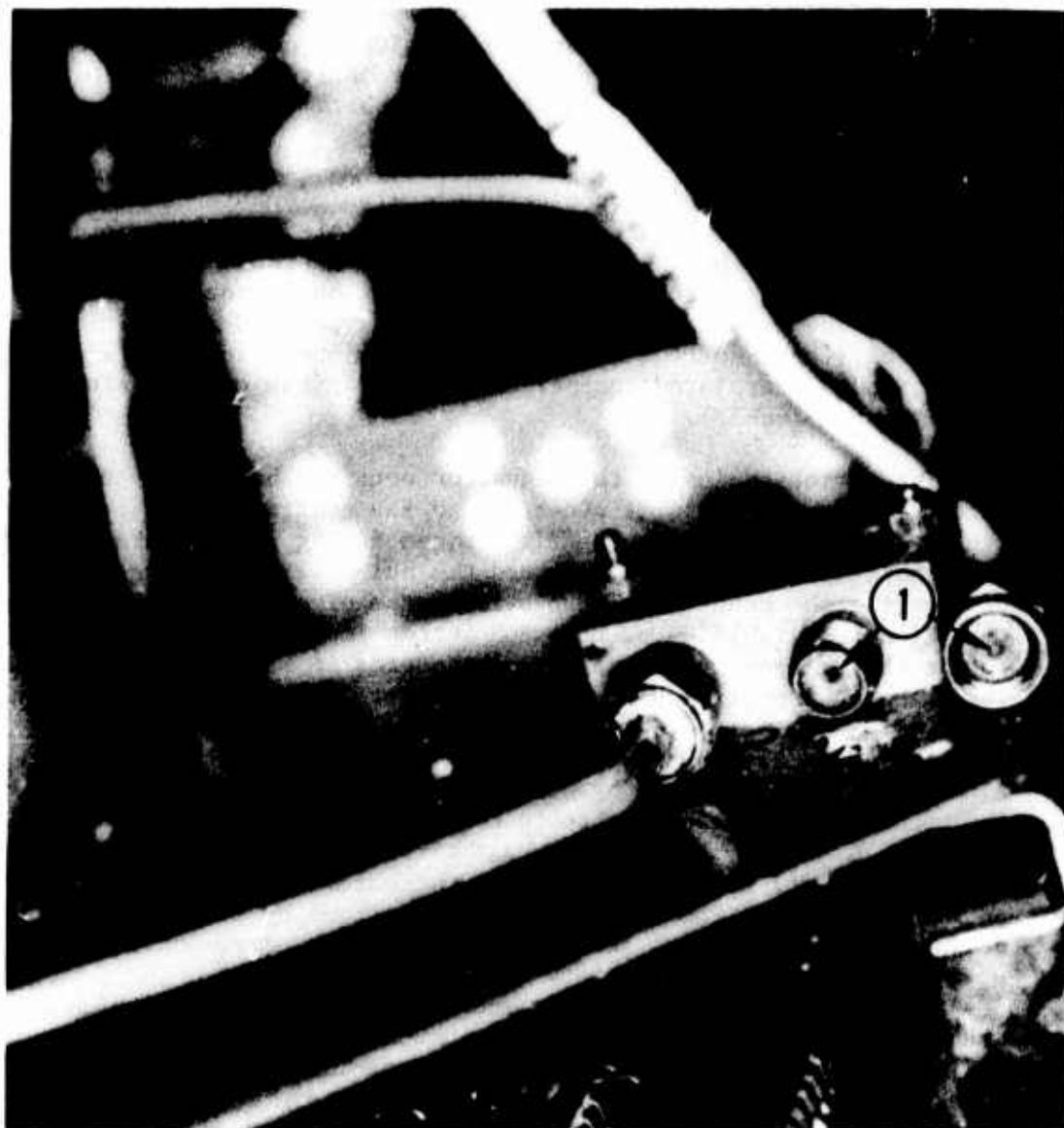
FIGURE 4 – Corrosion inside hard coaxial connector. Note that exfoliation of the 6061-T6 aluminum also occurred near the connector nut.

2.6X

FIGURE 5 – Photomicrograph showing exfoliation in 6061-T6 aluminum alloy.

Exfoliation corrosion of the aluminum alloy structure could have been prevented by designing the connection so that the nut was physically more distant from the plate, (i.e., so that a drop of water could not be supported between them). It could also have been avoided or greatly reduced by the application of a primer coat to the conversion coated aluminum alloy surfaces.

CONCLUSION

The examples of corrosion which have been shown are only a few of those which have occurred in ECM systems. Since dissimilar alloys will continue to be used in closely-packed electronic components, it is vital to provide corrosion protection to these systems. ECM component materials are selected on the basis of their electronic properties; in many cases inherent corrosion resistance is not a materials selection factor. Environmental protection is therefore mandatory if corrosion is to be avoided.

Improved manufacturing process control is necessary to avoid the use of methods which can result in corrosion of the end item in service. Thorough removal of corrosive substances such as etchants, soldering and brazing fluxes, good cleaning practices, and correct heat treatment of alloys are all effective methods of reducing the probability of corrosion.

Protective coatings can also provide effective corrosion protection. Whether they are protective covers and closures for maintenance use, primers and finish systems for coating structural components, conformal coatings for circuitry, or hermetrically sealed containers for particularly critical items, protective coatings help isolate susceptible materials from hostile environments. Greater use of protective coatings appears to be a convenient and effective way to reduce corrosion in ECM equipment.

When ECM equipment is shipped or stored the packing materials must provide adequate environmental protection. Attention must be given to providing packaging which provides protection from hostile environments and yet which is inexpensive and easy to use.

Corrosion can also be avoided by improved design. Features such as drain holes, seals, careful component placement, and the elimination of pockets which trap fluids reduce corrosion susceptibility. A designer's judicious choice of materials and processes, coupled with his knowledge of and desire to avoid corrosion creating situations

can greatly increase ECM system reliability and reduce the life
cycle cost of this vital military equipment.

REFERENCES

1. MIL-P-23377C, Primer Coating, Epoxy Polyamide, Chemical and
    Solvent Resistant, 26 August 1969.

2. MIL-F-7179E, Finishes and Coatings; Protection of Aerospace
    Weapon Systems, Structures and Parts; General Specification
    for, 15 November 1972.

3. MIL-C-5541B, Chemical Conversion Coatings on Aluminum and
    Aluminum Alloys, 14 October 1968.

4. MIL-STD-889, Dissimilar Metals, 25 September 1969.

5. Metals Handbook, Vol. 2, American Society for Metals, 1963,
    pp. 339-340.

6. J.W. Denison, Jr., Cleaning of Printed Circuit Boards to
    Remove Ionic Solis, Paper #27, CORROSION/74, Chicago, IL.,
    4-8 March 1974.

PROTECTIVE COATINGS FOR JET ENGINE COMPRESSOR COMPONENTS

Dr. Martin Weinstein

Turbine Support Division
Chromalloy American Corporation
San Antonio, Texas 78219

ABSTRACT

General corrosion mechanisms of alloy steel jet engine compressor components are discussed. Basic emphasis is placed on the effects of oxidation-aqueous corrosion on component integrity and engine performance. The effect of protective coatings will also be discussed both in terms of effectiveness of protection as well as engine performance characteristics. Examples of coating performance in such engines as the Pratt and Whitney J-57, Allison/Rolls Royce TF-41 and United Aircraft of Canada T400 will be given.

I.   INTRODUCTION

The excellent performance of the gas turbine engine in commercial and military aviation is a matter of record. It is questionable whether the extent of commercial air travel presently taken for granted could have been possible without the reliability and quality built into the Pratt & Whitney JT3D, JT4 and JT9D, the G.E. CJ610/CF700 and CF6 and the Rolls Royce Spey and RB211 engines. These engines have performed remarkably well and have maintained their basic economic position through many years of service.

The characteristics of these engines in combination with their commercial air frames, however, vary considerably from those of their military counterparts, such as, the Pratt & Whitney J57, J75 and TF33, the G.E. J79, J85 and TF39 and the Rolls Royce/Allison TF41. These engines in combination with their air frames normally experience much higher stress levels as well as considerably more severe environmental conditions. For this reason, one immediately assumes that more complex mechanical designs, as well as without question, superior grade materials would be used in the military counterpart engines. Although often military hardware initially assumes complex geometries as well as utilizes higher grade materials, the facts of engineering life-cost, maintainability, and reliability often take precedence.

The bulk of this paper will be spent describing what can be classified as an engineering approach to the reliability and cost effective design of military jet engine compressor hardware. By utilizing surface treatments such as pack aluminizing, one can produce a component that often can more effectively perform in the environmental conditions encountered in severe military missions than more expensive homogeneous materials. Where possible presently utilized designs are

45   **Preceding page blank**

described and comparative cost factors are introduced indicating the benefits o
utilizing composite coating-base metal technology rather than designing utilizir.
bulk properties.

II. MATERIALS USED IN JET ENGINE COMPRESSOR COMPONENTS

In order to help describe the fundamental mechanisms and methods for
prevention of corrosion in jet engine compressors a description of materials used in
present day engines is given. Figure 1 is a schematic of a jet engine compressor
pointing out the placement of rotor blading, rotor spacers, rotor disks, stator vanes
and air seals that make up the assembly. Table 1 gives a summary of the major
materials utilized in conventional gas turbine engine compressors. Rather than
going over detailed metallurgical reasons for the specific use of each material a
short generalized description of each material, enough to aid in the evaluation of
corrosion phenomena and related protective coatings is given.

A Description of the Material Applications

(1) Disks and Spacers

AMS 4340 and AMS 6304 are the most often utilized materials for com-
pressor disks and spacers. These are normally used in the forged condition. The
use of very high strength low alloy steels is necessary since these components are
very highly stressed particularly during aircraft takeoff and landing. Disks are
therefore often low cycle fatigue limited. These low alloy steels are obviously ex-
tremely susceptible to marine corrosion damage, therefore, they are almost always
coated. Since these materials lose their strength above 800°F, in new compressors
nickel base alloys such as Inco 718 are often used. Ti-6Al-4V disks are often used
in the cooler front end of the compressor when engine weight is an especially criti-
cal design requirement. Higher temperature titanium disk materials are also being
utilized in some of the newer engines in order to maximize thrust to weight ratios.

(2) Blades, Vanes and Shrouds

AMS 5616 and its counterpart "Greek Ascoloy" along with AMS 355 are
the work horse materials of jet engine, blading and vanes. These stainless steels
possess excellent high temperature fatigue strength along with reasonable process-
ing costs. Where higher temperatures above 900°F are experienced nickel base
alloys such as Inco 718 and Inconel X750 are utilized. These latter materials are
not susceptible to marine corrosion damage as are AMS 5616, AM 355, etc., how-
ever, they are extremely expensive to fabricate and difficult to repair. They are
also often brazed with expensive braze alloys in hard vacuum and cannot be in-
spected by high resolution flourescent magnetic particle techniques. Titanium alloys
such as Ti-6Al-4V have seen extensive use in fan blades because of their excellent
strength to weight ratios.

(3) Joining

The welding of 410 type stainless steel stationery non-air flow components such as shrouds and cases is accomplished using AMS 5776, 410 base welding rod, and tungsten inert gas weld techniques. No repair welding other than electron beam welding of Ti-6Al-4V fan blades is permitted on any rotating component or stationery airfoil component.

Applicable brazing alloys are shown in Table 1. AMS 4770 braze is used extensively in the low temperature section of most compressors while AMS 4772 is utilized with AMS 5616 stainless steel in slightly more severe and higher temperature environments. Silver-copper-palladium and gold-nickel brazes are often utilized in conjunction with nickel base alloys as well as with steel materials where more severe oxidation-corrosion environments are encountered.

III. CORROSION PROTECTION

A large number of coatings are available for the protection of metals against corrosion damage. In many cases where only surface protection is needed the visual appearance of the coated part will determine whether adequate protection has been obtained. More critical requirements will be placed on the coating when protection must be provided against corrosion related phenomena. Examples of these corrosion initiated mechanisms are corrosion fatigue, stress corrosion, and hydrogen induced embrittlement from external environments.

Interpretation of the coating performance in these cases becomes more complicated. For example, an analysis of degree of protection is not available through visual examination. As indicated, martensitic stainless steels are representative of steels which require protection from corrosion initiated damage particularly in the application of compressor vanes and blades. Coatings applied to cyclic stressed martensitic stainless steels must protect against pit formation because often the stress intensification induced by a corrosion pit can supply the initiation site for fatigue failure. Figure 2a is a photomicrograph indicating how what appeared to be a protected blade, in this case a NiCad coated 410 stainless steel J57 blade, has in fact developed corrosion pitting which is consistent with possible fatigue stress amplification. As can be seen a small discontinuity in the nickel plate lead to the corrosion pit. Figure 2b shows how corrosion occurred through the slight break in the Ni plate. This is indicated by analyzing the iron concentration by electron microprobe analysis.

In order to protect 410 stainless steels against temperature and other environmental conditions developed in jet engine compressors one must consider the use of truly sacrificial coatings, i.e. coatings which retain their anodic characteristic even after severe oxidation and/or salt corrosion.

47

Figure 3 is the electromotive series of various metals and coatings relative to saturated calomel electrode in 3% sodium chloride solution. It can be seen that it is desirable to use a coating exhibiting a potential of less than -0.40 volts for the protection of 410 stainless steels. The patented Chromalloy A12 coating is such a sacrificial type coating for 410 steels. It has been utilized on numerous airfoil components of military jet engine compressors. Specific applications will be described in the next section.

In Figure 4a it is clear that sacrificial corrosion has occurred rather than pitting corrosion on a component utilizing the A12 coating. A cross section, Figure 4b, through the coating indicates that only sacrificial corrosion products are formed on the coating rather than corrosion of the base material. Figure 4c shows the microprobe analysis of corrosion products indicating that the coating had corroded sacrificially to the base material. The sacrificial behavior of the A12 coating is very dramatically shown in Figure 5 which is a J57 blade in which the coating has been removed by grit blasting from the leading edge to mid-airfoil. It is clear that after salt spray exposure for 120 hours no corrosion is observed on the blade leading edge, however, substantial corrosion has been encountered on the uncoated blade.

The A12 coating is a diffusion produced coating in which aluminum vapors are utilized to form an aluminide on the surface of the part. This type of coating is an absolute requirement for close tolerance jet engine parts. For example, deviations of as little as half a thousand on a blade or vane airfoil can significantly affect the performance of a jet engine compressor. Figure 6 is a cross section through the leading edge of a J57 airfoil which clearly shows the coating coverage and uniformity available with the Chromalloy A12 system. A12 affords an order of magnitude improvement over that which could be attained by any painting or other overcoat process. Another illustration of the A12 diffusion coating is shown in the photomicrograph (Figure 7) of a section through a drilled and tapped hole. Note how the coating follows the contour of the thread.

Numerous engine tests on the J85, CJ610/CF700, TF41, J57 and JT3D have been carried out utilizing Chromalloy A12 coated airfoil components. In no case has performance degradation been encountered, in fact, as will be indicated in the next section, in numerous cases performance improvements have been encountered. As well, initial performance characteristics have been maintained during service due to improved surface conditions and lack of corrosion product build-up.

The protection of low alloy steels such as AMS 6304 is a much more difficult problem. As can be seen in Figure 3, aluminum base coatings are only slightly more anodic than low alloy steels. Aluminum based coatings therefore often lack significant sacrificial characteristics to protect these low alloy steels against marine corrosion damage. To protect these materials the TSM coating utilizing magnesium as the base element has been developed. Magnesium is tied up in TSM as a complex intermetallic such that only limited sacrificial corrosion occurs in environments such as would normally actively react with pure magnesium. Electromotive measurements in 3% sodium chloride solution against a saturated

calomel electrode indicates a potential of less than -0.9 volts for TSM coated
materials. Significant testing has been carried out indicating that the TSM coating
can protect low alloy G.E. Chromalloy cases, AMS 6304 disks, etc., in the tem-
perature regime normally experienced by these components. The TSM coating is
compatible with the dimensional requirements of various jet engine components.
For example, the fit tolerances of stator vanes in a casing of the type utilized in
the J85 indicate that less than .0003" build-up is required to ensure optimum
assembly. In this case again only a diffusion process would meet the tolerance
requirements, the internal dovetail slot being impossible to coat uniformly by any
standard plating, spray or dip process.

IV.   SPECIFIC MILITARY ENGINE APPLICATIONS

(1)   United Aircraft of Canada T400 Engine

Figure 8 shows the gas generator case of the T40u engine manufactured by
United Aircraft of Canada, Limited. The T400 engine which has application on the
UH-1N Iroquois helicopter generates approximately 1,800 shp. The gas generator
casing is the major central body of the engine and comprises an integral diffuser as
well as a central portion of the compressor section. The case contains a multipli-
city of flanges, screw holes, as well as an integral type diffuser. The gas gener-
ator case is a particularly good application for the A12 coating. It is possible with
the A12 gaseous diffusion process to coat the internal diffuser as well as all tapped
holes and flanges. History on uncoated cases utilized in marine environments in-
dicated significant reductions in performance after 100 to 200 hours of operation.
Recently, an A12 coated case was flown in the Baltic for more than 5,000 hours
without any performance degradation or attack of the basis material. More than
1,000 gas generator cases have already been coated. Excellent field experience
has been reported.

During the initial development period of the T400 engine a study was
made to determine the possibility of fabricating the gas generator case of Inco 718
to eliminate marine corrosion. Although data was generated internally at UACL, an
independent estimate of the cost of the case indicated a two to three fold increase
if fabricated with Inco 718. Since the 410 stainless case cost is in the vicinity of
$6,000.00, a $6,000 to $12,000 increase in engine cost was estimated. This in-
crease would have been incompatible with total systems costs.

(2)   Rolls Royce/Allison TF41 Stator Assembly

Figure 9 is a photograph of a TF41 split compressor stator assembly.
The stainless steel vanes of this assembly have been A12 coated for approximately
three years. At the inception of the engine program NiCad plating was employed
for corrosion prevention. It was found however, after a relatively short period of
engine service, approximately 100 hours, that due to the high temperatures ex-
perienced by the compressor the Cd sacrificial overplate was oxidized thereby re-
ducing completely its sacrificial behavior. The presence of microscopic defects

in the nickel plating consequently produced a severe corrosion pitting condition. Scrap rates of approximately 35%, as a consequence of corrosion pitting, were encountered during this period. Since the introduction of the A12 coating system pitting scrap rates have continually decreased. More than 700 engine compressors have been coated with the A12 coating. The coating did not effect compressor performance. In fact, in a test carried out at the Naval Air Systems Test Facility, Newark, New Jersey, five A12 coated compressors were evaluated relative to uncoated compressors. No change in performance was determined which was in contrast to spray coated compressors, similarly tested, where significant reductions in performance were found.

(3) Pratt & Whitney Aircraft J57, J75 and TF33 Blades and Vane Shroud Assemblies

The application of the A12 coating to military Pratt & Whitney engines was initiated in 1968. Figure 10 is a photograph of some of the components presently coated with the A12 system. Up to the present more than 40,000 vane shroud assemblies have been coated. Overall engine performance has been shown to improve with this coating and pitting corrosion damage has been totally eliminated. The scrap rates due to corrosion damage have been reduced to zero from a range of 5-15% prior to the application of the A12 coating. The scrap rate on blades due to corrosion has been reduced from a high of 20% to zero over this period of time. In excess of 10,000,000 compressor blades have already been coated with A12.

(4) General Electric J85 Compressor Stator Assembly

The J85 is the most power dense engine presently in the Air Force and Navy inventory. Because of its extremely tight dimensional requirements, all previous attempts to coat the airfoils of this engine including complex aluminum vapor deposition, have failed in the past. In the last two years extensive performance testing has been carried out on A12 coated J85/CJ610/CF700 compressors. In no case has degradation of the performance of the compressor been found. Also because of the extremely tight fit requirements the dovetail slots in the Chromalloy (CrMoV steel) compressor case were masked prior to standard spray or dip coating. The use of the TSM coating to coat the dovetail slots has allowed the overall coating of the stator assembly thereby eliminating the severe corrosion problem associated with the corrosion freezing of the stator segments in the case. (See Figure 11). Navy J85 engines are presently being TSM coated to eliminate this severe maintenance problem. This problem could have been resolved by a change in the casing material, however, economic factors did not allow such a material selection change.

CONCLUSIONS

The present paper has outlined some fundamental requirements for the protective coating of jet engine compressor airfoil and case components. An attempt has been made to describe the engineering factors which are often the principal factors in material selection. Descriptions of diffusion coating applications, including the TF41 compressor stator assembly, J85 stator assembly, T400 gas

generator case and J57 vane/shrouds and blades have been described. The basic advantages of diffusion coatings, such as improved uniformity, thickness control and most importantly controlled production reproducibility have been briefly presented. Although future engine designs have not been discussed, it should be clear that in order to meet the requirements of both advanced performance and decreased cost, consideration should be given to the application of composite diffusion coating/base metal systems. Utilization of diffusion coated low alloy and stainless steels, rather than across the board implementation of expensive titanium or high nickel base alloy systems, should be considered.
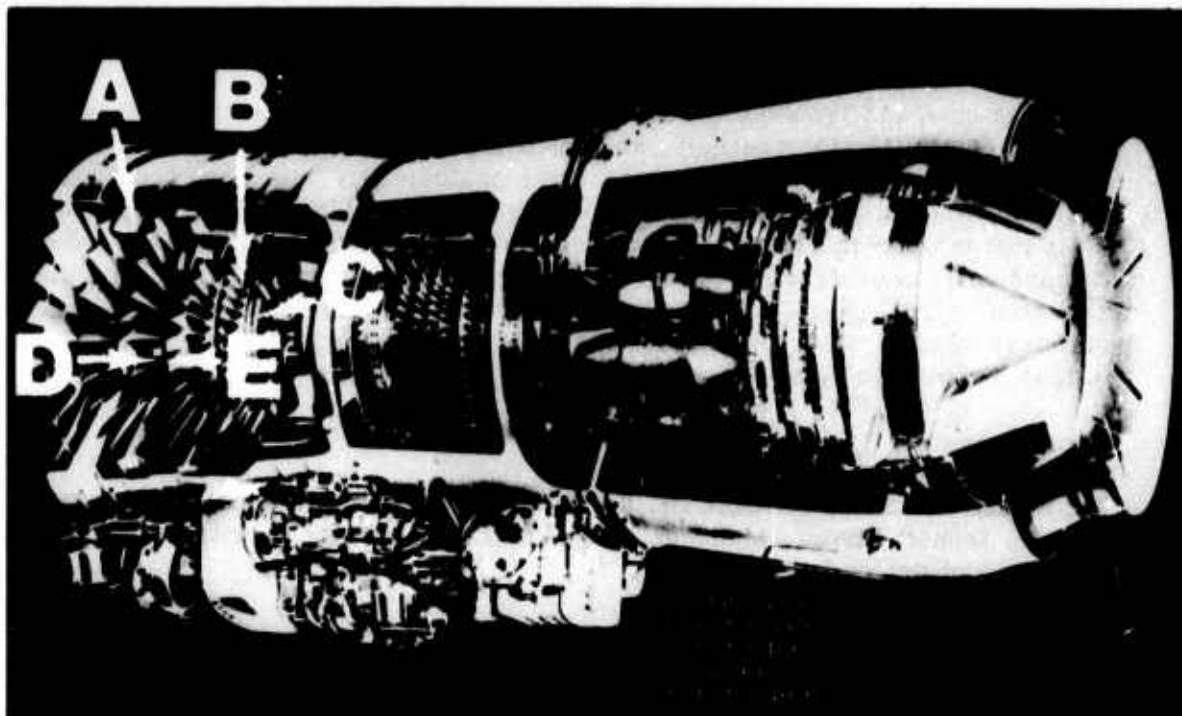
Figure 1. Sectional view of Rolls-Royce/Allison TF-41 engine which powers the LTVA-7 aircraft showing major compressor components. Compressor is of axial variety with a 3-stage low pressure, 2-stage intermediate compressor with steel stators and titanium rotor blading and 11 stage high pressure compressor with stainless steel vanes, case, disks and spacers, titanium rotor blades, stage 1-8, and stainless steel blades, stages 9-11.

Table 1. Base and braze alloys utilized in military jet engine compressors.

COMMON COMPRESSOR MATERIALS		
ALLOY	COMPOSITION	APPLICATION
AISI 4340	0.40 C, 0.8 Cr, 1.8 Ni, 0.25 Mo	Disks, Spacers
Chromalloy (G.E.)	0.20 C, 1.0 Cr, 1.0 Mo, 0.1 V	Cases
AMS 6304	0.40 C, 0.95 Cr, 0.30 V	Disks, Spacers
AISI 410	12.5 Cr, 0.15 C	Blades, Vane/shrouds
AM 355	0.13 C, 15 Cr, 4.25 Ni, 2.75 Mo	Vanes, Blades, Cases
AMS 5616	13.0 Cr, 2 Ni, 0.12 C, 3 W	Blades, Vane/shrouds
Ti 6 Al, 4 V	6.0 Al, 4.0 V	Blades, Disks
Inco 718	53 Ni, 19 Cr, 3.0 Mo, 0.8 Ti, 0.6 Al, 19.0 Fe, 5.3 (Cb + Ta)	Blades, Vane/shrouds
Inconel x - 750	73.0 Ni, 7.0 Fe, 15.5 Cr, 0.7 Al, 2.5 Ti, 0.9 (Cb + Ta)	
BRAZE ALLOY		
AMS 4770	50 Ag, 15.5 Cu, 16.5 Zn, 18 Cd	Stainless Steel
AMS 4772	54 Ag, 40 Cu, 5 Zn, 1 Ni	Stainless Steel
PWA 706	54 Ag, 25 Pd, 21 Cu	Stainless Steel
PWA 698, AMS 4787	82 Au, 18 Ni	Inconel, Stainless Steel

Figure 2a. Photomicrograph of Ni-Cad coated AMS 5616 J57 compressor blade with small discontinuity in nickel plate leading to corrosion pit.

500x

Figure 2b. Iron X-ray image (electron-microprobe) of nickel-cadmium coating in **2a** showing sub-coating corrosion pit.

53
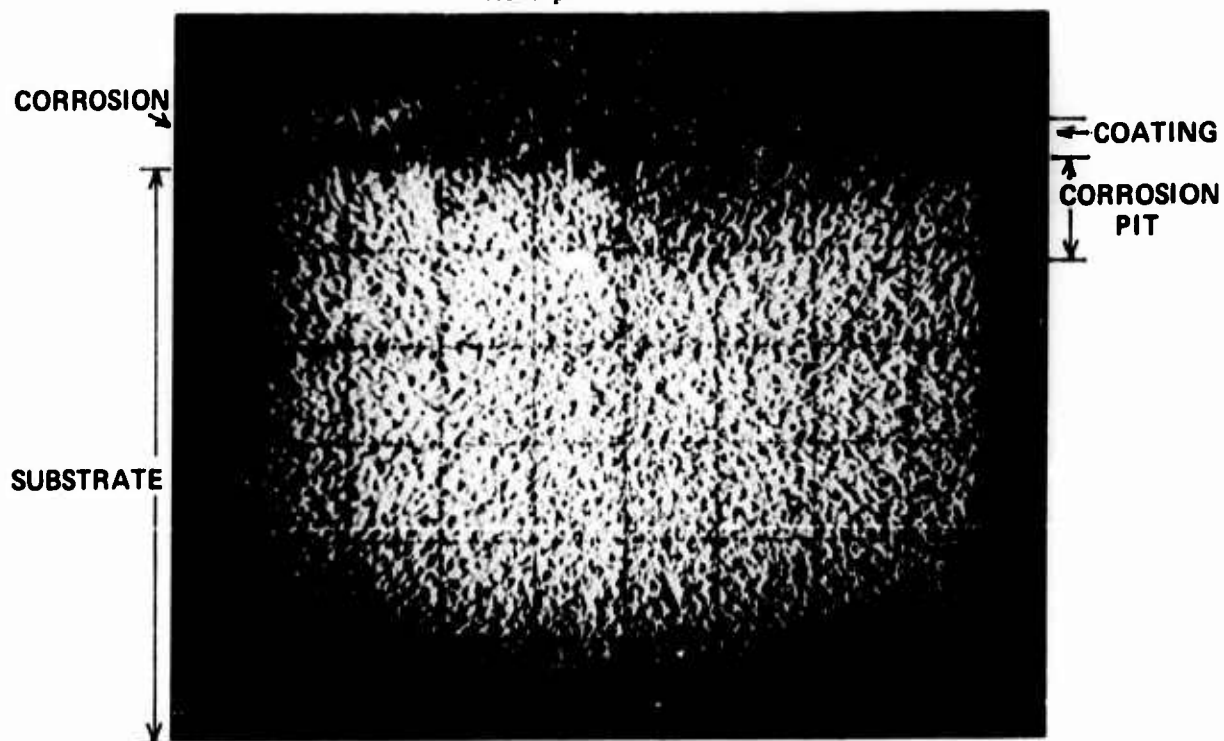
practical galvanic series
of metals and alloys
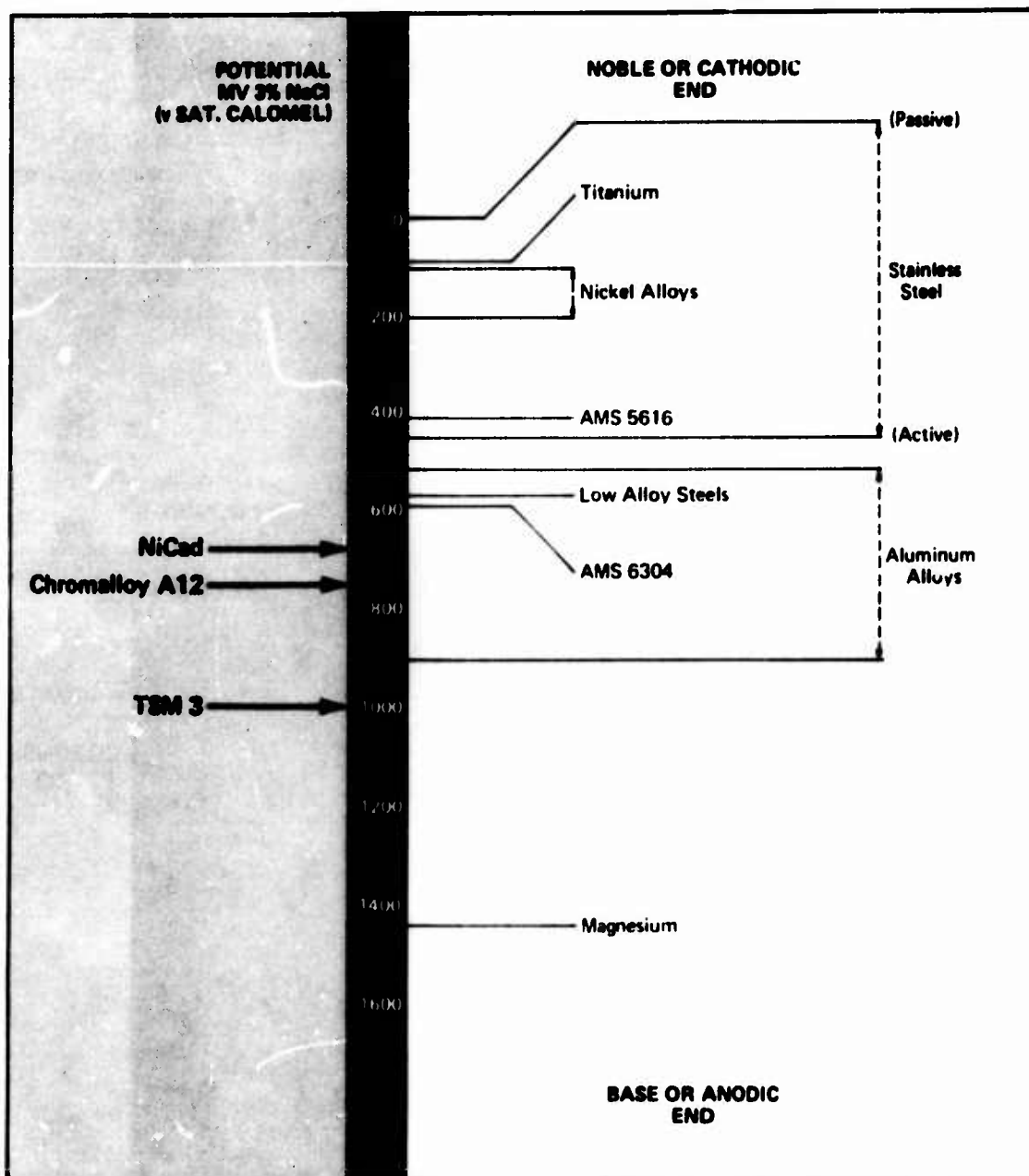
Figure 3. Electromotive series of various metals and coatings relative to saturated Calomel electrode in 3% sodium chloride solution. The A12 coating (iron alumi-nide) 0.73 and the TSM-3 (magnesium intermetallic) 0.98 are shown to be anodic to stainless steel and low alloy steels respectively.
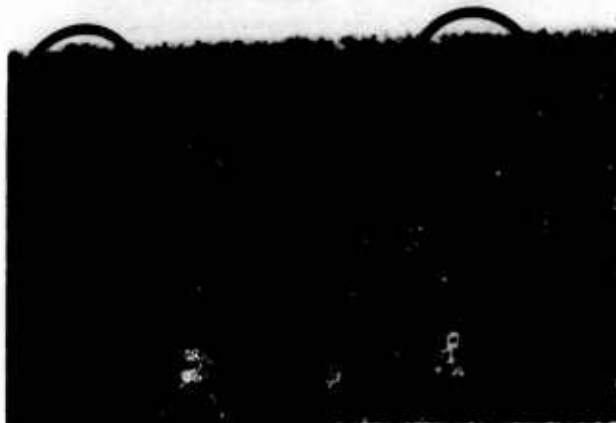
7x

Figure 4a. Sacrificial surface corrosion products on the surface of A12 coated Chromalloy A12 J57 compressor blade.
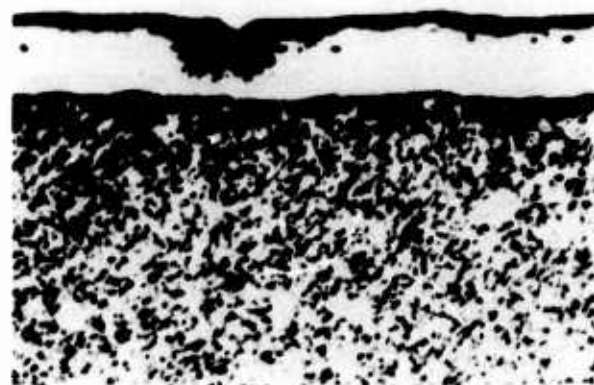
500x

Figure 4b. Cross-section through sacrificial corrosion products showing no attack of basis material (electrolytic oxalic acid etch).

NICKEL PLATE

26% IRON

CORROSION

COATING

37% IRON

38.4% IRON

SUBSTRATE
83.3% IRON ——●
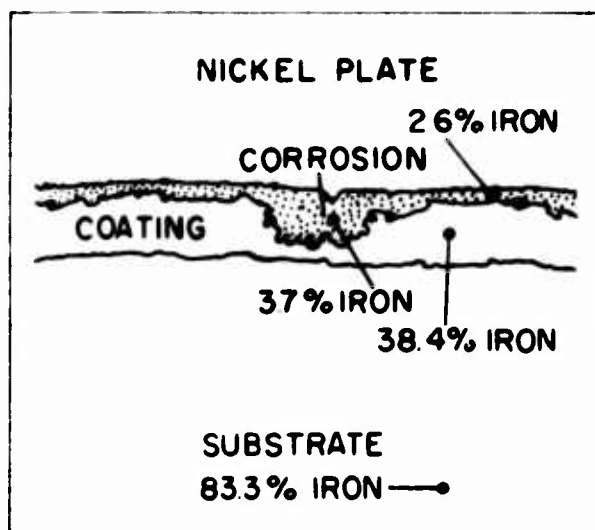
Figure 4c. Electron-microprobe point counts for iron made on 4b section indicating again sacrificial protection afforded by A12 coating.

55

SACRIFICIAL PROTECTION OF "A 12" COATING DURING 120 HOURS SALT SPRAY EXPOSURE

UNCOATED   "A12" COATED

LEADING EDGE REMOVED BY EROSION
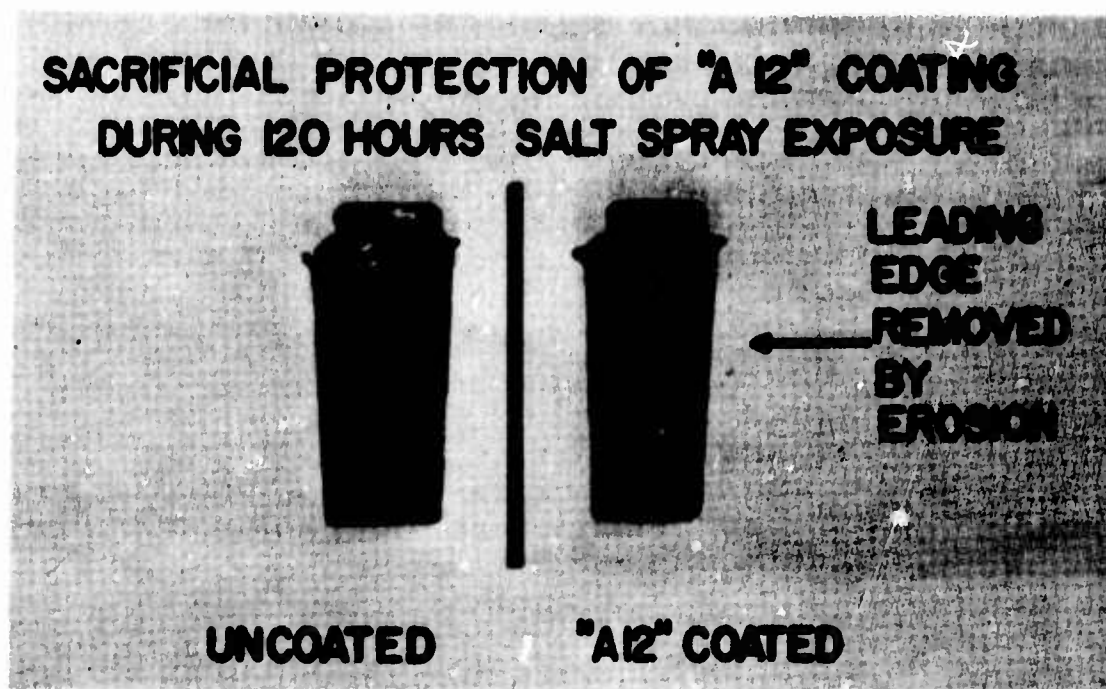
Figure 5. Sacrificial protection of A12 coating exhibited during 120 hr. salt spray exposure. AMS 5616 J57 blades were utilized. Prior to testing the coating was removed from the leading edge up to the center of the airfoil. As can be seen, no pitting of the basis material occurred in the uncoated area.

SACRIFICIAL PROTECTION OF "A 12" COATING

uncoated   "A 12" coated

leading edge coating removed

A·12 COATING

AIRFOIL

100x
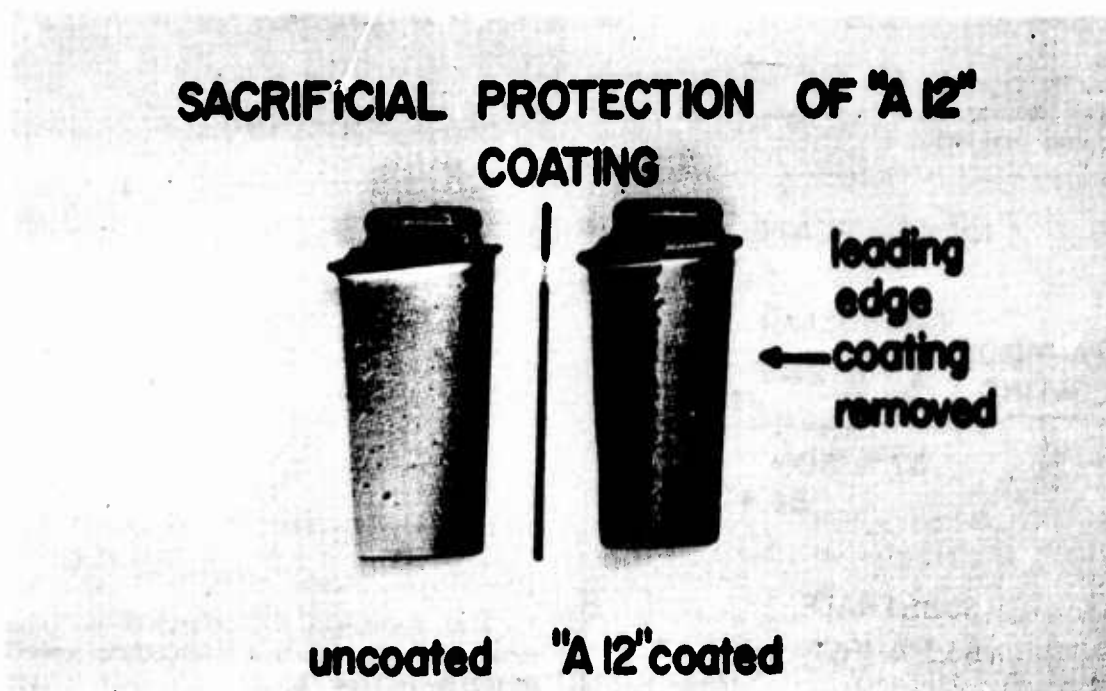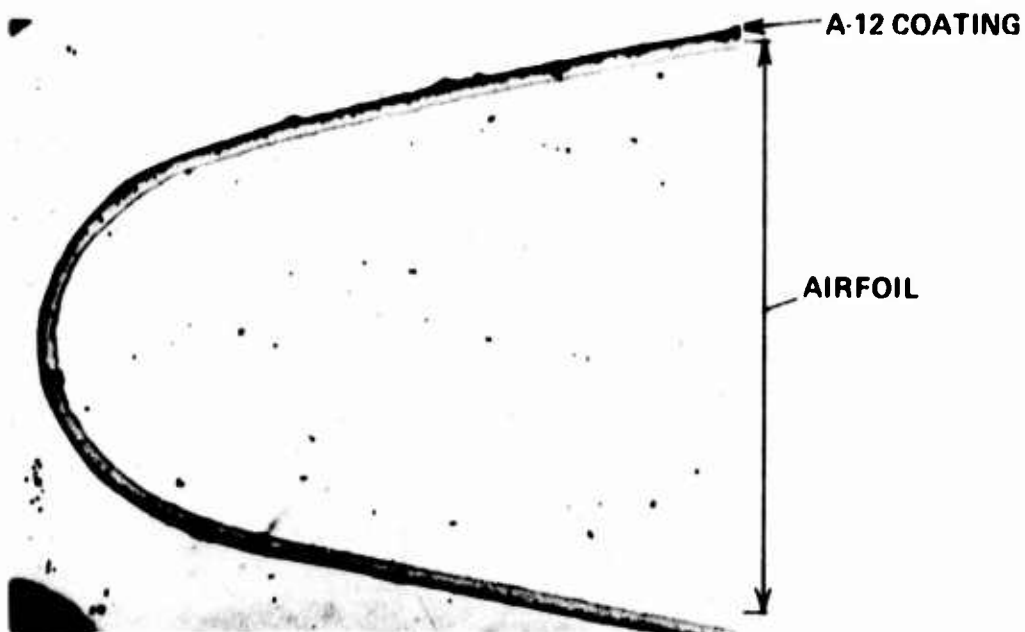
Figure 6. Photomicrograph of AMS 5616 compressor blade leading edge indicating uniformity and coating coverage only available with the Chromalloy A12 pack diffusion process.

100x
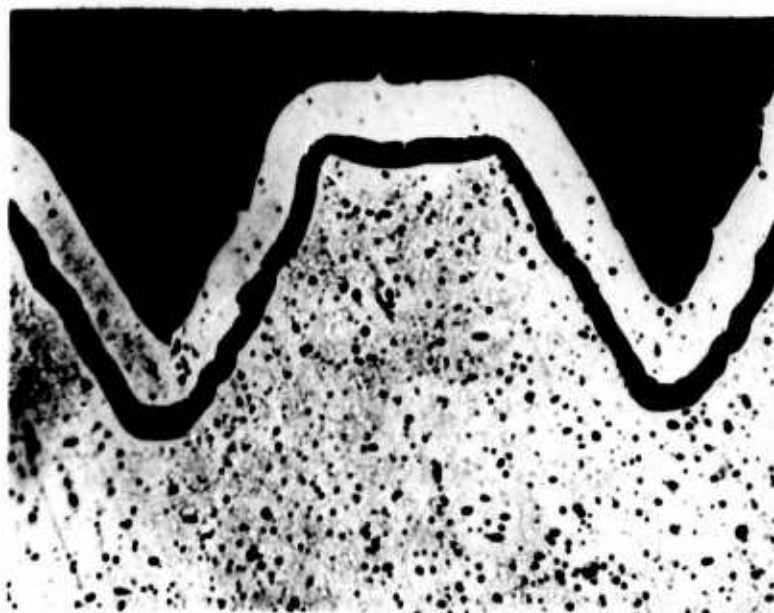
Figure 7. Photomicrograph of section through a drilled and tapped hole. Notice should be taken of the uniformity of the coating around the complex contour of the thread.

57
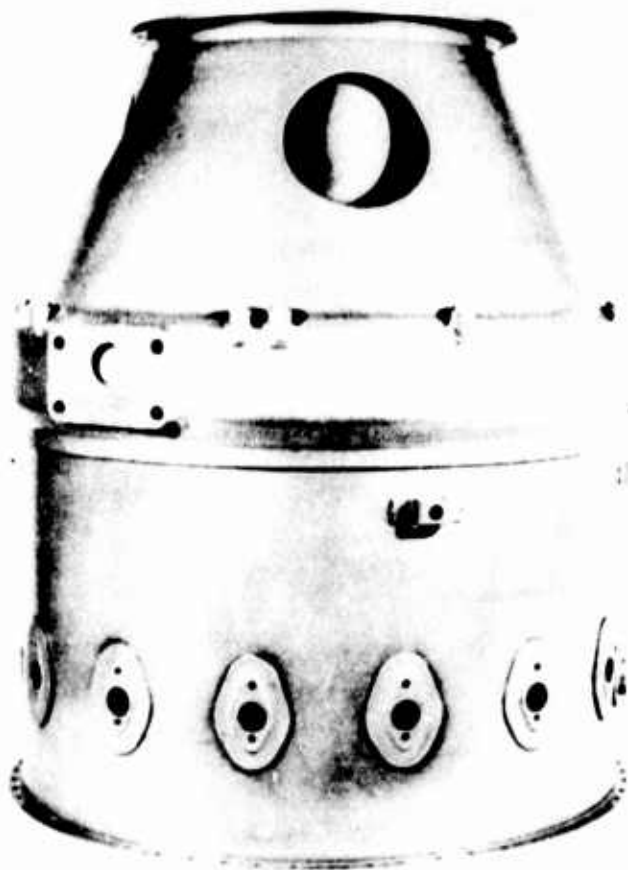
Figure 8. The T400/PT6 gas generator case shown in the above figure represents an ideal application for the A12 coating since complete protection can be offered in chanels, diffusion tubes and other irregular surfaces. This protection could not be obtained with any spray or plating technique.
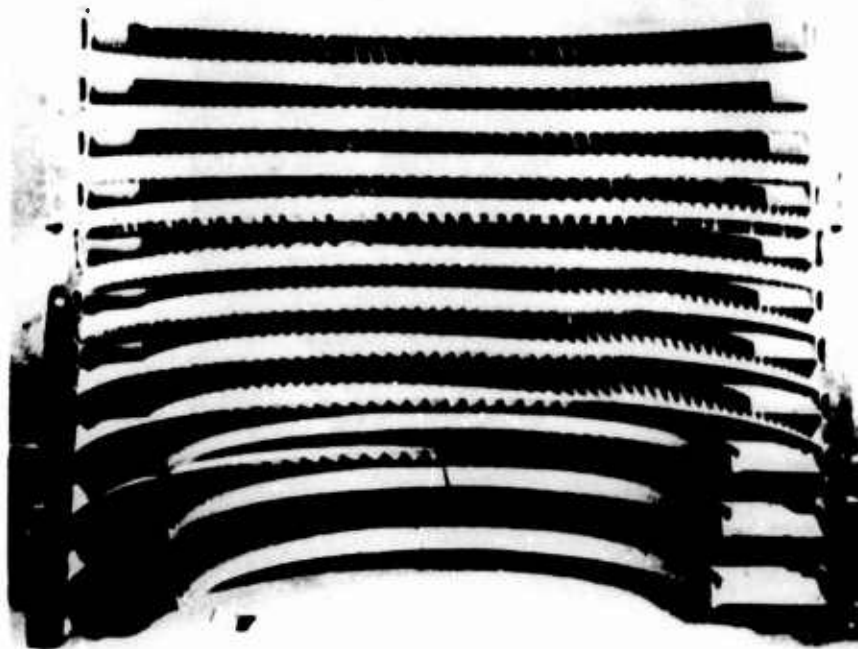
Figure 9. TF-41 stator assembly containing A12 coated stator vanes. Vanes and compressor casing are "410" type stainless steel.
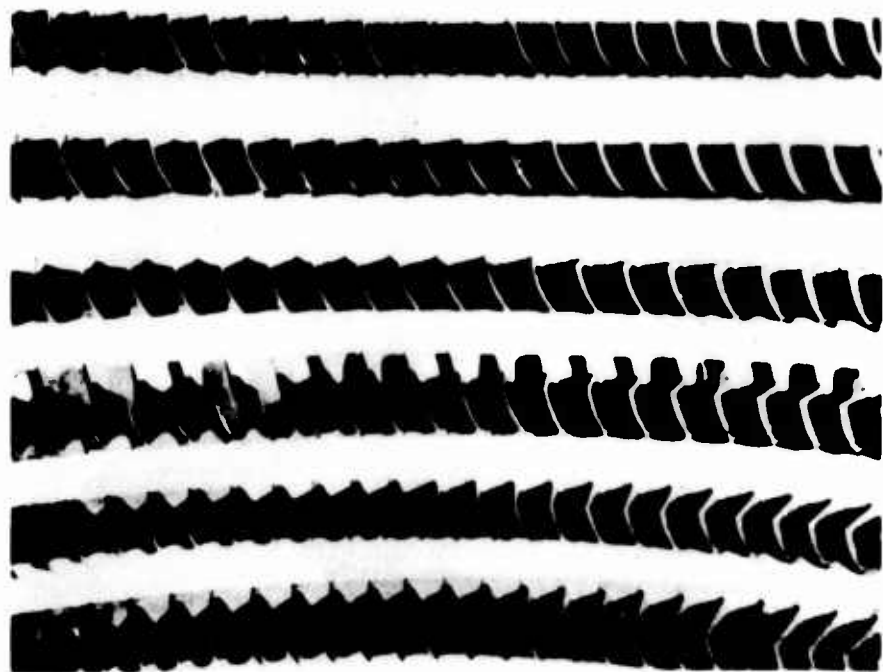
Figure 10. A12 coated Pratt and Whitney J57, J75 and
TF33 vane-shroud assemblies and blades.

Figure 11. J85 stator assembly with TSM-3 coated Chromalloy (CrMoV) case and A12 coated 410 S.S. vane segments. Thickness of TSM-3 coating controlled to less than 0.0002" build-up without negatively affecting corrosion protection.

STRESS CORROSION HISTORY OF APOLLO-SATURN LAUNCH VEHICLE AS-208
(SKYLAB IV) AND ASSOCIATED COMPONENTS

BY
H. L. GILMORE and C. E. CATALDO

Metallic Materials Division
Materials and Processes Laboratory
George C. Marshall Space Flight Center
National Aeronautics and Space Administration

Stress Corrosion History of Apollo-Saturn Launch Vehicle AS-208
(Skylab IV) and Associated Components

By H. L. Gilmore and C. E. Cataldo

Abstract

The history of aluminum 7178-T6 and 7079-T652 forgings through
design, fabrication, testing,and storage to the successful flight of
the Skylab IV mission is documented. The decision process, inspection
routine,and repair which led to safe operation of the boost vehicle are
related. Specific forgings involved are 7178-T6 E-Beams and 7079-T652
fin spars in the base of the S-IB first stage, vertical reaction beams
(7079-T652) in the S-IB/S-IVB interstage, among other components. The
lessons learned from the Saturn experience in terms of material control,
systematic inspection, laboratory simulation,and guidelines developed
are vital to future systems in aerospace and ground-based structures.

Stress Corrosion History of Apollo-Saturn Launch Vehicle AS-208 (Skylab IV) and Associated Components

Prior to launch of the Skylab IV crew on the AS-208 [*] launch vehicle (see Figure 1), several major materials problems were encountered that required the concentrated efforts of a large number of people to resolve and to establish the subsequent flight worthiness of the vehicle. During pre-launch preparations, bulkheads on two fuel tanks were accidentally collapsed; stress corrosion cracks were discovered in several locations on two major components of the stage structure; fatigue cracked skin stringers were found; and a cable-harness had to be replaced when broken wires were detected. This paper describes the stress corrosion problems encountered and the actions taken to correct them and to verify the structural integrity of the vehicle, with respect to the materials applications. Similar problems on the two stages of launch vehicle AS-209 are discussed also.

Decisions to remove and replace, repair, and/or fly as is on these components were made on the basis of the following considerations:

(1) Analysis of cracks
(2) Proof test parameters and life cycle determination
(3) Repair methods
(4) Safety

Launch Vehicles Background

The two launch vehicles to be discussed in this paper were assembled and static fired in 1966 for launches scheduled in 1967 and 1968. Although a total of 14 S-IB stages were built for qualifying Apollo hardware as well as for actual Apollo missions, the Saturn V lunar program accelerated to such an extent and confidence in the Apollo hardware increased, the S-IB missions were reassigned and flown on the Saturn V configuration. Five Saturn IB missions were flown successfully, hence eliminating the need for the nine additional stages to back-up the Apollo missions. The remaining nine S-IB stages were placed in storage within the Michoud Plant beginning in 1968 with stringent controls of temperature, humidity and contaminants in the enclosures. Storage was

----

(*) Three R and D vehicles (SA-201 through SA-203) and twelve operational vehicles (SA-204 through SA-214) constitute the Saturn IB program. Each Saturn IB launch vehicle consists of an S-IB stage (i.e. S-IB-8), an S-IVB stage (i.e. S-IV-B-8), an S-IB/S-IVB interstage, and an instrument unit. When the launch vehicle combines with the Apollo payload, its configuration is designated Apollo-Saturn (AS); hence, AS-208, AS-209, and so forth.

discontinued for each Skylab assigned S-IB stage in 1972 according to the scheduled requirements of checkout, preparation for shipment and launch.

Because of additional knowledge learned about the stress corrosion cracking (SCC) behavior of the high strength 7000-series aluminum alloys during the late 1960's, and considering the age of the S-IB and S-IVB stages in 1972, an inspection procedure was prepared for selected SCC susceptible materials in the Skylab launch vehicles. Periodic inspections were made at Michoud and Kennedy Space Center (KSC) with the final inspection to be achieved within 30 days of launch.

Although the stress corrosion inspection for the S-IB-6 and S-IB-7 stages were negative, S-IB-8, S-IB-9 and the assigned S-IB/S-IVB inter-stages were not quite so fortunate.

S-IB Thrust Structure E-Beam Cracking

Stress corrosion cracks were found in the outboard end of a thrust outrigger upper E-Beam (see Figure 2) during installation of stabilizing and support fins on the S-IB-9 stage in late August of 1973. These cracks, shown as dye penetrant indications in the four photographs shown in Figure 3, were found by an observant technician as he was installing fin attachment bolts in the immediate vicinity of the Fin 7 E-Beam. As a result, immediate visual examination was made of all the forged 7178 aluminum E-Beams installed on the S-IB-9 stage which was located in the Vertical Assembly Building at KSC. Another crack was found also in the same E-Beam located near the center, as shown in Figure 3. A third crack was found in a beam toward the inboard end at position Fin 4; this crack is shown also in the composite Figure 3, note the straightness of the dye bleed-out initiating in the hole under the fastener nut. Dye penetrant inspections were made of several other questionable visual indications; however, no additional cracks were found in the E-Beams on the S-IB-9 stage.

A similar inspection of the S-IB-8 stage located on the launch pad and undergoing preparation for launch of the Skylab IV Crew, re-vealed only one crack which was found near the inboard end of the upper E-Beam at position Fin 4. The decision was made to remove this crack for failure analysis. The coupon containing the crack is shown in Figure 4. Note that the crack did not originate or terminate in a fastener hole, nor did it propagate through the thickness of the beam material, as shown in the lower left and right side photographs in Figure 4. A slight bowing of the material can be seen also in the right side view.

66

To expose the fracture surface for study on the scanning electron microscope (SEM) as well as to retain intact cracks for metallographic study, the sample was cut in a manner to leave both ends of the crack undisturbed. A flat view shown in the upper right corner of Figure 5 shows the end of the intergranular crack; whereas, a cross-sectional view made near the opposite end depicts the crack traversing intergranularly in the transverse direction. The SEM photograph in the lower right corner of Figure 5 shows the typical intergranular cracking along the fracture face. Mud crack patterns in corrosion deposits were found near the initiation, as shown in Figure 6.

With the cause of cracking verified for the beam in Fin 4 of the S-IB-8 stage, stress calculations were made to determine if an inplace repair could be made safely to insure structural integrity of the E-Beam. The calculations were favorable with the recommended fix being a spacer and doubler as shown in Figure 7.

The S-IB-9 stage E-Beam cracks were removed and examined similar to the one from S-IB-8. Stress calculations and repairs were made on an individual basis for these cracks.

Failure Analysis Summary for E-Beams

The following comments summarize the findings made on the E-Beam cracking:

1. The cracks were caused by stress corrosion.
2. The E-Beam material (7178-T6) is highly susceptible to stress corrosion cracking.
3. Stage environmental exposure is favorable for long crack free life.
4. Applied stress (residual plus assembly) is sufficient to cause cracks. Measured data indicate levels on the order of 10,000 psi.
5. Failure data on bare samples of 7178-T6 at 10,000 psi, resulted in failure in 3 to 4 years under inland environment, and 2 to 4 months under seacoast environment.
6. Use of a zinc chromate system extends time to failure by a factor of 2 to 4.
7. There is a probability that additional E-Beam cracks may develop but all applied stress data indicate that they will initiate on the visible surfaces.
8. Periodic visual inspection will detect any significant crack.

Rationale for Acceptable Flight Risk

The following rationale indicated that the E-Beams were flight worthy:

1. Cracks were caused by stress corrosion.
2. Residual stress in E-Beams was prime contributing factor.
3. Process review showed that the S-IB-7 stage beams should have had highest residual stresses and greatest potential for cracked beams, although none were reported.
4. All cracks found in the investigation would not have resulted in structural failure; i.e., loss of fin, tank or engine support.
5. Highest residual stresses were on surfaces between flanges resulting in greatest likelihood of cracking on visible surface.
6. Stress corrosion cracks will occur only in transverse grain direction which is not the flight direction.

Stress Corrosion Cracking of the Rear Spar of the S-IB-8 Stage Fins

During a scheduled inspection on November 6, 1973, of all components previously determined to be stress corrosion susceptible, cracks were found in 15 of 16 attach fittings for the stabilizing and support fins on the S-IB-8 stage. This was the final stress corrosion inspection scheduled for the launch vehicle and was performed after full propellant loading was completed as a part of the Count Down Demonstration Test (CDDT) conducted 4 days earlier. At the time of inspection, the fuel tanks were loaded and the extent of cracking in the lower spot face area of the left and right hand mounting pads of the rear spars was clearly visible. The rear spar fitting shown in Figure 8 is processed as a closed die forging of 7079-T652 aluminum alloy. It is approximately 42" X 24" X 12" in size and the final machined part weighs 52 pounds.

Three previous inspections of these parts, as assembled, had been made, two at Michoud in accordance with routine inspection specifications and one at KSC during the period of September 25 to October 4, 1973. No cracks were found during these previous inspections even though statements by inspection personnel asserted that these critical areas had been examined. Yet, the type of crack found could possibly have been missed due to the locations and characteristics of the cracks. They originated in a sharp radius of a bolt hole spot face as shown in Figure 9.

Analysis Results and Discussions

An initial metallurgical analysis was made on Fin 4, which was
the first fin removed from the stage, the mating pad of the lower
fitting assembly contained a crack large enough to be seen with the
unaided eye. The typical crack found propogated from a sharp radius
in the spot face for the main attach bolts. The crack did not originate
in the bolt hole itself (see Figure 9). A section of the Fin 4 spar
containing a crack was removed at KSC and a metallurgical examination
was made. The crack was confirmed to be stress corrosion cracking by
visual, metallographic and Scanning Electron Microscope (SEM) examinations.
It was noted also that considerable pitting corrosion existed on the
mating surface of the connecting pad. Pits were noted with depths up to
about .002 inch. The microstructure of the material showed a normal
grain structure although there was some evidence of slight overheating,
as could have been caused during initial processing; this would not
result in any cracking susceptibility.

A stress analysis of the fitting showed that static stresses in the
lower pad ranged from 7500 to 7900 psi. The stress corrosion cracking
(SCC) threshold for the 7079-T6 material is less than 8000 psi. Along
with the constantly applied stress, installation stresses, and the
hostile seacoast environment, conditions for cracking in these parts
were very favorable.

Mechanical properties of the 7079-T652 die forgings (5-6 inches
thick) are as follows:

MIL-HDBK-5 MIN.

	Longitudinal. psi	Short Transverse, psi	Typical Valves, psi
F_{TU}	70,000	68,000	78,000
F_{TY}	59,000	58,000	68,000
%EL	7	3	14

Stress Corrosion Threshold stresses are:

    Longitudinal   -   > 50,000 psi
    Long Transverse   -   50,000 psi
    Short Transverse -   < 8,000 psi

Thus, the threshold stresses, for sustained service, are quite low,
compared to the typical mechanical properties of the material.

Stress corrosion failure of aluminum alloys is more often due to residual stresses in the material than to short-time service stresses. 7079-T652 forgings, when compressive surface areas are machined away, are highly susceptible to stress corrosion cracking, and minute cracks, once formed, propogate much more rapidly than in most other aluminum alloys. The initiation site of such a crack might be detected as a corrosion pit, or it might not be evident at all. In previous failure of components of this alloy, no evidence of actual corrosive effects could be detected in some cases, yet the failures were inter-granular and branching, characteristic of stress corrosion failures.

While the residual stresses that may be present in the S-IB fin attachment fittings are unknown, we must assume that they might be quite high in very localized areas. Based on previous tests on a very similar part, the residual stresses in the fin fittings could be on the order of 12,000 to 18,000 psi tensile.

Tests on 7079-T651 have been made under various test site exposures and using different surface treatments on the material. A summary of the data is as follows:

DAYS TO FAILURE AT 55,000 psi STRESS

TEST SITE OR CONDITION	UNPROTECTED	$ZnCrO_3$ PRIMER	SHOT PEENED
		(RANGE OF 5 SPECIMENS)	
3.5 NaCl (A.I.)	10-17	115 (4-190)	200 (60-520)
Pt. Judity, R.I.	35-45	70 (56-240)	1460 N.F. *
Pt. Comfort, Texas	35-87*	1000 (628-1230)	1460 N.F.
Industrial Atmos., Pa.	35-76	150 (59-222)	1500 N.F.

* One specimen out of 5 failed in 7 days. N.F. means "none failed."

Stresses on the fin attach fittings were calculated as follows:

CONDITION	STRESS, psi
On Pad - Empty	4,000
Loaded with Fuel Only	11,500
Fueled + 32 Kt. Wind	16,400
Fully Loaded	34,000
Fully Loaded + 32 Kt. Wind	39,000

In addition to these stresses, we could conceivably experience an additional 18,000 psi stress due to residual stresses in the part, resulting in total stresses on the order of 52,000 to 57,000 psi in the fully loaded condition.

Thus, the stresses experienced during fully loaded conditions are approximately the same as those for which the test data were generated in the exposure tests shown above. On this basis, it appears reasonable to consider that the fittings should withstand at least 10 days of exposure to a fully loaded condition, with winds, where the metal was completely unprotected and a salt water environment was present.

In one sense that is extremely conservative, in that it is based on the worst possible environment with no protection at all. On the other hand, it does not account for possible additional stresses that may have occurred due to attachment mismatch and bolting stresses. If severe enough, such stresses could easily exceed the yield strength of the material.

The fact that all of the S-IB-8 stage fittings were cracked in essentially the same place indicates that all were equally loaded, or that all of the these areas exceeded the "threshold" stress for stress corrosion. The failures are obviously due more to applied stresses rather than residual stresses, because none of the residual stresses must have been below 9,000 psi, short transverse. Adding this figure to the applied stresses during loading gives a maximum stress of 47,000 psi which is close to the stress value that was used for the SCC tests in the table above.

Failure Analysis Summary for S-IB-208 Fins

1. Cracking resulted from stress corrosion.
2. The forging process produced a grain flow transition which resulted in a short transverse grain direction in the area of the cracks.
3. Evidence of pitting corrosion was found.
4. Spectrographic analysis and hardness of Rockwell "E" 109 confirmed the composition to be 7079 as specified.
5. The cracking of the fin spars in fifteen of sixteen locations presents a classical case of stress corrosion.
6. The sharp notch in the spot face, the short transverse grain direction, damage to the protective coating, exposure to the corrosive environment, and the sustained tensile stresses and age resulted in the failure by stress corrosion cracking.

Rationale for Acceptable Flight Risk

1. New fins installed within 5 days of launch.
2. Reinforcement fittings installed on fins to transfer load away from problem area in spar.
3. Cracks were caused by stress corrosion cracking.
4. Calculations showed safety factor sufficient to warrent safe launch.

S-IVB Reaction Beam Cracking

On November 11, 1973 during the final scheduled inspection, cracks were discovered near the centerline of the inboard flanges of the S-IVB-8 aft interstage reaction beams. Subsequently, cracks were found also on the S-IVB-9 aft interstage reaction beams of the Skylab rescue vehicle, and on a similar test article at the Marshall Space Flight Center (MSFC). The aft interstage contains eight reaction beams which are machined from 7079-T652 aluminum alloy die forgings.

While the reaction beams described above plus those on vehicles in storage at Michoud, LA were being examined for cracks, a parallel effort was undertaken at the McDonnel Douglas Facility at Huntington Beach, CA, on thirty-one surplus unmachined reaction beam forgings. All thirty-one were found to contain cracks in similar locations as those in the flight interstages. Failure analysis investigations were undertaken on the beams at MSFC and on the unmachined forgings at Huntington Beach to determine the cause of these cracks.

Two of the interstage test article beams were removed at MSFC for metallographic and fractographic analyses. A compilation of the findings are shown in Figure 10. Note the intergranular crack progression shown in the photomicrographs for beam forging No. 38. The cracks were located near the centerline (parting plane) of the forging. Scanning Electron Microscope (SEM) photographs also depict intergranular fracture morphology plus typical mud crack patterns in the corrosion products on the fracture surface. Photomicrographs of the cracked area in Forging No. 49 show intergranular cracking initiating at the bottom of surface pits in the 7079-T652 aluminum. Note that a single crack was found in Forging No. 19 whereas two cracks were discovered in Forging No. 38.

Chemical analysis indicated that the beam forgings met the specifications for 7079 aluminum alloy. The average hardness of Rockwell B 89 and electrical conductivity of 33.5% IACS indicated that the forgings were heat treated to the specified strength requirements.

A typical cross-section near the centerline of an inboard flange (forging flash area) is shown in Figure 11A. The highly directional grain flow in the flash area is typical and normal. Figure 11B shows the branching intergranular cracking further into the cracked beam. The microstructure within the flash area exhibited areas of large elongated grains as well as regions of small grains. This type of microstructure is normal for the flash area of 7079 aluminum when die forged.

Reaction Beam Forging History

A look at the history of these beam forgings show that the material was supplied by the Aluminum Company of America as 11-inch square billets and were die forged in a temperature range of 800°F to 650°F and subsequently heat treated to the T652 condition by Wyman Gordan Company, Worchester, MA. The aged forgings were ultrasonically inspected per NAS 824, Grade A and B; however, due to the configuration of the forging, certain areas with non-parallel surfaces were not inspectible by ultrasonic techniques. One such area, the outer flange, could contain a crack nearly an inch deep and would not have been detected by this method. Although fluorescent penetrant inspections were made on the machined parts, no cracks were detected prior to installation because the parts were not etched prior to penetrant application. It is highly probable that tight cracks could have been smeared over during machining.

Examination of S-IVB-8 Aft Interstage

During the final inspection of the S-IVB-8 stage and aft interstage, cracks were found in the base of seven of the eight reaction beams. The cracks were located on the inboard face, varying in length, and on three beams extending into the center pocket area a maximum of approximately 1/4 inch from the edge of bevel.

As the result of finding a crack about 36 inches above the base on the back-up S-IB/S-IVB-8 interstage in the Vertical Assembly Building, a dye penetrant inspection was performed not only on the inboard and outboard surface of the fat end of the inboard cap of the S-IB/S-IVB-8 interstage reaction beams, but on a one inch wide length of all 8 beams. No cracks were found except in the base area as previously stated.

73

Failure Analysis Summary of S-IVB Aft Interstage Reaction Beams

1. MSFC and McDonnel Douglas studies indicated that failure of the 7079-T6 beams resulted from stress corrosion cracking.

2. Residual stresses from forging operation caused failure.

3. Preferential grain direction in the flash area contributed to failure.

4. Machining operation would have smeared over any cracks and would have precluded dye penetrant detection prior to installation.

Rationale to Leave Reaction Beams Intact on SA-208

1. Known cause of failure was stress corrosion cracking.

2. Stress analysis of the cracked beams indicated a Factor of Safety in excess of 1.5.

3. The minimum required Factor of Safety is 1.4

4. Repair of the beams would require extensive rework and possibly effect the S-IB stage.

5. Removing and replacing the beams would require demating the aft interstage from the vehicle.

6. Stress direction was parallel to crack direction.

In conclusion, the lessons learned from the Saturn experience in terms of material selection and control, systematic inspections, laboratory simulation and guidelines developed are vital to future systems in aerospace and ground based structures.

FIGURE 1 - APOLLO-SATURN LAUNCH VEHICLE AS-208
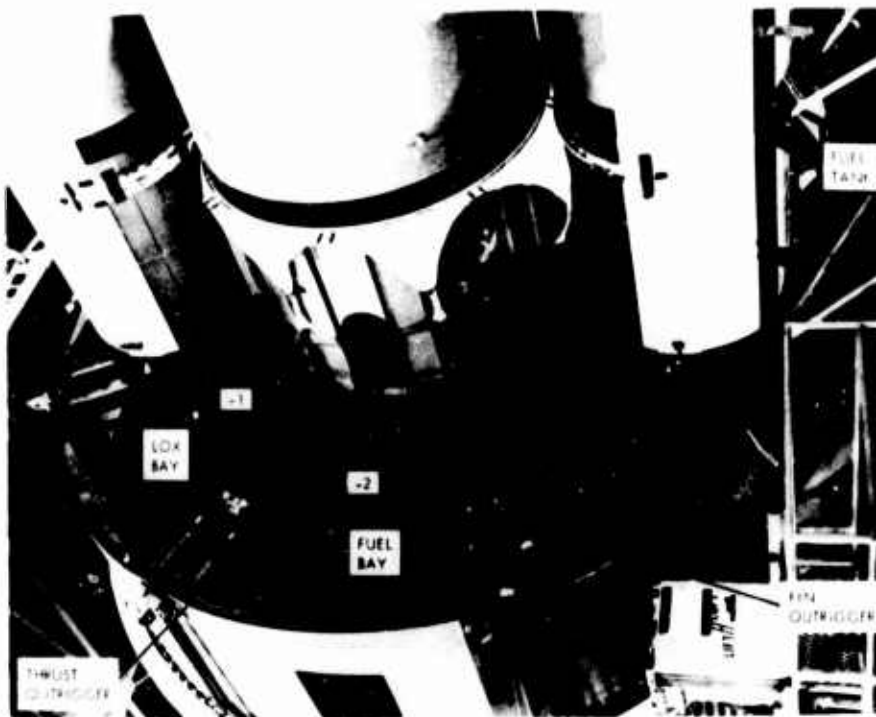
A. S-IB E-BEAM LOCATIONS

B. S-IB E-BEAM

FIGURE 2
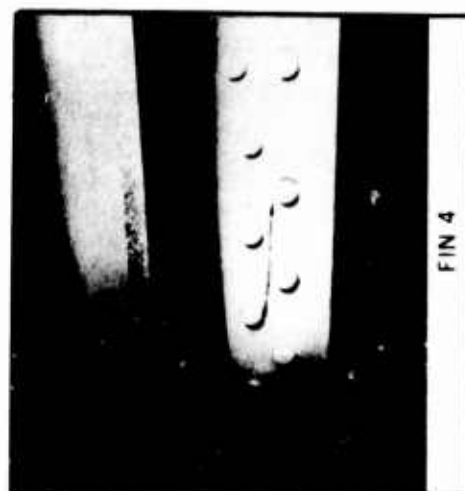
S-IB E-BEAM CRACK LOCATIONS

FIGURE 3
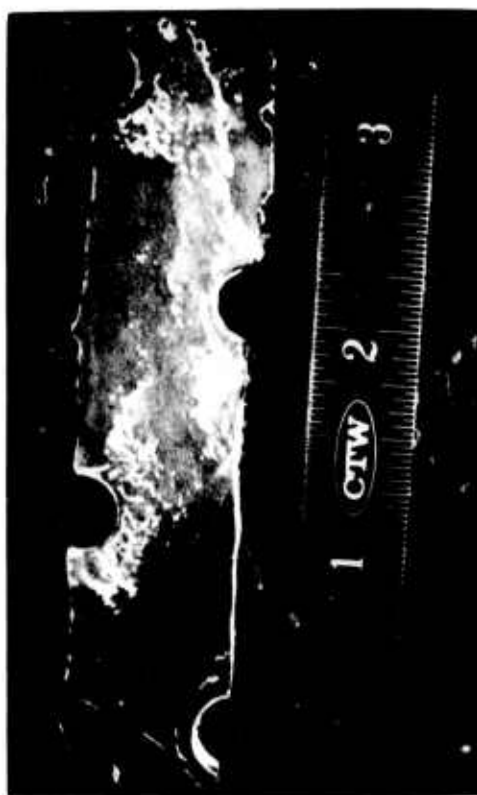
SIB 8 FIN 4 SAMPLE AS RECEIVED

FIGURE 4

78
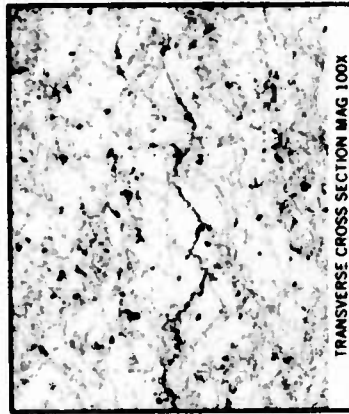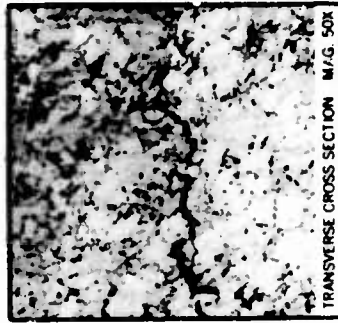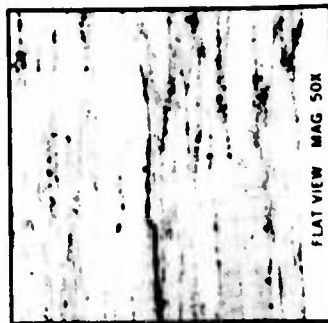
METALLOGRAPHY OF 7178-T6 ALUMINUM E-BEAMS

FIGURE 5

79

FIGURE 6 - MUD CRACK PATTERNS IN CORROSION PRODUCTS ON FRACTURE

AFTER SPLICE PLATE

BEFORE SPLICE PLATE

SIB 8 FIN 4 REPAIR

FIGURE 7

81

S-1B-8 REAR FIN SPAR FORGING

FIGURE 8

FLORESCENT DYE INDICATION SHOWING CRACK LOCATION

FIGURE 9

S-IVB INTERSTAGE TEST ARTICLE
7079-T652 FORGING CRACKS

FORGING NO. 49

FORGING NO. 38

FIGURE 10

83
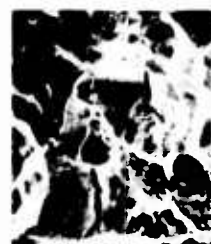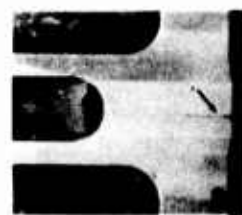
A. CROSS-SECTION   MAG. 100X

B. CROSS-SECTION   MAG. 100X

SCC IN SIV-B REACTION BEAM FORGING

FIGURE 11

Environmental Corrosion of L605 and Improved Monopropellant

Catalyst Screen Materials for Low Thrust Rocket Engines

A. N. Ewing[1], K. T. Kamber[2],
E. G. Kendall[3], and R. G. Sherman[4]
The Aerospace Corporation
El Segundo, California

ABSTRACT

A major difficulty encountered in designing long life monopropellant
hydrazine thrusters is that of providing structural elements, particu-
larly catalyst bed containment screens, capable of withstanding the
severe nitriding environment of hydrazine decomposition.   The use of
cobalt-based alloys such as Haynes 25 (L605) has gradually evolved.
Although much more durable than stainless steel, the Haynes 25 screens
are still subject to nitriding; after extneded usage, they become brittle
and crack, typically about 100, 000 pulses. It has long been known that
platinum is not susceptible to nitriding; however, its low tensile strength
makes it unsatisfactory for a containment screen material. For this
experimental investigation, platinum-iridium alloys were selected due
to the large tensile strength enhancement available from small per-
centages of iridium.

Metallurgical tests were conducted to define the basic characteristics
of the materials involved as an aid in material selection and to help
understand the basic phenomena involved in screen degradation.   Wire
samples and woven wire screens of Haynes 25, Pt-15% Ir, Pt-10% Rh
and Nichrome V were exposed to a nitriding ammonia atmosphere at
temperatures from 1300°F to 1700°F for up to 5000 min.   Metal-
lographic examinations were made to determine any microstructure
changes and to measure depth of nitride, if any; microhardness
measurements were made, and tensile tests at room temperature and
at elevated temperatures were run on the wire samples.   In addition,
woven screen samples were exposed to the nitriding atmosphere, then
subjected to applied loads from a spherical-ended rod at ambient and
elevated temperatures, as a measure of both strength and ductility.

The data indicate that the nitriding rate of Haynes 25 increases with
temperature.   The brittle nature of the nitride case suggests that the
failure mechanism at work in a thruster is one of progressive growth
of fatigue cracks formed in the brittle surface due to thermal cycling.
The platinum-iridium alloy did not exhibit any nitriding and remained

---

1.   Research Associate, Metallurgy Department
2.   Manager, Applied Metallurgy Section, Metallurgy Department
3.   Head, Metallurgy Department
4.   Consultant

ductile at all temperatures. The strength of the platinum-iridium alloy, while considerably less than that of Haynes 25 at lower temperatures, is about the same as Haynes 25 at the typical thruster catalyst bed maximum temperature of 1800°F.

I. INTRODUCTION

Hydrazine thruster requirements have increased to the point where Haynes 25 screens can no longer withstand thruster life testing without degradation to the point of hole formation and general embrittlement and loss of strength due to extensive nitriding. An improved material is needed for catalyst bed screens to withstand more than 10^6 pulses and 500 lb of hydrazine. Evaluation of such materials has generally consisted of empirical engineering data acquired from thruster testing. After the time and expense of such testing, it is often found that the selected material does not live up to expectations.

A series of metallurgical and engineering tests were conducted on screens made of Haynes 25 and platinum-iridium alloys and on wire of these materials and wires of nichrome and platinum-10% rhodium.

II. DISCUSSION

A. Metallurgical Considerations

Nascent nitrogen is a hydrazine decomposition product which can affect the chemical composition and physical properties of screen materials. The result of nitrogen attack on Haynes 25 is the formation of a hard case consisting of chromium, iron, and tungsten nitrides. This case is brittle and can be the cause of crack formation in stressed areas, such as the instance in which the woof wire in a screen bends around a warp wire. It is postulated that the additional stresses, caused by thermal cycling during pulse operation, cause the brittle outer nitrided case to crack. The cracks form during the quenching period and expose additional parent material to the nitriding atmosphere. During the subsequent quench, the weakened material cracks deeper in a self-propagating manner until the wire is completely severed.

Neither platinum nor iridium react with nitrogen, and an alloy of the two is expected to be equally inert. The basic tensile strength of platinum is low - 18,000 psi compared to 195,000 psi for cold drawn Haynes 25 at 70°F. The difference is less pronounced at 2000°F (see Table I). It was felt that sufficient iridium should be added to raise the tensile strength of the alloy as close to Haynes 25 as possible within the limits of ductility required for weaving. Several samples of 25% iridium were acquired; however, a screen lot containing 15% iridium was ultimately selected due to difficulties encountered in weaving the 25% iridium alloy. The resultant strength was predicted to equal that of Haynes 25 at 2000°F, and to be approximately 70,000 psi at 70°F. This was considered sufficient, based on a calculation of the stress incurred by a 10-mil diameter wire

86

Table I. Physical Property Comparison

Nitriding Susceptibility (in./min):

	$1300^{\circ}F$	$1700^{\circ}F$
Platinum - 10% Iridium	0*	0*
Platinum - 15% Iridium	0*	0*
L-605		
500 min	1×10^{-6}*	3×10^{-6}*
5000 min	0.2×10^{-6}*	1×10^{-6}*

Ultimate Tensile Strength ($lb/in.^2$)

	$70^{\circ}F$	$2000^{\circ}F$
L-605	195,000/185 000/ 165,000*†	14,000*
Platinum	18,000	4,400
Iridium	150,000	75,000
Platinum - 10% Iridium	55,000	10,000
Platinum - 15% Iridium	83,000*	15,000*
Platinum - 25% Iridium	125,000	30,000

Coefficient of Thermal Expansion (in./in. $-^{\circ}F$):

	$200^{\circ}F$	$2000^{\circ}F$
L-605	6.9×10^{-6}	10×10^{-6}
Platinum	5.1×10^{-6}	5.7×10^{-6}
Iridium	3.8×10^{-6}	4.3×10^{-6}
Platinum - 10% Iridium (estimated)	5.0×10^{-6}	5.5×10^{-6}
Platinum - 25% Iridium (estimated)	4.7×10^{-6}	5.2×10^{-6}

---

*Data derived from Aerospace laboratory tests

†Data for straight wire/kinked wire/nitrided wire, respectively

in a 40-mesh screen. If a single layer of unsupported screening were to withstand the upper catalyst bed pressure drop of 30 psi, the tensile loading would be 4850 lb/in^2.

The major stress placed on the screen is due to its thermal expansion and contraction, as well as that of the chamber and support ring to which it is brazed or welded. Analysis of this effect was not attempted; however, the coefficient of thermal expansion for platinum and its alloys appears favorable (Table I) compared to Haynes 25. The coefficient is lower by approximately one-half, indicating a potentially favorable reduction in the expansion and buckling forces on a contained screen. Resistance to crack formation during cooldown is a balance between tensile strength to withstand the stress and ductility to relieve it. Platinum and Haynes 25 represent two opposite ends of the spectrum. It was intended to reach the appropriate compromise with the Pt-Ir alloy, which would also exclude further reduction in both properties due to nitriding.

B. Apparatus and Procedure

1. Nitriding

Test specimens were nitrided in a 2-1/2 in diameter quartz tube which was inserted in a 12-in. long resistance heated tube furnace capable of temperatures up to 2000°F. An ammonia nitriding atmosphere was passed through the tube (see Figure 1) at a flow rate sufficient to maintain 70 to 90% dissociation. The temperature in the furnace was controlled by feedback from a platinum-rhodium thermocouple.

The specimens were placed in a quartz boat of sufficient size to ensure adequate specimen separation and ammonia circulation. In turn, the quartz boat was inserted into the quartz furnace tube adjacent to the control thermocouple. Test durations of 500 min and 5000 min were used. Early tests included cyclic heating to 1700°F and cooling to 250°F for 500 cycles, but did not cause cracking of L605 wire, probably because the screen was not stressed, and this technique was discarded.

The apparatus was used to condition wire and screen specimens prior to other tests, as well as to establish the nitriding characteristics of all materials at 1300, 1500 and 1700°F.

2. Tensile Tests

A 10,000-lb Instron machine was used. A 3-1/2 in. long resistance tube furnace with a 3/16-in. diameter inner ceramic muffle, was positioned vertically around the wire test specimen. The temperature field was plotted for each test temperature and calibrated to a control thermocouple on the outside of the muffle.

All tests were run in air. The 0.010-in. wire specimens were allowed to equilibrate for one minute prior to loading. The data were reduced in terms of ultimate and fracture strength and reduction in area at various temperatures and nitriding conditions.

88

3.   Screen Deflection Test Apparatus

The same tensile machine was used to apply a push load to screen specimens 1/2 in. in diameter. A fixture, shown in Figure 2, held the screen securely around its perimeter while a 1/2-in. diameter rod was pushed against it into a 5/16-in. diameter hole. The fixture was positioned within a standard 2200°F Marshal Furnace 14 in. long with a 2-1/2 in. inside diameter. Also shown are typical yielded "hat" sections formed in the test specimens.

All the samples (Haynes 25 and Pt-15% Ir) were first heat treated in the nitriding atmosphere at 1700°F for 500 min. Traces of load versus deformation length were developed for various temperatures.

4.   Microhardness Testing

Tests were run using a diamond pyramid impressor with a 10 and 50 gm load. Measurements were made along the end diameter of a wire potted in lucite, and converted to equivalent Rockwell readings.

C.   Results

1.   Nitriding

Nitriding is a chemical and diffusion process whose rate is controlled by time and temperature. In commerical terms, L605 is not considered a nitriding material because the rate is extremely slow as compared to nitriding steels at conventional nitriding temperatures (1050°F). However, at the higher temperatures encountered in thruster applications, the nitriding rate of L605 is increased as much as fivefold. Also, since the wire is of small diameter, a nitride case of 0.001 in. becomes significant. Figures 5 and 6 show the as-received microstructure and the 1500°F, 500-min nitride case, respectively, using a modified Fry's etch and 250X magnification. The fact that the nitriding reaction is time and temperature dependent is shown by comparing the nitride case formed after 500 and 5000 min at 1500°F, and 5000 min at 1700°F, as shown in Figures 6 through 8. At the higher temperature and longer time, the case is approximately 90% of the entire cross section.

Previous published work indicated that Nichrome V did not nitride. However, Figure 9 shows that this material will nitride, under the environmental conditions of the present study, at a rate less than that of L605. Figure 10 shows that the Pt-15% Ir does not nitride, and there were no surface effects from a 5000 min exposure at 1700°F.

2.   Tensile Strength

The differences are quite large at room temperature but decrease markedly at temperatures above 1300°F. Listed below in Table II and plotted in Figure 11 are the ultimate strengths of the as-received materials

89
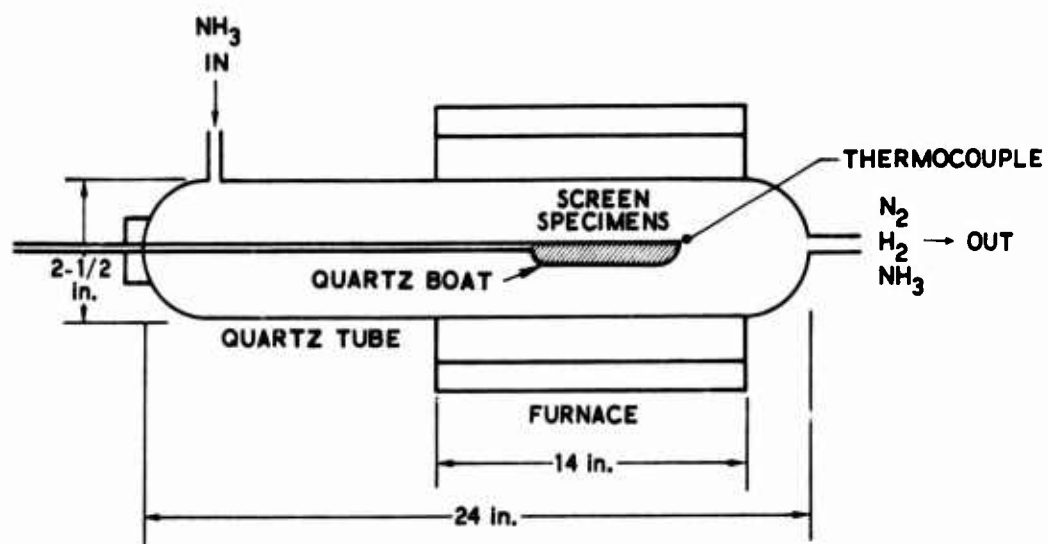
Fig. 1.   Laboratory Nitriding Apparatus

Screen Deflection Test Fixture

L-605   Pt - 15% Ir

TYPICAL TEST SPECIMENS
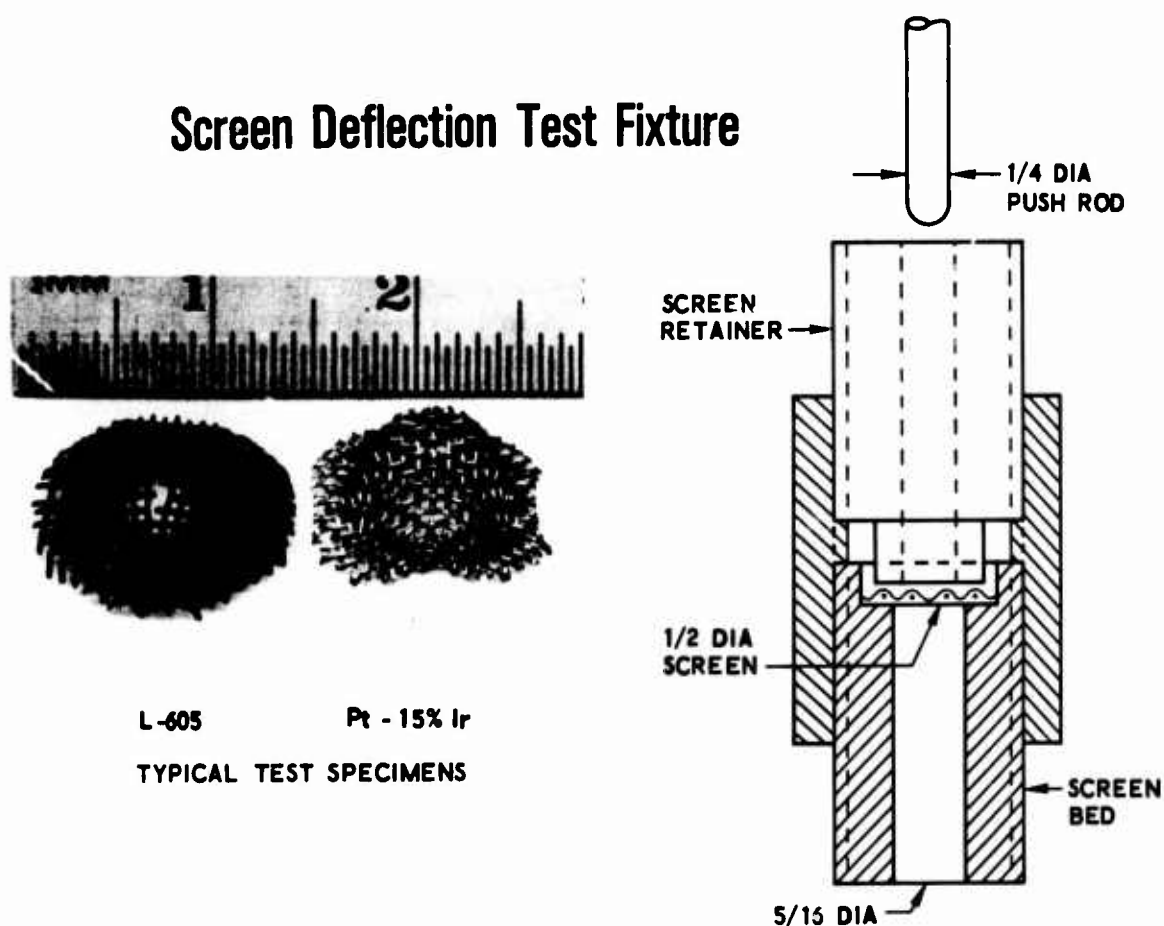
Fig. 2.   Screen Deflection Test Fixture

Fig. 5   L-605 Wire, As Received
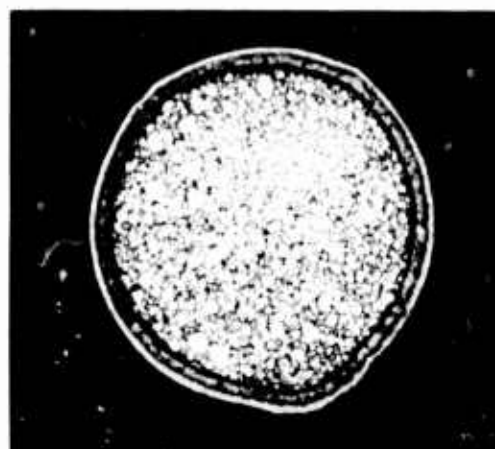
Fig. 6   L-605 Wire, Exposed to NH$_3$ at 1500°F for 500 min

Fig. 7   L-605 Wire, Exposed to NH$_3$ at 1500°F for 5000 min

Fig.   8 L-605 Wire, Exposed to NH$_3$ at 1700°F for 5000 min
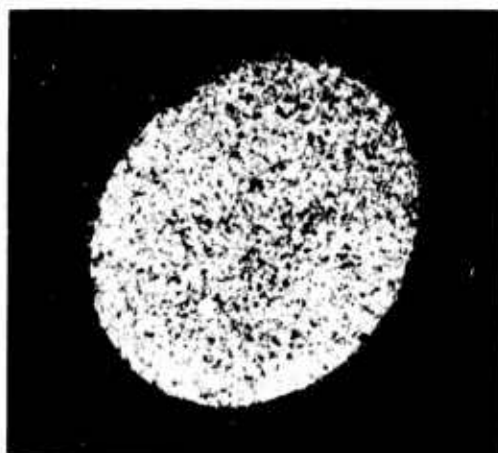
Fig. 9   Nichrome V Wire, Exposed to NH$_3$ at 1300°F for 5000 min
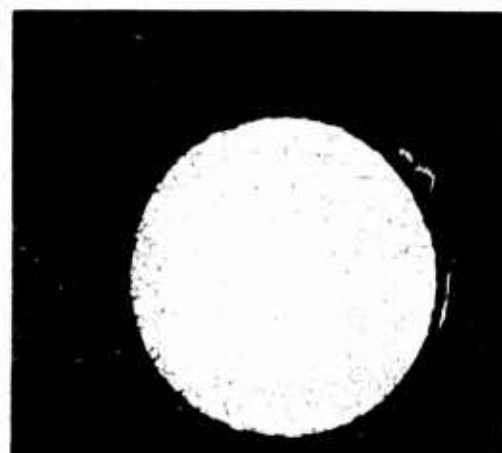
Fig. 10   Pt-15% IR Wire, Exposed to NH$_3$ at 1700°F for 5000 min

91

at room temperature, 1700°F and 2000°F. The platinum base alloys retain a greater percentage of their room temperature strength at high temperatures but, in absolute terms, L605 has higher strength at temperatures up to 2000°F.

Table II. Ultimate Tensile Strength of Un-nitrided Wire

Material	70°F (ksi)	1700°F (ksi)	2000°F (ksi)
L-605	195	36	14
Nichrome V	132	8	4
Pt-15% Ir	83	24	15
Pt-10% Rh	48	10	8

More important for thruster applications is the strength after exposure to the severe service conditions. The relative tensile characteristics, after long-time nitriding exposure, are shown in Figures 12 through 14, and the individual characteristics of each material are shown in Figures 15 through 18. The tensile strength of the platinum alloys was unaffected by the severe simulation of service environment; however, the strengths of the Nichrome V and, to a greater extent, the L-605 were degraded by the exposure.

This degradation in L-605 tensile strength is exhibited at room temperature and up to 1300°F. At higher temperatures, the metal nitrides appear to increase strength slightly, as computed using the original cross-sectional area of the 0.010-in. diameter wire. Actually, the L-605 nitriding caused an increase in diameter of up to 0.001 in. Use of this enlarged area would decrease the strength up to 21%. Therefore, the cross-over effect illustrated in Figure 16 should not be considered a real effect.

In order to compare the effect of the nitride case on the L-605 woven wire and on the smooth wire, individual strands of the woven wire were tested. These strands had kinks from weaving which could act as notches if the material were embrittled. The results are shown in Table III.

The data indicate a 10 to 45 ksi reduction due to kinks, and the severe degradation caused by the nitrided case. The 1700°F - 5000 min exposure results in a cross-section almost entirely of nitrided L-605. The shorter times and lower temperature samples are, in actuality, composite materials with a hard case ar i soft core. The brittle case is cracked as the kinks attempt to straigh.en under the tensile load. The apparent increase in strength with nitriding temperature is due principally to the area effect and may also be related to the fact that the nitride formed at high temperature is softer and less friable than that formed at the lower temperatures (see Section C-3).

92

No data are presented on the reduction of area prior to specimen fracture because it was so erratic. Generally, the platinum alloys were ductile and exhibited good reductions of area at all temperatures and after all exposures. The L-605 in the as-received condition also showed excellent ductility. However, after nitriding the reduction in area was nil.

Table III. Ultimate Tensile Strength of Individual L-605 Woven Wire Strands After Exposure to Various Temperatures and Atmospheres

Atmosphere	Condition	Ultimate Strength at $70^{\circ}F$ (psi)
- - - -	As received	185,000
NH_3	$1300^{\circ}F$ - 500 min	98,000
NH_3	$1300^{\circ}F$ - 5000 min	90,000
NH_3	$1500^{\circ}F$ - 500 min	110,000
NH_3	$1500^{\circ}F$ - 5000 min	90,000
NH_3	$1700^{\circ}F$ - 500 min	141,000
NH_3	$1700^{\circ}F$ - 5000 min	98,000
VAC	$1700^{\circ}F$ - 5000 min	169,000

3.   Hardness

The microhardness measurement results are shown in Table IV. The higher hardness of the $1700^{\circ}F$ core is attributed to some partial nitriding, as shown in Figure 8.

Table IV. Rockwell Hardness Values for 0.010-in. L-605 Wire Nitrided at Various Temperatures for 500 Min

Sample	Core, R_c	Case, R_c
As received	45	- -
$1300^{\circ}F$ Nitride	45	67
$1500^{\circ}F$ Nitride	45	60
$1700^{\circ}F$ Nitride	47.5	53

For thruster fabrication, the bed screens are typically brazed to their supports at $1950^{\circ}F$ for 5 min. Therefore, a series of nitriding and hardness tests were performed on woven wire samples after a $1950^{\circ}F/5$ min vacuum treatment. This resulted in annealing and also a significantly lower core hardness. The depth of case was not affected; however, the final case hardness was as described in Table V.
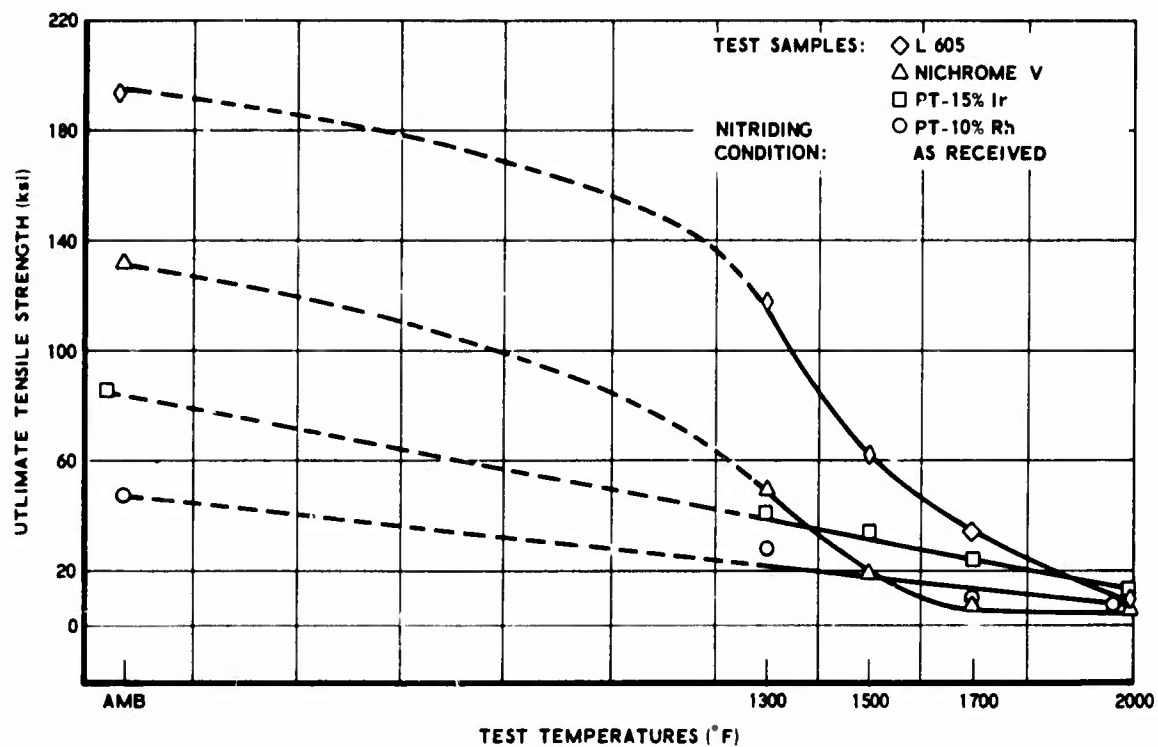
Fig. 11 Tensile Strength at Various Temperatures
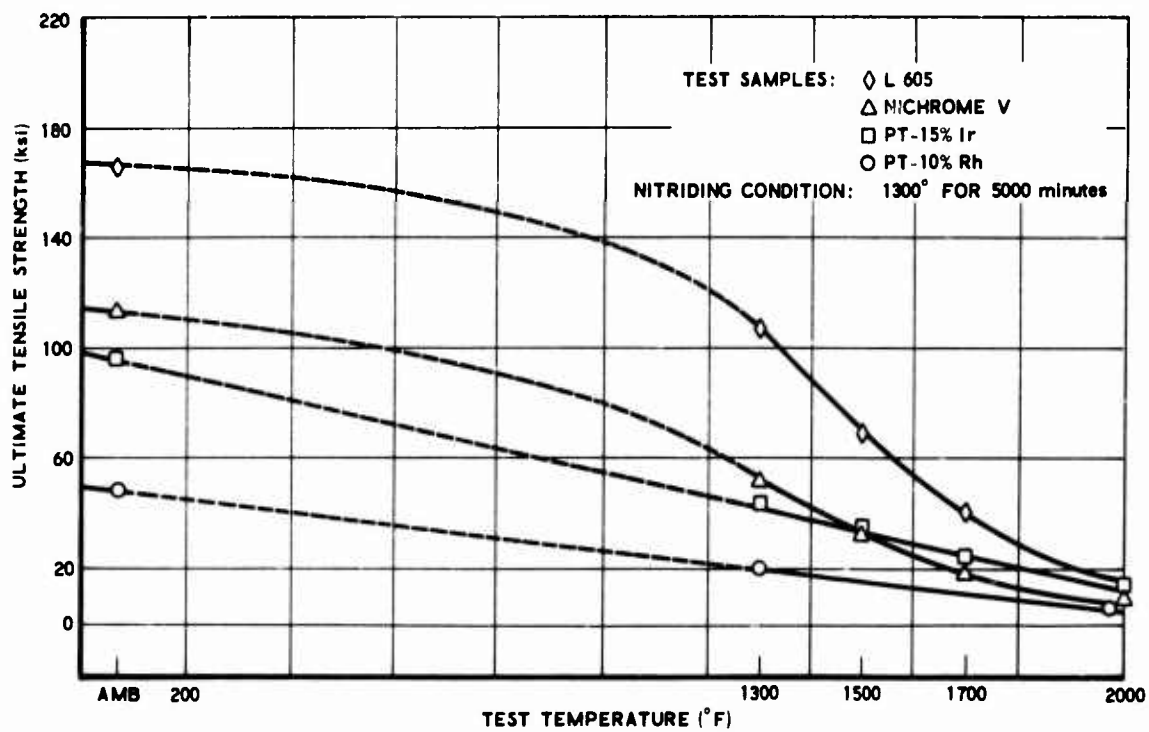
Fig. 12 Tensile Strengths at Various Temperatures

94
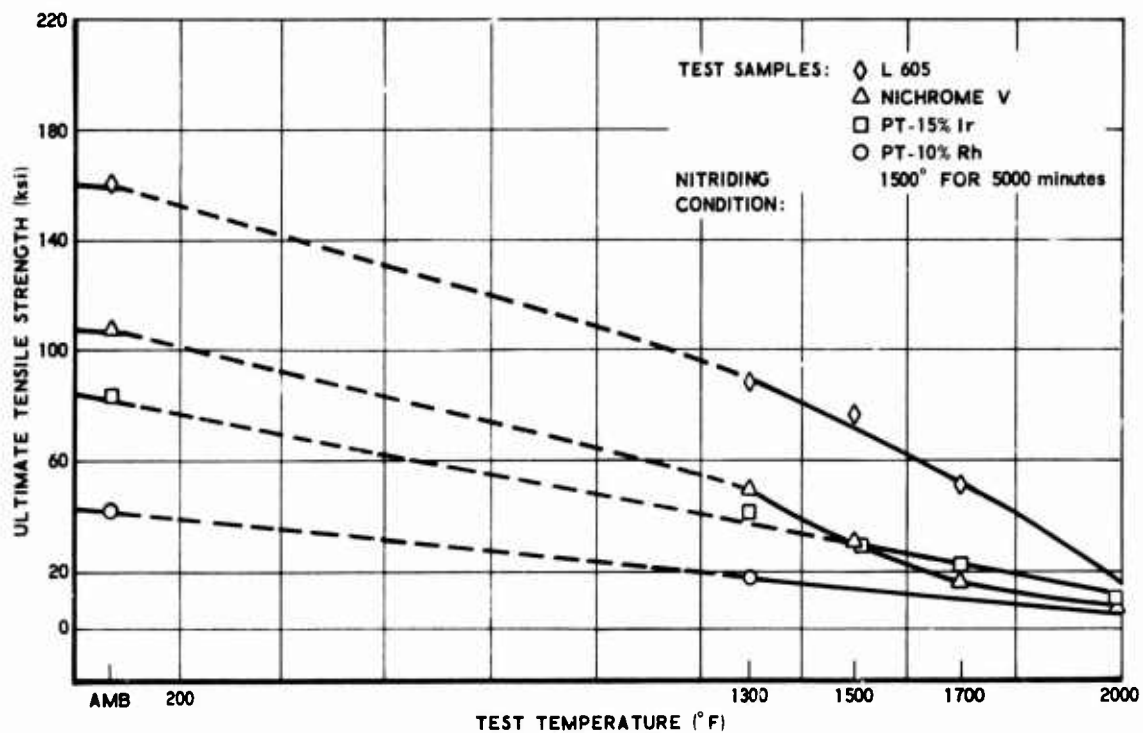
Fig. 13   Tensile Strengths at Various Temperatures
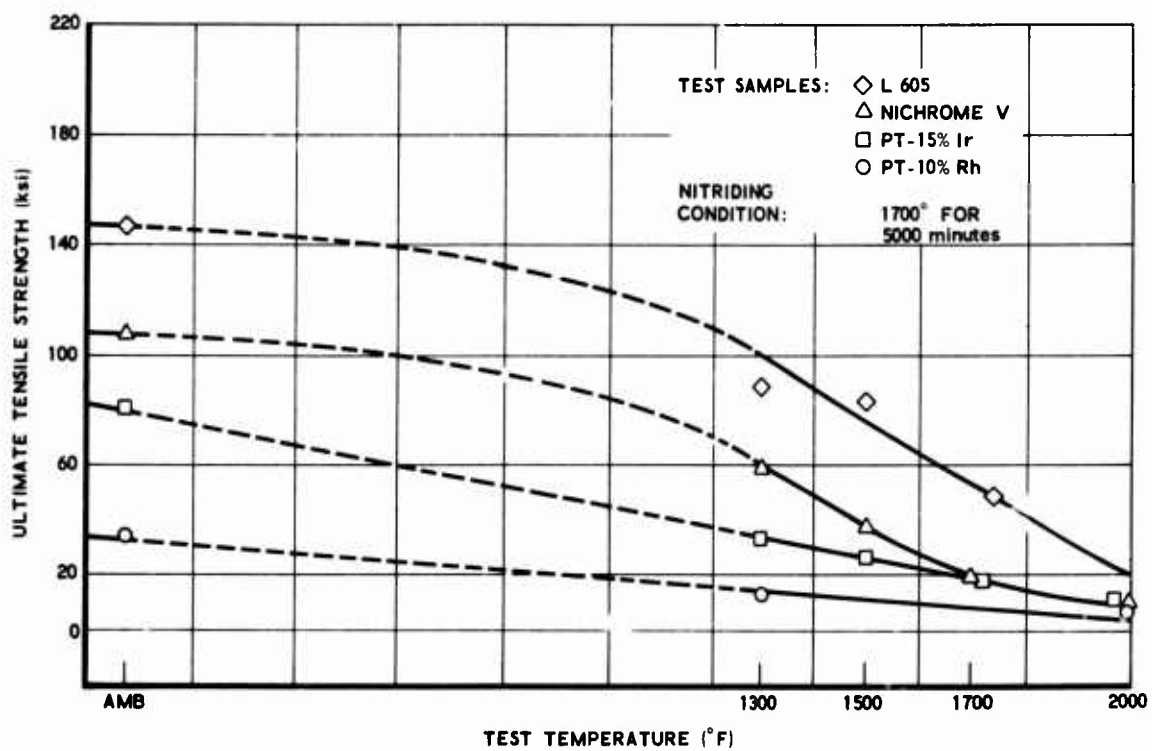
Fig. 14   Tensile Strengths at Various Temperatures
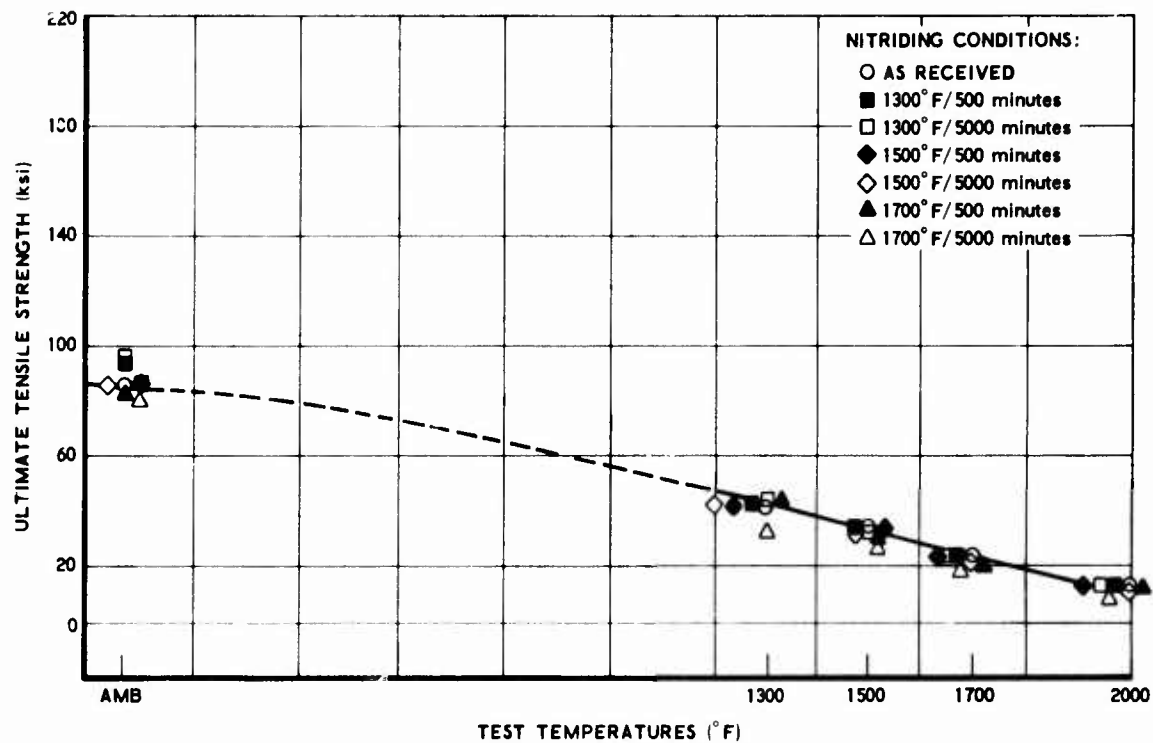
Fig. 15   PT-15 IR Tensile Strengths at Various Temperatures
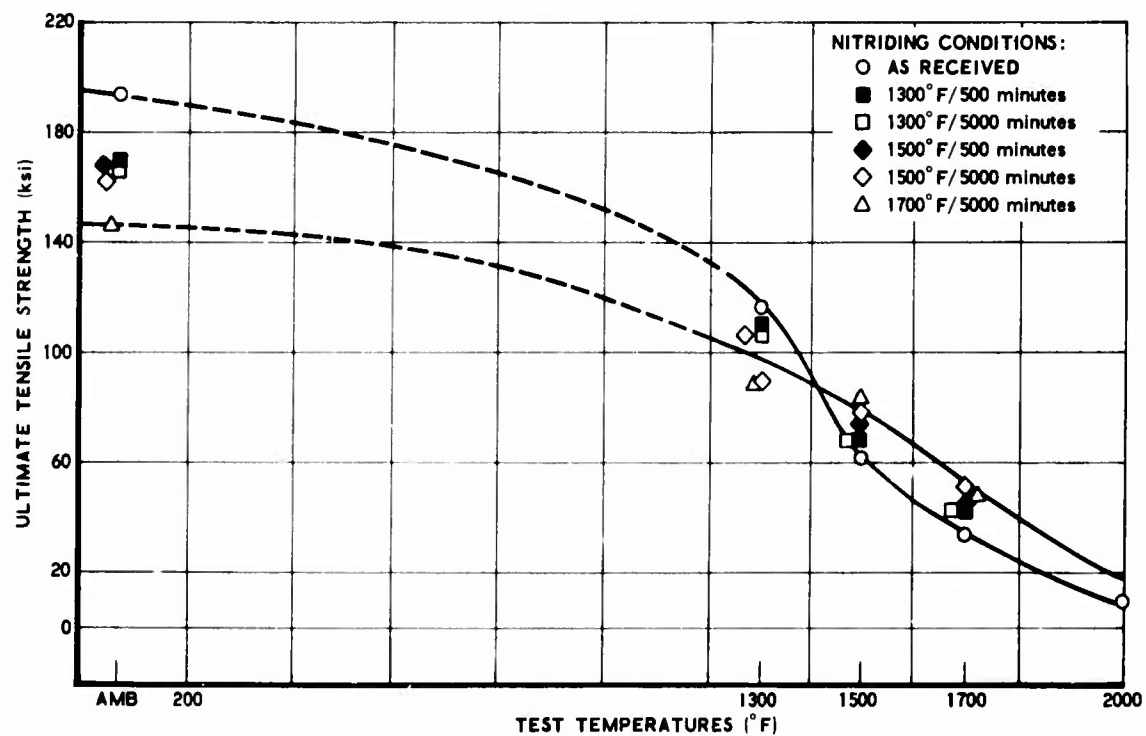
Fig. 16   L-605 Tensile Strength at Various Temperatures

96
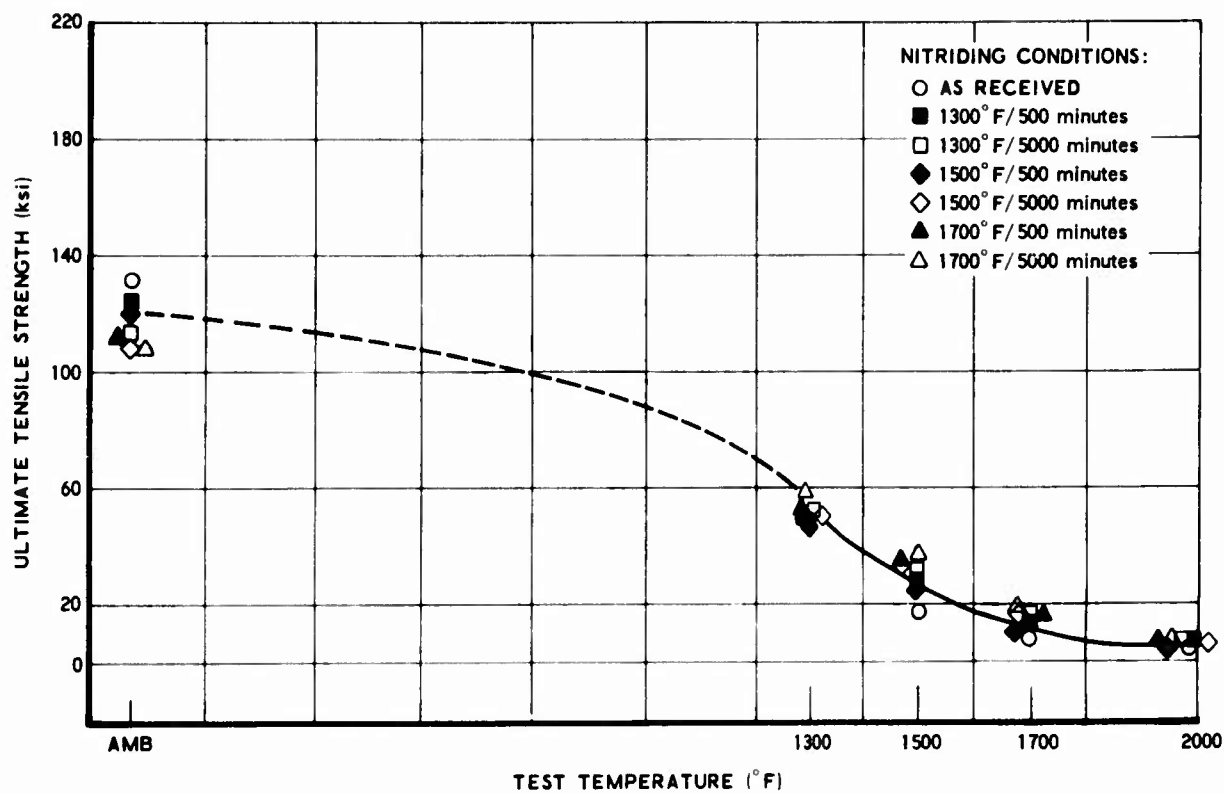
Fig. 17   Nichrome Tensile Strength at Various Temperatures
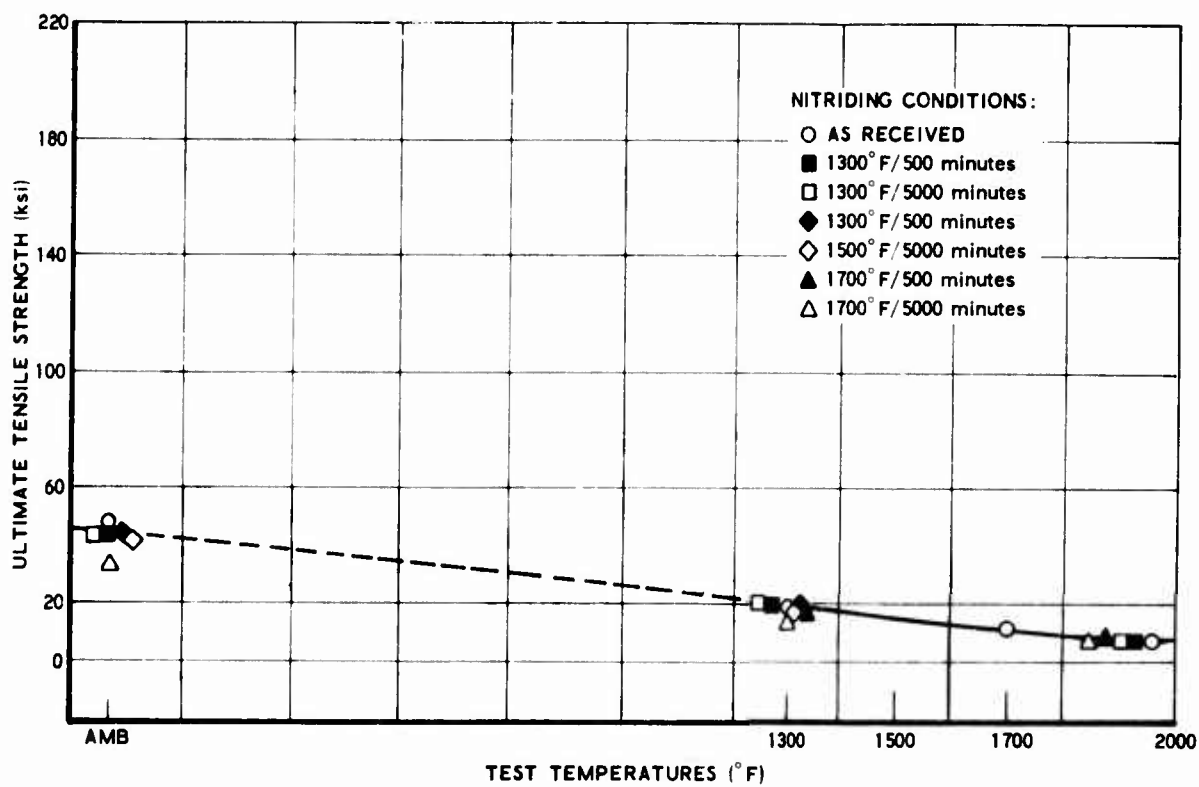
Fig. 18   PT-10 RH Tensile Strengths at Various Temperatures

97

Table V.   Rockwell Hardness Values for 0.010-in. L-605
          Wire Annealed at 1950°F for 5 min and Then Nitrided

Sample	Core, R_b	Case, R_c
As annealed	98	--
1050°F Nitride*	98	58
1300°F Nitride	97	56.5
1500°F Nitride	97	56
1700°F Nitride	97	43.5

*Normal commercial nitriding temperature

The data in Tables IV and V indicate that nitride case hardness is directly affected by the basic hardness of the starting material and is dependent upon the nitriding temperature.

4.   Screen Deflection Tests

The results of the screen deflection tests of Haynes 25 (L605) and Pt-15% Ir woven screen samples are shown in Figure 19, wherein the maximum load sustained by the screen specimen prior to yielding or failure is plotted versus test temperature.   Because of the constraints of the compression test fixture and the ductility of the Pt-15% Ir material, those screen samples had a much higher maximum load than the L-605 samples over much of the test temperature range.   The maximum loads for the L-605 samples exceeded those for the Pt-15% Ir samples only after the test temperature reached approximately 1500°F.   All the samples were initially subjected to the same nitriding atmosphere at 1700°F for 500 min.

Figure 20 illustrates the typical L605 "saw-tooth" load curves which correspond to a load reduction as individual strands crack and break.   Up to   1000°F there is an initial discontinuity (at a load of   6 lb) which was accompanied in some cases by an audible "tink" sound resulting from fracture of the first wire.   This point is the initial failure load which is also plotted in Figure 19.   Also shown is the specific depressed "hat" section test specimen, which incurred strand failure.

Figure 21 illustrates that at temperatures above 1500°F the nitrided layer on the L605 samples makes a transition from a brittle to a ductile material, and the load deflection curves take on the appearance of the Pt-15% Ir curves.   The Pt-15% Ir screen samples were ductile throughout the entire test temperature range of 70°F to 1900°F, as evidenced by the yielded but unbroken test specimens.

98
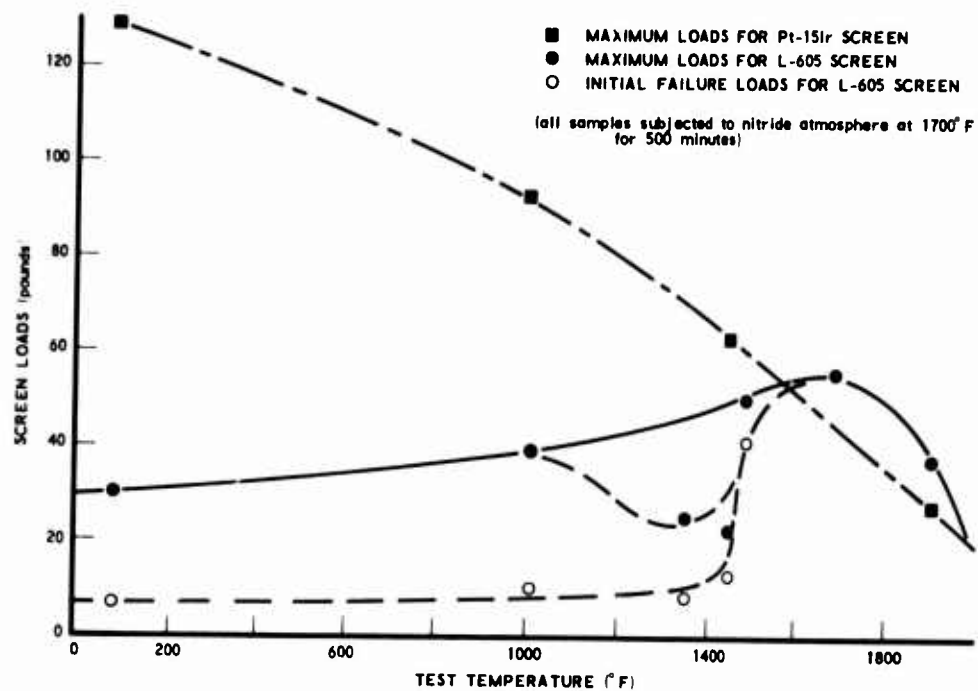
Fig. 19.   Screen Deflection Test
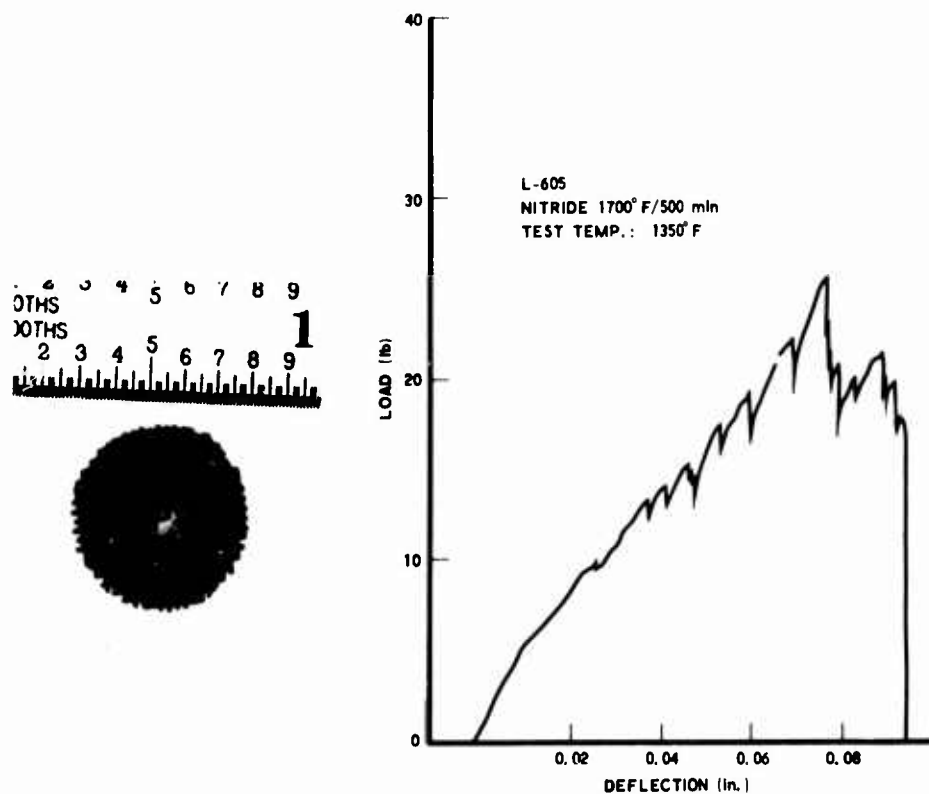
Fig. 20.   Screen Deflection Test

99
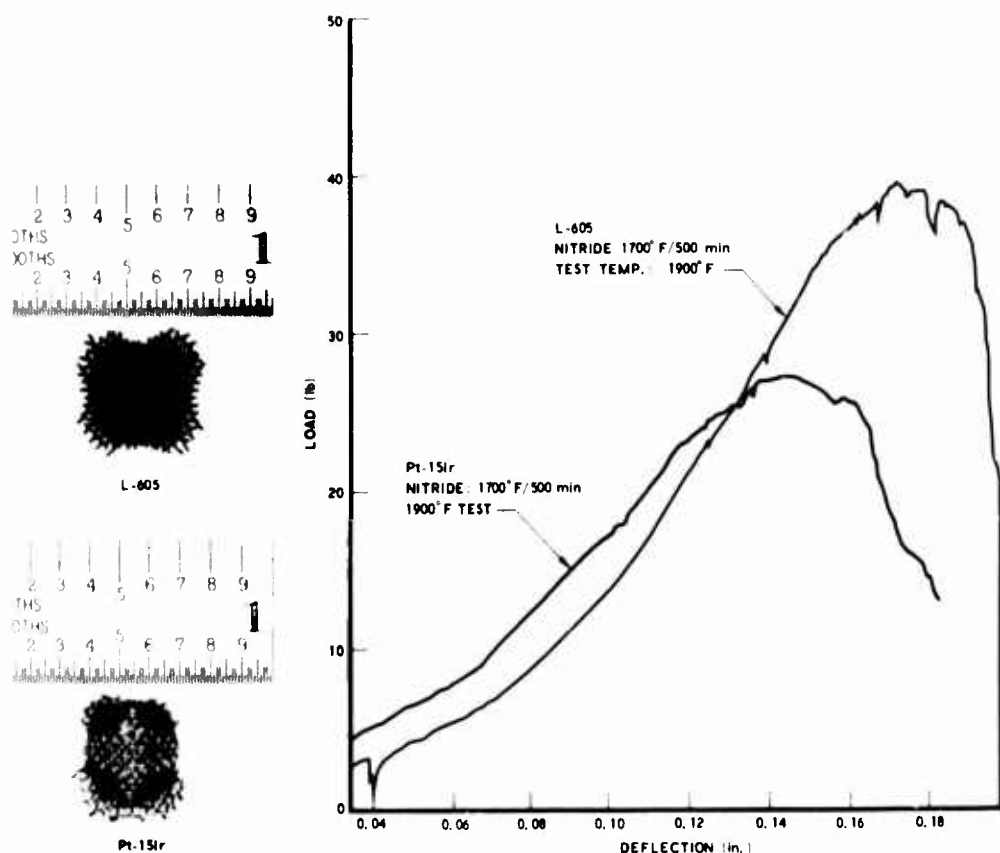
Fig. 21. Screen Deflection Test

III. CONCLUSIONS

The following conclusions are drawn from the results presented in this paper:

Pt-15% iridium is more suitable than Haynes 25 (L605) for hydrazine thruster catalyst bed retention screens. The increase in ductility is more significant than the accompanying loss in ultimate tensile strength.

Fundamental metallurgical laboratory tests can be used for catalyst bed screen material selection to reduce the scope of thruster development programs.

IV. RECOMMENDATIONS

It is recommended that metallurgical investigation of Pt-Ir alloys should continue for possible improvement of resistance to crack formation in a screen matrix. Included in the study should be a stronger alloy (20 to 25% iridium) and a more ductile alloy (10% iridium).

100

Similar metallurgical properties for alternate materials in use should be established for correlation with thruster life test results.

Finally, an improved laboratory test should be developed to force crack formation in a screen matrix due to thermal cycling in a nitriding atmosphere.

SATURN IB/SKYLAB IV STRESS CORROSION PROBLEMS

P. M. MUNAFO
T. O. KNIGHT

CHRYSLER CORPORATION SPACE DIVISION

SATURN IB/SKYLAB IV STRESS CORROSION PROBLEMS

INTRODUCTION

The highly successful NASA Skylab Program was completed upon the return of the third crew on February 9, 1974 after 84 days in earth orbit. Each of the crews composed of three astronauts had been launched to their Skylab missions by Saturn IB vehicles designed and built as part of the Apollo Program. A typical view of the launch vehicle, in the process of rollout from the Vehicle Assembly Building to Launch Complex 39B at the Kennedy Space Center, is shown in Figure 1. Saturn Vehicles 206, 207, and 208 were used for crew launch.

The three Saturn IB stages flown in the Skylab Program (S-IB-6, S-IB-7, and S-IB-8) were assembled and static fired in 1966 for launches scheduled in 1967. They were part of the Saturn IB series of launch stages originally intended for the purpose of qualifying Apollo hardware in earth orbit prior to the lunar landing. Many dual launches were planned and a total of fourteen S-IB stages were built. However, as the Saturn V lunar program accelerated, and confidence in the Apollo were increased, S-IB missions were reassigned and flown on a Saturn V Stage. The five Saturn IB missions flown were successful, thereby eliminating the need for S-IB Stages to back up subsequent Apollo missions. The nine remaining stages from the Apollo Program were placed in storage.

The potential for problems arising from the extended life of the S-IB Stages was recognized and a storage plan was placed in effect. Each stage was stored in a tent enclosure within the Michoud Plant, beginning in 1968. The control of temperature, humidity and contaminants in the enclosure was subject to specified verifications. Storage was discontinued for each Skylab assigned stage in 1972 according to the scheduled requirements of checkout, preparation for shipment and launch.

Design applications of stress corrosion susceptible alloys became a matter of concern as additional technical knowledge of such alloys was generated and the age of the hardware increased. An inspection procedure was prepared for selected structural and mechanical parts. Periodic inspections were to be performed at the Michoud Plant after each stage was removed from storage and at Kennedy Space Center after erection for launch. The final inspection was required to be accomplished within thirty days of launch.

All stress corrosion inspections were negative for the S-IB-6 and S-IB-7 Stages, but two incidents of stress corrosion cracking of primary structural parts occurred on the S-IB-8 Stage. This paper presents the rationale that was used to assure the structural integrity of that stage as a result of the cracks in the rear spar attach points for the fins and in one E-beam of the thrust support structure.

The science of Linear Elastic Fracture Mechanics was used to develop a systematic approach to the problem of fracture control of stress corrosion susceptible structure. The basic elements of the approach are shown in Figure 2. The rectangular elements are fracture mechanics properties or calculations and the circular elements are inputs from other disciplines. A flaw must already be present in the material, having been produced by chemical or mechanical means (e.g., corrosion or fatigue) or introduced during the manufacturing process. Sustained stress is introduced into the part as residual stress from the fabrication process, assembly stress from clamp-up effects or long-time service loads. Through the use of the stress intensity, K, as a data correlation parameter, laboratory data on stress corrosion

threshold (K_{ISCC}) and crack growth rate ($\frac{da}{dt}$) can be used to define service conditions which will cause initiation of crack growth, crack growth rate and eventual crack size. Laboratory data on fatigue crack growth rate ($\frac{da}{dN}$) and critical stress intensity (K_c) can be used with design stress data to predict in-service crack growth and critical crack size. Results of these analyses provide input to the formulation of a fracture control approach, which can lie within a spectrum ranging from "use as is" to "change design."

The fin analysis focused on the mechanism of crack formation, while the E-beam analysis involved almost the full procedure outlined in Figure 2. A discussion of those problems and their solution follows.

STRESS CORROSION CRACKING OF THE REAR SPAR OF THE S-IB-8 STAGE FINS

The inboard rear spar, Figure 3, is processed as a closed die forging of 7079-T652 Aluminum Alloy. It is approximately 42" x 24" x 12" in size and the final machined part weighs 52 pounds. It is one of two inboard spars which attach each of the eight fins to the S-IB Stage, Figure 4. Fins are shipped separately to the Kennedy Space Center in containers and are attached to the stage upon erection in the Vehicle Assembly Building. The fins have a flight function and, in addition, are the support base for the stacked space vehicle, Figure 1, prior to launch.

Stress corrosion inspections of the S-IB-8 Stage fins, prior to shipment to the Kennedy Space Center and reinspection during the period September 26, 1973 to October 2, 1973 while on the launch pad, did not reveal any cracks.

The cracked spars were discovered on November 6, 1973 during the final stress corrosion inspection which was performed after full propellant loading of the space vehicle had been performed as part of the Countdown Demonstration Test conducted four days earlier. At the time of inspection, the fuel tanks were loaded and the extent of cracking in the lower spotface area of the left and right hand mounting pads of the rear spars was clearly visible, Figure 5. Fifteen of the total sixteen locations on the eight fins exhibited cracks of varying lengths extending from the edge of the mounting pad to approximately 3/4 inch inboard of the spotface.

Although the cracks differed in length, the upper circumference of each spotface was involved. A typical view is shown by fluorescent dye in Figure 6. The absence of a radius on the spotface tool, which created a sharp notch effect in the corner of the spotface, is apparent in Figure 7. Also, damage to the protective coatings is evident. Damage to protective coatings is incurred in the process of attachment of the fins to the S-IB Stage and also because this bolt hole is an attach point for holding fins in shipping containers.

Macro examinations of metallurgically polished sections of the mounting pads revealed that the forging process produced a grain flow transition which resulted in a short transverse grain in the area of the cracks, Figures 8 and 9.

Evidence of pitting corrosion, Figure 10, was observed. However, a clear indication of a point of initiation for any of the fractures was not determined. The microstructure, Figure 11, is typical for a 7079-T652 aluminum forging alloy. The hardness was Rockwell "E" 109 and spectrographic analysis confirmed the composition to be 7079, as specified.

Fracture studies conducted by the Metallurgical Analysis Branch, Materials and Process Laboratory, MSFC, confirmed that stress corrosion cracking was the mode

of failure. The SEM micrograph, Figure 12, indicates an intergranular fracture with secondary cracking and corrosion products. The fractograph, Figure 13, depicts the "rock candy" appearance characteristic of stress corrosion.

The cracking of the fin spars in fifteen of sixteen locations presents a classical case of stress corrosion. The sharp notch in the spotface circumference, coincident with the short transverse grain, damage to the protective coatings and exposure to the corrosive environment at the launch pad, are factors which, combined with sustained tensile stresses and age, resulted in cracking of this stress corrosion susceptible alloy.

The criteria flight loads and crack geometry were sufficient to cause propagation of the existing cracks during flight. It was impractical to predict final crack length and net structural capability without testing one or more cracked fins. Because replacement fins were available, the decision was made to replace all of the cracked fins. The fact that cracking had occurred at fifteen of sixteen possible locations during an apparently short time frame raised the question of the cause of the cracking. More specifically, it was necessary to determine whether it was possible for the cracking to occur again during the time period preceding launch.

The most significant fracture mechanics properties for this problem pertain to sustained stress flaw growth behavior. Figure 14 is from the Damage Tolerant Design Handbook, MCIC-HB-01, and represents a composite plot of available crack growth data, with crack growth rate plotted as a function of the stress intensity parameter, K. This represents averaged data for plates and die forgings in a salt solution, hence is not strictly applicable to this problem, but it was an adequate representation for the purpose at hand. Figure 14 shows a plateau value of 2-3 inches per hour for the flaw growth rate, at stress intensities ranging from 11 KSI $\sqrt{in}$ upward. This is a very high sustained stress flaw growth rate - the highest reported in the Damage Handbook for any aluminum alloy. Figure 14 also shows that flaw growth has been observed at stress intensities as low as 4 KSI $\sqrt{in}$, but in consideration of the less severe environment and the short service life of the replacement fins the threshold stress intensity (K_{ISCC}) was taken as 7 KSI $\sqrt{in}$.

The initial flaw depth was taken as .002 inches, which was the depth of corrosion pits which had been observed at the fin spar pad location on the cracked fins, Figure 10. This is a resonable assumption, since all fins receive the same protective coatings and are stored under the same conditions.

The constant stress required for stress corrosion crack growth is induced in the fin spar pad by three mechanisms - residual stress due to the manufacturing process, assembly stress due to clamp-up effects during fin installation and stresses resulting from normal service loads. Residual stress measurements were made by the blind hole drilling method at thirteen locations on each of two production fin spar forgings. The highest tension stress recorded was 8.0 KSI, and the mean residual tension stress was 3.5 KSI. Typical residual stress profiles are shown in Figure 15. Assembly stress was evaluated experimentally using an instrumented fin assembly, and it was determined that a stress of 3.0 KSI could be expected in the crack-opening direction due to clamp-up effects. Service stress levels were determined by extrapolation of structural test data. These are introduced at the fin attachment locations by "heel and toe" loads due to vehicle weight, so they vary with the amount of fuel on board. During most of the prelaunch period, the vehicle is empty and the service stress is 3.1 KSI. The non-cryogenic fuels are loaded approximately two to three weeks preceding launch and stay on board thereafter. The service stress for this condition is 7.7 KSI. The cryogenic fuels are on board for

several hours during Countdown Demonstration Test (CDDT), which is approximately one week before launch, then are reloaded a few hours before launch. This produces a stress of 22.3 KSI.

Stress concentration effects cause a sharp increase in the sustained stress level in the vicinity of the sharp corner of the spotface. This stress concentration factor was estimated from handbook data as lying within the range of 3.0 to 8.0. The stress level is increased by this factor immediately at the corner, but drops off sharply with distance from the notch. In consideration of the spar pad geometry and the loading conditions, .050 was taken as a reasonable estimate of the zone of influence of the stress concentration effect.

Figure 16 is a plot of stress level required for crack growth versus effective surface flaw depth ("a/Q"), assuming a threshold stress intensity of 7.0 KSI $\sqrt{in}$. Figure 16 shows that a flaw depth of .002 requires a sustained stress level of 82 KSI to initiate crack growth. This is an invalid flaw growth threshold because it is above the material yield strength of 60 KSI. In such cases, the conservative approach is to set the threshold equal to the yield strength, hence the criterion for initiation of flaw growth from a corrosion pit was set at 60 KSI. Another significant criterion is the stress required to sustain flaw growth outside of the zone of influence of the stress concentration effect. This is the stress level corresponding to a stress intensity of 7.0 KSI $\sqrt{in}$. at a flaw depth of approximately .050, which is shown in Figure 16 to be 16 KSI. Hence the minimum design stress level which can cause extensive cracking was taken as 16 KSI.

Table 1 summarizes the crack growth potential for each of the on-pad design conditions. The maximum stress range represents a stress concentration factor of 3.0 to 8.0 applied to the total mean stress level defined earlier, and is the range of stress levels which are possible at the corner of the spotface. As stated above, initial crack propagation from a corrosion pit can occur within the stress concentration zone if the maximum stress exceeds 60 KSI and propagation can continue if the sustained stress exceeds 16 KSI. Table 1 shows that limited crack growth is possible prior to loading cryogenics and that extensive crack growth can occur while the vehicle is fully loaded. Referring to Figure 14, flaw growth rate increases sharply with stress intensity for this material until the limiting "plateau" value is attained. Since stress intensity varies linearly with the stress level, and the on-pad fully-loaded condition produces a stress which is significantly above the threshold, it appears that rapid flaw growth is possible at this time. Although this condition exists for only two to three hours prior to launch, the possibility of cracking on the replacement fins could not be ruled out.

A fitting was designed to provide local reinforcement at the fin attach points in the event of further cracking. This fitting is shown in Figure 17. A structural test of a cracked fin with fittings installed demonstrated an adequate factor of safety. Based on that test result, the decision was made to resume the countdown procedure following installation of uncracked, reinforced fins.

STRESS CORROSION CRACKING OF UPPER E-BEAM OF THE S-IB-8 STAGE THRUST STRUCTURE

The upper E-beam is processed from a hand forged billet of 7178-F aluminum alloy. The process sequence is: rough machine, solution treat, straighten, age to T6, finish machine and apply alodine plus two spray coats of zinc chromate primer. The part is approximately 82" x 7" x 6" in size and the final machined part weighs 50 pounds.

The E-beams are the upper and lower structural members for the eight outrigger assemblies. They are fastened to the outrigger shear panels, Figure 18, and

107

a pair of these assemblies is joined together to form one outrigger assembly. The outriggers are attached to the center barrel, Figure 19, and extend radially outboard to provide attaching points for the fins, support the eight 70-inch diameter propellant tanks and resist the thrust loads of the four outboard engines.

E-beam cracks were first discovered on S-IB-9 which was the backup stage for the Skylab 4 mission. Cracks were noted on two upper E-beams during the installation of fins on August 24, 1973. Inspection of the complete inventory of E-beams revealed one crack in the Fin 4 upper E-beam of the S-IB-8 Stage. The crack was located in the lower bay of the beam eight inches from the inboard end and was approximately 2.5 inches long, Figure 20.

A coupon, containing the entire crack area, was removed from the E-beam and subjected to metallurgical examination. Fracture studies conducted by the Metallurgical Analysis Branch, Materials and Process Laboratory, MSFC, confirmed that stress corrosion cracking was the mode of failure, reference Figure 21. The microstructure was normal for a 7178 T6 alloy in all areas where cracks occurred. It was noted that the fracture surfaces were very close together (tight cracks) and a tenacious oxide film existed on all fracture faces. Because the stages were stored from August 1968 to March 1972 in a controlled environment, it is reasonable to assume that it took a long time to build up such an oxide film and that these were old cracks. The discovery of zinc chromate primer in one crack (S-IB-9) further substantiates this assumption. It was significant to note that the E-beam cracks all occurred in planes parallel to the long dimension of the part, but there was no preferred location or orientation otherwise.

The E-beams were repaired by replacing the cracked material with auxiliary hardware. A typical repair is shown in Figure 22. Because the possibility of additional cracks occurring could not be excluded, a fracture control rationale was required for the E-beams. The basis for that rationale was in linear elastic fracture mechanics, and it encompassed most of the procedure outlined in Figure 2. Standard fracture mechanics tests were conducted, using specimens cut from production E-beams to establish Mode I and Mode II fracture toughness (K_{IC} and K_{IIC}), sustained stress flaw growth threshold (K_{ISCC}) and sustained stress flaw growth rate (da/dt). Residual stress measurements were taken on flight configuration spare parts. The test data were used with stress analysis results to quantitatively evaluate the possible extent of cracking and resulting structural behavior.

Static fracture tests were conducted on thru-thickness cracked specimens, with all cracks in the transverse grain direction. The specimen load lines were oriented at varying angles to the crack to impose combined tension and shear loading in varying ratios. This "mixed mode" loading condition exists in most areas of the E-beams which are susceptible to cracking. The test results are presented in Figure 23 as a plot of Mode I vs. Mode II stress intensity at failure, each one normalized by the single-mode critical stress intensity, 24 KSI $\sqrt{in.}$ and 26 KSI $\sqrt{in.}$, respectively.

Sustained stress flaw growth behavior was evaluated using double cantilever beam (DCB) specimens. The DCB specimen provides a decreasing stress intensity with crack growth for constant displacement of the load points. The specimens were initially loaded to a stress intensity close to the failure point. The crack growth rates measured early in the test gave an indication of the maximum crack growth rate attainable under stable conditions. The stress intensity at crack arrest was taken as K_{ISCC}, the minimum stress intensity for flaw growth under sustained stress conditions. A total of eight specimens were tested, four each in distilled water and salt water to bracket the seacoast environment at the launch facility. Five of the eight specimens showed no growth at stress intensities ranging from 7.0 to 28.0 KSI $\sqrt{in.}$

108

Of the remaining three specimens, the lowest stress intensity at which crack growth occurred was 12.0 KSI $\sqrt{in}$. and the highest crack growth rate observed was .0043 in/hr. The test results for these three specimens are shown in Figure 24.

Figure 25 shows typical results of residual (processing) stress measurements made on an E-beam taken from storage. This data was generated by the blind hole drilling method. The residual stress survey concentrated on the web and ribs because these areas experience the highest service stresses in the crack-propagating directions. Additional measurements were taken on the flanges at two external points (not shown) which indicated residual compression stresses in the potential crack opening direction of the same magnitude as those on the web. The results of the residual stress measurements can be summarized as follows:

1. The web stress was low (less than 7.0 KSI), varying along the length in an irregular manner.

2. Extremely high residual tension stress (>45 KSI) was measured in the inboard rib just below the surface. This stress was always in the 7-inch direction, tending to produce a crack in the 3-inch direction.

3. In all areas of high residual tension or compression, the stress approaches zero at the surface.

Potential locations for stress corrosion cracks were established in consideration of grain direction, residual stress and assembly stress. Cracks were assumed possible wherever the combined residual and assembly stress exceeded the stress corrosion threshold of 7 KSI in the transverse grain direction. The potential crack locations for the upper E-beams are shown in Figure 26. Most of these were in areas of high potential assembly stress, the residual stress not being high enough alone to cause cracking. The exceptions are the end rib cracks (A_1, A_2, G_1, G_2 and G_3) which were postulated because of the extremely high residual stresses that had been measured in those areas. The tail section assembly procedure included precision alignment and shimming methods which virtually eliminated assembly stress at these locations.

The sustained stress crack growth data obtained on this program were combined with existing data on 7178-T6 material to formulate criteria for quantitatively assessing the possible crack length at each potential crack location. As ground rules for this study, a stress corrosion threshold stress of 7.0 KSI and a K_{ISCC} value of 10.0 KSI $\sqrt{in}$. were assumed. The method for predicting potential crack size is shown schematically in Figure 27. The dotted line depicts one half of a typical sustained stress profile (assembly plus processing residual), which is usually locally symmetric about an attach point. If this stress exceeds 7 KSI, a crack will form and grow by the standard stress corrosion mechanism. It will continue to grow as long as the stress near the crack tip exceeds 7 KSI and it will also grow if the combination of stress and crack length produces a stress intensity above that required for sustained stress flaw growth, K_{ISCC}. In the plot shown, the solid line represents a crack arrest envelope within which a crack will not grow under sustained stress conditions. The intersection of that line with the sustained stress line defines the maximum possible extent of a crack. It should be noted that this representation does not take into account secondary effects associated with crack growth, such as the stress relieving effect of a growing crack due to decreased structural stiffness.

The critical crack size was calculated for each potential crack location, using design stress levels and the failure criterion shown in Figure 23. Table 2 shows the results of that study and compares them to the corresponding potential crack size, estimated by the preceding method. Assessment categories were assigned to each crack location based on the following criteria:

- o **Category X**: The possible crack size exceeds the critical crack size.

- o **Category Y**: The critical crack size exceeds the possible crack size by a significant margin.

- o **Category Z**: The design stress level in the crack-opening direction is so low that unstable crack propagation is not possible.

In consideration of the slow flaw growth rate for the E-beam material, periodic inspection was considered a sufficient safeguard against calculational inaccuracies for all Categories Y and Z locations.

The Category X cracks were analyzed to determine likelihood of detection, possible extent of unstable crack propagation and resulting structural capability. All Category X cracks are located in the inboard ribs and would be due entirely to the high residual tension stress that was measured in this area. All of the data were consistent in showing tension stress on the visible surface and compression stress on the hidden surface, so it was unlikely that a crack would form in an area that was inaccessible to inspection. However, the minimum critical crack size in this area is 0.18 inches and a crack of this size could conceivably exist under a bolt head or could develop from a smaller crack after the final inspection. The crack would be in the 3-inch direction, normal to the high residual tension stress (see Figure 26). There are two main tension bolts in this area, and the failure mode would be loss of effectiveness of a single bolt with crack arrest in the vicinity of the rib-web interface. The other bolt would still be active, and by analysis, would be able to carry the total E-beam load with an adequate factor of safety for all design load conditions. If two failures occurred at the same end of an E-beam, the total load capability at that point would be lost. This condition was also analyzed and it was found that there is sufficient structural redundancy in the outrigger assembly to transfer all loads to the adjacent structural and maintain an adequate factor of safety.

The E-beams were also analyzed for possible structural deficiencies which might result in the event of nominal-sized cracks occurring at each of the Categories Y and Z locations. It was determined that a potential problem existed at the upper E-beam "C-2" location, which is the support point for the 70-inch LO_2 tanks. Although the crack size required for unstable crack propagation is very large, the reduction in local stiffness, resulting from the introduction of a three inch crack at this location, would cause a reduction in overall vehicle stability against wind loading. It was determined that after rollback of the Mobile Service Structure, the required safety factors against this failure mode would not be met if the winds exceeded 31 knots.

The results of the E-beam study were presented to a committee of fracture control experts and Skylab program officials. The decision was made to continue the periodic stress corrosion inspections and, in the absence of further cracking, to fly the S-IB-8 with the repaired E-beams. A launch rule was established precluding rollback of the Mobile Service Structure if peak winds were predicted to exceed 30 knots.

110

CONCLUSION

The Chrysler Corporation Space Division approach to fracture control of stress corrosion susceptible hardware in the as-built state has been outlined. The establishment of a fracture control plan for each critical structural component on the S-IB Stage that is fabricated from stress corrosion susceptible material, has become a formal requirement for the Apollo-Soyuz mission next year. Each detail part will be analyzed to assess the potential for stress corrosion cracking and subsequent structural behavior, in essentially the manner presented in this paper.

Figure 1.   Saturn 1B Launch Vehicle
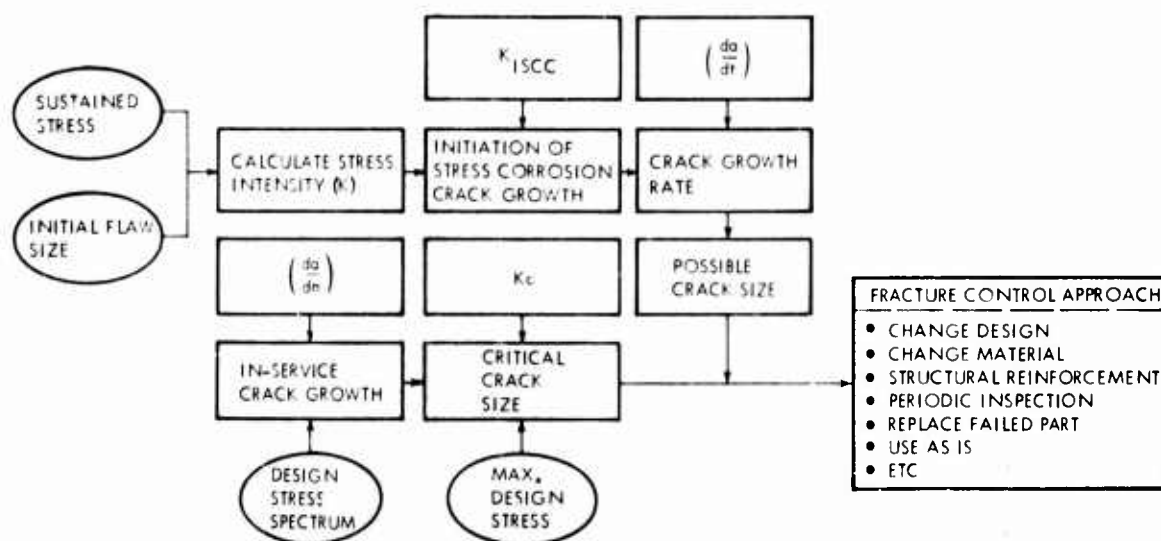
Figure 2.   Fracture Mechanics Approach to Stress
Corrosion Control
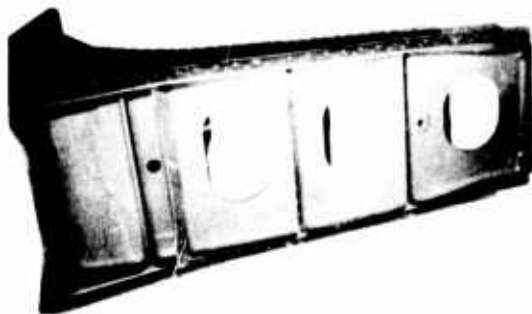
Figure 3.   Rear Spar (MSFC photo)
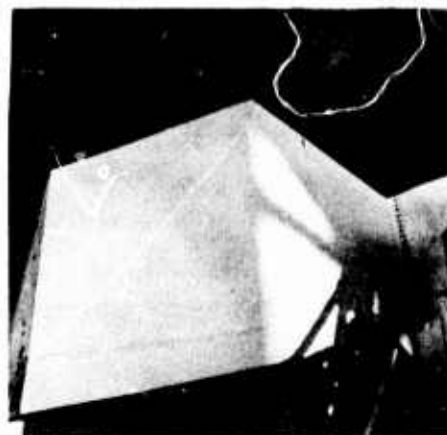
Figure 4.   Fin, S-IB Stage (KSC photo)
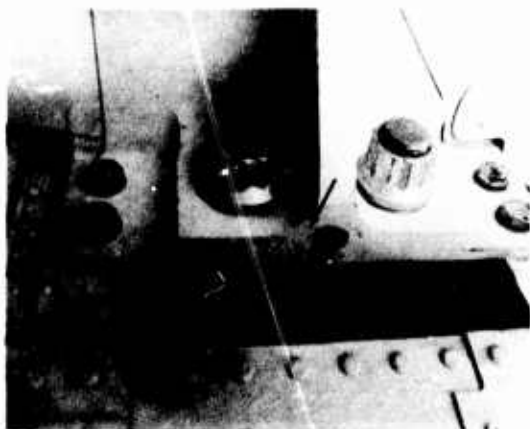
Figure 5.   Cracked Mounting Pad - Rear Spar
(KSC photo)

Figure 6.   Typical Crack - Rear Spar

Figure 7.   Spotface Area - Cracked Rear Spar
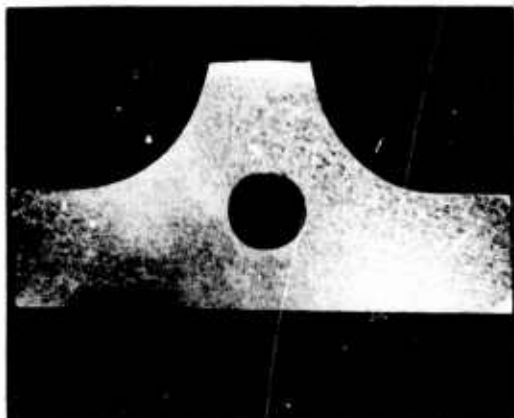
Figure 8. **Forging Grain Transition - Mounting Pad, Outboard**

Figure 9. **Forging Grain Transition - Mounting Pad, Inboard**
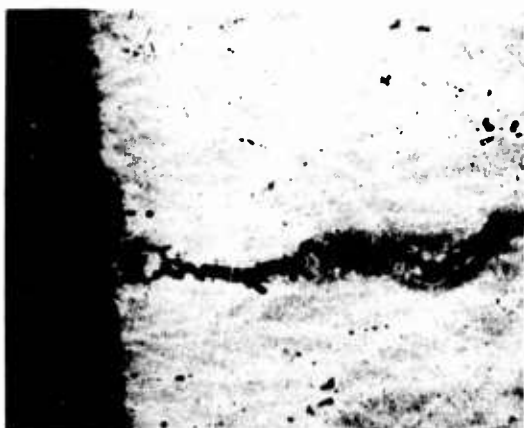
Figure 10. **Typical Spar Crack with Pit - 50X (KSC photo)**
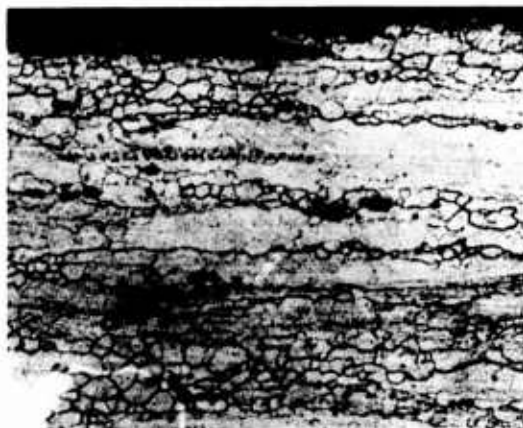
Figure 11. **Rear Spar Microstructure - 200X, Keller's Etch**
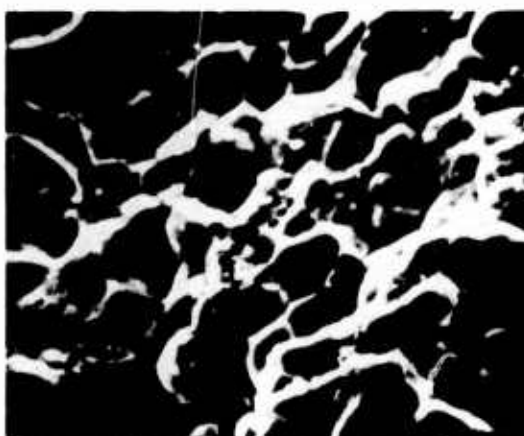
Figure 12. **SEM Micrograph - Fracture Surface, 1000X (MSFC photo)**
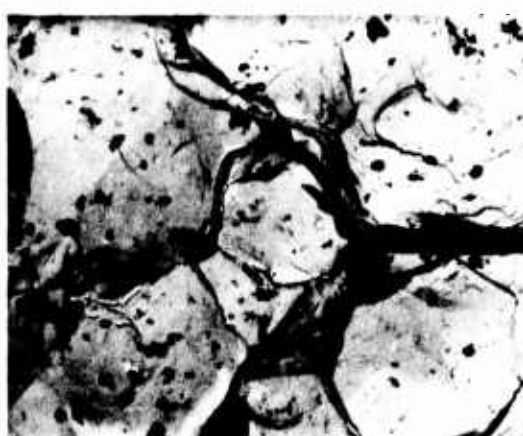
Figure 13. **Fracture Surface - TEM, 3150X (MSFC photo)**

114
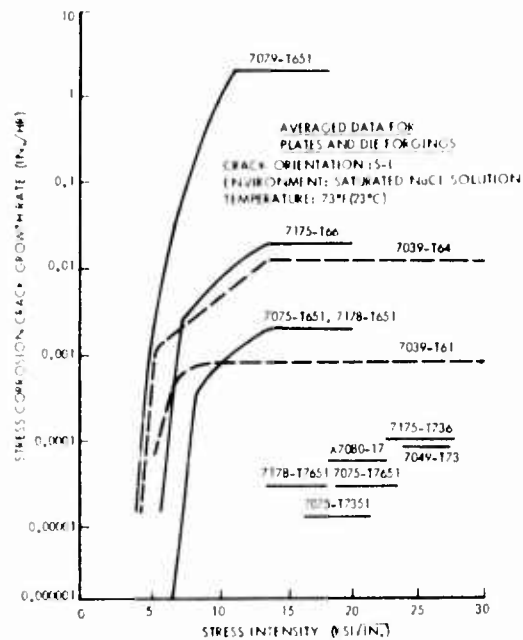
Figure 14. Sustained Load Crack Growth Rate Data for Aluminum Alloys in Saturated Na Cl Solution
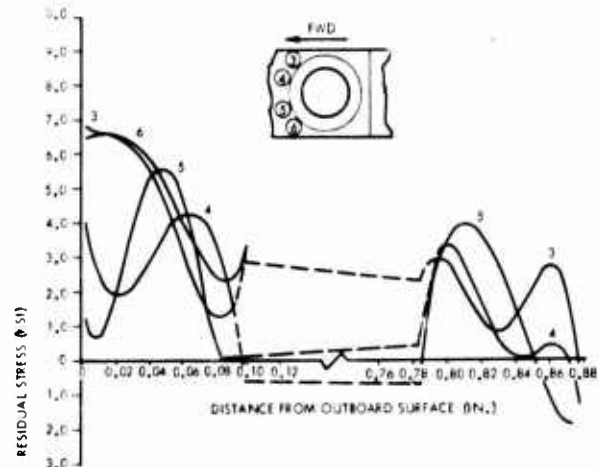
Figure 15. Typical Fin Spar Residual Stress Levels at the Aft Bolt Hole
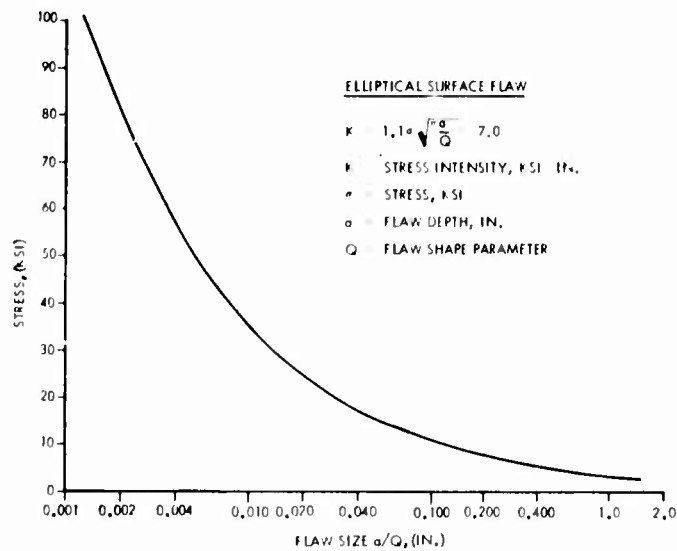
Figure 16. Fin Spar Threshold Stress for Flaw Growth vs. Flaw Size, Assembly $K_{ISCC} = 7.0$ KSI$\sqrt{in}$.
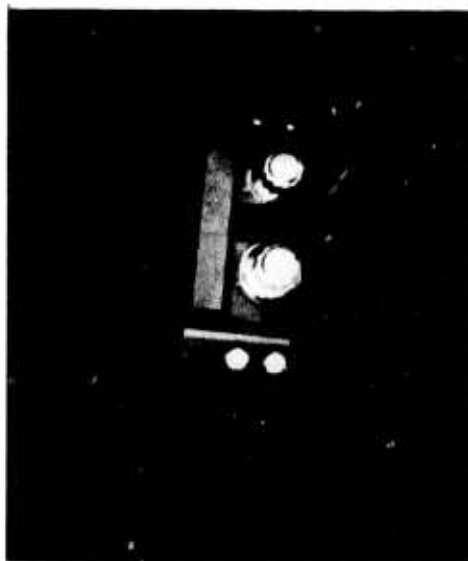
Figure 17. S-IB-8 Fin Reinforcement Fitting
(KSC photo)
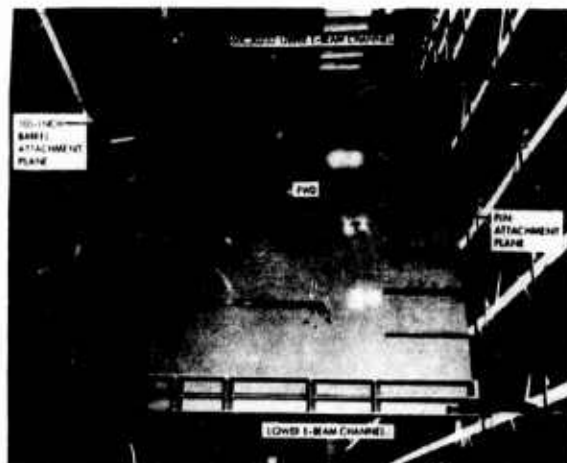
Figure 18. Shear Panel Assembly - Outrigger
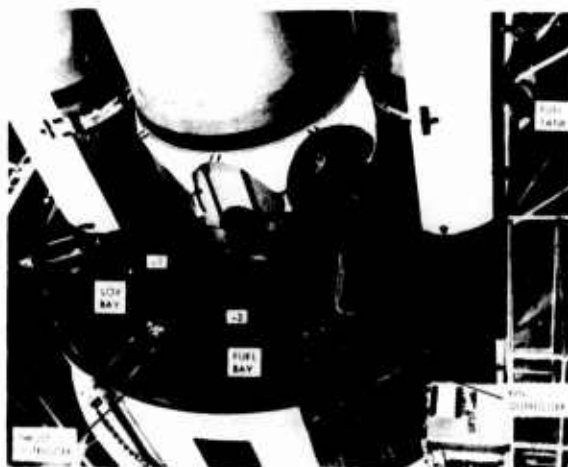
Figure 19. S-IB Stage Assembly

Figure 20. E-Beam Crack - S-IB-8 (KSC photo)

Figure 21. Stress Corrosion Crack - S-IB-8
E-Beam, 50X (MSFC photo)

Figure 22. Typical E-Beam Repair

$$\left(\frac{K_1}{24}\right)^2 + \left(\frac{K_{II}}{26}\right)^2 = 1.0$$

Figure 23. Normalized Mixed-Mode Unstable Crack
Propagation Criteria
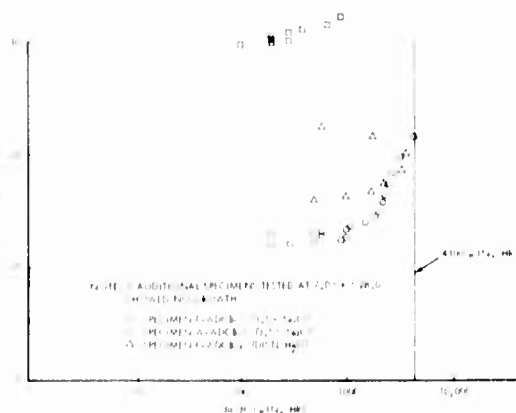
Figure 24. Test Results - Sustained Stress Crack Growth
of E-Beam Material
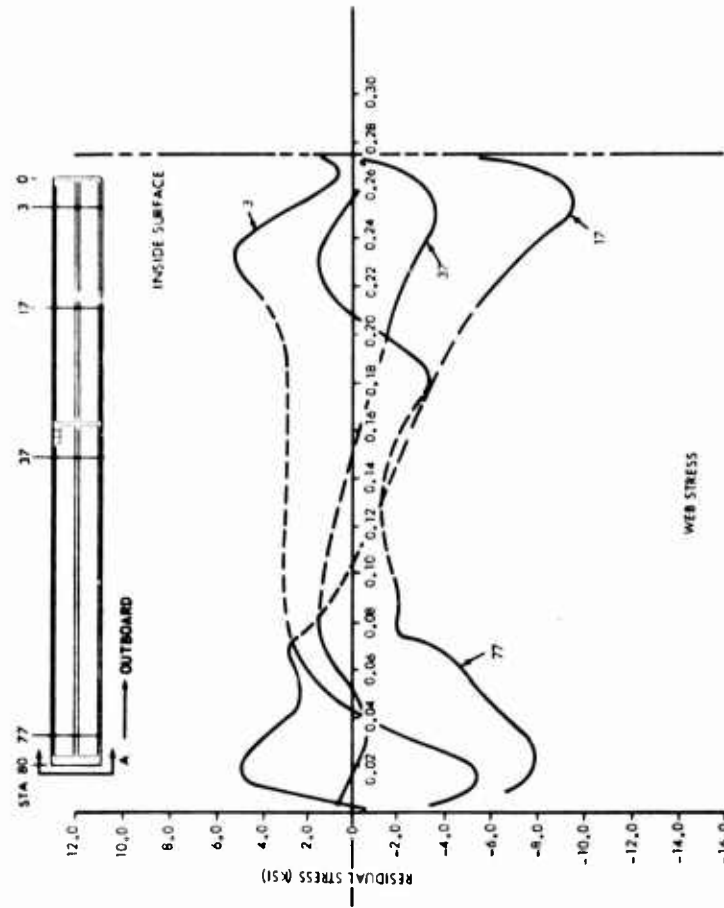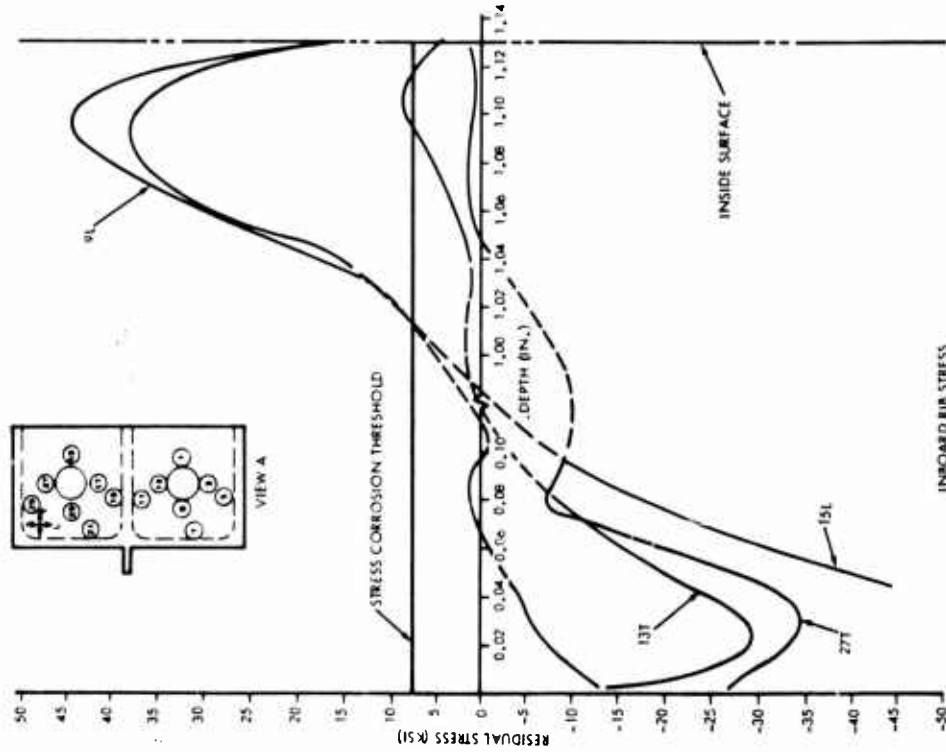
Figure 25. Residual Stress Measurements – Upper E–Beam

118
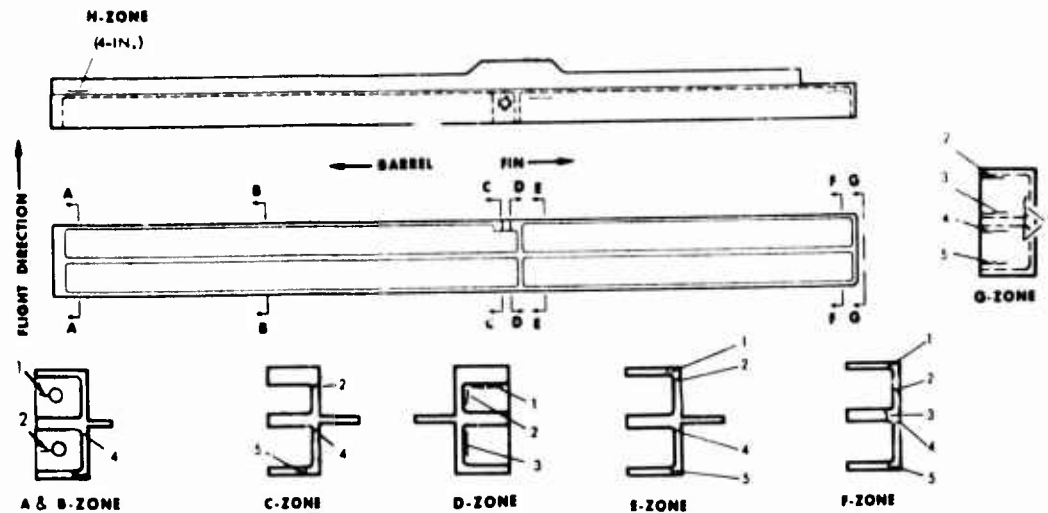
Figure 26. Potential Crack Locations - Upper E-Beam
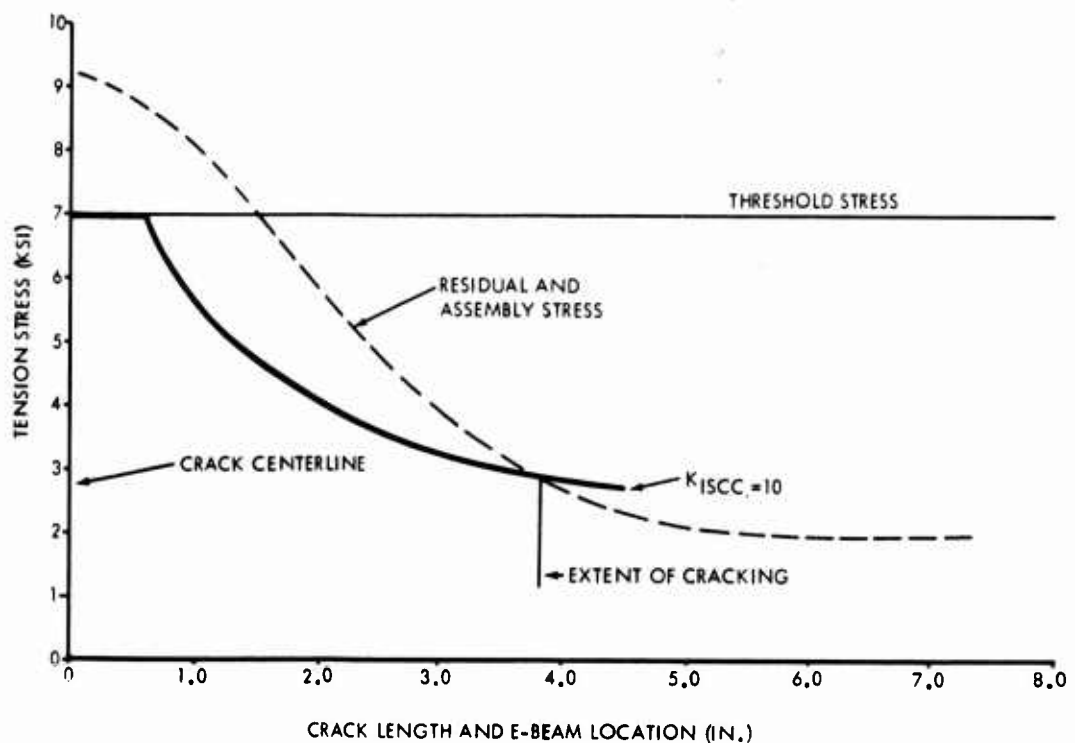
Figure 27. Crack Initiation and Growth-Sustained Stress
Conditions

119

Table 1. Crack Growth Potential in the S-IB Fin Spar Pad for the Three On-Pad Load Conditions

| Condition | Sustained Stress ,KSI | | Assessment |
	Beyond Stress Conc. Zone	Within Stress Conc. Zone	
On-Pad, No Fuel	9. 6	29-77	Limited crack growth possible, within stress concentration zone. No extensive cracking.
On-Pad, With Fuel	14. 2	43-114	Limited crack growth likely, within stress concentration zone. No extensive cracking.
On-Pad, Fuel Plus Cryogenics	28. 8	86-230	Extensive crack growth likely.

Table 2. Assessment of E-Beam Stress Corrosion Cracking Potential

| UPPER E-BEAM | | | | LOWER E-BEAM | | | |
LOCATION	POSSIBLE CRACK LENGTH (IN.)	CRITICAL CRACK LENGTH (IN.)	ASSESSMENT CATEGORY*	LOCATION	POSSIBLE CRACK LENGTH (IN.)	CRITICAL CRACK LENGTH (IN.)	ASSESSMENT CATEGORY*
A, 1, 2	3.0	0.18	X	A, 1, 2	3.0	0.44	X
A, 4	1.25	10.5	Y	A, 4	2.0	10.8	Y
A, 5	1.25	40	Z	A, 5	2.0	144	Z
B, 4	1.25	12.8	Y	B, 4	2.0	23.6	Y
B, 5	1.25	191	Z	B, 5	2.0	330	Z
C, 2	5.0	55	Z	C, 4	9.0	23.7	Y
C, 4	1.25	12.8	Y	C, 5	9.0	330	Z
C, 5	1.25	191	Z	D, 4	7.0	18.7	Y
D, 1	0	23	Y	D, 5	7.0	540	Z
E, 1, 2	3.0	168	Z	E, 1	0	365	Z
E, 4	0	7.3	Y	E, 2	3.0	17.4	Y
E, 5	1.25	168	Z	F, 4	2.0	10.5	Y
F, 1, 5	1.0	18.4	Y	F, 5	2.0	166	Z
F, 2	5.0	9.4	Y	G, 1	3.0	1.23	X
F, 4	5.0	7.0	Y	G, 2	3.0	.87	X
G, 1, 5	7.0	∞	Z	G, 3	3.0	.87	X
H	2.0	51	Z	H	1.0	46	Y

*DESCRIPTION OF ASSESSMENT CATEGORIES:
    CATEGORY X - POSSIBLE CRACK LENGTH > CRITICAL CRACK LENGTH
    CATEGORY Y - POSSIBLE CRACK LENGTH < CRITICAL CRACK LENGTH
    CATEGORY Z - CRITICAL CRACK LENGTH LARGE

INCIDENTS OF CORROSION ON MANNED SPACECRAFT
- THEIR CAUSE AND PREVENTION -

H. M. Clancy
Space Division
Rockwell International
Downey, California

ABSTRACT

The Apollo program has spanned twelve years and, following the Mercury and Gemini programs, is the culmination of the first phase of this country's exploration of space. Apollo also plays a major role in the second phase, the Skylab program. We are now undertaking the third phase of man in space with the Shuttle program which will affect the consolidation and application of this new frontier for the benefit of all mankind.

At the start of the Apollo program there were many unknowns and much concern regarding the corrosion resistance of a manned space vehicle:

- How would the exotic materials behave on the ground and in space?

- What would be the effects of using minimum gage metals to save weight?

- What would be the effects of extremely corrosive fluids?

- Would corrosion be accelerated by extended pad "holds" just a few hundred feet from the ocean?

- What would happen if an astronaut spilled a bag of urine inside the crew bay?

These and many other questions were raised and eventually answered. We learned many things; most of which were simply a reiteration of classic corrosion problems. We learned how to handle the "exotic" materials and that once their limitations were known, they become ordinary. We learned that our concern for a multitude of unknowns was indeed extreme and largely unfounded. We learned that corrosion problems on a manned space program are the usual problems of any new product - aluminum corrodes and must be adequately protected, dissimilar metal couples corrode vigorously, parts must be adequately protected through in-plant processing, water is one of the most corrosive fluids aboard.

INTRODUCTION

In 1963, early in the Apollo program, NASA asked many of the major subcontractors to attend a corrosion control conference at the site of future Apollo launches, Kennedy Space Center. At that time the Vertical Assembly Building was a skeleton of steel barely visible under mass of construction workers. In the lobby to the conference room were displayed numerous photographs and bottled specimens of alligators, rodents, spiders and snakes captured on previous Cape construction sites. One rattlesnake had the dimensions of a boa constrictor and rattlers as big as your thumb. The whole Cape area at that time typified man's struggle against nature. Indeed, the conference continued this theme, emphasizing the extreme tropical sea coast environment. Needless to say, NASA got its point across quite well that day. However, as in all programs, this apprehension gradually gave way to the work-a-day problems associated with hardware production. Over the ensuing years the program developed and matured until today KSC with its freeways and sight-seeing buses has become an adjunct to Disneyworld. Likewise, the corrosion incidents that occurred on Apollo were similar (with a few exceptions) to those encountered on any aerospace program. Actually, very few corrosion problems occurred at KSC due to the fact that the spacecraft was so well protected. The first indications of corrosion problems came from early fluid compatibility tests; later there were in-process and in checkout corrosion incidents; and finally post-flight inspection showed some corrosion. Test failures re-emphasized the importance of early material/fluid compatibility evaluation and the need for special tests like the NASA fracture mechanics test developed for evaluation of tank materials. The need for good "in process corrosion control" was illustrated by aluminum corrosion while still on the shelf in the warehouse or using department.

Problems which occurred during checkout were usually traced to fabrication process control and GSE/Facilities equipment which interfaced with spacecraft systems. Postflight corrosion was particularly bothersome because it was necessary to demonstrate beyond any doubt that the corrosion was due to salt water ingested on landing and was not due to material deficiency. Actually the spacecraft interior was showed to be extremely resistant to various (inadvertent) fluid spills including water glycol, water, various food stuffs and urine - but not salt water.

Apollo did provide one new lesson: the smallest indication or suspicion of corrosion had major program impact and was sufficient to stop a launch. In the space effort there is no such thing as cleanup and repaint; every corrosion incident must be totally understood and corrected. For these reasons, often as much time was spent in understanding a suspected corrosion problem as if it were real.

The corrosion engineer, if he has learned anything, has learned to be "light on his feet." This is certainly the case today when he is asked to apply all he has learned from Apollo in the reduction of corrosion incidents on the Shuttle with associated program cost savings. However, he must now recognize that Shuttle is a spacecraft that will be like a commercial aircraft; it will be reused; it will be repeatedly exposed to the Cape elements. We must build that corrosion resistance into the vehicle - we must remember that corrosion conference of 1963.

SUMMARY

The attachments summarize some of the incidents and suspected incidents of corrosion which occurred on the Apollo program.

CORROSION INCIDENT SUMMARY

1. **Incident:** Failed parachute link

2. **Vehicle:** Apollo 15

3. **System:** Recovery

4. **Part:** Parachute riser to suspension line link

5. **Date:** November 1971

6. **When (Operation):** Postflight

7. **Material:** Link - 4130 steel; nut - A286 CRES

8. **Heat Treat:** Link - 200 ksi

9. **Surface Preparation:** Link - electroless nickel and tin plated
   Nut - silver plated

10. **Welding or Brazing Involved in Corrosion:** No

11. **Analysis:** Initially chute collapse which occurred during landing was thought to be related to link failure. Subsequent investigation showed chute failure due to ignition of fuel dumped during descent. Failed link found on postflight inspection of recovered chutes. Rust on fracture surface. Tests to demonstrate stress corrosion or hydrogen embrittlement from plating were inconclusive.

12. **Cause:** SCC (most probable) resulting from salt water exposure on landing

13. **Corrosion Type:** SCC aggravated by dissimilar metal contact in thread area (silver vs 4130 steel)

14. **Fix:** Change links to Inconel 718 with no plating

15. **Finding:** Protective plating must remain intact

Failure point

Main parachute connector link failure.

125

CORROSION INCIDENT SUMMARY

1. Incident: Cracked frangible nut and washer - 1/16-inch gap in nut
    five days after inspection for integrity

2. Vehicle: AS/202 mission

3. System: Launch escape

4. Part: Frangible nut attaching launch escape tower to C/M

5. Date: August 21, 1966

6. When (Operation): Prelaunch checkout at John F. Kennedy Space Center

7. Material: Nut - 4340 steel, electroless nickel and tin plated
    Washer - 4130 steel, electroless nickel and tin plated with
    dry film lube

8. Heat Treat: Nut, 200-200 ksi and washer, 180-200 ksi

9. Surface Preparation: Plated

10. Welding or Brazing Involved in Corrosion: No

11. Analysis: Macro's, fractographs. Salts (green) identified by X-ray diffraction
    and emission spectrograph to be fluorides. Electroless Ni cracked.

12. Cause: Rain dissolved ammonium fluoroborate (NH_4BF_4) ablator material on
    launch escape engine skirt which ran down tower leg and puddled
    in leg well. Solution stress corroded nut and washer in five days.
    Plating had cracked exposing base metal.

13. Corrosion Type: SCC

14. Fix: Seal ablator, cover and seal leg well

15. Finding: Components must be protected from possible fluids running down stack.
    Integrity of protective finish on SCC susceptible material is essential.

LAUNCH ESCAPE SYSTEM
SEPARATION MECHANISM

EXPLOSIVE BOLT CHARGE

FRANGIBLE NUT

SHAPE CHARGE CUTTING ASSEMBLY

TOWER JETTISON MOTOR

LAUNCH ESCAPE MOTOR

STRUCTURAL SKIRT

(AMMONIUM FLUOROBORATE ABLATOR)

LAUNCH ESCAPE TOWER

TOWER FLAPS

PASSIVE TENSION

FORWARD HEAT SHIELD THRUSTERS

FORWARD HEAT SHIELD

PASSIVE TENSION

COMMAND MODULE

-Z AXIS
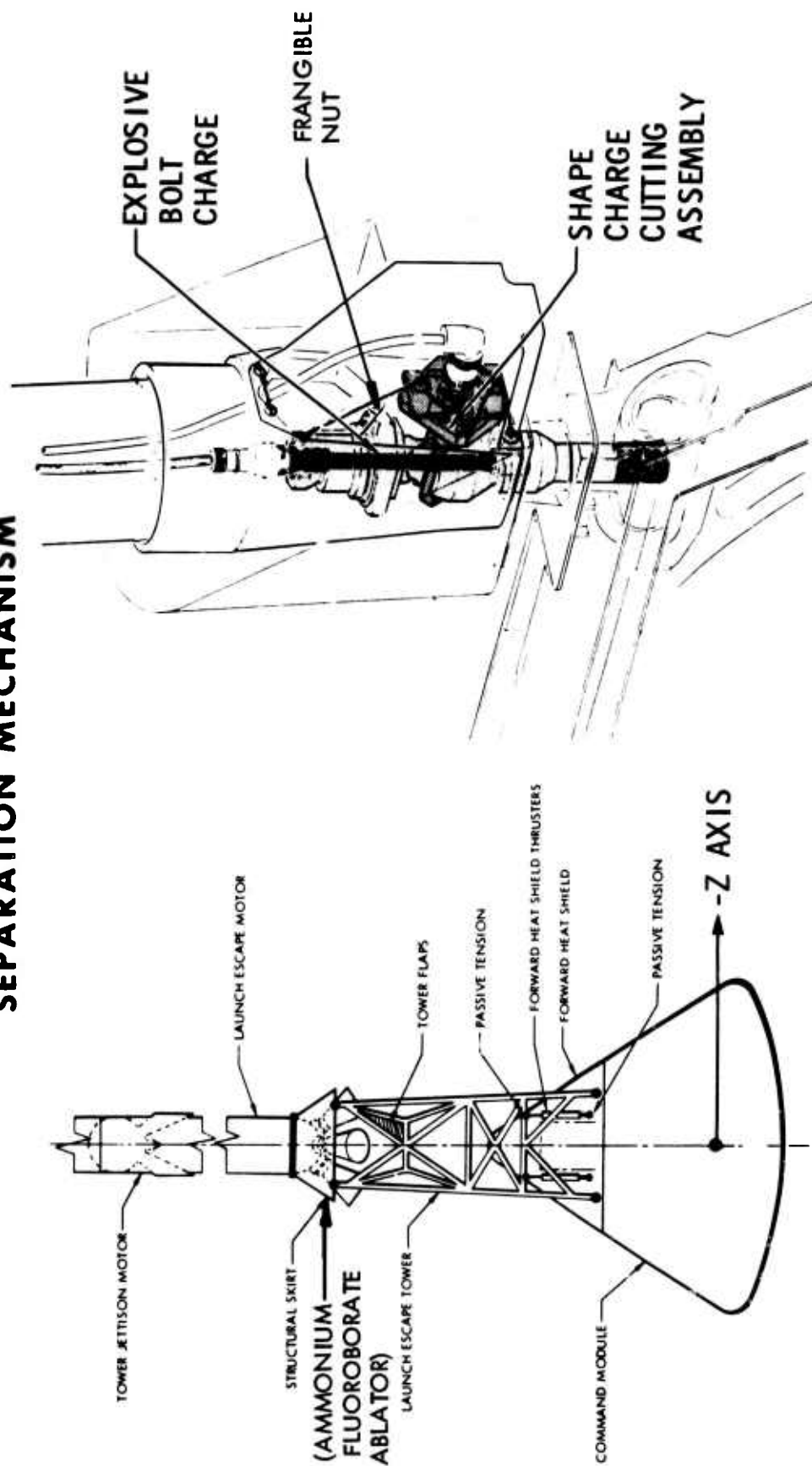
End-view of the Nut. The Dark Lower Portion of the
Part had been Submerged in Water While in Service

128

CORROSION INCIDENT SUMMARY

1. Incident: Rust in CM RCS

2. Vehicle: Skylab 3 mission

3. System: RCS

4. Part: RCS assembly

5. Date: June 1970

6. When (Operation): Cleanliness verification (system flushing)

7. Material: Various but primarily 304L CRES

8. Heat Treat: Condition B

9. Surface Preparation: Passivated

10. Welding or Brazing Involved in Corrosion: No

11. Analysis: X-ray diffraction showed iron-oxide hydroxide and trace of ferrous chloride. Particles were 20-40 microns in size.

12. Cause: The Freon MF (fluorotrichloromethane) previously used for flushing had backed up into flushing unit gaseous nitrogen heater which oxidized and continued to blow particles into RCS during subsequent drying operations.

13. Corrosion Type: Thermal chemical

14. Fix: Added check valve upstream and depth filter at system interface

15. Finding: GSE and facilities corrosion control can be as critical as flight hardware

CORROSION INCIDENT SUMMARY

1. Incident: Failure of rotation hand controller in checkout

2. CSM: None

3. System: Guidance and navigation

4. Part: Astronaut's hand controller

5. Date: November 1972

6. When (Operation): Checkout following rework

7. Material: 7075

8. Heat Treat: -T6510

9. Surface Preparation: Chem filmed

10. Welding or Brazing Involved in Corrosion: No

11. Analysis: Fractography, microprobe showed typical stress corrosion cracking through short transverse section of part

12. Cause: Gear pushed onto shaft and clamped up with screw putting section under sustained load (tensile stress)

13. Corrosion Type: SCC

14. Fix: Change to 7075-T73; selectively machine to eliminate short transverse loading

15. Finding: Prohibit use of 7075-T6 in miniature electro-mechanical unit where slight interference on shaft or small differences in torque on miniature fasteners can significantly increase stress levels

Yaw Section Gear Crack

131

CORROSION INCIDENT SUMMARY

1. <u>Incident</u>: Check and relief valve leakage from particulate contamination

2. <u>Vehicle</u>: Apollo 15 (check valve); Apollo 16 (relief valve)

3. <u>System</u>: Cryo (fuel cell)

4. <u>Part</u>: Check valve and relief valve

5. <u>Date</u>: 10-5-70 (check valve); 2-71 (relief valve)

6. <u>When (Operation)</u>: System checkout prior to delivery to
   John F. Kennedy Space Center

7. <u>Material</u>: 304L CRES tubing

8. <u>Heat Treat</u>: Condition B

9. <u>Surface Preparation</u>: Electropolish

10. <u>Welding or Brazing Involved in Corrosion</u>: Yes, brazing at 1875 F.

11. <u>Analysis</u>: X-ray diffraction showed particles to be ferrous chloride ($Fe\ Cl_2 \cdot 2H_2O$).

12. <u>Cause</u>: Use of Freon TF (1,1,2-trichloro-1,2,2-trifluoroethane) to clean
    parts assembled for brazing just prior to brazing. Particles caused
    by thermal decomposition of Freon and high-temperature reaction
    with CRES. Some operators were found to use Freon TF spray
    rinse just prior to installation of the induction brazing tool. Usually
    the Freon evaporated and was carried away by the argon purge.
    However, where adjacent components did not allow the internal flow
    of argon (dead-end purge), the Freon could not complete escape.

13. <u>Corrosion Type</u>: Thermal chemical

14. <u>Fix</u>: Eliminate use of Freon TF just prior to brazing

15. <u>Finding</u>: Improper use of cleaning agent
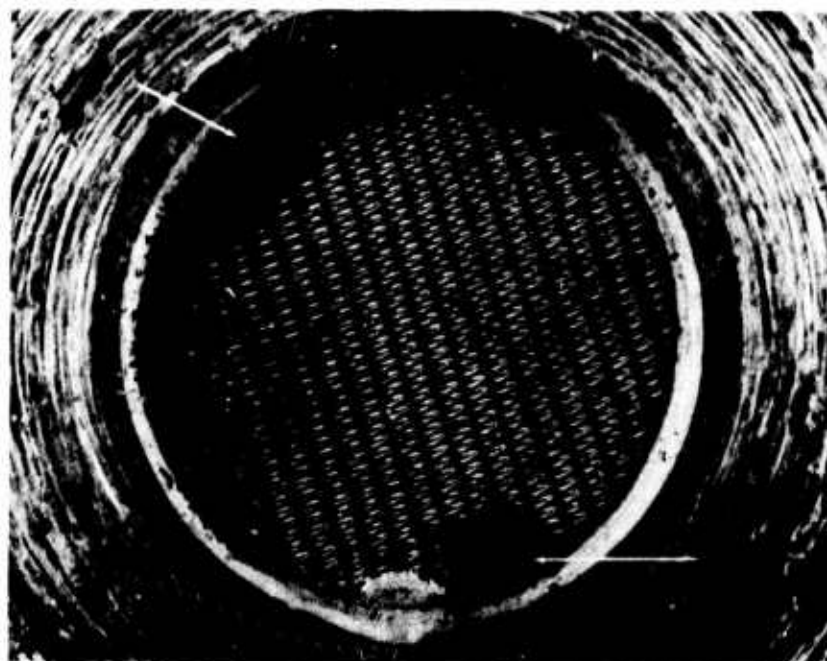
Ferrous Chloride Contamination Trapped on the Upstream Side
of the Wafer Filter in Check Valve

CORROSION INCIDENT SUMMARY

1. **Incident:** Leakage of 321 CRES flex hose

2. **Vehicle:** Skylab 3 and Apollo 17

3. **System:** RCS

4. **Part:** Flex hose to RCS engine

5. **Date:** 11-10-71 (Apollo 17); 1-10-73 (Skylab 3)

6. **When (Operation):** Skylab 3 leaked Freon during system flushing prior to John F. Kennedy Space Center delivery

   Apollo 17 leaked helium during postflight inspection

7. **Material:** 321 CRES convoluted tubing with 321 CRES wire overbraid

8. **Heat Treat:** Condition B

9. **Surface Preparation:** Passivated

10. **Welding or Brazing Involved in Corrosion:** No

11. **Analysis:** Through corrosion pit from outside. Photomicrographs, emission spectograph, X-ray diffraction and electron microprobe showed rust and trace of chlorides.

12. **Cause:** Crevice corrosion underneath braid from salt water exposure during landing. Skylab 3 was reuse hose which had been cleaned prior to reuse but after corrosion had occurred.

13. **Corrosion Type:** Crevice

14. **Fix:** None

15. **Finding:** Rate of crevice corrosion. The hose experienced 0.010 penetration in approximately thirty days.

Path of Corrosion Through Tube Wall
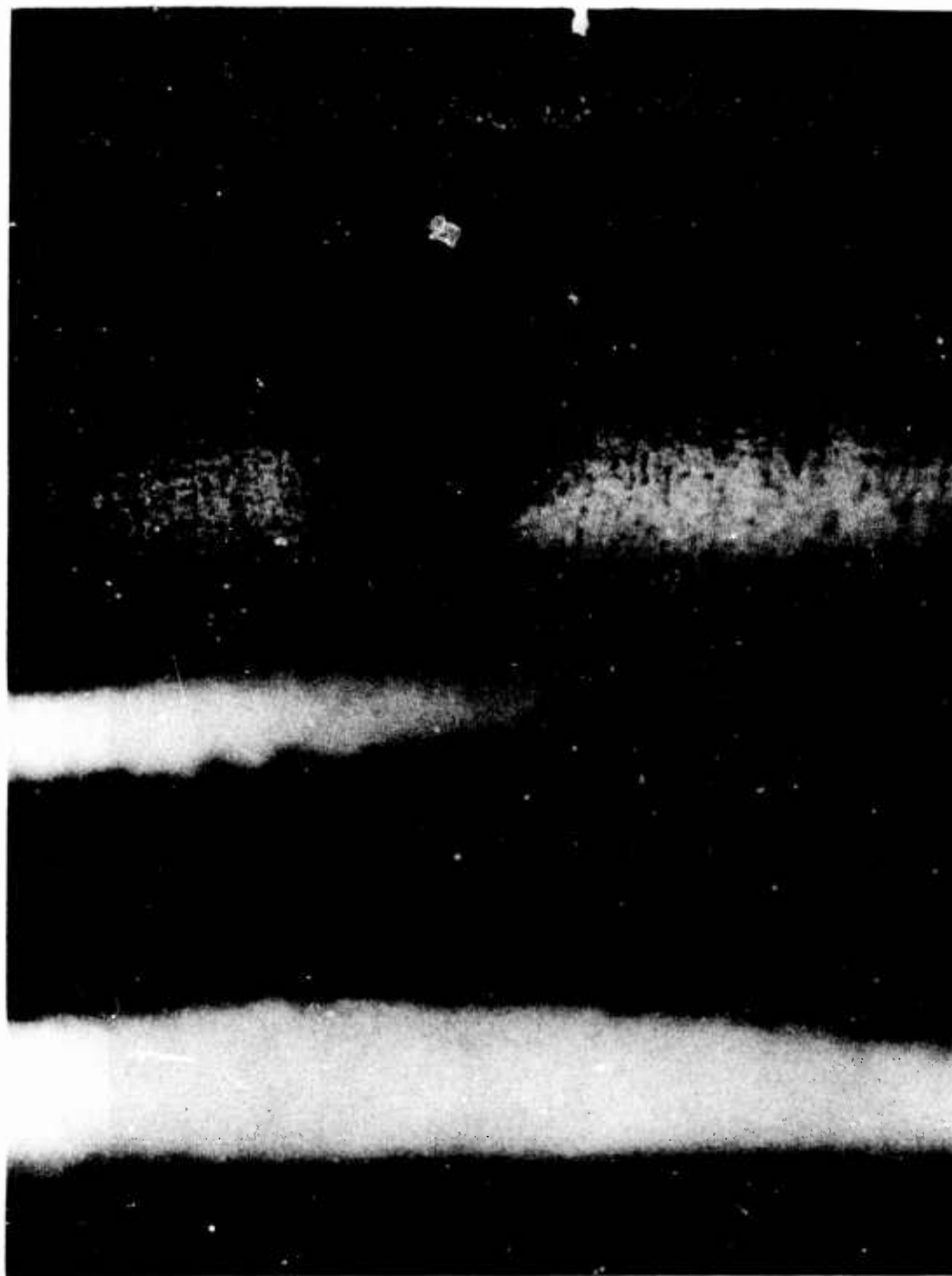
Corrosion Pit on Inside Diameter of Tube

CORROSION INCIDENT SUMMARY

1. Incident: Leaking cryo vent disconnect

2. Vehicle: Skylab 4

3. System: Fuel cell cryo storage (oxygen)

4. Part: Vent quick disconnect

5. Date: April 1972

6. When (Operation): System leak check prior to delivery to John F. Kennedy
    Space Center

7. Material: 304L CRES tubing

8. Heat Treat: Condition B

9. Surface Preparation: Passivated

10. Welding or Brazing Involved in Corrosion: Brazing

11. Analysis: Nondispersive X-ray analysis and microprobe showed zinc
    on fracture surface

12. Cause: QD returned to supplier to rework valve seat. Supplier hand
    brazed temporary extension to valve for leak check using QQ-S-561
    (Ag-Cu-Zn) alloy. Residual alloy left on surface cracked tubing
    during subsequent system braze installation (1875 F).

13. Corrosion Type: Liquid metal embrittlement

14. Fix: Use mechanical fitting for leak check

15. Finding: Zinc bearing braze alloys must be used with caution

Supplier Union – Braze Temperature – 1325 F to 1450 F

SD Union – Braze Temperature – 1800 F to 2000 F

Quick Disconnect

$\frac{5}{8}$"

1"
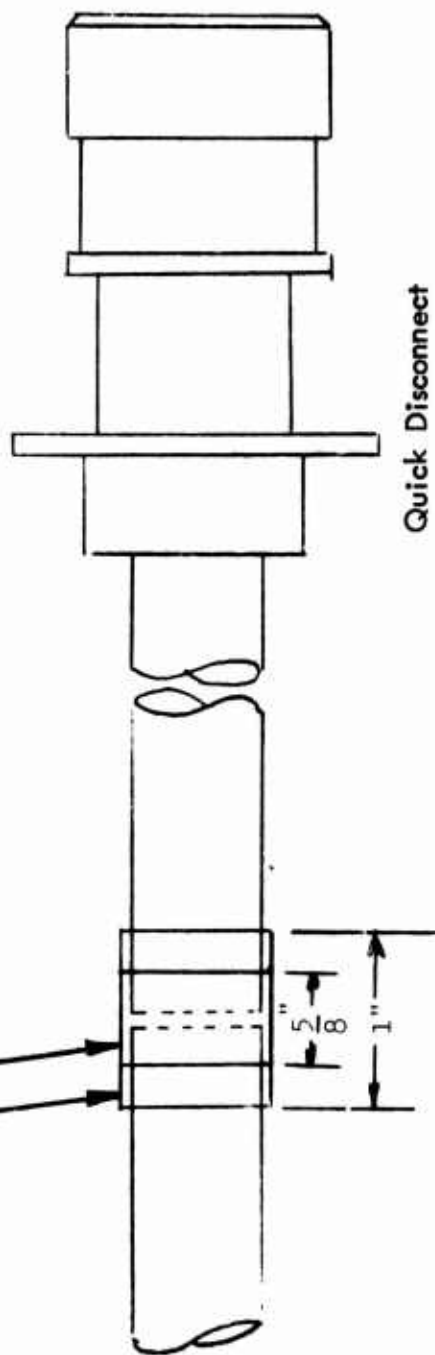
Unions and Braze Temperatures

CORROSION INCIDENT SUMMARY

1. Incident: Corrosion of aluminum during machining

2. Vehicle: Apollo/Soyuz Test Project (ASTP)

3. System: Docking

4. Part: Docking system base

5. Date: May 1973

6. When (Operation): Manufacturing

7. Material: 7075

8. Heat Treat: T73

9. Surface Preparation: Machined

10. Welding or Brazing Involved in Corrosion: No

11. Analysis: Pitting on certain surfaces

12. Cause: Machine coolant sitting for several days between part and steel machine base

13. Type of Corrosion: Galvanic

14. Fix: Change machine coolant

15. Finding: Coolant successfully used previously because parts were small and only on machine short time. A more severe corrosion condition may exist in manufacturing than in service.

CORROSION INCIDENT SUMMARY

1. **Incident:** Suspected hydrogen embrittlement of titanium cryogenic storage tank (investigation initiated as the result of SIVB tank failure)

2. **CSM:** None

3. **System:** Cryo storage

4. **Part:** Tank

5. **Date:** March 1967

6. **When (Operation):** Scrap tank dissection

7. **Material:** Titanium 5 Al-2.5 Sn Eli

8. **Heat Treat:** As welded

9. **Surface Preparation:** As machined

10. **Welding or Brazing Involved in Corrosion:** Yes, welded with CP titanium wire

11. **Analysis:** Photomicro's to show titanium hydrides

12. **Cause:** Precipitation of hydrides in welds caused by heating and slow cooling from adjacent subsequent weld including hydride precipitation caused by use of CP titanium weld wire and thickness of parent material which determine degree of dilution of CP material

13. **Corrosion Type:** Hydrogen embrittlement

14. **Fix:** None, but specification changed to carry precautionary note, "Do not use CP weld wire on joints greater than 0.150 thick."

15. **Finding:** Careful (selected) use of CP titanium for welding and structural elements required

Cracks from Titanium Hydrides

CORROSION INCIDENT SUMMARY

1. __Incident:__ Cracked spring in rotation controller

2. __Vehicle:__ Skylab 3

3. __System:__ Guidance and navigation

4. __Part:__ Return spring in rotation hand controller

5. __Date:__ May 1973

6. __When (Operation):__ Unit rework

7. __Material:__ 17-7 PH CRES wire

8. __Heat Treat:__ CH900

9. __Surface Preparation:__ Pickled and passivated

10. __Welding or Brazing Involved in Corrosion:__ No

11. __Analysis:__ Cracks were parallel to the axis of the wire in the spring. Contaminants were found on spring surface but fracture was ductile.

12. __Cause:__ Mechanical overstress during manufacturing/assembly

13. __Type of Corrosion:__ None (suspected only)

14. __Fix:__ None

15. __Finding:__ Mechanical cracking in spring difficult to interpret since cracking due to torsional shear
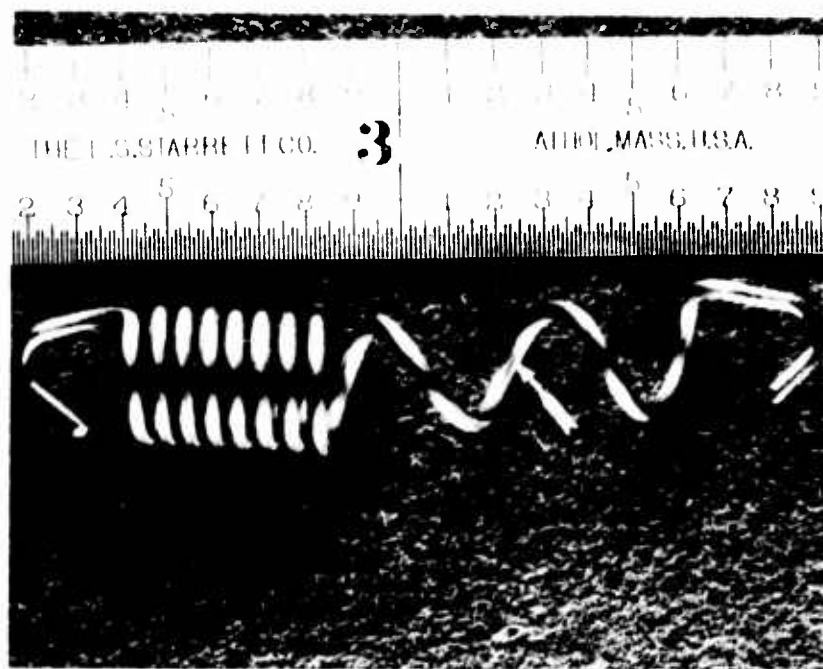
Photograph of Spring After Extension to Failure
Arrow Points to Crack

Macrograph of Crack Shown in Magnification 13X

CORROSION INCIDENT SUMMARY

1. <u>Incident</u>: Broken springs on electrical connector

2. <u>Vehicle</u>: Apollo 16

3. <u>System</u>: Optical unit assembly

4. <u>Part</u>: Connector

5. <u>Date</u>: August 10, 1972

6. <u>When (Operation)</u>: Postflight inspection (approximately 35 days after landing)

7. <u>Material</u>: Beryllium copper

8. <u>Heat Treat</u>: Unknown

9. <u>Surface</u>: Gold plating (0.00015 inch)

10. <u>Welding or Brazing Involved in Corrosion</u>: No

11. <u>Analysis</u>: SEM shows intergranular fracture

12. <u>Cause</u>: Compression of spring cracked gold plating causing exposure of base material to salt water on landing

13. <u>Type of Corrosion</u>: SCC

14. <u>Fix</u>: None, postflight anomaly

15. <u>Finding</u>: Protective plating must be carefully engineered to make sure it does not crack in service

CORROSION INCIDENT SUMMARY

1. Incident: Leakage of CRES tee in cryo system (hydrogen)

2. Vehicle: Apollo 16

3. System: Fuel cell gas storage system

4. Part: Machined tee (.020 wall)

5. Date: October 7, 1971

6. When (Operation): Prelaunch checkout at John F. Kennedy Space Center

7. Material: 304L CRES bar

8. Heat Treat: Condition B

9. Surface Preparation: Electropolish

10. Welding or Brazing Involved in Corrosion: No

11. Analysis: Photomicrographs, microprobe showed oxide inclusion

12. Cause: Nonmetallic inclusion in air melt 304L CRES.
    Material should have been vacuum melt.

13. Corrosion Type: None (suspected only)

14. Fix: Reaffirm use of vacuum melt material and helium leak
    check at supplier

15. Finding: As much effort may be expended in proving a leak is not due
    to corrosion as if it were.

CORROSION INCIDENT SUMMARY

1. Incident: Cracking of 304L CRES tubing during brazing

2. Vehicle: Apollo 15

3. System: SPS and ECS

4. Part: Helium check valve (SPS); O_2 isolation valve (ECS)

5. Date: July 1971

6. When (Operation): Prelaunch checkout

7. Material: 304L tubing

8. Heat Treat: Condition B

9. Surface Preparation: Passivated

10. Welding or Brazing Involved in Corrosion: Yes. Brazed with gold-copper-nickel alloy at 1875 F.

11. Analysis: Intergranular cracking; crack filled with braze alloy

12. Cause: Liquid metal embrittlement by copper in braze alloy under elevated temperature and thermal stresses of brazing

13. Corrosion Type: Liquid metal embrittlement

14. Fix: None. Cracks always under braze sleeve. Burst tests showed all failures to occur outside sleeve in tubing. Specimen with simulated cracks beyond sleeve withstood thermal shock, vibration and near burst pressure.

15. Finding: Very rare occurrence. Of the approximately 30 thousand brazed joints made on the Apollo program, a total of 36 were found to be cracked.

VIEW 1   VIEW 2

POLAROID OF X-RAY FILM - 5.5X MAG - SM 117

Shown in Views 1 and 2 are two sections of a continuous .700 long crack found in a 304L tube, V57-470850-3 that was brazed to a 304L fitting
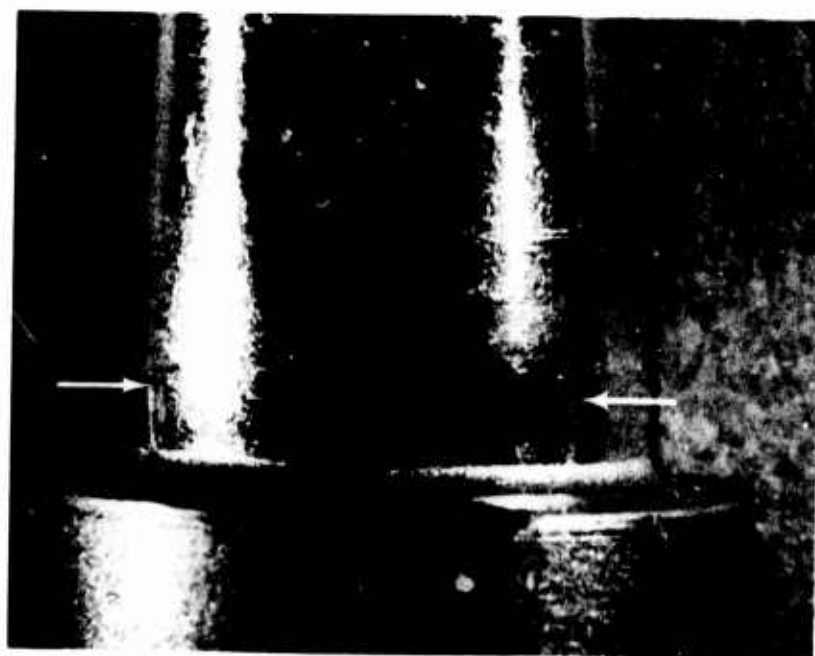
Brazed Slots After Pressure Testing
(showed that even if cracks ran
beyond sleeve they would fill with
braze alloy and function adequately)

CORROSION INCIDENT SUMMARY

1. <u>Incident</u>: Suspected SCC of Belleville spring in oxygen regulator. Investigation initiated by failure of similar regulator spring on Skylab.

2. <u>CSM</u>: None (investigation only)

3. <u>System</u>: ECS

4. <u>Part</u>: Oxygen regulator

5. <u>Date</u>: March 1971

6. <u>When (Operation)</u>: Parts on shelf

7. <u>Material</u>: Vascomax 300 maraging steel

8. <u>Heat Treat</u>: 280 ksi

9. <u>Surface Preparation</u>: Electroless nickel plated

10. <u>Welding or Brazing Involved in Corrosion</u>: No

11. <u>Analysis</u>: Lab tests showed failure of spring under stress after one day alternate water immersion and salt spray exposure and after twenty days humidity <u>without electroless nickel plating</u>.

12. <u>Cause</u>: Skylab springs baked four hours at 375 F following plating. Space Division springs received no bake. Baking embrittled nickel which cracked on spring flexing, allowing exposure of Vascomax 300.

13. <u>Corrosion Type</u>: None found on Apollo parts

14. <u>Fix</u>: No change. Parts inspected and additional failure mode effects analysis performed.

15. <u>Finding</u>: Subtle differences in processing can produce significantly different environmental resistance. When base metal has known SCC susceptibility, protective coating becomes very critical.

Heat treatment curve of Kanigen chemical nickel alloy coating

The curve was made by heating the parts in an inert atmosphere to the specified temperature, then holding at the temperature for one hour. At the expiration of the heating period, the parts were cooled slowly to 200°C then removed from the oven. All measurements of hardness were made at room temperature. All samples were plated on cold rolled steel. Measurements were taken on the top surface of plating 0.005" thick.

Final Vickers hardness number measured at room temperature

Heating Temperature (°C)

150

CORROSION INCIDENT SUMMARY

1. <u>Incident</u>: Corroded aluminum tubing

2. <u>CSM</u>: None (in process)

3. <u>System</u>: ECS

4. <u>Part</u>: Tube details

5. <u>Date</u>: April 1971

6. <u>When (Operation)</u>: Tube bending and storage

7. <u>Material</u>: 6061 tubing

8. <u>Heat Treat</u>: T6

9. <u>Surface Preparation</u>: As received

10. <u>Welding or Brazing Involved in Corrosion</u>: No

11. <u>Analysis</u>: No corrosion on inside of tubes. Corrosion on outside of tubes consisted of pitting which opened and became pronounced on bending. Subsequent investigation showed other corroded tubing in department stowage area.

12. <u>Cause</u>: Atmospheric corrosion in plant handling

13. <u>Corrosion Type</u>: Atmospheric

14. <u>Fix</u>: Chem film or oil and cover aluminum in process

15. <u>Finding</u>: Reemphasized need for "In-Process" corrosion control
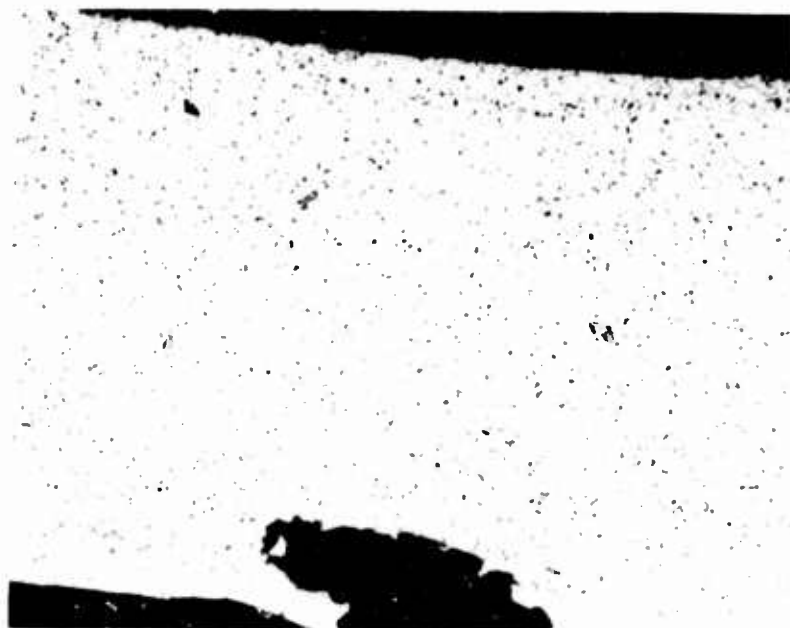
Section from Bend of Tube

Section from Straight Portion of Tube

Photomicrographs of Inactive Corrosion Pits from Detail Tube Assembly

152

CORROSION INCIDENT SUMMARY

1. Incident: Titanium tank failure (methanol)

2. Vehicle: Apollo 4

3. System: Service Propulsion System (SPS)

4. Part: Titanium fuel tank

5. Date: October 25, 1966

6. When (Operation): Proof test

7. Material: Ti-6Al-4V

8. Heat Treat: 160 ksi

9. Surface Preparation: As heat treated (blue oxide)

10. Welding or Brazing Involved in Corrosion: No

11. Observations and Analyses: Tank ruptured two hours after being pressurized
    with methanol. Fractography showed brittle fracture. SCC test
    showed reagent grade methanol to crack Ti-6Al-4V in time
    inversely proportional to stress. Methanol with more than one
    percent H_2O inhibits SCC.

12. Cause: SCC in dry methanol

13. Corrosion Type: SCC

14. Fix: Discontinue use of methanol

15. Finding: Purer fluids are not necessarily better. All fluids coming in
    contact with titanium under stress must be evaluated prior to
    use.
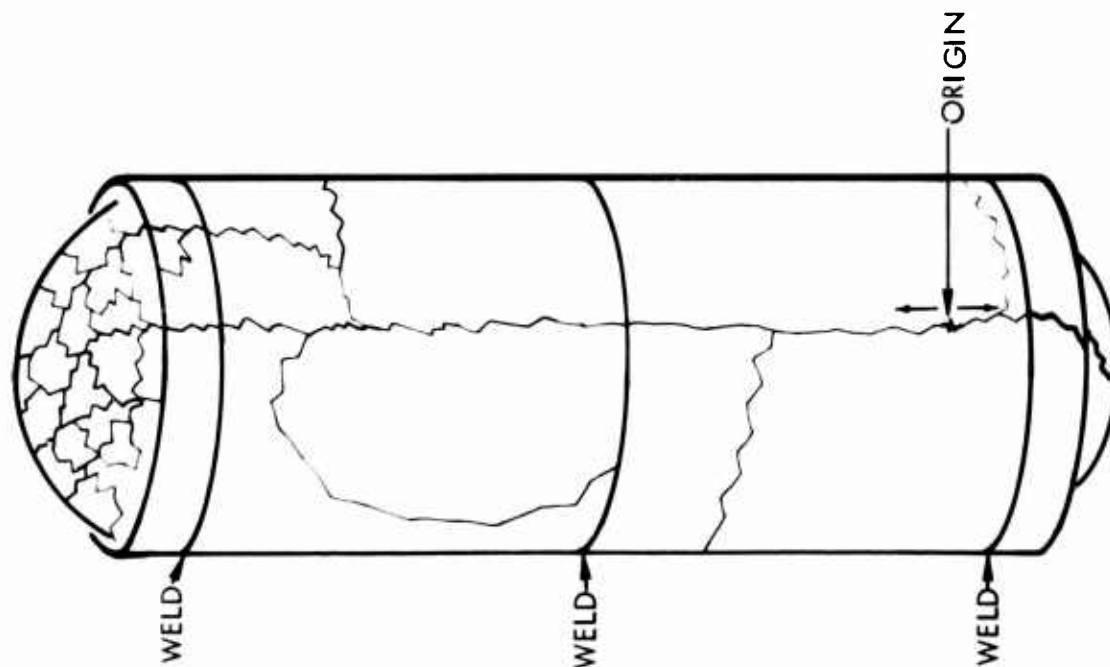
- FLAT FRACTURE WITH "POP-INS"

- RIPPING GOES BOTH DIRECTION

- MAIN FRACTURE - SAWTOOTH + YIELDING

- MAIN FRACTURE - $\perp$ TO MAX STRESS

- REMAINING CRACKS DUCTILE & NO YIELDING

- LOCAL AREA HAD MANY FINE CRACKS

WELD

WELD

WELD

ORIGIN

SPS TANK FAILURE

154

CORROSION INCIDENT SUMMARY

1. <u>Incident:</u> Titanium tank failure (NTO)

2. <u>Vehicle:</u> None

3. <u>System:</u> RCS

4. <u>Part:</u> Oxidizer stowage tank

5. <u>Date:</u> July 12, 1965

6. <u>When (Operation):</u> 30-day NTO exposure test, 160 F, 250 psig

7. <u>Material:</u> Ti-6Al-4V

8. <u>Heat Treat:</u> 160 ksi

9. <u>Surface Preparation:</u> Ti-Brite cleaned

10. <u>Welding or Brazing Involved in Corrosion:</u> No

11. <u>Observations and Analyses:</u> Tank ruptured seven hours after pressurization fractography showed brittle fracture and stress corrosion cracks

12. <u>Cause:</u> Reduced nitrous oxide (white NTO) stress corrodes titanium

13. <u>Corrosion Type:</u> SCC

14. <u>Fix:</u> Increase and control nitrous oxide in NTO

15. <u>Finding:</u> Purer fluids are not necessarily better. All fluids must be evaluated for compatibility with titanium.

Appearance of RCS Tank After Failure

156

CORROSION INCIDENT SUMMARY

1. __Incident:__ Freon MF-titanium tank incompatibility

2. __Vehicle:__ None (laboratory test only)

3. __System:__ RCS, SPS

4. __Part:__ All titanium tanks

5. __Date:__ January 12, 1967

6. __When (Operation):__ Laboratory compatibility tests at Lyndon B. Johnson Space Center

7. __Material:__ Ti-6Al-4V

8. __Heat Treat:__ 160 ksi

9. __Surface Preparation:__ As heat treated (blue oxide)

10. __Welding or Brazing Involved in Corrosion:__ No

11. __Analysis:__ Laboratory tests showed SCC of titanium 6Al-4V in Freon MF. Tests eventually allowed plotting toughness in any given fluid vs time.

12. __Cause:__ Freon MF used for cold flow checkout of propellant tanks. Although no tank failure occurred, use of Freon MF discontinued based on laboratory tests.

13. __Corrosion Type:__ SCC

14. __Fix:__ Use Freon TF in place of Freon MF and conduct compatibility (fracture mechanics) tests on each lot of Freon TF prior to test.

15. __Finding:__ Laboratory tests can accurately predict tank/fluid compatibility problem.
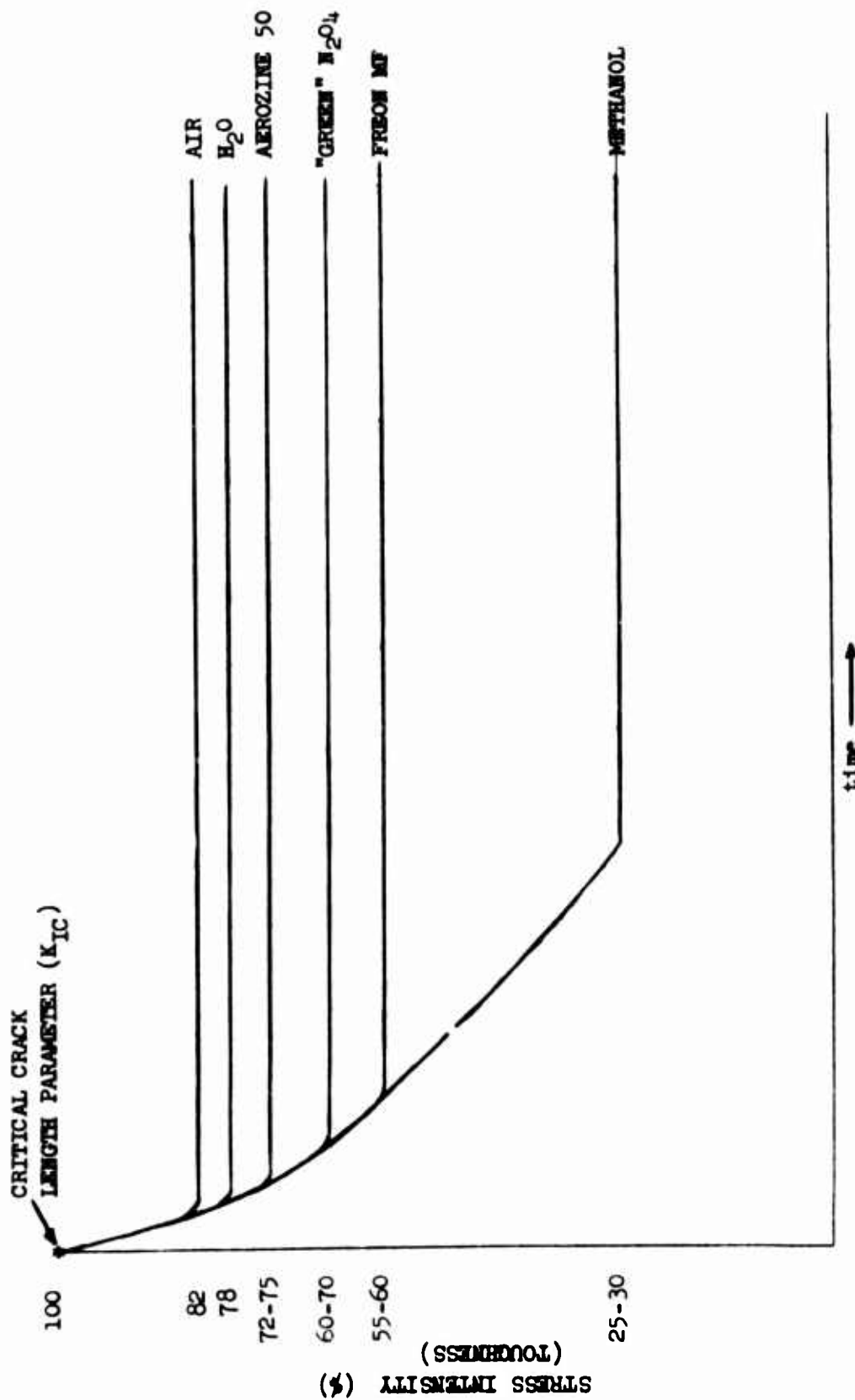
RELATIONSHIP OF "TOUGHNESS" OF Ti-6Al-4V MATERIAL
IN VARIOUS FLUIDS AS A FUNCTION OF TIME TO FAILURE
WITH CRITICAL CRACK LENGTHS

INTEGRATING THE AIR FORCE CORROSION CONTROL PLAN

AND ITS EFFECT ON THE F-15 EAGLE

by

A. W. Morris
McDonnell Aircraft Company
St. Louis, Missouri

ABSTRACT

This report discusses the Air Force Corrosion Plan and the McDonnell Aircraft Company's Corrosion Control Program for the Eagle Air Superiority Fighter. The key Program activities necessary for providing the Eagle with the capability of operating for a 10 year period without serious corrosion problems are identified. These include the selection of structural materials, protective finishes and the methods used to disseminate these requirements through the Project related entities including the Customer, Prime Contractor, Subcontractor, Supplier System.

TABLE OF CONTENTS

Page

1.0 INTRODUCTION

The Air Force Eagle designed and manufactured at the McDonnell Douglas Corp. St. Louis facility is the first conventionally fueled aircraft to have a thrust-to-weight ratio greater than one. This characteristic gives the Eagle an exceedingly high rate of acceleration and rate of climb capability. When these features are combined with light wing loading and large control surfaces, the end result is an aircraft with the superior maneuvering capability necessary for a state-of-the-art air superiority fighter. The 10 ft. canopy and the low wing design gives the pilot a 360° viewing angle above the aircraft fore and aft axis. An unusual feature of the McDonnell Aircraft Company's (MCAIR) design is the fact that the front of the engine air inlet ducts are pivoted at the bottom so that they rotate in the vertical plane. This provides the necessary control over inlet air to enable the engines to maintain full power throughout the F-15's wide ranging speed/altitude flight envelope and during violent air combat maneuvers. See Figure 1.

However, it is not the purpose of this paper to dwell on the Eagle's flight characteristics but to discuss a far more interesting subject to a corrosion engineer - the corrosion control features used in its design and the corrosion control program used to implement these design features.

In order to put the F-15's corrosion control technology in perspective it is necessary to look back and see what we had in the way of technology a few years ago. Until the 1960's, military aircraft were selected on the basis of "fly-away" cost and flight performance. In the immediate post-World War II era this was a successful policy from a corrosion control standard because the materials used were relatively corrosion resistant. The structure was made out of light gauge material and the skins were generally alclad light gauge aluminum sheet. Because only a minimum of protection from corrosion was required, protective methods were held to a low key effort both in the research and development field and in the application area. In contrast to the stagnation which existed in corrosion control methods, rapid advances were made in the development of higher strength structural materials. For example, the use of 7075-T6, 7178-T6 and 7079-T6 aluminum alloys as well as the use of higher strength steels and magnesium alloys became increasing popular. As a result, airframe structures became more efficient but the impact of using these corrosion susceptible materials was not seriously assessed because of the fragmented responsibility for corrosion control in both the corporate and military organizational structure.

When aircraft representing the ultimate in structural efficiency were exposed to corrosive operating conditions, such as aircraft carrier deployment, whole aircraft models were scrapped because the cost of repairing corrosion damage would have exceeded the value of the aircraft[1]. We now realize that the combined effect of using bare aluminum skins instead of alclad skins, the use of materials at their highest strength level and the use of heavy gauge aluminum was such that conventional protective systems were no longer capable of protecting these ultra efficient structural materials.

The need for corrective action accelerated corrosion research and development to an unprecedented level. One of the most significant advances was made by aluminum suppliers in the development of the intergranular corrosion resistant overaged tempers. The use of magnesium alloys was restricted. The shot peening of high strength steels became a mandatory operation for stress corrosion prevention. MCAIR funded a 5 year in-house corrosion control research and development program. This program made it possible to evaluate the corrosion resistance of newly developed materials and the protection provided by the use of fastener and joint sealing techniques. Through the Navy's encouragement in the use of this technology, the F-4 became one of the first aircraft to make use of the overaged aluminum alloy tempers to prevent stress corrosion and exfoliation problems and to use sealants to control corrosion at fastener locations and joint interfaces. As a result, when the Air Force F-15 contract was awarded, MCAIR was in a position to appreciate the need for application of the state-of-the-art corrosion control methods and was experienced in dealing with the problems associated with their implementation.

Because protective finishes are no longer regarded as the only corrosion control method, the finish specification by itself is no longer an adequate method of specifying and controlling corrosion control technology useage. Utilization of the state of the art technology required a new approach to aircraft design. The Air Force had the foresight to introduce their corrosion control plan as a contractual requirement at a time when corrosion specialists were needed as part of the design team to promote full utilization of the advances in corrosion resistant materials. Also, the scope of corrosion control technology has increased to a point where a program which is an integral part of the design, manufacturing, and deployment activities is required to coordinate corrosion control related activities. The Air Force corrosion control plan meets this requirement by providing a framework of program activities and controls upon which a successful corrosion control program can be built.

2.0 SUMMARY OF THE AIR FORCE CORROSION CONTROL PLAN REQUIREMENTS

The stated objective of the plan is to "provide an effective corrosion preventive and control plan on a total system basis. To assure that corrosion considerations and control measures are properly integrated during contract definition, engineering development, and operational phases in consonance with the designated life cycle of the system and mission objectives." In order to meet this objective, the plan requires the contractor to design, implement and maintain a corrosion control program and to identify the office or individual responsible for administering the program.[2] The plan goes on to detail the scope and structure the program must have to receive Air Force approval. The principal requirements for the program are summarized below:

o Selection of corrosion control design features such as materials, protective coatings, drainage and sealing requirements on the basis of an environmental analysis.

o Review of Engineering drawings by corrosion control specialists.

o Development and maintenance of a corrosion control training program.

o Submittal of a finish specification for Air Force Approval.

o Control of manufacturing processes and methods to ensure the intrinsic
   corrosion resistance of structural materials will not be jeopardized.

o Control of subcontractors and suppliers to ensure compliance with program
   structural material, finish, sealing, processing and drainage requirements.

o Customer and contractor reviews during design, manufacturing and deploy-
   ment until system obsolescence.

o Specification of Quality Assurance's corrosion control functions.

Although the above summary is not complete, it outlines the scope of the pro-
gram the contractor must maintain from design concept to obsolescence. All con-
tractor supplied equipment including ground support equipment must be covered by
the contractor's corrosion control program. The only hardware not under full con-
trol of the plan is government furnished equipment and standard parts. Technically
standard parts fall under the plan's provisions, but the fact is, government and
industry specifications to which standard parts are fabricated have not been
reoriented to meet the more stringent plan requirements.

The plan revolutionizes the concept of aircraft corrosion control in these
respects:

o It provides a balanced system of activities and controls as a framework
   for a contractual corrosion control program to be maintained from design
   to obsolescence.

o It requires that the administrator of the program be identified.

o It requires that the customer and the contractor cooperate in regular
   program reviews.

o It requires a training program be set up so that Engineering, Quality
   Assurance and Production are familiar with corrosion control methods and
   technology.

In other words, the plan is based on a systems engineering concept in which
the network of corrosion control related activities which are diffused through
company divisions, and which interlock with another network in the Air Force are
defined in such a way that they can be monitored and correlated as required.

3.0 THE MCAIR CORROSION CONTROL PROGRAM[3]

The prime objective of the MCAIR program is to build a weapon system which
can operate for a 10 year period without the need for scheduled depot maintenance
to repair corrosion damage. Our experience indicates that by maximizing the use
of alclad aluminum and the overaged aluminum alloy temper conditions and by using
state-of-the-art protective systems, this goal can be achieved. To realize this
difficult objective it would be necessary to make effective use of the Air Force
Corrosion Control Plan in designing a program which would effectively implement
the required technology. Selecting technology which would meet our 10 year objective

is a relatively simple task compared to the task of communication. Any weak spots in communicating the plan requirements to Engineering, Quality Assurance and Manufacturing personnel assigned to the project by MCAIR or contractors would result in nonuniformity in corrosion control design features. Communicating these more stringent requirements to specialized equipment suppliers was also a challenging problem.

The principal features of the program used to select the F-15 corrosion control design features and to communicate these requirements to outside and in-house personnel is summarized in Table 1.

TABLE 1 MCAIR CORROSION CONTROL PROGRAM SUMMARY

Program Phase	Activities & Controls
Design	o Select corrosion control design features based on a 10 year operational life criteria o Document selected design features in: "Corrosion Control Plan", "Air Vehicle Specification", "Finish Specification" and "Corrosion Control Guidelines" o Corrosion specialist review of Engineering drawings, process specifications, procurement specifications, proposals and equipment supplier's proposed usage of materials, finishes and processes o Participate in Customer/MCAIR corrosion control design reviews o Utilize a corrosion control training program to acquaint Engineering - in-house and contractor personnel - with the program requirements and their individual responsibilities
Manufacturing	o Utilize a corrosion control training program to acquaint Production and Quality Assurance - in-house and contractor personnel - with the program requirements and their individual responsibilities o Monitor process controls, assembly operations, and supplier environmental qualification test results. Participate in Customer/MCAIR reviews on in-house and major subcontractor manufacturing facilities and operations
Deployment	o Participate in Customer/MCAIR inspections of aircraft after environmental hangar test, after 1 year squadron deployment and at Customer scheduled intervals thereafter o Recommend appropriate design changes or maintenance corrective action as required o Provide technical support at the request of the Customer

Now that the program has reached the point where production aircraft are on the assembly line with the first delivery to Tactical Air Command scheduled for November of this year, it is possible to look back on the design and manufacturing elements of the program and identify some activities which had a major impact in helping MCAIR meet the program objectives.

3.1 Corrosion Control Design Feature Selection - The initial and one of the key program activities was the selection of the corrosion control design features such as structural materials, protective finishes and water trap drainage provisions. The approach taken was to avoid design features which caused, or contributed to, corrosion problems in older designs and to substitute materials and preventive methods which had proved themselves over the years such as alclad coatings on aluminum or which, although recently developed, had sufficient service history behind them to prove their superiority over less successful design features. The following discussion illustrates how these concepts were implemented first in selecting and then in documenting F-15 design features.

Finish Deficiencies - In older designs, corrosion problems were related to the following protective finish inadequacies:

o There was no established criteria for protecting surfaces which because of functional or fabrication method reasons could not be painted.

o Exterior paint systems such as lacquers, acrylics and epoxies were subject to cracking with resultant exposure of the substrate in locations where it was most vulnerable to attack - moldline fastener locations.

o The less protective interior finish systems were often used instead of the exterior system in areas which are interior located but are in fact exposed to the exterior environment.

o Dissimilar metal joints were not identified and given adequate protection.

o Cadmium plating on standard parts such as fasteners was too thin to provide adequate protection (.0002 in min).

3.2 F-15 Finish Specification Requirements - For the purpose of protective finish application the aircraft was divided into three environmental areas: exterior, interior and jet fuel. When the paint finish system applicable to an environmental area could not be applied for functional reasons, emphasis was placed on the concept that the alternate protective system must be at least as protective as the paint finish or the component material must be a corrosion resistant type that does not require a protective finish. For example, if paint were removed from an area to provide electrical grounding and an environmental sealing technique could not be used, the area is electroplated or the material is required to be corrosion resistant [4]. Low alloy steel parts with a functional wear surface received as a minimum, a .002 in. thick electroplate of nickel or chromium. A large number of functional surfaces do not require protection because of the extensive use of stainless steel and titanium fittings in the F-15 design.

The following excerpt from the F-15 Finish Specification shows that all areas exposed to the exterior environment are clearly identified [5]. In so doing, we are meeting the corrosion control plan requirements that protective methods be related to environmental conditions.

165

EXCERPT FROM F-15 FINISH SPECIFICATION

"3.0 REQUIREMENTS

Exterior Surfaces - Component part surfaces which comprise or lie in the following areas shall be considered exterior surfaces:

o Airframe moldline

o Landing gear and arresting gear exterior, cutouts, fold areas, doors, and wells

o Speedbrake moldline and edges, cutouts, and compartment

o Missile wells

o Refueling well

o Gun compartment

o Chaff dispensing wells

o Air inlet and exit ducts

o Cockpit floor

o Pylons and external stores moldline (except external fuel tanks)."

End of excerpt.

Exterior Finish Requirements - Exterior surfaces receive the following finish system on nonfunctional surfaces:

o All skins and attachments are coated with sealant on faying surfaces to preclude moisture entrapment

o All permanent fasteners in aluminum and low alloy steel components are installed with sealant. - Removable fasteners are installed after the access door countersinks have been painted

o Surfaces receive an epoxy primer coat and a two-coat linear polyurethane enamel paint systems except for some titanium and stainless steel components in "hot" areas. The polyurethane enamel topcoat used on the F-15 had shown its superior anti-cracking and weather resistant characteristics over a two year test period on operational Air Force and Navy Phantom aircraft

The F-15 landing gear finish requirements are an example of using field experience to correct problem areas. During a tour of the Warner Robins AFB overhaul facilities it was noted that most landing gear corrosion damage occurred in the I.D. of bushed holes and in the I.D. of tubular struts containing air spaces. These problems result from the policy of inserting bushings into unprotected holes and from applying only one coat of primer to the landing gear I.D. surfaces in spite of the fact that exterior air has free access to areas not submerged in hydraulic oil.

To overcome these deficiencies, the bushed holes in the F-15 300M alloy gear components are cadmium plated as are the O.D. of the bushings. The I.D. of the F-15 tubular gear components which enclose air spaces have the same protective finish as the O.D. - a .005 in. minimum coating of low embrittlement cadmium which is first chromated and then painted with the exterior paint finish.

Fasteners - Each aircraft is assembled using thousands of fasteners and the installed cost runs into thousands of dollars. Yet fasteners tended to be ignored in industry and military finish specifications. The question of whether a titanium or stainless steel fastener in aluminum structure should be treated as a dissimilar metal interface or not, is not directly addressed. In addition, there seemed to be an assumption that all fasteners are a monolithic item like a rivet. In fact, structural engineers tend to use the most weight effective fastener types. Therefore it is common practice to use an aluminum collar on a titanium or stainless steel pin when using a pin and collar type fastener instead of a stainless collar. Aluminum nut plates may contain stainless steel nut elements with cadmium plated screws and stainless steel retainers.

As a result of the large number of possible fastener element material combinations, there was a lot of confusion on the assembly floor about when to seal a fastener and when not to seal it, or whether to paint it for corrosion protection or to leave it bare. Corrective action included emphasizing rules governing fastener/structural interface protection during the Corrosion Control Training sessions. This training course is discussed in a subsequent chapter.

All project personnel who complete the training program are issued a pocket sized "Corrosion Prevention Procedures" manual[6]. This manual contains the following sealing instructions:

"Sealing Requirements for Permanent Fasteners: There are approximately 442,000 fasteners used in the F-15 airframe assembly. Therefore, the most common functional surface sealing operation involves the sealing of fastener holes. Fasteners are sealed for two general reasons - to prevent corrosion and to prevent leakage from wet fuel cells or pressurized compartments. The following general rules apply to permanent fastener installations.

General Rule #1 - Coat all fasteners with sealant before insertion in aluminum, composite, or cadmium plated components which are on the moldline or in exterior locations as defined by the Finish specification.

General Rule #2 - Seal all fasteners located in holes which penetrate into a pressurized compartment or wet fuel area.

The following requirements apply to all fasteners which are not covered by the two general rules specified above. The following applications may be sealed either with sealant or with wet paint primer.

Seal all stainless steel fasteners or aluminum fasteners elements such as rivets, collars, or washers which contact titanium, stainless steel or Inconel type alloys.

167

Seal all cadmium plated fasteners or fastener elements which contact stainless steel, brass, copper, or Inconel.

NOTE:
1) Cadmium plated fasteners are prohibited in applications which would bring them into contact with titanium, and titanium fasteners are prohibited in applications which would bring them into contact with cadmium plated components.

2) Monel fasteners or copper plated fasteners should not be used in contact with aluminum components.

3) Violations of 1) or 2) above should be brought to the attention of the supervision for corrective action."

The above instructions permit the use of sealant or paint primer to protect fastener interfaces on interior components but require the use of sealant on exterior located fasteners. The reasoning behind these requirements stems from the fact that exterior skins and doors are subject to a greater degree of flexure under cyclic loads than interior structure. Therefore, sealant is required on exterior located fasteners because its superior flexibility allows it to accommodate to the flexing and relative movement between fastener and component without rupturing. Paint is permitted in lieu of sealant on interior located fasteners because in-house corrosion exposure tests indicate it provides corrosion protection equal, or superior to sealant.

Cadmium plated fastener corrosion problems are avoided through the use of stainless steel, titanium and aluminum fasteners for 95% of the moldline applications. The cadmium plated fasteners that are used are MCAIR specials because they have a thicker cadmium plating requirement than standard fasteners - Class 2 instead of Class 3.

Magnesium Alloys - There are only three airframe components fabricated from a magnesium alloy. These are AZ91C magnesium castings. Their configuration was carefully studied to ensure freedom from water traps before permission was requested from the Air Force for magnesium utilization. They are required by the Finish Specification to have all assembly line fitting and hole drilling accomplished before the finish system is applied. The parts are brought to the assembly line match drilled and fitted; then they are given a heavy (Type I) Dow 17 coating as well as an extra coat of primer and an extra topcoat. Therefore, all surfaces including fastener holes are completely incapsulated by the anodic coating and paint system. In addition, all faying surfaces and fasteners are coated with a polysulfide sealant immediately before assembly.

Composite Structures - All aluminum honeycomb core used on the F-15 is the non-perforated type and has a proprietary corrosion resistant coating on the surface. Both aluminum and titanium skins are coated with a corrosion inhibiting adhesive primer for corrosion protection before the structural adhesive is applied for bonding purposes. In addition, all honeycomb assemblies including those with composite skins are leak tested after the exposed bondlines are sealed by application of a polysulfide sealant. This is accomplished by submerging the assembly in hot water and looking for air bubbles produced when the positive pressure generated as the air in the honeycomb is heated forces its way through any voids which may be present in the sealant coated bondline. Any "leakers" are resealed and retested.

168

3.3 F-15 Material Selection - The most damaging types of corrosion experienced by aircraft using the 7XXX and 2XXX series alloys in a T6 temper condition are stress corrosion cracking and exfoliation. Stress corrosion caused more component failures but exfoliation is more expensive to repair because it normally affects a large number of parts instead of a few. In-house experience backed up with data from aluminum suppliers indicated that thin gauge sheet less than .080 in. was generally resistant to this type of attack if good quenching practices after solution treatment were applied. Our selection criteria required that the more susceptible products be used in temper conditions formulated to resist stress corrosion and exfoliation attack as shown in Table 2.

TABLE 2 - ALUMINUM ALLOY SELECTION CRITERIA
FOR THE PREVENTION OF CORROSION THAT TYPIFIES T6 USAGE

Product	Type of Attack Typical of T6 Temper (7XXX and 2XXX Series Alloys)	F-15 Usage
Sheet less than .080 in. thick	Pitting	*2024-T81 *7075-T6 *2024-T6 6061-T6
Sheet thicker than .080 in.	Exfoliation	*7075-T76 *2024-T72 *2024-T81 6061-T6
Plate	Exfoliation, Stress Corrosion	*7075-T73 *2024-T851 6061-T6
Forgings	Stress Corrosion	**7075-T73XXX

NOTES: Extrusions are similar to sheet and plate in corrosion susceptibility
   *Alclad materials are used where environmental conditions could cause pitting.
   **7075-T73XXX is the only aluminum material recommended for forgings.

The F-15 aluminum product usage is unique in that the areas identified in the Finish Specification as "exterior" are alclad or anodized or are fabricated from 6061-T6. Alclad was used in perference to anodize except when product type, fabrication or functional requirement precluded its use. Our experience indicated that alclad provided sacrificial protection to adjacent non clad areas such as edges and countersinks. In contrast, anodized coatings lack the capability to protect non-anodized countersinks and other adjacent non-anodized surfaces. Access doors with removable fasteners proved to be the most susceptible type of component to exfoliation corrosion attack on previous aircraft designs. Fortunately, in order to meet "turnaround" requirements, a large number of F-15 access doors are either secured by latches or quick release type fasteners. Other doors are corrosion resistant becuase they are fabricated from titanium. Aluminum doors secrued with removable fasteners in addition to being alclad must be fabricated from the exfoliation resistant 7075-T76, 7075-T73, 2024-T72, or 2024-T851 materials.

Exfoliation and stress corrosion resistant overaged tempers were also used for aluminum extrusions. 7075 alloy extrusions in the medium gauge sizes were overaged to the T76511 temper and heavier gauges to the 7075-T73511 temper. The exfoliation and stress corrosion resistant 2024-T8511 alloy temper was also used in many applications. Another important corrosion control design factor is that hundreds of lightly loaded miscellaneous items such as shims, spacers, brackets and some fairings are fabricated from an alloy with superior resistance to intergranular and pitting corrosion - 6061-T6. Formerly such items were fabricated from 2024-T4 or 2024-T3. Naturally aged 2XXX series alloy tempers such as 2024-T4, T42, T3, T351 and T3511 were prohibited because their instability in the F-15 thermal environment invited intergranular corrosion attack (7).

Titanium Alloys - All titanium alloys are used in the annealed condition. Ti-6Al-4V is used in applications where toughness and fatigue resistance are prime requirements. In other applications, Ti-6Al-6V-2Sn is used where its superior strength-to-weight ratio can be used to advantage. High pressure hydraulic tubing is fabricated from Ti-3Al-2.5V.

Ferrous Alloys - Stainless steel selection was controlled to prevent the use of alloys or microstructures which are susceptible to intergranular attack (300 series alloys) or stress corrosion (precipitation hardening alloys). The SAE 4340 type alloy forgings which caused stress corrosion problems in older designs when they were heat treated to high strength levels are restricted to the 180-200 ksi ultimate tensile strength range for F-15 applications. The high strength landing gear components are fabricated from 300M steel. This material has been used successfully for commercial aircraft gear components.

Material Distribution - The manner in which these materials are distributed throughout the airframe is shown in Figure 1. Alclad aluminum alloy skins predominate in the forward fuselage and the forward part of the center fuselage. In contrast, the aft part of the airframe is fabricated from titanium alloys, boron epoxy composites, brazed titanium composites and aluminum honeycomb.

3.4 Program Controls - It is not difficult to select materials which have the required corrosion resistance properties for a 10 year service life and to draw up another list of materials which do not have the required properties. The difficult part of the program is to communicate this information in such a way that it will be accurately utilized thoughout the prime contractor, subcontractor and component supplier system.

There is no traditional vehicle for specifying material usage that parallels the use of a finish specification for control of finish usage. In order to provide a working document to aid all designers to select materials approved by structures, metallurgists and corrosion specialists, a MCAIR Report, "F-15 Corrosion Control Guidelines" (8) was compiled by corrosion specialists and approved by the Project Engineering Manager to give it the required authority. This report was distributed to the program design team before any drawings were released. The report not only minimized the number of drawings rejected by the corrosion specialist during his review but also reduced communication problems with the designers.

The report also provided guidance on methods for water trap elimination including the use of drain holes at low spots or for sealant utilization to raise the level of a low spot if a drain hole could not be drilled at that particular location.

170

The E33 Data Item - Procurement Specifications required suppliers of components and systems - electronic equipment excepted - to submit an E33 data item for approval. This data item requires full disclosure of the material, finish and processes used to fabricate each detail part. These data items were reviewed by corrosion specialists to ensure conformance with our material and finish requirements. Although these requirements were clearly stated in the Procurement Specification a substantial number of data item responses indicated they were not taken seriously and that the suppliers intended to continue using materials that were responsible for corrosion problems on previous aircraft designs. Therefore, without the E33 data item submittal and review requirement, airborne systems and components would not have met F-15 material and finish requirements.

Engineering Drawing Review - Besides providing the necessary control to ensure only approved materials and finishes are used, the drawing review also provides an opportunity to suggest changes which reduce dissimilar metal interfaces or which reduce costs through standardization of material usage. Most dissimilar metal contacts involve the selection of standard parts such as fasteners, clamps and plumbing or electrical system details which are not compatible with interfacing structure.

3.5 The Corrosion Control Training Program - Just as the Corrosion Control Guidelines Report was a major factor in familiarizing design personnel with the corrosion control Design Features and was a major factor in ensuring compliance, so that Corrosion Control Training Program was a major instrument for performing the same functions during the manufacturing phase of the program. The training program is a mandatory requirement for all in-house and major subcontractor personnel assigned to the F-15 project. Two different programs are available for presentation.

Engineering, Quality Assurance and Manufacturing supervision are given classroom training sessions by a corrosion specialist which included the following subject matter:

o Corrosion theory

o Typical corrosion problems and causes

o Corrosion control program contractual requirements

o The F-15 corrosion control design features

o Mechanisms by which F-15 design features avoid or prevent corrosion problems

o Detail and assembly operations which have a critical effect on weapon system corrosion resistance.

Production Training Program - Because of the large number of Production personnel and production floor Quality Assurance personnel who were required to participate in the Training program (approximately 1200), this presentation was automated. A tape recording was used in conjunction with a slide projector.

This training program was based on the pocket sized reference book mentioned previously (6), a copy of which was given to all in-house and contractor personnel who attended the course. The presentations and the training sessions are organized by the MCAIR F-15 Training Department.

The program content was divided into two sections:

Section I discusses detail part fabrication and finishes with emphasis on
the importance of: 1) protecting parts from corrosion or mechanically induced
surface damage during handling, processing and storage, 2) F-15 contractual
mechanical, thermal and chemical processing requirements, 3) finishes for painted
parts and finishes for surfaces which cannot be painted because of functional re-
quirements.

The second section addressed itself to assembly operation corrosion control
requirements such as compartmental drainage, mold line sealing, removal of foreign
objects from compartments, dissimilar metal protection as well as paint finish
requirements for subassemblies.

The pocket sized Corrosion Prevention Procedure handbook in addition to pro-
viding the above detailed information cautioned all personnel to be on the "look-
out" for any of the following violations and to report them to their supervision
for corrective action:

o Bare structural materials in contact with aluminum (unless contact area
  is environmentally sealed).

o Cadmium or silver plated parts in contact with titanium.

o Assembly line drilling or "fitting" of painted magnesium parts.

o Unprotected aluminum fastener elements such as screws, washers, collers,
  etc., in contact with titanium or stainless steel.

The reason that bare structural materials in contact with aluminum - unless
contact areas are environmentally sealed - is a violation is that materials which
do not have a protective finish are corrosion resistant and therefore incompatible
with aluminum. The finish specification requires that all such dissimilar metal
joints be assembled with a coating of uncured paint or primer on the mating sur-
faces so that a "squeeze out" of excess material is obtained. This ensures that
all voids in the joint are filled with paint or sealant to deny access to moisture
and other corrodents.

The interfacing of any cadmium plated parts with titanium is prohibited not only
because it may cause embrittlement and cracking of the titanium microstructure, but also
because the materials are galvanically incompatible. Silver in contact with ti-
tanium alloys has an adverse effect on their stress corrosion resistance at tem-
peratures in excess of 450°F and therefore the use of standard silver plated stain-
less steel fasteners or other silver plated components is prohibited in applica-
tions where they would contact titanium.

Magnesium parts are supplied to the assembly line in a painted condition.
Drilling of holes or any other operation which would damage the anodized Dow 17
coating and the paint finish are prohibited because there is no touch-up treat-
ment which supplies equivalent protection to Dow 17. And magnesium needs all the
specified protection to remain corrosion free for the life of the airframe.

Aluminum fastener elements in an aluminum structure would be automatically
painted with the rest of the subassembly. In contrast, an interior located tita-
nium or stainless steel structure is normally not painted. Therefore, aluminum
fastener elements located in such a structure must be touched up by hand.

There are two general points of interest concerning the training program:

1. A computer program is used to keep track of personnel changes so that the Training Department can arrange training sessions as new personnel are assigned to the project.

2. More than 1,500 MCAIR personnel and a large number of prime contractor personnel have been exposed to the corrosion control training and have received a copy of the "Corrosion Control Handbook".

4.0 CONCLUSION

There can be a significant gap between the quality of the technology built into a product and that which has been made available for use through research and development programs. This is generally true immediately following rapid technology advances and is especially true if the new technology cannot be applied by traditional application methods. Corrosion control technology in the middle 60's is a case in point. It had suddenly expanded in scope and sophistication to the extent that it was no longer solely concerned with protective finishes. If advances in corrosive resistant material technology were to be fully exploited, the corrosion engineer had to move from the traditional peripherial role of writing a finish specification to one of active participation in the conceptual and detail design of the product. Acceptance of this concept and its implementation would normally be a slow process and during such a transition a significant gap in applied technology and state-of-the-art technology would exist.

The Air Force Corrosion Control Control Plan played a vital role in speeding up the transition process. By making the plan contractual and having the contractor identify the plan manager, corrosion control was no longer everybody's and nobody's responsibility. The Plan outlined the scope of the contractor's program and set the ground rules for developing a program which had the necessary management and technical attributes for success.

The Eagle Corrosion Control Program which has been discussed in general terms is one example of an infinite variety of plans which can be built around the Corrosion Control Plan Blueprints. The program built on these blueprints can be a facade or an efficient corrosion control implementation tool depending on the type of support it receives from project management and depending on the skill and dedication of the hundreds of personnel who have a direct or peripherial part in its function.

In the writer's opinion a successful program should have the following characteristics.

° The program must have a clearcut objective

° Selected corrosion control technology must be compatible with the program objective

° Materials and finishes must be selected on environmental basis

° Component materials which would normally be painted but which cannot be painted must be given equivalent protection by another corrosion prevention method

173

o Materials which are too corrosion prone to be capable of protection by
conventional finishes should be avoided. If this is not possible, then
they must be protected by a special finish tailor-made to meet their
requirements. The shot peened, chromated cadmium, paint system combina-
tion finish used on high strength steels is an example of a special finish
combination required for a potentially corrosion succeptible material.

o The program objectives must be kept in mind during day to day decision
making to prevent a gradual deterioriation in applied technology quality.

It is felt that the Eagle's Corrosion Control Program is successful by
today's standards. However, the moment of truth will not arrive until a signi-
ficant number of aircraft have been in service for the duration of their design
life. Therefore, it would be interesting to compare the conclusions drawn at
that time with the conclusions that appear valid today.

5.0 REFERENCES

1. Samual Goldberg, Head Metals Section, Department of the Navy, Naval Air Systems Command (Private Communication)

2. AFLC/AFSC Data Item No. S138, "Corrosion Prevention and Control Program"

3. CDRL A066, "F-15 Corrosion Prevention and Control Program", McDonnell Aircraft Company, St. Louis, Missouri 63166

4. A. W. Morris, J. J. Reilly, "Corrosion Control Methods For Electrically Bonded Joints. MCAIR Report No. 73-026. Presented at the 1974 National Association of Corrosion Engineers, Chicago, Illinois, 2-8 March 1974.

5. R. A. Lammers III, A. W. Morris, R. A. Williams, "Finish Specification For F-15 Aircraft"

6. A. W. Morris, "F-15 Corrosion Prevention Procedures", Published by MCAIR Training Department, March 1972, McDonnell Aircraft Company, St. Louis, Missouri 63166

7. J. A. Nock, Jr., Reheating of 2024 and 7075 Sheet, Alcoa Research Laboratories, Aluminum Company of America, New Kensington, Pennsylvania

8. A. W. Morris, R. A. Williams, F-15 Corrosion Prevention Guidelines, MDC Report No. A0448, 1 July 1970.
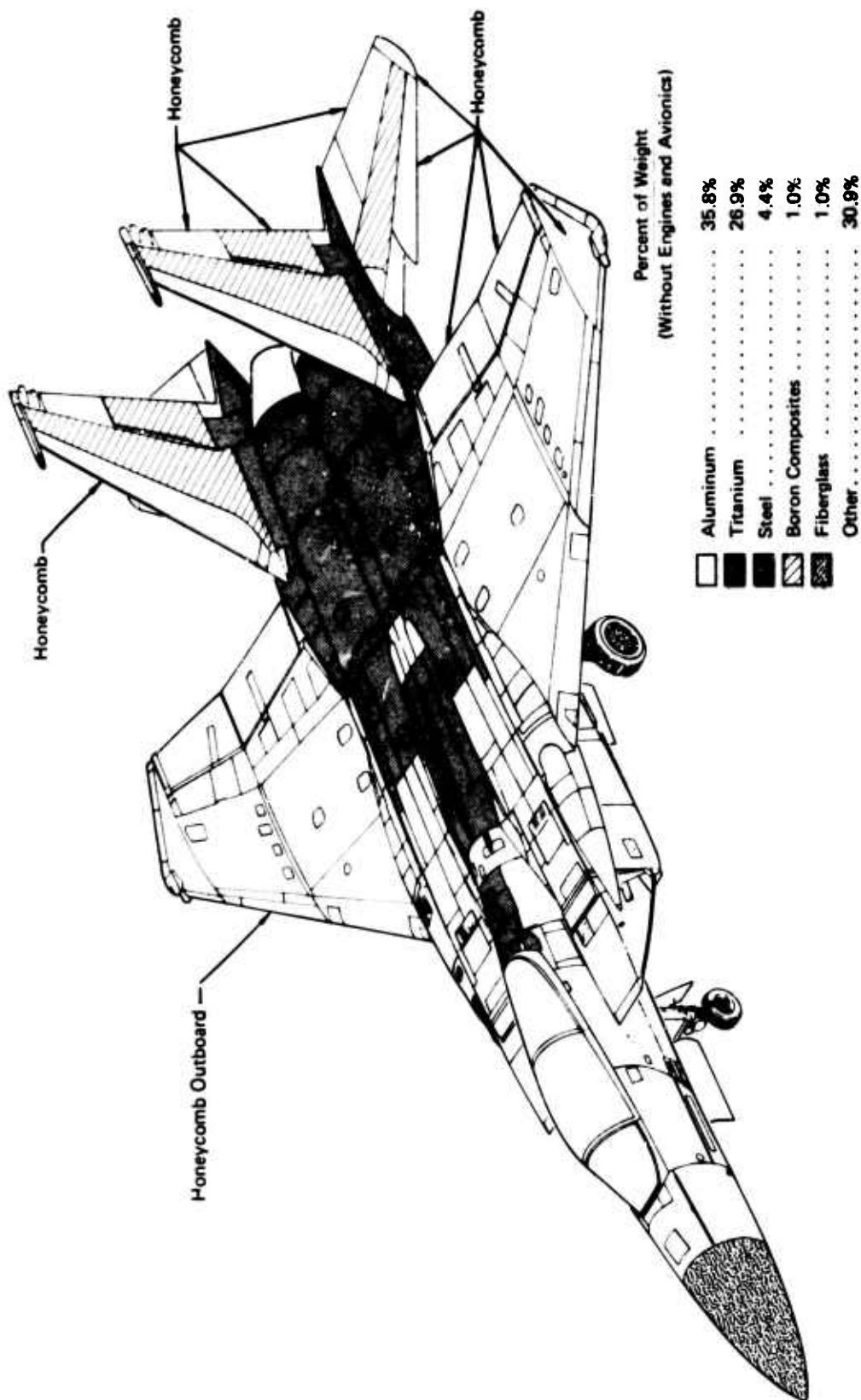
FIGURE 1
MATERIAL DISTRIBUTION

Honeycomb

Honeycomb

Honeycomb

Honeycomb Outboard

Percent of Weight
(Without Engines and Avionics)

☐	Aluminum	35.8%
■	Titanium	26.9%
■	Steel	4.4%
☐	Boron Composites	1.0%
▨	Fiberglass	1.0%
▨	Other	30.9%

GP74-0826-1

176

STRESS CORROSION CRACKING SUSCEPTIBILITY OF
β TITANIUM ALLOY 38-6-44:   CANDIDATE ALLOY
FOR SCOUT TORSION BAR

by

Walter F. Czyrklis and Milton Levy
Army Materials and Mechanics Research Center
Watertown, Massachusetts   02172

ABSTRACT

The threshold stress intensities for stress corrosion crack propagation
in beta titanium alloy 38-6-44, Ti-3Al-8V-6Cr-4Mo-4Zr, has been determined
in salt water and methanolic solutions. The alloy was immune to SCC in aqueous
sodium chloride solutions. However, in methanolic solutions, the alloy was
very susceptible to SCC. This marked susceptibility in methanolic solutions
can be mitigated by the addition of an inhibitor sodium nitrate. Crack exten-
sion in the alloy was transgranular and failure occurred by brittle quasicleav-
age in methanolic solutions.

INTRODUCTION

The newer beta-type titanium alloys are finding increasing use because of their excellent fabricability, corrosion resistance, and heat treatment respons. In the ductile solution treated condition, these alloys are easily formed and cold headed for applications such as honeycomb, thin sheet, and fasteners. The excellent deep hardening characteristics of beta titanium alloys also make them attractive for thick section parts.

One of these newer β alloys, titanium alloy 38-6-44, nominal composition Ti-3Al-8V-6Cr-4Mo-4Zr, has been selected as the candidate material for the Scout Army Vehicle dual rate torsion bar application. The selection of this alloy appears to be an excellent materials choice because of its superior spring rate characteristics. Also, depending on the heat treat cycle, many strength-ductility combinations can be produced and, unlike some of the other beta alloys, the brittle omega phase does not form during the heat treatment. By proper aging of the solution treated material, ultimate tensile strengths in excess of 200 ksi can be obtained.

Other β alloys, including Beta III[1], have been reported as susceptible to SCC in aqueous solutions. The strength level of Ti-38-6-44 proposed for the Scout torsion bar application is relatively high and usually susceptibility to SCC increases with increasing strength level. For these reasons, SCC of Ti-38-6-44 may be a potential problem for Scout and ATAC requested that AMMRC investigate the alloy's SCC susceptibility. Reported herein, is the alloys response to SCC in the solution treated and aged condition that is identical to the heat treatment proposed for the Scout torsion bar application.

178

EXPERIMENTAL PROCEDURE

Materials

Titanium alloy 38-6-44 was obtained from Reactive Metals Inc. in the form of 9/16-inch thick plate which had been solution treated at 1700°F for thirty minutes and air cooled, then aged at 875°F for 24 hours and air cooled. The chemical composition and mechanical properties of the material are shown in Table I.

Single edge notched cantilever beam specimens, 6 x 1 x 0.5 inch with a 0.3-inch deep, 45° included angle notch were fabricated from the plate material in order to determine this alloys susceptibility to stress corrosion cracking. The specimens were of L-T orientation, that is, they were cut with the long dimension parallel to the direction of grain flow and notched so as to cause crack growth and fracture during testing to take place through the long transverse direction.

Metallographic examination of the alloy shows a microstructure of equiaxed beta grains with a finely dispersed alpha phase (dark) in the beta (light) matrix. Note the α precipitation at the grain boundaries and the enriched β region adjacent to the β grain boundaries. See Figure I.

The environments used for testing were 3.5% sodium chloride, methanol, and methanol to which a small amount of hydrochloric acid was added. Reagent grade chemicals and distilled water were used to prepare the solutions. The sodium chloride was used to simulate a sea water environment while methanol has been used as a de-icing solution in both automotive and aircraft applications. The methanol plus hydrochloric acid solution is a convenient way of introducing

179

chloride ion into methyl alcohol. Titanium alloys have been found to be susceptible to stress corrosion in all of these environments.[1-5]

TEST PROCEDURE

The cantilever beam test developed by Brown and Beachem[6] was used to determine the alloy's degree of susceptibility to SCC. In this test, specimens containing a sharp flaw (a notch which is sharpened by fatiguing) are deadweight loaded in cantilever bending with a plastic cell containing the desired environment surrounding the pre-cracked central portion of the specimen. Stress intensity was calculated from the Kies equation given in Figure 2. Also shown in Figure 2 is the specimen geometry and test rig. The results of the stress corrosion tests were plotted as initial applied stress intensity K_{Ii} vs. time to failure, and the plane-strain threshold stress intensity level, K_{Iscc}, below which crack growth did not occur, was determined.

Fracture surfaces were replicated by the plastic carbon technique and examined by electron microscopy. Chromium was used as a replica pre-shadowing material.

RESULTS AND DISCUSSION

Figure 3 contains plots of critical stress intensity vs. time to failure for Ti-38-6-44 in 3.5% NaCl, CH_3OH, CH_3OH + 0.5% HCl, and CH_3OH + 0.5% HCl + 0.5% $NaNO_3$ solutions. These plots show that K_{Iscc} is 34.5 ksi $\sqrt{in}$. in NaCl, 16 ksi $\sqrt{in}$. in CH_3OH, and 6 ksi $\sqrt{in}$. in CH_3OH + HCl. The air value, K_{Ix}, is 35 ksi $\sqrt{in}$. These data indicate that the alloy is immune to sodium chloride

SCC and is very susceptible to SCC in methanolic solutions, particularly in methanol + HCl solution. Thus, the measure of susceptibility K_{Iscc}/K_{IX}, decreases from 0.46 in CH_3OH to 0.17 in CH_3OH + HCl solution. Average crack growth rates (based on optical comparator measurement of the total crack extension in the SCC zone as a function of time) were 1.4×10^{-2} in/hr (3.6×10^{-1} mm/hr) and 3×10^{-2} in/hr (8.2×10^{-1} mm/hr) in CH_3OH and CH_3OH + HCl solutions respectively. The stress intensities at failure were 56 ± 2 ksi $\sqrt{in}$. and 44 ± 2 ksi $\sqrt{in}$. respectively. The addition of 0.5% HCl increased the average crack growth rate in methanol by a factor of ~ 2. Figure 3 also shows that $NaNO_3$ increases K_{Iscc} for the alloy in CH_3OH + HCl from 6 to 30 ksi $\sqrt{in}$. which approaches the air value of 35 ksi $\sqrt{in}$. Thus, $NaNO_3$ markedly reduces the susceptibility of the alloy to SCC in this extremely aggressive environment.

Macroscopic examination of the fracture surfaces of specimens which exhibited environmental cracking revealed three distinguishable zones, namely, the fatigue zone under the notch, the slow crack growth or SCC zone, and finally the fast fracture area (see Figure 4). There was no apparent SCC zone for specimens showing immunity to SCC. Figures 5-10 are high magnification replica fractographs which show the effect of environment on the fracture mode of the alloy. Crack extension in all environemnts, including air, was transgranular. The transgranular plastic fracture shown in Figure 5a-5c is typical for specimens fractured in air as well as for the fast fracture zone of specimens tested in aqueous and methanolic solutions. The main feature of their fracture topologies is that they all contain dimples. In Figure 5c,

the dimples are relatively small and shallow, whereas the dimples are larger
and more pronounced in Figure 5a and 5b.

The fracture surfaces of the specimens tested in NaCl solution (immune
to SCC) and inhibited CH_3OH + HCl solution (little susceptibility to SCC)
showed no discernible slow crack growth area. See Figures 6 and 7. Note the
similar ductile rupture topologies (shallow dimples).

Fractographs of the specimens stress corroded in uninhibited methanolic
solutions (very susceptible to SCC) are shown in Figures 8-10. Figure 8
shows the interface of the fatigue and slow crack growth areas and Figure 9
the center of the slow crack growth area. The SCC failure mode is transgranu-
lar brittle quasi-cleavage. Figure 10 shows that there is an intermediate
zone in the transition from slow crack growth to fast fracture which is
characterized by cleavage tongues. The fast fracture zone, as mentioned
earlier, has a ductile dimple rupture topology.

CONCLUSIONS

1. The solution treated and aged titanium alloy 38-6-44 is immune to sodium
chloride stress corrosion when the alloy is tested in the L-T direction. Thus,
SCC in salt water environments is not expected to be a problem.

2. Methanolic solutions provide extremely aggressive environments for the
SCC of Ti-38-6-44. The susceptibility is markedly increased in CH_3OH + HCl
solution.

3. The SCC resistance of Ti-38-6-44 in CH_3OH + HCl solution can be signifi-
cantly improved by the addition of sodium nitrate to the solution. Thus, care
should be taken that the Ti-38-6-44 components do not come in contact with

methanolic solutions unless the methanol is inhibited with $NaNO_3$.

4. Fractographic analysis of the stress corroded specimens showed that crack extension in the alloy in all environments was transgranular. Failure in the methanolic solutions was by brittle quasi-cleavage fracture. The alloy exhibited fractographic ductile characteristics (dimple rupture) in air, 3.5% NaCl and inhibited CH_3OH + HCl environments.

LITERATURE CITED

1. J.A. Feeney and M.J. Blackburn, "Effect of Microstructure on the Strength, Toughness and SCC Susceptibility of a Metastable β Titanium Alloy", Met. Trans., Vol. 1, Dec. 1970, p. 3309.

2. B.F. Brown, "A New Stress Corrosion Cracking Test for High Strength Alloys", Materials Research and Standards, Vo. 6, No. 3, March 1966, p. 129.

3. E.G. Haney and W.R. Wearmouth, "Effect of 'Pure' Methanol on the Cracking of Titanium", Corrosion, V. 25, 1969, p. 87.

4. K. Mori, A. Takamura, and T. Shimose, "Stress-Corrosion Cracking of Titanium and Zirconium in HCl Methanol Solutions", Corrosion, V. 22, 1966, p. 29.

5. M. Levy and D.W. Seitz, Jr., "Stress Corrosion of Ti-8Al-1Mo-1V in Methanol + HCl solutions", Corrosion Science, Vol. 9, 1969, p. 341-351.

6. B.F. Brown and C.D. Beachem, "A Study of the Stress Factor in Corrosion Cracking by Use of the Pre-Cracked Cantilever Beam Specimen," Corrosion Science, Vol. 5, 1965, p. 745.

CHEMICAL ANALYSIS (WEIGHT PERCENT)									MECHANICAL PROPERTIES			
Al	V	Cr	Mo	Zr	C	N	O	H	UTS PSI	YS PSI	Elong.	RA
3.34	7.95	5.70	4.03	3.83	0.029	0.006	0.100	0.0118	207,200	183,300	6.3	12.9

TABLE I. Chemical Composition and Mechanical Properties of Titanium Alloy 38-6-44 in the As Received STA Condition

185
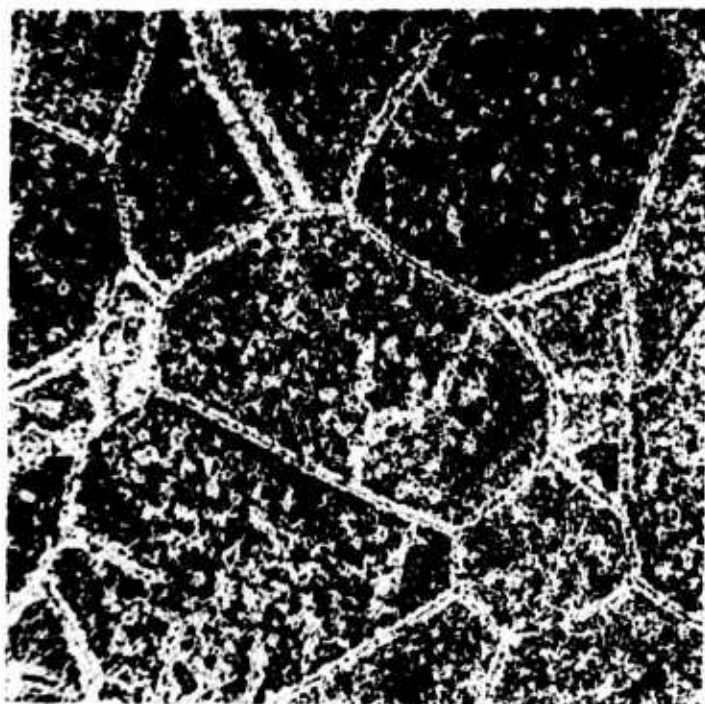
Figure 1. Photomicrograph of Ti-38-6-44 in the as-received STA condition. Mag. 250X
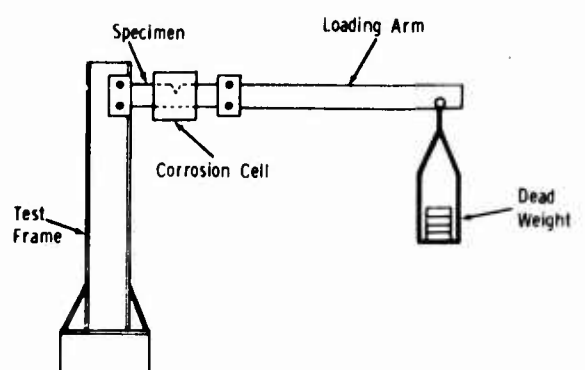
Figure 2. Cantilever rig, specimen geometry and equation for stress intensity values

L = 6 inches
W = 1 inch
B = 0.5 inch

$$K_1 = \frac{\beta M}{BW^{3/2}}$$
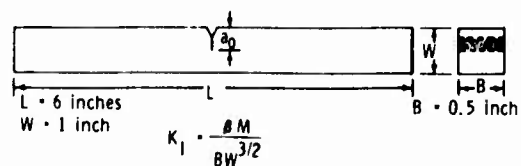
where:

M = the bending moment at the notch
B = the thickness of the specimen
W = the depth of the specimen

$$\beta = 4.12 \sqrt{\frac{1}{(1-a/W)^3} - (1-a/W)^3}$$
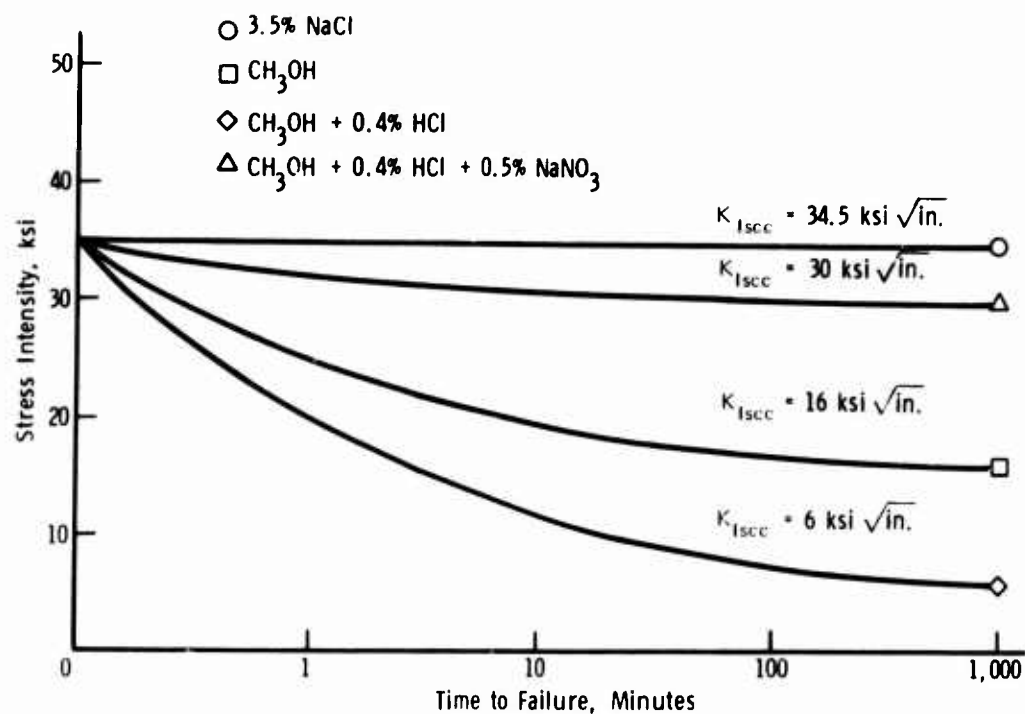
Figure 3. Stress corrosion curves for titanium alloy 38-6-44
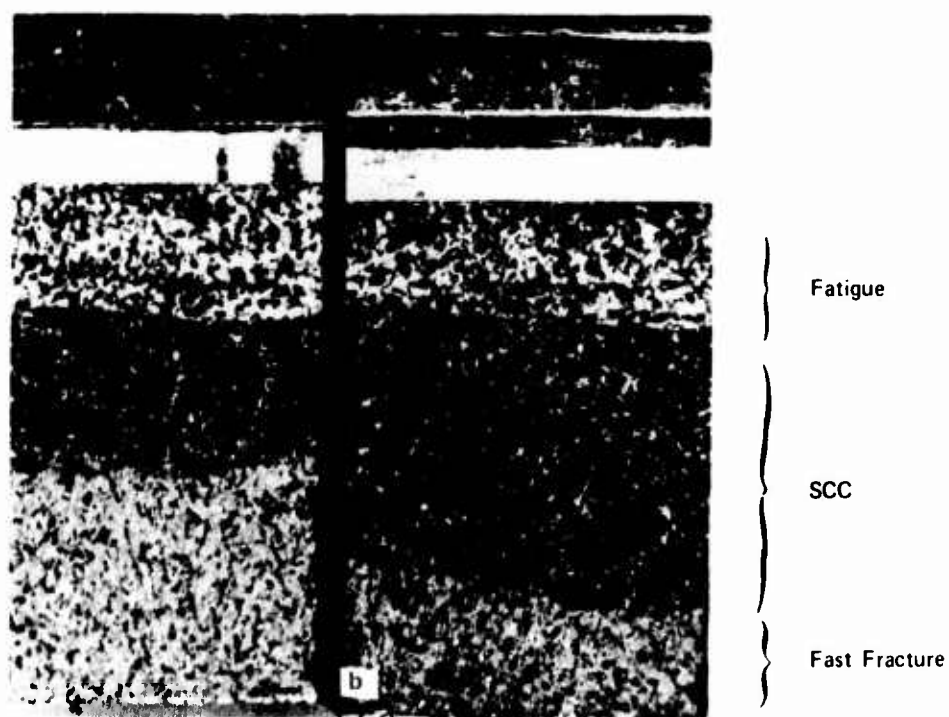
Figure 4. Fracture surfaces of specimens stress corroded in (a) CH_3OH and (b) CH_3OH + HCl. Mag. 4X
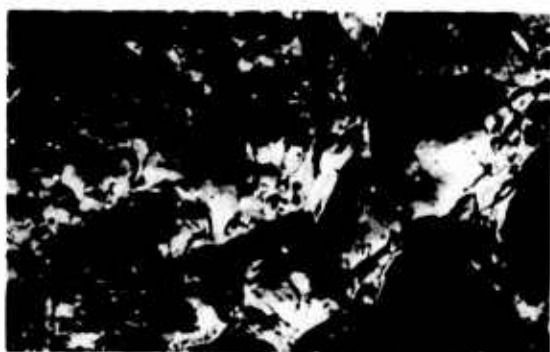
a. Mag. 3,200X

b. Mag. 3,500X

c. Mag. 3,500X

Figure 5. Fractographs of Ti-38-6-44 showing ductile rupture in the rapid fracture zone.

Fracture

Fracture

Fatigue

Fatigue

Figure 6. Fracture topology of Ti-38-6-44 showing fatigue and fracture zones resulting from stressing in aqueous NaCl and inhibited CH_3OH + HCl Mag. 2,500X
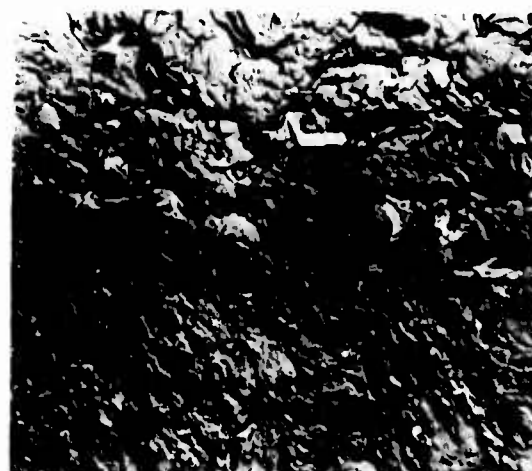
Figure 7. Fracture topology of Ti-38-6-44 showing fatigue and rapid fracture zones resulting from failure in air. Mag. 2,200X

188

SCC

Fatigue

Figure 8. Fractograph of Ti-38-6-44 showing fatigue and SCC zones resulting from stressing in methanolic solutions. Mag. 2,800X
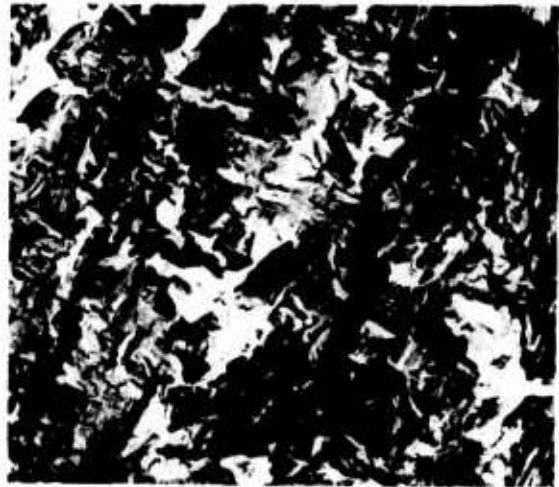
Figure 9. Topology of Ti-38-6-44 of the SCC zone resulting from stressing in methanolic solutions. Mag. 6,300X

SCC

Figure 10. Fracture topology of Ti-38-6-44 of the SCC and rapid fracture zones for specimen failed in CH_3OH. Mag. 4,600X

Fracture

189

SESSION II

MATERIALS REQUIREMENTS IN A HYDROGEN ECONOMY--NEW CHALLENGES?

By

B. C. Syrett, R. L. Jones, and N.H.G. Daniels*

ABSTRACT

It is anticipated that the energy shortages already experienced in the United States will develop into a serious crisis before the end of the twentieth century. The supply of gaseous and liquid fossil fuels, barely adequate for our needs today is expected to fall short of the demand in the years to come. Consequently, there has been an increasing recent effort to develop alternative fuels. One fuel that has received much attention is hydrogen, which has the advantages of being clean (its combustion product is nonpolluting) and in plentiful supply (in the form of water).

Numerous publications discuss the merits and feasibility of a national, hydrogen-based fuel system (a "hydrogen economy"), and many predict the widespread use of hydrogen by the year 2020.

Of the wide variety of problems that could occur with the introduction of a hydrogen economy, those related to materials are considered in this paper. The transmission, storage, and use of hydrogen are discussed briefly, but major emphasis is placed on the materials research and development needs related to large-scale, low-cost hydrogen production.

INTRODUCTION

This paper is based on portions of a study[1] conducted for De'ense Advanced Research Projects Agency (ARPA) dealing with materials problems that would be encountered with the widespread introduction of advanced nonfossil fuel systems. The fuel considered in greatest detail in this study was hydrogen.

There have been an increasing number of publications in recent years that have discussed the merits and feasibility of a national hydrogen-based fuel system--the so-called hydrogen economy. Because of the ever increasing shortage of fossil fuels, many predict the widespread use of hydrogen by the year 2020. Its chief advantages are that it is in plentiful supply (in the form of water) and that its combustion product is nonpolluting (unlike fossil fuels).

The merits or financial feasibility of a hydrogen economy will not be discussed here. Instead, it will be assumed that a fuel system based on hydrogen will be

---

*Stanford Research Institute, Menlo Park, California.

introduced, and that, because of a shortage of fossil fuels, hydrogen will be produced entirely from a nonfossil source, namely water. It will further be assumed that a primary source of energy, (e.g., nuclear, solar, wind) will be available in sufficient quantities to allow the extraction of the required amount of hydrogen from water. Of the wide variety of problems that could occur with the introduction of a hydrogen economy, only problems related to materials will be discussed, and particular emphasis will be placed on problems that need immediate attention to permit the successful introduction of a hydrogen economy in 40 to 50 years.

THE HYDROGEN ECONOMY

It appears that there is a deep-seated feeling in a large number of the population that hydrogen is a "dangerous gas." Frequent mention is made of the Hindenberg disaster and of the embrittlement and slow crack growth that have long been observed in metals exposed to hydrogen environments. On the other hand, the familiar laboratory gas bottles containing hydrogen have apparently had a perfect safety record for more than 50 years, and many years of practical experience have already been amassed in the transmission of gaseous hydrogen for industrial uses-- admittedly over relatively short distances and at relatively low pressures. So what is the truth?

In the study[1] conducted for ARPA, the materials problems that might be encountered in a hydrogen fuel economy were examined in detail. Four major aspects of the hydrogen fuel system were studied: (1) production, (2) transmission and distribution, (3) storage, and (4) end use. Although important materials research and development needs were identified in each of these four areas, it is the belief of the authors that no insurmountable materials-related obstacles exist to prevent the safe and successful transportation, storage, and use of hydrogen fuel. It was apparent that the major effort must go into developing improved methods of producing hydrogen in large volumes at minimum cost. Materials research and development needs related to large-scale, low-cost hydrogen production will now be discussed in greater detail.

LARGE-SCALE, LOW-COST HYDROGEN PRODUCTION

Even a partial hydrogen fuel economy would require the production of enormous quantities of hydrogen. The quantity of hydrogen required to have entirely replaced the 1970 U.S. fossil fuel consumption would have been about 631 million tons. Replacing the 1970 U.S. natural gas supply alone would have required 215 million tons of hydrogen. (See Table 1.) In a future total hydrogen economy, billions of tons per year would be required. Contrast this need with the world production of hydrogen in 1970 of about 17 million tons, only 5% of which was derived from nonfossil sources.

Water is the only credible nonfossil source of the required quantities of hydrogen, and, in the short-to-mid-term future, nuclear fission appears to be the only possible source of the energy needed to extract hydrogen from water; in the longer term, other energy sources such as solar heat and nuclear fusion may become important.

Table 1

ANNUAL U.S. ENERGY SUPPLY (1970)

Energy Source	Energy Content (10^{15} Btu)	H_2 Equivalent* (10^6 Tons)
Fossil fuels		
– Natural gas	22.1	215
– Coal	13.5	131
– Liquid hydro- carbons	29.4	285
Total fossil fuels	65.0	631
All other	2.8	27

'Based on the lower heating value of H_2 (51,571 Btu/lb).

Three possible routes can be suggested for using nuclear energy to extract hydrogen from water: electrolysis, direct thermal splitting, and thermochemical splitting. Electrolysis is the only proven method, but electrolysis requires an inefficient intermediate step in which heat energy is converted into electricity. A process for splitting water using thermal energy alone would avoid this intermediate step and might, therefore, be capable of producing hydrogen with a higher overall efficiency and at a lower cost. The direct thermal dissociation of water, requiring temperatures in excess of 2500°C for appreciable conversion, is not feasible within the limitations of foreseeable reactor technology. However, it is theoretically possible to split water by a combination of chemical and thermal steps at temperatures below the $\sim$ 1000°C level anticipated in future high-temperature gas-cooled reactors. A considerable effort is now underway in laboratories around the world to reduce to practice the thermochemical splitting concept.

The type of process being sought is a closed chemical cycle in which the maximum process temperature is below 1000°C, and only water is consumed, any chemical intermediates being completely recycled. A large number of possible cycles have now been proposed, and the range of possibilities is still growing with several groups using computerized search routines to identify promising reaction sequences. However, none of the proposed cycles have yet been integrated into even a bench-scale process, and it is not yet clear which cycle or cycles should be selected for further development. In fact, it seems likely that three to five years of additional research into reaction thermodynamics and kinetics will be required before the most attractive cycles and their associated materials problems can be clearly defined.

An indication of the types of materials problems that are likely to be encountered in future thermochemical splitting plants can be obtained by reviewing the

general nature of the cycles now under consideration. All water splitting cycles involve some sort of hydrolysis step in which hydrogen or oxygen is generated, either directly or via one or more chemical intermediates. Because of their strong tendency to hydrolyze, metal halides are involved in many of the proposed thermochemical splitting cycles. Other proposed species include halogens, hydrogen halides, liquid metals, metal oxides and metal hydroxides, as well as hydrogen, oxygen, and steam. A typical example of a reaction sequence, the Mark IB process proposed by the EURATOM group in Italy, is shown here:

(1)	$CaBr_2 + H_2O \rightarrow Ca(OH)_2 + 2HBr$	$780°C$
(2)	$Hg_2Br_2 + 2HBr \rightarrow 2HgBr_2 + H_2$	$120°C$
(3)	$HgBr_2 + Hg \rightarrow Hg_2Br_2$	$120°C$
(4)	$HgBr_2 + Ca(OH)_2 \rightarrow CaBr_2 + HgO + H_2O$	$200°C$
(5)	$HgO \rightarrow Hg + \frac{1}{2}O_2$	$600°C$
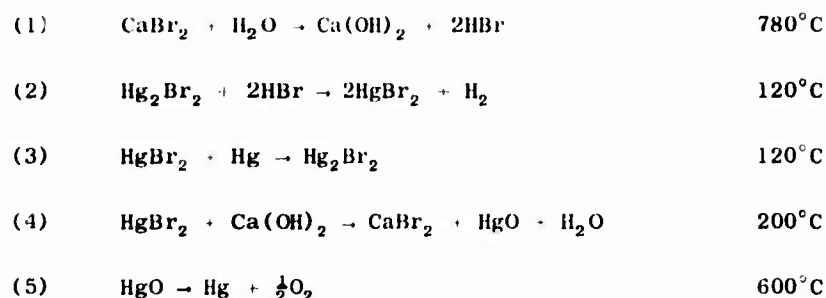
It seems probable that corrosion of containment vessel materials will be a major problem in the chemically aggressive, high-temperature environments involved in this and all other thermochemical splitting cycles. In addition to the need for corrosion resistant materials and coatings, materials with good high-temperature strength will be needed, especially for reaction vessels required to operate at high pressures. For instance, the calcium bromide hydrolysis step in the above EURATOM Mark IB process is to be carried out at $780°C$ and at a system pressure of 30 atmospheres.

As for the proven hydrogen production route, electrolysis, it should be noted first that electrolysis is an old technology. The electrolytic decomposition of water was first demonstrated in 1800, and electrolysis has been used for the commercial production of hydrogen for more than 60 years. Electrolyzer design remained virtually unchanged until recently, and, as a consequence, conventional electrolyzers are characterized by conservative design and engineering, which leads to low energy efficiency, low cell capacity, and high capital costs.

Table 2 shows that, for a typical large conventional electrolyzer, the cost of electric power consumed is by far the major contributor to the cost of the hydrogen produced. If electrolytic hydrogen was to be produced on the vast scale required for its use as a fuel, the mass production of electrolyzers of advanced design would be necessary. This would probably result in a decrease in the capital cost contribution to below the 24 percent shown in Table 2 and so would further increase the percentage of product cost attributable to the electric power consumed. Therefore, to minimize product cost, electrolyzer development must be directed to optimizing the utilization of electric power, i.e., to maximizing the electrolyzer efficiency.

The thermal efficiency of electrolysis is commonly defined as the ratio between the gross heating value of the hydrogen produced and the heating value of the electrical energy expended. By this definition, the theoretical thermal efficiency

194

of electrolysis is 120 percent at STP because of the endothermic nature of elec-
trolysis. The thermal efficiency increases as the temperature is increased, such
that at 550°F (1 atmosphere pressure) the theoretical efficiency has reached about
150 percent. In comparison, the actual thermal efficiencies of today's commercial
electrolyzers range from about 50 percent for older units to about 80 percent for
the best current units.

Table 2

BREAKDOWN OF COSTS FOR ELECTROLYTIC HYDROGEN PRODUCED
BY A LARGE CONVENTIONAL ELECTROLYZER

Cost contribution	Percent of Product Cost
Electric Power Consumed	69.5
Capital Costs	24
Other Consumables	4.5
Operation and Maintenance	2
	100

The discrepancy between theoretical and practical efficiencies is associated
almost entirely with the extra voltage above theoretical that must be applied to
the electrodes of a real cell in order to achieve a reasonable rate of hydrogen
production. A number of factors contribute to this overvoltage. Concentration
polarization of the anode and cathode and resistive voltage drops in the electron
conduction path account for minor contributions to the overvoltage, but, in today's
commercial electrolyzers, the major contributions are due to activation polarization
of the electrodes and the resistive voltage drop in the ion conduction path.

Resistive voltage losses can be minimized by minimizing interelectrode spacing,
keeping product gases out of the current path, using a high-conductivity electrolyte,
maximizing the ionic conductivity of the separator, and increasing the operating
temperature. Activation polarization can be minimized by using electrocatalysts, by
increasing the effective area of the electrodes, and by increasing the operating
temperature. It will be noted that an increase in the operating temperature decreases
both resistive voltage losses and activation polarization. Temperature increases and
the use of electrocatalysts are considered most likely to lead to the desired sub-
stantial improvements in efficiency. Materials research and development needed to
allow these advances will now be discussed.

Most of today's commercial electrolyzers use aqueous solutions of potassium
hydroxide as the electrolyte. Before any substantial operating temperature increase
is possible in these alkaline electrolyzers, the materials problems that must be
overcome include severe corrosion of the nickel anode and rapid deterioration of
separator and cell frame materials at temperatures above about 100°C.

Because the materials currently used for the anode and cathode structures
(nickel and iron respectively) are themselves fairly good catalysts for oxygen and

hydrogen evolution, it has been suggested that significant improvement in catalytic
activity can be obtained only by using noble metals such as platinum. However, the
use of noble metal catalysts on a hydrogen economy scale can probably be ruled out
for reasons of cost and availability. For instance, at a moderate catalyst loading
of 1 gram/ft^2 (about 1 mg/cm^2), the amount of catalyst required for a hydrogen pro-
duction capacity equivalent to the 1970 U.S. consumption of natural gas would be of
the order of 2 million pounds, compared with a current annual world production of
platinum of about 0.1 million pounds and a U.S. annual production of a mere 620
pounds. (See Table 3.) These figures emphasize the need for the development of
improved, nonnoble electrocatalysts.

Table 3

CATALYST REQUIREMENTS OF NOBLE METAL CATALYZED ELECTROLYZERS

Catalyst loading of 1 gram/ft^2	$\equiv \sim 20$ grams of catalyst per pound/hour of H$_2$ production capacity
1970 U.S. natural gas consumption	$\sim 5 \times 10^7$ pounds/hour of H$_2$ production capacity
$\therefore$ Catalyst required	$= \sim 2 \times 10^6$ pounds
World production of platinum	$= \sim 1.2 \times 10^5$ pounds/year
U.S. production of platinum	$= \sim 620$ pounds/year

An entirely different type of electrolyzer, prototypes of which have shown
potential for high thermal efficiency, is based on the use of a hydrogen-ion con-
ducting membrane of perfluorinated sulphonic acid--the so-called solid polymer elec-
trolyte. This 12-mil thick polymer membrane combines the functions of the electro-
lyte and the separator. Prototype cells of this type currently use noble metal
electrocatalysts but, for the reasons discussed above, these would probably have to
be replaced with nonnoble catalysts in the event of a hydrogen economy. Improvements
in performance could be obtained by decreasing the thickness of the polymer membrane;
this approach is presently limited by the difficulty of producing thin, pinhole-free
membranes. Further improvements in performance could be obtained by increasing the
operating temperature above the current value of about 80°C. At present, the maximum
operating temperature is limited by chemical and mechanical stability of the membrane
to about 125°C. Thus, for a temperature increase much above the present value, a new
ion-conducting membrane material would have to be developed.

SUMMARY AND CONCLUSIONS

The materials research and development programs that we feel are needed in
support of the further development of alkaline electrolyzers are as follows:

● Development of improved corrosion-resistant materials for use in the
  anode electrode structure.

196

- Development of separator materials with improved conductivity and with temperature capability to about 200°C.

- Development of inexpensive polymeric materials with temperature capability to about 200°C for use in cell frames.

- Development and fabrication of gas diffusion electrode structures with high effective electrode areas.

- Development of active, nonnoble electrocatalysts for both the anode and cathode.

Research and development needs in the field of solid polymer electrolyzers are summarized as follows:

- Development of inexpensive ion-conducting membranes with superio

        - Ionic conductivity (H^+, O^- or OH^-)
        - Temperature capability
        - Mechanical and chemical stability.

- Development of active nonnoble electrocatalysts for both the anode and cathode.

If these materials challenges can be successfully met, the development of electrolyzers showing thermal efficiencies of about 100 percent will become possible at current densities up to a factor of 5 higher than in present units. With this performance, plus the reduction in electrolyzer capital costs that could be anticipated as a result of mass production, future electrolyzers could produce hydrogen costing little more per unit energy than electricity. In addition, an ecologically sensible fuel system would be one step closer to practical reality.

REFERENCE

1. N.H.G. Daniels, B. C. Syrett, and R. L. Jones, "Materials Requirements for Advanced Energy Systems--New Fuels," [Vol. I, "Interactions of Materials with New Fuels;" Vol. II, "Materials Aspects of the Use, Production, Transportation and Storage of New Fuels;" Vol. III "Materials Research Needs in Advanced Energy Systems Using New Fuels"]. Prepared for Defense Advanced Research Projects Agency (Contract No. DAC-15-73C-0313, 1 May 1973), July 1974.

Chemical Corrosion Inhibition of Steel in Hydrofluoric Acid

by

F. Pearlstein and R. F. Weightman
Pitman-Dunn Laboratory
U. S. Army Frankford Arsenal
Philadelphia, Pa. 19137

Binary chemical munitions are designed to produce toxic chemical agents by the reaction of relatively nontoxic ingredients. To readily combine ingredients at the time of usage, binary projectile designs necessarily incorporate separating membranes. One of the reactants employed in the G-agent binary process is classified as corrosive and represents a potential hazard to the integrity of its separating 0.25 mm thick steel membrane. The corrosive action is believed to stem primarily from the presence of small quantities of hydrofluoric acid either as a production impurity or a degradation product.

The use of more corrosion resistant membrane materials has been considered for the binary chemical munitions and 321 stainless steel was indicated potentially suitable (1). Another approach towards solving the problem is the addition of chemical corrosion inhibitors to the corrosive reactant (CR) for mitigating attack of the steel membrane material. It is well known that numerous chemical agents are very effective for inhibiting corrosion of steel in hydrochloric or sulfuric acid solutions (2-6). Little specific data has been published on corrosion inhibition of steel in hydrofluoric acid solutions but one might expect that the compounds effective in the other acids would also apply. In the study described herein, selected corrosion inhibitors were added to hydrofluoric acid solution or to the corrosive reactant (CR) and the effectiveness in reducing corrosion of steel membrane material was determined. Initial studies were conducted with hydrofluoric acid solution since the CR was not immediately available and it was expected that results with the two liquids would probably be comparable.

Experimental Procedure

All corrosion inhibition tests, unless otherwise specified, were conducted in duplicate by immersion of 20 cm^2 (1.3 cm x 7.7 cm x 0.25 cm) metal sample in 200 ml of solutions at ambient temperature (23 ± 2°C) in 330 ml capacity polyethylene plastic jars tightly sealed during exposure. Corrosion weight loss measurements were made after suitable exposure periods.

Initial tests were conducted with S.A.E. 1010 cold-rolled steel (binary chemical munitions membrane material) in aqueous 0.59 N hydrofluoric acid solution to which was added 1 g/l candidate corrosion inhibitor, i.e., gelatine (GEL), o-tolylthiourea (OTTU), benzotriazole (BT), quinoline ethiodide (QEI), n-lauryl pyridinium chloride (NLPC), and oxides of arsenic, antimony and tin. Combinations of two inhibitors, each at 0.5 g/l concentration, were also studied for inhibition effectiveness. A newly developed proprietary corrosion inhibitor useful in hydrofluoric acid solution for cleaning boiler tubes (7) was also tested. Limited studies were also conducted on corrosion of metals such as 321 stainless steel, 99.5% purity nickel and AZ31b magnesium.

199

The steady-state corrosion potential of steel in aqueous 0.59 N hydrofluoric acid solution containing corrosion inhibitor was determined using the Orion 801 Ionanalyzer[a] with Orion Ag/AgCl reference electrodes #90-01 filled with 90-00-01 solution. The electrodes are fabricated with plastic outer sleeves that provide resistance to attack by hydrofluoric acid and the electrode potential characteristics are equivalent to those of conventional saturated KCl calomel electrodes. The solutions were open to the atmosphere and potential measurements taken periodically up to 48 hours exposure. Corrosion weight loss measurements were taken at the end of the 48 hour period. Potential measurements were also made on stainless steel, nickel, tin, magnesium, lead and antimony.

Two hundred ml samples of the corrosive reactant (containing 1.9 mole percent active hydrogen compounds[b]) were poured into polyethylene bottles within a dry box maintained at low relative humidity with phosphorus pentoxide. Selected inhibitors were added at 1 g/l concentration and a steel specimen immersed in each. Nickel and stainless steel specimens were also immersed into uninhibited corrosive reactant (CR). Four ml of diisopropylcarbodiamide (DICDI) was added to 200 ml samples of CR to determine the effectiveness of this acid-neutralizing compound[c] in reducing corrosion of steel. After 30 days' exposure, the jars were uncapped and corrosion weight loss measurements made on the metal specimens.

Results and Discussion

The results of corrosion tests on steel in aqueous 0.59 N hydrofluoric acid solution containing inhibitors are shown in Table I. It is readily evident that the organic inhibitors tested were all quite effective for retarding corrosion of steel in the hydrofluoric acid solution. Extrapolating the initial corrosion rate of steel in uninhibited acid to the 21 day test period, the inhibitor effectiveness[d] achieved by the organic compounds listed in Table I ranged from about 95 to 99 percent. Although GEL and BT were less effective than NLPC and QEI, the latter two had a greater tendency to produce edge corrosion or pitting than the former. OTTU was an effective inhibitor and there was little tendency for nonuniform attack on steel. In most instances, combinations of organic inhibitors yielded lower corrosion weight losses than when either of the inhibitors was used alone. Exceptions to this were the following combinations: OTTU-QEI, QEI-GEL, BT-GEL and NLPC-BT (at > 21 days exposure). Of the inhibitors tested, only OTTU appeared to be insoluble in the hydrofluoric acid solution at 0.5 or 1 g/l additions. One might thus expect all combinations with OTTU to be more effective than the OTTU alone since a saturated solution of OTTU is present in both instances and the addition of 0.5 g/l of another inhibitor would be expected to enhance effectiveness. The OTTU-QEI combination provided a lower degree of inhibition than the OTTU alone and, for some exposure periods, the combination was lower in inhibitor effectiveness

---

a. Orion Research Inc., Cambridge, Mass. 02139.
b. Determined from NMR studies, Edgewood Arsenal, Edgewood, Md.

c. $isopr-N=C=N-isopr + 2HF \rightarrow isopr-N-C-N-isopr$

d. $(1 - \dfrac{\text{corrosion weight loss, inhibited acid}}{\text{corrosion weight loss, uninhibited acid}}) \times 100$

(higher corrosion weight losses) than either alone. The combination of OTTU-BT provided the lowest corrosion rate of the organic additive with little tendency for nonuniform attack.

The proprietary corrosion inhibitor (M107) was more effective than the organic compounds tested and corrosion was quite uniform. Although As_2O_3 in the acid resulted in a higher degree of inhibition than the proprietary inhibitor, numerous blisters in the metal surface were visible at 7X magnification after exposures of 21 days or more. It is believed that arsenic increases the hydrogen overvoltage of the surface which greatly retards the hydrogen evolution reaction, but increases diffusion of atomic hydrogen into the surface. Sub-surface combination of atomic hydrogen to the molecular form could provide the pressure to account for blister formation. It is interesting to note that tin or antimony oxide provided little inhibitive properties though tin and antimony are also considered metals of high hydrogen overvoltage.

Corrosion weight loss with time of various metals in 0.59 N hydrofluoric acid solution is shown in Figure 1. Corrosion of steel is very rapid as indicated earlier. The corrosion rate of stainless steel is considerably lower than steel but is nevertheless substantial. The rate of nickel corrosion in uninhibited acid approximates that of steel in acid solutions containing the more effective inhibitors tested. However, the nickel undergoes pitting-type corrosion. There was virtually no change in weight of magnesium exposed to the acid and the only visible change was the formation of a very thin gold-colored film. It should be noted that during the first few minutes after immersion of the magnesium in the acid, there was active hydrogen gas evolution from the surface indicative of corrosion, but the rate of gassing decreased rapidly and ceased after about five minutes. While magnesium could be considered as an alternative to steel membrane material on the basis of its corrosion resistance, other factors such as mechanical properties and difficulties in joining make such recommendations premature. Magnesium may also be considered as a vessel for holding the corrosive reactant during storage though long term exposure tests would first be necessary. Antimony was available only as rocky lumps, so the area exposed to the hydrofluoric acid was difficult to estimate. The corrosion rate of antimony shown in Figure 1 is thus an approximation, but is greater than that of any of the other metals tested except steel.

The corrosion potential of steel in hydrofluoric acid solutions containing additive is shown in Table II. The organic compounds were at a concentration of 1 g/l while the metal salt overvoltage-modifiers were at a metal ion molar concentration equivalent to 1 g/l SnO. The corrosion weight loss after 48 hours is also shown. It is evident from the data that a general relationship exists between potential and weight loss since the more effective inhibitors resulted in substantially higher (less negative) corrosion potentials than the ineffective ones. Since all inhibitors shifted the corrosion potential of steel in the less negative direction, they are indicated to have had greater influence on the anodic than cathodic processes (8). The metal salts, which were believed to function by increasing the hydrogen overvoltage of the surface (9), would have been expected to reflect predominant action on cathodic processes by shifting the corrosion potential in the negative direction (10). The reverse was found from this investigation and it must be concluded that the metal salts predominantly stifled the anodic reaction.

The log corrosion weight loss vs steady-state corrosion potential of steel in the acid solution containing various inhibitors is shown in Figure 2. It is interesting to note that the metal ions produce potentials that approximate a linear

201

relationship with corrosion weight loss reminiscent of the Tafel slope for hydrogen evolution. Bockris and Drazic (11) showed that the Tafel slope should be -120 mv per decade when the proton-discharge is the rate determining slope and -30 mv per decade when the combination of adsorbed hydrogen atoms is rate determining. The experimental slope in Figure 2 is about -45 mv per decade. Further studies are to be conducted in order to more clearly elucidate the relationship between corrosion rate and corrosion potential of steel in acid containing various inhibitors.

The organic compounds tended to result in steel corrosion potentials higher than that of the metal salts but there was little relationship between corrosion rate and potential. The results in Figure 2 show that OTTU caused the most pronounced shift in corrosion potential indicating a highly preferential effect on the anodic reaction. The results with the proprietary compound, M107, were similar to OTTU. See Table I.

The corrosion potentials of a number of metals in uninhibited 0.59 N hydrofluoric acid solution after a 48 hour immersion period are shown in Figure 3. Corrosion weight loss after 48 hours is also given in parenthesis in the figure; additional corrosion date are shown in Figure 1 and discussed earlier. Antimony is considerably more noble than steel and the reason for the inability of Sb_2O_3 to inhibit acid corrosion of steel (Figure 2) may lie in the adverse galvanic cell formed when a film of antimony is electrochemically displaced (immersion deposited) on the steel. Lead is more galvanically compatible with steel than antimony and lower corrosion rates resulted from additions of PbO (Figure 2). It is probably not advisable to attempt protection of steel with deposits of metals of more noble electrode potential (e.g., Ni, Sb, Pb) since there would be danger of corrosive penetration of the steel at sites of porosity or defects in the coating.

Tin acquires a slightly more active corrosion potential than steel and addition of SnO (Figure 2) to acid was relatively ineffective for corrosion inhibition of steel because complex tin fluoride ion that is formed probably prevents immersion deposition and thus cannot function as an overvoltage modifier. The potential of tin indicates that a tin coating on steel would be sacrificially protective to the basis metal. It was indeed found that when a 15 μm thick deposit of tin was applied to steel from an alkaline stannate bath and then immersed in the 0.59 N hydrofluoric acid solution, corrosion of the tin deposit ensued at a substantially lower rate than does steel but even when significant areas of basis metal had become exposed, there was no evidence of acid attack on the steel; after all of the tin had been removed by dissolution, rapid attack of the steel ensued.

The electrode potential of magnesium was highly active though the corrosion rate was extremely low. Apparently, a thin oxide or fluoride film is formed that essentially prevents acid attack. The results indicate that a magnesium plated steel surface would be quite effective for sacrificially protecting steel against acid corrosion while the coating itself would be resistant to attack. Unfortunately magnesium cannot be electrodeposited from aqueous solution but may be plated from organometallic solution (12), flame sprayed or deposited by sputtering.

Arsenic metal in bulk-form was unavailable for test but it would be of interest to ascertain its electrode potential in the hydrofluoric acid solution. If arsenic was found to provide sacrificial protection to steel, its potential value as a protective coating would be indicated. Arsenic can be plated from aqueous solutions and studies with electroplated arsenic are contemplated.

Consideration should also be given the fact that the potential of steel is made considerably more noble by addition of OTTU to the hydrofluoric acid solution and other metals not so affected could then provide sacrificial protection to steel. Lead coatings, for example, might be more active than steel in hydrofluoric acid solution containing OTTU and provide sacrificial protection and then additionally might provide even more effective corrosion inhibition by introduction of lead ions into the acid.

Corrosion of steel in the corrosive reactant (CR) was slower than that in aqueous 0.59 N hydrofluoric acid by a factor of about twelve which nonetheless represents a considerable rate of attack. Corrosion weight losses of steel immersed for 30 days in CR containing inhibitors are shown in Table III. None of the additives were very effective for reducing corrosion rates in CR and some actually accelerated dissolution. The proprietary material (M107) was the most effective of the inhibitors but provided only about 70 percent effectiveness. When DICDI was added to the (CR) samples, white fumes were generated and the solution became green in color. Although sufficient DICDI had been added to theoretically neutralize all the acid present, acid attack of the steel was still considerable. The results with DICDI and the chemical corrosion inhibitors indicates that the corrosion mechanism in CR differs from that in hydrofluoric acid solution.

Corrosion of nickel and stainless steel in CR is shown in Table III. Though the corrosion weight loss for nickel was lower than that of stainless steel, there was a tendency for pitting of the nickel while corrosion of the stainless steel was relatively uniform.

Conclusions

Corrosion of steel in dilute (0.59 N) hydrofluoric acid solution is greatly retarded by the addition of small amounts of As_2O_3, o-tolylthiourea (OTTU), benzotriazole (BT), gelatine (GEL), quinoline ethiodide (QEI), or n-laurylpyridinium chloride (NLPC). However, hydrogen blistering of steel results from use of As_2O_3 and there is a tendency for pitting-type corrosion when QEI and NLPC are used. The combination of OTTU-BT provides quite effective inhibition with little tendency for pitting corrosion; somewhat superior results were, however, obtained with a newly developed proprietary inhibitor (M107). The addition of inhibitor to acid results in an increase in the corrosion potential of steel indicative of predominant inhibition of the anodic reaction; the highest potentials are obtained with OTTU or M107 addition. The corrosion potential of steel in acid containing organic inhibitors is unrelated to degree of inhibitor effectiveness but with metal salt addition, the log corrosion weight loss is linearly related to the potential.

Steel is rapidly attacked in uninhibited 0.59 N hydrofluoric acid. The metals: steel, antimony, 321 stainless steel, tin, lead, nickel, and magnesium are in the order of increasing resistance to acid dissolution. Magnesium corrosion is apparent from active gassing during the first few minutes of exposure to acid but, thereafter, corrosion of magnesium is nil. Both magnesium and tin acquire more active steady-state potentials than steel. Electrodeposited tin provides sacrificial protection to steel in hydrofluoric acid solution. Nickel, antimony, stainless steel and lead are more noble in corrosion potential than steel in the acid solution.

Corrosion of steel in corrosive reactant (CR) is not as rapid as in 0.59 N hydrofluoric acid but the inhibitors that are effective for retarding corrosion in the latter solution provide little or no inhibitive action in the former liquid. The least corrosion of steel in (CR) is obtained when diisopropylcarbodiamide or proprietary inhibitor M107 was added. Neither nickel nor 321 stainless steel can be considered resistant to attack by CR though both are substantially more resistant than steel.

References

1. A. Gallaccio, "Corrosive Effects of Methyl Phosphonic Acid and HF Solutions on Thin-Sheet 1010 Steel, 321 Stainless Steel and 200 Nickel", F.A. Memorandum Report M74-2-1 (1974) January.

2. H. H. Uhlig, "The Corrosion Handbook", John Wiley & Sons, Inc., New York, pp. 910-912 (1948).

3. U. R. Evans, "An Introduction to Metallic Corrosion", Edward Arnold & Co., London, pp. 144-145 (1948).

4. I. N. Putilova, S. A. Balezin, V. P. Barannik, "Metallic Corrosion Inhibitors", Pergamon Press, New York (Translated from the Russian), pp. 76-85 (1960).

5. E. S. Snavely, L. H. Williamson, "Proc. Nat'l Assoc. Corrosion Engineers", Paper No. 28, Anaheim, Calif. (1973) March.

6. R. J. Chin, D. Altura, K. Nobe, Corrosion, 29, 185 (1973).

7. E. A. Rodziewich, "Proc. Nat'l Assoc. Corrosion Engineers", Paper No. 74, Chicago, Ill. (1974) March.

8. T. P. Hoar, "Proc. Pittsburgh International Conference on Surface Reactions", p. 127, Corrosion Publ. Co., Pittsburgh (1948).

9. H. C. Gatos, "Symposium on Corrosion Fundamentals" (Chapter X), University of Tennessee Press, Knoxville, Tenn., p. 142 (1956).

10. T. P. Hoar, Trans. Faraday Soc., 45, 683 (1949).

11. J. O'M. Bockris, D. M. Drazic, "Electro-Chemical Science", Barnes & Noble Books, New York, pp. 115-117 (1972).

12. A. Brenner, "Record of Chemical Progress", 16, No. 4, 241 (1955).

Table I. Corrosion of Steel in 0.59 N HF Solution at 23 ± 2°C Containing Chemical Corrosion Inhibitors.

Inhibitor, 1 g/1 total	Corrosion Weight Loss, mg/20 cm^2 after various exposure times				
	7 days	14 days	21 days	28 days	42 days
None	disintegrated*	—	—	—	—
OTTU	35	72	135	229	422
QEI	45	86	165	260	461
NLPC	60	130	222	357	597
BT	57	185	363	536	825
GEL	91	191	352	544	876
OTTU + QEI	38	76	156	335	520
OTTU + NLPC	20	41	93	183	409
OTTU + BT	29	63	112	198	326
OTTU + GEL	27	54	100	172	363
QEI + NLPC	21	48	99	183	363
QEI + BT	30	71	140	229	413
QEI + GEL	43	97	176	290	605
NLPC + BT	42	85	201	387	862
NLPC + GEL	33	71	143	283	399
BT + GEL	73	256	409	579	954
M107	25	46	79	112	176
SnO	disintegrated**	—	—	—	—
Sb$_2$O$_3$	disintegrated***	—	—	—	—
As$_2$O$_3$	20	41	63	104	—

*Corrosion weight loss 824 mg after two days exposure.
**Corrosion weight loss 359 mg after two days exposure.
***Corrosion weight loss 811 mg after two days exposure.

205

Table II. Steady-state Corrosion Potential of Steel in 0.59 N HF Solution
at 23 ± 2°C Containing Inhibitor; Corrosion Weight Losses After
48 Hours Immersion.

Inhibitor	Conc, g/1	Corrosion Potential vs. S.C.E. of Steel in HF Solution After Various Exposure Times					Corrosion Weight Loss After 48 Hours, mg
		2 hrs	4 hrs	7 hrs	24 hrs	48 hrs	
OTTU	1.0	-445	-450	-447	-439	-426	15
QEI	1.0	-502	-506	-506	-496	-498	16
NLPC	1.0	-504	-509	-511	-501	-499	18
BT	1.0	-494	-495	-496	-492	-488	12
GEL	1.0	-524	-516	-515	-560	-507	17
Sb_2O_3	1.1	-562	-572	-582	-589	-591	762
SnO	1.0	-555	-555	-559	-566	-586	359
PbO	1.7	-548	-551	-555	-562	-571	190
As_2O_3	0.73	-481	-504	-503	-523	-517	13
Hg_2O	1.6	-534	-556	-560	-585	-594	642
None	——	-577	-579	-583	-589	-588	824
M107	1.0	—	—	—	-436	-418	16

Table III. Corrosion of Steel After 30 Days in Corrosive Reactant (CR) at 23 ± 2°C
Containing Various Inhibitors; Corrosion of Steel, Stainless Steel and
Nickel in (CR)

Metal	Inhibitor	Inhibitor Concentration	Corrosion Weight Loss, $mg/20cm^2/30$ days
Steel	OTTU	1 g/l	1036
Steel	NLPC	1 g/l	737
Steel	BT	1 g/l	1076
Steel	OTTU-NLPC	0.5 g/l each	1073
Steel	OTTU-BT	0.5 g/l each	1269
Steel	NLPC-BT	0.5 g/l each	931
Steel	As_2O_3	1 g/l	635
Steel	Proprietary M107	1 g/l	330
Steel	DICDI	20 ml/l	300
Steel	None	—	1043
Nickel	None	—	189
Stainless Steel	None	—	312
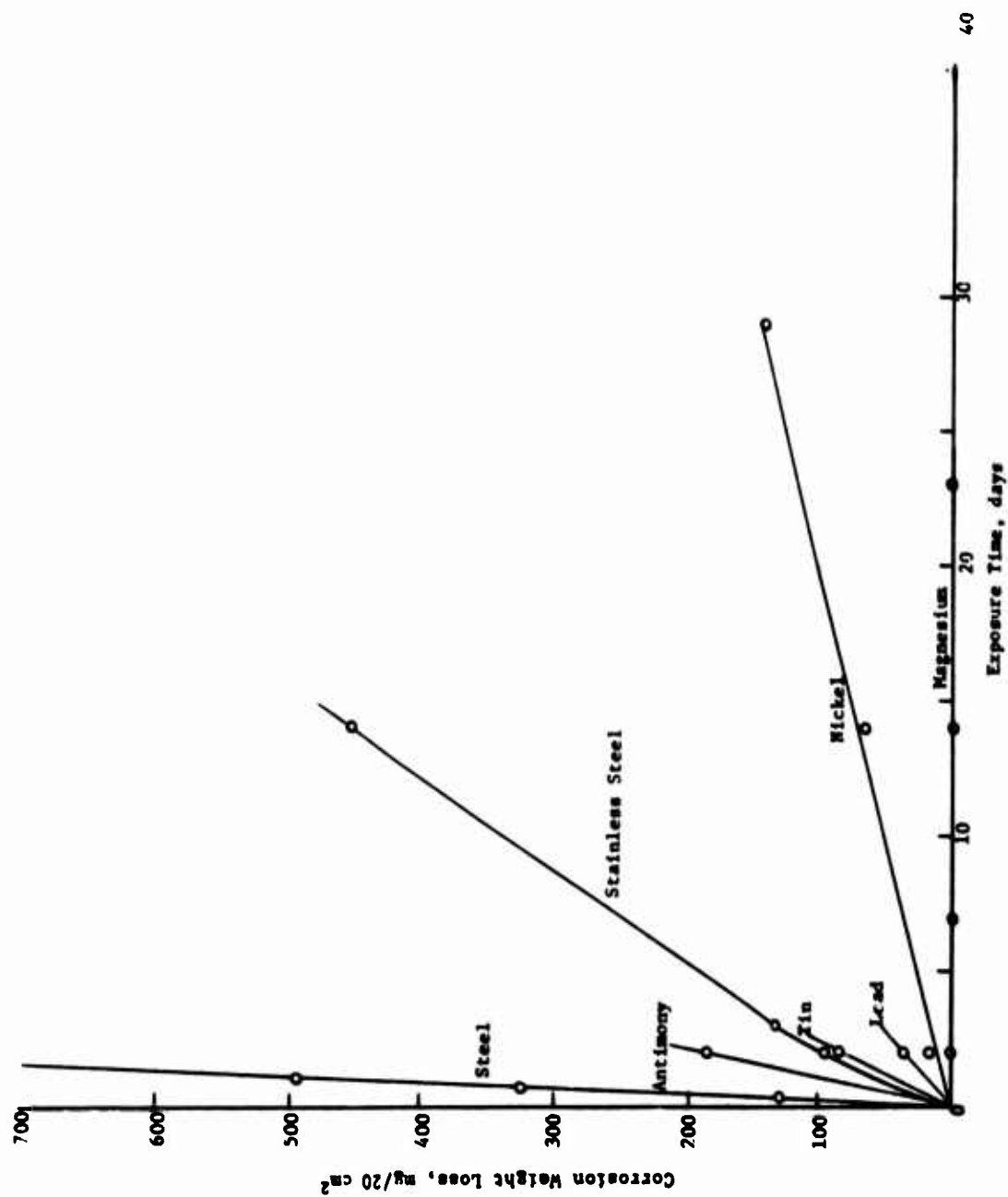
Figure 1. Corrosion of Various Metals in 0.59 N HF Solution at 23 ± 2°C.
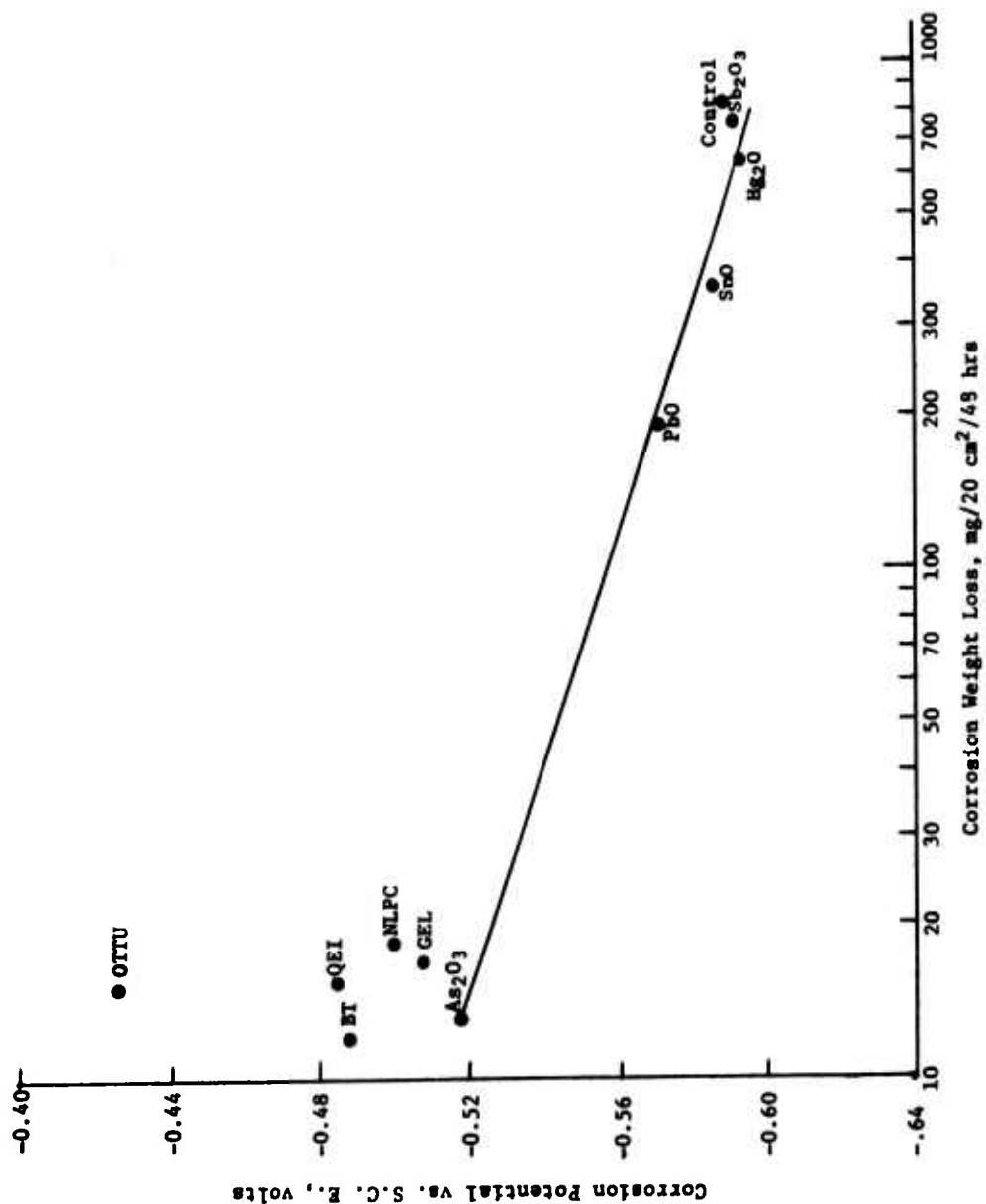
Figure 2. Potential of Steel vs Corrosion Weight Loss After 48 Hours in 0.59 N HF Solution at 23 ± 2°C Containing 1 g/l Organic Inhibitor or ½ Metal Oxide Equivalent in Molar Concentration of Metal Ions to 1 g/l SnO.
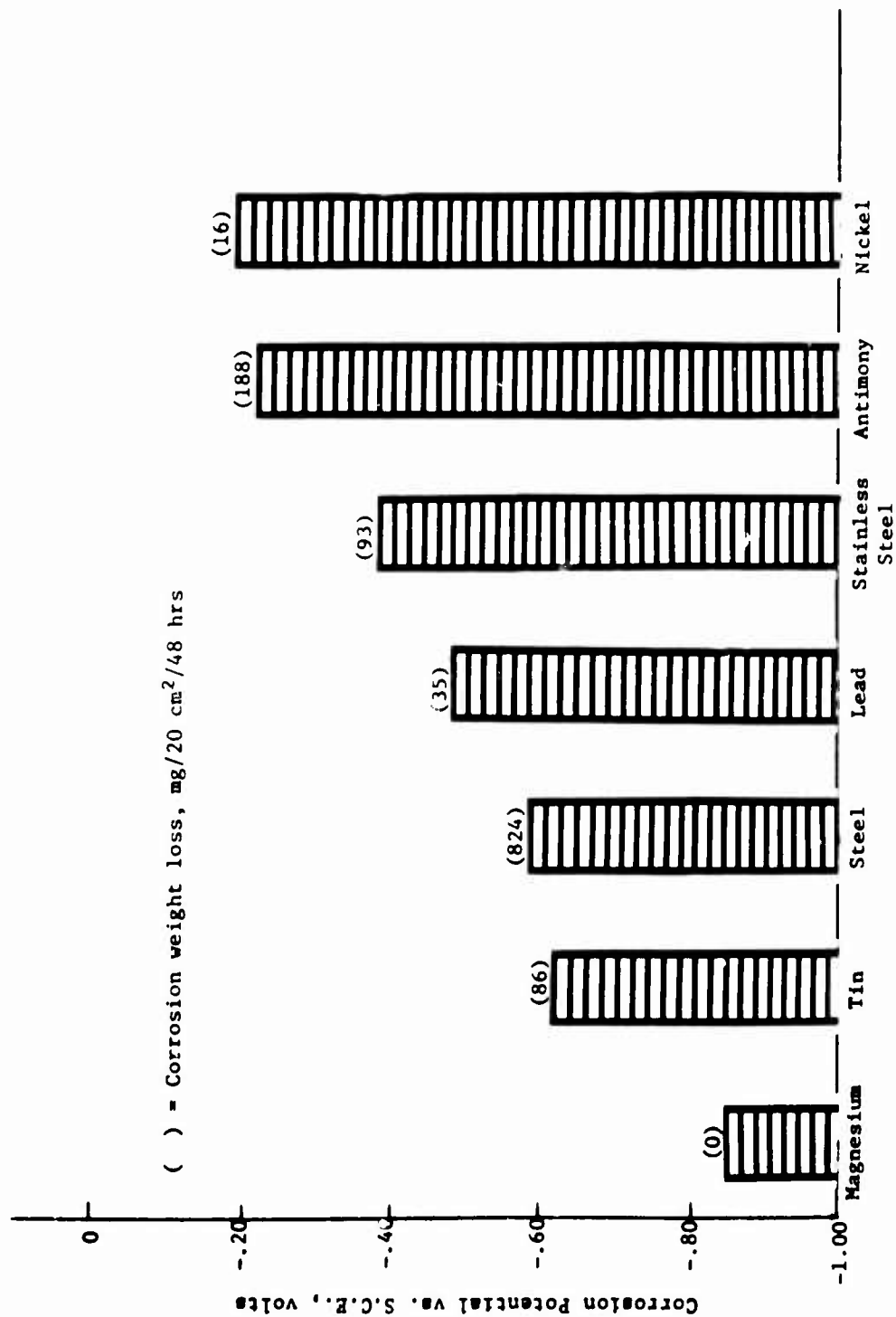
Figure 3. Potential of Various Metals After 48 Hours in 0.59 N HF Solution at $23 \pm 2°C$.

The Influence of Carbon Dioxide
on
The Corrosion of Magnesium Alloys
in
Solutions

by

F.J. Dougherty
A. Gallaccio

Pitman-Dunn Laboratory
FRANKFORD ARSENAL
Philadelphia, PA 19137

211

ABSTRACT

The role of carbon dioxide in the corrosion of 99.999 percent magnesium and AZ31B and HK31A magnesium alloys was investigated in distilled water, and in 0.1, 1.0 and 3.0 percent sodium chloride solutions. Solution volume influences with and in the absence of dissolved carbon dioxide also were examined.

It was found that carbon dioxide increases the corrosion rate of magnesium and the magnesium alloys in distilled water. The effect of carbon dioxide on corrosion in the sodium chloride solutions varies with the alloy and the sodium chloride concentration; in each case the carbon dioxide influence diminishes with increasing salt concentration.

With pure magnesium and HK31A alloy, a larger volume of solution was found to have a marked positive effect on corrosion, whereas with AZ31 alloy, the effect was less marked.

212

INTRODUCTION

There is little data in the literature on the effect of atmospheric carbon dioxide, in equilibrium with distilled water or with sodium chloride solutions, on the corrosion of pure magnesium and magnesium alloys. Godard, et al,[1] states that in static experiments covering 14 days, the corrosion rate of magnesium metal (99.95 percent purity) immersed in open containers was 1.2 to 12 mils per year, depending on the ratio of the air-solution interface to the area of the specimen. When carbon dioxide of the atmosphere was excluded by an Ascarite trap, the corrosion rate was 0.6 mpy.

Further, there is no information in the literature on the effect of different volumes of solution containing dissolved carbon dioxide, in equilibrium with the atmosphere, on the corrosion of magnesium or magnesium alloys. Emley[2] reported an increase in the corrosion of magnesium with increase in volume of pure water, but made no mention of carbon dioxide effects.

This report furnishes data concerning the role of carbon dioxide on the corrosion of pure magnesium and two commercial magnesium alloys in distilled water and sodium chloride solutions. The effects of different volumes of distilled water also are presented.

EXPERIMENTAL

Three magnesium metals, rolled sheets, 0.1 cm thick, were included in the study: 1) pure magnesium 99.999 percent, tripley distilled, supplied by Dow Chemical Company from a supply of experimental stock; 2) HK31A alloy (2.91 percent thorium, .68 percent zirconium); 3) AZ31A alloy (3.03 percent aluminum, 1.25 percent zinc). The HK31A and AZ31B were commercially produced stock and rectangular specimens (2.6 x 3.8 cm) were cut from the sheets using a power shears.

Four solutions were used; distilled water, and 0.1, 1.0, 3.0 percent sodium chloride solutions.

The source of air for the experiments was from a central compressed air source via a service line to the laboratory. The carbon dioxide content of the line air was analyzed using a Precision Wet Test Meter, and found to be 0.033 percent by volume (0.046 percent by weight). This is in close agreement with values given in the literature.[3] During the experiments, the line air was passed through a glass-wool packed column to remove particulate matter. For experiments requiring carbon dioxide, the line air was regulated by needle valve to a flow of 112 ml/min, and led into the test solution. Tygon tubing was used to carry the air from

the valve to polyethylene tubing extending into the test solution. Agitation of the solutions was adequately accomplished by the bubbling air. Solutions of all experiments were so agitated to help minimize scatter in results. Earlier investigations indicated that "still" solutions yielded results of wide scatter.[4] For experiments performed with air devoid of carbon dioxide, the line air was passed through a 13 cm column packed with Ascarite (sodium hydroxide-asbestos granules).

The containers in which the tests were run were heavy-walled, polypropylene beakers with tapered closures, that are friction secured by pressing into the beaker mouth. A rubber stopper, with appropriate holes through it to communicate with similar holes through the plastic cover, was used to support the air inlet and exhaust tubes, was fitted into each closure. Two sizes of containers were used, one for the smaller volume (300 ml) test, and a larger size for the greater volume (1200 ml).

The metal specimens were first washed with dichloromethane to remove oily soil. A 0.1397 cm diameter hole was drilled at one end of each specimen to receive the dacron thread by which the specimens would be suspended during the tests. These were then manually cleaned with water-wet Scotch-Brite scouring pads containing a very fine abrasive (aluminum oxide in open-mat plastic fibers). This was followed by usual metal cleaning operations, namely, cleaning in hot alkaline solution (15 minutes), dipping into two percent chromic acid solution (one minute, 85°C), dipping (one second) into a nitric acid sulfuric acid solution (80 ml 70 percent HNO_3, 20 ml 98 percent $H_2SO_4/1H_2O$) to finish with a bright surface.[5] The specimens were well rinsed with water at each step, and after the bright dip were rinsed with distilled water, then with "dry" acetone. After thorough drying in the atmosphere, and conditioning in a desiccator, the specimens were weighed to 0.1 mg and stored in a desiccator, over Drierite, in readiness for testing.

Tests conducted in distilled water comprised two groups, one involving a 300 ml volume, the other a 1200 ml volume. The ratio of liquid volume to metal surface area for the smaller volume was 15, for the larger volume, 60. All experiments conducted in salt solutions were with 300 ml volume only.

The exposure intervals were 6, 18, 40, and 66 hours.

Each test involved four replicates, for each metal, each solution, each air, each volume, and each exposure period. Each replicate was new and was immersed in a fresh solution.

After a set of tests was completed, the specimens were rinsed with distilled water, dried with acetone, conditioned in a desiccator containing Drierite for 15 minutes and reweighed. Each specimen was then individually placed for 90 seconds in 100 ml of boiling 15 percent chromic acid solution contained in a 150 ml beaker. In determinations in which sodium chloride was used as the test solution, one percent silver chromate was added to the chromic acid solution as a scavenger for

214

residual chloride anions. One 100 ml portion of the chromic acid was used for eight specimens and the solution then discarded. The specimen was washed thoroughly with distilled water, rinsed with acetone, dried at room temperature, conditioned in a desiccator, and weighed again.

All solutions for the 300 ml volume tests were prepared using water "as distilled" and not sparged with carbon dioxide-free air. The water "as distilled" contained approximately 1.6 mg CO_2/1. In using the 300 ml of distilled water the removal of carbon dioxide in the starting solution was found to make no difference in the result if carbon dioxide containing air was subsequently passed into the liquid. If air devoid of carbon dioxide was passed into the same starting solution a very slight depression of weight loss occurs and based on initial tests these values were calculated and are listed for comparison purposes in Table VIII.

The experiments with 1200 ml of distilled water were in two groups, one with the water at the start containing carbon dioxide at approximately 1.6 mg CO_2/1, the other free of carbon dioxide. The water free of carbon dioxide was prepared by continuously sparging distilled water with oil pumped nitrogen for at least two days.

After transferring nitrogen sparged water into the test cell, further bubbling of nitrogen through the water in the container was continued for 18 hours additional. Following this conditioning step, tests were performed, one group receiving carbon dioxide free air, the other group, line air containing carbon dioxide.

RESULTS AND DISCUSSION

The weight loss/area obtained with specimens of the three metals in 300 ml volumes of distilled water or salt solutions are listed in Tables I, II, and III.

From Table I it is seen that the weight losses in distilled water for pure magnesium, AZ31B, and HK31A alloys show approximately an eight-fold increase when air with carbon dioxide is passed through the water, as compared to when air free of carbon dioxide is used. In the sodium chloride solutions sparged with air containing carbon dioxide, pure magnesium yields a slightly higher weight loss at 66 hours, compared to when air free of carbon dioxide is used. In the sodium chloride solutions sparged with air containing carbon dioxide, pure magnesium yields a slightly higher weight loss at 66 hours, compared to that in distilled water (ca. 165 mg/dm^2, dist. H_2O vs. ca. 208 mg/dm^2, 3% NaCl soln.). However, when carbon dioxide-free air is passed through, weight loss increases with salt concentration, compared to distilled water, and in the 3 percent salt solution is twice as much (ca. 18 mg/dm^2, dist. H_2O vs. ca. 39 mg/dm^2, 3% NaCl soln.).

TABLE I

Weight Loss of Pure Magnesium Specimens[a] in Solution[b] and Sparged With Air
Either Containing Carbon Dioxide or Devoid of Carbon Dioxide

Weight Loss/Area (mg/dm^2)

Sodium Chloride Solution (300 ml) Wt. %	Air	6 Hrs.	18 Hrs.	40 Hrs.	66 Hrs.
0	No CO_2	10.40	15.07	16.05	17.89
	CO_2	16.42	51.87	101.00	165.44
0.1	No CO_2	16.79	20.73	22.54	22.94
	CO_2	26.82	59.30	116.66	197.54
1.0	No CO_2	23.28	27.07	27.07	27.94
	CO_2	32.35	68.00	133.33	199.06
3.0	No CO_2	33.77	34.07	35.54	38.72
	CO_2	37.26	74.63	151.46	207.84

[a]Average of four determinations
[b]Starting solution "as distilled" carbon dioxide content approximately 1.60 mg/1

216

On the whole, a similar situation is observed for HK31 alloy (Table II), although throughout, the corrosion of this alloy is somewhat greater than pure magnesium under like conditions. However, the effect of salt concentration is more pronounced with HK31 alloy. In distilled water and in the absence of carbon dioxide, corrosion is least. In the salt solutions weight loss increases progressively, reaching, at 66 hours in 3 percent sodium chloride solution, about $2\frac{1}{2}$ times the loss in distilled water (ca. 24.7 mg/dm^2 vs. 68.5 mg/dm^2). Comparisons of test results with air containing carbon dioxide show the effects of carbon dioxide in accelerating corrosion of HK31 alloy in distilled water and in the salt solutions, also the enhancement of corrosion with increase in salt concentration.

Table III reveals somewhat different effects on the AZ31 alloy. These include a noticeably stronger influence of the presence of salt and the concentration of the salt solution in promoting corrosion. Further, it is evident that while carbon dioxide in solution promotes corrosion in distilled water, it diminishes corrosion attributable to the presence and concentration of the salt electrolyte. Weight loss in 3 percent salt solution after 66 hours in the absence of carbon dioxide is ca. 57 times that in distilled water; and in the presence of carbon dioxide, ca. three times. Smaller differences prevail for the 0.1 and 1.0 percent salt solutions with and without dissolved carbon dioxide.

In distilled water devoid of carbon dioxide, each metal exhibits a substantial retardation of corrosion with extended exposure time; whereas with carbon dioxide in solution, only a slight diminution occurs. Pure magnesium and HK31 alloy are similar in their general behavior, but weight loss data differ in magnitude. The AZ31 alloy on the whole is indicated less corrodable in distilled water, either in the absence or in the presence of carbon dioxide than pure magnesium or HK31 alloy. But, in the salt solutions, with or without carbon dioxide present AZ31 alloy is generally more susceptible to dissolution.

Solution, NaCl Conc. (Wt. %)	Air – W or W/O CO_2	Metal and Comparative Corrosion (rate)
0	W/O	HK31 > Mg $\overline{>}$ AZ31
0	W	HK31 > Mg > AZ31
0.1	W/O	AZ31 > HK31 > Mg
0.1	W	HK31 > Mg > AZ31
1.0	W/O	AZ31 > HK31 > Mg
1.0	W	AZ31 > HK31 > Mg
3.0	W/O	AZ31 > HK31 > Mg
3.0	W	AZ31 > HK31 > Mg

TABLE II

Weight Loss of Magnesium Alloy HK31A Specimens[a] in Solution[b] and Sparged With Air Either Containing Carbon Dioxide or Devoid of Carbon Dioxide

Sodium Chloride Solution (300 ml) Wt. %	Air	Weight Loss/Area (mg/dm^2)			
		6 Hrs.	18 Hrs.	40 Hrs.	66 Hrs.
0	No CO_2	14.35	20.59	23.66	24.65
	CO_2	21.57	60.18	120.80	187.12
0.1	No CO_2	21.94	26.38	28.10	32.54
	CO_2	33.52	69.75	137.57	199.70
1.0	No CO_2	26.00	35.37	38.46	48.32
	CO_2	35.25	78.76	168.64	252.46
3.0	No CO_2	31.55	45.74	52.76	68.53
	CO_2	40.19	85.30	176.52	269.72

[a] Average of four determinations

[b] Starting solution "as distilled" carbon dioxide content approximately 1.50 mg/l

TABLE III

Weight Loss of Magnesium Alloy AZ31B Specimens[a] in Solution[b] and Sparged With Air Either Containing Carbon Dioxide or Devoid of Carbon Dioxide

Sodium Chloride Solution (300 ml) Wt. %	Air	Weight Loss/Area (mg/dm^2)			
		6 Hrs.	18 Hrs.	40 Hrs.	66 Hrs.
0	No CO_2	11.13	12.40	15.39	17.53
	CO_2	15.38	38.55	68.25	122.34
0.1	No CO_2	20.91	45.44	99.0	163.24
	CO_2	20.41	42.69	88.60	137.00
1.0	No CO_2	61.58	176.00	290.43	434.65
	CO_2	56.83	111.00	158.73	202.80
3.0	No CO_2	121.30	421.87	548.0	1006.90
	CO_2	87.38	279.12	294.44	365.01

[a] Average of four determinations

[b] Starting solution "as distilled" carbon dioxide content approximately 1.60 mg/1

The normal hydroxide film which develops on the metal surfaces in distilled water, or in dilute (o.1%) sodium chloride solution[2,6], acts to diminish, with time, dissolution of pure magnesium or the alloys. This condition unquestionably is modified or altered when carbon dioxide is available to act on the film, to form carbonates of the metals involved, which are more soluble than the respective hydroxides. In the presence of chlorides, the chloride ion penetrates and sufficiently damages the hydroxide film to promote corrosion[7,8]. Bothwell[1] states that in the presence of chloride ion, magnesium hydroxide film is rendered porous, resulting in promotion of corrosion.

Differences in corrosion among the three metals may be related to the alloying constituents, the contribution of the constituents in providing films of different solubilities, in test media, and the action of the chloride ion on the films produced. For example, solubilities of hydroxides and carbonates of magnesium and the principal alloying constituents of the AZ31 and HK31 alloys are as follows:

Metal	Solubility, Cold H_2O, ppH	
	Hydroxide	Carbonate
Mg.	0.009 $\begin{array}{l}3\ Mg\ CO_3.\\ Mg\ (OH)_2.\ \}\\ 3\ H_2O\end{array}$	0.04
Al.	0.0001	– *
Th.	1.2×10^{-13}	– *
Zn.	0.0005	0.001
	0.02 $\begin{array}{l}Zr.\ O_2CO_2.\\ 3\ H_2O\ \ \ \}\end{array}$	– *

* Not available

From the solubility data, it would appear that the corrodability of the metals in distilled water with or without carbon dioxide should follow the order: AZ31B alloy < pure magnesium < HK31A alloy. This is the order derived from the experimental data. But in the salt solutions, the effect of the chloride ion in reducing the effectiveness of the film formed on the metal surfaces and in each case resulting in the promotion of corrosion, is manifested. The combined effects on the corrosion of the metals contributed to by the specific film susceptibility to salt solution and carbon dioxide conditions involved are not known. Yet, the relative order of attack on the metals has been demonstrated by the weight loss data.

The alloys are more attacked than is pure magnesium, whether or not the solutions are free of carbon dioxide, with the exception of the 0.1 percent sodium chloride solution containing carbon dioxide. In this case, HK31 is more susceptible and AZ31 less susceptible than pure magnesium. The greater activity of the alloys is attributed to impurities[9,10], e.g.,

in HK31 (% Weight): Cu 0.01, Mn 0.05, Ni 0.005, Fe 0.005; in AZ31: Cu 0.01, Mn 0.48, Ni 0.005, Fe 0.005 and in addition AZ31B also contains 0.04 percent calcium. Marked retardation of attack of the AZ31 alloy in the presence of carbon dioxide, suggests a combined effect of resistance of the carbonate film to chloride ion and solubility.

Corrosion potentials were measured for each metal in three percent sodium chloride solution saturated with air containing carbon dioxide or with air free of carbon dioxide. The potentials, vs. S.C.E. were:

	Pure Magnesium	AZ31B	HK31A
Air no CO_2	-1.68	-1.60	-1.80
Air with CO_2	-1.87	-1.56	-1.81

Carbon dioxide influence on the corrosion potential of pure magnesium is evident from the higher negative potential, and is in line with the greater tendency of pure magnesium to corrode in salt solutions containing carbon dioxide. It is noteworthy that whether or not carbon dioxide is present, the corrosion potentials are the same in each case for HK31 and essentially similar for AZ31. Yet from the weight loss measurements in three percent sodium chloride solution, attack of HK31 is greater when carbon dioxide is present. Under the same conditions, attack of AZ31 is reduced. Two principal anomalies are apparent. First, there is non-agreement between the significance of corrosion potentials obtained for HK31 or for AZ31 and the corrosion performance of each alloy in salt solutions either containing carbon dioxide or free of it. Second, AZ31 demonstrates the least active potential, yet is overall more reactive in each condition. As was mentioned above, metallic alloying constituents, corrosion film composition and morphology, and chloride ion influence on the transfer characteristics of the film contributes in modifying the corrosion behavior of the magnesium metals.

Corrosion rate data for each of the metals are listed in Tables IV, V, and VI. Ratios of weight loss/area (mg/dm^2) for each metal in the different solutions, with or without carbon dioxide, are given in Table VII, and plotted in Figures 1 and 2. A ratio greater than one indicates that carbon dioxide promotes corrosion; whereas a ratio less than one signifies a suppression of corrosion by carbon dioxide. The larger the ratio, the more is the effect of carbon dioxide. Table VII includes the interactions of all the parameters examined in the experiments - the significance of carbon dioxide, salt concentration, and exposure time. The influence of alloy composition also may be inferred from the data.

Comparison data of weight loss/area (mg/dm^2) of the three metals in 300 ml and 1200 ml of distilled water, with and without carbon dioxide, are shown in Table VIII; corrosion ratios for the larger volume (1200 ml) are given in Table IX; and comparative weight loss/area ratio in 300 ml and 1200 ml, with and without carbon dioxide are presented in Table X.

221

TABLE IV

Corrosion Rate of HK31A Alloy Specimens[a] in Solution[b] and Sparged With Air Either Containing Carbon Dioxide or Devoid of Carbon Dioxide

Sodium Chloride Solution (300 ml) Wt. %	Air	Corrosion Rate (mdd)			
		6 Hrs.	18 Hrs.	40 Hrs.	66 Hrs.
0	No CO_2	57.4	27.4	14.2	8.8
	CO_2	86.3	80.0	72.5	67.4
0.1	No CO_2	87.8	35.1	16.8	11.7
	CO_2	134.1	92.8	82.5	71.8
1.0	No CO_2	104.0	47.0	23.1	17.4
	CO_2	141.0	104.8	101.2	90.9
3.0	No CO_2	126.2	60.3	31.7	24.7
	CO_2	160.7	113.4	105.9	97.1

[a] Average of four determinations

[b] Starting solution "as distilled" carbon dioxide content approximately 1.60 mg/l

TABLE V

Corrosion Rate of AZ31B Magnesium Alloy Specimens[a] in Solution[b] and Sparged With Air Either Containing Carbon Dioxide or Devoid of Carbon Dioxide

Sodium Chloride Solution (300 ml) Wt. %	Air	Corrosion Rate (mdd)			
		6 Hrs.	18 Hrs.	40 Hrs.	66 Hrs.
0	No CO_2	44.5	16.5	9.2	6.3
	CO_2	61.5	51.3	41.0	44.0
0.1	No CO_2	83.6	60.4	59.4	58.7
	CO_2	81.6	56.7	53.1	49.3
1.0	No CO_2	246.3	234.1	174.3	156.5
	CO_2	227.3	147.6	95.2	73.0
3.0	No CO_2	485.2	561.1	328.8	362.5
	CO_2	349.5	371.2	176.7	131.4

[a] Average of four determinations
[b] Starting solution "as distilled" carbon dioxide content approximately 1.60 mg/l

223

TABLE VI

Corrosion Rate of Pure Magnesium Specimens[a] in Solution[b] and Sparged With Air Either Containing Carbon Dioxide or Devoid of Carbon Dioxide

Sodium Chloride Solution (300 ml) Wt. %	Air	Corrosion Rate (mdd)			
		6 Hrs.	18 Hrs.	40 Hrs.	66 Hrs.
0	No CO_2	41.6	20.0	9.6	6.4
	CO_2	65.7	68.9	60.6	59.5
0.1	No CO_2	67.1	27.6	13.5	8.2
	CO_2	107.8	78.9	69.9	71.1
1.0	No CO_2	93.1	36.0	16.2	10.1
	CO_2	129.4	90.4	80.0	71.6
3.0	No CO_2	135.1	45.4	21.3	13.9
	CO_2	149.0	99.2	90.9	74.8

[a]Average of four determinations
[b]Starting solution "as distilled" carbon dioxide content approximately 1.60 mg/1

TABLE VII

Ratio of Corrosion[a] From Presence and Absence of Carbon Dioxide Data For Pure Magnesium, HK31A and AZ31B Magnesium Alloys in Distilled Water and Sodium Chloride Solutions

Exposure Hours

Sodium Chloride Solution (300 ml) Wt. %	AZ31B			HK31A			Pure Magnesium		
	6	18	40	66	6	18	40	66	6	18	40	66
0	1.38	3.11	4.44	6.98	1.50	2.92	5.11	7.59	1.58	3.44	6.29	9.25
0.1	0.98	0.94	0.89	0.84	1.52	2.62	4.90	6.14	1.72	2.86	5.18	8.61
1.0	0.92	0.63	0.55	0.47	1.36	2.23	4.38	5.22	1.39	2.51	4.95	7.12
3.0	0.72	0.66	0.53	0.36	1.27	1.88	3.35	3.94	1.10	2.19	4.26	5.37

$$a = \frac{\text{Weight Loss/Area (mg/dm}^2) \text{ with carbon dioxide}}{\text{Weight Loss/Area (mg/dm}^2) \text{ without carbon dioxide}}$$

Figure 1. Ratio of Corrosion[b] from Presence and Absence of Carbon
Dioxide Data for Pure Magnesium, HK31A and AZ31B Magnesium
Alloys in Distilled Water and Sodium Chloride Solutions
(300 ml).
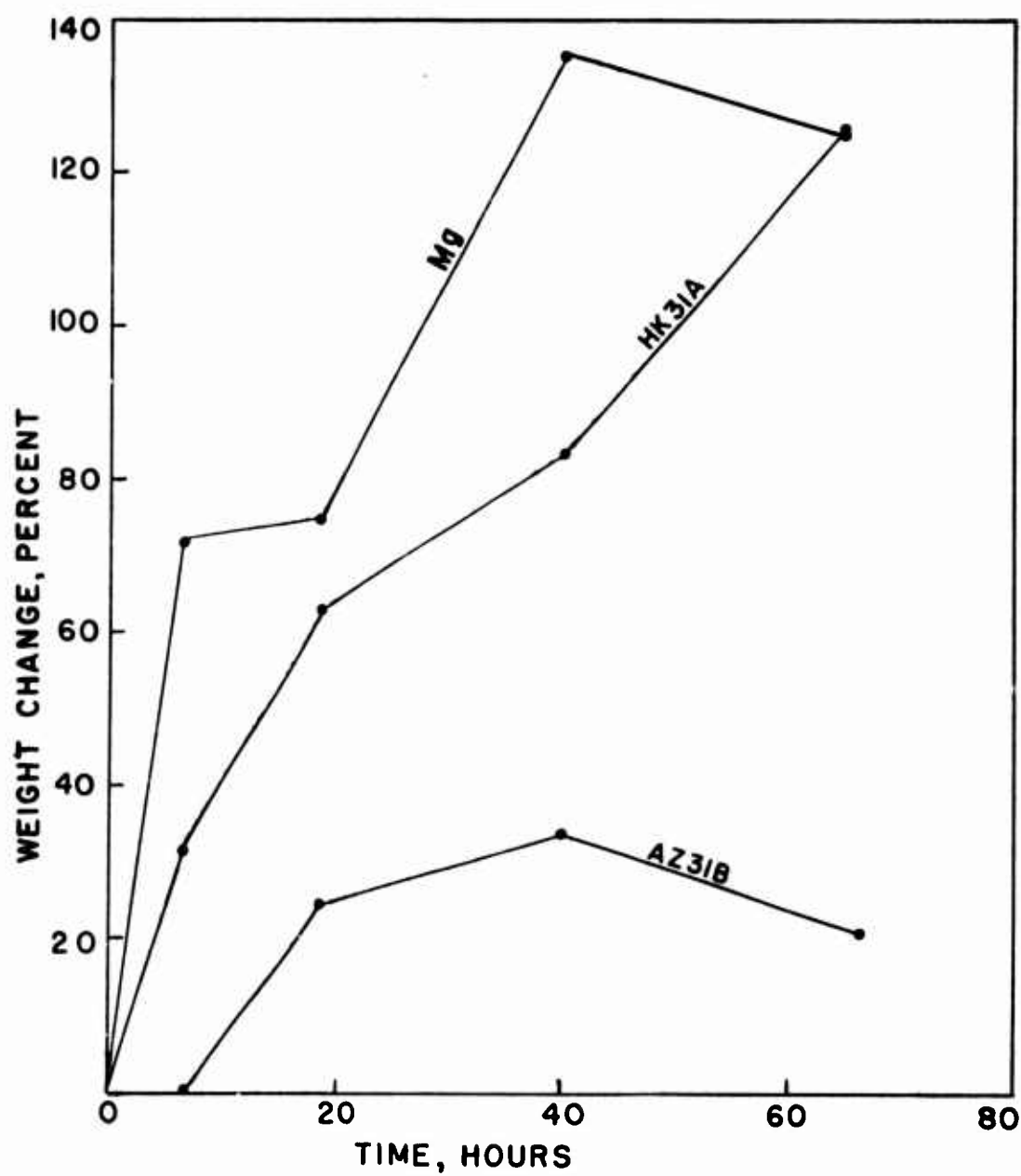
Figure 2. Percent Change (Weight Loss) of Pure Magnesium and HK31A and
AZ31B Magnesium Alloys Sparged with Air Devoid of Carbon
Dioxide, 300 ml/1200 ml.

TABLE VIII

Weight Loss/Area (mg/dm^2) of Metal Specimens
Submerged at Various Time Intervals in Distilled Water, 300 ml/1200 ml

Volume (ml)	Starting Solution	Air	AZ31B 6	18	40	66	HK31A 6	18	40	66	Pure Mg 6	18	40	66
300	as dis-tilled*	No CO$_2$	11.13	12.40	15.39	17.53	14.35	20.59	23.66	24.65	10.40	15.07	16.05	17.89
		CO$_2$	15.38	38.55	68.25	122.34	21.57	60.18	120.80	187.12	16.42	51.87	101.00	165.44
300	CO$_2$ free	No CO$_2$	10.00	11.51	14.52	16.52	13.31	19.72	22.68	23.66	8.82	13.72	15.19	16.66
		CO$_2$	15.38	38.55	68.25	122.34	21.57	60.18	120.80	187.12	16.42	51.87	101.00	165.44
1200	as dis-tilled*	No CO$_2$	11.68	19.23	21.18	23.50	23.42	36.48	44.37	51.77	20.44	29.90	40.19	41.7
		CO$_2$	14.79	41.91	79.38	133.10	31.06	72.48	125.73	230.76	24.02	62.74	124.50	193.13
1200	CO$_2$ free	No CO$_2$	10.00	14.52	19.52	20.03	17.75	32.05	41.42	49.30	15.19	24.02	36.76	36.80
		CO$_2$	16.52	39.55	84.62	130.19	26.62	72.48	118.69	229.78	22.54	60.78	125.00	178.92

(Exposure Hours)

*Carbon dioxide content, approximately 1.60 mg CO$_2$/l

TABLE IX

Corrosion Rate (mdd) of Metal Specimens in Distilled Water
With Air Containing Carbon Dioxide or Devoid of Carbon Dioxide, 300 ml/1200 ml

Exposure Hours

Volume (ml)	Starting Solution	Air	AZ31B				HK31A				Pure Mg			
			6	18	40	66	6	18	40	66	6	18	40	66
300	as distilled*	No CO$_2$	44.5	16.5	9.2	6.3	57.4	27.4	14.2	8.8	41.6	20.0	9.6	6.4
		CO$_2$	61.5	51.3	41.0	44.0	86.3	80.0	72.5	67.4	65.7	68.9	60.6	59.5
1200	as distilled*	No CO$_2$	46.7	25.5	13.3	8.5	93.3	48.5	26.6	18.6	81.7	39.8	24.1	14.8
		CO$_2$	59.2	55.7	46.4	47.9	124.2	96.4	75.4	83.1	96.1	83.4	74.3	59.5
1200	CO$_2$ free	No CO$_2$	40.0	19.3	11.7	7.2	71.0	42.6	24.9	17.8	60.7	31.9	22.1	13.2
		CO$_2$	66.1	52.6	50.7	46.8	106.5	96.4	77.2	82.7	90.2	80.8	75.0	64.4

*Carbon dioxide content approximately 1.60 mg CO$_2$/1

TABLE X
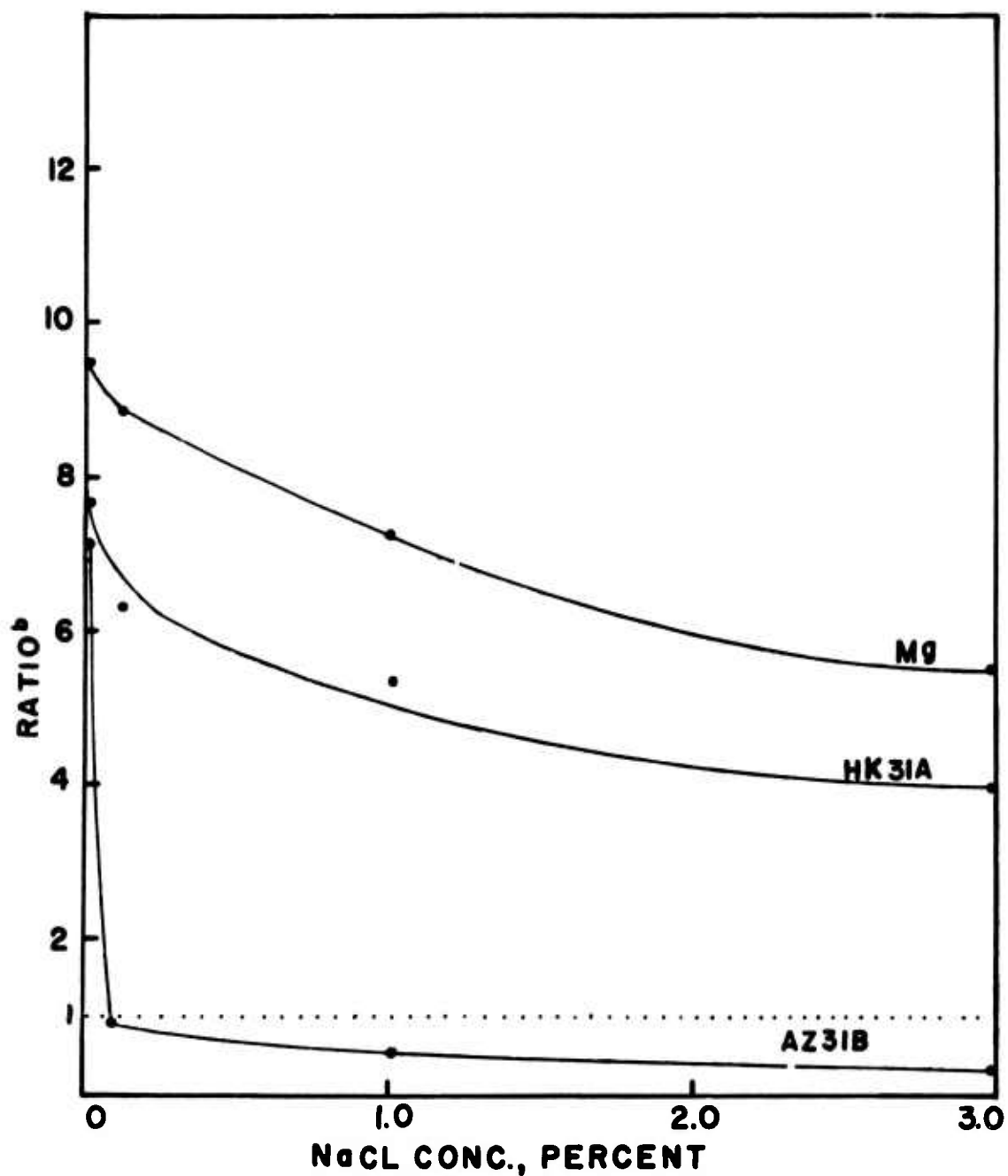
Ratio of Corrosion[a] in Presence and Absence of Carbon Dioxide for Pure Magnesium, HK31A and AZ31B Magnesium Alloys in Distilled Water, 300 ml/1200 ml

Exposure Hours

Volume (ml)	Starting Solution	AZ31B				HK31A				Mg			
		6	18	40	66	6	18	40	66	6	18	40	66
300	as distilled*	1.38	3.11	4.44	6.98	1.50	2.92	5.11	7.59	1.58	3.44	6.29	9.25
1200	as distilled*	1.27	2.18	3.58	5.66	1.33	1.99	2.82	4.46	1.18	2.10	2.95	4.69
1200	CO_2 free	1.65	2.72	4.34	6.50	1.50	2.26	3.11	4.67	1.48	2.53	3.40	4.86

a = $\dfrac{\text{Weight loss/area } (mg/dm^2) \text{ with carbon dioxide}}{\text{Weight loss/area } (mg/dm^2) \text{ without carbon dioxide}}$

* Carbon dioxide content approximately 1.60 mg CO_2/l

230

Corrosion of the three metals increases in the larger volume of distilled water free of carbon dioxide. The volume effect is least with AZ31 alloy. With the larger volume of distilled water with carbon dioxide, a marked increase in corrosion occurs, again with least effect on AZ31 alloy. Corrosion of AZ31 alloy is only mildly affected in the larger volume of water with carbon dioxide.

The ratios of corrosion of the three metals in the different volumes of distilled water with and without carbon dioxide for the exposure periods involved are given in Table X. Table XI shows the percent change in weight loss which occurs as a result of going from 300 ml to 1200 ml of distilled water, with and without the addition of carbon dioxide. Pure magnesium and HK31A are more significantly affected compared to AZ31B which is only mildly affected. For the pure magnesium and HK31A in the solution with carbon dioxide the percent increase in the larger volume is only 20 percent of that of the carbon dioxide free water. Changes in the same direction are noted with AZ31B magnesium alloy, but the differences are much smaller. The AZ31B magnesium alloy shows virtually no change at six hours with increased volume. This is probably due to the initial protection of hydroxide film which tends to mask the effects which might be attributed to the larger volume of distilled water. Figures 2 and 3 are plots of these results. Figure 3 shows that the presence of carbon dioxide overshadows the volume effect and only small increases in volume effects are seen especially at the longer time periods.

The findings are summarized:

Mg Alloy	Air W or W/O CO2	Solution and Relative Order of Corrosion 300 ml		1200 ml
Pure Magnesium	W/O	3% > 1% > 0.1% > DW	<	DW
		∧ ∧ ∧ ∧		∧
	W	3% > 1% > 0.1% > DW	<	DW
AZ31B	W/O	3% > 1% > 0.1% > DW	<	DW
		∨ ∨ ∨ ∧		∧
	W	3% > 1% > 0.1% > DW	<	DW
HK31A	W/O	3% > 1% > 0.1% > DW	<	DW
		∧ ∧ ∧ ∧		∧
	W	3% > 1% > 0.1% > DW	<	DW
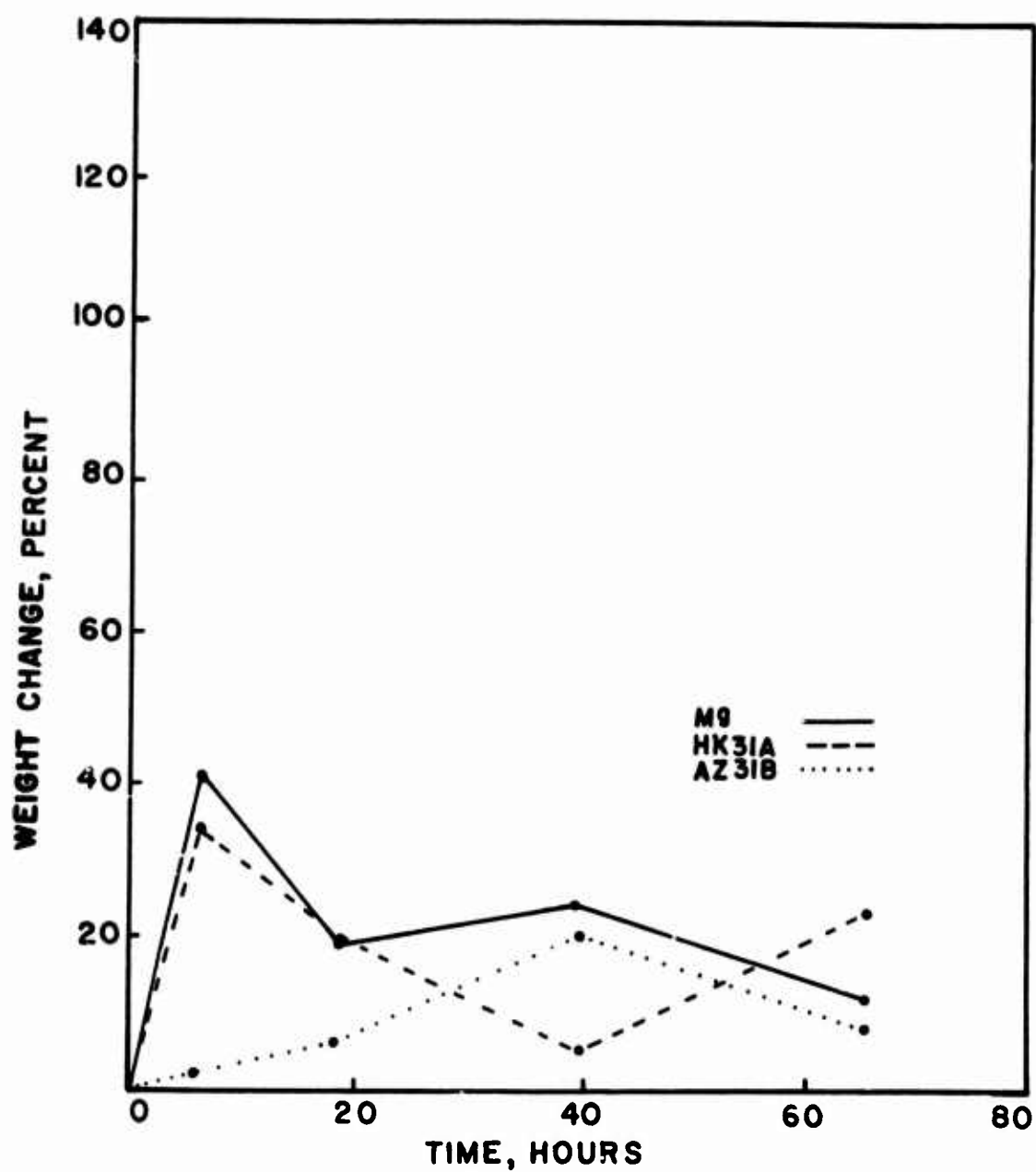
Figure 3. Percent Change (Weight Loss) of Pure Magnesium and HK31A and AZ31B Magnesium Alloys Sparged with Air Containing Carbon Dioxide, 300 ml/1200 ml.

232

TABLE XI

Percent Change Weight Loss of Pure Magnesium, HK31A and AZ31B Magnesium Alloys Sparged With Air, With and Without Carbon Dioxide in Distilled Water,[a] 300 ml/1200 ml

Alloy	Air	Exposure Hours				
		6	18	40	66	Average
Pure Mg	No CO_2	72	75	135	125	102
	CO_2	41	19	24	12	24
AZ31B	No CO_2	0	26	34	21	20
	CO_2	2	6	20	8	9
HK31A	No CO_2	33	63	83	126	76
	CO_2	34	20	5	23	21

[a] Distilled water devoid of CO_2 at start of experiment.

233

CONCLUSIONS

1. Atmospheric carbon dioxide in distilled water in equilibrium with the air accelerates the corrosion of pure magnesium, AZ31B and HK31A magnesium alloy. The degree of corrosion is more drastic as the volume of distilled water is increased (300 - 1200 ml) for pure magnesium and HK31A magnesium alloys.

2. The effect of carbon dioxide in a small volume (300 ml) on the corrosion process shows the following:

   a. Reduces corrosion ratio by approximately 50 percent for pure magnesium and HK31A magnesium alloy as the sodium chloride concentration is increased to three percent.

   b. An increase in corrosion ratio with lengthening exposure time for pure magnesium and HK31A magnesium alloy.

   c. Shows a significant change, and actually retards the corrosion of AZ31B in sodium chloride solutions. Also diminishes the corrosion ratio of AZ31B magnesium alloy with increasing sodium chloride concentration from 0.1 to 3.0 percent and further diminishes with prolonged exposure.

   d. The compositions of magnesium alloy affects whether carbon dioxide suppresses or increases the corrosion process in sodium chloride solution.

3. Influences on corrosion attributable to different volumes of distilled water, 300 ml/1200 ml, are as follows:

   a. Corrosion rate increases by ca. 100 percent for pure magnesium and HK31A magnesium alloy with air devoid of carbon dioxide. When air containing carbon dioxide is passed into the solution the corrosion is increased approximately by an additional 20 percent.

   b. AZ31B magnesium alloy is less affected (20 percent) in solution receiving air without carbon dioxide and only a nine percent increase in carbon dioxide containing air.

   c. The larger volume (1200 ml) causes a significant reduction in the corrosion ratio of pure magnesium and HK31A magnesium alloy while little change is seen with AZ31B.

REFERENCES

1. H.P. Godard, W.P. Jepson, M.R. Bothwell and R.L. Kane, "The Corrosion of Light Metals", p. 16, 282-285, John Wiley and Sons, New York, (1967).

2. E.F. Emley, "Principles of Magnesium Technology", p. 689, Pergamon Press, New York, (1966).

3. "Handbook of Chemistry and Physics", 46th Edition, F-116, Chemical Rubber Company, Cleveland, Ohio, (1962).

4. G. Norwitz and A. Gallaccio, "Corrosion of Magnesium and Magnesium Alloys", Frankford Arsenal Summary Report, Phila., PA, July 1972.

5. "Magnesium Finishing", p. 27, The Dow Chemical Company, Midland, Michigan, (1958).

6. H. Uhlig, "Corrosion and Corrosion Control", p. 191, John Wiley and Sons, New York, (1964).

7. N.D. Tomashov, "Theory of Corrosion and Protection of Metals", p. 691, The Macmillan Company, New York, (1966).

8. "Metals Handbook", Volume I, Properties and Selection of Metals, p. 926, 1086-1088, American Society for Metals, Metals Park, Ohio, (1961).

9. J.P. Hanawalt, C.E. Nelson and J. Peloubet, "Trans. Am. Inst. Mining and Met. Eng.", 147 pp. 273-99 (1942).

10. Ref. 1 - pp. 286-288.

THE EFFECT OF TEXTURE ON THE ELECTROCHEMICAL BEHAVIOR OF TITANIUM ALLOYS

by

David W. Seitz
Army Materials and Mechanics Research Center
Watertown, Massachusetts 02172

and

Michael Kurek
Federal Agency for Procurement and Technology
Koblenz, Federal Republic of Germany

ABSTRACT

Studies are reported on the electrochemical behavior of highly textured Ti-4Al and Ti-4Al-4V alloys. Specimens were fabricated to expose surfaces having preferential basal or prism orientation. Potential sweep anodic polarization experiments were carried out to determine the effects of specimen orientation, hence texture, on the dissolution characteristics of the alloys. The environments were sulfuric and hydrochloric acid solutions. After polarization, the specimen surfaces were examined by scanning electron microscopy and the findings correlated with the electrochemical data.

237

INTRODUCTION

Most of the reported work on the anisotropic behavior of titanium has focused on mechanical behavior. It has been shown that significant improvement in the strength of biaxially stressed components can be realized through the use of controlled texture (detailed crystallographic structure) titanium[1]. Until quite recently, little work has been done on the effect of texture on corrosion and stress corrosion cracking of titanium alloys. However, recently Fraker and Ruff at NBS and Green at Martin Marietta, utilizing titanium single crystals, have shown a marked difference in the electrochemical behavior of the various crystal surfaces[2,3,4]. These results suggest the possibility of utilizing texture controlled α titanium alloys to achieve enhanced corrosion resistance combined with improved strength characteristics. It is the purpose of this work to extend the single crystal work to polycrystalline alloys.

MATERIAL

The two materials tested were a 0.25 in. thick Ti-4Al sheet and a 0.5 in. thick Ti-4Al-4V plate; the chemistries of which are given in Table I. Mechanical property data on the Ti-4Al-4V alloy is given in Table II. Note the effect of the preferred orientation on the transverse versus longitudinal properties. No mechanical property data was available on the Ti-4Al material. The Ti-4Al-4V alloy has an α + 10% β phase composition and, although its thermomechanical history is unknown, the texture present and the microstructure indicate that this alloy was hot rolled low in the α-β field. The Ti-4Al alloy has an all α equiaxed grain structure with the final heat treatment for this material consisting of a twenty hour solution treat at 1625°F and water quenched.

238

The pole figures shown in Figure 1 indicate both materials to be strongly textured with respect to basal plane orientation. In the case of the Ti-4Al alloy, the basal planes are sharply aligned in the plane of the sheet with random orientation of the prism planes about the c axis. In the case of the Ti-4Al-4V alloy, the basal planes are parallel to the rolling direction with the $(10\bar{1}0)$ prism planes parallel to the transverse direction and the $(11\bar{2}0)$ prism planes parallel to the plane of the sheet. The procedure and equipment utilized in obtaining the pole figures in Figure 1 have been described elsewhere[5,6].

PROCEDURE

The polarization specimens used were in the form of cubes cut from the plate and sheet stock (see Figure 1) to expose the desired crystalline planes having approximately 1 sq cm surface area. One face of each cube was drilled and tapped for attaching the specimen to the electrode holder. The face to be studied was metalographically polished with all other faces being coated with a non conductive coating prior to testing.

The polarization cell was basically that described by Green[7] but modified to use only one counter electrode positioned opposite to the specimen face to be tested. A heating mantel was used to regulate the temperature of the environment ± 2°C. Potential sweep anodic polarization measurements were made utilizing a Wenking potentiostat in conjunction with a moto-potentiometer and x-y recorder to automatically record the current versus potential data. The potential was changed at a constant rate of 5,000 mv/hr and all potential measurements were made versus a saturated calomel electrode via a Luggin probe.

The environments utilized were 1.5N H_2SO_4, 5N H_2SO_4, and 5N HCl and tests were conducted at room temperature, 50°C, and 65°C.

RESULTS AND DISCUSSION

The polarization curves in Figure 2 show the effect of texture on the anodic polarization behavior of the Ti-4Al alloy in 5N H_2SO_4 at 25, 50, and 65°C. In all cases the peak dissolution current for specimens which preferentially expose basal planes is less than that for specimens exposing a mixture of prism planes. The critical potential for passivity is the same for both types of specimens at a given temperature but shifts (cathodically) in the more active direction with increasing temperature. Regardless of crystallographic plane exposed, the maximum dissolution current increased with increasing temperature. Also the higher the temperature, the greater the effect of texture.

Figure 3 shows similar data for the Ti-4Al alloy in 5N HCl. Again, the peak dissolution current for specimens which preferentially expose basal planes is less than that for specimens exposing a mixture of prism planes. However, increasing the solution temperature reduced the texture effect for this alloy in 5N HCl.

In the case of the Ti-4Al-4V alloy, it was possible to preferentially expose and test two different prism planes; namely, $(11\bar{2}0)$ and $(10\bar{1}0)$, rather than the mixture of prism planes tested in the Ti-4Al specimens. Figure 4 shows the polarization curves obtained for these two prism planes as well as for the basal plane in 1.5N H_2SO_4 at room temperature (25°C). The basal plane oriented specimens are again found to be less reactive, as reflected in the dissolution currents for the active as well as passive and transpassive regions. There is very little difference

in the behavior of the two prism planes in this environment. Increasing

the H_2SO_4 concentration to 5N (Figure 5) served only to increase the

peak dissolution currents for the three types of specimens. When the

temperature of the 5N environment is increased to 50°C, a difference in

behavior between the two prism planes becomes evident as shown in Figure 6.

The $(10\bar{1}0)$ plane specimens show a higher dissolution current than the

$(11\bar{2}0)$ specimens with the basal oriented specimens showing, as in all

other cases reported here, the lowest peak dissolution current. Once

again the critical potential is the same for all orientations at a given

temperature, but shifts in the active direction as the temperature of the

5N H_2SO_4 environment is increased.

METALLOGRAPHY

Specimen surfaces which had been used in the anodic polarization

experiments were examined in the scanning electron microscope to elucidate

the morphology of corrosive attack on the various specimen orientations.

Figure 7 shows the effect of the anodic polarization runs on the

surfaces of basal (A,C,E, and G) versus prism (B,D,F, and H) oriented Ti-4Al

specimens (specimens used to obtain the 50°C data shown in Figure 2).

A-D are light micrographs while E-H are scanning electron micrographs. A

and B show typical areas of basal, (0001), and prism oriented specimens,

respectively; while C and D are a greater magnification of the areas circled

in A and B. What is shown in this series of photos is that the contrast,

light versus dark grains, in A and B is attributable to the surface roughness

of the grains and not to faceting. Note the relationship between the grain

surface roughness shown in C and D and the contrast between these same

grains as seen in A and B. The lighter a grain appears in A or B the

smoother its surface appears under higher magnification in C or D; and the darker it appears, the rougher its surface. The morphology of the grain surface roughnesses evident in the higher light magnification photos C and D are more clearly illustrated in the scanning electron micrographs E-H. E and G are typical areas of the surface of a basal oriented specimen while F and H are typical of a prism oriented surface. Note the three fold symmetry of the surface features found on grains marked a and b in photo E and c in photo G. This form of attack has been observed by other authors[3,4] and indicates that these grains probably have near basal orientations. These grains show a reduced severity of attack (i.e. material loss) when compared with the grains shown in photos F and H. This difference in reactivity accounts for the difference in the magnitude of the dissolution currents observed for these two surfaces in the anodic polarization experiments.

The surface features found upon examination of the Ti-4Al-4V alloy specimens exposed to the same conditions were quite different as illustrated in Figure 8. This alloy had an elongated α,β microstructure. Scanning electron micrographs A, B, and C show representative areas of, (0001), $(11\bar{2}0)$, and $(10\bar{1}0)$ preferentially oriented specimen surfaces. As can be seen in these photos, the loss of material was least from the (0001) surface and greatest from the $(10\bar{1}0)$ surface. These observations are in agreement with the relative magnitude of the dissolution currents in Figure 6. There appears to be three types of material present in these photos. The areas marked (a) appear as flat unaffected plateau regions and probably represent the original surface of the sample (note the presence of polishing marks here). Since the area of this material decreases as we progress from (0001) to $(11\bar{2}0)$ to $(10\bar{1}0)$ it is assumed to be basal oriented α.

The areas marked (b) appear as depressed areas where dissolution has taken place. As the area of this type of material increases from (0001) to $(11\bar{2}0)$ to $(10\bar{1}0)$ it is assumed to be prism oriented α. The island material marked (c) consists of the ~10% β found in this alloy.

SUMMARY AND CONCLUSIONS

1. The basal (0001) oriented specimens of both alloys exhibited lower critical current densities for passivity than the prism oriented specimens.

2. Microscopic examination of the specimen surfaces revealed preferrential corrosive attack depending on grain orientation. Basal oriented specimen surfaces were corroded less than prism oriented surfaces of the same alloy under identical exposure conditions. Thus, microscopic observations support the anodic polarization data.

These results indicate that controlled basal (0001) texture in polycrystalline α titanium alloys can be utilized to provide improved corrosion resistance under active anodic dissolution conditions. Figure 9 illustrates how textured titanium can be used to produce more corrosion resistant tubing and pressure vessels (i.e. by orienting the basal surface of the textured material toward the environment). This configuration will also provide increased biaxial strength or "burst strength".

REFERENCES

1. Lockheed Missiles and Space Company, Palo Alto, CA, AF Contract No. FO4611-67-C007Y, February 1969.

2. J.A.S. Green, Corrosion, Vol. 30, p. 175 (1974).

3. A.C. Fraker, A.W. Ruff, J.A.S. Green, and C.J. Bechtoldt, Corrosion, Vol. 30, p. 203 (1974).

4. A.W. Ruff and A.C. Fracker, Corrosion, Vol. 30, p. 259 (1974).

5. S.L. Lopata and E.B. Kula, Transaction AIME, J. of Metals, Vol 224, p. 865 (1962).

6. A.G. Martin and F.R. Larson, Army Materials and Mechanics Research Center, AMMRC TR-71-33, (1971).

7. N.D. Greene, Corrosion, Vol. 15, p. 369t (1959).

TABLE I

COMPOSITION FOR Ti-4Al and Ti-4Al-4V
ALLOYS (in weight percent)

	C	O	V	Al	H	N
Ti-4Al	0.01	0.07	-	4.1	0.004	0.008
Ti-4Al-4V	0.012	0.15	4.12	4.15	0.009	0.019

Table II
MECHANICAL PROPERTIES OF TEXTURED Ti-4Al-4V PLATE

Orien-tation	Thick (in.)	Yield Strength (psi)		Tensile Strength (psi)	Elon. (%)	E x 10⁶ (psi)
		0.1%	0.2%			
L	0.359	100,600	101,200	109,500	21.0	16.3
T	0.358	119,300	119,300	120,400	18.5	18.6
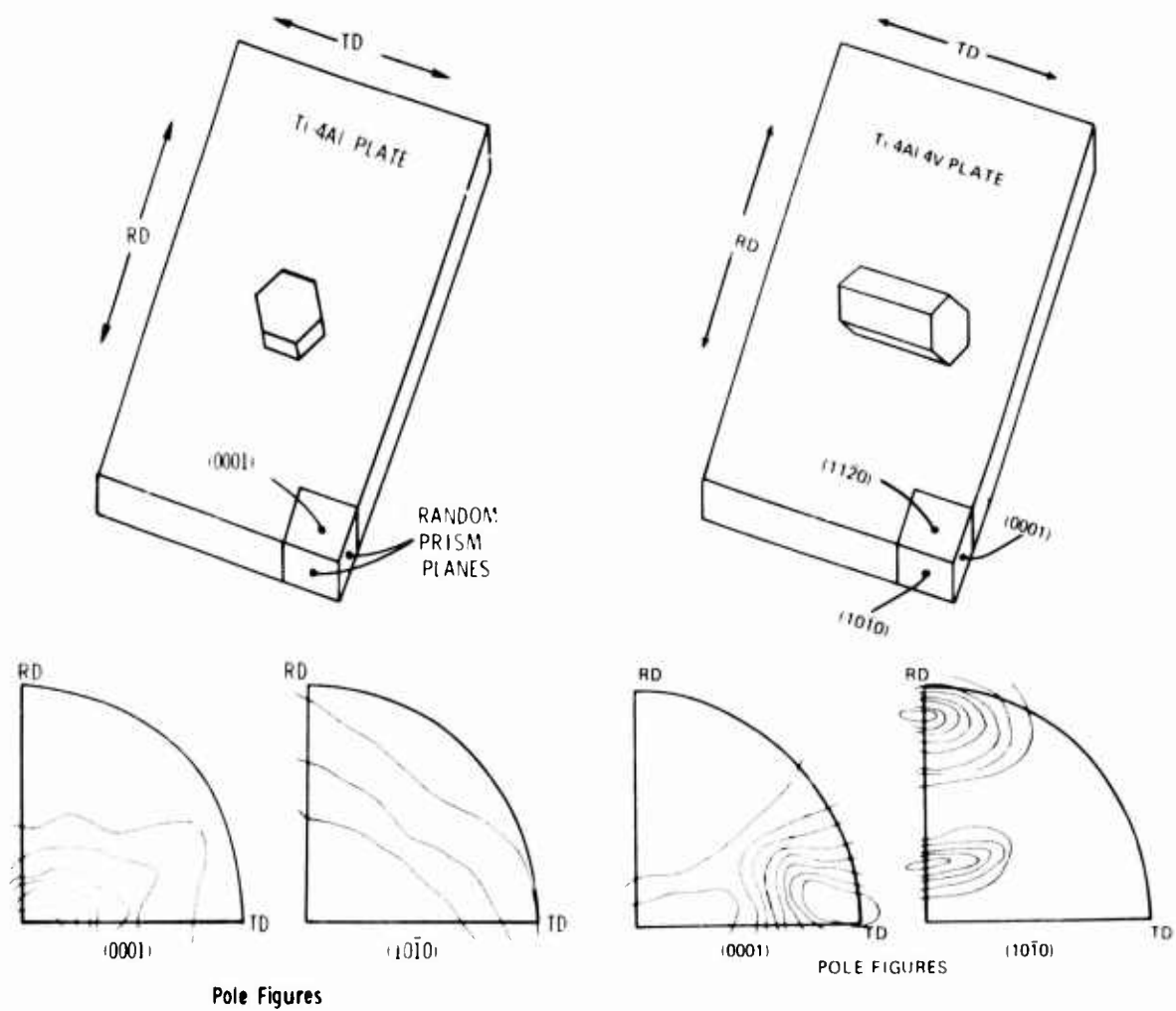
Figure 1. Texture in the Alloys Tested
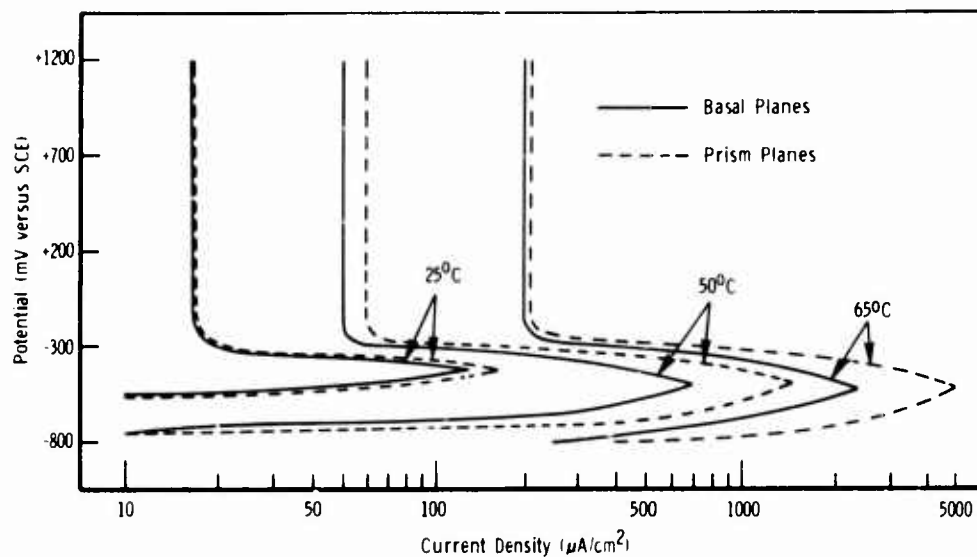
Figure 2. Polarization Curves for Ti-4Al in 5N H_2SO_4
at 25, 50, and 65 C
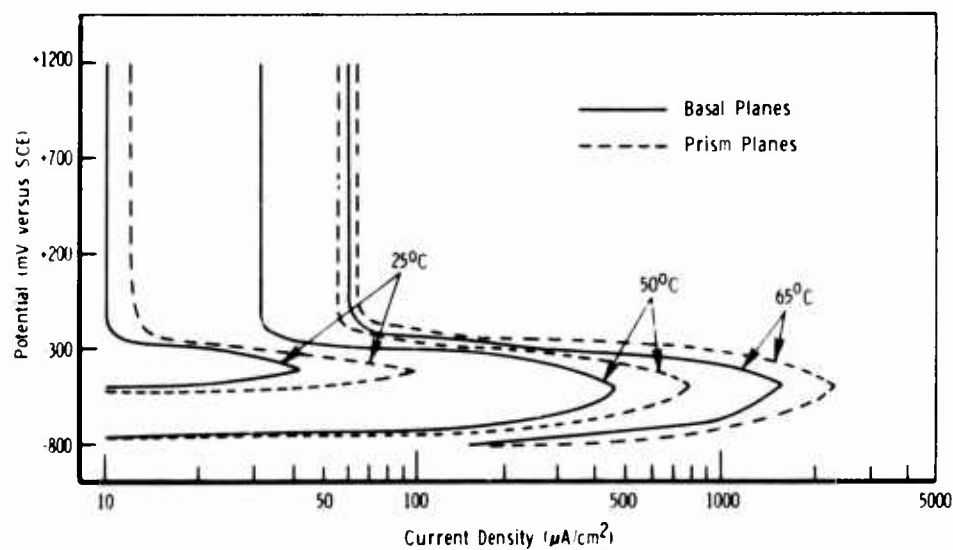
Figure 3. Polarization Curves for Ti-4Al in 5N HCl
at 25, 50, and 65 C

247
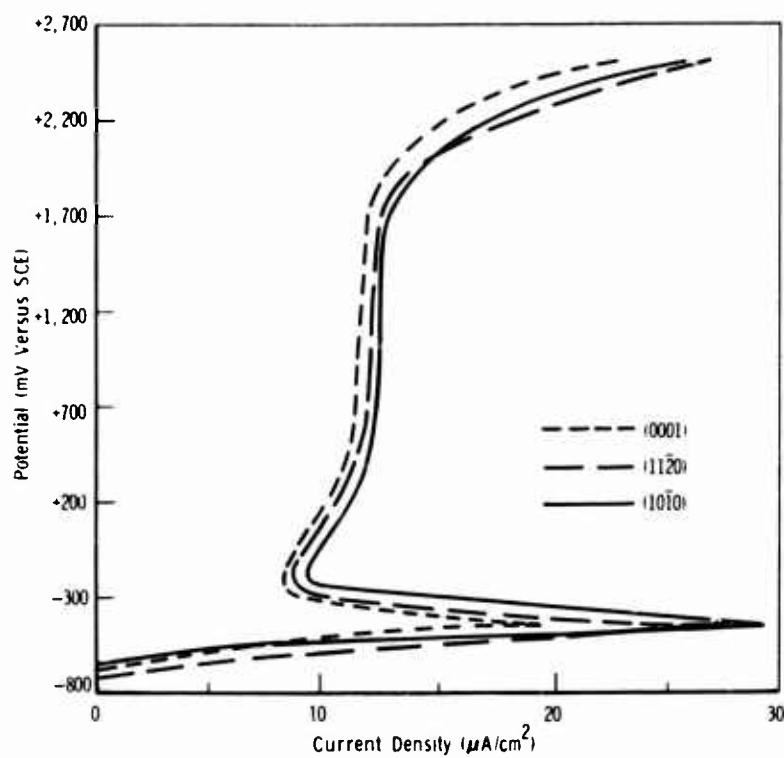
Figure 4.   Polarization Curves for Ti-4Al-4V in 1.5N H_2SO_4 at 22 C
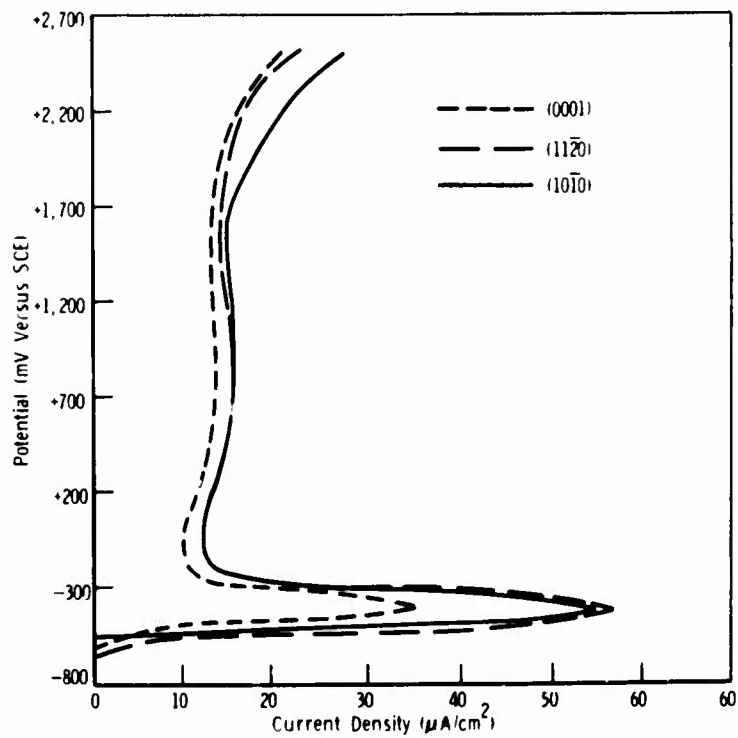
Figure 5.   Polarization Curves for Ti-4Al-4V in 5N H_2SO_4 at 22 C
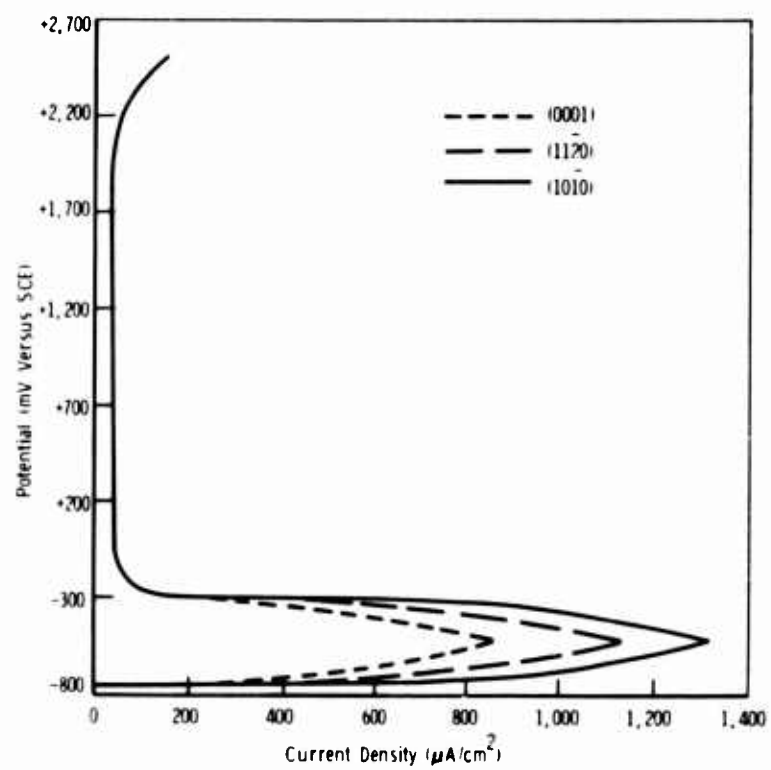
Figure 6. Polarization Curves for Ti-4Al-4V in 5N H_2SO_4 at 50 C
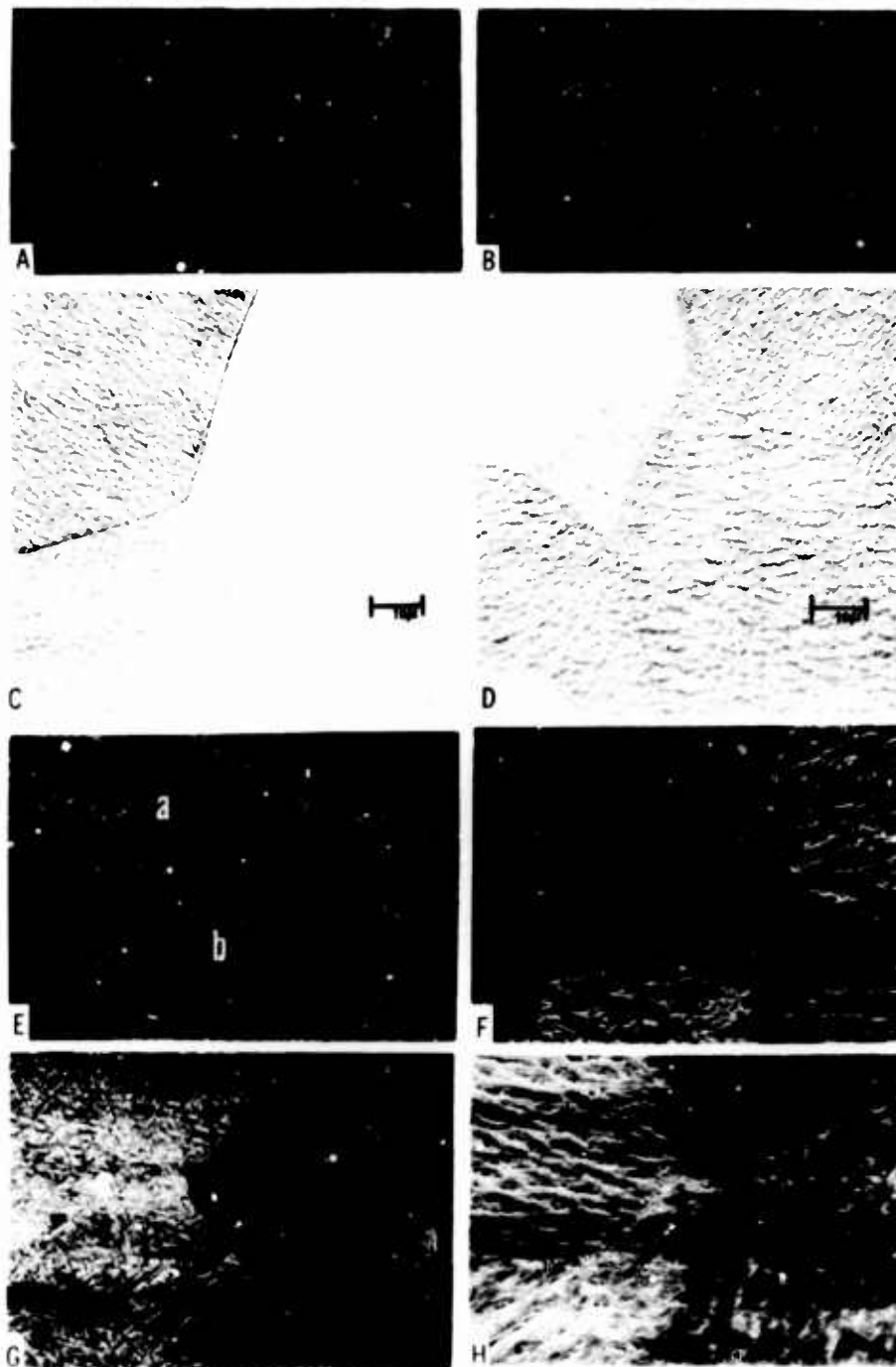
Figure 7. Effect of Anodic Polarization on Ti-4Al Specimen Surfaces
in 5N H_2SO_4 at 50 C

Figure 8. Effect of Anodic Polarization on Ti-4Al-4V Specimen Surfaces
in 5N H_2SO_4 at 50 C
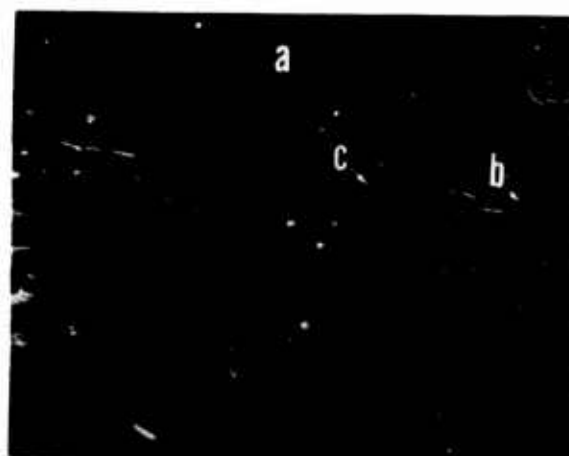
A
(0001) Oriented Surface

B
(11$\bar{2}$0) Oriented Surface

C
(10$\bar{1}$0) Oriented Surface

251
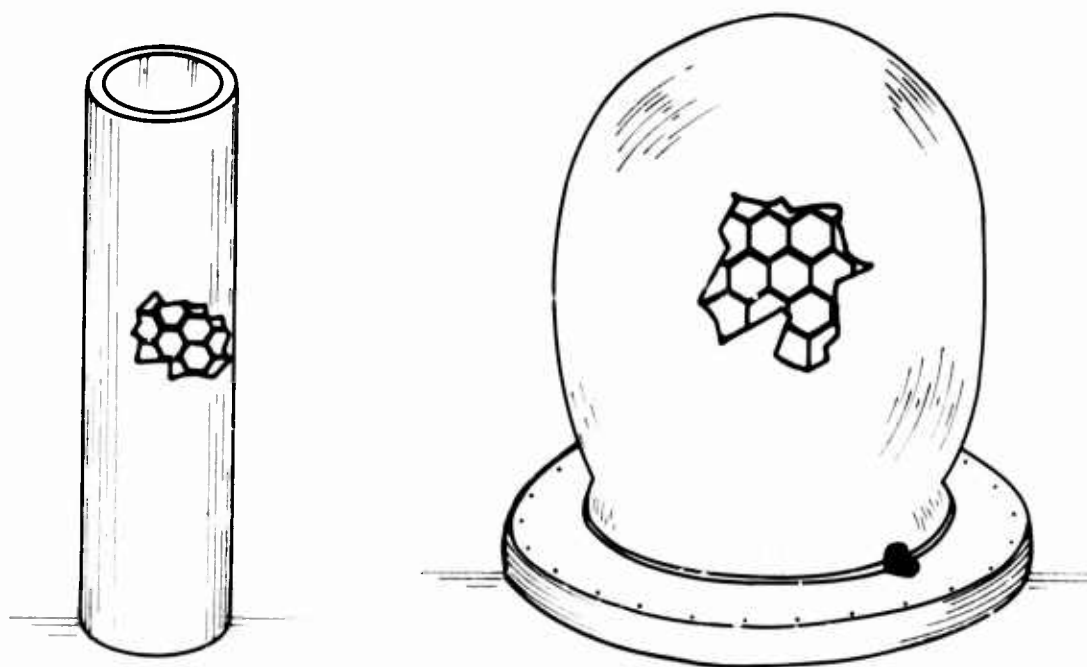
Figure 9. Examples of Textured Titanium Utilization

THE ADHESION OF Al_2O_3 SCALES ON ALLOYS

by

C. S. Giggins, E. J. Felten and F. S. Pettit
Materials Engineering and Research Laboratory
Pratt & Whitney Aircraft
Middletown, Connecticut 06457

Abstract

A number of mechanisms have been proposed to explain the effects of oxygen-active elements or oxide dispersions on oxide adhesion. These include: the vacancy sink mechanism, the enhanced oxide plasticity mechanism, the graded seal mechanism, the chemical bonding mechanism, and the mechanical pegging mechanism. Evaluation of some of these mechanisms became possible during an investigation of the morphological features of the oxide and substrate from which the oxide had spalled on a number of alloy systems. Alloy systems evaluated included NiCrAl(Y), CoCrAl(Y), FeCrAl and Pt-6.6Al. The enhanced adherence of oxides on the yttrium-modified NiCrAl and CoCrAl alloys was found to be due to the presence of an irregular oxide-alloy interface resulting from the formation of yttrium-rich macro and micro oxide pegs protruding into the metal at this interface. Similarly, platinum-rich metallic protrusions into the oxide formed on a Pt-6.6Al alloy also produce an irregular oxide-alloy interface and result in excellent oxide adhesion.

Introduction

The adhesion of Al_2O_3 scales to alloy substrates under the influence of thermally-induced stresses is of extreme importance since the most oxidation resistant coatings for nickel- and cobalt-base superalloys are designed to form Al_2O_3 on exposure to corrosive environments at elevated temperatures.[1] Spalling of the Al_2O_3 scale results in a loss of alloy protection and requires reformation of the protective alumina scale. Repeated spallation, as frequently occurs in practice, causes severe depletion of aluminum in the alloy or coating, eventually resulting in the formation of less protective scales.

It has been found that small additions of oxygen active elements, such as yttrium,[2-4] as well as oxide dispersions[5-7] can be used to improve the adherence of oxide scales to alloy substrates. More recently it has been observed that the addition of platinum to coatings or alloys is also effective in promoting oxide adherence.[8]

A number of mechanisms have been tentatively proposed to account for the improvement of oxide adhesion, namely:

The Vacancy Sink Mechanism is based on the assumption that the presence of voids at the oxide/substrate interface results in poor external oxide scale adhesion. Oxide particles or oxygen active elements in the alloy are proposed to act as sinks which annihilate the vacancies generated during the oxidation process, thus preventing the formation of voids at the oxide/substrate interface.

The Enhanced Oxide Plasticity Mechanism is based on the assumption that elements such as yttrium may improve the adhesion of Al_2O_3 by causing the Al_2O_3 to be more easily deformed and thereby allowing the relief of growth and thermally-induced stresses which would otherwise cause spalling of the oxide scale.[10]

The Graded Seal Mechanism is based on the assumption that a layer of oxide is developed between the oxide scale and the alloy which possesses a thermal expansion coefficient that gradually changes from values similar to those of the alloy to values close to those of the oxide scale as one proceeds through this layer from the alloy to the external scale.[11]

The Chemical Bonding Mechanism proposes that the adhesion of Al_2O_3 scales is dependent upon the nature of the atomic bonds which are developed across the oxide/substrate interface. Yttrium dissolved in the alloy and oxide may alter the nature of the chemical bonds developed at the oxide/alloy interface.[12]

The Mechanical Pegging Mechanism proposes that oxide pegs are developed at the oxide/alloy interface which mechanically key the oxide scale to the alloy.[3,4,13]

The purpose of this paper is to present the results of recent experiments involving alloys which form external Al_2O_3 scales during high temperature exposure. On some of these alloys the Al_2O_3 scale was adherent, while on others it was non-adherent. The morphological features of the oxides and the metal substrates from which they spalled were examined in light of the oxide adherence mechanisms described above. New evidence in support of the pegging mechanism is presented.

Experimental

Alloys used in this program were Ni-15Cr-6Al,* Fe-25Cr-4Al and Co-25Cr-6Al, with and without 0.1 or 0.5% yttrium. These alloys were studied in three fabrication conditions, namely: as-cast, hot worked and annealed and vapor-deposited. Also evaluated was a cast and annealed Pt-6.6Al alloy. Specimens of the NiCrAl, FeCrAl and CoCrAl alloys were isothermally oxidized between $1000°$ and $1200°C$ in 1 atm of dry air, the Pt-6.6Al alloy to $1400°C$. The oxide scales and alloy surfaces were examined using scanning electron microscopy. Standard metallographic techniques were also used to examine the oxidized specimens. Adherent oxides were separated from their respective alloys by dissolving the alloy in either 10% bromine-methanol or for the Pt-6.6Al alloy, warm aqua regia.

Results and Discussion

The results presented here were selected from a more comprehensive study concerned with the morphological features of adherent and non-adherent Al_2O_3 scales.[14] The evidence presented, is in support of a particular mechanism (mechanical pegging) but does not completely exclude participation of other mechanisms in contributing to Al_2O_3 scale adherence.

It was observed that the Al_2O_3 scale which formed on the Ni-15Cr-6Al, Co-25Cr-6Al and Fe-25Cr-4Al alloys (i.e. those alloys which do not contain yttrium) during oxidation tends to spall during cooling.[14] Typical features observed on the metal surfaces of NiCrAl and CoCrAl alloys from which the oxide had spalled are shown in Figure 1. It can be seen that there are two types of structural features on the metal surface. There are areas where the imprints of oxide grains are observed, but there are also numerous areas which

---

*All compositions are given in weight percent.

256

are smooth and contain no such imprints. It is believed that at these smooth areas the oxide became detached from the alloy substrate at temperature, during oxidation since they contain numerous thermal facets, Figure 1b.

As pointed out in a previous study[15] concerned with the spalling of Al_2O_3 from an Fe-25Cr-4Al alloy, void formation is frequently associated with oxide scale spalling. It can be shown, however, that void formation is not absolutely necessary for oxide scale spalling to occur. To illustrate this point, an electropolished specimen of Fe-25Cr-4Al was oxidized for 24 hours at $1200^{\circ}C$ in 1 atm of air. The external Al_2O_3 scale spalled from this specimen, but no smooth areas were observed on the substrate surface, Figure 2. Rather, the substrate was totally covered with imprints of oxide grains, Figures 2b and 2c. The oxide surface at the substrate interface contained only a few isolated voids. The structures observed in Figure 2 are not consistent with the vacancy sink mechanism since this mechanism presumes that void formation is a precursor to spalling of the oxide.

It has been proposed that elements such as yttrium may improve the adhesion of Al_2O_3 on alloys by causing the Al_2O_3 to be more easily deformed and thereby allowing the relief of growth and thermally-induced stresses which would have otherwise caused spalling of the scale. In the present studies more apparent deformation of the Al_2O_3 has been observed on the alloys which did not contain yttrium than on those containing yttrium, Figure 3. Oxides formed on alloys not containing yttrium were often highly wrinkled, Figure 3a, while those formed under the same conditions on alloys containing yttrium were flat, Figure 3b. The wrinkles in the former alloys frequently occurred at sites where the oxide had become detached at temperature, Figure 1a. It is therefore proposed that the presence of yttrium in the oxide does not result in increased oxide plasticity.

257

The graded seal mechanism is based on the supposition that a layer of oxide other than Al_2O_3 is developed between the external oxide scale and the alloy. In this study no such continuous layer was observed. However, the zone of alloy beneath the Al_2O_3 scale may become deformed to accommodate growth stresses generated as a result of the formation of oxide protrusions and particles of yttrium oxide within this region.

It is possible that alloying elements may promote oxide adherence through chemical effects, i.e. by developing stronger atomic bonds across the oxide-substrate interface. It has been proposed[12] that impurities which have a greater affinity for oxygen than other elements in the alloy can play a dominant role by developing stronger atomic bonds across the oxide-substrate interface. In the alloys used in this investigation, the standard free energy of formation of Y_2O_3 is more negative than those of NiO, FeO, CoO, Cr_2O_3 and Al_2O_3. Consequently it is possible that in addition to providing vacancy sinks via the formation of internal oxide particles or the formation of large atom-vacancy complexes, yttrium as well as other oxygen active elements may also promote oxide adherence by developing stronger bonds across the oxide-substrate interface. It is difficult to prove or disprove this proposition. It is worth noting, however, that Al_2O_3 particles in a FeCrAl alloy have been observed to significantly improve the adhesion of Al_2O_3.[15] Such results indicate improved adhesion can be achieved without any chemical bonding effects.

In the mechanical pegging mechanism it is proposed that oxide pegs are developed at the Al_2O_3-alloy interface which mechanically key the Al_2O_3 to the alloy and adherence of the Al_2O_3 to the alloy is therefore improved. In the present study, pegs extending into alloys containing yttrium were observed,

Figure 4. Since the Al_2O_3 scales which formed on the NiCrAlY and CoCrAlY alloys were usually adherent, the surfaces of these scales at the substrate interface were examined by dissolving the alloys in a 10 percent bromine-methanol solution. The extracted oxide flakes were separated from the solution by filtering and subsequently were washed in pure methanol. Typical features of the Al_2O_3 at the substrate interface are presented in Figure 4. The oxide contained a network of oxide protrusions, Figure 4a, which extended into grain boundaries of the alloy, Figure 4b. Electron-beam microprobe analyses showed that these protrusions contained predominantly yttrium. These yttrium-rich protrusions will be referred to as macro pegs.

The surfaces of extracted Al_2O_3 flakes at the substrate interface always exhibited the coarse network of oxide protrusions, Figure 4a. On numerous flakes much smaller oxide protrusions were also evident, Figure 4c. The density of these smaller protrusions was observed to vary from flake to flake. An attempt was made to determine the composition of these particles by using an energy dispersive technique. Yttrium was detected in the large particles, but was not detected in the smaller particles. However, it is believed that these particles may have been too small to generate detectable intensities. Nonetheless, these smaller particles are also believed to be yttrium-rich. These small oxide protrusions are considered to be micro pegs. It is believed that the combined effects of macro and micro pegs on the alloys containing yttrium contributes in a significant way to oxide adherence by producing an irregular interface between the oxide and alloy.

In common with the alloys containing yttrium, the Al_2O_3 scale formed on the Pt-6.6Al alloy at temperatures up to 1400°C was very adherent. The substrate interfaces of oxide flakes obtained from this alloy were compared

to those described above. The surfaces of the oxide flakes obtained from a specimen oxidized at 1200°C contained a small number of depressions or voids in addition to a continuous network of oxide crystals, Figure 5a. Also observed in the microstructures of these specimens were numerous pegs at the oxide-alloy substrate, Figure 5b. The pegs at this interface in the case of the Pt-6.6Al alloy were metallic as opposed to the oxide pegs in the NiCrAlY and CoCrAlY specimens. The specimen shown in Figure 5b had been oxidized for 7.5 hours at 1350°C and was metallographically polished, then etched in hot phosphoric oxide.

The number of these metallic pegs increases with time and temperature, Figure 6, as illustrated for a specimen oxidized for 2 hours at 1400°C. Where a slight amount of spalling had occurred, Figure 6a, due to fracturing the specimen after oxidation, the density of the metallic pegs which had protruded into the oxide scale is clearly evident. The substrate interface of the oxide scale was examined after dissolution of the alloy substrate in warm aqua regia. It can be seen, Figure 6b, that there are voids in the oxide scale and the relative densities of the metal protrusions and voids in the oxide, Figures 6a and 6b, are the same, and coincident with one another. It is believed that these metallic pegs contribute in an important way to the excellent adherence of Al_2O_3 on the Pt-6.6Al alloy, by forming an irregular interface between the oxide and the alloy substrate.

Summary and Conclusions

At this time it is believed that the oxide pegging mechanism best explains the improved oxide adhesion attributed to oxygen active elements, oxide particles and platinum in alloys which contain one or more of these additives. While other mechanisms may contribute synergistically to oxide adherence, less evidence in support of these mechanisms has been obtained to date. Therefore,

260

while the exact mechanism(s) for oxide adherence remain uncertain, it is believed that where improved adhesion is obtained, an important characteristic is the development of an irregular interface between the oxide and the alloy. Macro and micro oxide pegs in NiCrAlY and CoCrAlY alloys and metallic pegs in Pt-6.6Al produce such an irregular interface.

Acknowledgment

References

1. G. W. Goward, "Current Research on the Surface Protection of Superalloys for Gas Turbine Engines", Journal of Metals, Vol. 22, No. 10, October 1970, pp. 31-39

2. W. Hessenbruck, "Metallen und Legierungen fur Hohe Temperaturen", Teil I, J. Springer Publishing Co., Berlin (1940).

3. E. J. Felten, "High Temperature Oxidation of Fe-Cr Base Alloys with Particular Reference to Fe-Cr-Y Alloys", J. Electrochem. Soc., Vol. 108, 1961, pp. 490-495.

4. C. S. Wukusick and J. F. Collins, "An Iron-Chromium-Aluminum Alloy Containing Yttrium", Mat. Res. and Standards, Vol. 4, 1964, pp. 637-646.

5. A. V. Seybolt, "High Temperature Oxidation of Chromium Containing Y_2O_3", Corrosion Science, Vol. 6, 1966, pp. 263-269.

6. J. Stringer, B. A. Wilcox, and R. I. Jaffee, "The High Temperature Oxidation of Nickel-20 wt. % Chromium Alloys Containing Dispersed Oxide Phases", Oxidation of Metals, Vol. 5, No. 1, 1972, pp. 11-47.

7. M. S. Seltzer, J. Stringer, B. A. Wilcox, and R. I. Jaffee, Final Report NASA, NAS3-14326 (November 1971).

8. G. Lehnert and H. W. Meinhardt, "A New Protective Coating for Nickel Alloys", Electrodeposition and Surface Treatment, Vol. 1, 1972/73, pp. 189-197.

9. J. Stringer, "The Effect of Alloying on Oxidation: Quantitative Treatments", Met. Rev., Vol. 11, 1966, pp. 113-128.

10. J. M. Francis and J. A. Jutson, "High Temperature Oxidation of an Iron-Chromium-Aluminum-Yttrium Alloy in Carbon Dioxide", Corrosion Science, Vol. 8, 1968, pp. 445-449.

11. H. Pfeiffer, "Influence of Trace Elements on Anti-Scaling Properties of Heat Resistant Alloys", Werkst. Korros., Vol. 8, 1957, pp. 574-579.

12. J. E. McDonald and J. G. Eberhart, "Adhesion in Aluminum Oxide-Metal Systems", Trans. TMS-AIME, Vol. 233, 1965, pp. 512-517.

13. B. Lustman, "The Intermittant Oxidation of Some Nickel-Chromium Base Alloys", Trans. TMS-AIME, Vol. 188, 1957, pp. 995-996.

14. C. S. Giggins and F. S. Pettit, "Oxide Scale Adherence Mechanisms, Second Annual Report", for the Aerospace Research Laboratories, WPAFB, Ohio (Contract No. F33615-72-C-1702) July 1974.

15. J. K. Tien and F. S. Pettit, "Mechanism of Oxide Adherence on Fe-25Cr-4Al (Y or Sc) Alloys", Metallurgical Transactions, Vol. 3, 1972, pp. 1587-1599.

Figure 1 - Typical morphological features on the metal
surfaces of CoCrAl (a) and NiCrAl (b) alloys after 100
hours at 1100°C in 1 atm. of dry air. Wrinkles in the
Al_2O_3 coincided with smooth areas in the alloy surface
and voids (arrows) were occasionally observed in the
smooth areas (a). Smooth areas on the alloy surfaces
contained thermal facets (black arrows) whereas rough
areas contained imprints of oxide grains (b).

263
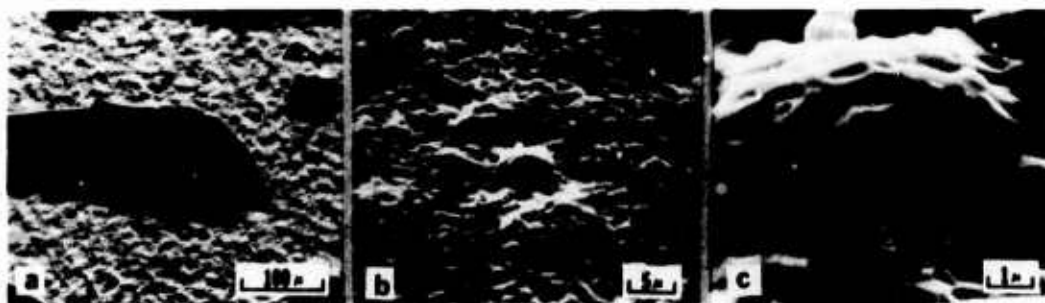
Figure 2 - Oxide scale and alloy surface morphologies of
electropolished Fe-25Cr-4Al after isothermal oxidation
at 1200°C for 24 hrs in air. (a) General structure of
oxide flakes and bare alloy surface. (b) and (c) Low and
high magnification of alloy surface specifically showing
that the mounds of alloy were not smooth but faceted
by imprints of the oxide grains.

264

Figure 3 - Typical morphological features developed at
the Al_2O_3-gas interface of Al_2O_3 scales after 100 hours
at 1200° C in 1 atm. of dry air.   The oxide scale is
highly wrinkled on NiCrAl and CoCrAl alloys (a) but smooth
on NiCrAl and CoCrAlY alloys (b).

Figure 4 - Macro and micro oxide protrusions which were
formed on CoCrAlY alloys during oxidation. (a) Oxide
scale morphology at alloy-oxide interface illustrating
concentrations of yttrium-rich macro-pegs (arrows).
(b) Metallographic section shows that the macro-pegs
are found in the alloy grain boundaries. (c) Physical
evidence for the presence of micro-pegs at the alloy-
oxide interface.

Figure 5 - Morphological features typical of the Al_2O_3 scales formed on Pt-6.6Al. (a) Oxide flake at gas interface contains a small number of depressions or voids. (b) Voids are sites where metallic pegs protruded.
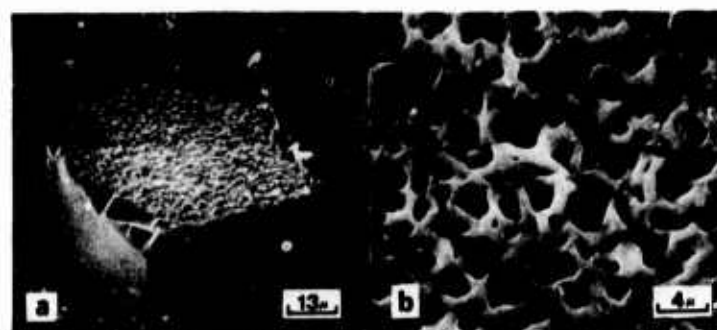
Figure 6 - Morphological features of the metal surface
of Pt-6.6Al (a) and the detached Al_2O_3 scale at the
metal-oxide interface (b) after 2 hours at $1400°C$ in
1 atm. of dry air.   It is apparent that a highly
irregular metal-oxide interface has developed.

COMPARISON OF THE HOT CORROSION DEGRADATION OF NICKEL
AND COBALT-BASE ALLOYS

by

J. A. Goebel, E. J. Felten and F. S. Pettit
Pratt & Whitney Aircraft
Middletown, Connecticut   06457

Abstract

The mechanisms for Na_2SO_4-induced hot corrosion of nickel and cobalt and

alloys of these metals containing chromium and/or aluminum are compared in

order to determine if there are any fundamental reasons for the apparent superior

hot corrosion resistance of cobalt-base alloys compared to nickel-base alloys.

It is shown that cobalt-base alloys are much more resistant to the initiation of

hot corrosion than nickel-base alloys when these alloys contain both chromium

and aluminum but that for the both types of alloys the hot corrosion degradation

mechanisms are virtually the same.

Introduction

Alloy components in the turbine sections of both marine and aircraft gas
turbine engines are often subjected to unusually severe corrosion. This type
of attack, usually referred to as hot corrosion, has been found to be caused
by molten salt or ash deposits. Both nickel and cobalt-base alloys are subject
to hot corrosion attack. However, from experiments using burner rigs it appears
as though at temperatures on the order of 900° C that the commercial cobalt-base
alloys are more resistant to hot corrosion than the commercial nickel-base
alloys.[1] The reasons for this difference in performance have been the subject
of considerable speculation.

Seybolt and Beltram[2] observed that the basic mechanism of hot corrosion
was essentially the same for nickel, cobalt and binary alloys of these elements.
Deleterious reactions occurred at a lower temperature for nickel-base systems
than for the cobalt-base systems. Wheatfall[3] has summarized the considerable
amount of laboratory and rig testing of nickel and cobalt binary and ternary
alloys as well as that of some more complex superalloys. Again, the commercial
cobalt-base superalloys were found to be more corrosion resistant than alloys
based on nickel. However, burner rig tests on unalloyed nickel and cobalt
revealed that these materials had similar corrosion resistances at 1675° and
1750° F (913° and 954° C). The Ni-25Cr and Co-25Cr binary alloys also had comparable
corrosion rates at all temperature levels. The purpose of this paper is to
examine the hot corrosion degradation mechanisms of nickel, cobalt and alloys

of these metals in order to determine if there are any fundamental reasons
for the apparent differences in the resistances of these materials.

Experimental

Binary alloys of Ni-25Al,* and Co-25Al were prepared by casting and
annealing. Alloys of Ni-30Cr and Co-35Cr were cast, hot worked and annealed.
The aluminum and chromium concentrations of these alloys were sufficient to
allow during oxidation the development of continuous, external scales of Al_2O_3
and Cr_2O_3, respectively. Alloys of Ni-25Cr-6Al (NiCrAl) and Co-25Cr-6Al (CoCrAl)
were prepared by vapor deposition. (The vapor deposition fabrication procedure
was used to examine the influence of microstructure on the initiation of hot
corrosion and results obtained for this part of the investigation will be reported
elsewhere.) External scales of Al_2O_3 were formed on both of these alloys during
oxidation.

The hot corrosion testing consisted of either isothermal or cyclic oxidation
at 1000°C in oxygen or air using deposits of Na_2SO_4. Sodium sulfate was used
to initiate the hot corrosion since it is well established that deposition of
principally Na_2SO_4 is a precursor to the initiation of hot corrosion in gas
turbines. Specimens of the alloys were polished through 600 grit SiC paper
and degreased prior to testing. The specimens were then coated with Na_2SO_4
and isothermally or cyclically oxidized. In the cyclic test, the specimens
were cycled to room temperature once every hour (50 minutes hot, 10 minutes
cold) and removed from the test once every 20 hrs. Every 20 hrs the specimens
were washed, weighed and visually examined before a fresh coating of Na_2SO_4
was applied.

---

*All compositions are given in weight percent.

271

Results

1. Hot Corrosion Behavior of Nickel and Cobalt

Oxidation experiments performed with specimens of nickel and cobalt at
$1000^\circ C$ have shown that if Na_2SO_4 is present on the metal surface, accelerated
oxidation occurs during the initial stages of oxidation.[4,5] It has also been
observed that the accelerated rate of oxidation does not persist, and for periods
beyond approximately 15 min. the oxidation rate of Na_2SO_4-coated specimens is
identical to that of uncoated specimens.

Examination of Na_2SO_4-coated specimens after oxidation has revealed two
morphological features which are not found in equivalent uncoated specimens.
It appears that during the period of accelerated oxidation, the oxide scales
formed on Na_2SO_4-coated nickel and cobalt are porous and non-protective. In
addition, it has been determined that during this same period sulfur from the
Na_2SO_4 reacts with the metal to form a liquid sulfide layer separating the
oxide scale from the metal. After longer oxidation times dense, protective
oxide scales are eventually formed beneath the initial porous scales, and the
oxidation rate decreases toward that which is characteristic of nickel and
cobalt in the absence of Na_2SO_4.

Based upon an examination of the thermodynamic properties of molten Na_2SO_4,
it has been possible to propose a mechanism to explain the attack of nickel
and cobalt by molten Na_2SO_4.[6] According to the proposed mechanism, an oxide
film initially forms on the metal beneath the liquid sulfate by consuming oxygen
from the melt. Consequently an oxygen gradient is established across the molten
salt such that the oxygen activity of the scale-salt interface is reduced. The
decreased oxygen activity results in an increased sulfur activity, and sulfur
diffuses through the oxide scale to form sulfides beneath the scale. The loss
of sulfur and oxygen from the Na_2SO_4 results in a sufficiently large increase in

272

the oxide ion activity of the melt that dissolution of the oxide scale by the basic melt can occur. Dissolution (fluxing) of the oxide films is believed to occur at local sites in the oxide scale, such as grain boundaries, to the extent that the liquid penetrates the scale and subsequently spreads laterally, stripping the oxide from the metal. Repetitive stripping of the oxide film by the Na_2SO_4 results in rapid oxidation of the metal.

Based upon the results of these studies it has been concluded that the attack of nickel and cobalt by Na_2SO_4 occurs by essentially the same mechanism.

3. Hot Corrosion of Co-25Al and Ni-25Al

Binary alloys of cobalt and nickel containing 25 weight percent Al derive their high temperature oxidation resistance from protective Al_2O_3 oxide barriers. When specimens of these alloys are coated with Na_2SO_4 and then oxidized, kinetic data which has been obtained indicate that no accelerated oxidation occurs for periods up to 10 hrs. After this initial incubation period, a brief period of very rapid oxidation is observed, after which the oxidation rate decreases, but nevertheless remains greater than would be expected in the absence of Na_2SO_4.

Detailed examination of Co-25Al and Ni-25Al hot corrosion specimens as a function of time has shown that during the initial stages of oxidation, protective films of Al_2O_3 are formed on these alloys beneath the molten Na_2SO_4. The termination of the incubation period and the onset of rapid oxidation has been found to correspond to the rapid destruction of the Al_2O_3 scale, followed by the formation of less protective scales which are rich in nickel or cobalt oxides. A typical microstructure resulting from this type of attack is shown in Figure 1. It is evident that in addition to the formation of a thick, non-protective oxide scale, sulfur from the Na_2SO_4 reacts with these alloys to form aluminum sulfide particles beneath the oxide scale.

273

The mechanism of attack for both of these alloys in the presence of Na_2SO_4 is believed to be similar to that for cobalt and nickel. In particular, it has been proposed that during the incubation period conditions are developed in molten sulfate such that penetration of the Al_2O_3 scales can occur by basic fluxing of the Al_2O_3 in localized areas. Once it is penetrated, rapid stripping of the Al_2O_3 occurs, and large amounts of sulfur react with the alloy to form aluminum sulfides preventing the reformation of a protective Al_2O_3 barrier, and therefore the accelerated oxidation rate persists.

3. Hot Corrosion of Co-35Cr and Ni-30Cr

Weight-change versus time data obtained for the cyclic hot corrosion testing of Co-35Cr and Ni-30Cr alloys are presented in Figure 2. No significant difference between the results obtained with the cobalt or nickel-base alloy is evident. Metallographic examination of the specimens from this test were consistent with such a conclusion. On both alloys continuous layers of Cr_2O_3 were formed above an internal zone of chromium sulfide particles. The results which have been obtained for these two alloys indicate that the hot corrosion resistance and degradation mechanism of Ni-Cr and Co-Cr alloys, with chromium concentrations such that continuous external layers of Cr_2O_3 are developed on the alloys, are not markedly different. In the case of these two alloys, however, it is necessary to emphasize that severe hot corrosion degradation was not observed in either alloy. More severe degradation would be expected to be observed eventually after sufficiently long periods of testing and it is possible that one of the alloys may be more resistant to the initiation of the more severe degradation.

4. Hot Corrosion of CoCrAl and NiCrAl

The weight-change versus time data obtained from the cyclic hot corrosion and cyclic oxidation testing of Ni-25Cr-6Al and Co-25Cr-6Al alloys are presented in Figures 3a and 3b, respectively. Data obtained with alloys having the same

274

compositions but which also contained yttrium are also included. The Al_2O_3 scales were more adherent on the alloys which contained yttrium. Adherent Al_2O_3 scales were evident on the NiCrAlY and CoCrAlY alloys after 350 hours of cyclic oxidation. The Al_2O_3 spalled from the NiCrAl and CoCrAl alloys in the cyclic oxidation test and continuous scales of Cr_2O_3 were eventually developed on these alloys above subscale zones of Al_2O_3 particles. In the cyclic hot corrosion test, the NiCrAl and NiCrAlY alloys were very severely degraded after less than thirty hours, Figure 3a. The severe degradation was caused by the development of sulfide stringers in these alloys, Figure 4a, which were subsequently preferentially oxidized, Figure 4b. It appeared as though the sulfide stringers may have been liquid at temperature, Figure 4c. Severe degradation of the CoCrAl alloy in the cyclic hot corrosion test was observed after about 300 hours, Figure 3a. The microstructural features were the same as those observed with the NiCrAl and NiCrAlY alloys. Severe degradation of the CoCrAlY alloy in the cyclic hot corrosion test was not observed, but degradation similar to that of NiCrAl, NiCrAlY and CoCrAl should occur at some test time beyond 300 hours. The points to be emphasized are that the hot corrosion mechanisms of NiCrAl and CoCrAl alloys are the same but the CoCrAl alloys are much more resistant to the initiation of this type of degradation.

Concluding Remarks

The results obtained in the present studies show that there is no signif-icant difference between the hot corrosion degradation mechanisms for nickel and cobalt or alloys of these metals containing the same amounts of chromium and/or aluminum. It has also been determined that the resistance of such alloys to the initiation of hot corrosion degradation are about the same except for the alloys containing both chromium and aluminum, in which case the cobalt-base alloys are much more resistant. In view of these results, it is proposed that cobalt-base alloys are only more resistant to the initiation of hot corrosion degradation

than nickel-base alloys containing the same types and amounts of alloying elements, when these alloys contain chromium and aluminum. Moreover, in such alloys, the chromium and aluminum concentrations must be sufficient that continuous layers of Al_2O_3 are developed upon the alloys during oxidation in the absence of hot corrosion attack.

Acknowledgements

References

1. C. T. Sims, P. A. Bergman and A. M. Beltran, Naval Engineers Journal, p. 39, April 1970.

2. A. U. Seybolt and A. M. Beltran, "High Temperature Sulfur-Oxygen Corrosion of Nickel and Cobalt" in ASTM Special Technical Publication 421, 1967, p. 21.

3. W. L. Wheatfall, "Are Cobalt-Base Alloys Intrinsically More Resistant to Hot Corrosion than Alloys Based on Nickel?" in Agard Conference Proceedings No. 120, 1973, p. 237.

4. J. A. Goebel and F. S. Pettit, "First Annual Report on the Hot Corrosion of Cobalt-Base Alloy Program", for The Aerospace Research Laboratories, WPAFB; Ohio, (Contract No. F 33615-72-C-1757), June 1973.

5. J. A. Goebel, E. J. Felten and F. S. Pettit, "Hot Corrosion Mechanisms for Nickel and Cobalt Base Alloys" in the Proceedings of the Conference on Gas Turbine Materials in the Marine Environment; Castine, Maine (1974).

6. J. A. Goebel and F. S. Pettit, Met. Trans. 1, 1943, July 1970.
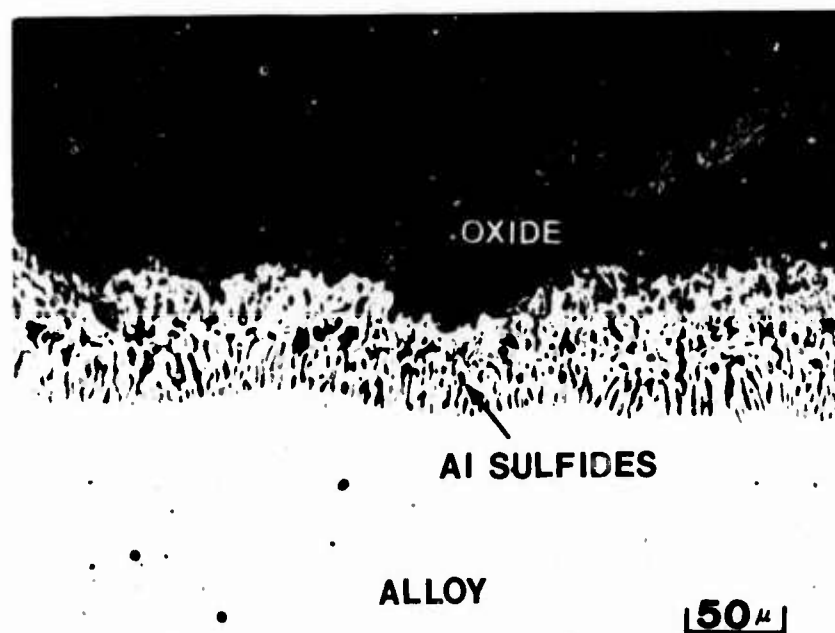
Figure 1. Transverse microstructure of Co-25Al coated with 0.5 mg/cm^2 Na$_2$SO$_4$ and cyclically oxidized at 1000°C in 1.0 atm of oxygen for 80-one hour cycles. Scale contains oxides of cobalt and aluminum, while the subscale consists mainly of aluminum sulfide particles.

278
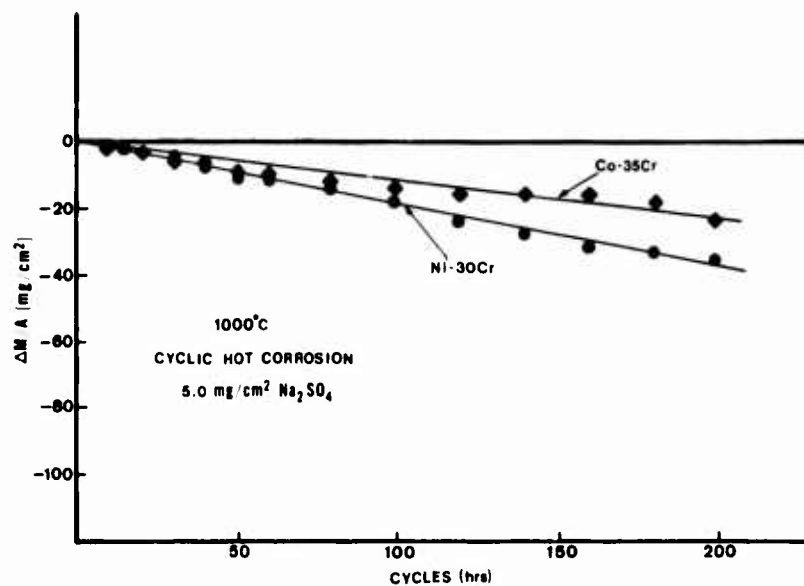
Figure 2. Weight-change versus time curves for the cyclic hot corrosion of Co-35Cr and Ni-30Cr alloy specimens coated with 5 mg/cm² at approximately 20 cycle (hr) intervals. After 200 cycles the difference in total weight change between each alloy is considered insignificant.
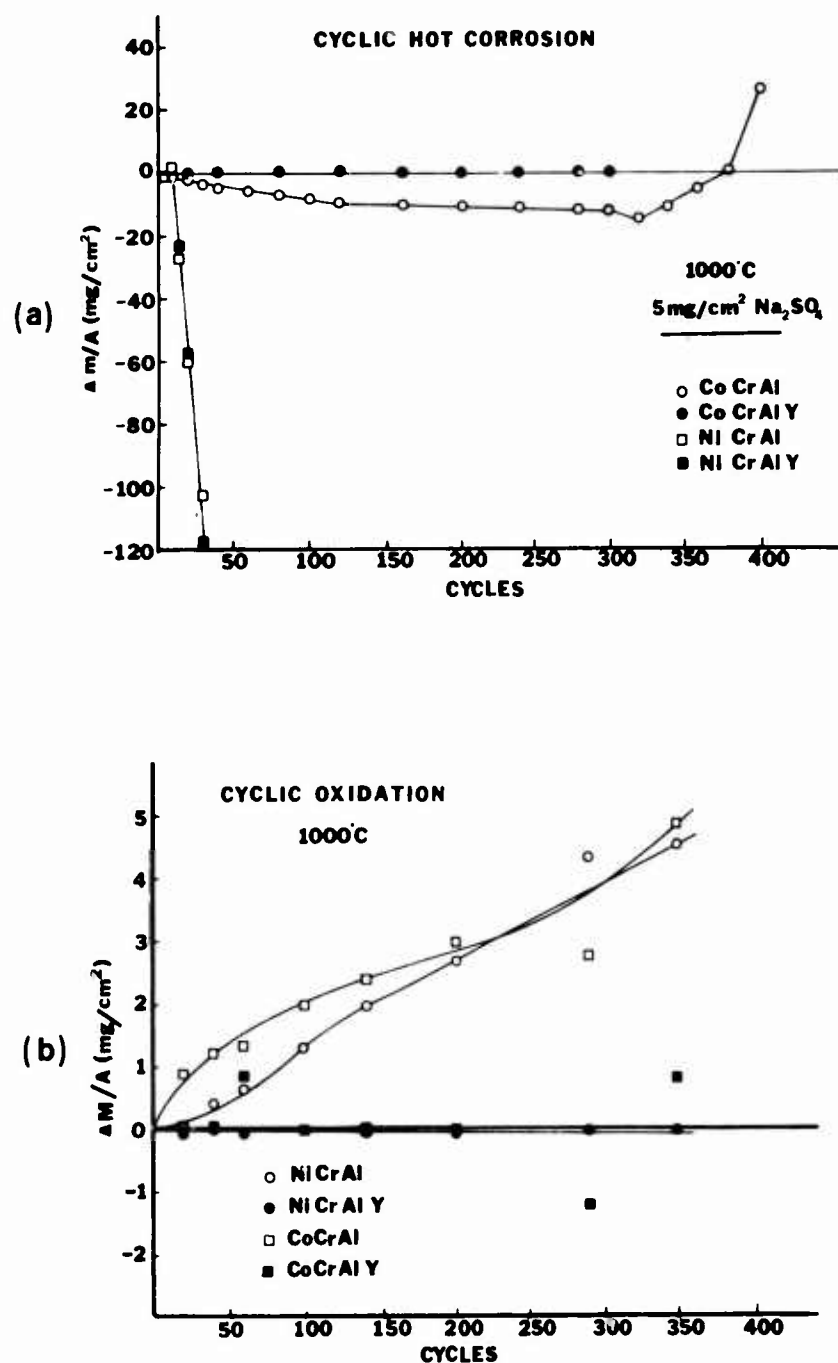
Figure 3. Comparison of the weight-chan e versus time curves obtained
from the cyclic testing of NiCrAl(Y) and CoCrAl(Y) alloys at 1000°C;
(a), cyclic hot corrosion using 5 mg/cm² Na₂SO₄, and (b), cyclic oxidation
without Na₂SO₄. Severe corrosion of the NiCrAl, NiCrAlY and CoCrAl
specimens has occurred in the hot corrosion test, although the scale
on the CoCrAl alloy has only partially spalled.

280
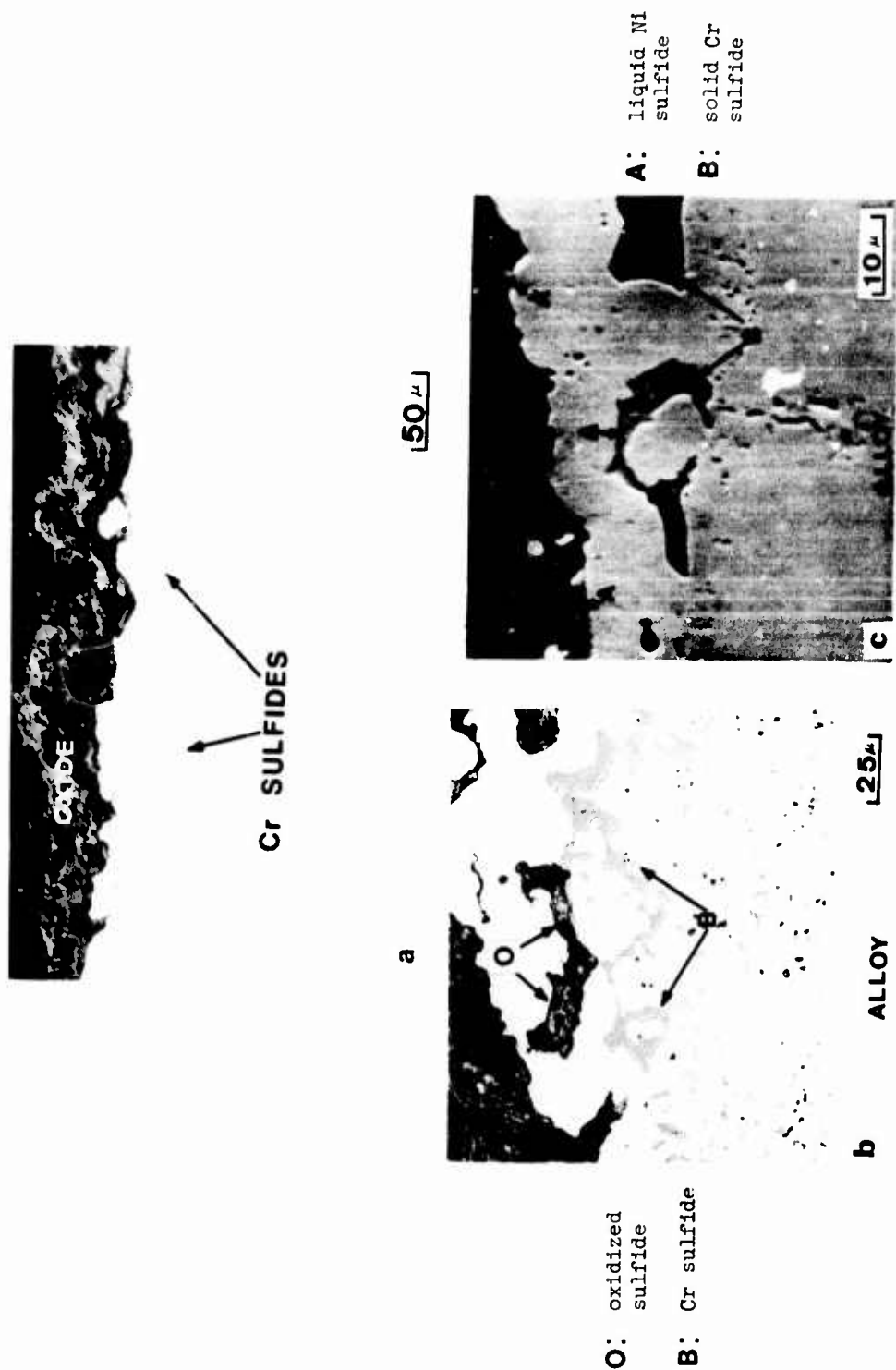
Figure 4. Photomicrographs showing features typical of hot corrosion of NiCrAl and CoCrAl alloys. A thick oxide scale, (a), develops as a result of preferential oxidation of sulfides, (b), which appear to have been liquid, (c).

O: oxidized sulfide

B: Cr sulfide

A: liquid Ni sulfide

B: solid Cr sulfide

CORROSION FATIGUE OF 4340 AND D6AC

STEELS BELOW K_{ISCC}

C. S. Kortovich

TRW INC., CLEVELAND, OHIO 44117

ABSTRACT

The corrosion fatigue behavior of low alloy martensitic AISI 4340 and D6AC steels in distilled water below K_{ISCC} was studied. The results indicated that crack growth rates for both steels obeyed power law relationships which were not invariant with respect to each other or to results obtained in an inert argon environment. As a result, the environmental contribution to fatigue crack growth diminished as cyclic stress intensity factor range increased.

Activation energy for corrosion fatigue crack growth in 4340 (750°F temper) below the threshold stress intensity factor for stress corrosion cracking, K_{ISCC}, compared more favorably with the value for hydrogen adsorption onto a clean iron surface than for hydrogen diffusion through a steel lattice. However, the values obtained in this study indicated that the rate controlling factor was probably not associated with such idealistic processes. The crack growth rates for 4340 (750°F temper) increased with loading time in tension and the trend of the data indicated a possible maximum at lower frequencies than those included in this investigation.

Preceding page blank

INTRODUCTION

The performance of high strength steel components subjected to cyclic loading has been observed to be seriously impaired when exposed to an aqueous environment (1,2). This effect is called corrosion fatigue and can be characterized in terms of two approaches, the numbers of stress or strain cycles to produce failure, N_f, or the rate of fatigue crack growth, da/dn, under given loading conditions. Studies of corrosion fatigue have been reported as early as 1917 (3), and utilized primarily the first of the two approaches. More recently, however, the emphasis has been shifted to considerations of fatigue crack growth. Two factors are responsible for this change (4). First, current structural design procedures utilize fail-safe concepts that assume the presence or early initiation of cracks in the structures, and therefore necessitate considerations of crack growth. Second, because of the inability to clearly separate crack initiation from crack growth, N_f data have failed to provide information that is useful either for quantitative design or for understanding the mechanisms for corrosion fatigue (4).

Corrosion fatigue may be broadly characterized in terms of three general patterns of behavior as illustrated in Figure 1 (5). For this figure, K_{max}, ΔK, K_{Ic} and K_{Iscc} refer to the maximum stress intensity in a given fatigue cycle, the cyclic stress intensity factor range, the plane-strain fracture toughness, the "thin section" fracture toughness and the stress intensity below which failure does not occur under static load as a result of stress corrosion cracking, respectively. The lower portion of the curves correspond to some apparent limiting stress-intensity level for crack growth, $K_{THRESHOLD}$, and appears to be related to the metallurgical structure (6-9) while the upper portion, near K_{Ic} or K_c, corresponds to the onset of unstable crack growth.

The three fatigue behavior patterns may be discussed in terms of K_{Iscc}. At one extreme, Type A behavior represents those steel-environment systems where K_{Iscc} approaches K_{Ic} or K_c, and the environmental effects result from the synergistic actions of fatigue and corrosion (5,10). The environmental effect is characterized by a reduction of "$K_{THRESHOLD}$" for crack growth from a to b and by increased crack growth rates at given K_{max} or ΔK levels compared to that obtained in an inert environment. As K_{max} approaches K_{Ic} or K_c, the environmental influences are diminished as a result of either the rate limiting nature of the hydrogen transport processes or other mechanical-chemical interactions (4).

At the other extreme, Type B fatigue behavior represents those systems with K_{Iscc} substantially less than K_{Ic} or K_c (5,10). The environmental effects in fatigue are quite strong above K_{Iscc} and are negligible below this level. A broad range of steel-environment (and other alloy-environment) systems exhibit Type C behaviors that fall between these two extremes, with Type A behavior at K_{max} levels below K_{Iscc} and Type B behavior above K_{Iscc}. The overall behavior of any particular system depends on the complex interactions between environmental, metallurgical and mechanical loading variables. Crack growth response can thus differ and provide insight into the possible mechanisms for environment-enhanced fatigue crack growth.

The combined role of corrosion and fatigue in nucleating cracks and in producing accelerated growth below K_{Iscc} has only received very limited study, and only a general mechanism to explain the effects is available (12). Barsom has found that cycling below K_{Iscc} in a stress corrosive environment causes crack growth acceleration that is dependent on the loading time in tension; hence, the type of loading wave form and not on the total time at maximum load (12). His results for 12Ni-5Cr-3Mo steel showed that wave forms that have a slow rise time (such as sine waves) produced an appreciable environmental effect, while waveforms with fast rise-times (such as square waves) produced little or no environment enhancement of crack growth, Figure 2A. For this material the environment merely displaced the curve while keeping the same functional dependence on ΔK. Results obtained by Gallagher on HY80 steel (13) and Crooker and Lange on a number of steels (1), however, differ from Barsom's with respect to the constant ratio of corrosion fatigue to air fatigue crack growth rate, Figure 2B (1). Since fatigue crack propagation laws usually involve a power law relationship of ΔK, it is generally believed that this term is the most significant variable governing fatigue crack growth. Since Barsom's data show that the curves for crack growth in an inert and corrosive environment remain parallel, the environment-metal reaction is at least as important to crack growth as ΔK. When the curves converge, however, the effect of environment becomes diminished, and fatigue crack growth becomes a function primarily of ΔK.

Frequency is another important loading variable which can have a significant effect on corrosion fatigue crack growth below K_{Iscc}. Recent experimental results suggest that some synergistic effect of corrosion and fatigue may be present, and that the effect may be influenced by both frequency and by the waveform of the applied load (14,15). Corrosion fatigue crack growth exhibits a maximum at some intermediate frequency depending on the steel-environment system, and approaches the growth rate in an inert environment at high frequencies and, presumably, at very low frequencies (14). The observed frequency dependence suggests a complex interplay involving the rate of production of fresh surfaces by fatigue, the kinetics of absorption, the rate of repassivation, and the rate of transport. Further fundamental studies are needed for a better understanding of frequency and waveform effects.

The purpose of the present study was to develop a model for explaining environmentally accelerated fatigue crack growth below K_{Iscc} in high strength steels. The experimental results were analyzed to provide an indication of the factors controlling corrosion fatigue and to determine whether power law relationships could accurately predict corrosion fatigue kinetics below K_{Iscc}.

EXPERIMENTAL PROCEDURE

Commercial heats of 5/8" thick air melted SAE-AISI 4340 and D6AC steels with the following compositions were used for the study:

Table I

Composition of 4340 and D6AC Steels (w/o)

Alloy Source and Heat No.	C	Si	Mn	Cr	Mo	Ni	P	S	Cu	Fe	V
4340 Allen-Fry Heat 6790388	.39	.30	.76	.74	.23	1.77	.010	.015	.11	Balance	-
D6AC American Alloy Metals Heat 3962772	.48	.26	.79	1.05	.98	.63	.008	.005	-	Balance	.10

All tests were conducted on precracked compact K_{Ic} plate specimens 0.450" thick. The specimens were heat treated prior to finish machining according to the following sequences:

4340 Heat Treatment

1. Normalize 15 minutes, salt bath at 1700°F, air cool.

2. Austenitize 30 minutes, salt bath at 1550°F, oil quench.

3. Temper in air, 1 hour plus 1 hour at 750°F or 450°F, air cool.

D6AC Heat Treatment

1. Normalize 15 minutes, salt bath at 1700°F, air cool.

2. Austenitize 20 minutes, salt bath at 1500°F, oil quench.

3. Temper in air, 1 hour plus 1 hour at 850°F.

Duplicate room temperature tensile tests were conducted on material receiving these heat treatments and the average of the results are listed in Table II.

Table II

Room Temperature Mechanical Properties of 4340 and D6AC Steels

	4340-750°F Temper	4340-450°F Temper	D6AC
Ultimate Tensile Strength (ksi)	225.1	286.0	239.7
0.2% Offset Yield Strength (ksi)	211.4	233.6	223.8
% Elongation	12.4	11.5	9.8
% Reduction Area	47.4	47.8	35.4
Rockwell C Hardness	43.7	48.4	47.8

In order to determine K_{Iscc} for these various materials, sustained load delayed failure tests were conducted on self-leveling lever-loaded Satec creep rupture machines in distilled water at 32°F, room temperature and 212°F for 4340 - 750°F temper and room temperature for 4340 - 450°F temper and D6AC.

Load control corrosion fatigue tests were performed on an Instron tensile testing machine using various ΔK levels depending on the alloy and heat treatment, and at frequencies of 2.4 and 24 cpm. The cyclic loading mode was tension-tension below K_{Iscc}. Crack growth kinetics were determined with a cantilever beam clip gauge designed for these single-edge notch specimens. The compliance was measured by strain gauges attached to the upper and lower faces of the gauge beam with the strain bridge output being fed into a Datronic amplifier and then into a Moseley single pen recorder. Crack growth characteristics were measured by recording changes in the specimen compliance for test conditions involving an inert atmosphere of dehumidified argon at room temperature and distilled water at 32°F, room temperature and 212°F. The dehumidified argon atmosphere was obtained by passing the inert gas through a column of magnesium perchlorate before entering the sealed plexigalss environmental test chamber. Barsom (12) has observed that environmental effects in corrosion fatigue near or below K_{Iscc} do not occur during the constant-load portion of each load excursion. Therefore, a varying load-time profile was established for this study.

RESULTS AND DISCUSSION

1.   Frequency and Temperature Effects

The frequency and temperature effects were studied by tension-tension fatigue tests conducted under load controlled conditions in distilled water at 32°F, room temperature and 212°F utilizing 4340 in the 750°F temper condition. The fatigue crack growth kinetics as a function of ΔK are shown in Figures 3-5. The bar across each curve indicates where K_{max} exceeded K_{Iscc} as the crack grew into the specimen. Because of the geometry of the compact K_{Ic} plate specimens used in this study, K at the crack tip increases as the crack travels and hence, after a period of time K_{max} went above K_{Iscc}.

The damaging effect of room temperature distilled water on fatigue crack growth rate is dramatically shown in Figure 4, which includes test results for 4340 steel (750°F temper) tested in room temperature dehumidified argon. Considering the argon to be an inert nonaggressive reference environment, the deliterious effect of the water on fatigue crack growth behavior can be readily seen by the fact that growth rates below K_{Iscc} are approximately two orders of magnitude higher in water and approximately one order of magnitude higher at loads above K_{Iscc}.

Frequency of applied load and environment temperature had a considerable effect upon the interaction between the fatigue and environmental processes. For all three temperatures, as frequency decreased the fatigue crack growth rate increased in magnitude indicating that the time-dependent action of the corrosive environment had more influence than the cycle dependent fatigue damage alone. A number of investigators have observed this frequency effect in various steels tested in a variety of environments (4,12,16,17,18) at loads both above and below K_{Iscc}. These results have been explained in terms of Troiano's hydrogen embrittlement theory (19) which requires a critical combination of triaxial stress and hydrogen concentration in the region of maximum stress triaxiality. At lower frequencies more time per cycle is available for the hydrogen to diffuse to the region of maximum stress triaxiality and hence to enhance the crack growth process. It is suggested that the same explanation is applicable in the present study involving low alloy martensitic 4340 steel tested in a distilled water environment at initial loads below K_{Iscc}.

Comparison of Figures 3-5 also indicates that the severity of environmental embrittlement in this high strength steel was also quite temperature deoendent, particularly for loads below K_{Iscc}. This effect was greatest for the lower test frequency, 2.4 cpm. As test temperature increased from 32°F to 212°F, the crack growth rate below K_{Iscc} increased by approximately one and one half orders of magnitude. At the 24 cpm test frequency, the effect below K_{Iscc} was slightly less, with the crack growth rate increasing approximately one order of magnitude for the same temperature range. While the detailed mechanism for this temperature-frequency enhanced environmental failure is not completely understood, it is suggested that temperature increases the reaction rates for the various processes associated with failure, including the hydrogen generating metal-environment reaction, the transfer processes enabling hydrogen to enter the specimen and finally the stress induced lattice diffusion of hydrogen to the front of the crack tip. Both of these frequency and temperature effects were observed in a previous study of 4340 steel tested under load conditions entirely above K_{Iscc} (16).

288

2.   Tempering Temperature and Composition Effects

Tempering temperature and composition effects were studied by fatigue tests at 24 cpm with initial K below K_{Iscc} in room temperature distilled water and dehumidified argon utilizing 4340 (750°F and 450°F temper) and D6AC. The fatigue crack growth kinetics as a function of ΔK are shown in Figure 6. In the inert atmosphere, there appeared to be little difference in fatigue behavior between the three materials, at least until high values of ΔK were reached. This would indicate that fatigue crack growth was primarily a function of ΔK, and not of either tempering temperature or composition.

There was, however, an appreciable environmental effect which extended from the region below K_{Iscc} into the region above K_{Iscc} which indicated that 4340 in the 450°F temper was most susceptible while D6AC was the least susceptible to environmental embrittlement. The effect of tempering temperature has been attributed to the influence of yield strength on a material's basic ability to resist hydrogen embrittlement (17). Rowland has observed that the sharpness of a crack tip decreases as the yield strength of a material decreases due to the increase in the amount of plastic deformation caused by the lack of a plane strain situation (17). As shown by Troiano, the point of maximum stress triaxiality and hence, the origin of cracks in hydrogen embrittled material, is closer to the base of a sharp notch or crack than in the case of a blunt crack (19). Thus, the lower the yield strength of the material, the further away from the crack tip is the point of maximum stress triaxiality. This means that the hydrogen must diffuse further in the low than in the high yield strength material to reach the critical region of maximum stress triaxiality. In addition, the lower yield strength material has an inherent toughness of its own due to its ability to plastically deform. Hence, the observed decrease in the severity of room temperature environmental embrittlement in the 750°F temper 4340 material (211.4 ksi yield strength) compared to the 450°F temper 4340 material (233.6 ksi yield strength).

Using the yield strength criterion discussed previously, the corrosion fatigue characteristics of D6AC (223.8 ksi yield strength) should have fallen roughly in between those of the two 4340 temper conditions. However, the D6AC was more resistant than the 4340, indicating the significance of composition. These results confirm the importance of higher Mo (20) and Cr (20,21) for enhanced resistance to environmental embrittlement in D6AC as well as other high strength steels.

3.   Predictability of Experimental Results

For loading below K_{Iscc}, a number of observers have suggested the power law relationship first developed by Paris (22) for sinusoidal loading in an air environment,

$$da/dn = A \, (\Delta K)^n$$

where   a = crack length, inches

             n = number of cycles

             ΔK = stress intensity factor range, ksi $\sqrt{in.}$

             A and n are constants for a given material

289

The exponent n can be evaluated from the slope of the log-log plot of test data. Both Paris, testing in air, and Barsom (12), testing in salt water, found n to be invariant for test data gathered from a wide variety of materials. Paris' value for n was 4 while Barsom's value was 2.25. For these results the environment only influenced the constant A and therefore merely displaced the curve while keeping the same functional dependence on ΔK. Other investigators have found, however, that n is not an invariant interger for the environment-material systems studied, but rather, is inversely related to the fracture toughness of the material (1,17,23). Hence, it was suggested that any attempts to describe the crack growth behavior of a wide variety of materials with an invariant power law should be subjected to careful scrutiny.

As shown in the log-log plots of Figure 6 for 4340 (750°F and 450°F temper) and D6AC steels tested in room temperature distilled water and dehumidified argon at 24 cpm, the portions of the curves below K_{Iscc} do follow a power law relationship. In the inert dehumidified argon atmosphere an approximate slope (n value) of 4.19 was obtained for all three materials and the crack growth rates were quite similar. In the distilled water environment the crack growth rates were different for each material but also followed a power law relationship below K_{Iscc}. The slopes, however, were not invariant, ranging from 1.08 for D6AC to 0.9 for 4340 in the 450°F temper to 0.391 for 4340 in the 750°F temper. This indicated that as ΔK increased, the curves below K_{Iscc} for each material tested in water approached those for material tested in the inert environment. Thus, as ΔK increased the environmental contribution towards fatigue crack propagation diminished slightly but remained the predominant factor, however, because the crack growth curves in water never met the corresponding curves in the inert atmosphere.

Comparison of these results with other data for different steel-environment systems (1,17,23) revealed that the slopes in the present study were smaller. This suggested that the 4340 and D6AC steel-distilled water system was characterized by environmental contributions to fatigue crack growth which diminished more rapidly with increases in ΔK than in the other, more aggressive environments. In addition to this, the fact that the slopes were not invariant agreed with the results of Crooker and Lang (1), Rowlands (17), Gallagher (13) and Miller (23), as opposed to the results of Barsom (12) and Paris (22) in which the slopes were invariant and the environmental contribution remained constant with increasing ΔK.

Both tempering temperature and composition had an effect upon the slopes of these curves. For the 4340 steel, n decreased with the yield strength indicating that the environmental contribution to crack growth diminished more rapidly with the lower yield strength material. As is also evident from Figure 6 the environmental embrittlement was less severe in the lower yield strength 4340. Both the embrittlement behavior and change in n with respect to yield strength have also been observed in other steel-environment systems (17). Of the three materials D6AC exhibited the highest n value, 1.08. Thus, although characterized by increased resistance to environmental embrittlement, D6AC also exhibited a lesser tendency for this embrittlement to diminish with an increase in ΔK.

4.   Corrosion Fatigue Cracking Activation Energy

The activation energy for corrosion fatigue crack growth rate was determined by plotting the logarithm of the growth rate as a function of the reciprocal of the absolute temperature. The results for crack growth rates <u>at 24 cpm</u>, obtained from Figures 3-5 are shown in Figure 7 for ΔK = 13 ksi $\sqrt{in}$. (below

K_{Iscc}) and $\Delta K = 20$ ksi $\sqrt{in.}$ (above K_{Iscc}). For comparative purposes the 5200 cal/mole which corresponds to the activation energy for hydrogen adsorption onto a clean iron surface (24) and the 9000 cal/mole which corresponds to the activation energy for hydrogen diffusion through a lattice (25,26,28) are also presented in the figure. Activation energy, Q, is obtained from the slopes of these plots. Results for crack growth below K_{Iscc} (Q = 3710 cal/mole) and for growth above K_{Iscc} (Q = 3000 cal/mole) were closer to the 5200 cal/mole value for surface adsorption of hydrogen than for hydrogen diffusion. While this ruled out lattice diffusion as the possible rate controlling factor, it also indicated that surface hydrogen adsorption was too simplistic a mechanism. The actual mechanism is more likely a complex surface process consisting of the hydrogen generating metal-environment reaction, the alternate formation and penetration of protective surface films and the transfer processes enabling hydrogen to enter the material (molecular physisorption and dissociation, atom surface migration and chemisorption and atom solution).

5.   Influence of Loading Time on Corrosion Fatigue Below K_{Iscc}

For environment-enhanced fatigue crack growth below K_{Iscc}, a number of investigators have shown that wave form can have a significant and unusual effect (12,15). These results showed that waveforms that have a slow load rise time (such as sine waves) produced full environmental effect, while waveforms with fast load rise-times produced little or no environmental enhancement of crack growth. The rate of environment-enhanced fatigue crack growth exhibited a maximum at some intermediate frequency depending on the steel-environment system, and approached the growth rate at high frequencies and, presumably, at very low frequencies (14). These data indicated that the time during which the tensile load increases controls the crack growth acceleration, with the greater time yielding the greatest degree of embrittlement. However, the increase in crack growth rate with increased time in the tensile loading cycle cannot continuously increase since very long loading times approach static loading where no environment effect exists.

In order to determine the effect of loading time in tension on cyclic crack growth rate below K_{Iscc}, tension-tension fatigue tests at three frequencies in room temperature distilled water were conducted utilizing 4340 steel in the 750°F temper condition. The crack growth rates have been plotted for these tests as a function of ΔK in Figure 4. These crack growth data are replotted in Figure 8 as a function of loading time in tension for ΔK at 13 ksi $\sqrt{in.}$ (below K_{Iscc}). Although a maximum was not obtained in the curve, the fact that the slope steadily decreases indicates that the plot may go through a maximum beyond 20 seconds/cycle loading time in tension, or a frequency of 1.5 cpm. The trend of the present data on low alloy martensitic 4340 steel compares favorably with the frequency effects observed in 12Ni-5Cr-3Mo maraging steel (12), HY-80 steel (13) and RQ-360A steel (15). Wei suggests that the observed frequency dependence below K_{Iscc} implies a complex interplay involving the rate of production of fresh surfaces by fatigue, the kinetics of hydrogen adsorption, the rate of repassivation and the rate of hydrogen transport (4). Further fundamental studies are needed to separate and analyze the importance of these process rates for better understanding of these frequency effects.

SUMMARY

Experiments were conducted to study the corrosion fatigue of high strength AISI 4340 and D6AC steels below K_{Iscc} in a distilled water environment. The investigation included a study of the frequency, environment temperature, tempering temperature and composition effects as well as the predictability of crack growth rates by power law relationships, crack growth activation energies and the effect of loading time in tension on crack growth rates. In order to evaluate these characteristics below K_{Iscc}, sustained load tests were conducted in a distilled water environment to determine K_{Iscc} and were combined with fatigue tests with initial loading below K_{Iscc}.

Comparison of the crack growth kinetics for environmentally accelerated fatigue with those for fatigue in the inert dehumidified argon atmosphere illustrated the degrading influence of the aqueous environment. The effect became more pronounced as frequency decreased and temperature increased. At any given frequency the corrosion fatigue crack growth rates were at least one order of magnitude greater than the cycle dependent argon fatigue crack growth rates, indicating that the kinetics were controlled primarily by environmental attack. At lower frequencies more time per cycle was available for the hydrogen to diffuse to the region of maximum stress triaxiality and hence to enhance the crack growth process. Temperature increased the reaction rates for the various processes associated with failure, including the hydrogen generating metal-environment reaction, the transfer processes enabling hydrogen to enter the specimen and finally the stress induced lattice diffusion of hydrogen to the front of the crack tip.

Tempering temperature and composition, while not affecting the fatigue properties of 4340 and D6AC in the inert argon environment, had a considerable effect on the embrittlement characteristics in distilled water. 4340 steel in the 450°F temper condition was most susceptible while D6AC was the least susceptible. This was explained in terms of the higher yield strength of the 450°F temper 4340 steel and the higher Mo and Cr content of the D6AC steel.

Both the 4340 and D6AC steels exhibited crack growth behavior below K_{Iscc} which followed a power law of the form $da/dn = A\Delta K^n$. The slopes of the lines, however, were not invariant in distilled water, but decreased compared to the slope for those materials tested in argon. This indicated that as ΔK increased, the environmental contribution towards fatigue crack propagation diminished. These results agreed with those observed by Crooker and Lang (1), Gallagher (13), and Miller (23). Both tempering temperature and composition had an effect upon the slopes of these curves. For 4340, the slope decreased with yield strength indicating that the environmental contribution to crack growth diminished more rapidly with the lower yield strength material. Although characterized by increased resistance to environmental embrittlement, D6AC was also characterized by a decreased tendency for this embrittlement effect to diminish with an increase in ΔK.

The activation energy for corrosion fatigue crack growth rate above and below K_{Iscc} compared more favorably with the value for hydrogen adsorption onto a clean iron surface than for hydrogen diffusion through a steel lattice. However, the values obtained in this study indicated that the rate controlling factor was probably not associated with such idealistic processes. The corrosion fatigue crack growth rates for 4340 steel in the 750°F temper condition increased with loading time in tension and the trend of the data indicated that a maximum point may be reached at lower frequencies than those included in this investigation.

292

ACKNOWLEDGEMENT

REFERENCES

1. T. W. Crooker and E. A. Lange: NRL Report 6944, October 14, 1969.

2. I. M. Austen and J. M. West: Engineering Fracture Mechanics, Vol. 4, March 1972, p. 181.

3. P. B. Haigh, J. Inst. Metals, 18. 55, 1917.

4. R. P. Wei and G. W. Simmons: Contract N00014-67-A-0370-0008, March 1973.

5. A. J. McEvily, Jr. and R. P. Wei, Proceedings - International Conference on Corrosion Fatigue, University of Connecticut, 1971, NACE, 381, 1972.

6. A. J. McEvily, Jr. and W. Illg, NACA TN 4394, 1958.

7. J. A. Fe ney, J. C. McMillan and R. P. Wei, Met. Trans. 1, 1741, 1970.

8. P. C. Paris, R. J. Bucci, E. T. Wessel, W. G. Clark, Jr. and T. R. Mager, ASTM STP 513, 1972.

9. R. J. Bucci, W. G. Clark, Jr. and P. C. Paris, ASTM STP 513, 1972.

10. R. P. Wei, J. Eng'g, Fract. Mech. 1, 633, 1970.

11. R. P. Wei and J. D. Landes, Mat'l. Res. & Std., ASTM 9, 25, July 1969.

12. J. M. Barsom: International Conference on Corrosion Fatigue, June 1971, University of Connecticut.

13. J. P. Gallagher: NRL Report 7064, May 28, 1970.

14. J. M. Barsom, Ph.D. Dissertation, University of Pittsburgh, 1969.

15. G. A. Miller, S. J. Hudak, Jr. and R. P. Wei, "The Influence of Loading Variables on Environment-Enhanced Fatigue Crack Growth in High Strength Steels," to be published by ASTM (copies available from authors on request).

16. C. S. Kortovich and E. A. Steigerwald: Contract N00014-69-C-0286, July 1972.

17. R. C. Rowlands, M.S. Dissertation, Cornell University, September 1972.

18. T. C. Babcock, M.S. Thesis, Cornell University, 1969.

19. A. R. Troiano: Trans. ASM, 1960, Vol. 52, p. 54.

20. E. A. Steigerwald and W. D. Benjamin, Met. Trans. Communications, July 1970.

REFERENCES (cont'd)

21. W. Beck and E. J. Jankowsky, Metal Progress 84, 1963.

22. P. C. Paris, Proc. of the 10th Sagamore Army Materials Research Conference, Syracuse Univ. Press, 1964, p. 107.

23. G. A. Miller, Trans. ASM Vol. 61, 1968, p. 442.

24. C. M. Sturgess and A. P. Miodownik: Acta Met., 1969, Vol. 17, p. 1206.

25. E. A. Steigerwald, F. W. Schaller and A. R. Troiano: AIME Trans., Vol. 215, 1959, p. 1048.

26. J. D. Hobson: Journal Iron and Steel Inst., 1958, Vol. 189, p. 315.

27. R. C. Rank: Journal Applied Phys., 1958, Vol. 29, p. 1262.

28. R. Gibala: Trans. AIME, 1967, Vol. 239, p. 1574.

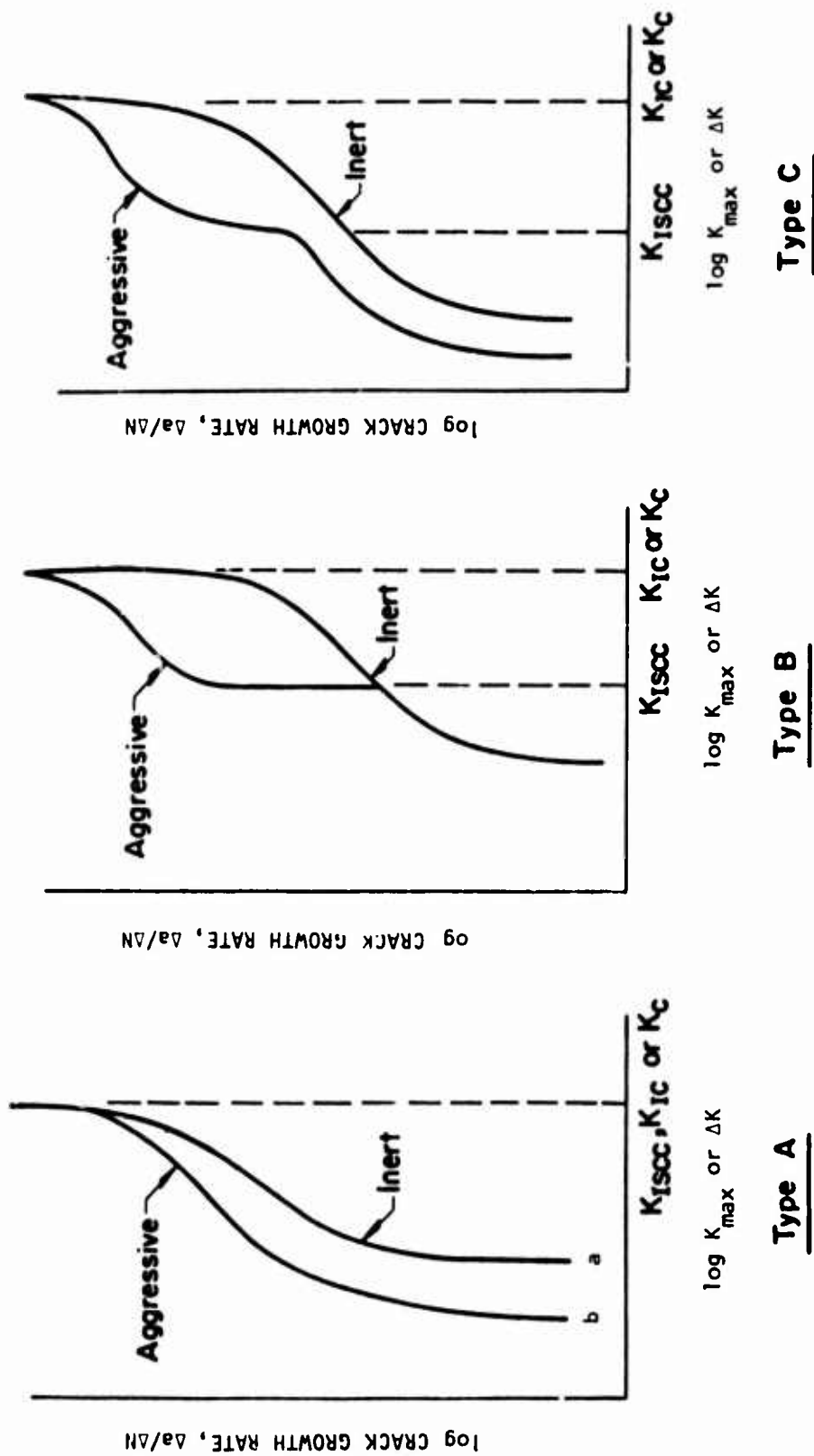Figure 1. Types of Fatigue Crack Growth Behavior in Aggressive Environments (5).
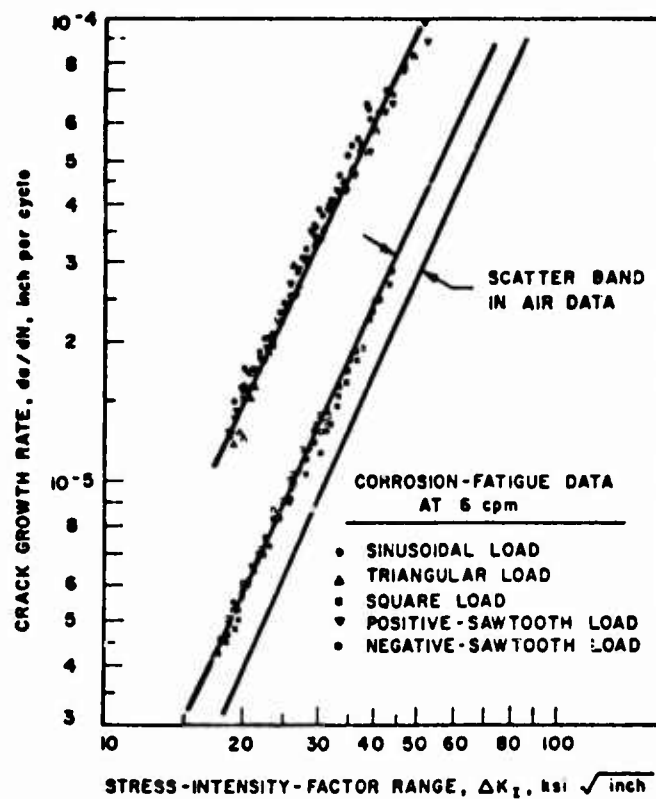
a. Influence of wave form on crack growth acceleration and constant ratio of corrosion fatigue to air fatigue da/dn (12).
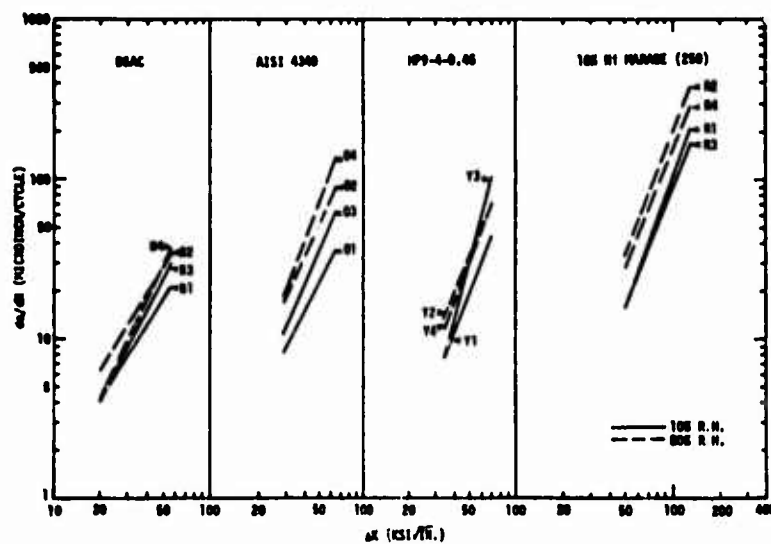
b. Comparative plots of fatigue crack growth rates for D6AC, AISI 4340, HP9-4-.45, and 18% Marage (250) steels (1).

Figure 2. Anomalous Corrosion Fatigue Crack Growth Behavior Below K_{Iscc}.

Figure 3. Fatigue Crack Growth Rate for 4340 Steel, 750°F Temper, Tested in Distilled Water at 32°F and Two Frequencies.
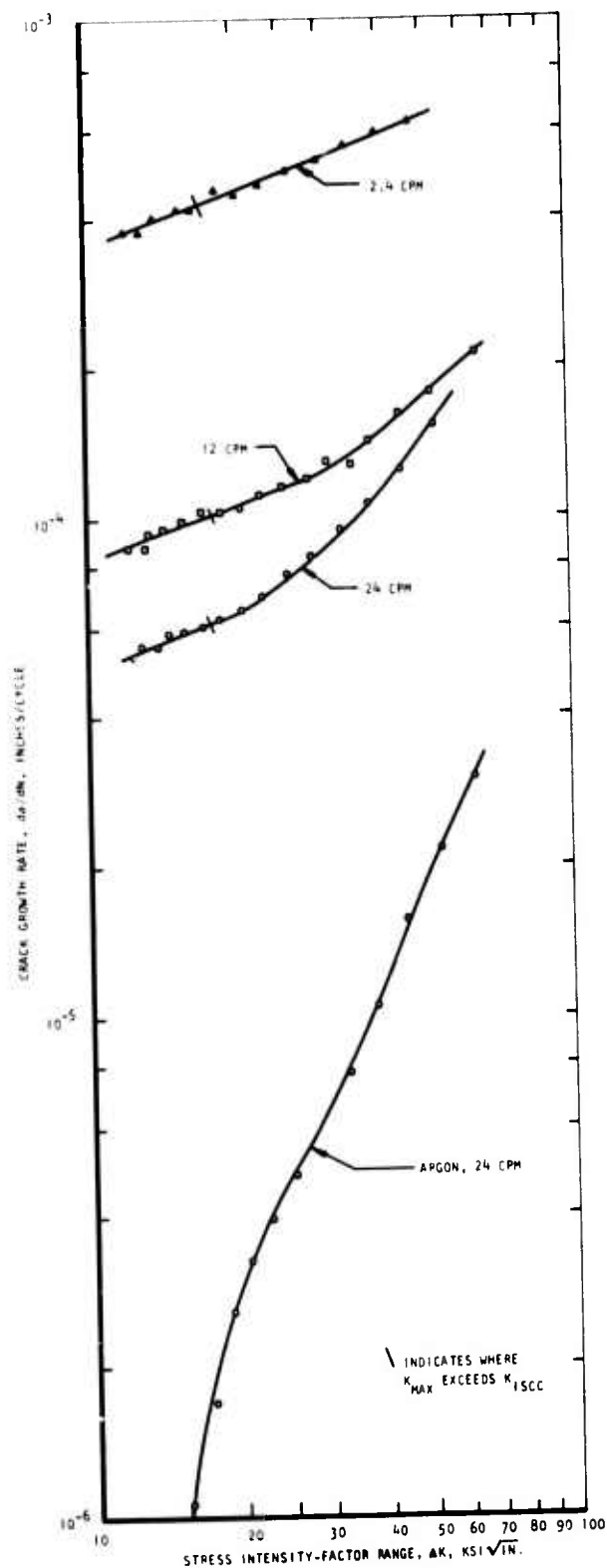
Figure 4. Fatigue Crack Growth Rate for 4340 Steel, 750°F Temper, Tested in Room Temperature Distilled Water and Three Frequencies and Argon at Room Temperature 24 cpm

299
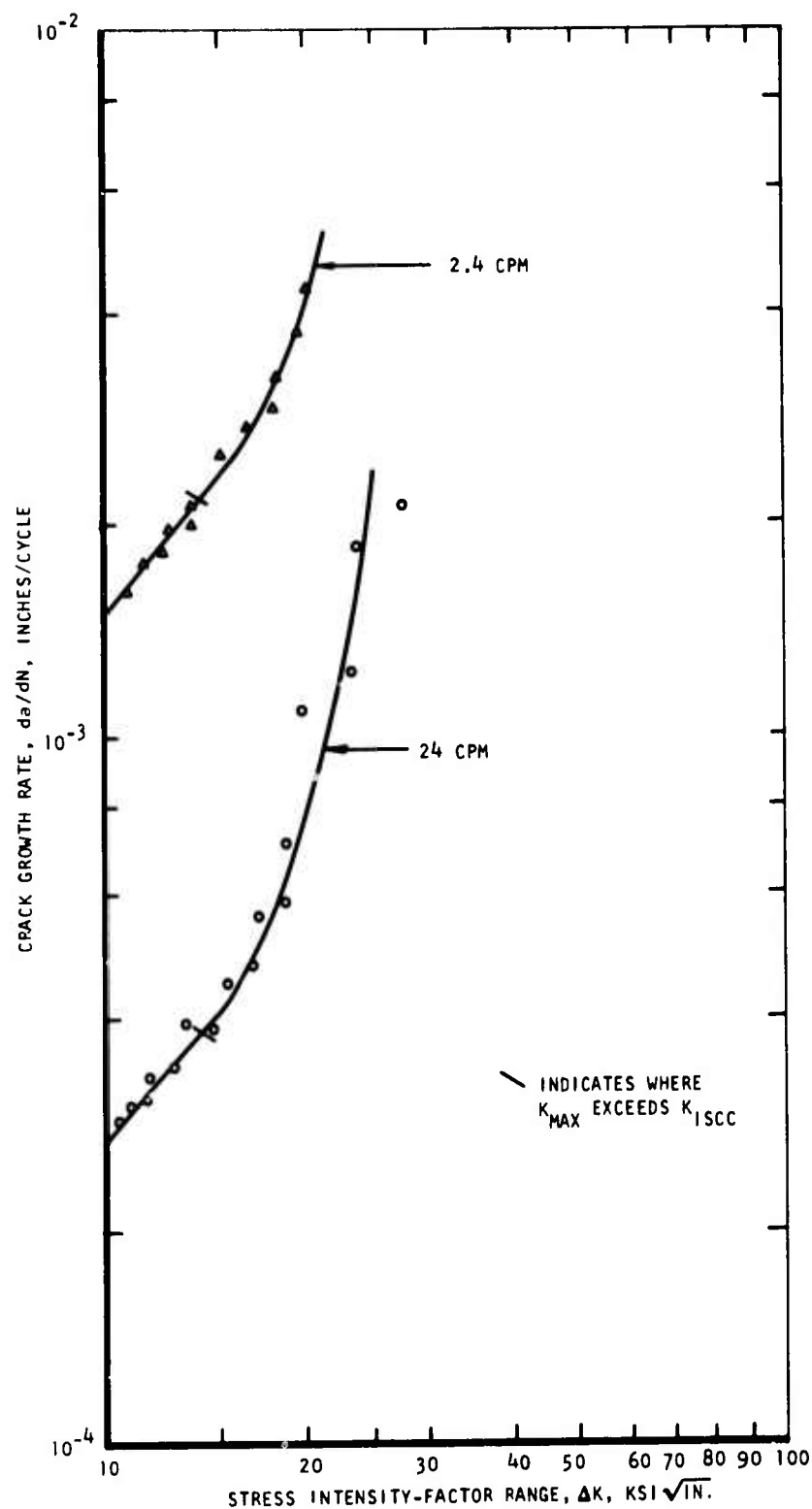
Figure 5. Fatigue Crack Growth Rate for 4340 Steel, 750°F Temper, Tested in Distilled Water at 212°F and Two Frequencies.

300

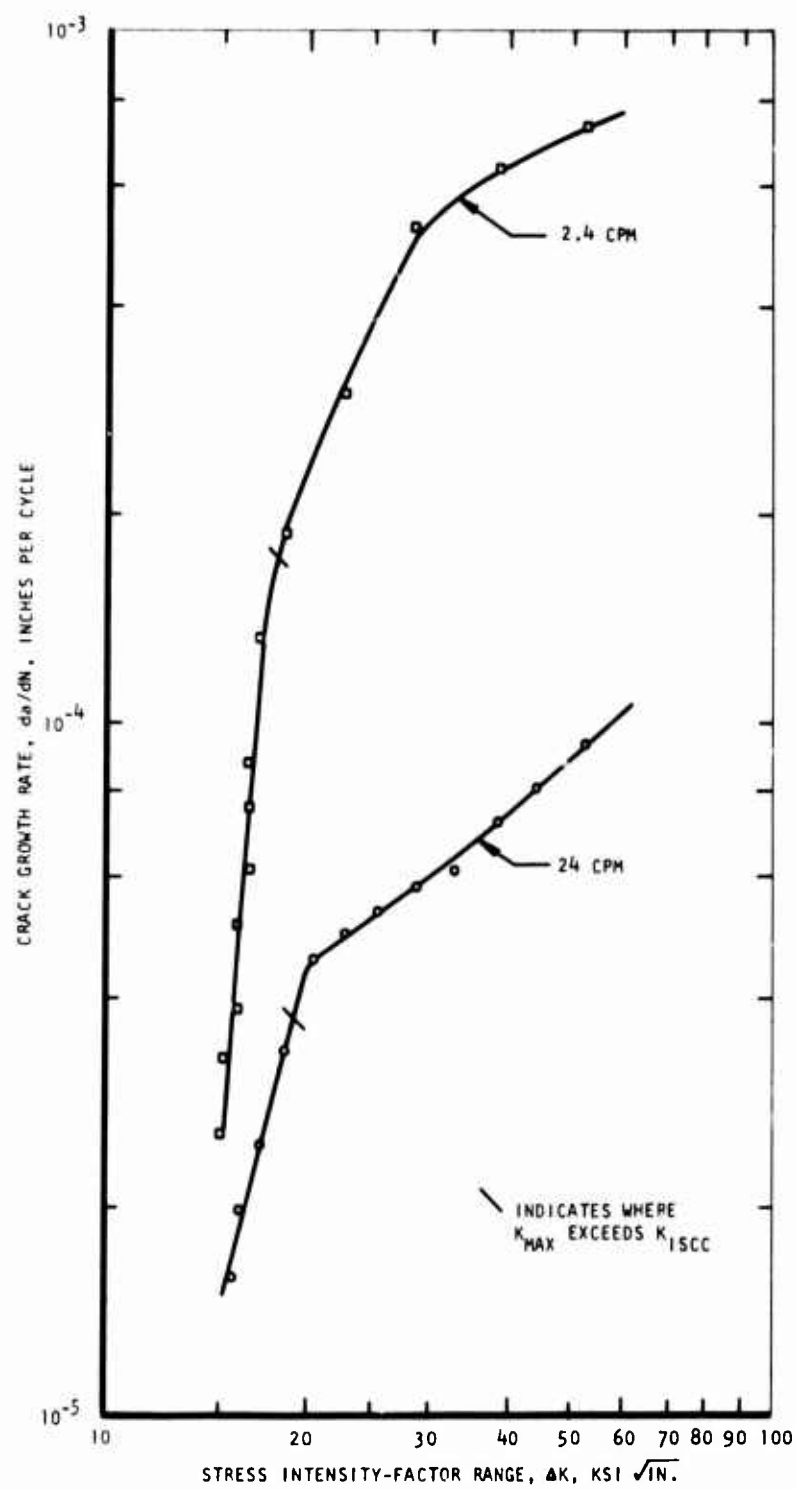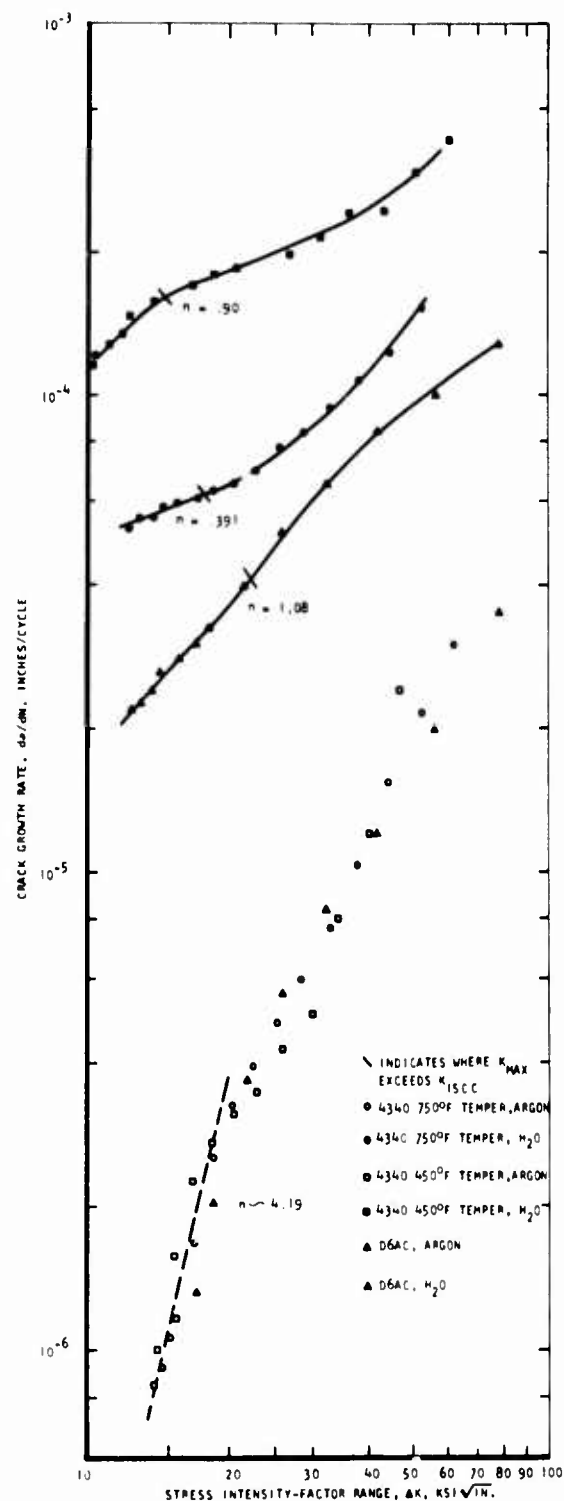Figure 6. Fatigue Crack Growth Rate for 4340 Steel, 750°F and 450°F Temper, and D6AC Steel Tested in Room Temperature Distilled Water and Dehumified Argon at 24 cpm. The n Values are the Slopes of the Straight Line Portion of the Curves.

301
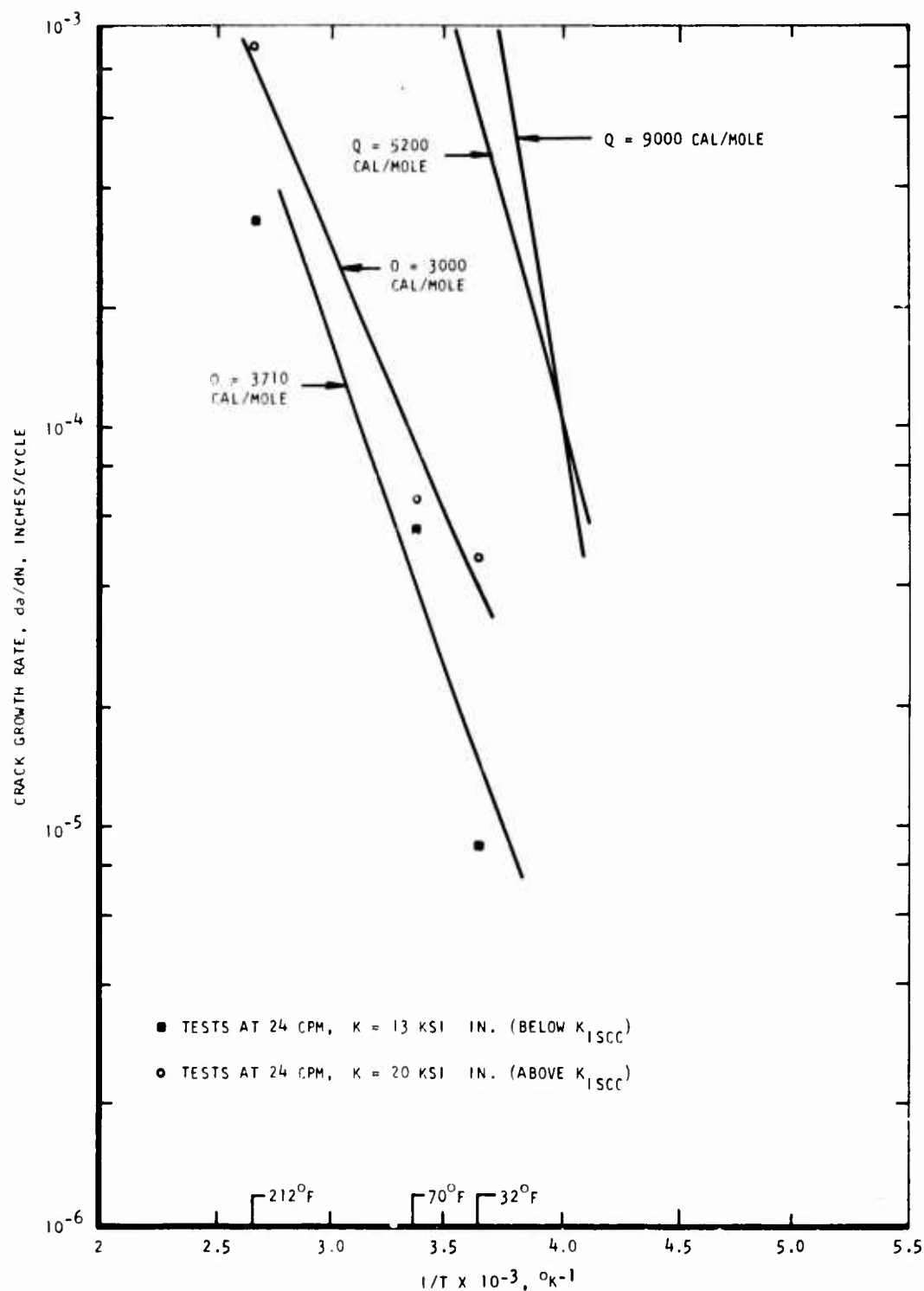
Figure 7. Activation Energy for Corrosion Fatigue Crack Growth Kinetics Both Above and Below K_{Iscc} for 4340 Steel, 750°F Temper, Tested in Distilled Water at Room Temperature and 24 cpm. Activation Energy for Hydrogen Adsorption onto a Clean Iron Surface (5200 cal/mole) and for Hydrogen Diffusion in a Steel Lattice (9000 cal/mole) Have Been Included for Comparative Purposes.

302
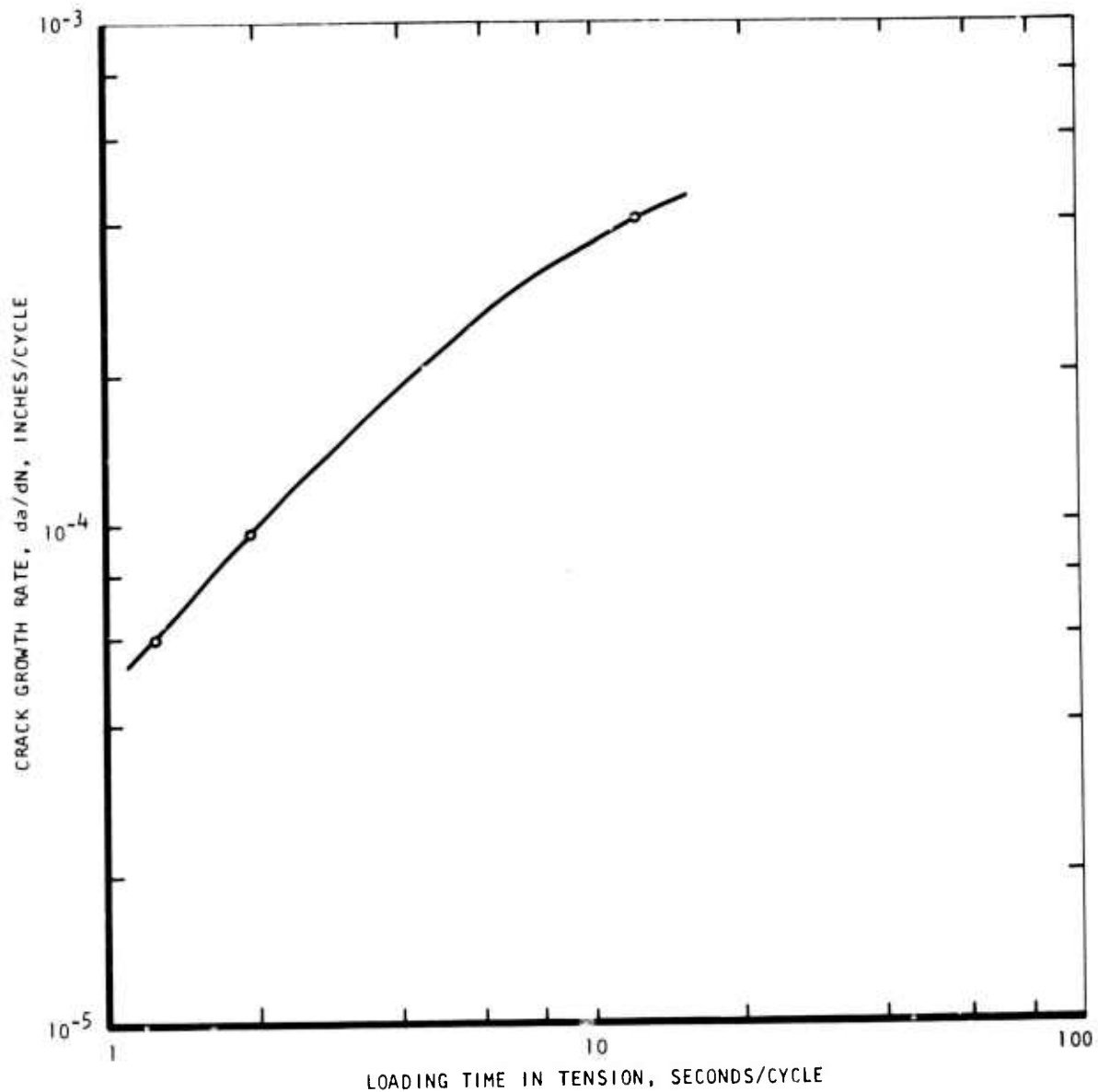
Figure 8. Increase in Cyclic Crack Growth Rate as a Function of Loading Time in Tension Below K_{Iscc} for 4340 Steel, 750°F Temper, Tested in Room Temperature Distilled Water.

INTERACTION BETWEEN PERFLUOROALKYL POLYETHER LINEAR AND CYCLIC DERIVATIVE FLUIDS AND HIGH TEMPERATURE BEARING STEELS IN OXIDATION CORROSION ENVIRONMENT

by

George J. Morris

AIR FORCE MATERIALS LABORATORY
LUBRICANTS AND TRIBOLOGY BRANCH

305

The trends of advanced performance aerospace systems toward high temperature operation have led to the development of both metals and fluid lubricant materials over the past decade that are capable of withstanding stringent thermal and oxidative stresses without undergoing appreciable degradation. However, in the gas turbine engine oil area high thermal and oxidative stability must also be accompanied by other specific attributes such as metal compatibility, lubricity, and reasonable rheological properties at low temperatures. This has presented a problem, for example, in the case of the polyphenyl ethers typified by the 5P4E structure. They have outstanding oxidative and thermal stability but are unfortunately accompanied by poor low temperature flow characteristics and poor lubricating capability (without additives) which fall short of meeting gas turbine engine oil needs. Currently used silicones have excellent rheological properties, fairly good lubricating capabilities, but were found to be lacking in moderately high ($428^{\circ}F$ to $465^{\circ}F$) temperature oxidative environment. Another class of fluids that appeared to provide most of the above-mentioned properties consisted of a series of polymeric perfluorinated polyether fluids that also provided chemical inertness, complete nonflammability, and non-sludging or lacquer formation tendencies. The first of these known as the "Krytox" oils was produced by duPont with varying molecular weight ranges and was recommended for use in applications such as high temperature hydraulic fluids and gas turbine engine oils. Their fluid range was not fully acceptable because of a sacrifice of proper fluidity at $-20^{\circ}F$ to maintain reasonable viscosity above 1.0 centistoke at $500^{\circ}F$ and sufficient volatility at $400^{\circ}F$. It was also demonstrated by former workers in this laboratory that these fluids could be inhibited with additives (solubility sometimes difficult) to increase their useful range at high temperatures by approximately $100^{\circ}F$. A similar fluid was also commercially produced by another manufacturer at a later date. This technology was further extended by duPont by synthesizing the perfluoro-aklylpolyether with one or more triazine structures included. The fluids described above were evaluated with metals of interest under oxidation corrosion conditions from $500^{\circ}F$ up to $700^{\circ}F$.

In the metals area the Metals and Processing Branch of the Metals and Ceramics Division, Air Force Materials Laboratory, efforts were directed toward developing bearing materials with superior elevated temperature properties over $900^{\circ}F$. One of the most commonly used bearing steels, 52100, could no longer be considered in this high temperature regime ($1000^{\circ}F$) because of a rapid loss of hardness and dimensional stability. Hot worked die steels and high speed tool steels met the requirements for aircraft bearings with only varying degrees of success. As a result of the work carried out by Crucible Steel under AFML contract, a prototype high temperature alloy designated WB-49 was developed for aircraft bearing application over $900^{\circ}F$. This technology was extended to incorporate corrosion resistance to the already attained high initial hardness, adequate temper resistance (in the range of $600^{\circ}F$ and $900^{\circ}F$), and good dimensional stability of the alloy. This composition designated as WD-65 was recommended for use as a corrosion resistant bearing steel for 500 hours of operation at temperatures up to $900^{\circ}F$.

Since the perfluorinated fluids had been shown to have outstanding thermal and chemical stability at high temperature, their interaction with high temperature

metals that they might encounter was of immediate interest. Several concurrent studies were carried out when the fluids were first introduced with emphasis on oxidation stability and metal corrosion tendency. One of these was performed by duPont in a semi micro oxidation-corrosion test rig. This study showed that the perfluoroalkylpolyether fluid, then identified as PR-143 could be used without deleterious effects up to 550°F on most 400 series stainless steels, a high speed tool steel and the bearing steels such as M-1, M-50, 52100 and WB-49. It was also noted that above 600°F, several of the frequently used titanium alloys caused severe degradation to the PR-143 fluid even in the absence of oxygen. An unexpected improvement up to 650°F in corrosion behavior of the bearing steels M-1, M-50, and WB-49 was observed when these materials were hardened and configured for use in ball bearing hardware instead of the washer shaped metal specimens normally used in current oxidation-corrosion testing.

Laboratory investigations conducted by this laboratory on the perfluoroalkyl-polyether fluid utilizing slightly different oxidizing conditions showed a considerable corrosive effect on most ferrous metals and certain titanium alloys at 550°F and above. Included in these ferrous alloys were M-1, M-10, 52100, and 440 C that were included in the previously described program.

A more recent evaluation of the interaction between M-50 and WD-65 aircraft bearing steels and perfluoroalkylpolyether gas turbine engine oil grade, by this time identified as Krytox 143 AC, was performed by the Air Force Aero Propulsion Laboratory. The conditions were again of the oxidation-corrosion variety conducted in accord with the Coordinating Research Council (CRC) procedure L-53-368 at 644°F for 48 hours. This test method was the forerunner of the current Method 5307 for Federal Test Method Standard 791b used to evaluate the oxidation stability of candidate gas turbine engine oils directed toward the requirements of specification MIL-L-27502. Both metals suffered excessive corrosion by our current standards with the M-50 appearing worse than the WD-65 with the naked eye and under the microscope. The M-50 showed a coated, very rough and pitted surface while the WD-65 was only coated and not as rough (Table I). Based on previous experience within this laboratory and that of outside workers reviewed herein, these results could be expected at the test temperature that was selected. However, since these high temperature alloys were considered to be the aircraft bearing steels of the future and similarly the perfluorinated fluids were considered to be the future high temperature class of lubricants, the question arose as to the mutual compatibility of these materials under severe projected use conditions. In order to answer this compatibility question with a relative degree of certainty, a study was conceived utilizing the micro oxidation-corrosion test. This method, which has previously been used in high temperature fluid studies, incorporates the severity and repeatability necessary to reliably project the interaction of both metals and perfluorinated fluids at high temperatures. The data accumulated in this study are reported herein.

TABLE I

TEST RESULTS FROM A REFLUX OXIDATION-CORROSION TEST
48 HOURS @644°F

PROCEDURE: CRC DESIGNATION L-53-368 (FTMS791b, METHOD 5309)

METAL SPECIMEN DATA:	Weight Change mg/cm^2	DESCRIPTION:
WD-65		
Before cleaning	+0.96	Dark brown and black coating
After electrocleaning	-1.54	Rough
M-50:		
Before cleaning	+1.42	Dark brown and black coating
After electrocleaning	-0.72	Very rough and pitted

NOTE: Pretest appearance both specimens:
Bright, shiny and polished finish
Approx: 5μ in. rms

Oxidation-corrosion (o-c) studies were performed under two basic conditions with the perfluorinated fluids identified below:

Sample Identity	Fluid Identity
MLO-73-20	Perfluoroalkylpolyether, from manufacturer Nr 1
MLO-73-21	Inhibited perfluoroalkylpolyether
MLO-73-22	Perfluoroalkylpolyether (HFPO) triazine
MLO-73-23	Perfluoroalkylpolyether, from manufacturer Nr 2

These fluids were furnished as laboratory samples from interested suppliers and are not necessarily typical of fluids that would be supplied on a full scale production. The assumption is made that refinements and improvements on the finished product would be incorporated in scaling up from the laboratory bench to larger scale manufacturing.

All investigations were made in micro scale apparatus. When dissimilar metal specimens were employed, the glassware configuration contained a condenser for refluxing fluid vapors. When ferrous metals were tested, the condenser was replaced with a side arm adapter in an "overboard" configuration which allowed for collecting and measurement of condensed fluid vapors. All metal specimens were separated by glass spacers as illustrated in Figure 1.

The metal specimens were selected from combinations previously evaluated in perfluoroalkylpolyether fluid (their compositions where possible are covered by federal, military, or industrial specifications as listed on Table II). The term

TABLE II

METAL TEST SPECIMEN IDENTITIES

Test Specimen Identity	Specification
Dissimilar	
Titanium, 6 Al-4V	MIL-T-9046, titanium and titanium alloy sheet, strip and plate, type III, composition C
Aluminum, 2024	QQ-A-250/4, aluminum alloy 2024, plate and sheet
Tool Steel, M-10	AISI, Type M-10, machined from bar
Silver	MIL-S-13282, electrolytic, 99.9, Grade A
301 Corrosion Resistant	MIL-S-5059, Type 301, Half Hard
Ferrous	
4140 Steel Alloy	Steel alloy, grade 4140 machined from annealed bar
52100	MIL-S-7430B, Grade E, from annealed strip
410	Stainless steel, Type 410 from annealed sheet
M-50, Tool Steel	AMS 6490A, Grade M-50 from annealed sheet
440C	QQ-S-763, Type 440-C machined from annealed bar

"dissimilar" metals refers to a specific metal combination that includes two ferrous metals. The washer type specimens of WD-65 alloy were furnished for this evaluation by the Metals and Processing Branch (LLM) of the Metals and Ceramics Division of AFML. They are identified below:

309

Identity	Source
WD-65	Colt Industries, Crucible Inc., - fully hardened at heat treatment to Rockwell C "65.5"
WD-65-53	Federal Mogul - did not fully harden at heat treatment - Rockwell C "53"

Washer-shaped specimens of the material from both sources were heat treated as follows:

Preheat at 1550°F/5 min.

Austenitize at 2190°F/2 min; quench into salt at 1000/5 min; air cool to room temperature

Refrigerate at -100°F/30 min.

Triple temper at 1000°F/2 hr. with refrigeration step (-100°F/30 min) between each tempering step.

The final hardnesses were Rockwell "C" 65.5 for the Colt Industries, Crucible Inc., material and Rockwell "C" 53 for the Federal Mogul material. The reasons for the Federal Mogul material not responding to the above heat treatment cycle have not been explored.

The WD-65 and WD-65-53 specimens were investigated alone in each fluid and inserted into each combination of dissimilar and ferrous metals, first to determine single metal activity and second to determine the degree of interaction of both WD-65's with the metal combinations normally used in oxidation-corrosion studies and the fluids in question.

The failure criteria chosen for this study were essentially the same as those used in previous perfluoroalkylpolyether fluid studies. Attack on the metal specimens (either weight gain by deposition or weight loss by corrosion) was considered excessive if the observed change was greater than 0.2 milligrams per square centimeter of specimen area over the original weight. Fluid deterioration criteria were derived from the limits set for long-term gas turbine engine oil goals as shown below:

Total acid number	4.0 max
Viscosity change @ 100°F, %	±25.0 max

No oxidation-corrosion test was carried beyond 700°F since this is beyond the projected limit for the perfluoroalkylether fluids due to viscosity and volatility characteristics.

Oxidation-corrosion data obtained with the perfluoroalkylpolyether, MLO-73-20, and the various metals are summarized on Table III. The reactivity of WD-65-53

310

by itself was nil until 650°F was reached. At this temperature attacks on all the specimens were excessive with deposition ranging from heavy black to a heavy multi-colored (peacock) appearance. Degradation of the fluid was minimal at all temperatures, which was the rule rather than the exception with other fluids. Fluid condition, therefore, will be considered within the prescribed limits unless otherwise stated throughout the remainder of this report. The WD-65 by itself demonstrated erratic behavior at 550°F but through 575°F and 600°F appeared nonreactive before it finally failed completely at 650°F (showing heavy black deposits). This erratic behavior had been observed at the lower temperature by other investigators.

The WD-65-53 with dissimilar metals in the MLO-73-20 fluid did not show corrosive attack at 500°F. Corrosion began to develop at 550°F along with aluminum and titanium. All dissimilar metals and WD-65-53 showed excessive corrosion at 600°F with the WD-65-53 appearing with a tan tarnish and spotted. A similar behavior pattern was observed with WD-65 and the dissimilar metals.

In oxidation-corrosion characterization with ferrous metals, each hardness level of WD-65 showed no corrosion at 500°F along with the other alloys in MIL-73-20 fluid. This trend of nonreactivity of WD-65's continued to 600°F despite heavy corrosive attack on all other ferrous alloys. It is apparent that none of the other ferrous metals' failures could be attributed to the presence of either hardness level of WD-65 in this characterization or in others involving the different types of fluids in this study.

Oxidation-corrosion data with the perfluoroalkylpolyether base fluid formulated with a high temperature corrosion inhibitor additive C, identified as MLO-73-21, appears on Table IV. Initial work was begun at a higher temperature level of 650°F with WD-65-53 and WD-65 alone to determine the inhibitor effectivity. No metal attack was observed at 650°F or 700°F with the washers having a slightly stained appearance. Fluid deterioration at 650°F only was indicated for both hardness levels by a gross viscosity loss.

Dissimilar metals with WD-65-53 showed no reactivity with the inhibited fluid MLO-73-21 through 550°F and 600°F and slight reactivity at 700°F with aluminum and M-10. This same trend occurred with WD-65 through 700°F where no reactivity was observed even at that top temperature. All WD-65 specimens at the end of each test were slightly stained in appearance. Fluid deterioration was excessive with the WD-65-53 at 550°F and 700°F as indicated by high viscosity and high volatility losses. By comparison, the WD-65 fluid deterioration at 550°F and 700°F although not excessive were an order of magnitude or two beyond normal expectations.

Reactivity of the inhibited perfluoroalkylpolyether MLO-73-21 with WD-65-53 and ferrous metals was mixed. At 550°F M-50 was excessively corroded and at 600, the 4140 showed attack. Corrosion was excessive on all the ferrous metals at 700°F. With WD-65 the ferrous metal combination showed very little susceptibility to corrosion at 550 and 600°F. However, at 700°F high corrosion was observed. Interestingly through the above temperature range to 700°F, both hardness levels of WD-65 with both metal combinations were not attacked excessively by the inhibited fluid.

311

Oxidation-corrosion data on the perfluoroalkylpolyether (HFPO) triazine MIL-73-22 is summarized in Table V. Each hardness level of WD-65 when immersed in the above fluid showed no attack at 650°F. At 700°F the WD-65-53 remains non-reactive while the WD-65 at 700°F gave incipient corrosion. Both sets of specimens ranged from a light stain to spot deposits in appearance. With dissimilar metals the WD-65-53 and WD-65 showed no corrosion through 600°F and up to 700°F with the neat fluid and a formulation using the same oxidation inhibitor (additive C) previously used with the perfluoroalkylpolyether. At 700°F the dissimilar metal combination showed excessive corrosion of the titanium and M-10 in duplicate tests with the neat fluid and the inhibited fluid. In addition, the silver showed excessive weight change in the inhibited fluid only. Both WD-65's were characterized by a golden stain.

The study of the ferrous metal combination, WD-65's and HFPO triazine also incorporated an additive effectiveness evaluation in addition to the neat fluid reactivity. At 500°F all ferrous metals and WD-65's were not corroded excessively with the neat fluid but at 600°F most of the ferrous were attacked including M-50. Both WD-65's did not suffer excessive weight change. The addition of additive C to the fluid eliminated the corrosion at 600°F on the ferrous combination but was not effective at 650°F. At both of the above temperatures, neither WD-65's showed signs of corrosion. The other additives M-4 and additive B were not as effective as additive C in their recommended concentrations in the HFPO triazine at 600°F.

Oxidation-corrosion data with the perfluoroalkylpolyether fluid from manufacturer Number 2, MIL-73-23 appears on Table VI. Due to insufficient sample, complete characterization of the fluid with all metal combinations and all temperatures of interest was not conducted. Some inferences are made by relating the data obtained on this fluid to that obtained on the similar fluid produced by the other manufacturer.

The reactivity of WD-65 by itself was minimal at 500°F up to 600°F. This same performance could be attributed to WD-65-53 at those temperatures by extending the data accumulated on the perfluoroalkylpolyether of different manufacturer. Both hardness levels showed excessive attack at 650°F with a dark tarnish appearance. Interpolated data in Figure 2 shows failure would occur in the neighborhood of 630°F.

In combination with the dissimilar metals, both WD-65's remained passive from 500°F to 600°F with only the silver specimen exceeding the acceptable corrosion limits. This same behavior of nonreactivity of WD-65's was observed with the ferrous metal group at both of the above temperatures. At 600°F, however, all the other ferrous metals showed excessive corrosion in the presence of WD-65-53. Again utilizing previous data obtained on the similar fluid, corrosion of the ferrous metals in the presence of WD-65 could be assumed at 600°F. The appearance of the WD-65's throughout the dissimilar and ferrous metal evaluations was dull metallic with no discoloration. Fluid deterioration at 600°F with both mixed metal combinations ranged from borderline passing to failure as indicated by high viscosity changes, volatilities, and acid numbers.

312

As a result of this program the conclusions that were reached are as follows:

1. Both hardness levels of WD-65 showed little reactivity with the currently available perfluorinated fluids up to 700°F.

2. Both WD-65's were nonreactive in the presence of dissimilar metals up to 700°F.

3. Both WD-65's were nonreactive in the presence of ferrous metals up to 700°F.

4. Neither hardness level of WD-65 appeared to catalyze the failure of either dissimilar or ferrous metals.

5. Neither WD-65 contributed to any lack of additive response in the perfluorinated fluids.

6. Both WD-65's were substantially less reactive under all conditions and with all fluids than M-50 or 52100 bearing steels (Figures 3 and 4).

7. The difference in hardness level of R_c 12 between the two WD-65 alloys did not affect their reactivity in the perfluorinated fluids investigated up to 700°F.

TABLE III

WD-65 ALLOY EVALUATION IN PERFLUORINATED FLUIDS, MLO-73-20,
OXIDATION-CORROSION STUDIES RESULTS

Fluid Identity	Test Temp. °F	Viscosity Change @ 100°F %	Acid No. Mg KOH/g	Fluid Loss %	Metal Weight Change, Mg/cm²						Remarks: WD-65 Metal Appearance
								WD 65	Rc 53		
Perfluoro-alkylpoly-ether	550	+3.1	NIL	2.0	+0.03	+0.23	+0.05	+0.09	+0.02		Light tan stain; some peacock; no pitting
	575	+3.8	NIL	4.0	+0.03	+0.02	+0.02	0.00	+0.01		Light deposit; peacock coloration
	600	+2.8	NIL	4.0	+0.01	+0.06	+0.09	+0.10	+0.12		Slight peacock
	650	+2.8	NIL	4.4	+0.47	+0.31	+0.42	+0.30	+0.24		Heavy black deposit; heavy peacock
								WD-65	Rc 65		
MLO-73-2Q	550	+3.1	NIL	1.0	+0.52	+0.12	+0.07	+1.1	+0.10		Light tan stain; some peacock
	575	+3.8	NIL	4.0	-0.01	-0.02	-0.02	-0.07	-0.05		Light deposit; peacock
	600	+3.8	NIL	4.0	+0.08	+0.08	+0.08	+0.05	+0.02		Slight peacock
	650	+2.7	NIL	4.7	+0.34	+0.33	+0.44	+0.50	+0.70		Heavy black deposit
					Dissimilar Metals w/WD-65						
					Ti	Al	Rc 53	M-10	Ag	301 St.St.	
	500	+30.6	NIL	15.3	0.00	-0.04	—	-0.02	-0.06	-0.04	None
	500	+11.0	NIL	4.0	+0.04	+0.02	+0.03	0.00	-0.07	0.00	Tan tarnish
	550	+ 3.5	NIL	9.8	+0.36	+0.40	+0.33	+0.14	+0.04	+0.18	Tan tarnish
	600	+ 4.8	NIL	9.8	+0.35	+0.38	+0.52	+0.56	+0.47	+0.57	Tan tarnish, spotted
							Rc 65				
	500	+7.2	NIL	2.4	+0.04	+0.02	+0.05	0.00	-0.02	+0.04	Tan tarnish
	550	+3.5	NIL	10.0	+0.44	+0.28	+0.47	+0.13	+0.14	+0.12	Tan tarnish
	600	+5.5	NIL	10.0	+0.30	+0.23	+0.47	+0.52	+0.12	+0.25	Tan tarnish spots
					Ferrous Metals w/WD 65						
					4140	52100	Rc 53	410	M-50	440c	
	500	+2.4	NIL	0.5	+0.05	+0.02	+0.03	+0.03	+0.09	+0.02	Light tarnish
	600	+1.7	3.1	3.9	-6.90	+2.48	-0.04	-5.78	-8.27	-3.47	Light black tarnish
							Rc 65				
	500	+1.7	NIL	0.3	+0.05	+0.02	+0.05	+0.02	+0.03	-0.02	Light tarnish
	600	+1.7	3.1	6.1	-6.80	+1.51	+0.02	-0.45	-1.88	+2.38	Light black tarnish

TABLE IV

WD-65 ALLOY EVALUATION IN PERFLUORINATED FLUIDS, MLO-73-21, OXIDATION-CORROSION STUDIES RESULTS

Fluid Identity	Test Temp °F	Viscosity Change @ 100°F %	Acid No. Mg KOH/g	Fluid Loss %	Metal Weight Change, mg/cm²						Remarks: WD-65 Metal Appearance
					Ti	**Al**	**Rc 53**	**WD 65**	**Rc 53**		
Perfluoro-alkylpoly-ether plus proprietary inhibitor additive MLO-73-21	650	−89.5	0.06	5.5	−0.12	+0.10	−0.05	−0.060	−0.09		Slight stain
	700	+ 5.6	–	8.4	+0.03	+0.03	+0.01	+0.03	0.00		Slight stain
					Ti	**Al**	**Rc 53**	**WD 65**	**Rc 65**		
	650	−89.4	0.22	5.8	+0.05	+0.07	+0.04	+0.04	+0.06		Slight stain
	700	+ 5.6	–	8.4	+0.05	+0.07	+0.06	+0.04	+0.01		Slight stain
					Dissimilar Metal W/WD 65						
					Ti	**Al**	**Rc 53**	**M-10**	**Ag**	**301 St.St.**	
	550	+30.8	–	24.4	+0.02	0.00	+0.02	+0.03	+0.06	+0.01	Slight stain
	600	+11.2	–	6.9	−0.01	+0.02	0.00	−0.07	−0.02	−0.05	Slight stain
	700	−27.4	0.27	29.9	+0.09	+0.23	+0.08	−0.28	−0.17	+0.03	Slight stain with carbon spots
							Rc 65				
	550	+17.6	–	15.3	0.00	−0.02	+0.01	+0.02	+0.02	+0.27	Slight stain
	600	+10.9	–	6.1	−0.02	+0.03	−0.02	−0.04	−0.05	−0.03	Slight stain
	700	+17.2	–	16.6	−0.01	+0.07	+0.09	−0.03	−0.03	+0.09	Slight stain
					Ferrous Metals W/WD 65						
					4140	**52100**	**Rc 53**	**410**	**M-50**	**440c**	
	550	+ 1.9	–	0.03	+0.15	+0.15	+0.09	+0.08	+1.10	−0.03	Slight stain
	600	+ 2.6	–	0.6	+0.23	+0.15	−0.01	−0.04	+0.16	0.00	Slight stain
	700	+ 6.0	0.52	26.0	−7.14	+2.5	−0.14	−3.2	−9.63	−14.5	Slight stain with carbon spots
							Rc 65				
	550	+ 2.3	–	0.0	+0.16	+0.08	+0.02	+0.04	+0.06	+0.07	Slight stain
	600	+ 2.2	–	0.3	+0.18	+0.13	+0.04	0.00	+0.13	+0.07	Slight stain
	700	+ 4.1	–	25.0	−5.94	+1.62	−0.20	−7.88	−8.54	−15.4	Heavy mottled deposit

315

TABLE V

WD-55 ALLOY EVALUATION IN PERFLUORINATED FLUIDS, MLO-73-22, OXIDATION-CORROSION STUDIES RESULTS

Dissimilar Metals w/WD-65

Fluid Identity	Test Temp. °F	Viscosity Change @ 100°F %	Acid No. Mg KOH/g	Fluid Loss %	Ti	Al	Rc 53	M-10	Ag	301 St.St.	Remarks: WD-65 Metal Appearance
HFPO	650	+ 0.23	–	4.81	+0.06	+0.05	+0.04	+0.06	+0.04		No stain or deposits
Triazine	700	– 0.8	–	15.3	+0.09	+0.06	+0.05	+0.09	+0.08		Light stain to spot deposits
MLO-73-22	650	+ 0.63	–	4.52	0.00	+0.02	-0.03	-0.03	-0.03		No stain or deposits
	700	+ 0.7	–	16.8	+0.27	+0.22	+0.14	+0.20	+0.17		Light stain to spot deposits
	600	+11.2	–	6.86	-0.01	+0.02	0.00	-0.07	-0.02	-0.05	No stains or deposits
	650	+ 7.0	–	9.1	-0.10	+0.14	+0.10	+0.10	-0.06	+0.05	–
	650	+12.6	–	7.9	+0.05	+0.14	+0.03	+0.03	-0.06	+0.03	–
	700	+25.5	<0.1	26.7	+0.47	+0.14	-0.72	-0.72	-0.18	+0.04	Golden stain
	700	+12.3	0.11	21.1	+0.44	+0.10	-0.80	-0.80	-0.05	+0.04	Not recorded
+5% ADD C	600	+10.9	–	6.08	-0.02	-0.03	-0.02	-0.04	-0.40	-0.03	No stains or deposits
+5% ADD C	700	+21.4	<0.1	16.9	+0.30	+0.12	+0.13	-0.46	-0.46	0.00	Golden stain
+5% ADD C	700	+ 6.2	0.12	25.8	+1.48	+0.17	-0.01	-0.56	-0.54	+0.02	Not recorded

Ferrous Metals w/WD-65

Fluid Identity	Test Temp. °F	Viscosity Change @ 100°F %	Acid No. Mg KOH/g	Fluid Loss %	4140	52100	Rc 53	410	M-50	440c	Remarks: WD-65 Metal Appearance
+2% M-4	500	+ 1.8	<0.1	0.6	+0.05	+0.04	+0.03	+0.09	+0.11	+0.08	Tan tarnish
+5% M-4	600	+ 2.7	<0.1	0.3	+0.56	+0.33	+0.16	+0.14	+1.16	+0.17	Blue to tan stain
+2% ADD B	600	0.0	<0.1	2.7	+1.4	+1.1	+0.89	+1.1	+1.5	+0.72	Black spotted deposit
+5% M-4	600	0.0	<0.1	5.5	+1.8	+1.7	+2.9	+2.5	+2.2	+3.0	Heavy dark brown to black deposit
+2% ADD C	600	0.9	<0.1	2.4	+0.11	+0.12	+0.06	+0.07	+0.34	+0.06	No stain or deposit
+5% ADD C	600	+ 8.1	<0.1	0.5	+0.10	+0.02	+0.06	+0.07	+0.18	+0.10	No stain or deposit
+5% ADD C	650	+ 3.4	<0.1	0.3	+0.28	+0.19	+0.07	+0.19	+0.28	+0.50	Blue to tan stain
+2% M-4	500	+ 1.8	–	0.3	+0.06	+0.04	+0.05	+0.09	+0.11	+0.16	Tan tarnish
+5% M-4	600	+ 1.8	–	0.3	+0.24	+0.15	+0.04	+0.09	+0.58	+0.06	Blue to tan
+2% ADD B	600	+ 0.9	–	2.7	+1.5	+1.2	+1.1	+0.77	+1.1	+1.2	Black spotted deposit
+5% M-4	600	– 0.9	–	5.3	+2.6	+2.6	+2.0	+2.1	+2.9	+2.8	Heavy dark brown to black deposit
+2% ADD C	600	+ 0.9	–	2.1	+0.11	+0.08	+0.18	+0.07	+0.25	+0.11	No stain or deposit
+5% ADD C	600	+ 7.2	–	0.5	+0.07	+0.06	+0.08	+0.12	+0.14	+0.11	No stain or deposit
+5% ADD C	650	-12.7	–	0.4	+0.18	+0.19	+0.10	-0.12	-0.23	+0.28	Blue to tan stain

TABLE VI

WD-65 ALLOY EVALUATION IN PERFLUORINATED FLUIDS, MLO-73-23, OXIDATION-CORROSION STUDIES RESULTS

Fluid Identity: Perfluoro-alkylpolyether, Mfg No. 2, MLO-73-23

Test Temp. °F	Viscosity Change @ 100°F %	Acid No. Mg KOH/g	Fluid Loss %	Metal Weight Change, Mg/cm^2	Remarks: WD 65 Metal Appearance
500	+ 6.7	NIL	2.5	No Metals	
600	+405	not sufficient sample		No metals	

Metal Weight Change, Mg/cm^2 — Metals: Ti, Al, Rc 53, M-10, Ag

Test Temp. °F	Viscosity Change %	Acid No.	Fluid Loss %	Ti	Al	Rc 53	M-10	Ag	Remarks
650	-17.0	-	16.5	+0.25	+0.24	+0.38	+0.31	+0.30	Dark Tarnish

Metal Weight Change, Mg/cm^2 — Metals: Ti, Al, Rc 53, WD 65, Rc 65

Test Temp. °F	Viscosity Change %	Acid No.	Fluid Loss %	Ti	Al	Rc 53	WD 65	Rc 65	Remarks
500	+ 1.32	NII	1.69	-0.02	0.00	+0.01	0.00	+0.02	
600	- 1.08	NII	1.96	-0.01	-0.02	-0.03	-0.02	-0.01	
650	-11.2	-	10.7	+0.36	+0.41	+0.39	+0.24	+0.22	Dark tarnish

Dissimilar Metals w/WD 65, Rc 53 — Metals: Ti, Al, Rc 53, M-10, Ag, 301 St.St.

Test Temp. °F	Viscosity Change %	Acid No.	Fluid Loss %	Ti	Al	Rc 53	M-10	Ag	301 St.St.	Remarks
500	+ 6.81	0.3	1.93	0.00	-0.03	-0.01	0.00	-0.01	-0.01	Dull; no discoloration
500	-71.8	5.3	31.6	+0.01	-0.04	-0.11	-0.05	-0.45	-0.07	

Rc 65 — Metals: Ti, Al, Rc 53, M-10, Ag, 301 St.St.

Test Temp. °F	Viscosity Change %	Acid No.	Fluid Loss %	Ti	Al	Rc 53	M-10	Ag	301 St.St.	Remarks
500	+ 4.25	0.2	0.55	-0.01	-0.03	-0.01	0.01	0.00	0.00	Dull; no discoloration
600	-23.6	0.61	25.8	+0.02	+0.12	-0.09	+0.08	-0.39	+0.050	

Ferrous Metals — Metals: 4140, 52100, Rc 53, 410, M-50, 440c

Test Temp. °F	Viscosity Change %	Acid No.	Fluid Loss %	4140	52100	Rc 53	410	M-50	440c	Remarks
500	+ 2.76	NIL	0.0	+0.01	0.00	-0.03	-0.04	+0.01	+0.03	Dull; no discoloration
600	-82.9	6.6	48.6	-2.27	+0.68	+0.04	-4.07	-4.44	-5.34	

Rc 65 — Metals: 4140, 52100, Rc 53, 410, M-50, 440c

Test Temp. °F	Viscosity Change %	Acid No.	Fluid Loss %	4140	52100	Rc 53	410	M-50	440c	Remarks
500	+ 3.0	NIL	0.0	+0.05	+0.01	+0.02	0.00	+0.02	+0.02	Dull; no discoloration
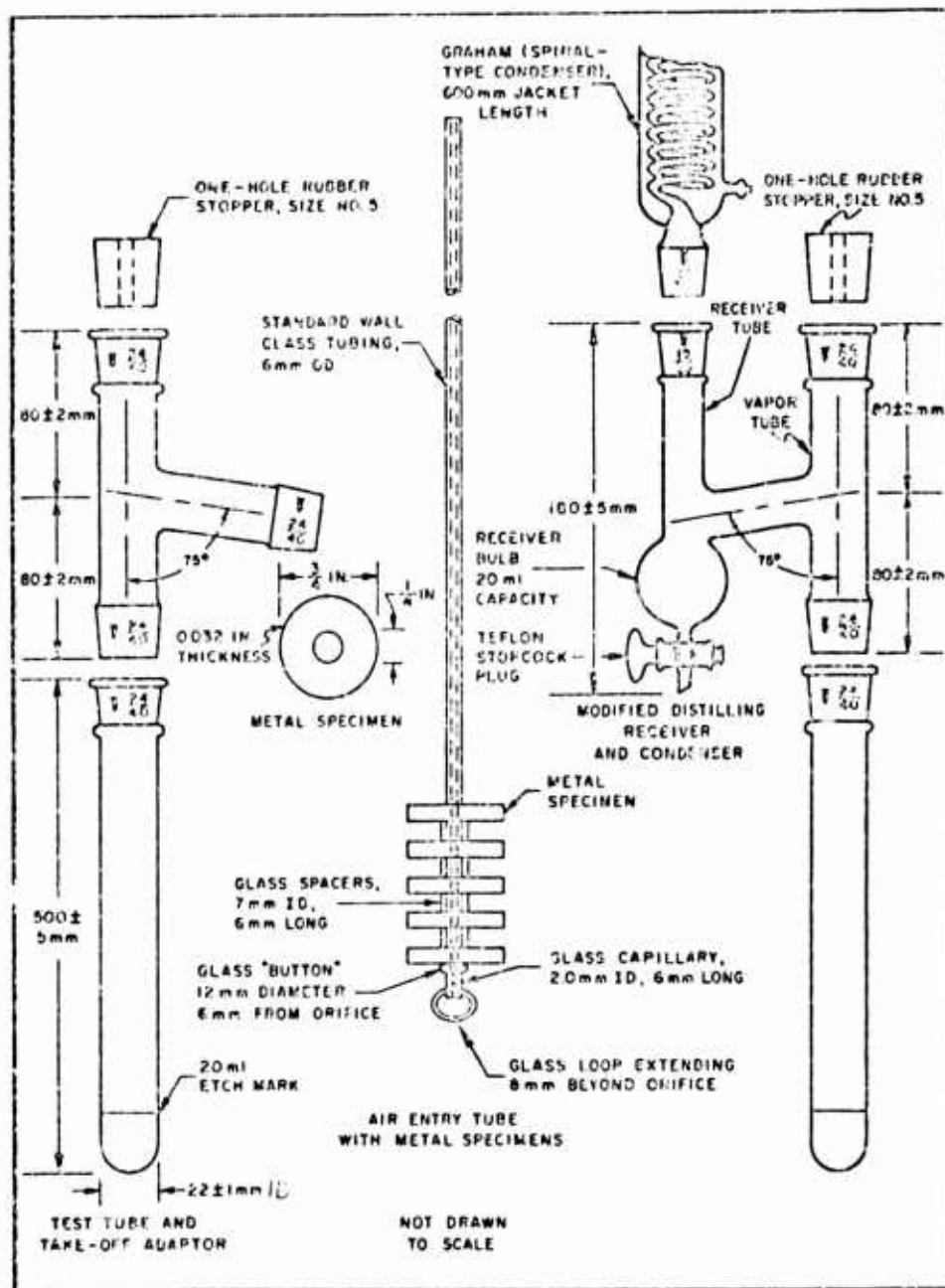
Figure 1. Micro-O-C Test Apparatus

318
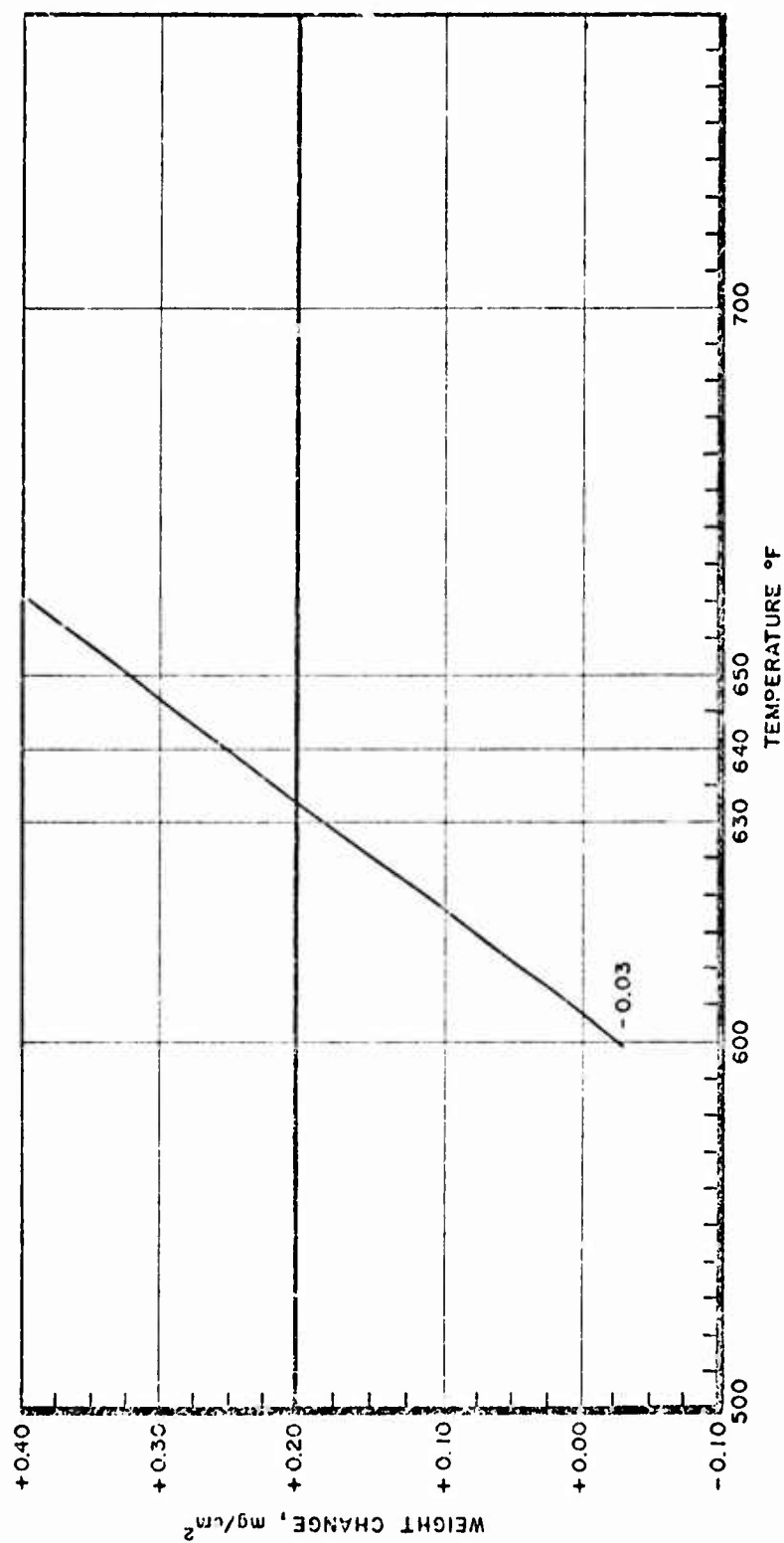
Figure 2. WD-65 Corrosion in MLO-73-23 Fluid

319
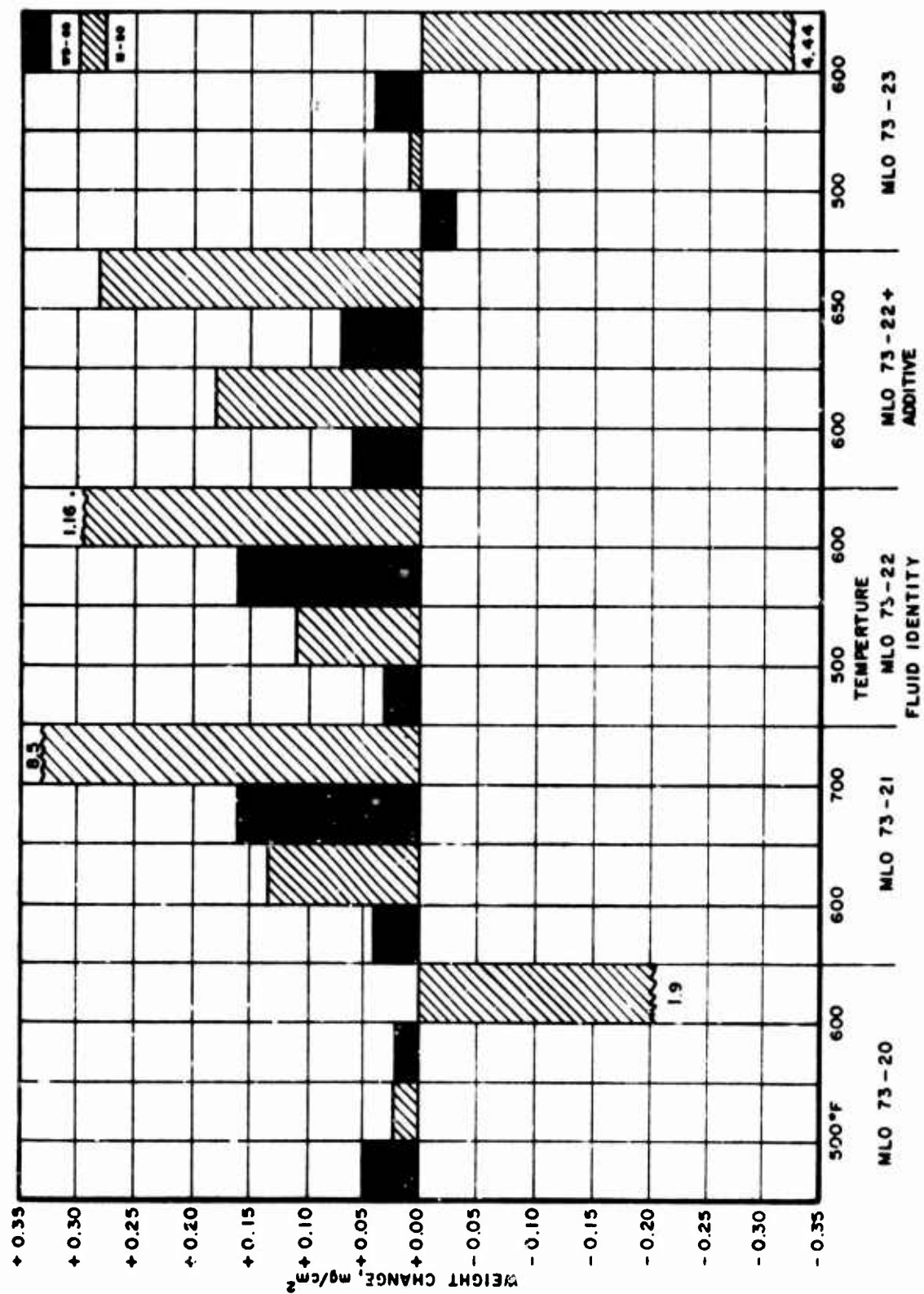
Figure 3. WD-65-M-50 Corrosion Comparison
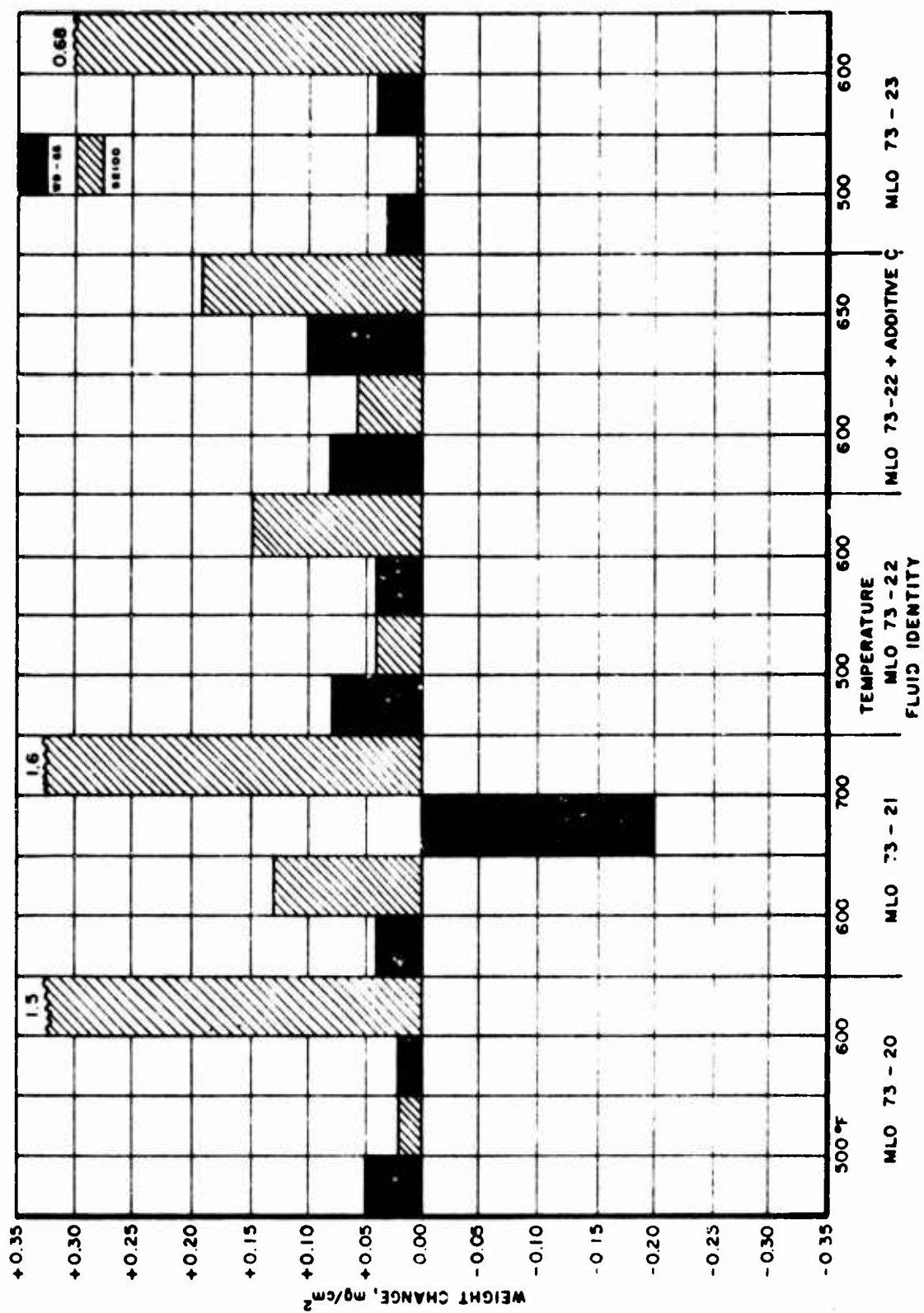
Figure 4. MD-65-52100 Corrosion Comparison

EFFECTS OF GRAPHITE-EPOXY COMPOSITE MATERIALS
ON THE CORROSION BEHAVIOR OF AIRCRAFT ALLOYS

Philip Fischer

and

John J. DeLuccia

Naval Air Development Center
Warminster, Pennsylvania 18974

ABSTRACT

Electrochemical tests were performed to show the nature of galvanic corrosion when graphite-epoxy composite materials are coupled to aluminum and titanium alloys. Open circuit potential measurements in 3.5% NaCl solution showed approximately one volt potential difference between the composite and 7075-T6 and 7075-T651 aluminum alloys. This relatively large potential dissimilarity provides the driving force for corrosion of the aluminum as an anode and is cause for concern. The potential difference between Ti-6-4 and the composite was about 0.3 volt for the as received unpolished metal surface vs. 0.5 volt for a freshly polished surface.

Corrosion current data (zero impedance technique) show that aluminum alloys, cadmium plate, cadmium plate + chromate conversion coat are much more reactive than Ti-6-4 when coupled to graphite-epoxy ($\sim$15 vs. 0.002 $\mu A/cm^2$). This technique provides a means of ranking the corrosion problem when graphite-epoxy is coupled to various aircraft alloys.

Flatwise tensile data indicated significant strength losses when graphite-epoxy composite sandwich specimens are exposed to salt spray and synthetic sea water + SO_2 spray environments. For two week exposure tests the comparative strength losses in the two environments were 41 vs. 78 per cent respectively. These strength losses were greater than those for all aluminum specimens and definitely shows the corrosion effect of coupling graphite-epoxy to aluminum as compared with specimens where galvanic effects are minimized.

Data obtained show that galvanic coupling of graphite-epoxy composite to 7075-T651 aluminum alloy has no effect on the stress corrosion cracking behavior of the alloy, but does increase its general corrosion.

INTRODUCTION

As a result of the demand for new materials that will outperform the traditional monolithic materials, organic matrix composites with inherent high strength to weight ratios and high moduli have been developed for use as an airframe material. Chief among these is the graphite-epoxy composite material that utilizes a number of plies of graphite fibers impregnated in an epoxy matrix. These composites offer engineers the opportunity to design with totally new materials to "tailor fit" a combination of properties for a specific task. The principal efforts to date have been directed toward graphite-epoxy's mechanical and structural behavior as well as its use in fabrication of components. Initial work on the compatibility of graphite-epoxy composites with metallic materials indicated a potential galvanic corrosion problem.[1]

Due to the inherent nobility of the filamentary graphite, it is anticipated that this problem will surface as the use of composites increases, and may be compounded by new methods of attachment, e.g., adhesive bonding, stepped structures, mechanical fastener configurations, etc. These combinations can lead to multi-component galvanic couples with the problem being particularly aggravated by the carrier based environment that naval aircraft must endure. Quantifying these areas of concern is of vital interest for the eventual use of filamentary graphite composites in optimizing design concepts.

In this study electrochemical, mechanical and stress corrosion cracking (SCC) data were obtained to define and evaluate the potential galvanic corrosion problem in the naval air-sea environment. The electrochemical approach has become an important technique for studying corrosion problems from a design engineering point of view because it provides rapid and accurate information indicating the severity of the corrosion problem[2,3]. Mechanical tests were performed to determine the degree of degradation (loss of strength) of the composite and "sandwich specimens" (composite faces bonded to aluminum honeycomb), when subjected to salt spray, synthetic sea water + SO_2 and high humidity environments. A study of the galvanic effects of graphite-epoxy composite material on the stress corrosion crack growth rate of 7075-T651 aluminum alloy was performed.

EXPERIMENTAL PROCEDURE

Test Specimens

The filamentary graphite-epoxy composite was made from Narmco 5206-II, a tape of "Modmor", Type II, coated with a modified epoxy resin system. The graphite-epoxy pre-impregnated layers were fabricated into 6 ply laminates, which were oriented $0° + 45°$, $-45°$, $-45°$, $+45°$, $0°$. The final thickness of the composite was 0.033 in. Details of the layup and cure procedures are given in reference (4).

The metal specimens of aluminum 7075-T6, 5052-H38, and titanium 6Al-4V were in sheet form. The aluminum 7075-T651 alloy was machined from plate stock. The cadmium plated and the chromate conversion coated cadmium plated specimens utilized low alloy steel as a substrate.

Specimen Preparation

All specimens received a cleaning treatment prior to making electrochemical potential measurements. The composite was rinsed with distilled water and air dried for one hour. The cadmium and chromate conversion coated steel specimens were cleaned in boiling benzene for 5 minutes. Measurements were made for sheet aluminum and titanium alloys in the as received condition and after polishing. The polishing procedure consisted of an initial polish with 320 grit silicon carbide paper followed by 4/0 grit paper. All metal specimens received a final 5 minute cleaning in boiling benzene. Measurements on the polished specimen were made approximately ½ hour after polishing. After the initial potential measurement, the polished specimen was rinsed in distilled water, dried in air and then measured again 24 hours later.

Open Circuit Potential Measurements

The open circuit potential or driving force associated with corrosion reactions was measured with an electrometer or a potentiostat. Measurements were made in 3.5% sodium chloride solution (wt %) with a saturated calomel electrode (SCE) as the reference standard. The output of either instrument was connected to a strip chart recorder and the potential was recorded until it became constant (approximately one hour).

Galvanic Current Measurements

The galvanic current which gives an indication of the couple's corrosion severity, was measured using the zero impedence technique. A potentiostat was used as a zero impedance instrument by appropriate external connections. The experimental setup for the measurements made in this study is shown in Figure 1 (5). In this mode one specimen of the galvanic couple was connected to the working electrode and the other specimen to the reference electrode shorted to the auxiliary electrode. With the potentiostat set at 0.000V applied potential, the galvanic current can be read directly or recorded continuously.

Stress Corrosion Cracking (SCC) Test

The objective here was to determine the effect, if any, that graphite-epoxy composite would have on a growing stress corrosion crack in a high strength aluminum alloy to which it was coupled. A fracture mechanics approach was used with the final result showing the stress corrosion crack growth rate vs. the stress intensity factor K_I.

Test Specimen

Specimens were machined from aluminum 7075-T651 plate 2-3/4 in. thick, 15 in. wide and 5 in. long so that the notch hence cracking would proceed in a direction normal to the short transverse direction. Mechanical properties are listed in Table I. T The double cantilever beam (DCB) configuration used in this study is shown in Figure 2.
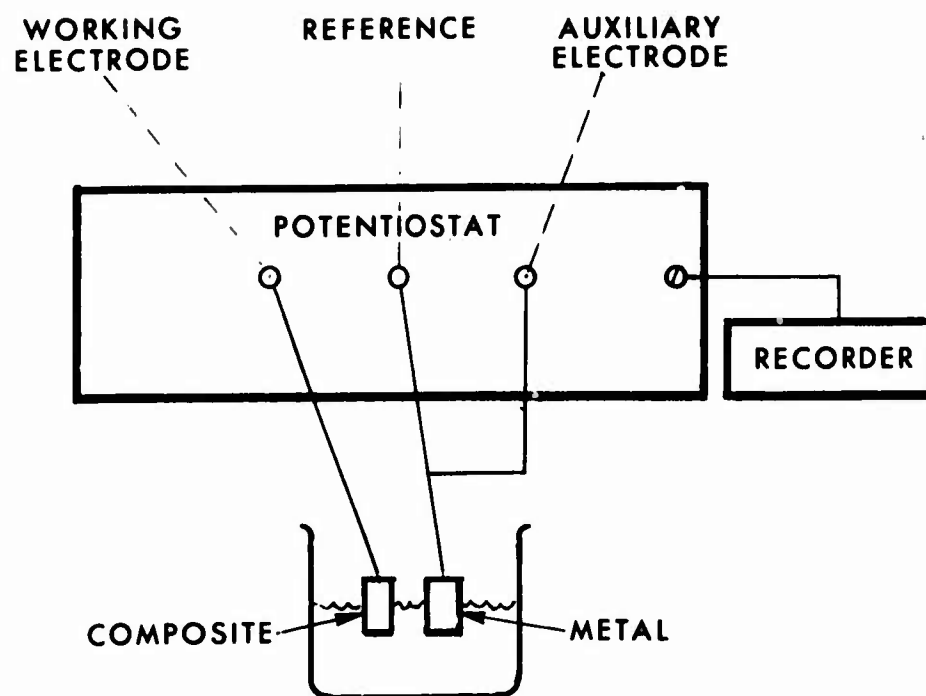
FIGURE 1   ZERO RESISTANCE CIRCUIT FOR MEASUREMENT OF
GALVANIC CORROSION CURRENTS
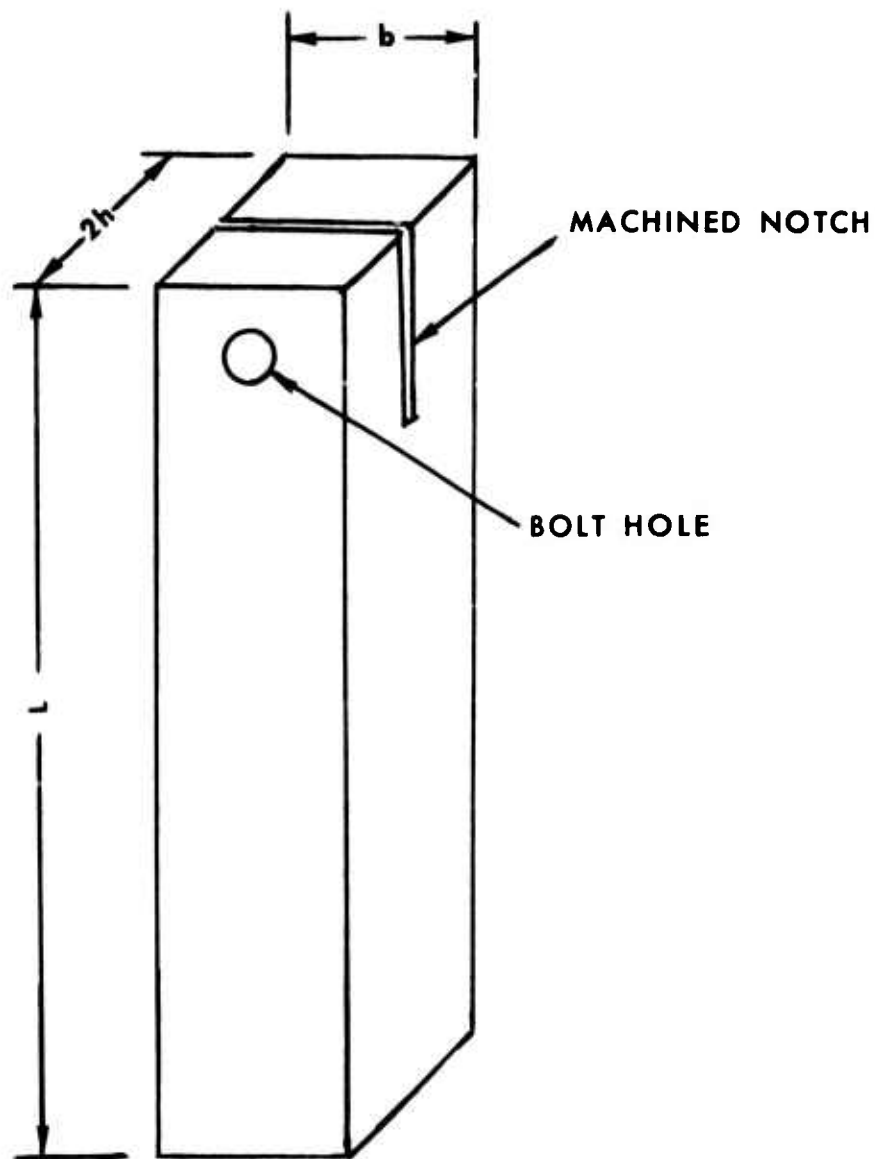
FIGURE 2   DOUBLE CANTILEVER BEAM SPECIMEN

TABLE I

MECHANICAL PROPERTIES OF 7075-T651 ALUMINUM ALLOY
STRESS CORROSION CRACKING TEST SPECIMENS

	Longitudinal		Short Transverse	Conductivity
	Yield Strength (KSI)	Tensile Strength T_u (KSI)	$K_{I_{SCC}}$ (KSI in)	% I.A.C.S.*
7075-T651 *	68	76	7	32
Test Material	74	81	11.5	32.5

* International Annealed Copper Standard

Side grooving was considered unnecessary since the elongated grain structure of the plate material and the intergranular nature of stress corrosion cracking in aluminum alloys combine to keep the cracks in a plane. The specimens were taken only from the center section of the plate thickness to insure uniformity, thus eliminating any possible structural discontinuities associated with the rolling surface. After the specimens had been milled, loading bolt holes were machined and a notch cut with a wafering saw. The surfaces along which the crack would be measured were polished with metallographic grinding paper down to a 600 grit finish.

The test set up designed and fabricated for this work is illustrated in Figure 3. The stand and bolts are made of Nylon so that for this particular situation they are essentially inert and non-conductive. With this fixture the DCB specimen stands in a vertical position and permits positioning a number of composite strips at a chosen distance from and parallel to the side of the specimen along which the crack will grow. The electrical circuit is completed by connecting a copper wire from the top of the graphite-epoxy composite strips to the DCB specimen by way of the high strength steel stressing bolts.

SCC TEST PROCEDURE

The test procedure consisted of measuring the specimen height (2h), width(b) and length(l). The steel bolt end of the specimen was then masked with a vinyl coating to prevent any galvanic action with the bolts. Once the coating dried, the machined notch was wet with a 3.5 percent aqueous NaCl solution and the crack was popped in by simultaneously advancing both bolts thus creating a wedging action k that results in tension at the root of the notch. When the crack had reached 0.1 inch in length, the stressing was stopped. A measurement was then made of the specimen height(2h) at the bolt centerline to determine the deflection(v). The specimens were then placed in the test environment, a 3.5 percent aqueous NaCl solution at 22°C (72°F). The salt solution was changed once a week and room temperature was kept constant. Crack lengths were monitored daily with measurements taken on both sides of the specimens. In order to determine the ultimate length of the stress corrosion crack, the specimens were broken open after a period of time when crack arrest was assumed. This provided the final point to the crack growth data.

Curves of crack length versus time were prepared from the resulting data. The slopes of the curves at different crack lengths provide crack growth rate data

---

* values according to Hyatt (6,7)

COUPLING WIRES

COMPOSITE STRIPS

NYLON STAND AND BOLTS
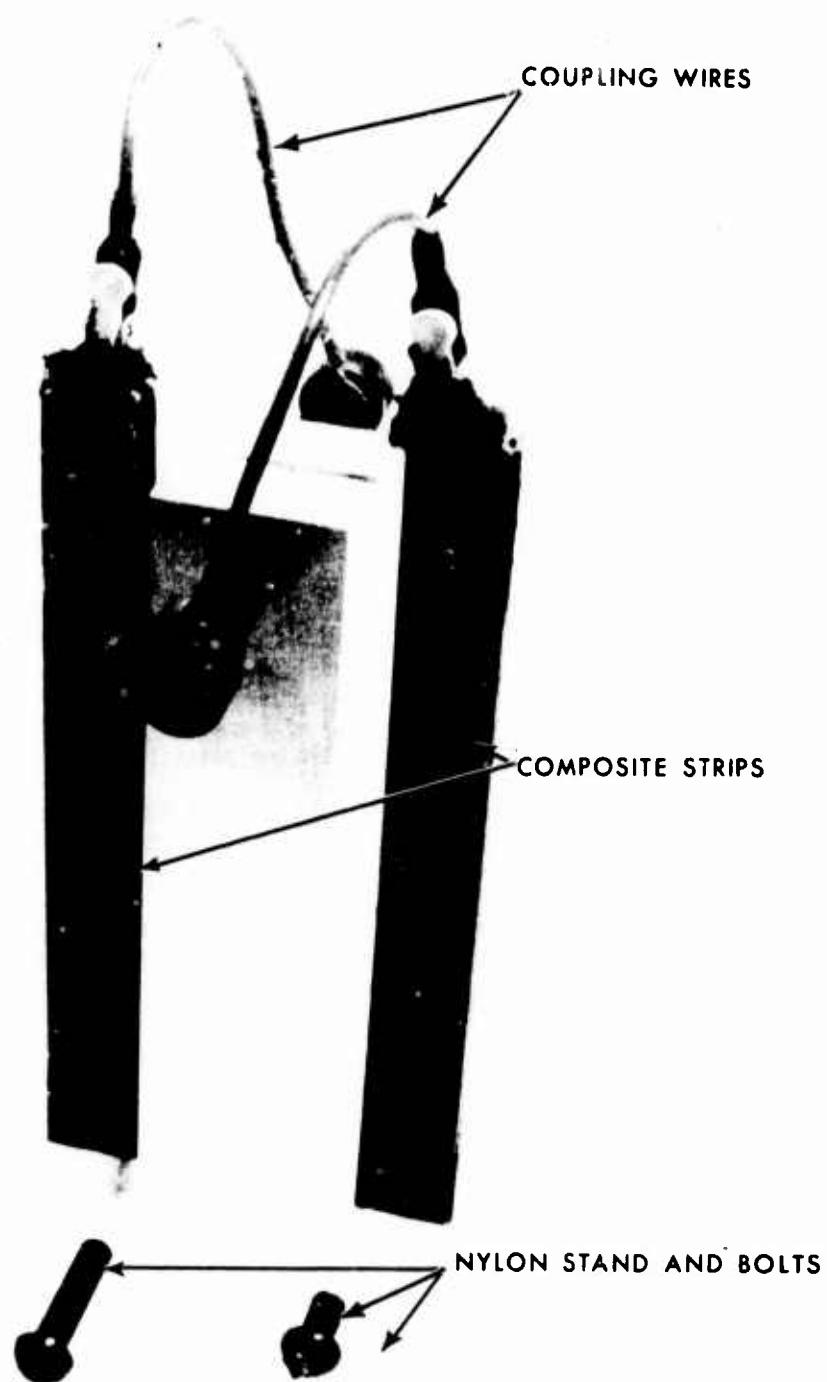
1.25X

FIGURE 3   TEST SETUP FOR GALVANIC COUPLING OF GRAPHITE-EPOXY
COMPOSITE TO DCB SPECIMEN

330

as a function of K_I. The crack length at which growth ceases was then used to determine $K_{I_{SCC}}$ that is the stress corrosion cracking stress intensity limit in 3.5% aqueous salt solution. The equation used (6,7) to calculate K is as follows:

$$K_I = \frac{vEh}{4} \frac{(3h(a + .6h)^2 + h^3)^{\frac{1}{4}}}{(a + .6h)^3 + h^2 a}$$

Though a true $K_{I_{SCC}}$ may not be feasible for the time limitation of this study, a relative value was chosen at a crack velocity of 1.4×10^{-5} inches per hour which is equivalent to one atomic bond fracturing along the entire crack front per second (8).

Corrosion Environments for Static Tests

Mechanical test specimens were exposed to the following three environments for one and two week periods:

Salt Spray (Fog) Test

The ASTM standard test method B117-64 was used for salt (NaCl) spray (fog) testing. The apparatus consists of a fog chamber, a salt solution reservoir, compressed air, heaters and controls to meet the requirements of the test method. The salt solution was composed of 5 ± 1 parts by weight of NaCl in 95 parts of distilled water. The temperature of the atomized solution was 35°C(95°F) and the pH of the collection solution was 6.5 to 7.2.

Synthetic Sea Water + SO_2 Spray (Fog) Test

This test environment employs a cabinet similar to that used in the above ASTM salt spray test method. Synthetic sea water was prepared by dissolving 41.953 grams of "sea-salt" (simulated sea salt mix) in one liter of distilled water, SO_2 gas was injected at regular intervals.

Conditions in the cabinet were as follows:

Synthetic sea water spray solution	pH 6.5 - 7.2
Cabinet temperature	35°C (95°F $\pm$ 2°)
Tower temperature	45.5°C (114°F $\pm$ 2°)
SO_2 gas injection cycle	1 hour every 6 hours
SO_2 gas flow	25 cc/min.

Conditions shall be such so as to maintain a:

Collection rate	1 to 2 ml/hr
pH	1.8 - 2.5
Specific gravity	1.025 - 1.040

Humidity Test

Relative humidity tests were performed at 95% relative humidity at 49°C (120°F). A controlled relative humidity cabinet was used.

331

Sandwich Flatwise Tension Test

The "sandwich" specimen used for flatwise tensile tests consisted of a core of honeycomb bonded with Metalbond 329 to 2 in. x 2 in. facings of either sheet aluminum or composite material. The three different material combinations of "sandwich" specimens tested were:

(1) Graphite-epoxy composite faces bonded to 5052 aluminum honeycomb

(2) Graphite-epoxy composite faces bonded to Nomex honeycomb

(3) 5052 aluminum alloy faces bonded to 5052 aluminum honeycomb

The aluminum honeycomb was 1/2 in. thick with a cell diameter of 3/16 in. and a cell density of 4.4 lb/cu.ft.

Flatwise tensile tests (application of forces in a direction normal to the plane of the sandwich) to pull the facings from the honeycomb core were performed in accordance with MIL-STD-401, Sandwich Constructions and Core Materials; General Test Methods (NOTE: ASTM C297 - Methods for Tension Test of Flat Sandwich Constructions in Flatwise Plane). The test was performed on specimens with faces bonded between metal loading blocks, 2 inches on a side, which are pulled apart in a testing machine. Tests were conducted at $177^\circ C$ ($350^\circ F$) with a 10,000 pound capacity Instron test machine at a grip separation speed of 0.05 in./min.

Horizontal Shear Test (Short Beam Test)

A composite specimen 0.6 in. long, 0.5 in. wide, and approximately 0.03 in. thick was used for the test. The force was applied by a 3/8 in. diameter pressure foot to the center of the specimen placed on 3.8 in. diameter rollers spaced 0.4 in. apart. Horizontal shear stress at failure was calculated using the following formula (9):

$$\text{stress (psi)} = \frac{3P}{4bt}$$

P = total load at failure (pounds)
b = specimen width (inches)
t = specimen thickness (inches)

Tensile Test

The graphite-epoxy composite tensile test specimens were one in. wide and nine in. long with 1½ in. long tabs at the ends. Longitudinal and transverse strain during loading was obtained from strain gages placed at the center of the specimen. A 10,000 pound capacity Instron test instrument was used and measurements made at a grip separation speed of 0.05 in./min.

RESULTS AND DISCUSSION

Galvanic Corrosion Experiments

The objective of the initial phase of the study of the galvanic corrosion problem was to perform fast simple tests to note the nature and degree of corrosion attack when graphite-epoxy composite material is coupled to structural metals and exposed

to a corrosive environment. This was accomplished by coupling the composite to aluminum 5052·H38, titanium 6Al-4V and by coupling aluminum to Plexiglas (as a control). The couples were exposed to the ASTM standard salt and synthetic sea water + SO$_2$ spray (fog) environments for one week. In order to conserve material, specimens 2 in. x 2 in. were used and were joined by two Nylon fasteners so that there was an overlap of two square inches of each material.

A summary of the test results are as follows:

TABLE II

GALVANIC CORROSION TEST RESULTS

Environment	Composite + Aluminum	Composite + Titanium	Plexiglas + Aluminum
Standard Salt Spray	Light Corrosion on surface	No corrosion	Very light corrosion
Synthetic Sea Water + SO$_2$ spray	Surface corrosion and pitting around drilled holes	No corrosion	Shallow pitting and slight corrosion on surface

Photographs of the disassembled couples of the aforementioned tests are shown in Figures 4 and 5. In Figure 4 (standard salt spray exposure) the 5052 Al coupled to the composite shows light surface corrosion, while that in contact with the Plexiglas shows very little, as evidenced by practically no corrosion products on the Plexiglas. In Figure 5 (synthetic sea water + SO$_2$ exposure) the 5052 aluminum in contact with the composite shows signs of surface corrosion and pitting around the drilled hole. For the aluminum Plexiglas couple there is evidence of some pitting and corrosion on the 5052 aluminum and corrosion products are visible on the Plexiglas. The anodic behavior of the aluminum is clearly evident when coupled to the more noble graphite-epoxy composite. Coupling to the inert Plexiglas caused no accelerated corrosion of the aluminum alloy.

Additional corrosion tests were performed on sandwich constructed specimens (synthetic sea water + SO$_2$ exposure). Honeycomb (5052 aluminum) was coupled by Nylon fasteners to faces of 5052 aluminum sheet. The specimens were coupled with and without a fiberglass interface. The purpose of the fiberglass was to isolate the metals to minimize galvanic corrosion. However, the specimens with the glass interface showed a marked increase in corrosion as is dramatically seen in Figure 6. The cause for this is most probably due to the wicking action of the fiberglass layer, thus creating a crevice to store corrodent. It should be emphasized that in actual practice the fiberglass layer would be continuously bonded to the honeycomb and the composite face so that the wicking problem would be minimized.

Electrochemical Measurements

Open circuit potential measurements (no current through the cell) were made in this study to show the degree of electrochemical disparity between the graphite-epoxy composite and structural aircraft alloys. The greater the electrochemical potential difference between the couples, the greater should be the galvanic corrosion experienced by them.

333

Results of open circuit potential measurements made in 3.5% NaCl solution (pH 7) are presented in Table III. A saturated calomel electrode was used as the standard against which all materials were measured. No attempt was made to remove dissolved oxygen from the solution.

TABLE III

OPEN CIRCUIT POTENTIAL MEASUREMENTS
VS. SATURATED CALOMEL ELECTRODE

Material	Potential
Graphite-Epoxy Composite (NARMCO 5206-II)	+170 mV
Aluminum 5052-H38	-760 mV
Aluminum 7075-T6	-770 mV
Aluminum 7075-T651	-780 mV
Cadmium	-865 mV
Cadmium plated steel (chromate conversion coating)	-735 mV
Titanium 6Al-4V (as received)	-140 mV
Titanium 6Al-4V (freshly polished surface)	-375 mV
Titanium 6Al-4V (above specimen 24 hrs. later)	-260 mV

The above results show potential differences of approximately 1 volt between the composite and the aluminum alloys as well as the cadmium and the cadmium plated steel which had a chromate conversion coating. These differences elicit a definite cause for concern. The potential difference between titanium-6Al-4V, although not quite as large, is quite revealing and indicates that a freshly polished surface, representative of a freshly drilled hole, is much more active than the as received material, whose surface has a more uniform and thicker inert oxide layer. Although the oxide reformation on a polished surface is considered to be rapid, the corrosion potential of the freshly polished surface after exposure to air for 24 hours is still more active than the as received sheet material. Similar corrosion potential measurements on freshly polished surfaces of the aluminum alloys showed only small differences.

It is to be noted that the potential difference between two metals only indicates the tendency of galvanic corrosion between a dissimilar metal couple and is not a measure of the corrosion rate. The size of the galvanic current, corresponding to corrosion rate of the anode in a galvanic couple is a function of the kinetic parameters, exchange current density, electrode polarization, as well as ratio of cathode to anode areas (2). The determination of corrosion rates is, therefore, the next study consideration.

The corrosion current (Imax) can be determined from the polarization diagrams of the materials of a galvanic couple (2). By Faraday's law, the corrosion rate of anodic areas on a metal surface is proportional to the corrosion current and can be expressed as a current density. However, this technique is a tedious one and obtaining good anodic polarization curves for aluminum alloys presents many problems.

The use of the zero impedance technique previously described provides a powerful tool for obtaining galvanic corrosion currents (I_{corr}) which approximates the corrosion current (Imax) determined from polarization diagrams (2). It must be

334

ALUMINUM 5052   ALUMINUM 5052
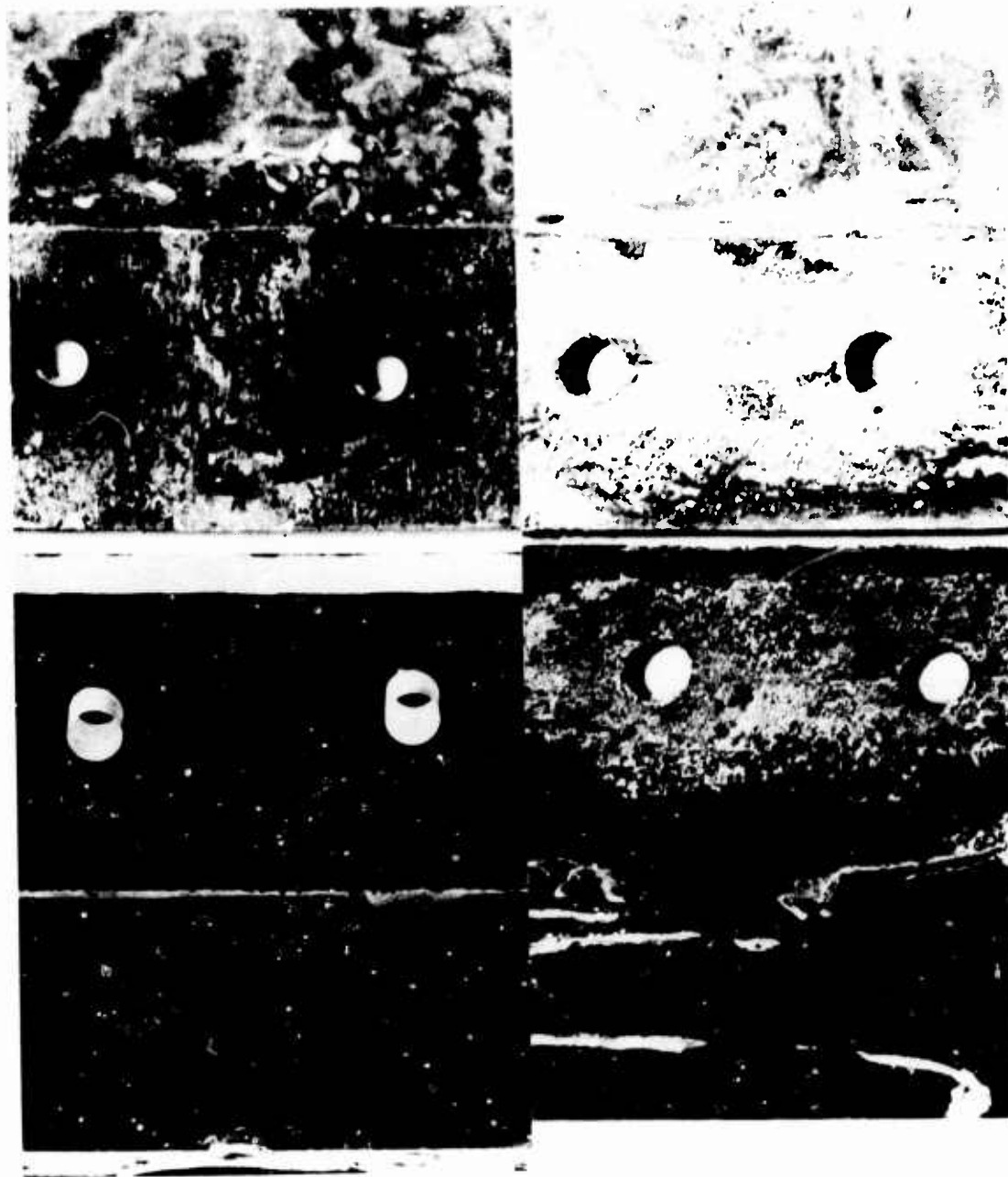
PLEXIGLAS   GRAPHITE-EPOXY COMPOSITE

FIGURE 4   GALVANIC CORROSION OF ALUMINUM 5052 COUPLED TO
GRAPHITE-EPOXY COMPOSITE AFTER ONE WEEK EXPOSURE
TO ASTM 5% SALT SPRAY TEST

ALUMINUM 5052   ALUMINUM 5052
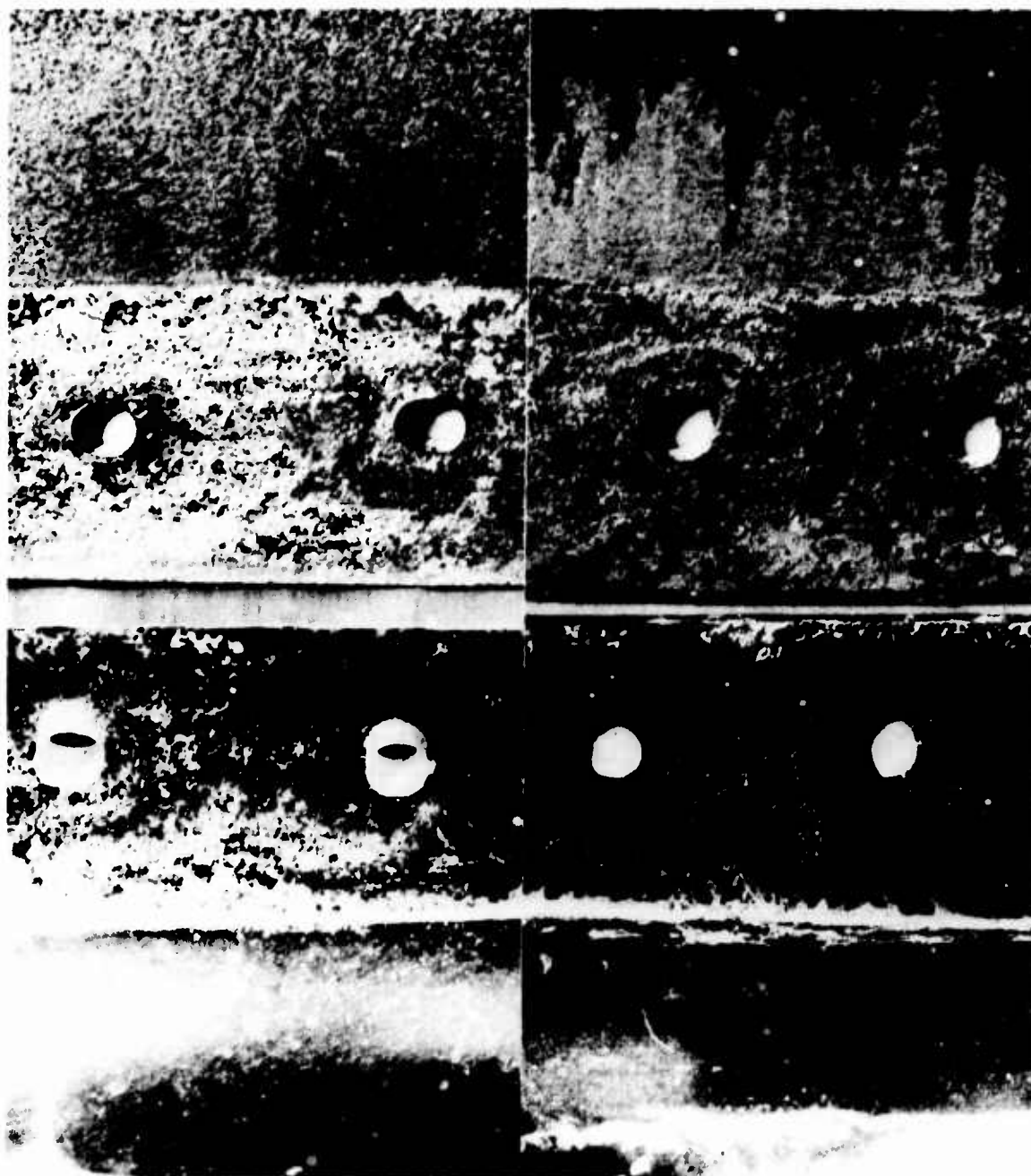
PLEXIGLAS   GRAPHITE-EPOXY COMPOSITE   2X

FIGURE 5 GALVANIC CORROSION OF ALUMINUM 5052 COUPLED TO
GRAPHITE-EPOXY COMPOSITE AFTER ONE WEEK EXPOSURE
IN SYNTHETIC SEA WATER + SO$_2$ SPRAY

NO GLASS INTERFACE   GLASS INTERFACE   1.5X

FIGURE 6 GALVANIC CORROSION OF ALUMINUM HONEYCOMB COUPLED TO ALUMINUM
5052 FACES BY NYLON FASTENER AFTER ONE WEEK EXPOSURE IN SYNTHETIC
SEA WATER + SO_2 SPRAY

337

mentioned that the dissolution rates calculated from galvanic current data and from weight loss data obtained for Al 7075-T6 differed (12 vs. 18 mdd* respectively). The weight loss measurement was based upon one week exposure of the aluminum alloy in 3.5% NaCl solution (no aeration); i.e., same composition for making the electro-chemical measurements.

This effect has also been observed by Mansfeld and Parry in their work with aluminum alloys coupled to coated stainless steel (10,11). It has been shown from theoretical considerations based on the mixed potential theory that in certain cases these deviations are to be expected. Correction procedures for aluminum alloys have been described (10-12).

Galvanic current measurements performed in 3.5% sodium chloride solution are pre-sented in Table IV. These results provide a means of ranking the galvanic corro-sion problem resulting from coupling graphite-epoxy composite material to the various aircraft alloys.

TABLE IV

ZERO IMPEDANCE GALVANIC CURRENT MEASUREMENTS
BETWEEN GRAPHITE-EPOXY COMPOSITE MATERIAL AND DESIGNATED ALLOYS

Couple	Galvanic Current $\mu A/cm^2$	mdd*
Composite Aluminum 5052-H38	12.7	10.3
Composite Aluminum 7075-T6	12.5	10.1
Composite Aluminum 7075-T651	14.4	11.7
Composite Cadmium	15.5	77.9
Composite Cadmium plate + chromate conversion coating	9.6	7.8
Composite Titanium 6Al-4V (as received)	0.002	.003
Composite Titanium 6Al-4V (freshly polished surface)	0.19	.27

*Corrosion rate calculated from the measured zero impedance currents, in milli-grams per square decimeter per day.

The calculated corrosion rate for the composite/aluminum couples shows that the aluminum 7075-T651 was slightly more reactive than the aluminum alloys 7075-T6 or 5052-H38. Cadmium was found to be about seven times more reactive. Although the chromate conversion coating over the cadmium reduced the galvanic current by 40 per cent, the reactivity was only slightly less than the aluminum alloys. The titanium alloys followed the expected pattern of having very low galvanic corrosion rates; e.g., four orders of magnitude lower than corresponding aluminum couples. However, the galvanic current for the freshly polished titanium was two orders of magnitude higher than that for the unpolished (as received) surface. The data clearly indicate that there is a galvanic corrosion problem for graphite-epoxy composites when coupled to structural aluminum alloys and cadmium plated high strength fasteners.

* mdd = corrosion rate in milligrams per square decimeter per day.

STRENGTH DEGRADATION DUE TO EXPOSURE TO DIFFERENT ENVIRONMENTS

Sandwich Specimens

Flatwise tensile tests were performed to assess degrading effects on the composite, bonding material and aluminum 5052 honeycomb subjected to high humidity, 95% RH at 49°C (120°F), the ASTM standard salt spray fog test, and synthetic sea water spray fog test environments. Flatwise tensile data were obtained at 177°C (350°F) on sandwich type specimens after a 30 minute soak at 177°C (graphite-epoxy composite faces bonded with Metalbond 329 an epoxy adhesive to aluminum 5052 honeycomb).

A second group of sandwich specimens were included in the same environmental tests in order to obtain more information on the controlling factors of strength degradation. This group consisted of the following material combinations:

Grapnite-epoxy faces bonded to aluminum 5052 honeycomb-with fiberglass interface.
Aluminum 5052 faces bonded to aluminum 5052 honeycomb.
Graphite-epoxy faces bonded to Nomex (organic) honeycomb.

The last two groups of specimens were considered non-galvanic controls because of the lack of dissimilarity of the couples. Results of flatwise tensile tests are presented in Table V.

The data show that there are significant reductions in strength of the sandwich specimens when subjected to the salt spray and synthetic sea water + SO_2 environments. A comparison of the standard deviation calculated from the flatwise tensile data for the control sandwich specimens (from one batch) is indicative of the rather wide scatter when testing this type of specimen (Table V).

It should be realized that galvanic effects might not be the sole factor for degradation, for example, the probable breakdown of the adhesive may be a contributing factor. An analysis of the data is displayed in Figure 7. Specimens with a fiberglass cloth interface did not conclusively show smaller strength losses as compared with specimens without a fiberglass interface. There is probably a lessened galvanic effect caused by the electrical insulation between the composite and the metallic core. For the one-week exposure tests comparative losses in strength (%) in 95% RH were 15.3 vs. 15.7, in the ASTM salt spray fog test, 19.3 vs. 36.1 and in the synthetic sea water + SO_2 test, 72.8 vs. 68.9, respectively. For the two-week exposure tests, the comparative losses in strength in 95% RH were 9.7 vs. 14.9 percent, in the ASTM salt spray fog test 38.0 vs. 41.3 percent, and in the synthetic sea water + SO_2, 63.0 vs. 78.0 percent. An examination of the strength loss data for the aluminum 5052 faces bonded to aluminum 5052 honeycomb (non-galvanic controls) indicated significant reductions in strength when exposed to the same three environments. However, the strength reduction was not as great as that obtained for the composite face bonded to aluminum honeycomb sandwich specimens. For one-week exposure tests comparative losses in strength in 95% RH were 6.4 vs. 15.7 percent, in the ASTM salt spray fog test 18.5 vs. 36.1 percent, and in the synthetic sea water + SO_2 test 52.6 vs. 68.9 percent. For the two week exposure tests, the comparative losses in strength in 95% RH were 8.8 vs. 14.9 percent, in the ASTM salt spray test 29.8 vs. 41.3 percent, and in the synthetic sea water + SO_2 69.1 vs. 78.0 percent. This categorically shows the galvanic corrosion effect of coupling graphite-epoxy to aluminum does result in a greater strength loss than the
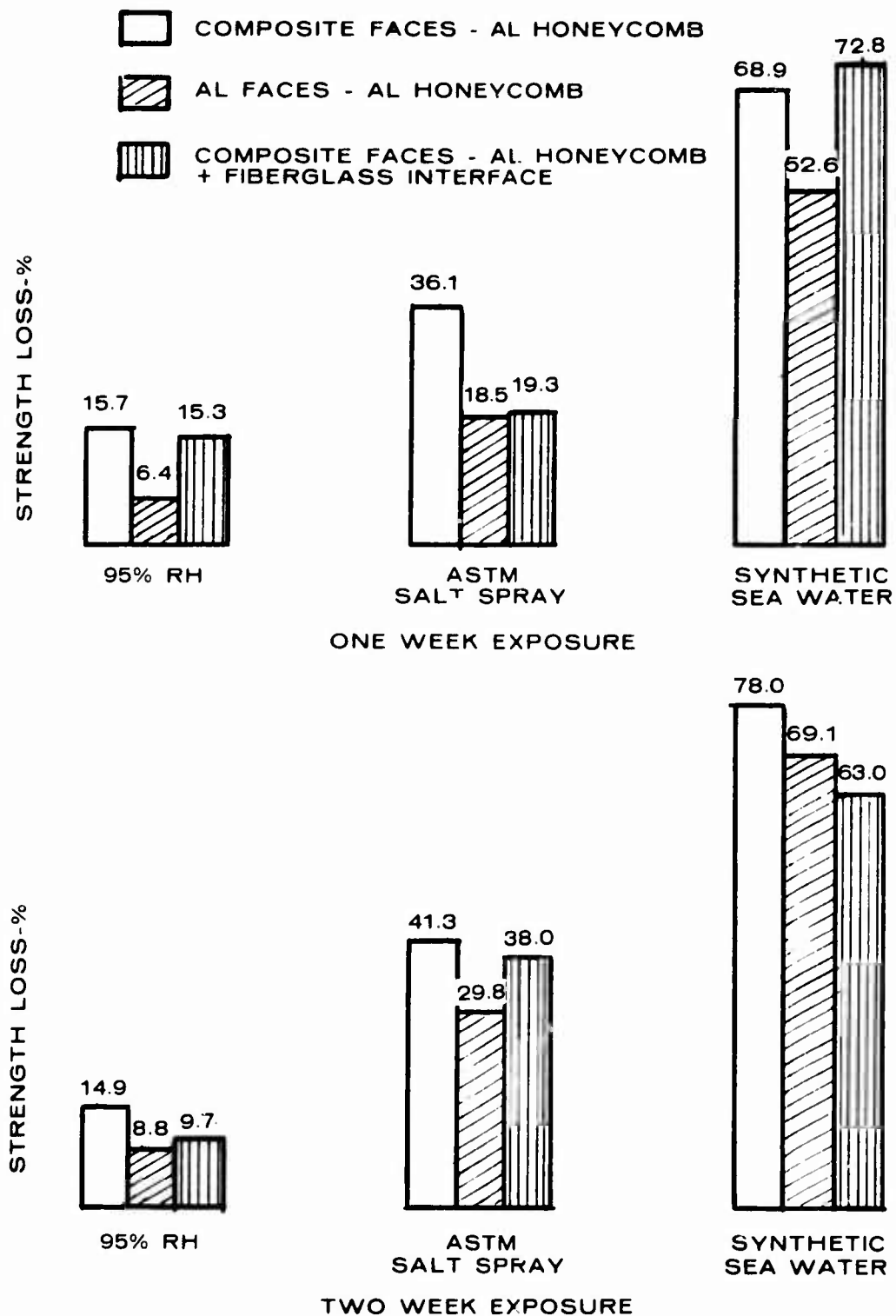
FIGURE 7 STRENGTH LOSS OF SANDWICH HONEYCOMB CONSTRUCTION
AS A FUNCTION OF ENVIORNMENTAL EXPOSURE

340

Flatwise Tensile Tests of Sandwich Constructed Specimens

GRAPHITE-EPOXY COMPOSITE FACES BONDED TO ALUMINUM HONEYCOMB

Environment	1 WEEK EXPOSURE		2 WEEKS EXPOSURE	
	Strength-psi	Loss	Strength-psi	Loss
Control (unexposed)	555 ± 18	--	510 ± 41	--
95% RH at 49°C (120°F)	468 ± 33	15.7%	434 ± 27	14.9%
ASTM Salt Spray	355 ± 23	36.1%	300 ± 86	41.3%
Synthetic sea water + SO_2	173 ± 21	68.9%	113 ± 9	78.0%

GRAPHITE-EPOXY COMPOSITE FACES BONDED TO ALUMINUM HONEYCOMB (GLASS INTERFACE)

Control (unexposed)	518 ± 47	--	432 ± 4	--
95% RH at 49°C (120°F)	439 ± 50	15.3%	390 ± 14	9.7%
ASTM Salt Spray	418 ± 13	19.3%	268 ± 57	38.0%
Synthetic Sea Water + SO_2	141 ± 11	72.6%	159 ± 16	63.0%

Flatwise Tensile Tests of Non-Galvanic Sandwich Constructed Specimens

ALUMINUM FACES BONDED TO ALUMINUM HONEYCOMB

Control	578 ± 43	--	543 ± 52	--
95% RH at 49°C (120°F)	541 ± 32	6.4%	495 ± 30	8.8%
ASTM Salt Spray	471 ± 69	18.5%	381 ± 56	29.8%
Synthetic Sea Water + SO_2	274 ± 16	52.6%	168 ± 17	69.1%

GRAPHITE-EPOXY COMPOSITE FACES BONDED TO NOMEX HONEYCOMB *

Control	267 ± 2.9		253 ± 10.6	
95% RH at 49°C (120°F)	272 ± 5.2		263 ± 15.5	
ASTM Salt Spray	264 ± 9.0		260 ± 0	
Synthetic Sea Water + SO_2	272 ± 24.3		268 ± 8.0	

Standard Deviation (±) calculated from three tensile tests. * All data are results due to core failures.

all aluminum specimens where no galvanic effect exists.

Unfortunately the data for the composite faced Nomex honeycomb sandwich specimens offer only a partial picture because failures occurred in the honeycomb structure rather than the bonded joint. This indicates that the bonded joint on the all organic sandwich specimens did not deteriorate upon exposure to any great degree and was stronger than the Nomex core.

The differences in severity of the ASTM salt spray and synthetic sea water + SO_2 environments have been clearly indicated in the flatwise tensile data. Figures[2] 8 and 9 are photographs of "sandwich" specimens after flatwise tensile testing. Prior to tensile testing the specimens are bonded to aluminum blocks and after testing the separation at the bond joint between the face and the aluminum honeycomb is easily seen. A comparison of the differences in corrosive attack on the aluminum honeycomb shows that there is considerably more pitting on the specimen subjected to the synthetic sea water + SO_2 environment.

Horizontal shear and tensile data were also obtained for graphite-epoxy composite exposed to the same three environments. Data were obtained on the composite for galvanically coupled as well as uncoupled specimens. Galvanic coupling was accomplished by sandwiching the composite between two sheets of aluminum 5052 with Nylon fasteners. Unexposed composite specimens were used as controls. Results of one-and two-week exposure tests are presented in Table VI.

The horizontal shear tests, using short single beam method, are essentially a measure of the interlaminar shear strength of the composite (the graphite fibers are not being tested). An examination of the data in Table VI for the three different environments, in general, shows a wide scatter, large standard deviations, in the strength for the controls as well as the tested specimens. It is understood that this type variation in mechanical property measurements is not uncommon for organic composite materials. This makes analysis of the data difficult but it appears that there is no major loss in strength when the uncoupled or the galvanically coupled specimens are exposed to the three environments.

The tensile data which is related to the graphite fiber strength also show a large scatter. The tensile strength for one tested panel was ~73,000 psi vs. ~50,000 psi for another panel. These data present the same difficulty for analysis and only a general statement that there is no apparent loss in strength can be made.

STRESS CORROSION CRACKING

This phase of the overall study is intended to determine the effect of coupling graphite-epoxy composite to aluminum 7075-T651 on stress corrosion crack propagation properties of the alloy. Stress corrosion cracking is defined by Champion (13) as, "greater deterioration of mechanical properties of a material through the simultaneous action of a static stress and exposure to a specific environment than would occur by the separate but additive action of those agencies." Implied in the definition is that S.C.C. is controlled by the electrochemistry, mechanics and metallurgy of the particular system. The effects of metallurgy and mechanics are held constant for all specimens in this study. Thus, electrochemistry is the only variable under consideration.

1.25X

FIGURE 8 SANDWICH SPECIMENS SHOWING SEPARATION AT BOND JOINT AFTER TENSILE TEST.
ONE WEEK EXPOSURE IN ASTM 5% SALT SPRAY

FIGURE 9 SANDWICH SPECIMENS SHOWING SEPARATION AT BOND JOINT AFTER TENSILE TESTING. ONE WEEK EXPOSURE IN SYNTHETIC SEA WATER + SO$_2$ SPRAY

1.25X

TABLE VI

TENSILE AND HORIZONTAL SHEAR MEASUREMENTS OF GRAPHITE-EPOXY COMPOSITE

Uncoupled Composite (NARMCO 5206-II)

Environment	1 WEEK EXPOSURE		2 WEEKS EXPOSURE	
	Shear (psi)	Tensile (psi)	Shear (psi)	Tensile (psi)
Control	6,752 ± 659	72,882 ± 876	6,653 ± 1,366	50,218 ± 3,252
95% RH at 49°C (120°F)	7,239 ± 496	70,155 ± 13,449	6,440 ± 531	49,543 ± 2,779
ASTM Salt Spray	7,049 ± 654	71,104 ± 3,712	6,998 ± 599	49,564 ± 6,728
Synthetic Sea Water + SO$_2$	6,426 ± 1,280	75,724 ± 1,280	5,676 ± 839	54,465 ± 4,531

Galvanically Coupled Composite + Aluminum 5052-H38

Environment	1 WEEK EXPOSURE		2 WEEKS EXPOSURE	
	Shear (psi)	Tensile (psi)	Shear (psi)	Tensile (psi)
Control	6,752 ± 659	72,882 ± 876	5,528 ± 777	50,218 ± 3,252
95% RH at 49°C (120°F)	7,225 ± 621	72,628 ± 3,993	5,564 ± 1,130	54,645 ± 4,867
ASTM Salt Spray	6,497 ± 896	72,304 ± 3,887	6,320 ± 699	61,106 ± 1,423
Synthetic Sea Water + SO$_2$	7,158 ± 581	65,590 ± 3,619	6,332 ± 1,012	60,979 ± 2,348

345

Stress Corrosion Cracking Results

Visual measurements of the crack lengths became increasingly difficult as the length of time of the test increased due to appearance of secondary cracks. Photomacrographs of the control and galvanically coupled specimens are shown in Figure 10. The lower magnification photographs show that the control specimen had little, if any, surface attack and had developed a black oxide film, while the galvanically coupled specimen had considerable amount of surface corrosion. From the higher magnification photomacrographs, it is seen that the area immediately surrounding the crack of the control specimen was heavily corroded, while on the galvanically coupled specimen the entire surface was corroded. This condition necessitated opening the specimen to determine the actual extent of the stress corrosion cracking.

Data for control and galvanically coupled specimens is plotted in Figure 11. All the points appear to fall into a common band that forms a dual slope relationship. Stress corrosion cracking stress intensity factor K_{ISCC} is determined through extrapolation to a crack growth rate of 1.4×10^{-5} inches per hour, which is considered crack cessation or the limit to testing since the actual K_{ISCC} is not absolutely determinable. Using Figure 11 K_{ISCC} is 11.5 KSI in. which is 4.5 KSI in. higher than that obtained by Hyatt (6,7) using the same aluminum alloy heat treated to the same condition. This difference can be explained by comparing the differences in the mechanical properties and chemical composition of the specimens used by Hyatt to those used in this study. In Table I the differences in properties are illustrated in the difference in ultimate strengths. In addition, the material used in this study exceeds the upper specification limits for magnesium and is low in iron and silicon. These facts help to explain the differences in mechanical properties. Additionally, the lower the iron and silicon contents of the alloy, the greater the fracture toughness which should result in a higher K_{IC} and a slower crack growth rate. The K_{IC} for the specimens used in this work was 26.7 KSI in. versus 25 KSI in. for the material in Hyatt's study. Figure 12 shows the presence of secondary cracks about the main crack tip. These secondary cracks would relieve the stress in the region of the crack tip and result in a false value of K_{ISCC} at the high end.

346

SUMMARY

The following phenomenology was established by this work:

1. Open circuit potential measurements in 3½% NaCl solution indicate that there is approximately one volt potential difference between graphite-epoxy composite and aluminum alloys 7075-T6 and 7075-T651. This relatively large dissimilarity in potential provides the driving force for corrosion of the aluminum as an anode and is cause for concern. The difference between the composite and titanium alloy, Ti-6-4, was about 0.3 volt for an as received unpolished surface vs. 0.5 volt for a freshly polished surface.

2. Corrosion current data employing the zero impedance technique show that aluminum alloys, cadmium plate, cadmium plate + chromate conversion coat are much more reactive than Ti-6Al-4V alloy when coupled to graphite-epoxy ($\sim$15 vs. 0.002 μ A/cm^2). These data provide a means of ranking the galvanic corrosion problem resulting from coupling graphite-epoxy composite to various aircraft alloys.

3. Flatwise tensile data indicate that there are significant strength losses when graphite-epoxy composite sandwich specimens are exposed to salt spray and synthetic sea water + SO$_2$ spray environments. For two-week exposure tests the comparative strength losses in the two environments were 41 vs 78 per cent respectively. These strength losses were greater than those for all aluminum specimens and definitely shows the corrosion effect of coupling graphite-epoxy to aluminum as compared with specimens where galvanic effects are minimized.

4. Data obtained shows that galvanic coupl'ng of graphite-epoxy composite to 7075-T651 aluminum alloy has no effect on the stress corrosion cracking rate of the alloy, but does increase the general corrosion.

ACKNOWLEDGMENTS
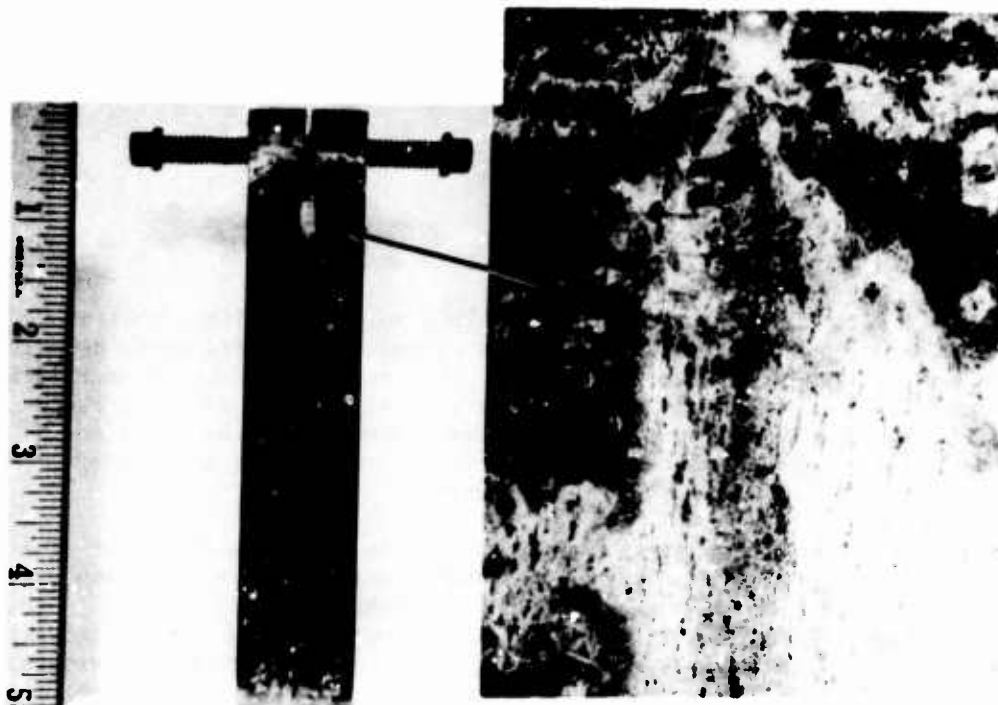
CONTROL SPECIMEN NO. 4   7.5X
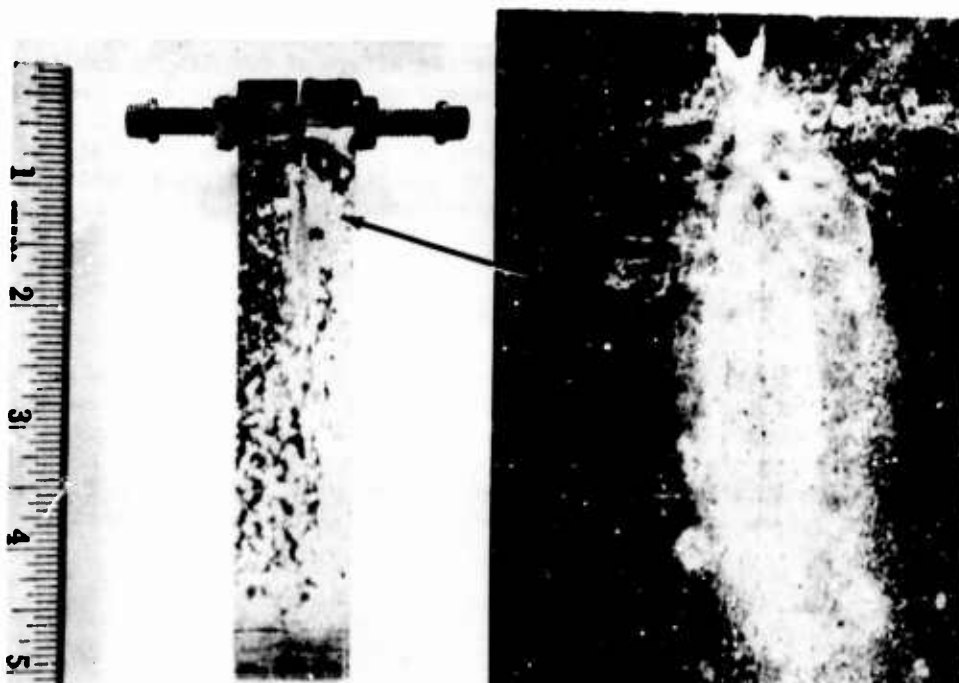
COUPLED SPECIMEN NO. 5   7.5X

FIGURE 10   PHOTOMACROGRAPH OF TESTED SPECIMENS
COMPARING SURFACE CONDITIONS
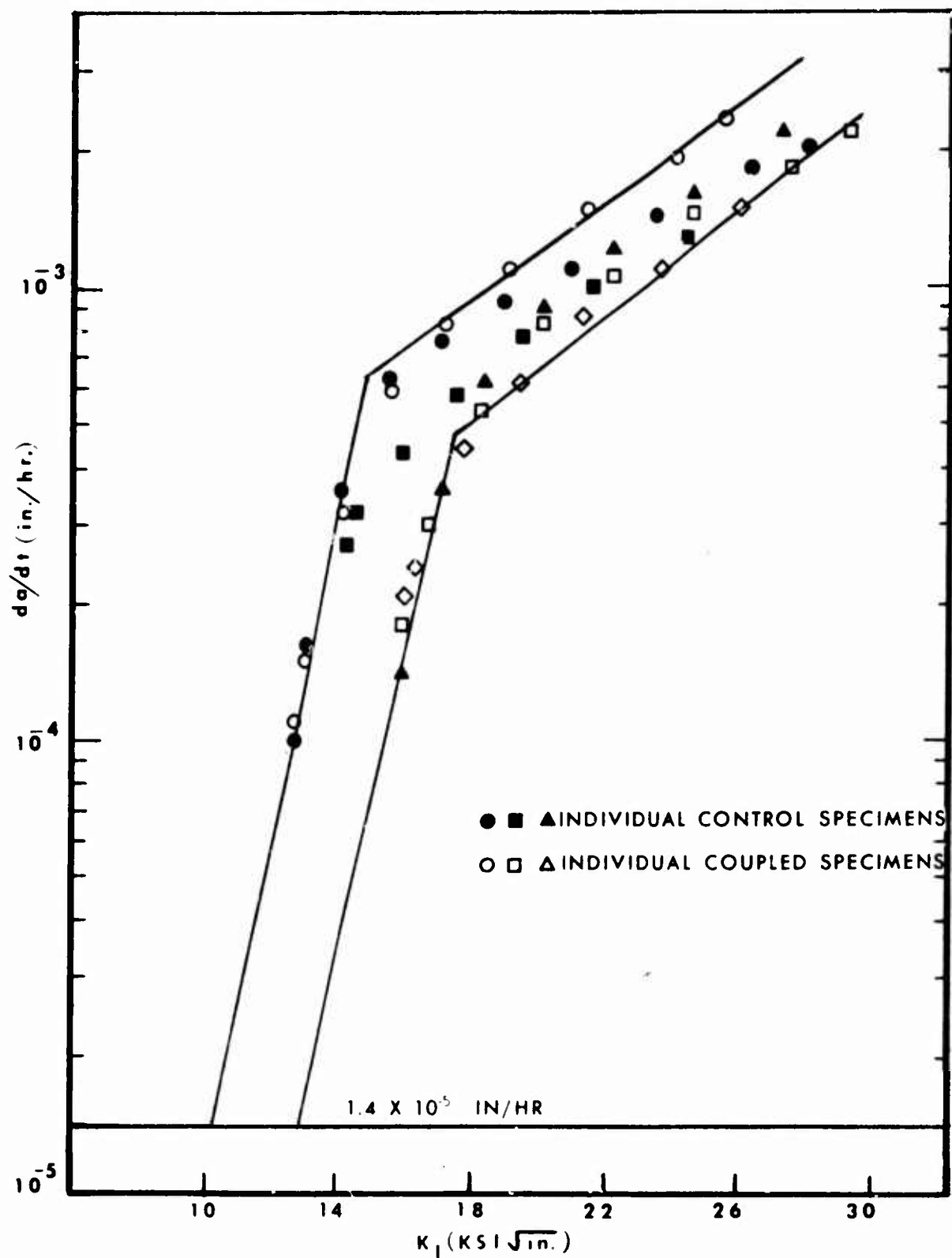
FIGURE II CRACK GROWTH RATE VERSUS STRESS INTENSITY FACTOR
FOR ALUMINUM ALLOY 7075-T651

NOTCH BOTTOM

100X

8X

100X

DIRECTION OF PROPAGATION
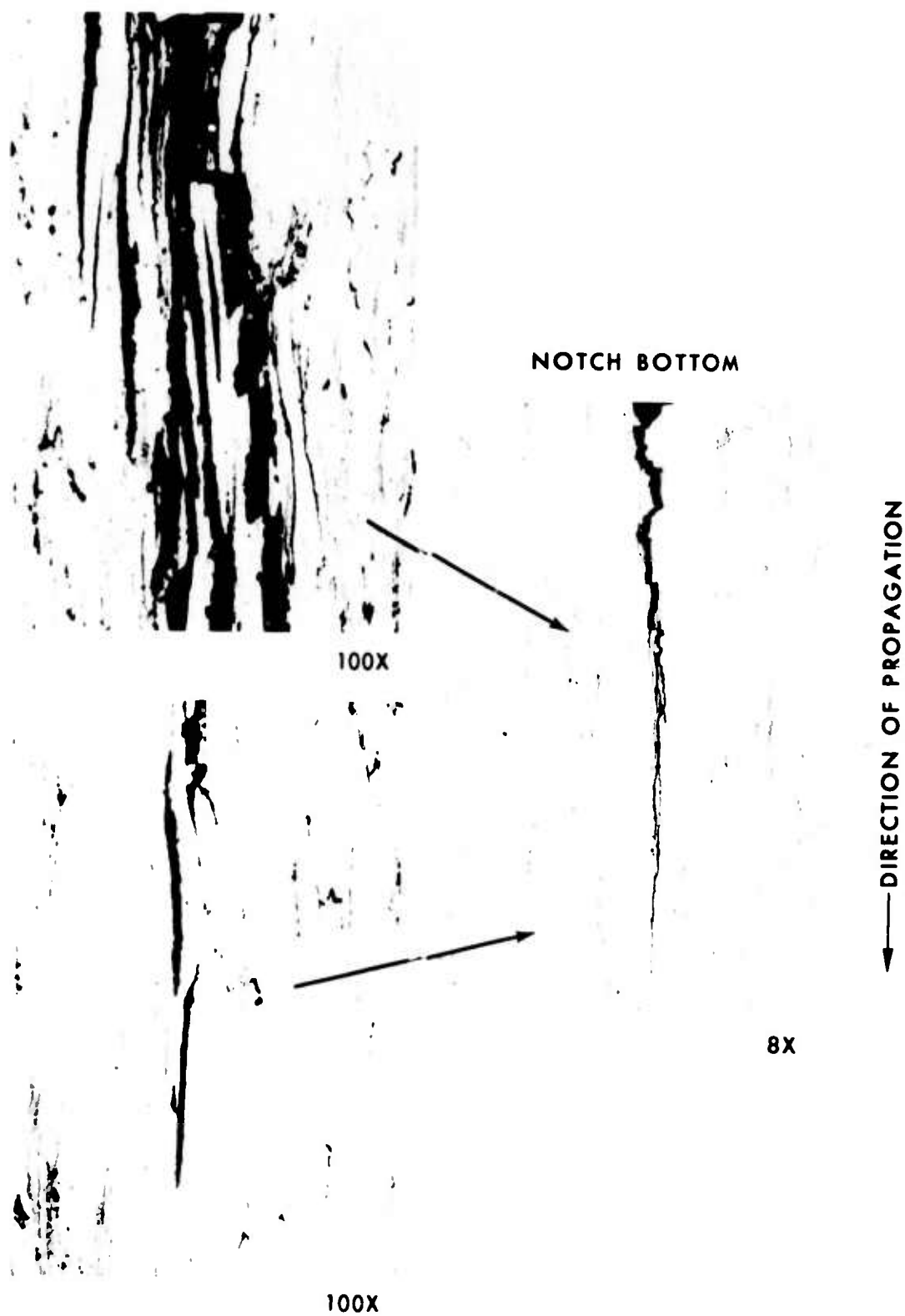
FIGURE 12   METALLOGRAPHY OF CRACKING

350

REFERENCES

(1) R. R. Sederman and K. E. Weber - Technical Brief, "Investigation of Galvanic Corrosion Associated with Filamentary Composites in Contact with Aircraft Structural Metals", Lockheed California Company, Burbank, California, 1970.

(2) H. H. Uhlig, "Corrosion and Corrosion Control", John Wiley and Sons, New York, 1971.

(3) M. G. Fontana and N. D. Greene, "Corrosion Engineering", McGraw Hill Book Company, New York, 1967.

(4) W. T. Kelly, "Development of Composite Joints in Graphite Laminates of Modulite 5206-II", Report No. NADC-73006-30, Naval Air Development Center, Warminster, Pennsylvania, 22 June 1973.

(5) J. A. von Fraunhofer and P. J. Staheli, "The Measurement of Galvanic Currents in Dental Amalgam", Corr. Sci. 12 p 767 (1972).

(6) M. V. Hyatt, "Effects of Specimen Geometry and Grain Structure on Stress Corrosion Cracking Behavior of Aluminum Alloys", The Boeing Company.

(7) M. V. Hyatt, "Use of Precracked Specimens in Stress Corrosion Testing of High Strength Aluminum Alloys", The Boeing Company (D6-24466) November 1969.

(8) M. G. Fontana and R. W. Staehle, eds. "Advances in Corrosion Science and Technology", Plenum Press, New York, 1972.

(9) W. T. Kelly, "Development of Optimum Joints in Graphite Composites-Carboform Material", Report No. NADC-MA-7142, Naval Air Development Center, Warminster, Pennsylvania, 25 August 1971.

(10) F. Mansfeld and E. P. Parry, "Galvanic Corrosion of Bare and Coated Al Alloys Coupled to Stainless 304 or Ti-6Al-4V", Corr. Sci., 13, p 605 (1973).

(11) F. Mansfeld, "Galvanic Corrosion of Al Alloys Coupled to Coated PH13-8Mo Stainless Steel", Corrosion, 29, No. 7, p. 276 (1973).

(12) F. Mansfeld, "The Relationship Between Galvanic Current and Dissolution Rates", Corrosion, 29, No. 10, pp 403-405 (1973).

(13) W. H. Ailor, "Handbook of Corrosion Testing and Evaluation", John Wiley and Sons, New York, 1971.

LIST OF FIGURES

1. Zero Resistance Ammeter Circuit Used for Measurement of Galvanic Corrosion Currents

2. Double Cantilever Beam Specimens

3. Test Set-up for Coupling of Composite to DCB Stress Corrosion Specimen

4. Galvanic Corrosion of Aluminum 5052 Coupled to Graphite-epoxy After One Week Exposure in ASTM Standard Salt Spray

5. Galvanic Corrosion of Aluminum 5052 Coupled to Graphite-epoxy Composite After One Week Exposure in Synthetic Sea Water + SO_2 Spray

6. Galvanic Corrosion of Aluminum Honeycomb Coupled to Aluminum 5052 by Nylon Fasteners After One Week Exposure in Synthetic Sea Water + SO_2 Spray

7. Strength Loss of Sandwich Honeycomb Construction as a Function of Environmental Exposure

8. Sandwich Specimens Showing Separation at Bond Joint After Tensile Testing. One Week Exposure in ASTM 5% Salt Spray

9. Sandwich Specimen Showing Separation at Bond Joint After Tensile Testing. One Week Exposure in Synthetic Sea Water + SO_2

10. Photomacrographs of Tested Specimens Comparing Surface Conditions

11. Crack Growth Rate versus Strength Intensity Factor for Aluminum Alloy 7075-T651

12. Metallography of Cracking

LIST OF TABLES

Effect of Vanadium Pentoxide on Accelerated
Oxidation of Nickel-Base Alloys

N. S. Bornstein, M. A. DeCrescente and H. A. Roth
United Aircraft Research Laboratories
East Hartford, Connecticut

ABSTRACT

The oxidation behavior of various nickel-base alloys in the presence of
gaseous and condensed vanadium pentoxide was studied. It was found that vanadium
pentoxide accelerates the oxidation rate of nickel-base superalloys. The product
of the reaction between V_2O_5 and the substrates is dependent upon the alloying
elements present in the alloy. In the absence of alloying elements such as aluminum
and titanium, the products are vanadates. However, when the alloys contain aluminum
and/or titanium, the product of the reaction appears to be a glass.

Preceding page blank

Introduction

Lower cost distillates, residual and certain crude oils may contain organo-
vanadium compounds which during combustion are converted to vanadium pentoxide,
V_2O_5. V_2O_5 is a low melting oxide and has been known to cause corrosion problems
in oil fired boilers. The purpose of this work was to determine the mechanism
and extent of corrosion of V_2O_5 on nickel-base superalloys.

The physical state of the V_2O_5 at gas turbine temperatures depends upon the
temperature, concentration of vanadium in the fuel and whether or not the fuel
is being combusted under near or extreme non-equilibrium conditions. Under these
different conditions the vanadium pentoxide can be present in either the gaseous
or condensed state. The work presented here will consider the effect of both
gaseous and condensed V_2O_5 on gas turbine alloys. Since the composition of the
protective scales depends upon the alloy composition, the approach taken in this
work was to determine the effect of V_2O_5 on nickel, nickel binary alloys, and the
nickel base superalloys currently used in gas turbine engines.

Gaseous Reactions

If the vanadium present in the fuel is completely oxidized to the pentoxide,
and the concentration of V_2O_5 in the combustion products is less than the critical
concentration necessary for condensation to occur, then the vanadium will be present
in the turbine in the gaseous state.

Fitzer, et al., (Ref. 1) has shown that $V_2O_5(g)$ markedly increases the
oxidation rate of copper and chromium, and has a smaller effect on iron and nickel.
All the oxides of the metals mentioned above are P type conductors. Thus, as
expected, the introduction of a higher valency cation in the metal oxide matrix
results in an increase in the specific rate constant as discussed by Hauffe (Ref.
2). The introduction of an alkali metal such as Li (lower valent cations) would
decrease the specific rate constant. The effect of Li^+ doping in NiO has been
verified by Pfeiffer and Hauffe (Ref. 2).

The oxides commonly encountered in superalloy systems are NiO, Cr_2O_3 and
Al_2O_3. Both NiO and Cr_2O_3 have been identified as P type conductors. However,
Al_2O_3 is, according to Hauffe, a probable N conductor. Thus, the incorporation of
higher valent cations in the Al_2O_3 lattice should decrease the rate of oxidation.

In order to determine the effect, if any, of gaseous V_2O_5 on the oxidation
behavior of nickel-base superalloys a series of TGA experiments was performed in
which nickel, Ni_3Al, B-1900, U-700, and NiAl specimens were exposed to oxygen
containing approximately 17.6 ppm $V_2O_5(g)$. The V_2O_5 vapors were generated from a
platinum crucible filled with V_2O_5 and maintained at 850°C. The experimental
apparatus is shown in Fig. 1.

1. Nickel and Ni-Cr Alloys

The rates of oxidation of nickel in oxygen and oxygen containing 17.6 ppm
V_2O_5 are shown in Fig. 2. The exposure of nickel to oxygen containing V_2O_5 vapors
results in an apparent increased rate of oxidation. This effect is reproducible
as shown in Fig. 2 and further supported by differences in scale thickness. The
thickness of the scale of the specimens exposed to pure O_2 is approximately 1.4 mils

and the thickness of the scale of the specimen exposed to O_2 containing 17.5 ppm $V_2O_5(g)$ is approximately 2.2 mils thick, Fig. 3. Portions of the oxide scales from both specimens were mechanically removed and examined by XRD techniques. All lines were accounted for and the only phase observed was NiO.

The addition of minor quantities of chromium to nickel increases the rate of oxidation of the alloy. The beneficial effect of chromium is not observed until the scale formed on the alloy is a mixture of NiO and Cr_2O_3 (spinel) or Cr_2O_3 and depends upon the temperature and chromium content of the alloy.

At 1000°C the oxide scale formed on the Ni-8 Cr alloy consists of NiO and spinel and that formed on Ni-17 Cr alloy is spinel and Cr_2O_3. The introduction of 17.5 ppm $V_2O_5(g)$ in the oxygen stream resulted in an increase in the magnitude of the weight gain, similarly to that observed for "A" nickel. Likewise, the thickness of the oxide scale at corresponding times was greater for the specimens exposed to O_2 + $V_2O_5(g)$ than those exposed only to oxygen. X-ray diffraction studies revealed in the case of the Ni-8 Cr alloy the phases NiO and $NiCr_2O_4$ and for the Ni-17 Cr alloy the phases $NiCr_2O_4$ and Cr_2O_3. No vanadium containing phase was identified. The representative weight gain curves are shown in Fig. 4.

2. Ni-Al Alloys and Superalloys

The oxide scale formed at 1000°C on the intermetallic compounds NiAl and Ni_3Al is alumina which is also the major constituent of the scale formed on most nickel base superalloys. If alumina is an N type oxide, then the introduction of V^{+4} or V^{+5} cations into the alumina lattice should decrease the number of lattice defects, the net result being a decrease in the rate of oxidation of the alloy. However, when NiAl, Ni_3Al or B-1900 alloy specimens were exposed in O_2 containing 17.5 ppm $V_2O_5(g)$ the rate of oxidation increased rather than decreased. A comparison of the rates of oxidation of NiAl, Ni and B-1900 at 1000°C exposed to oxygen and oxygen containing 17.5 ppm $V_2O_5(g)$ is shown in Fig. 5. The data for Ni_3Al is not shown since its data is coincident with that of the superalloy B-1900.

A comparison of the thickness of the oxide scale formed on the intermetallic compound Ni_3Al exposed to O_2 and O_2 + $V_2O_5(g)$ for 1000 min revealed the formation of thicker scales in the presence of V_2O_5 as was observed for nickel. Except for the differences in the thicknesses of the scales, the oxide scales appeared to be identical. X-ray diffraction studies failed to reveal any phase other than Al_2O_3.

Condensing V_2O_5

If it is assumed that the turbine metal components are cooler than the hot turbine gases and the metal temperature is below the dewpoint of the gaseous V_2O_5, then the V_2O_5 can continuously condense onto the turbine components. At any given time the quantity of condensed V_2O_5 may be very small; nevertheless based upon the ability of V_2O_5 to dissolve oxide scales, the effect of continuously condensing V_2O_5 on turbine parts may be catastrophic. In order to determine the effect of condensing V_2O_5, a series of experiments was performed in which the following specimens, Ni, IN-100, B-1900, NiAl, Waspaloy, Ni_3Al, and NiAl + 1 and 5 w/o Y_2O_3 were exposed at 900°C in flowing oxygen. The specimens were suspended by means of a platinum chain from one arm of a continuously weighing Ainsworth semi-microbalance A platinum crucible filled with V_2O_5 was positioned approximately 2 inches below

the specimen and with the aid of supplemental heaters, the platinum crucible was maintained at 1200°C ± 25. The rate of condensation of V_2O_5 onto the test specimens was determined by suspending a platinum specimen in place of the test specimen and continuously monitoring the weight change. After each run the change in weight of the specimen and that of the platinum chain was separately determined. The average rate of weight gain of the specimen was 1×10^{-4} mg/cm^2 min.

1. Ni and Waspaloy

The phases present on the surface of the specimens will depend upon the rate of condensation of V_2O_5 and the quantity of nickel (Ni + Cr) that has reacted with oxygen to form oxides. If the quantity of V_2O_5 is much greater than the oxide formed in situ then the major phase present on the surface would be a liquid. If the quantity of oxides is much greater than the amount of liquid V_2O_5 then the major phases present on the surface would be the solid phases, oxides and vanadates.

If it is assumed that the surface oxide is a liquid, the rate of oxidation would tend to be linear. Similar results would be observed if the liquid phase limited the thickness of an oxide scale, i.e., dissolving a portion of the scale as it forms. If a solid protective phase forms between the liquid and the substrate then the rate of oxidation would decrease as the scale thickens.

In the case of nickel and the nickel-base alloy, Waspaloy, the rate of oxidation of the test specimen was initially greater than that observed in the absence of condensing V_2O_5 but the rate of oxidation decreased with increasing time. The magnitude of the weight gain after 1200 min (20 hrs) was less than a factor of two greater than that observed in the absence of V_2O_5. The experimental data is shown in Fig. 6. Also shown in Fig. 6 is (1) the observed oxidation behavior in pure oxygen, (2) the measured rate of condensation of V_2O_5 onto a platinum specimen, and (3) a summation curve which consists of the data from (1) and (2) above. Metallographic examination of the scales formed on the nickel specimen revealed a single phase oxide scale with no apparent evidence of a vanadate or free V_2O_5. It should be noted that after 1200 min the weight of V_2O_5 which condensed onto the specimen is 0.12 mg/cm^2 which corresponds to a thickness of 0.014 mils (3.57×10^{-5} cm).

2. B-1900, IN-100, Ni$_3$Al and NiAl

Based upon the results observed for Ni and Waspaloy, similar results were anticipated for the aluminum rich alloys. However, this was not the case. Upon exposure to condensing $V_2O_5(\ell)$ the rate of oxygen pickup for NiAl, and Ni$_3$Al specimens appeared to be linear, Fig. 7. Similar results were noted for the superalloys B-1900 and IN-100 with the exception that the linear rate of weight gain was greater during the first 100 min than during the subsequent 1100 min. Metallographic examination of the aluminum containing alloys revealed rather thick multiphase scales and in the case of the NiAl specimen, a depleted zone metallographically identified as Ni$_3$Al beneath the oxide scale.

X-ray diffraction analyses of the surface of the NiAl specimen did not confirm the presence of any V_2O_5 but a nickel vanadate phase was tentatively identified.

Reactions with Condensed V_2O_5

The conditions that actually exist within the gas turbine engine are not fully known. It is possible that vanadium present in the fuel could be present in the turbine in the gaseous state, could be continually condensing onto turbine parts, or as a result of buildup within the burner, could be periodically released, then impact and adhere to turbine components. The crucible experiments in which alloy specimens are totally or partially immersed in liquid V_2O_5 try, in part, to simulate the latter condition. These types of experiments have been conducted for many years with almost every available alloy and in general the conclusions are the same, namely (1) vanadate corrosion involves removal of the normally protective oxide scale allowing increased diffusion rates of oxygen to the metal surface, and (2) the corrosion could be controlled by development of alloys (or coatings) which would form protective oxide layers between the liquid vanadate and the metal surface and/or alter the physical properties of the melt and the operating conditions in the engine to reduce the fluxing tendency of the corrodent.

Many experiments have been performed in which the corrodent is applied onto a test specimen and the rate of oxidation of the specimen monitored. The corrodent consists of a mixture of salts primarily V_2O_5 + Na_2SO_4, V_2O_5 + $NaVO_3$ or complex vanadium bronzes some with excess alkali. The test specimens are often complex alloys. The results of these experiments are usually reported relative to (a) an alloy system and/or (b) an anticipated corrodent composition. It appears that the goal of those programs was a definition of the best material, rather than the determination of the mechanism by which degradation occurs. It appeared obvious from the experiments previously reported (condensing V_2O_5) that the nickel and nickel chromium alloys were markedly different in their behavior with respect to V_2O_5 than the nickel-aluminum intermetallic compounds or the nickel-base superalloys.

1. Nickel

In order to determine the static oxidation behavior of V_2O_5 coated specimens, the specimens were dipped into a reservoir of liquid V_2O_5 (700°C), quickly cooled and weighed. The quantity of V_2O_5 adhering to the surface is reported as mg/cm^2. The V_2O_5 coated specimens were then exposed at 830°C in a stream of flowing oxygen.

The comparison in behavior between vanadium free and 17.31 mg/cm^2 V_2O_5 coated nickel oxidized at 830°C is shown in Fig. 8. In the presence of V_2O_5, the initial rate of oxidation is greater than that observed for the vanadium free alloy, but the magnitude of the change cannot be described as catastrophic nor is the rate of oxidation linear, but as shown, the rate of oxidation of the V_2O_5 coated alloy decreases with increasing time.

The V_2O_5 coated nickel specimen was after oxidation, scraped on a bias in order to determine if more than one solid phase could be easily identified. It was immediately apparent that the scale consisted of three layers. The surface had a "wet" look as if a liquid was present at all times. Beneath the liquid phase was a purple to purple black phase and separating this phase from the nickel substrate was a greenish oxide which appeared to be NiO, Fig. 9. A cross-section under polarized light shows the V_2O_5 phase and the vanadates are optically active. It appears that for the V_2O_5 coated nickel, the outer phase is primarily vanadium pentoxide, the inner phase is nickel vanadate and the phase adjacent to the nickel substrate is nickel oxide.

The differences in the rates of oxidation between the uncoated and V_2O_5 coated

specimens could be the initial dissolution or reaction between V_2O_5 and NiO to form vanadates and during subsequent oxidation the rate of oxygen pickup is controlled by diffusion through the nickel oxide scale. If this is the case, then if a nickel specimen is preoxidized to a given weight gain and coated with a given amount of V_2O_5 such that at temperature the molar percentages of V_2O_5 to NiO correspond to the solidus of the V_2O_5-NiO phase diagram, it would be expected that (1) the rate of oxidation of the specimen would increase and (2) if the rate of oxygen pickup is replotted, it would appear as if only simple oxidation is occuring. This experiment was performed and the results are presented in Fig. 10. Initially a nickel specimen was oxidized for approximately 1000 min at 830°C in pure oxygen. The weight gain was approximately 1.05 mg/cm² which corresponds to 4.91 mg/cm² of NiO. After exposure for 1000 min, the oxidized nickel specimen was dipped into molten V_2O_5(700°C) and the amount of V_2O_5 retained was 10.0 mg/cm². Thus, the molar ratio of V_2O_5 to NiO is 1.25. When the specimen was reinserted into the TGA apparatus, the rate of oxygen pickup increased (Fig. 10) and if the data for the oxidation of the V_2O_5 coated preoxidized nickel specimen are replotted on the original coordinate (0,0) the resultant curve is almost identical to that of the simple oxidation of nickel.

A second series of experiments were then performed in which nickel was coated with V_2O_5 and oxidized for a predetermined length of time after which the specimen was removed from the furnace, recoated with a comparable amount of V_2O_5 and further oxidized. If the scale formed during the initial treatment consists of V_2O_5, a vanadate and nickel oxide, then the addition of more V_2O_5 would not markedly influence the rate of oxygen pickup. The results of this experiment are shown in Fig 11.

Initially a nickel specimen was coated with 17.31 mg/cm² of V_2O_5 and oxidized for approximately 120 min at 830°C in flowing oxygen. After 120 min, the specimen was removed from the furnace, recoated with 12.43 mg/cm² of V_2O_5 and oxidized an additional 80 min. The data generated during the initial 120 min is shown by the open circles and the data generated after reapplication of 12.43 mg/cm² V_2O_5 is shown by the filled in circles. It is apparent that a smooth curve connects all of the data points. When the weight gain for the initial experiment is plotted as weight gain squared vs time, the data fall on a straight line indicative of parabolic behavior. If the data from the subsequent experiment are added to the original data, the straight line can be continued to 200 min, the duration of the experiment. These results indicate that the additional quantity of V_2O_5 did not change the rate of oxidation of the V_2O_5 coated nickel and the rate of oxidation of the V_2O_5 coated nickel can be described by a parabolic equation.

It appears, based upon the results of the experiments conducted at 830°C, that unalloyed nickel can, under the experimental conditions, resist V_2O_5 corrosion. If similar experiments are conducted at 900°C, it would be anticipated that during exposure for prolong durations the rate of weight gain would actually decrease and become negative since the weight loss associated with evaporation of V_2O_5 would exceed the weight gain associated with the oxidation of nickel.

Two experiments were conducted in which nickel specimens were coated with 21 and 14 mg/cm² of V_2O_5 respectively and exposed at 900°C in flowing oxygen for 1200 min. As had been anticipated, after approximately 200 min, the specimens started to "lose" weight. The experimental data are shown in Fig. 12. Also shown in Fig. 12 are the data for simple oxidation of nickel and the rate of weight loss of V_2O_5 based upon the vapor pressure data of Pegg (Ref. 3). The dotted lines shown in

Fig. 12 are the summation curves obtained by ad__ing the weight loss data from evaporation of V_2O_5 to the observed oxidation curves for V_2O_5 coated nickel.

2. Superalloys

The majority of the experiments described herein were conducted at 830°C only because the initial rate of oxidation of the V_2O_5 coated superalloys exposed at 900°C was so rapid, that the automatic recording balance could not keep up with the rate of weight gain. The experimental problems encountered at 900°C, were alleviated when the temperature was reduced to 830°C. It is also possible that the reactions which occur at 830°C are not the same that occur at the higher temperatures and that the results reported herein are valid for the temperature range studied and care should be taken when extrapolating the data to higher temperatures.

When V_2O_5 was applied onto the superalloys, the immediate effect was a marked increase in the initial rate of oxidation. The magnitude of the weight gain is related to the amount of V_2O_5. A comparison of the oxidation behavior of uncoated and V_2O_5 coated B-1900 and IN-100 specimens is shown in Fig. 13. Also shown in Fig. 13 is the effect of different quantities of V_2O_5 (B-1900 alloy, 15 mg/cm^2 V_2O_5 and 20 mg/cm^2 V_2O_5). Note also that the rate of oxygen pickup does decrease with increasing time although as clearly shown, the differences in specific rates of oxidation are orders of magnitude apart.

The oxide scale formed on the V_2O_5 coated superalloys does not spall when V_2O_5 coated specimens were removed from the furnace. In general, the scales were adherent and had the appearance of minute cubic crystals randomly placed on the faces and edges of a specimen. A cross-section through a V_2O_5 coated B-1900 specimen exposed approximately 900 min at 830°C is shown in Fig. 14. Protrusions or pimples were also noted on the surface of the specimens and it appears that the protrusions or pimples are reaction products whose specific volume is much greater than the arithmetical volumes of its constituents.

When the V_2O_5 coated superalloys were exposed at 830°C and after a predetermined time, removed and recoated with V_2O_5, the rate of oxidation increased nonlinearly for about the first 400 min and then the rate of oxidation decreased with increasing time, Fig. 15. When the specimen was removed from the furnace, the scales were again adherent with no visible sign of spallation. The microstructure was identical, independent of the number of applications of V_2O_5.

If the scale had spalled or was cracked, (i.e., no barrier to liquid V_2O_5) then when the specimens were recoated with V_2O_5, the oxidation behavior would have been similar to that initially observed. If an adherent scale at temperature contains liquid V_2O_5, then the addition of more V_2O_5 may cause some increase in the rate of oxidation (solutionizing of the oxide scale), but not the marked increase observed. It appears then as if the superalloy specimens are coated with a glass and the glass has the capability of dissolving metal oxides or incorporating metal oxides into its structure. It should be noted that V_2O_5 like SiO_2 and B_2O_3 is classified as a strong glass former.

Glass modifiers are elements which do not enter into the glass structure. In general, for polycomponent glasses it is not essential that all constituents be glass-forming cations. For example, sodium silicate can form a glass in which sodium ions do not contribute to the network formation. Examples of glass modi-

fing oxides are Ca, Ba, Tn, Pb, Mg, Sn, Y, etc.

In between the glass formers and glass modifiers, is another group of oxides called intermediates. Intermediates do not form glasses themselves but can enter into the network of polycomponent glasses. The oxides of aluminum, titanium and zirconium are classified as intermediates.

3. Intermetallic compounds.

a. Ni_3Al and $NiAl$

The intermetallic compounds, NiAl and Ni_3Al, form upon exposure to oxygen a thin adherent film of alumina. At $830^{\circ}C$, the weight gain associated with the oxidation of NiAl or Ni_3Al exposed up to 1000 min in oxygen is less than 0.1 mg/cm^2.

When V_2O_5 was applied onto Ni_3Al or NiAl specimens, the rate of oxidation increased orders of magnitude. The response of Ni_3Al and NiAl to V_2O_5 and oxygen is shown in Figs. 16 and 17 respectively. Surprisingly, there does not appear to be any quantity effect, since the magnitude of the weight change at any given time for the 18 and 10 mg/cm^2 V_2O_5 coated Ni_3Al and the 15 and 10 mg/cm^2 V_2O_5 coated NiAl do not differ appreciably.

When either NiAl or Ni_3Al are coated with V_2O_5, exposed a predetermined length of time and then recoated with V_2O_5, the behavior of the specimen is similar to that noted for the superalloys. As previously observed the scale formed after the initial application of V_2O_5 is adherent, with no visible signs of spallation or cracking. The same is true after reapplication of V_2O_5.

Metallographic examination of the V_2O_5 coated nickel-aluminum intermetallic compounds revealed a microstructure similar to that observed with the V_2O_5 coated superalloys, namely a thick outer oxide scale and a thin (0.3 mils) adherent inner scale. When the scales formed on V_2O_5 coated nickel were examined under polarized light, the solidified V_2O_5 and nickel vanadates are readily identifiable since they are birefringent. However, the scales formed on the aluminum-nickel intermetallic compounds as well as those formed on the superalloys appear glassy.

b. NiTi

Since titanium is an important alloying element in superalloys (present in gamma prime, $Ni_3(TiAl)$, and in carbides, (MC and M_6C) and since its oxide is listed as an "intermediate" with the respect to glass formation, a series of experiments were performed to determine the effect of V_2O_5 on the oxidation behavior of NiTi.

Unlike NiAl, NiTi cannot be considered as an oxidation resistant material at elevated temperatures. The oxidation behavior of NiTi at 830° C is shown in Fig. 18. When V_2O_5 is applied onto NiTi the initial rate of oxidation is so rapid that the automatic recording balance could not keep up with the rate of oxygen pickup. The comparison of the oxidation behavior of uncoated and V_2O_5 coated NiTi is also shown in Fig. 18. It should be noted that after 1200 min exposure the change in weight as determined by the differences in initial and final weights is 25 mg/cm^2 as opposed to the 17.2 mg/cm^2 noted in the figure. The differences are believed to be the weight gain which occurred in the first minute of exposure.

The oxide scale formed on NiTi is protective and based simply upon the weight gain data, after exposure for 1200 min the scale is also quite thick. However, when the oxidized NiTi specimen is coated with V_2O_5, the response of the alloy is almost the same as that of an unoxidized specimen, Fig. 19. Immediately after application of the V_2O_5, the rate of oxidation of the alloy began to increase and within 50 min the rate of oxidation is extremely rapid. With prolonged exposure the rate of oxidation decreases, and it appears that the rate at which oxygen is consumed is linear with respect to time.

The oxide scale formed on the V_2O_5 coated NiTi was examined under normal and polarized light and the vanadate phases or solidified V_2O_5 were not observed. The appearance of the scale under polarized light was identical to that described for V_2O_5 coated NiAl.

CONCLUSIONS

A. Vanadium Corrosion

1. Under the experimental conditions imposed in this study, nickel and nickel-chromium alloys form protective scales in the presence of V_2O_5. The apparent rate of dissolution of the vanadates formed in liquid V_2O_5 is slow such that if additional quantities of V_2O_5 are deposited onto the vanadium oxide coated substrate, no increases in the rates of oxidation of the substrates are observed.

2. The initial rapid rates of oxidation between V_2O_5 and a metal substrate are due to the reduction of the V_2O_5 by the substrate.

3. Alloys based upon the intermetallic systems Ni_3Al and NiAl(As well as NiTi) are particularly susceptible to V_2O_5 corrosion.

4. The product of the reaction between V_2O_5 and alloys which tend to form alumina or titania rich scales in simple oxidation is glass-like or amorphous.

ACKNOWLEDGEMENT

REFERENCES

1. Fitzer, E. and Schwab, J., Corrosion 12, 459t(1956).
2. Hauffe, K. Oxidation of Metals, Plenum Press, New York, 1965.
3. McFarlane, The Mechanism of Corrosion by Fuel Impurities, Butterworths Press, London, 1963.

APPARATUS FOR EXPOSING ALLOYS TO V₂O₅ VAPORS
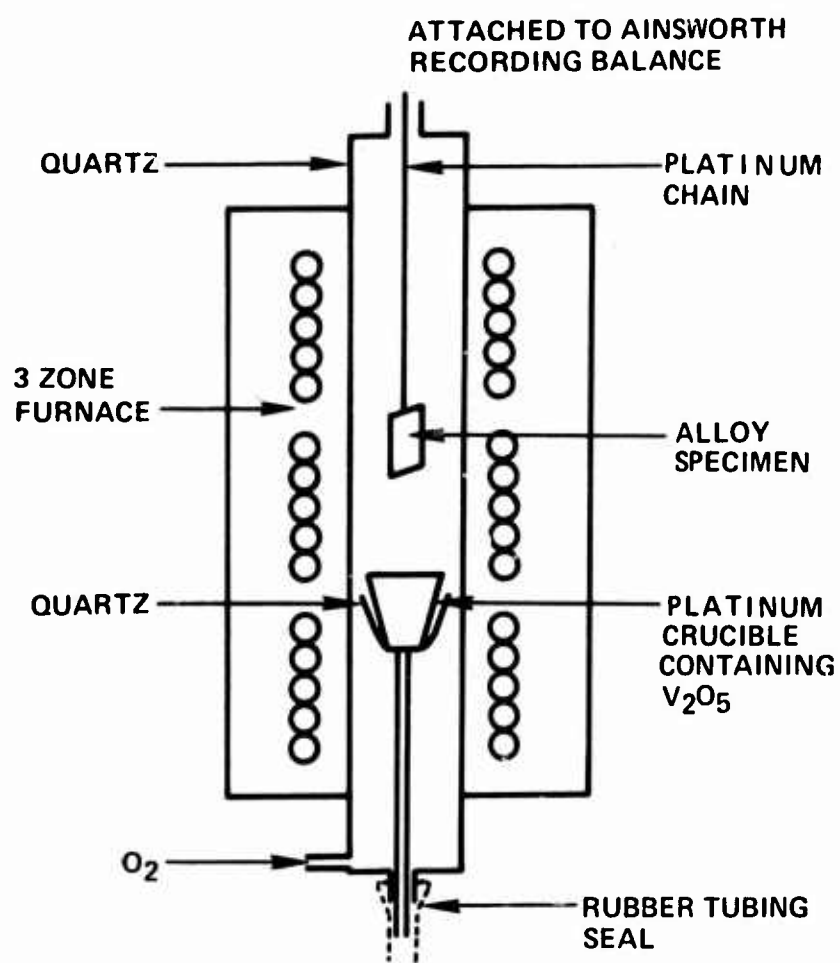
Figure 1

OXIDATION OF NICKEL EXPOSED AT 1000°C TO OXYGEN
AND OXYGEN + 17.5 PPM V_2O_5 (g)
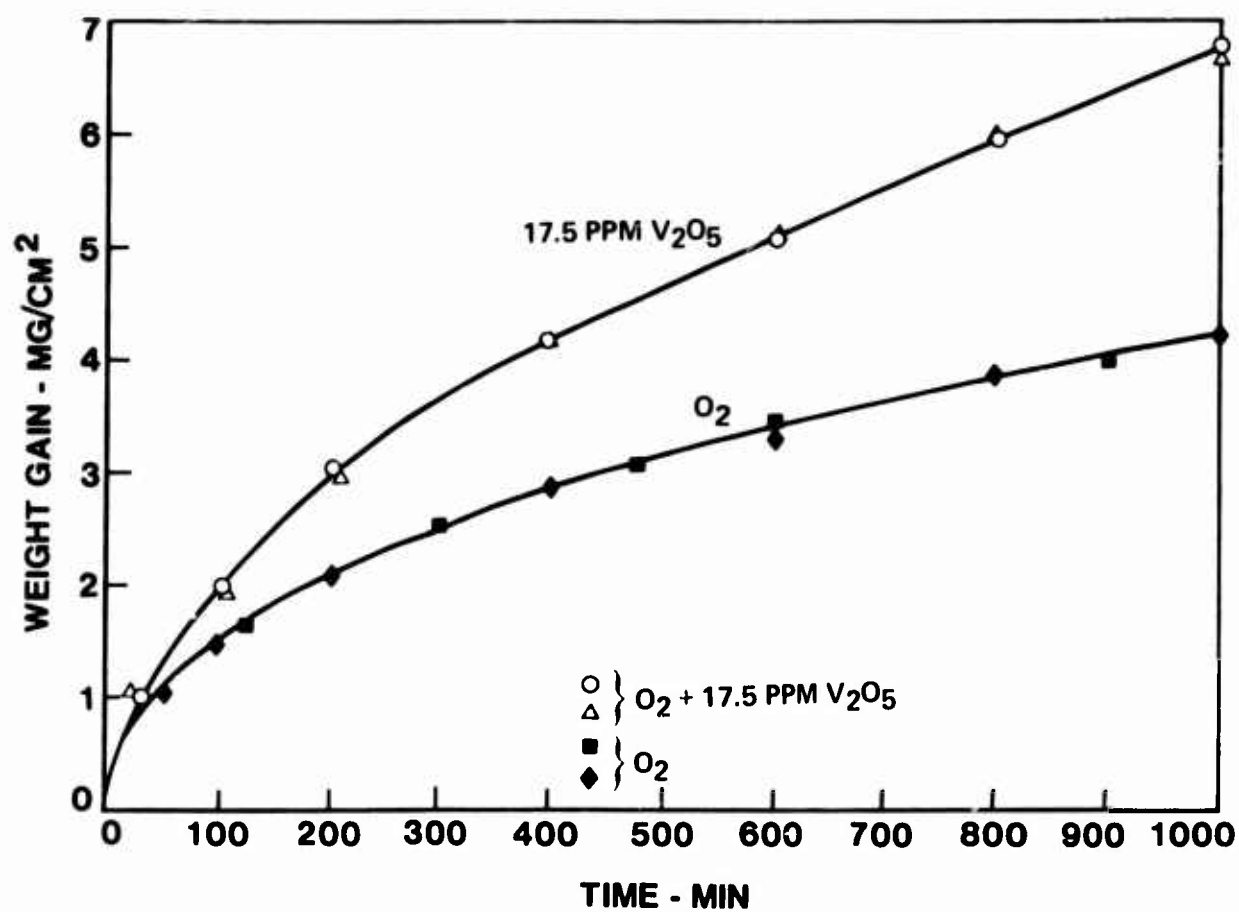
Figure 2

MICROSTRUCTURE OF "A" NICKEL EXPOSED AT 1000°C
FOR 1300 MINUTES TO V_2O_5 VAPORS

2.2 MILS

20 μ

OXYGEN + GASEOUS V_2O_5

1.4 MILS

20 μ

OXYGEN ONLY
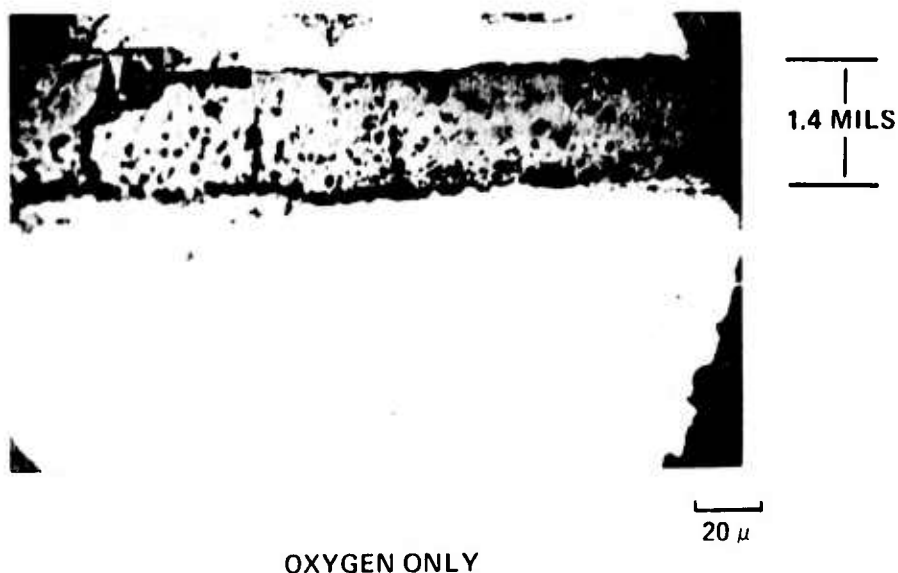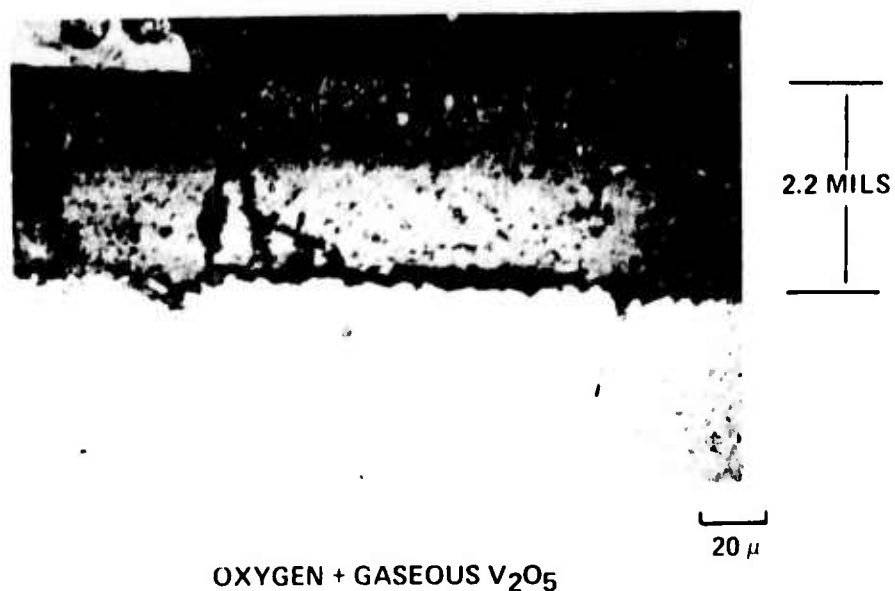
Figure 3

OXIDATION OF Ni-8 Cr ALLOY EXPOSED AT 1000°C TO CXYGEN
AND OXYGEN + 17.5 PPM V_2O_5 (g)
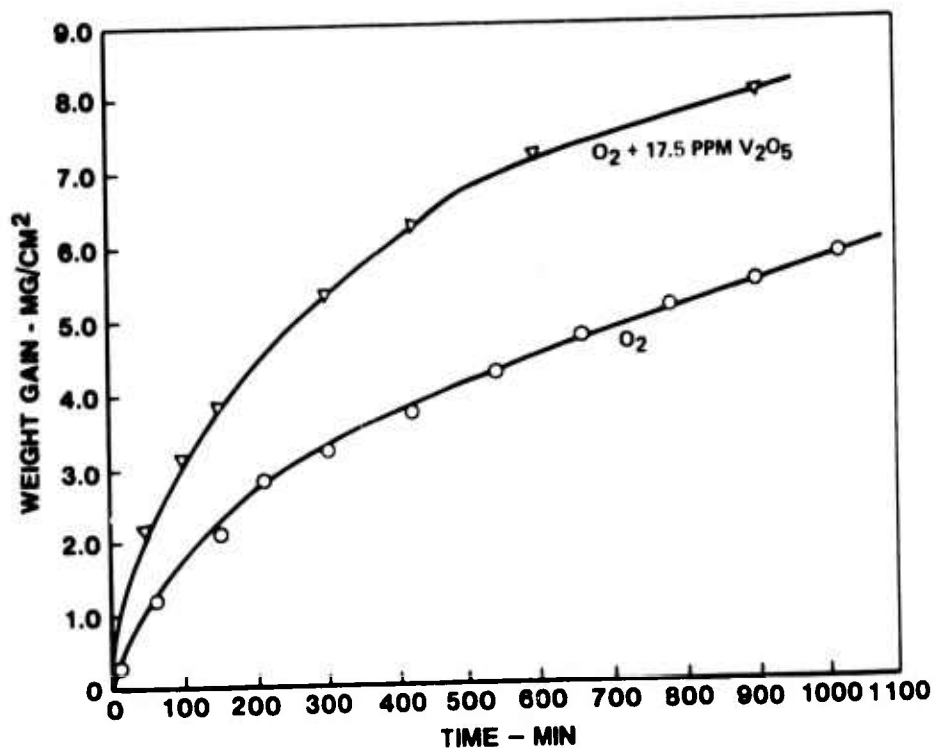
Figure 4

OXIDATION OF Ni-17 Cr ALLOY EXPOSED AT 1000°C TO OXYGEN
AND OXYGEN + 17.5 PPM V_2O_5 (g)

367
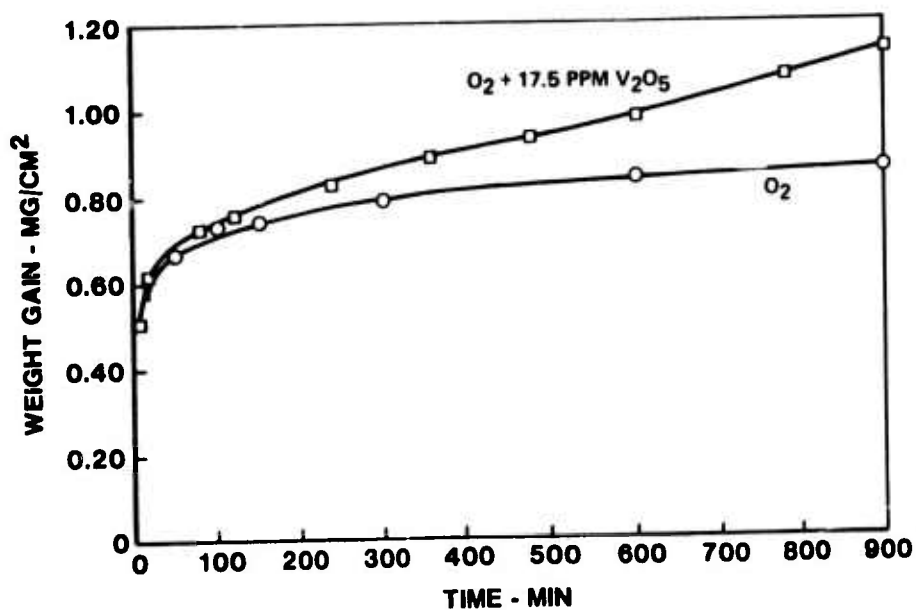
COMPARISON OF THE OXIDATION BEHAVIOR OF Ni, NiAl AND B-1900
EXPOSED AT 1000°C TO OXYGEN AND
OXYGEN +17.5 PPM V_2O_5 (g)
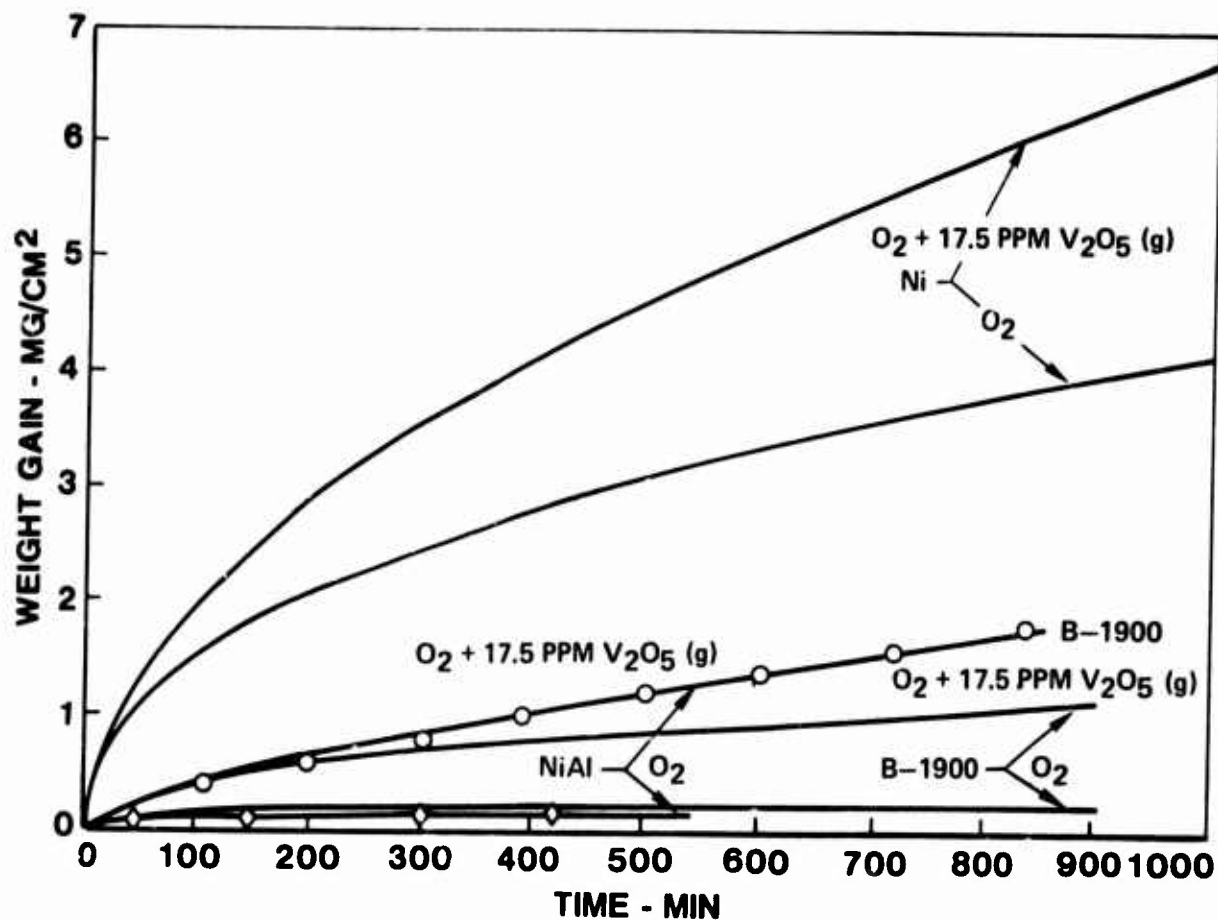
Figure 5

OXIDATION OF Ni AT 900°C IN THE PRESENCE OF CONDENSING V₂O₅ (ℓ)

Figure 6

369
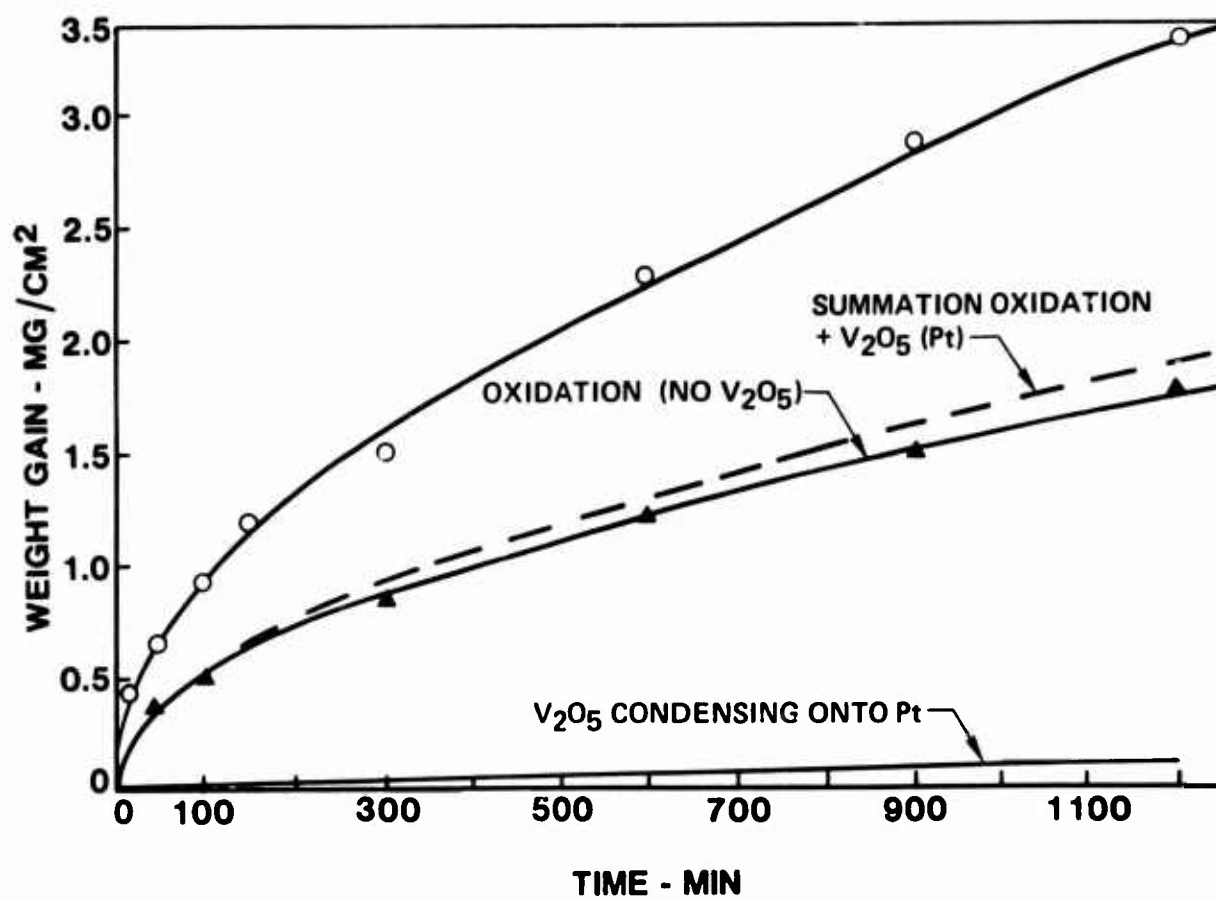
OXIDATION OF NiAl IN THE PRESENCE OF CONDENSING V$_2$O$_5$ (l)
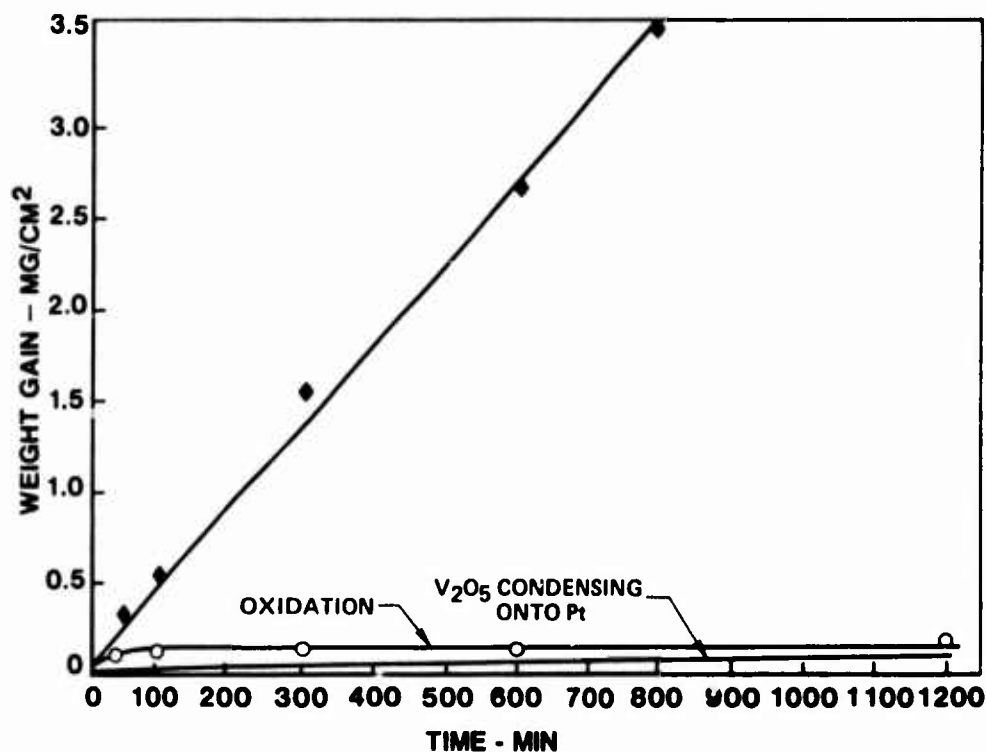
Figure 7

OXIDATION OF Ni$_3$Al AT 900°C IN THE PRESENCE OF CONDENSING V$_2$O$_5$ (l)

370
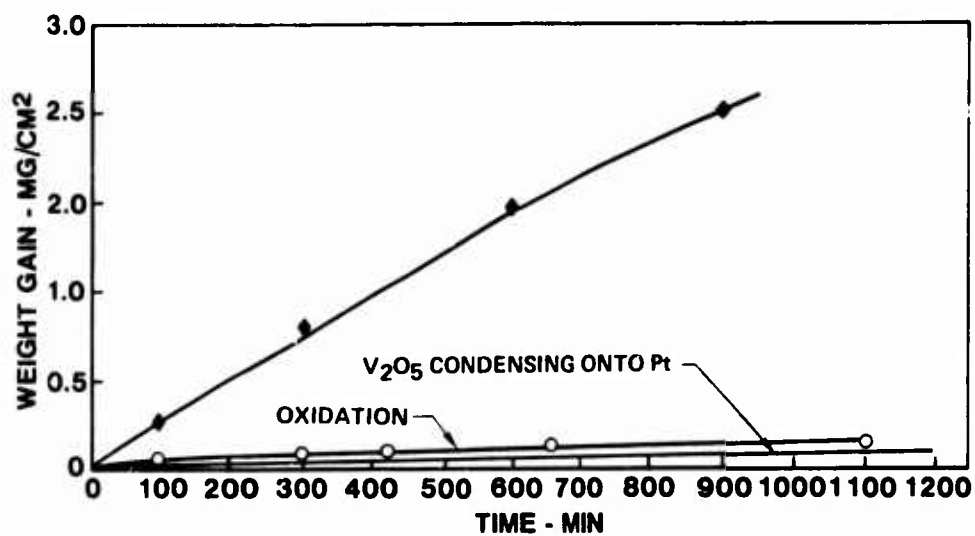
COMPARISON OF THE OXIDATION BEHAVIOR OF UNCOATED AND
V_2O_5 COATED A NICKEL - 830°C
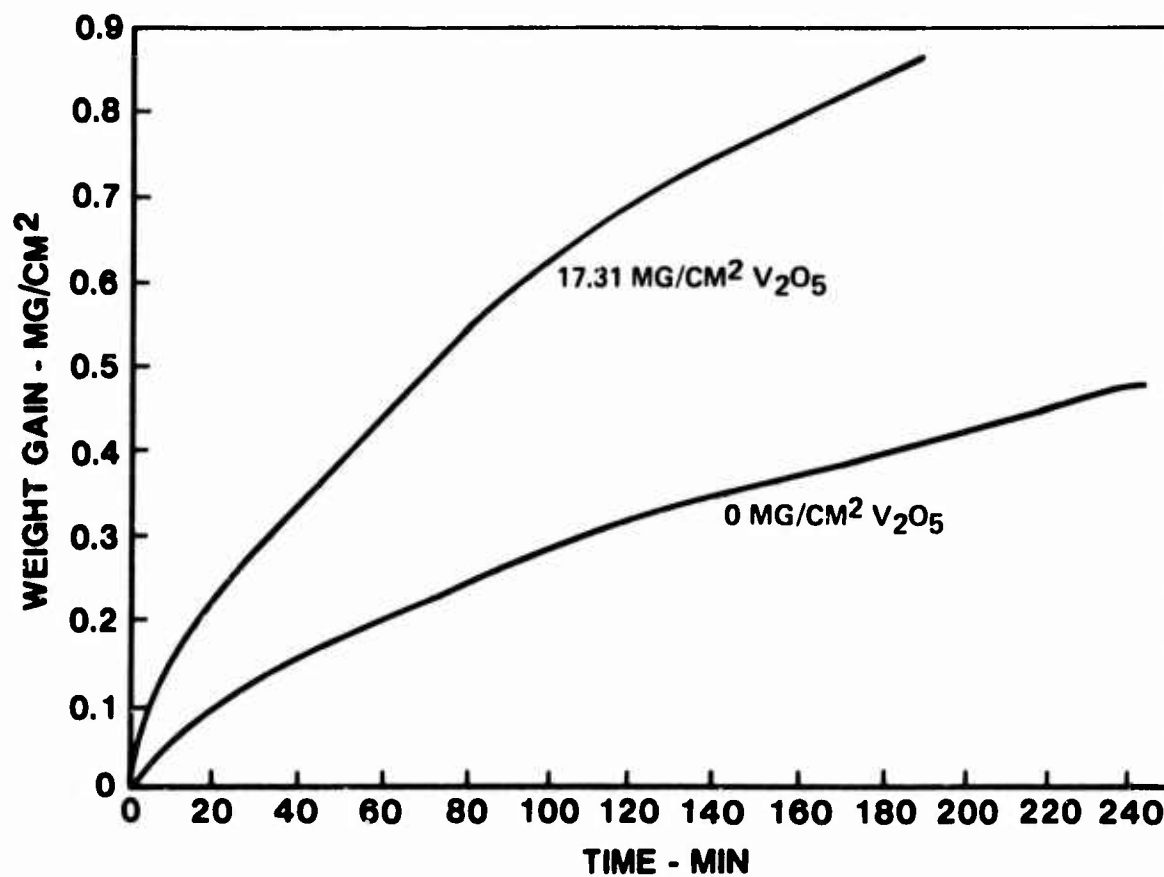
Figure 8

VANADIUM CORROSION STUDIES
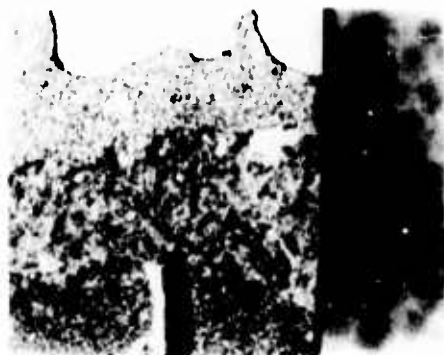
A NICKEL, 830°C

1.5x

NiO

VANDATE

V_2O_5

3x

Figure 9

VANADIUM CORROSION STUDIES
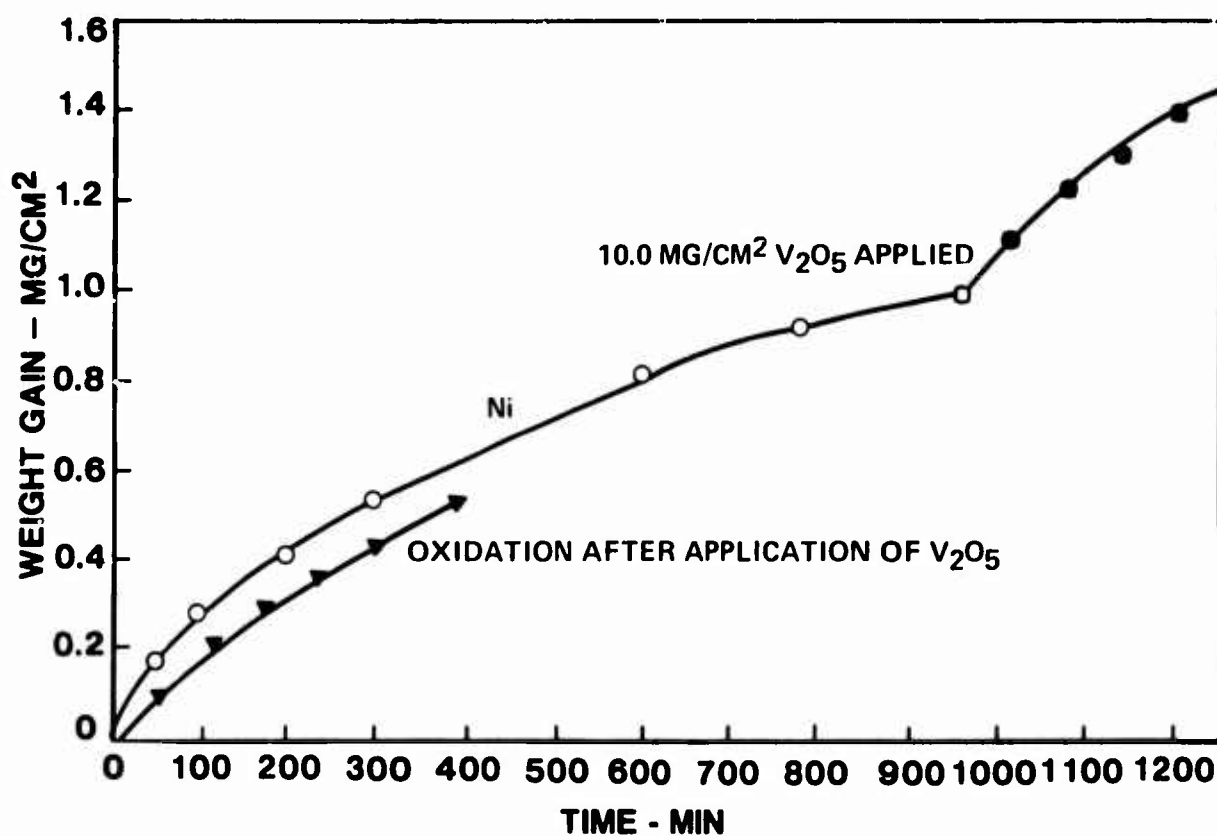
A NICKEL 830°C

Figure 10
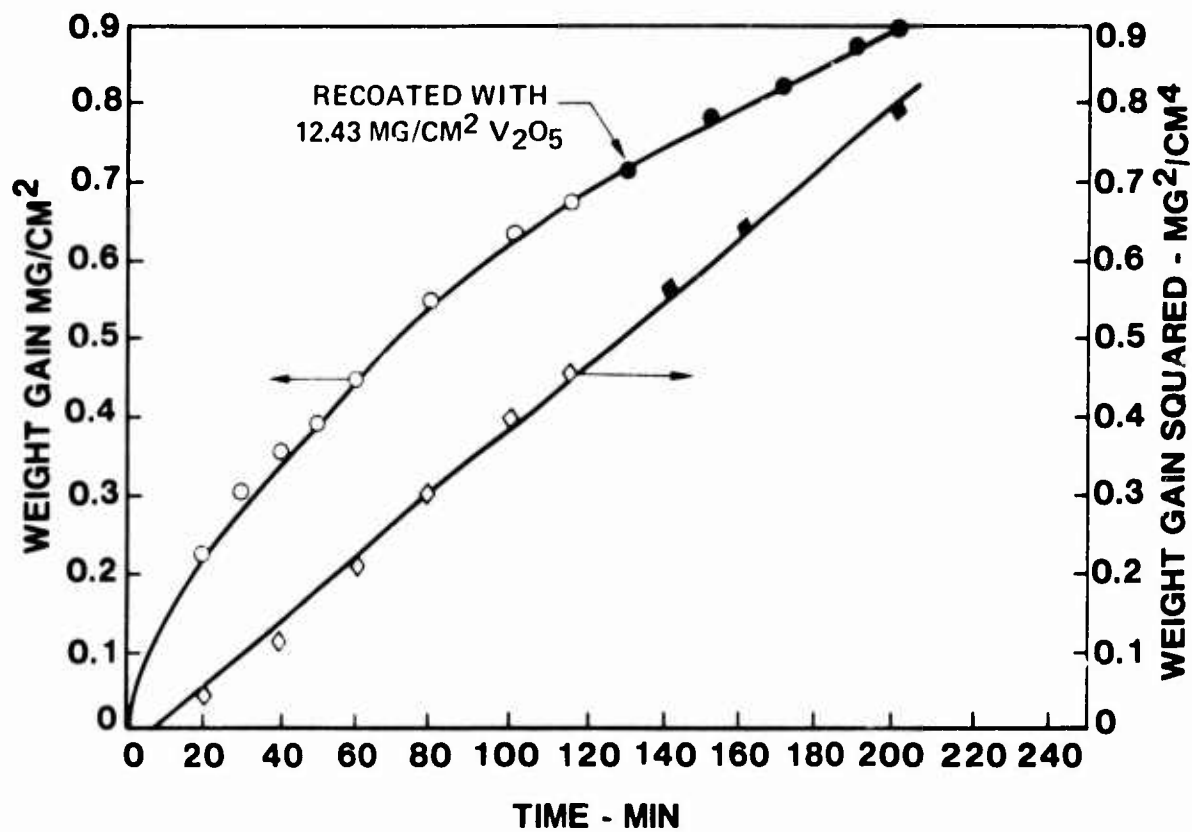
Figure 11

VANADIUM CORROSION STUDIES

A NICKEL – 900°C
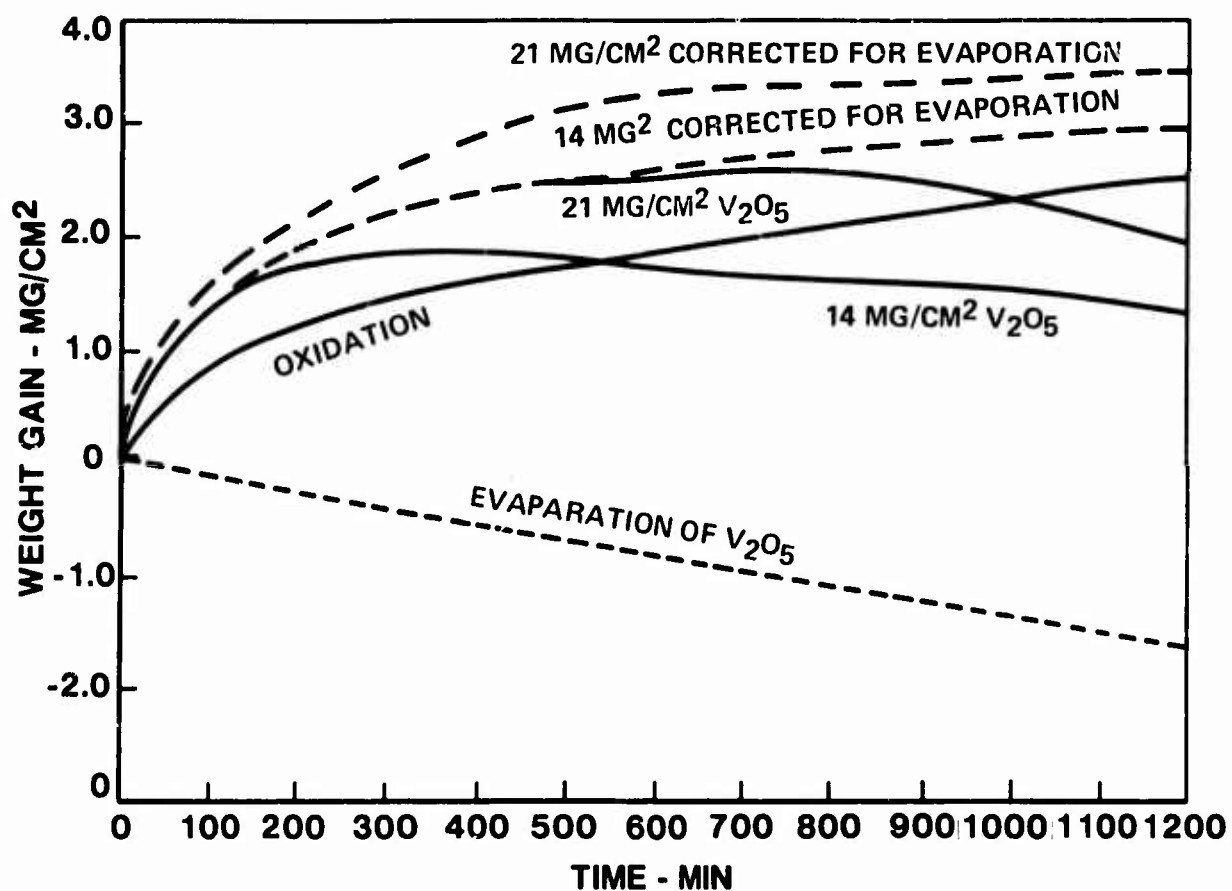
Figure 12

OXIDATION OF V_2O_5 COATED SUPERALLOYS AT 830°C
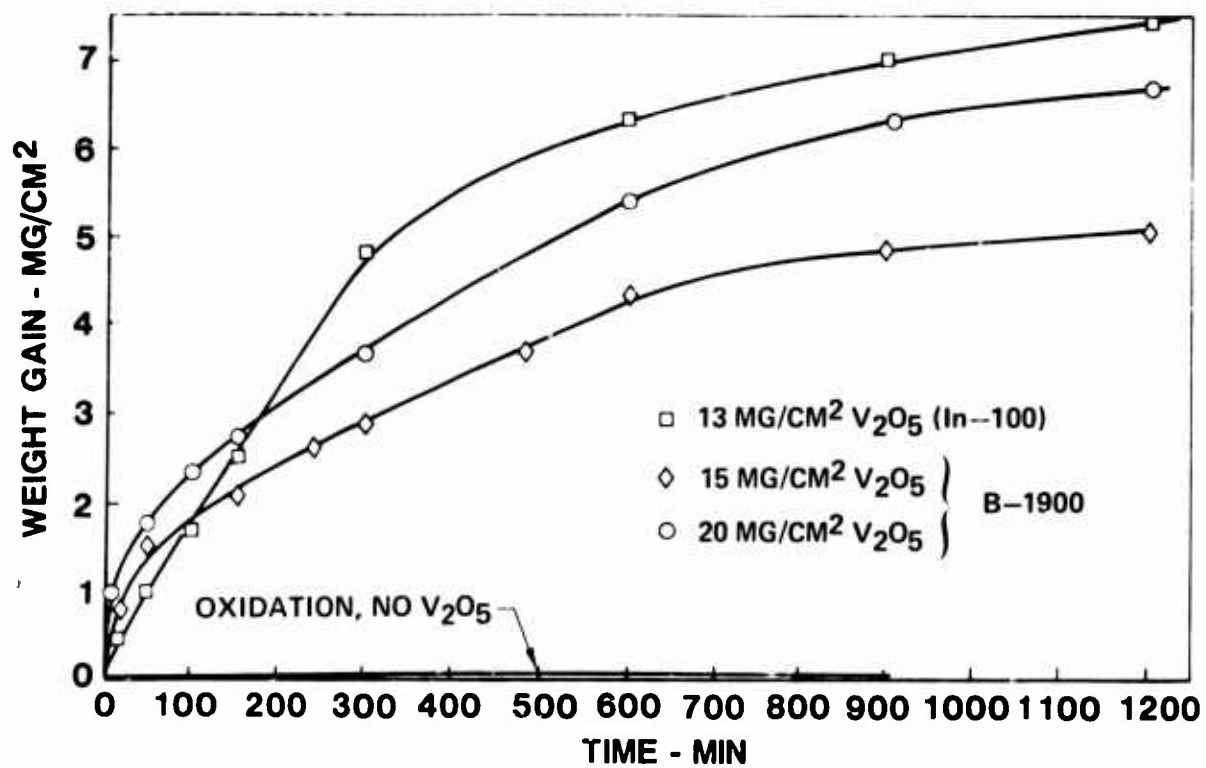
Figure 13

VANADIUM CORROSION STUDIES

B-1900, 830°C

L__J
100 μ

L__J
20 μ

ETCHED

Figure 14

VANADIUM CORROSON STUDIES

B–1900, 830° C
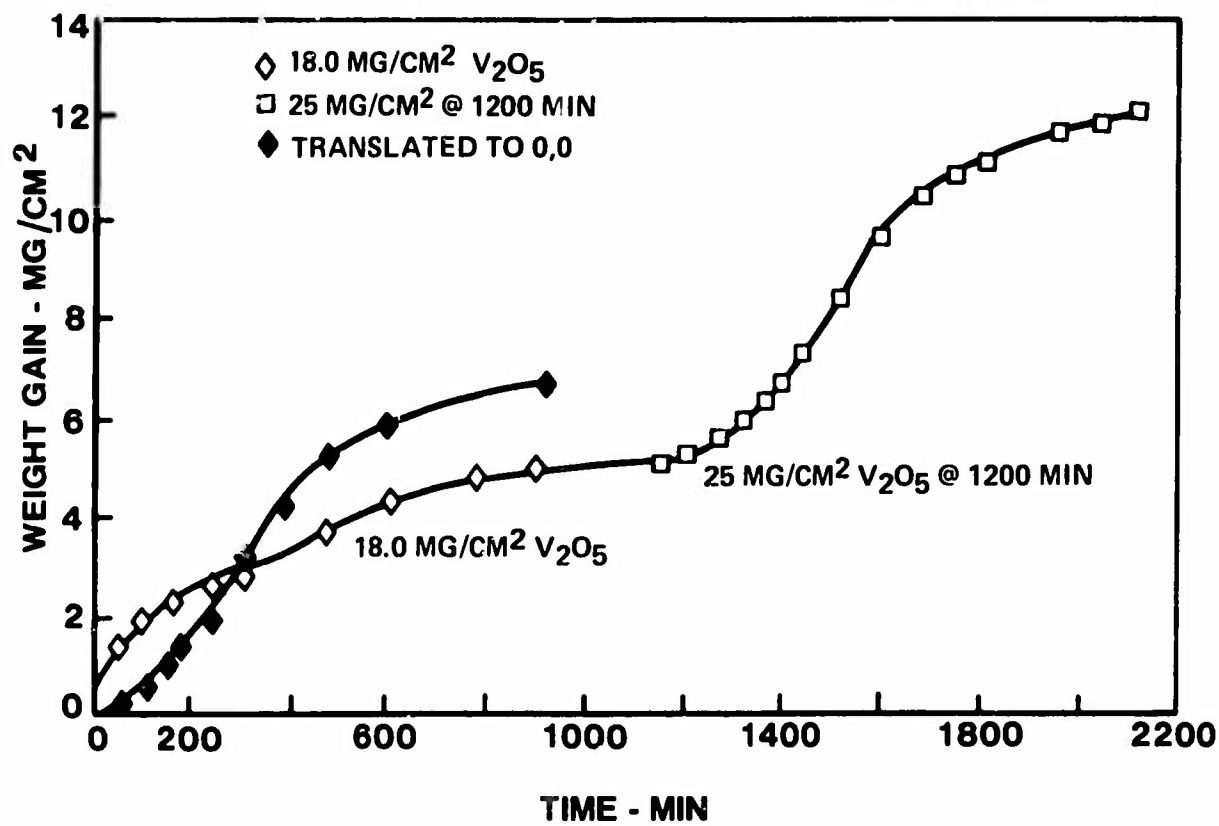
Figure 15

VANADIUM CORROSION STUDIES OF Ni₃Al AT 830°C
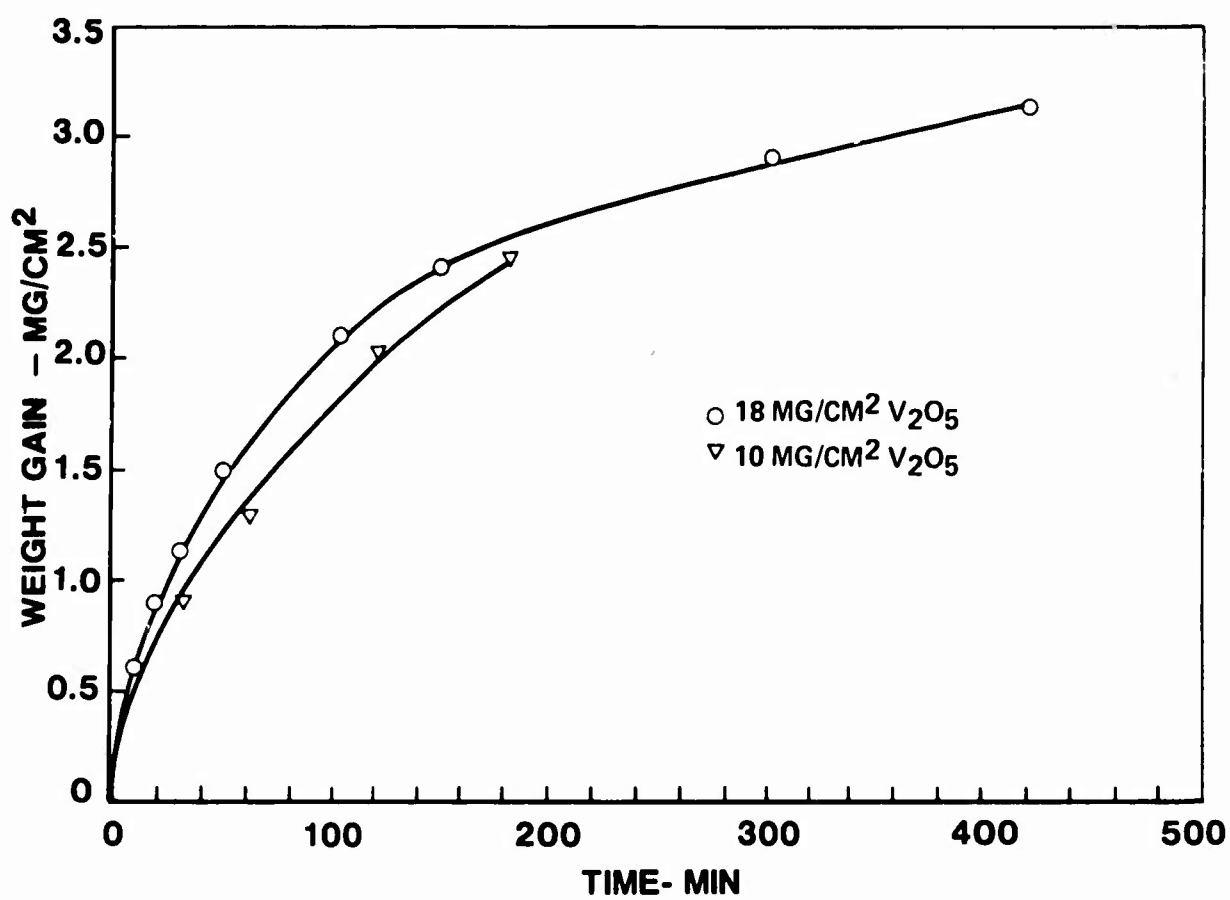
Figure 16

VANADIUM CORROSION STUDIES

NiAl, 830°C
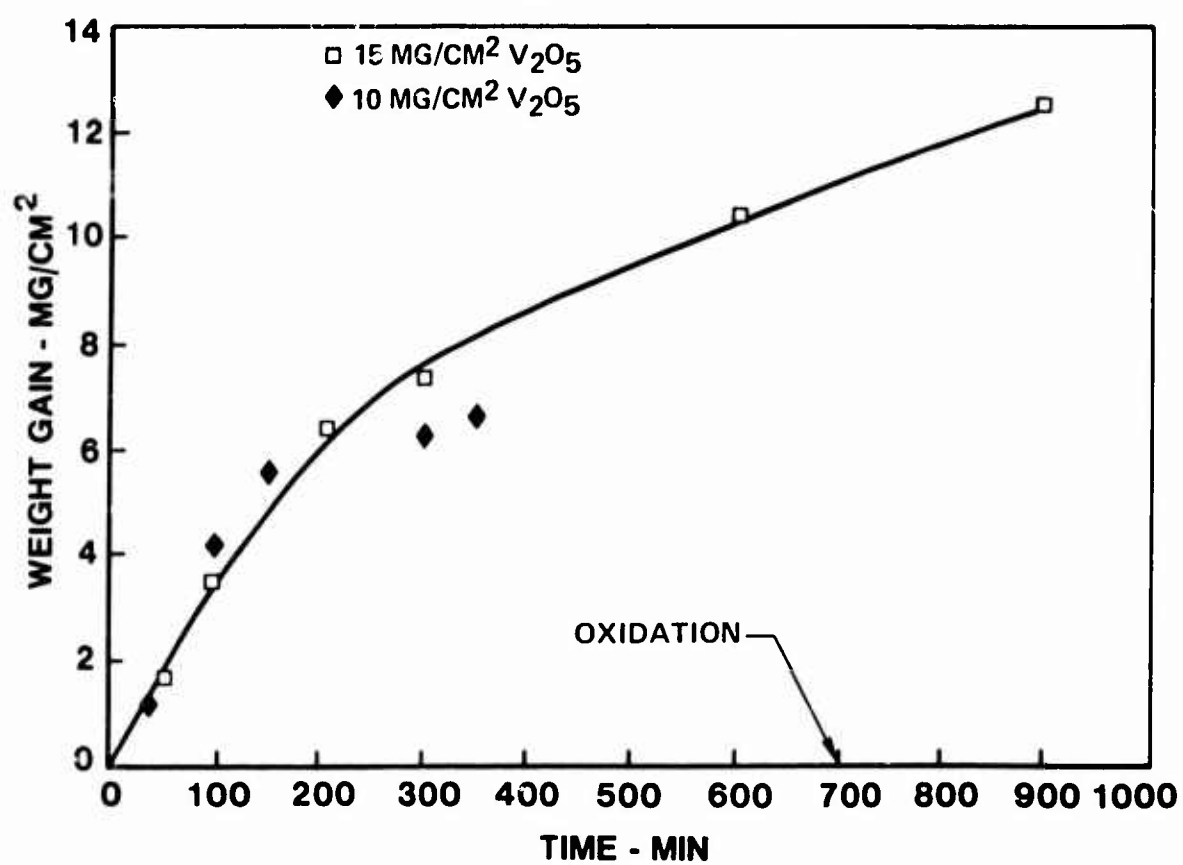
Figure 17

VANADIUM CORROSION STUDIES

NiTi, 830°C
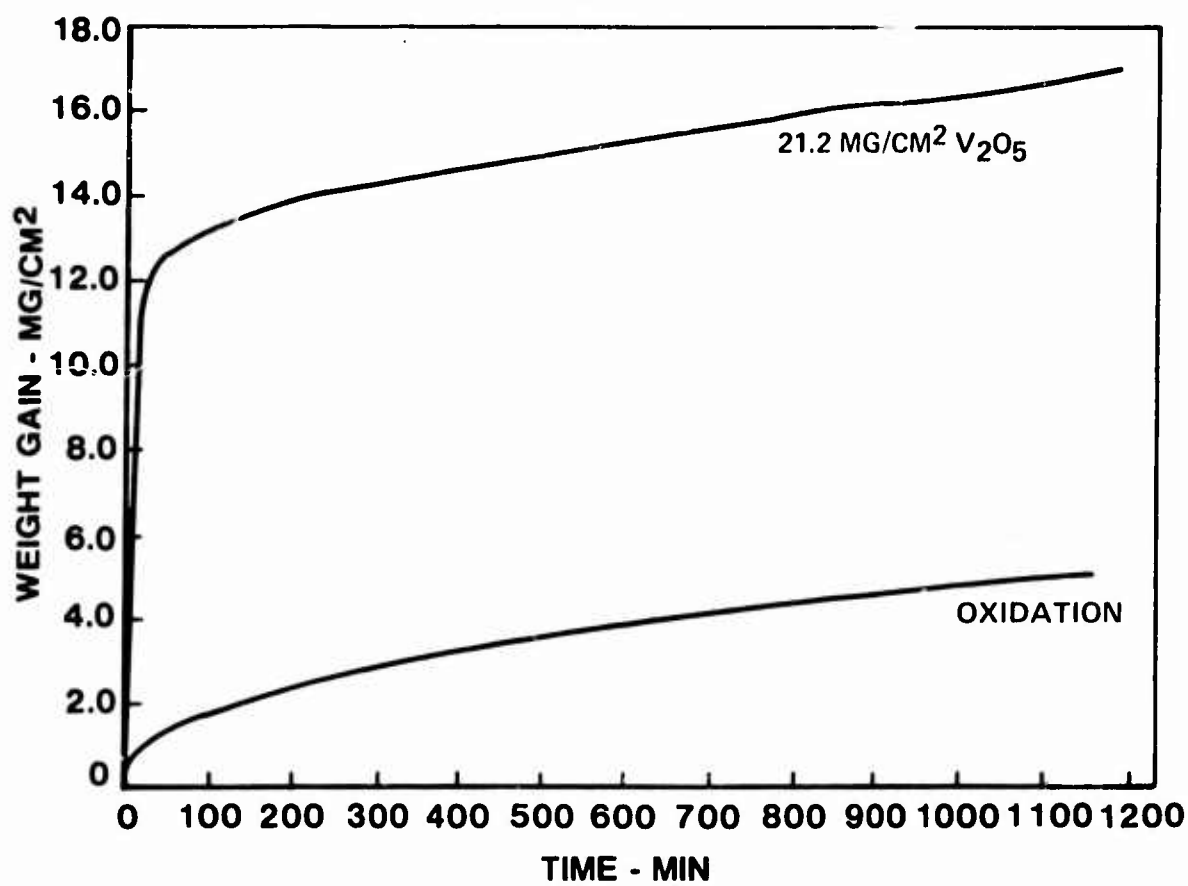
Figure 18

EFFECT OF V$_2$O$_5$ ON THE OXIDATION BEHAVIOR OF NiTi AT 830°C
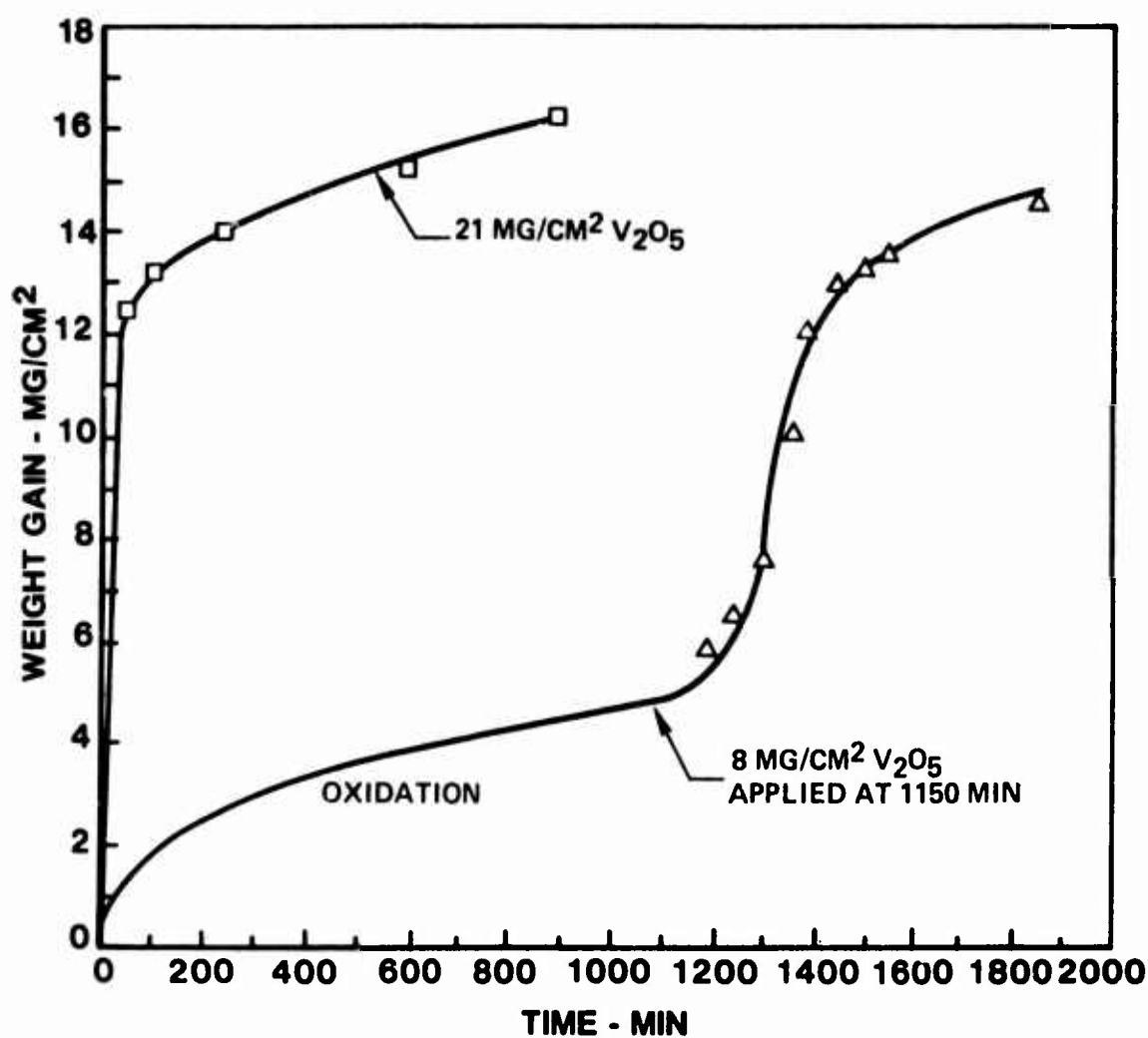
Figure 19

REDUCE MAINTENANCE WITH
IVD ALUMINUM COATINGS

E. R. Fannin and K. E. Steube
McDonnell Aircraft Company

Ion vapor deposited aluminum coatings provide good corrosion protection to both high strength aluminum and steel alloys without causing a reduction in fatigue life in aluminum or embrittlement in steel. The coating is also useful at temperatures to 950°F and is compatible with titanium. Neither the coating nor the coating process present ecology problems such as associated with cadmium coating processes. MCAIR has applied 8 years' development experience with IVD to establish production status which will result in reduced maintenance of weapons systems.

INTRODUCTION

Ion vapor deposition (IVD) is a process that can be used to deposit an aluminum coating uniformly on complex shaped parts with excellent coating to substrate adherence. IVD aluminum has definite advantages over vacuum deposited cadmium, electroplated cadmium, diffused nickel-cadmium and anodize and has great potential for replacing these coatings in the future.

IVD is a vacuum deposition process which differs significantly from the commonly-used physical vapor deposition (PVD) process in that during IVD the substrate or workpiece is the cathode of a high voltage circuit. By maintaining the proper inert gas pressure in the vacuum system a DC glow discharge is established about the workpiece wherein a portion of the evaporated aluminum is ionized and accelerated toward the part. This produces a more adherent coating.

Because the IVD process is not confined to line-of-sight deposition, parts having complex shapes can be plated with a uniform coating. This excellent throwing power makes the process very attractive for production applications.

McDonnell Aircraft has recognized the potential of IVD aluminum for reducing maintenance problems associated with some of the protective coatings used on weapon systems and has applied 8 years' development experience to establish IVD production coating capability.

MAINTENANCE PROBLEMS

Both aluminum and steel alloys are used extensively in the fabrication of weapon systems. Each of these materials must be protected from corrosion by some type of coating. The coatings selected must not only provide adequate protection from corrosion but must also be compatible with other materials they may contact. Coatings that do not satisfy both conditions can result in a high level of maintenance.

ALUMINUM ALLOYS

A typical maintenance problem with some aluminum alloys such as 7075-T6 and 7178-T6 is exfoliation corrosion. This type of corrosion is usually initiated at the base metal adjacent to a fastener hole as shown in Figure 1. Anodizing improves the corrosion resistance of the aluminum alloys; however, for most parts, the drilling and countersinking operation must be done last. Therefore, the holes and countersinks are not anodized and moisture penetration into the joints results in corrosive attack of the exposed grain boundaries. This exfoliation corrosion can be interpreted literally as deliminating or peeling of layers of the aluminum alloy panel.

The desirability of anodize as a protective coating for aluminum alloy structure has been reduced because of recent design innovations to improve fatigue life of these parts through the use of fatigue enhancing attachments.
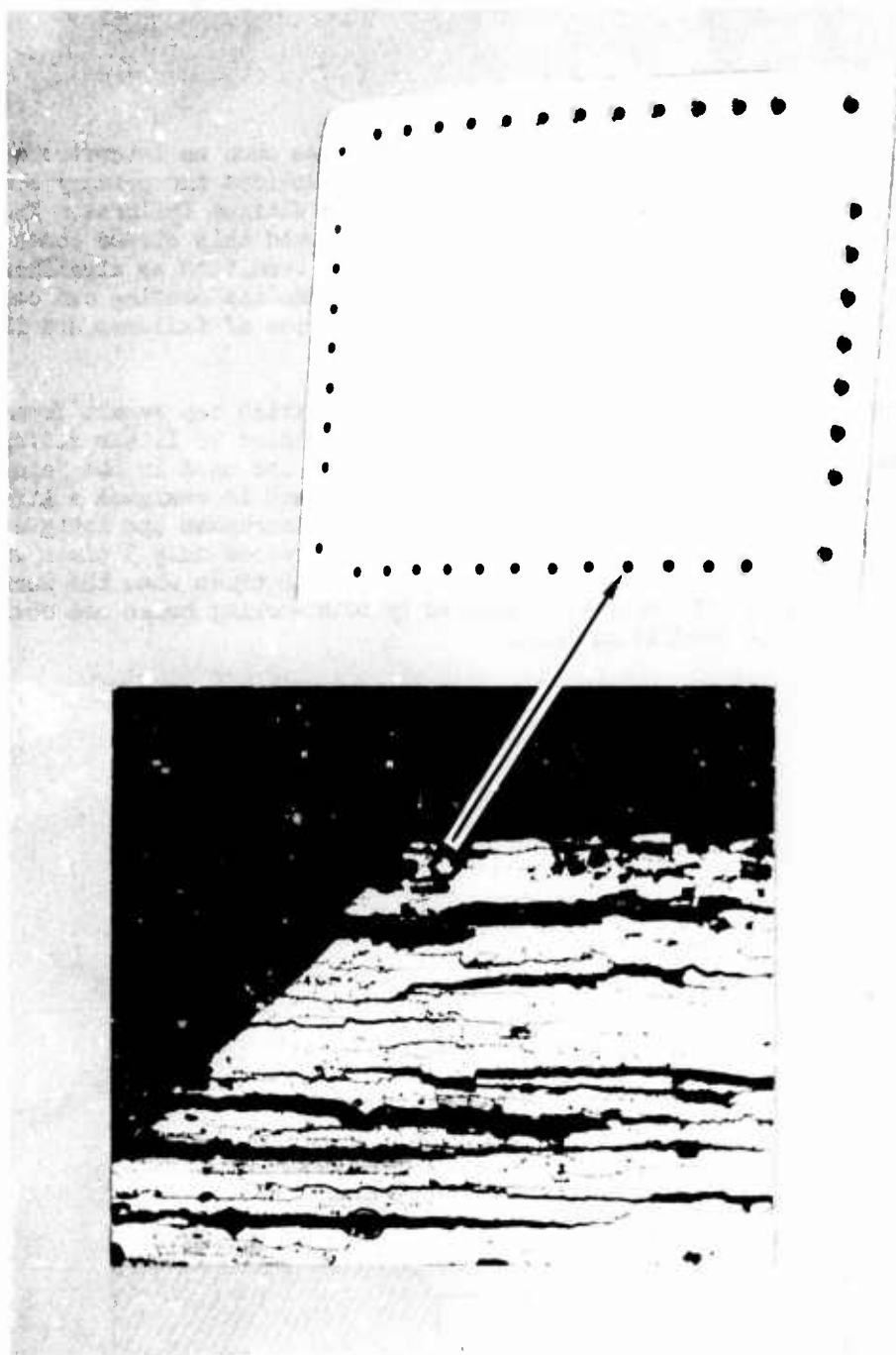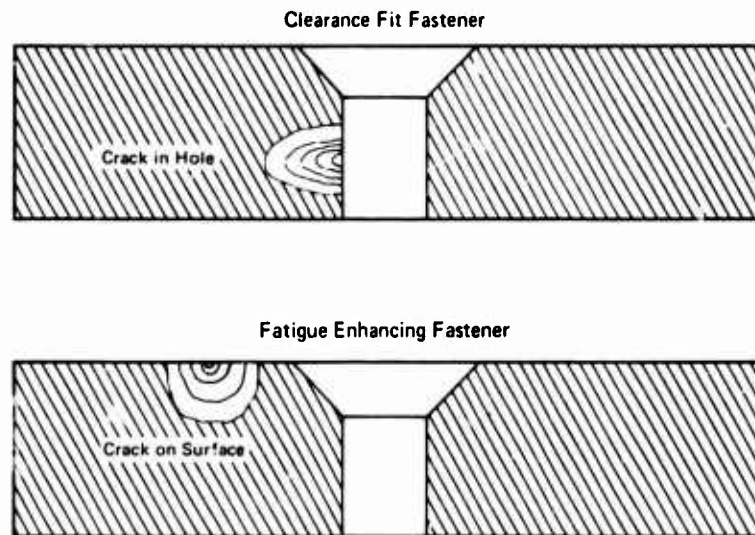
FIGURE 1
**EXFOLIATION CORROSION OF 7178-T6 ALUMINUM ALLOY PANEL**

Prior to the use of fatigue enhancement techniques such as interference fit fasteners and cold worked holes, the fastener holes provided the primary stress concentration and therefore were the location of most fatigue failures. The use of fatigue enchancement techniques has significantly reduced this stress concentration in and around the hole and has identified the surface condition as significantly influencing fatigue life. The brittle nature of the anodize coating can cause fatigue failures to initiate at the surface. These types of failures are illustrated in Figure 2.

The reduction of fatigue life of aluminum alloys which can result from anodize coatings is shown graphically in Figure 3. Note that there is little difference in fatigue life when conventional clearance fit fasteners are used in the joint. The uncoated material is used as the basis for comparison and is assigned a life of 1. Cold working the holes in joints in uncoated material increases the fatigue life 5.4 times. However, the fatigue life at joints is increased only 3 times when the surface of the material is chromic anodized and only 1.6 times when the surface is sulphuric anodized. The benefits obtained by cold working holes are obviously greatly reduced by the anodize coating.

Clearance Fit Fastener

Crack in Hole

Fatigue Enhancing Fastener

Crack on Surface

GP74 4367 15

FIGURE 2 FATIGUE OF ANODIZED ALUMINUM
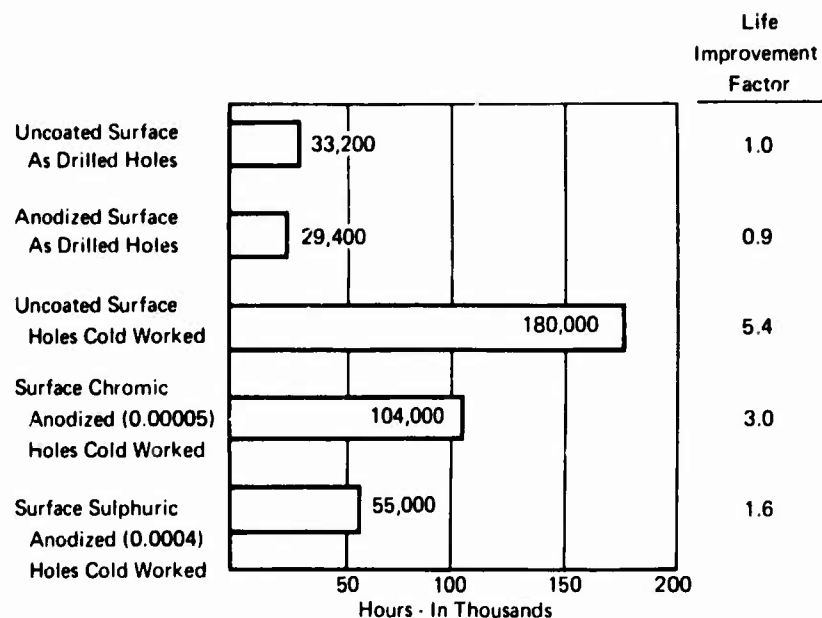
386

FIGURE 3
SPECTRUM FATIGUE LIFE/COLD WORKED HOLES IN
7075-T6 ALUMINUM (37.0 KSI-100% TLL)

STEEL ALLOYS

Corrosion of steel is another major source of maintenance problems. Steel parts must be protected with some type of coating to prevent rapid corrosion. These coatings often break down and leave the part unprotected. The result is that extensive rework or part replacement is required. An example of a part that has failed because of corrosion is shown in Figure 4.

Electroplated cadmium is the most widely used aerospace protective coating for steel parts. Hydrogen embrittlement of high strength steel parts (200 KSI) limits the type of coating system that can be used because of the evolution of hydrogen during electroplating.

Cadmium cannot always be used as a protective coating because it is not compatible with titanium. Under certain conditions a solid metal embrittlement failure can occur to a titanium part that is in contact with a cadmium coated steel part. This type failure is illustrated in Figure 5. A crack due to solid metal embrittlement has developed in the hole of a titanium plate. The hole contained a cadmium plated interference fit type. An electron microprobe scan (Figure 5) shows the presence of cadmium down the length of the crack. In addition, molten cadmium (M.?. 610°F) attacks most structural metals under stress, therefore, cadmium usage is limited to 450°F maximum applications.

387

GP74 4482-8

FIGURE 4
FAILURE OF PART DUE TO STRESS CORROSION
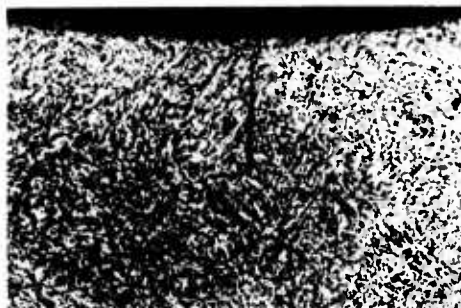
Cadmium Plated Interference
Fit Fastener in Titanium
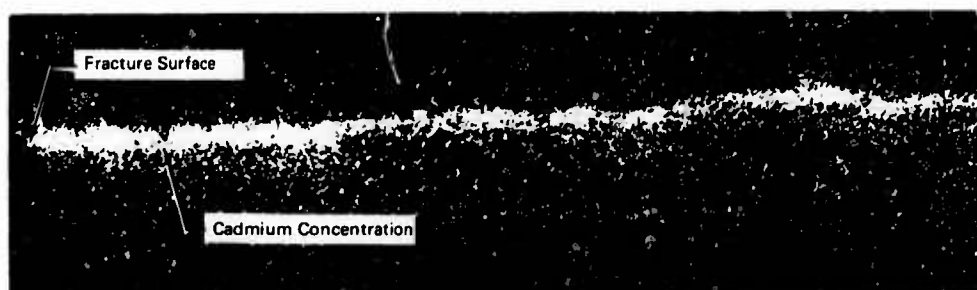
Microprobe Scan

FIGURE 5 SOLID METAL EMBRITTLEMENT

IVD ALUMINUM

IVD aluminum coatings are a solution to many of the current corrosion maintenance problems.

What is the IVD Process? – Ion vapor deposition is a plating process developed approximately ten years ago. The IVD process is similar to the familiar vacuum metallizing process, or physical vapor deposition (PVD) with one major difference – during plating the substrate is held at a high negative potential with respect to the vapor source (typically –2 to –3 kV). This potential, when applied at the proper inert gas pressure, causes a DC glow discharge to be established around the cathode or part to be coated. A portion of the evaporant is ionized in this region and accelerated toward the part. This produces greater adhesion and better thickness uniformity of the coating.

The IVD Process can be made applicable to large parts, and, since the plating is not confined to areas within line-of-sight, a very useful production process can be realized. Parts with complex shapes can be plated with a reasonably uniform coating even when some of the surfaces to be plated are recessed or otherwise not in line with the vapor source. The deposit extends into the recesses and holes of the part because of the many collisions of evaporant atoms with the gas molecules surrounding the workpiece. The schematic shown in Figure 6 illustrates the basic components of a production coater. This coater utilizes resistance heated boats to evaporate aluminum which is continuously supplied by a wire feeding system. Parts to be coated are held in place above the boats by a fixture that electrically insulates them from other internal structure while providing the contact to the negative lead of the high voltage power supply.
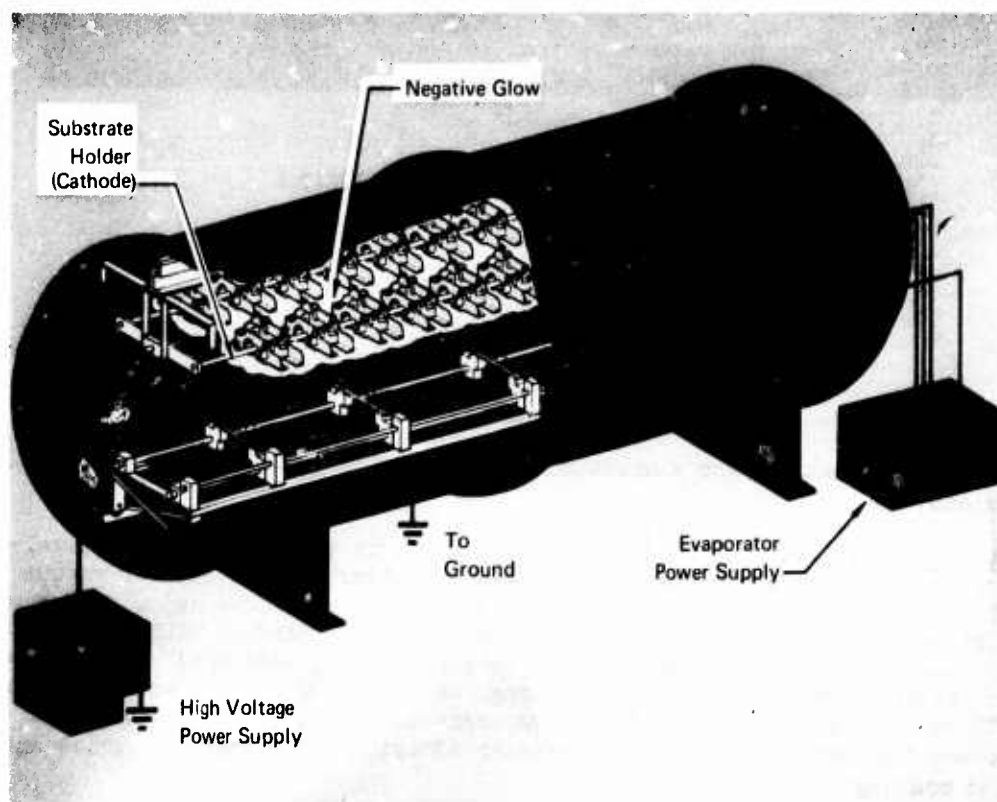
GP74 4482 1

FIGURE 6 ION VAPOR DEPOSITION CHAMBER

390

Advantages of IVD Over Other Processes - The several advantages of IVD aluminum over other protective coatings are summarized in Figure 7.

It can replace diffused nickel-cadmium plating on steel and provide better corrosion protection at all strength levels. Diffused nickel-cadmium plating is generally limited to steels having strengths below 200,000 psi because of hydrogen embrittlement. It can also be utilized in contact with titanium structure without causing solid metal embrittlement whereas cadmium is prohibited. Steel parts in contact with fuel can be IVD coated. Again, cadmium plating is prohibited. It can replace vacuum cadmium plating and be utilized at temperatures up to 950°F. Cadmium plating has a 450°F limitation.

IVD has several advantages over protective coatings commonly used on aluminum alloys. It provides better corrosion protection to high strength aluminum alloys than type II anodize in the real aircraft environment. In addition, IVD aluminum coatings are soft and ductile and do not adversely effect fatigue life of high strength aluminum alloys.

Aluminum coatings do not present any ecology problems. The future cost of vacuum cadmium coatings, for example, will be increased by strict OSHA requirements for the control of cadmium vapors and dust. EPA controls on the handling and disposal of waste liquors will increase the cost of electroplated cadmium coatings.

STEEL {
- Steel at all Strength Levels
- Contact Titanium
- 950°F
- Galvanic Protection
ALUMINUM {
- Fatigue
- Stress Corrosion Protection
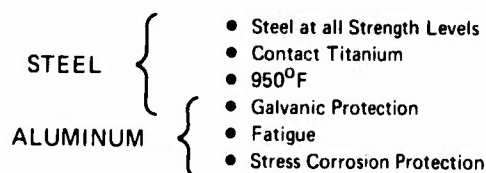
No Ecology Problems

GP74 4482 3

FIGURE 7 ADVANTAGES OF IVD ALUMINUM

391

COATING TEST RESULTS

IVD aluminum coatings were tested for protection of high-strength aluminum alloys. The coatings were adherent and afforded protection after 120 hours at 500°F followed by 120 hours in 5% salt spray.

Several small F-4 aircraft doors were coated for demonstration purposes and were used to illustrate the excellent adherence of the coating. Metallographic cross section of several countersink areas showed a uniform coating thickness and an excellent coating to substrate interface. In another series of experiments, the area in and around the countersinks of holes drilled in 7178-T6 aluminum alloy panels was coated with aluminum. These panels were compared with similar panels having unprotected countersinks. After exposure to alternate acidified salt spray for two weeks, the IVD protected counterskins showed only minimal corrosion. The unprotected countersinks were severely corroded.

Our assessment of the IVD coating system on aluminum is that it will provide better corrosion protection than anodizing in the real aircraft environment. Laboratory tests show undamaged anodize to provide the best corrosion protection; however, typically we trim edges and drill and countersink attachment holes on assembly. This leaves unanodized areas. IVD aluminum can be applied to detail parts in a manner similar to anodize; however, the trimmed and drilled areas are anodically protected by the IVD coating which functions like alclad on aluminum alloys. A chemical conversion coating is the least protective and most susceptible to damage of all the systems. Its primary function is to provide paint adhesion. IVD aluminum coating will provide much more effective corrosion protection.

Aluminum coatings are soft and ductile, and therefore do not have adverse effects on fatigue life. By comparison, type II anodize which is used extensively on aluminum structure, can limit the fatigue improvement resulting from the use of fatigue improving attachments such as interference fit fasteners. Fatigue tests show that no reduction in fatigue life results from the application of IVD aluminum coating (Figure 8) to aluminum alloys joined with interference fit fasteners.

Test results also show that IVD aluminum offers excellent protection to steel. A four year outdoor exposure test shows it to protect better than cadmium. This test exposure was accomplished on the roof of a McDonnell Aircraft building in St. Louis. The test samples, as they appeared after 4 years exposure, are shown in Figure 9. The cadmium protected samples were severely corroded because the cadmium had been sacrificially consumed while the aluminum coating remained intact and provided the necessary protection.

SCALE-UP TO PRODUCTION CAPABILITY

As a result of our in-house development and evaluation of the IVD aluminum process, NAVAIR awarded us a contract in March 1973 to fabricate a production coater for use at the Naval Air Rework Facility at North Island, California. This unit was successfully installed in April of this year.
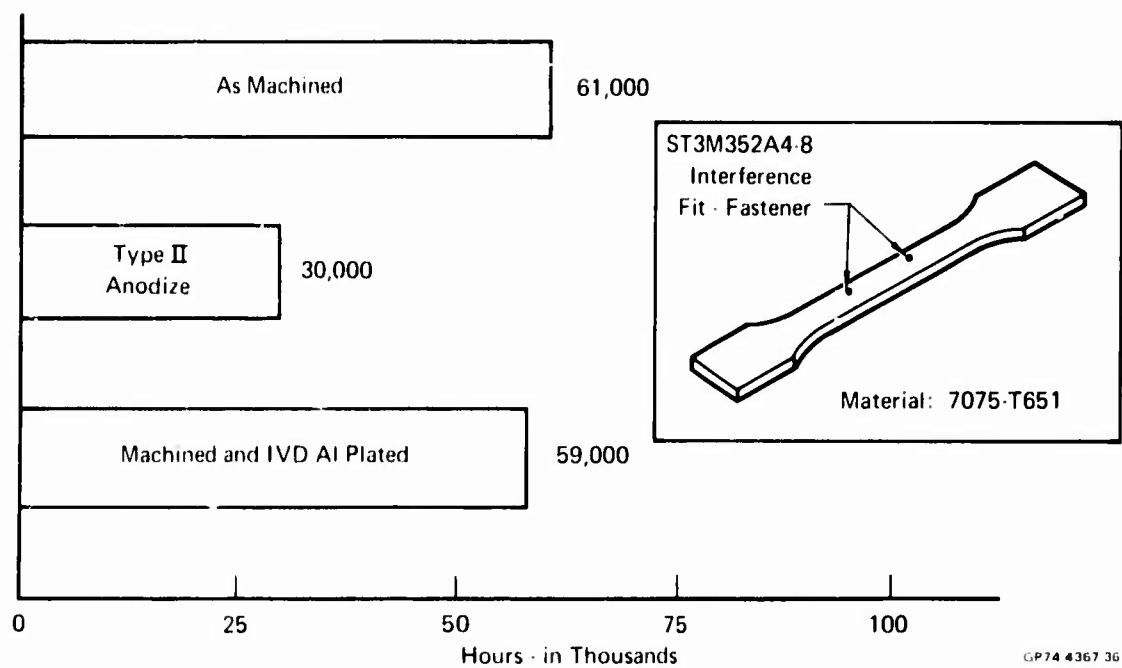
FIGURE 8 SPECTRUM FATIGUE LIFE/INTERFERENCE FIT FASTENERS
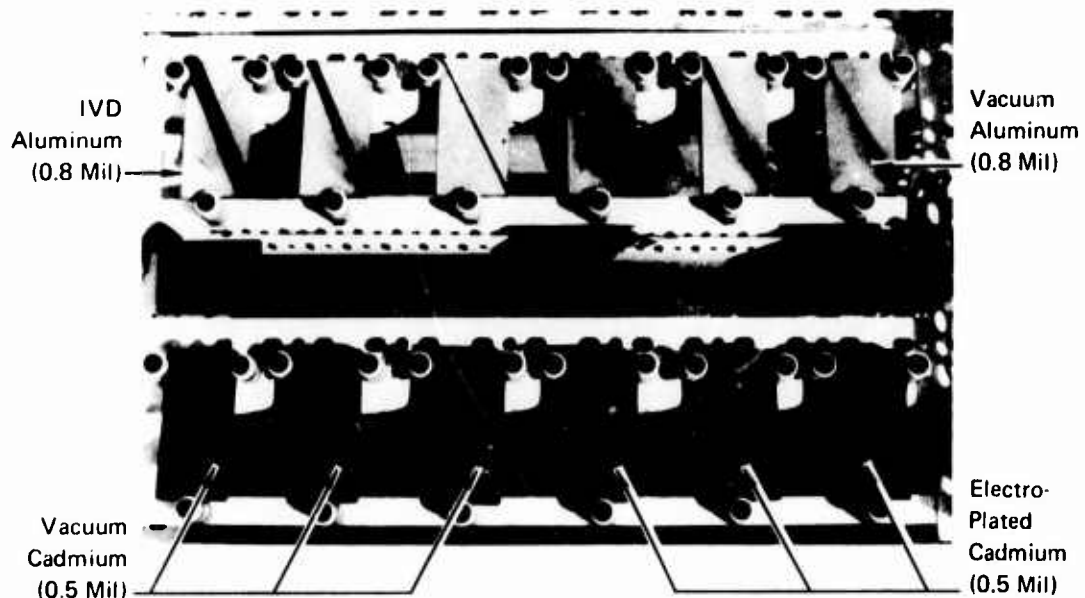
(34 KSI · 100% TLL)

FIGURE 9 FOUR YEAR OUTDOOR EXPOSURE TEST

The system developed for the Navy was enclosed in a vacuum chamber 4 ft. in diameter by 8 ft. long (Figure 10). Aluminum evaporators were positioned along the center axis of the chamber. Parts holders, located above the evaporators, can hold parts stationary, pass parts laterally, or rotate parts over the evaporators. This configuration allows the coating of flat sheet type parts approximately 2 ft. by 7 ft, cylindrically shaped parts approximately 15 in. diameter by 7 ft long, or numerous racked small parts.

Parts shown in Figure 11 are typical of those that have been plated in the Navy coater. Although all parts shown were not coated during the same coating cycle, it can be said that the coater is capable of doing so.

A plating thickness survey made on one of the complex shaped parts is illustrated in Figure 12. The results showed the coating uniformity to be at least equivalent to conventional coating processes.
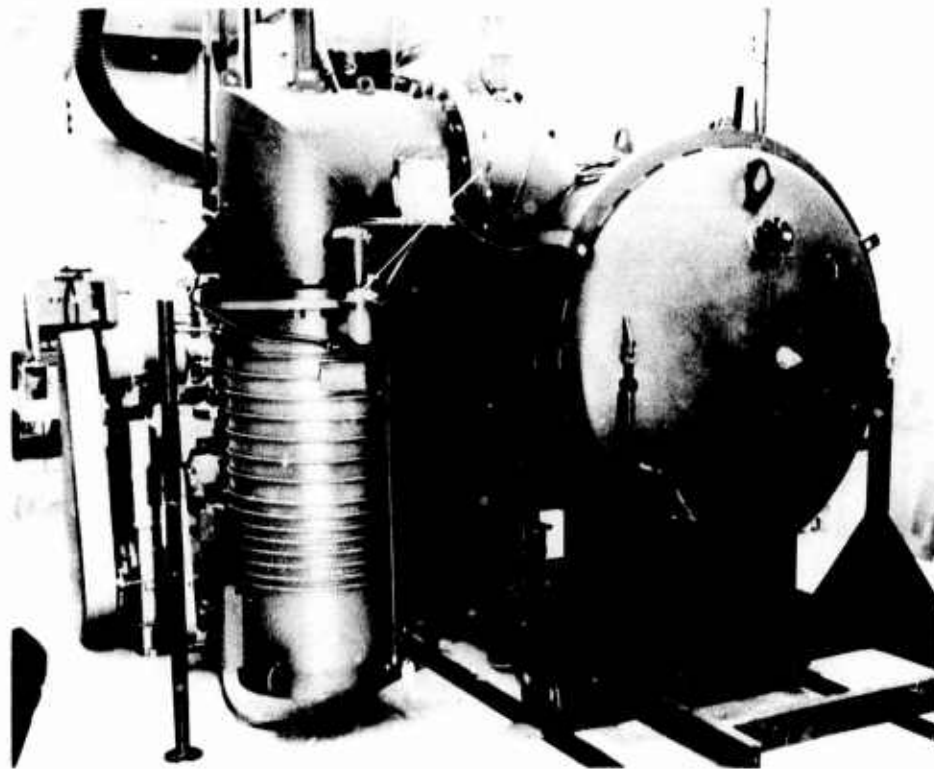
FIGURE 10
MCAIR PRODUCED COATER FOR NAVAL AIR REWORK FACILITY

394

FIGURE 11 IVD COATED PRODUCTION PARTS

Note: All dimensions in inches
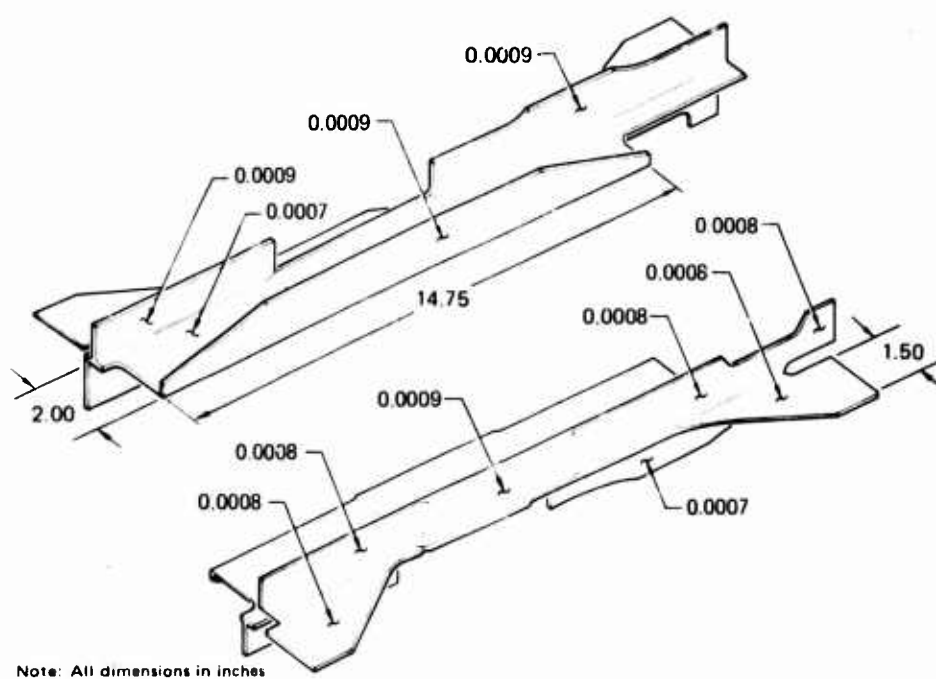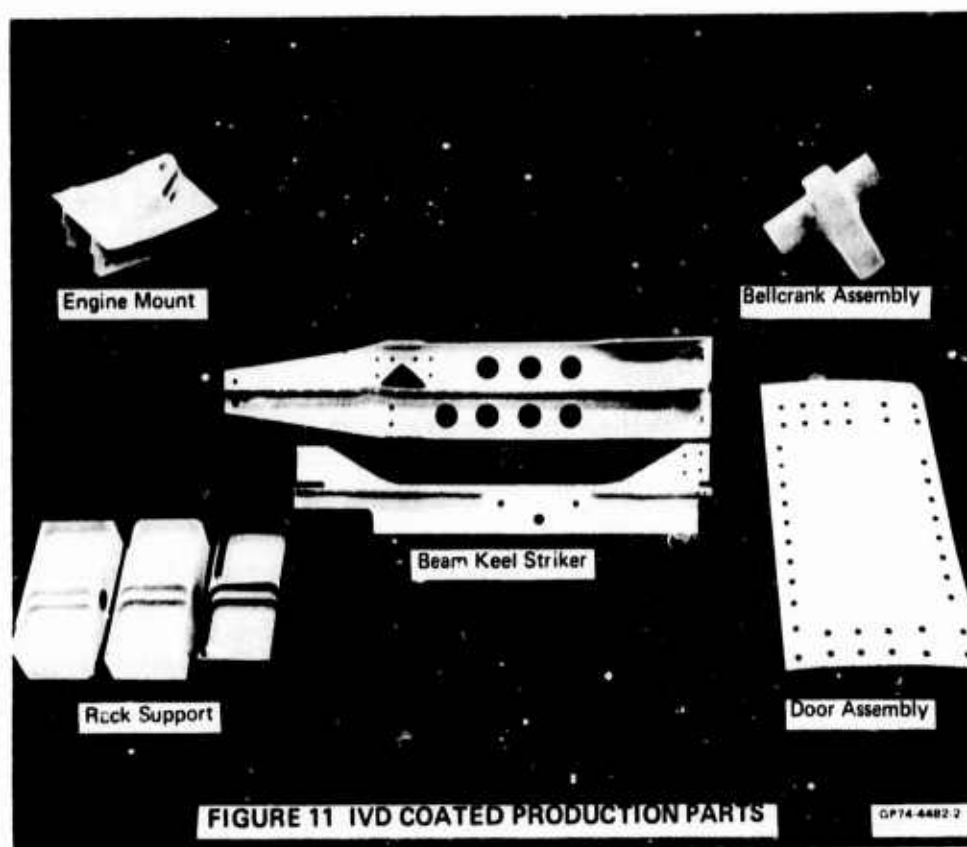
FIGURE 12 PLATING THICKNESS SURVEY

One of the primary benefits of IVD aluminum is that it allows the replacement of costly high strength stainless steel with lower cost aluminum coated low alloy steel. An estimate of cost savings was made for several aircraft parts based on this substitution. In each case the material substitution results in a significant savings.

As a part of the continuing IVD effort at McDonnell Aircraft, development effort has been concentrated on a technique for coating batch quantities (barrel plating) of small parts. The feasibility of using a rotating drum, as well as other type parts holders have been established and patent disclosures of the plating concepts have been made.

Laboratory tests were conducted to establish optimum parts cleaning and plating parameters. Barrel size and configuration were extensively evaluated for best coating results and coating efficiency. These tests provided the necessary information to design and build a full-scale IVD barrel coater for production use. A schematic of this facility is shown in Figure 13.

A chamber measuring 4 ft. diameter and 6 ft. long will be the basis of the coating facility. Two barrels positioned side by side, each measuring approximately 15 inches diameter and 4 ft. long, with evaporation boats located below, but centered between the barrels will comprise the coating apparatus. A two barrel configuration will be used to take advantage of the tendency of the parts to be coated to partially climb up the circumference or side of the barrel as it rotates. When the evaporation boats are placed between the two barrels and the barrels then rotated in opposite directions the coating region of each barrel is well within the vapor stream of the boats. The number of parts that can be coated per unit time is therefore doubled.

An estimate of cost savings was made based on replacing a combination of high strength stainless steel fastening devices with IVD aluminum plated alloy steel fastening devices for a specific aircraft application. This substitution would result in a savings of several thousand dollars per aircraft.

CONCLUSION

IVD aluminum has been shown to have significant advantages over other coatings commonly used to protect steel and aluminum alloys. Benefits of the coating are summarized in Figure 14. Previously, the IVD process was restricted to laboratory type equipment and substrates were limited to simple configuration and small size. McDonnell Aircraft's 8 years development experience with IVD provided the foundation for production exploitation of this plating process which will result in reduced maintenance of weapon system components because of the better corrosion protection and fatigue effects of IVD aluminum.

396

6 Ft

Small Parts

Evaporators

Barrels
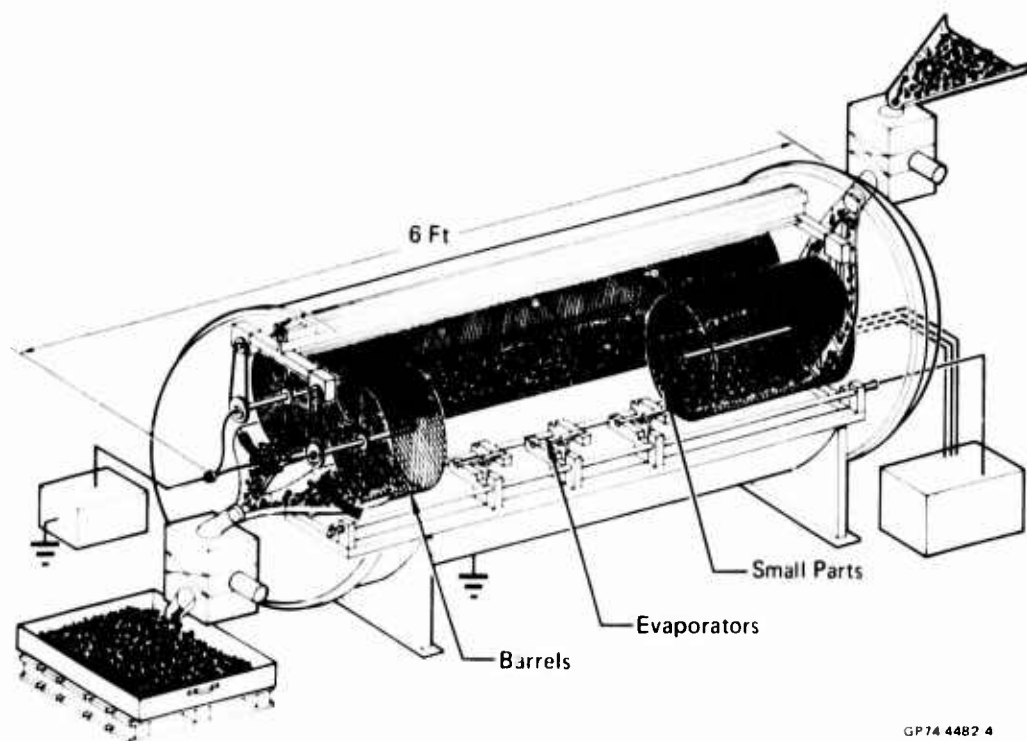
GP74 4482 4

FIGURE 13 SMALL PARTS COATER

REPLACE

- Stainless Steel with IVD Al Coated Alloy Steel
- Diffused Ni Cd
- Cd Electroplating
- Vacuum Cd Plating
- Sulphuric Acid Anodizing

APPLY

- To Unplated Parts

GP74 4482 6

FIGURE 14 BENEFITS

397

SESSION III

THE CORROSION OF 6061 ALUMINUM ALLOY - THORNEL 50 GRAPHITE COMPOSITE IN DISTILLED WATER AND NaCl SOLUTION

by

D. L. Dull, W. C. Harrigan, Jr., and M. F. Amateau
The Aerospace Corporation, El Segundo, Calif. 90245

ABSTRACT

The corrosion behavior of an 6061 aluminum alloy - Thornel 50 graphite composite has been examined in both distilled water and 3.5% NaCl solution at three temperatures 298K, 323K, and 348K. The corrosion rate was determined by the weight change and was monitored for times upto 1000 hours. The corrosion rates were maximum immediately after the initial immersion and decreased with increasing time of exposure. The NaCl solution was far more corrosive than the distilled water and increasing temperature resulted in increased corrosion rate. The mode of attack appears to be crevice corrosion promoted by galvanic coupling between the aluminum matrix and graphite fibers.

I. INTRODUCTION

Aluminum-graphite composites containing heat treatable matrix alloys have been developed for use as structural materials. The corrosion behavior of this class of materials during exposure to marine and atmospheric environments is of concern because of the expected galvanic coupling effect between fiber and matrix.

Previous qualitative studies of the corrosion behavior of A356 aluminum alloy - Thornel 50 graphite composite in NaCl solution have indicated that the corrosion rate of the composite is only slightly greater than the alloy matrix material (Ref. 1) This is attributed to the galvanic coupling effect of the graphite fibers that produce the anodic polarization of the aluminum matrix. Sedriks et al (Ref. 2) have studied the effects of galvanic coupling on the corrosion behavior of an aluminum -boron composite in a NaCl solution. Their results indicate that galvanic coupling was not a problem because of the low electrical conductivity of the boron. However, they did observe increased localized corrosion at the metal matrix-fiber interface.

This study was undertaken to examine the corrosion behavior of 6061 aluminum alloy - Thornel 50 graphite composites in distilled water and in a 3.5% NaCl solution from room temperature to 348K (75ºC). The objective was to identify corrosion problems typical of this class of materials. It is anticipated that the results will aid in the selection of new matrix compositions and fabrication techniques that will minimize corrosion.

II. EXPERIMENTAL

A. MATERIALS

The composite was produced by liquid-metal infiltration of the carbon yarn resulting in wire 1.6 mm (~63 mils) in diameter. The composite wire was consolidated into bars 6.5 mm (0.25 in.) square by 150 mm (6 in.) long by pressing at 895K (622°C) under 2.75 MPa (400 psi) pressure for 15 min. The resulting bars contained 30% fiber (0.114 x 10^5 kg/m^3 density). The composite bars were machined into specimens 5.85 mm (0.23 in.) square by 16.5 mm (0.65 in.) long. The 6061 aluminum alloy specimens were made from 0.25 in. (nominal) plate material in the T6 condition and annealed for 1 hr. at 773K (500°C). These specimens were machined to 6.35 mm (0.25 in.) by 7.82 mm (0.312 in.) by 15.9 mm (0.625 in.) long and ground with 600-grit silicon carbide paper.

B. TEST PROCEDURE

The specimens were cleaned by immersing them in an ultrasonic bath of methyl alcohol for 15 minutes, then drying in vacuum at 360K (87°C) for 30 min., and cooling in a desiccator. This procedure was applied before each specimen weighing. The corrosion rates were determined for 3.5% NaCl solution and distilled water at three temperatures 298K (25°C), 323K (50°C), and 348K (75°C). These temperatures were maintained in an isothermal bath to within ±0.5K. The specimens were weighed to the nearest 0.1 mg before they were immersed in separate jars containing glass beads to maximize surface exposure. The jars were loosely covered to minimize evaporation. The specimens were removed at approximately 48-hr. intervals and cleaned by the method described previously before being weighed. The total environment exposure was 500 to 1000 hrs.

II. RESULTS AND DISCUSSION

Typical weight change data for composite and alloy specimens in the NaCl solution and distilled water at 298K (25°C) are given in Fig. 1. The aluminum alloy-graphite composite undergoes an initial weight gain after immersion in the NaCl solution, while the alloy undergoes an initial weight loss. The weight change for both the composite and the alloy subsequently subsides with time. The initial weight gain of the composite is attributed to the formation of hydrated alumina on both the matrix and the exposed graphite fibers. This is probably caused by the alumina diffusing to and adsorbing on the exposed surface of the graphite fiber. The subsequent decrease in weight gain is probably the result of the spalling of the corrosion products from the surface once it has become totally covered with hydrated alumina. In distilled water, neither the composite nor the alloy showed any detectable change in weight over the 1000-hr. period, even though a very thin film covered the specimen after exposure. This apparent stability of the composite is attributed to the low conductivity of the water (>1 M Ω cm) used in this study. Low conductivity of water in a corroding system is electrically equivalent to producing an open circuit between the metal matrix and the graphite. The result is a reduction in the effect of the galvanic coupling and thus an overall reduction of the corrosion rate. The eventual stability of the alloy is due to the formation of a protective hydrated alumina film. The characteristics of the corrosion products on the composites for these conditions has been examined by means of

scanning electron microscopy. Although visual examination showed no evidence of corrosion products on the composite specimen exposed to distilled water at 298K (25°C), a surface film was detected by scanning electron microscopy. This film is shown in Fig. 2(a). In the NaCl solution (Fig. 2(b)), the film is considerably thicker and has a cracked, crazed, or granular appearance in the areas where the aluminum alloy had been exposed to the environment. In both cases, however, the corrosion product covers the graphite fibers that were exposed to the environment.

A summary of the rate of weight change at 0, 150, and 300 hrs. is given in Table I for the three temperatures used in this study. The reported corrosion rates are an average of measurements taken on two specimens except for the 298K (25°C) exposure, in which case, only one specimen was used. The corrosion rate was determined by taking the slope on the weight versus time plot. The trends are clear. Corrosion is most severe in the NaCl solution. In addition, the composites undergo a weight gain, and the alloy undergoes a weight loss. A general increase in corrosion rate with temperature for all materials and environments is also evident. This temperature effect is shown in Fig. 3. A significant increase in corrosion rate occurs above 323K (50°C) for the composites, especially in the NaCl solution.

The corrosion rates for various exposures for both the alloy and composite in distilled water are shown in Fig. 4. The corrosion rate was negligible for the alloys at all temperatures studied and negligible for the composite at 298K (25°C). At the higher temperatures, some weight gain was observed for the composite.

The behavior of the composite and alloy are considerably different in the NaCl solution (Fig. 5). The rate of weight loss for the alloy specimens in NaCl solution was maximum immediately after immersion and decreased slightly with time. Although the scatter in a few instances was great, the decrease in the rate of weight gain for the composite specimens at 298K (25°C) and 323K (50°C) was evident. At 348K (75°C), no decrease in the rate of weight change was evident. At 348K (75°C), no decrease in the rate of weight change was evident after 300 hrs. The chloride ion apparently increased the corrosion rate by promoting localized film breakdown, leading to crevice corrosion. The eventual decrease in corrosion rate generally observed can be attributed to hydrated alumina forming on the specimen surface.

A perpendicular cross section of a composite specimen exposed to the NaCl solution at 323K (50°C) is shown in Fig. 6 at a higher magnification. The typical mode of attack is the formation of a crevice at the surface and proceeding into the specimen along a region of high fiber density. The swelling of the composite, particularly at the higher temperatures, is the result of the rapid formation within the crevice of large amounts of hydrated alumina as evidenced from x-ray diffraction. The postulated model leading to swelling is based on the graphite fibers being able to catalyze hydrogen ion reduction faster than the aluminum matrix. The resulting effect is the stimulation of aluminum matrix dissolution to form aluminum ions. These aluminum ions can then hydrolyze to form hydrogen ions and aluminum hydroxide that is eventually transformed into hydrated alumina.

IV. CONCLUSIONS

1. The corrosion rate of the composite material in NaCl solution increases markedly with temperature, particularly above 323K.

2. The mechanism of attack is by crevice corrosion along the regions of high fiber density.

3. The galvanic couple effect between the matrix and the graphite fiber is the significant factor in the corrosive behavior of the composite.

4. A practical approach to eliminate this corrosion problem will be use use of aluminum cladding.

REFERENCES

1. E. G. Kendall and D. L. Dull, "Salt Water Corrosion Behavior of Aluminum-Graphite Composite", TR-0074(9250-03)-2, The Aerospace Corporation, El Segundo, California (March 74).

2. A. J. Sedriks, J. A. S. Green, and D. L. Novak, Metallurgical Transactions, March 1971, Vol. 2, pp. 871-875.

TABLE I

Corrosion Behavior of 6061 Aluminum Alloy-Thornel 50 Graphite Composite and
6061 Aluminum Alloy in 3.5 Percent (NaCl) Solution and Distilled Water

Material	Environment	Spec No.	Temperature K	Temperature (°C)	Corrosion Rate 10^{-9} kg/hr (Mils/yr) Initial	150 Hours	300 Hours
Composite	NaCl	6	298	25	+140 (+46)	+42 (+14)	-11 (-4)
		13A	323	50	+230	+68	+63
		13B			+210	+20	+59
		Avg.			+220 (+73)	+44 (+15)	+61 (+20)
		21A	348	75	+410	+410	+410
		21B			+250	+410	+365
		Avg.			+330 (+109)	+410 (+136)	+388 (+128)
Alloy	NaCl	8	298	25	-6 (-2)	-17 (-6)	-11 (-4)
		15A	323	50	-38	-11	-16
		15B			-29	-9	-6
		Avg.			-34 (-11)	-10 (-3)	-11 (-4)
		23A	348	75	-44	-17	-8
		23B			-59	-13	-5
		Avg.			-52 (-17)	-15 (-5)	-7 (-2)
Composite	H$_2$O	2	298	25	Nil	Nil	Nil
		9A	323	50	+40	+9	-16
		9B			-14	+3	-11
		Avg.			+27 (+9)	+6 (+2)	-14 (-5)
		17A	348	75	+85	+85	+85
		17B			+87	+44	+85
		Avg.			+86 (+28)	+65 (+21)	+60 (+20)
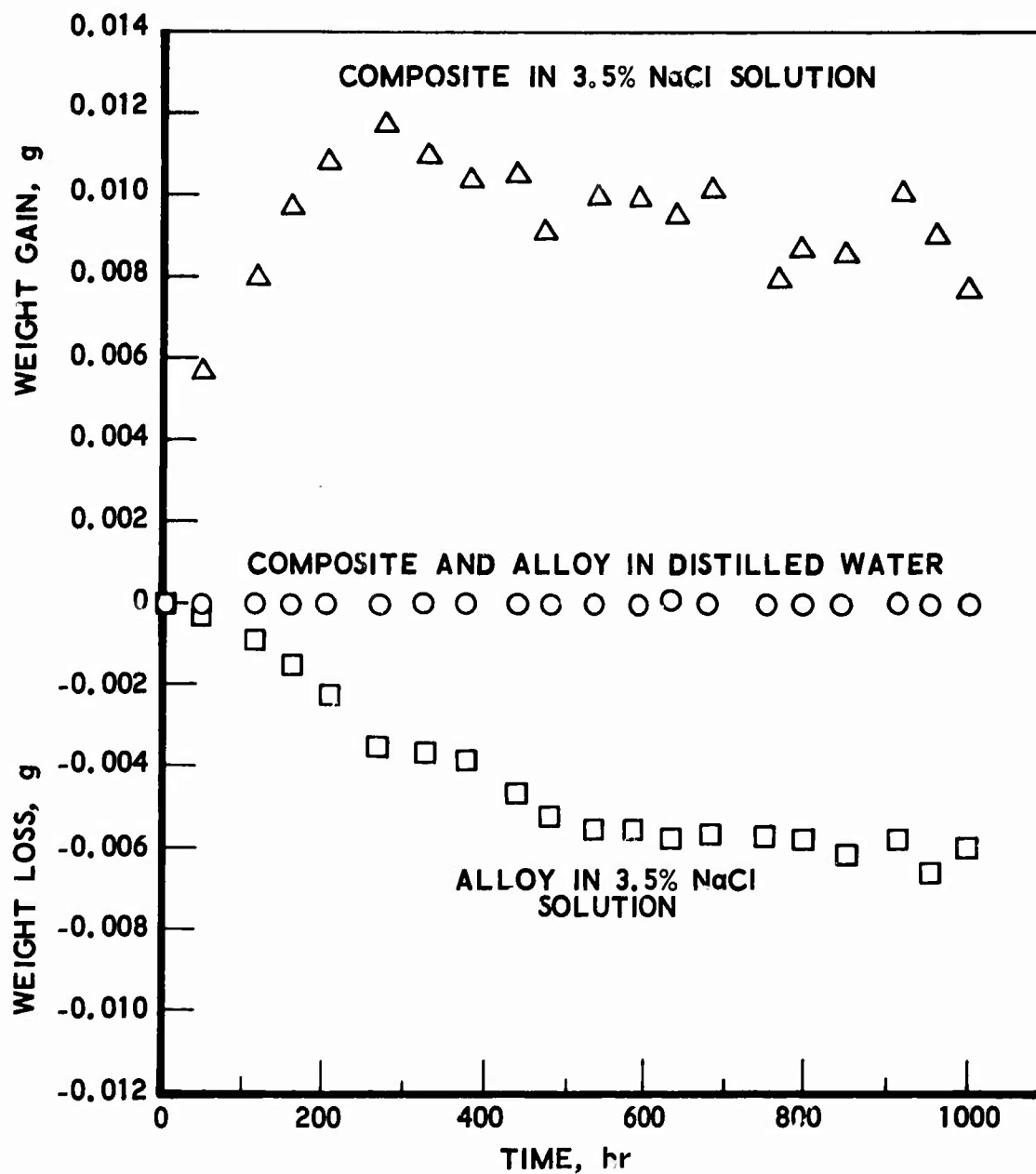
FIGURE 1. TYPICAL WEIGHT CHANGE BEHAVIOR FOR
6061 ALUMINUM ALLOY - THORNEL 50 GRAPHITE COMPOSITE
6061 ALUMINUM ALLOY IN 3.5% NaCl SOLUTION AND
DISTILLED WATER AT 25°C (298°K)

b. SODIUM CHLORIDE SOLUTION

a. DISTILLED WATER

FIGURE 2. SCANNING ELECTRON MICROGRAPHS OF
CORROSION PRODUCTS FORMED ON COMPOSITE AFTER
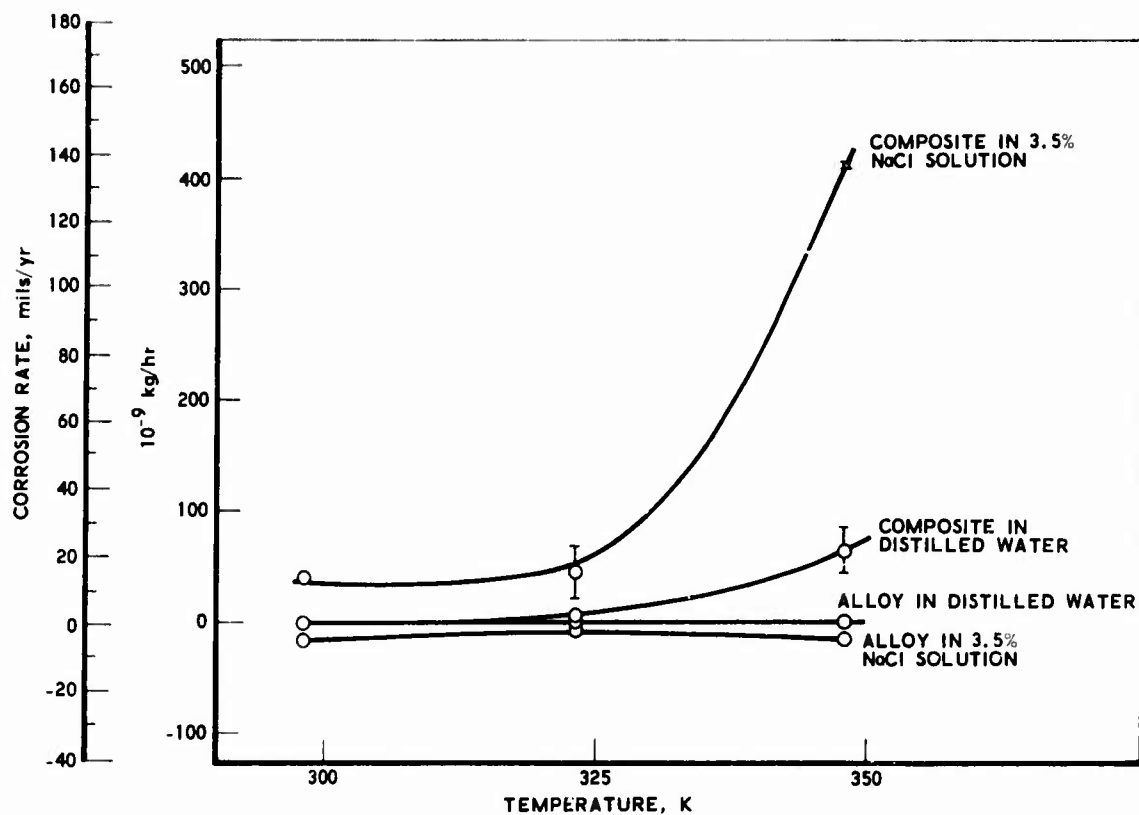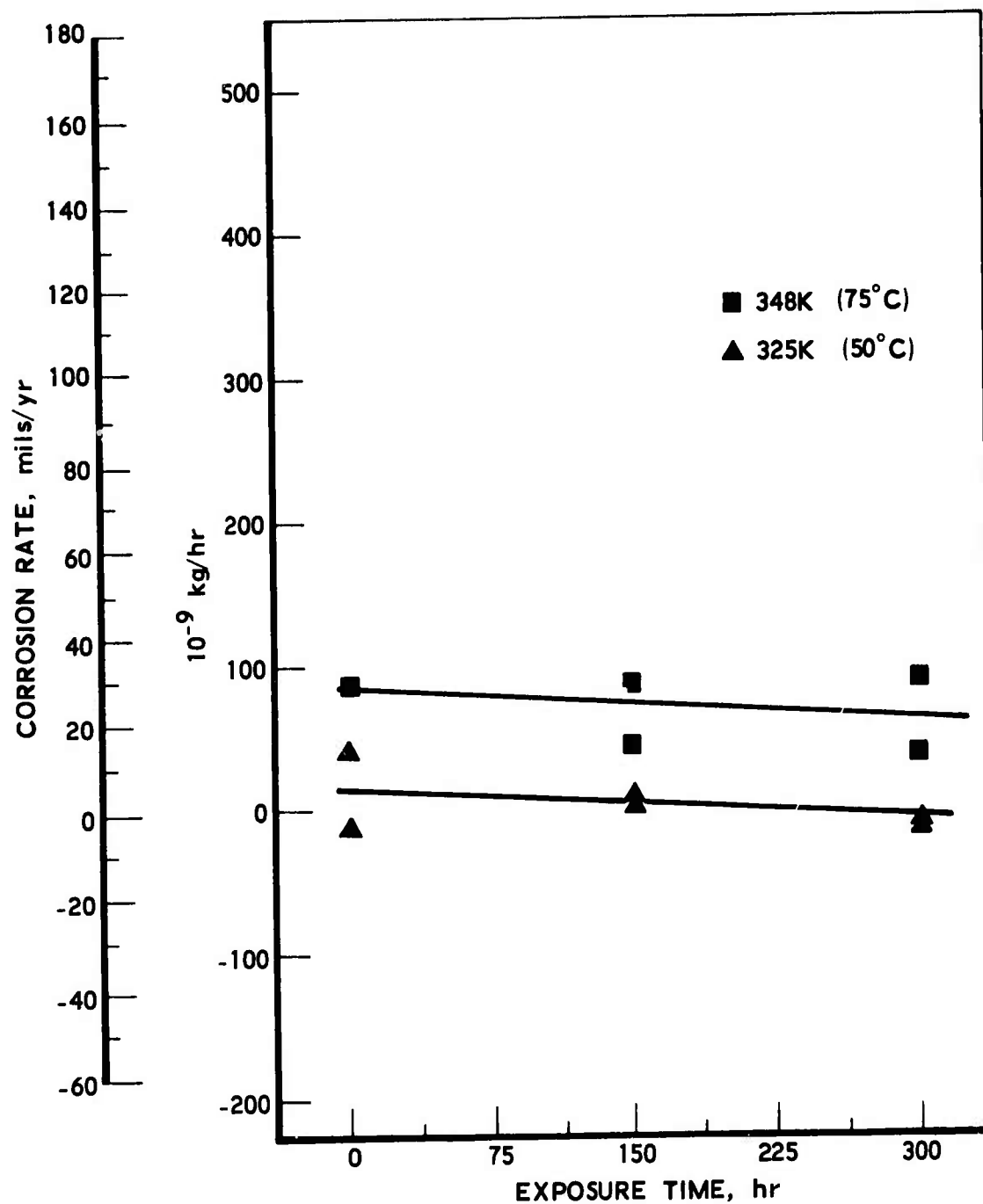1000 HRS. OF EXPOSURE TO SODIUM CHLORIDE SOLUTION AND
DISTILLED WATER AT 298K (300X)

FIGURE 3. CORROSION RATES AFTER 150 HR. OF
EXPOSURE FOR 6061 ALUMINUM ALLOY -
THORNEL 50 GRAPHITE COMPOSITE AND 6061
ALUMINUM ALLOY IN 3.5% NaCl SOLUTION
AND DISTILLED WATER AT VARIOUS TEMPERATURES

FIGURE 4. THE EFFECT OF EXPOSURE TIME ON THE
CORROSION RATE OF 6061 ALUMINUM ALLOY-THORNEL 50 GRAPHITE
COMPOSITE IN DISTILLED WATER AT 323K AND 348K
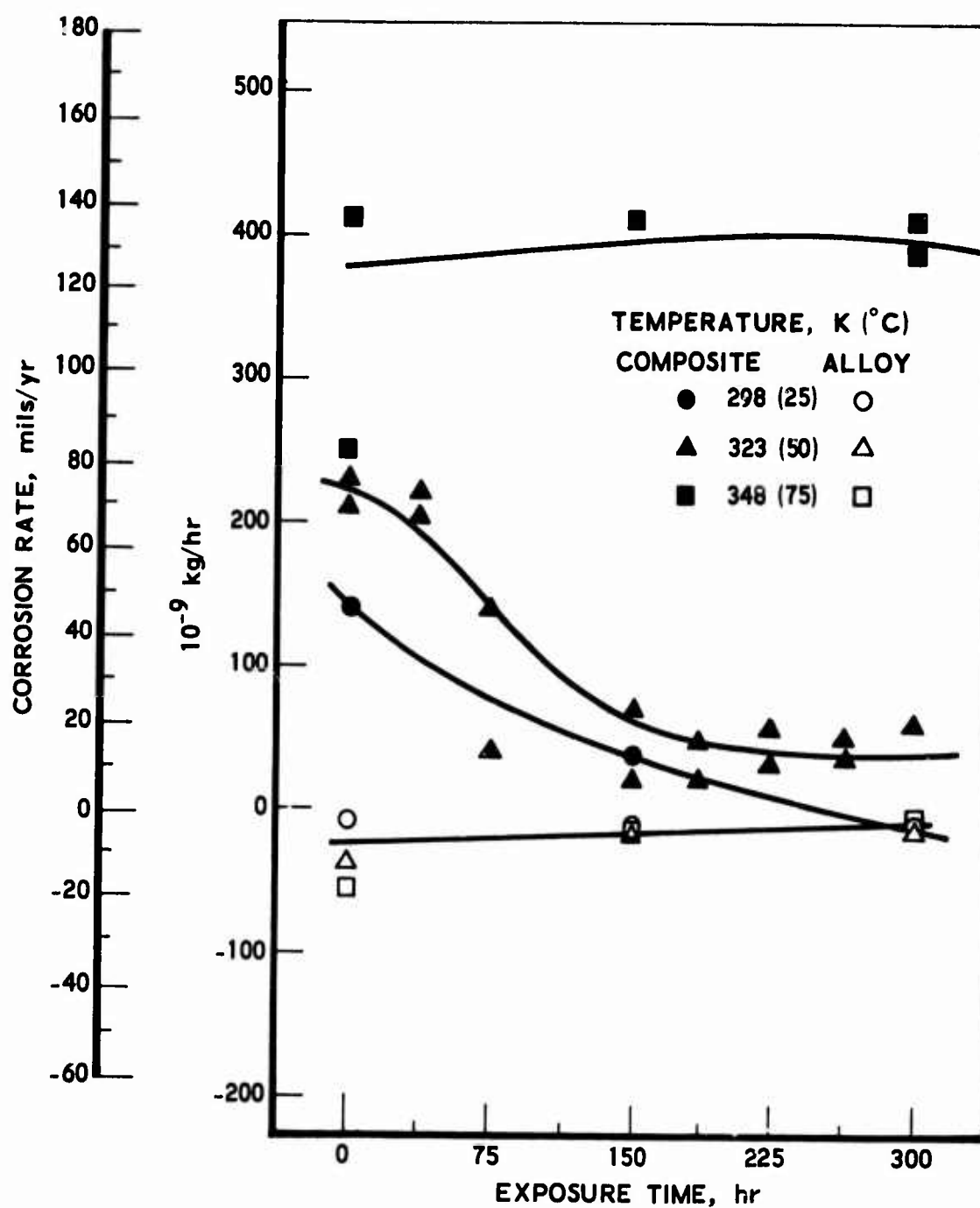
FIGURE 5. THE EFFECT OF EXPOSURE TIME ON THE CORROSION
RATE OF 6061 ALUMINUM ALLOY-THORNEL 50 GRAPHITE COMPOSITE
IN 3.5% NaCl SOLUTION BETWEEN 298K AND 348K

FIGURE 6. CROSS SECTION OF COMPOSITE SPECIMEN
EXPOSED TO SODIUM CHLORIDE SOLUTION AT 323 K
SHOWING CREVICE CORROSION IN AREAS OF
HIGH FIBER DENSITY (150X)

ULTRA HIGH STRENGTH CORROSION-IMMUNE BOLTING ALLOYS

Edward Taylor
Standard Pressed Steel Co.
Jenkintown, Pa. 19046

INTRODUCTION:

Higher speeds, higher temperatures, and higher loads necessitate higher strength bolting for military aircraft. The movement to ultra high strength levels and high applied stresses usually causes concern over stress corrosion cracking and hydrogen embrittlement, both of which are arch enemies of metals. Extensive evaluations of materials have shown that 180,000 psi is a critical number above which caution is exercised to a much greater degree, because of increased susceptibility to metal failure. Even so, many applications now require strength levels of 220,000 and 260,000 psi where emphasis on structural integrity is of paramount importance.

A number of years ago, MP35N™, a member of the MULTIPHASE™ alloy family, was introduced to the aerospace industry as an alloy capable of 260,000 psi strength levels without the threat of stress corrosion cracking or hydrogen embrittlement.[1] Since then, the alloy has been used successfully in many applications ranging from below the surface of the sea to the moon and beyond. It is replacing martensitic age hardenable stainless steel bomb rack springs and pins, providing a 10 year minimum corrosion-free performance for a threaded connection in a Navy missile launch tube, designed into above and below waterline applications in the new surface effect ships, and is replacing high strength maraging steel missile fin deployment springs. MP35N bolts are also being used in the water brake system on steam catapults where they replaced cadmium plated alloy steel. The alloy was selected for interference fit and maximum galvanic compatibility with titanium for use on the F-14 aircraft. Inasmuch as no failures have yet been reported which are due to a corrosive attack, the MP35N alloy is enjoying a climate of trust and is guaranteeing structural integrity in many military applications.

Now, another alloy of the MULTIPHASE family has been introduced and is called MP159™. This alloy also provides 260,000 psi strength levels, is usable to 1100°F, and is not susceptible to stress corrosion cracking or hydrogen embrittlement based on standard laboratory test methods.[2] Efforts to initiate crevice corrosion and pitting attack have not been successful either.

PROPERTIES:

The nominal composition of the MULTIPHASE alloys contains liberal amounts of cobalt, nickel, chromium, and molybdenum as shown in Table I. The principal difference in composition between the two alloys is the addition of iron, titanium, and minor elements at the expense of nickel and molybdenum in the MP159 alloy.

TM - Trademarks of Standard Pressed Steel Co.

PROPERTIES - Continued

Strength, achieved by working and aging, results in values like those
given in Table II. The MP159 alloy provides a wider spectrum of mechanical
property capabilities than its predecessor the MP35N alloy, and many
other high strength alloys such as H-11, PH13-8 Mo, Custom 455, Maraging
steel and even high temperature materials such as Rene 95 up to 1200°F.
A plot of ultimate tensile strength vs. testing temperature (Figure 1)
reflects the ability of the MP159 alloy to exceed the service temperature
limits of other high strength alloys.

Based on stress relaxation and thermal stability studies, 1100°F appears
to be a safe temperature limitation in normal stress-life time applications.
In service applications where life expectancy is relatively short, 1150°F
and even 1200°F can be considered.

Although many of these properties are available from various alloys, the
MP35N and MP159 alloys offer high strength and corrosion resistance con-
currently as a functional feature.

ENVIRONMENTAL PERFORMANCE:

Resistance to crevice corrosion, as determined by immersion in 10% ferric
chloride solution at room temperature, yielded unattacked surfaces. Tape
and rubber bands applied around bolt shanks for up to 96 hours did not
initiate attack on the MULTIPHASE alloys, as they did on other corrosion
resistant alloys in only 6 hours, as shown in Figure 2.

A simulated service test, employing aluminum alloy cylinders was conducted.
External wrenching bolts were loaded at 75% of actual ultimate tensile
strength after being swabbed with a 3.5% NaCl solution. After a period
of approximately 100 hours, the cylinders were unloaded. No failures were
observed with MP35N or MP159 bolts for periods up to 10 cycles although
other high strength alloys did fail because of the hydrogen embrittlement
produced [2,3]. Atomic hydrogen, generated on the cathodic bolt during
sacrificial corrosion of the aluminum cylinder, diffused into the metal
and caused a brittle fracture.

Sustained load tests with cadmium plated and unbaked MP159 bolts did not
cause failure during 200 hours at 75, 85, and 90% of ultimate tensile
strength. Similarly, MP35N notched bars with a K_t of 6.0 were loaded
at 90% NTS after cadmium plating and did not fail during a 600 hour period[4].
This data is in contrast to failures observed for other high strength
materials under the same conditions.[3]

The MP35N and MP159 alloys are noble metals with sea water potentials near
that of titanium. When coupled to less noble metals, the latter are
attacked galvanically. Even in the salty air near the sea, aluminum panels
are attacked around fastener heads unless protective coatings are employed.
When installed in titanium alloy structure and exposed to a chloride
environment, no corrosion is observed on either metal.[5]

ENVIRONMENTAL PERFORMANCE - Continued:

Although the MP159 alloy is too new to have gathered long term corrosion data, the MP35N alloy has been tested in a number of environments which show off its uniqueness. For example, a wire rope (1/8 x 7 x 19) was exposed at Wrightsville Beach, N.C. so that 5 ft. were constantly exposed to the atmosphere, 4 ft. were bathed by the rising and falling tide, 2 ft. were in the muddy bottom and the remainder was constantly wet. After six years of this exposure, no apparent corrosion was observed during a careful metallographic examination.

In a solution of 3% NaCl, 0.5% acetic acid, saturated with H_2S, MP35N smooth bars were loaded to 75% yield strength, where they did not fail after 1100 hours of exposure, compared to just a few hours for alloy steels of the same strength level.[7] Based on these findings, a 20,000 foot instrumentation cable was constructed of MP35N alloy for use in sour oil wells where other corrosion resistant alloys lack the strength or cannot provide the same degree of resistance to stress corrosion cracking or hydrogen embrittlement.

In a severe electrochemical test, MP35N notched specimens were loaded to 90% notched tensile strength in salt solutions and electrolytically charged to generate hydrogen or oxygen. After a considerable period of time, MP35N specimens did not fail due to a stress corrosion cracking environment but did fail due to hydrogen embrittlement. However, it was far better than anything else tested.[8]

In chemical solutions, the MP35N alloy performs with behavior similar to Hastelloy C. It is readily attacked by boiling hydrochloric acid but holds up in the Streicher and Huey tests. Corrosion rates are also known for several other solutions.[9]

SUMMARY:

Ths superior corrosion resistance demonstrated for MP35N and MP159 alloys indicates their applicability for a variety of environments ranging from outer space to inner space. The corrosion immunity of these alloys, in combination with high strength and elevated temperature capability, allows them to provide fastening free of troubles. Protective coatings are not required, although they can be applied for lubrication or protection of mating surfaces.

ACKNOWLEDGEMENTS:

REFERENCES

1. A. C. Hood, "MP35N - A Multiphase Alloy for High-Strength Fasteners." Metal Progress, Vol. 93, No. 5, May 1968, p.81.

2. F. R. Varrese, "The Evaluation of a 260,000 psi High Temperature, High Strength, Corrosion Resistant, Tension Fastener Made from Multiphase Alloy MP159." SPS Report No. 5533, February, 1974.

3. S. Patel and E. Taylor, "New High-Strength Fastener Materials Resist Corrosion," Metal Progress, Vol. 100, No. 3, Sept. 1971, p.98.

4. E. Taylor, "The Corrosion Resistance of Multiphase Alloys," Materials Protection Vol. 9, No. 3, March 1970, p. 29.

5. E. Taylor, "Galvanic Compatibility of Coated and Bare MP35N Bolts with 6 Al-4V Ti, 7075-T6 Al, and Cadmium Plated Steel Structures," SPS Report No. 5302 Revised, September,1971.

6. Unpublished report, F.L. LaQue Corrosion Laboratory.

7. Unpublished work, U.S. Steel Research Laboratories.

8. D.L. Dull and L. Raymond,"A Test Procedure to Evaluate the Relative Susceptibility of Materials to Stress Corrosion Cracking," Aerospace Corporation Report No. TR-0073 (3250-10)-3, December, 1972.

9. Unpublished report, Climax Molybdenum Co.

TABLE I

Chemistry of MULTIPHASE Alloys

Alloy	Co	Ni	Cr	Mo	Fe	Ti	Cb	Al
MP35N	35	35	20	10				
MP159	35	26	19	7	8	3	.6	.2

TABLE II

Mechanical Properties of MULTIPHASE Alloys

Alloy	Stress, KSI			Elong-ation,%	Reduction of Area,%
	UTS	Yield	Shear		
MP35N	286	255	145	11	39
MP159	280	275	140	8	35
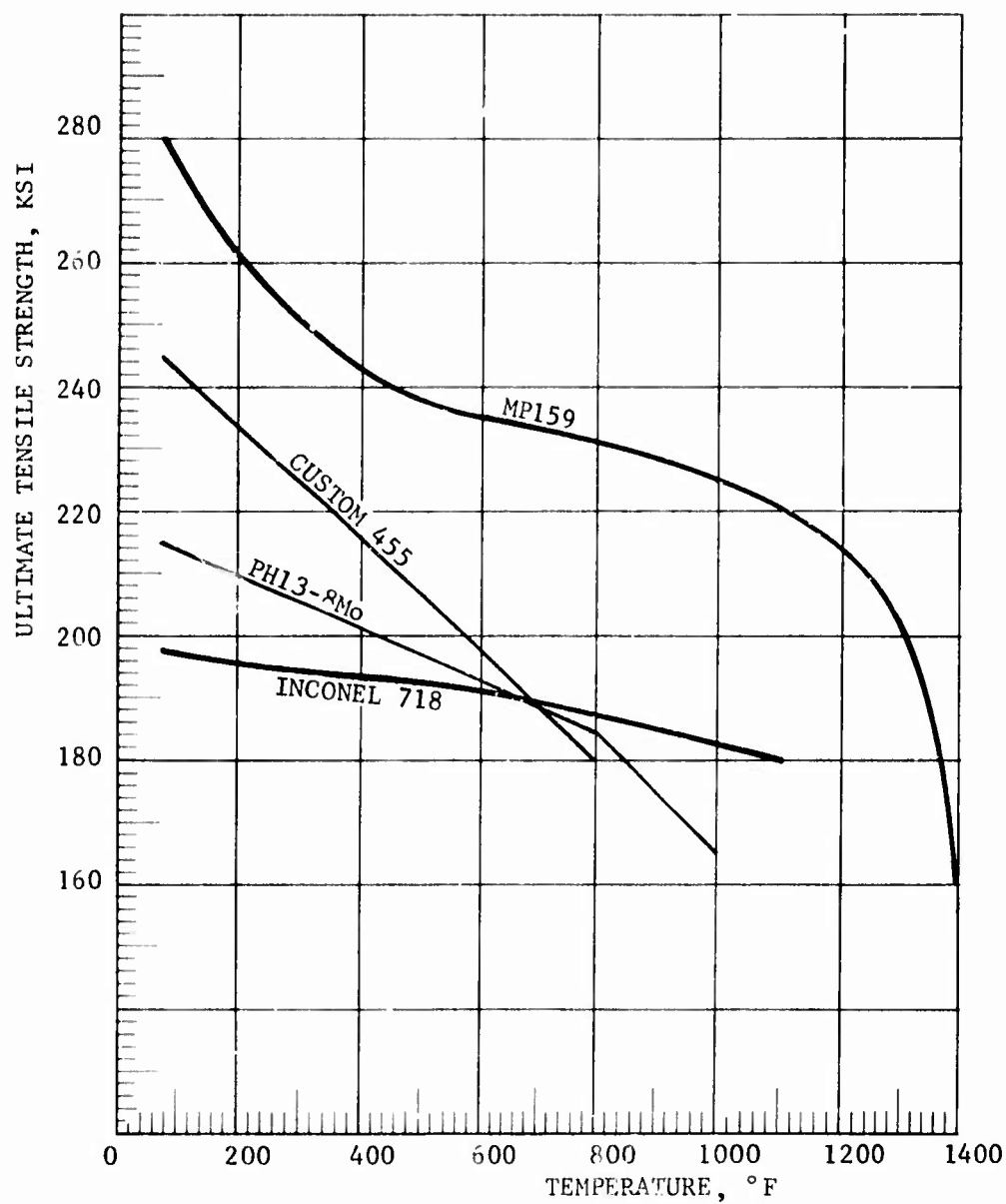
Figure 1. Ultimate Tensile Strength vs. Testing Temperature of High
Strength Alloys
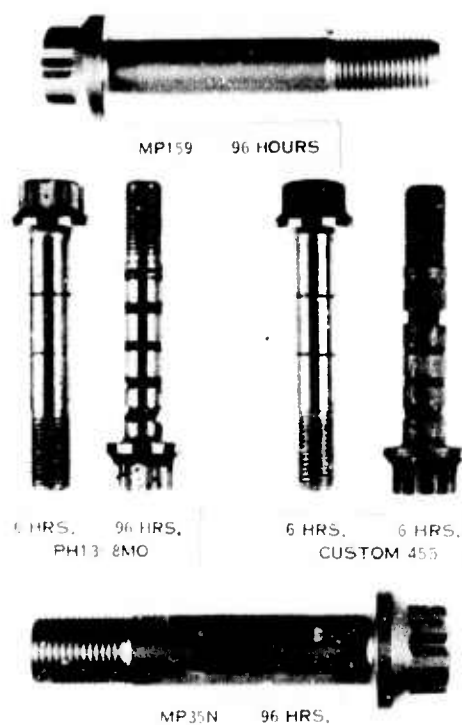
Figure 2. Crevice corrosion test in 10% FeCl₃ at room
temperature caused pitting and severe attack
of alloys other than the MULTIPHASE Alloys.
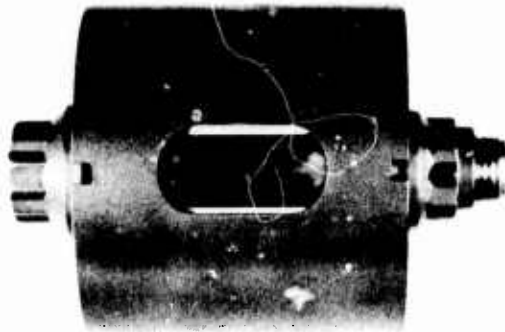
STRESS CORROSION CRACKING TEST

**NO FAILURE AFTER 5000 HOURS IN
3.5 NA CL ALTERNATE IMMERSION AT
75% U.T.S.**

Figure 3.   Stress corrosion cracking test assembly and
exposed MULTIPHASE bolt reveal no evidence of
corrosion due to crevice or galvanic conditions.

HOT CORROSION BEHAVIOR OF MAJOR COMPONENT
PHASES OF NICKEL-BASE SUPERALLOYS

G. Romeo and D.W. McKee
Corporate Research and Development
General Electric Company
Schenectady, New York 12301

ABSTRACT

A study has been carried out of the differences in hot
corrosion behavior of major component phases of Ni-base superalloys
at 850° and 900°C. Ni-Cr, Ni-Al, and Ni-Cr-Al alloys have been
coated with sodium sulfate and exposed to oxygen or H_2S-H_2 gas
mixtures, in order to provide large variations in oxygen and sulfur
potential at the gas-scale interface. The composition of the
alloys corresponded to the nominal gamma matrix, the gamma-prime
strengthening phase, and a system in which both these two phases
are present. The corrosive attack was monitored continuously by
thermogravimetry, and a morphological study of the corrosion
products was carried out by optical microscopy, electron microprobe
and X-ray diffraction. The results indicate that the extent and
mechanism of corrosion of the separate phases is strongly influenced
by the composition of the environment. Comparison between the
different phases under study has shown that the gamma-prime phase
is a weak link in the overall corrosion problem.

INTRODUCTION

Nickel base superalloys employed in gas turbines frequently
undergo accelerated corrosion in the presence of sodium sulfate
deposits. A high rate of degradation of the metal and the complex
morphology of the corrosion scales characterize this type of
attack, generally labeled as "hot corrosion" to distinguish it
from ordinary oxidation processes (1-6). In the past two decades
numerous studies have been carried out on the subject of hot
corrosion, and several mechanisms have been advanced to account
for it. Yet, to date a generalized explanation for hot corrosion
has not been made available, mainly because catastrophic attack
with comparable corrosion products can occur for different alloys
in a variety of environmental situations. However, the literature
data point out to two main aspects of hot corrosion:

1. Diffusion of sulfur from the salt/melt interface into
   the alloy. This favors internal precipitation of
   chromium/sulfide particles, which depletes the alloy
   in chromium and reduces its corrosion resistance (7-8).

419

2. Fluxing by the sodium sulfate film of oxides such as Al_2O_3 and Cr_2O_3, which would offer protection to the alloy in ordinary oxidation conditions. The solubility of these oxides in the salt melt can be influenced by elements such as molybdenum, vanadium, tungsten, etc., that diffuse outward from the alloy into the melt and modify the composition of the latter. (3)

On the other hand, catastrophic corrosion rates can be originated by transient reducing conditions in the environment. As Na_2SO_4 is reduced to Na_2S, the resulting increase in sulfur potential at the salt/scale interface can provide the driving force for sulfur penetration into the alloy. In this case sulfidation mechanisms may prevail over dissolution mechanisms, especially when formation of the liquid nickel-nickel sulfide eutectic can take place (9,10).

The correlation between alloy chemistry and rate of attack has been the subject of considerable investigation in the past years (3,4). However, little effort has been made to study the effect of alloy microstructure on corrosion rates. The microstructure of a nickel-base superalloy consists of several phases (4), the most important of which are the f.c.c. gamma matrix, a solid solution of chromium in nickel, with lesser amounts of other elements such as aluminum, titanium, etc.; and the gamma-prime phase, an ordered intermetallic compound of nickel and aluminum which imparts high temperature strength to the alloy.

Since both sulfur diffusivity and the capability of forming protective oxides (12) may be considerably different for the various phases present in a superalloy, we thought it useful to undertake a study in the temperature range 850° to 900°C of the hot corrosion behavior of alloys of nominal composition corresponding to the gamma matrix and the gamma-prime phases, in order to determine their separate influence on the overall hot corrosion resistance of the complex superalloy. This paper summarizes part of the results of experiments in which specimens of the nominal gamma matrix and gamma-prime phases were exposed to environments simulating oxidizing and reducing conditions in the presence of sodium sulfate deposites.

EXPERIMENTAL

Ingots of nominal composition (wt.%) Ni-35Cr, Ni-20Cr, Ni-13.3Al and Ni-10.4Cr-13.5Al were cast in argon after induction melting. Table I shows schematically the correspondence between these alloys and the phases of interest to this study. The gamma

matrix has a fairly wide range of existence in the Ni-Cr phase
diagram (13); accordingly, two compositions were chosen corre-
sponding to an upper and a medium level of chromium. The composi-
tion Ni-13Al corresponds to the center of the narrow range of
existence of the gamma-prime phase in the Ni-Al phase diagram (14).
Finally, the ternary Ni-10Cr-13Al alloy was used to simulate a
mixture of gamma matrix and gamma-prime phases (15).

TABLE I

ALLOY SYSTEMS

gamma matrix	$= \begin{matrix} Ni-35Cr \\ Ni-20Cr \end{matrix}$
gamma-prime	$= Ni-13Al$
gamma + gamma-prime	$= Ni-10Cr-13Al$

Platelets were machined out of each ingot, and after grind-
ing their surface through 600 grit silicon carbide paper they
were annealed in oxygen for 4 to 6 hours at reaction temperature,
in order to grow a layer of oxide which simulated the real condi-
tion of metal surfaces in a gas turbine during operation. The
specimens were then spray-coated with sodium sulfate, prior to
exposing them to the corrosive atmospheres. The extent of
corrosion was monitored with a continuous recording microbalance.
Standard metallographic examinations, electron microprobe and X-ray
diffraction analyses were carried out on the specimens at the end
of the experiments.

The specimens were exposed to two types of environments:
1) $Na_2SO_4 + H_2S-H_2$ and 2) $Na_2SO_4 + O_2$. Sodium sulfate coatings
and hydrogen-sulfide-hydrogen gas mixtures were used to simulate
high sulfur potentials, a situation that can occur in gas turbines
in the presence of transient reducing conditions. Sodium sulfate
coatings and oxygen were used to simulate oxidizing conditions,
which are prevailing in a gas turbine environment. The experiments
were carried out with the gases flowing at atmospheric pressure at
a rate of about 1/2 liter/minute, and the temperature was maintained
in most cases at 900°C.

RESULTS AND DISCUSSION

Reducing Environments

Fig. 1 shows the morphology of the corrosion product of a
Ni-35Cr alloy which was exposed for 2 1/2 hours to a 10% H_2S-Bal.

H_2 gas mixture at 850°C. The scale consisted of an outer layer of nickel sulfide (Ni_3S_2) which was molten at temperature, and an inner layer of chromium sulfide (Cr_3S_4). Nickel sulfide stringers can be noticed in this inner layer as a result of penetration of a liquid phase preferentially along grain boundaries (16). In this case fast formation of molten nickel sulfide was mainly responsible for accelerated corrosion of the gamma matrix-type alloy. Attempts were made to see whether a pre-existing layer of oxide could have prevented the formation of liquid nickel sulfide. Actually, the oxide layer only delayed catastrophic attack, which eventually took place

Fig. 2 shows the weight gain curves for specimens of a Ni-35Cr alloy treated directly with the hydrogen sulfide-hydrogen mixture or pre-oxidized prior to sulfidation. In all cases within the first two hours the weight gain amounted to about 30 mg/cm^2. However, in the case of the pre-oxidized specimen the attack was delayed because of the time required for sulfur to diffuse through the oxide layer. Instead, in the case of the specimen pre-oxidized and coated with 2 mg/cm^2 of sodium sulfate either a coherent protective oxide could not form or it was fluxed out by the film of molten salt so that the incubation period for accelerated corrosion was reduced. Concurrently, the composition of the salt melt was modified by the reducing action over Na_2SO_4 of hydrogen in the reaction atmosphere. The latter was partially converted into Na_2S, resulting in increased sulfur potential at the salt/melt interface. Analogous results were obtained with specimens of a Ni-20Cr alloy when exposed to H_2S-H_2 atmospheres.

In similar environmental conditions characterized by high sulfur potentials, the gamma prime phase shows some tendency to form a liquid nickel sulfide, although to a lesser degree than the gamma matrix. Fig. 3 shows the weight gain curves for two specimens of nominal gamma-prime. The lower curve (a) corresponds to a specimen treated directly with the 10% H_2S-H_2 gas mixture. The weight gain after several hours was not as marked as in the case of the upper curve (b) corresponding to a specimen pre-oxidized and coated with 9 mg/cm^2 of sodium sulfate. In this latter case any barrier to sulfidation provided by protective oxides was removed by the fluxing action of the sodium sulfate melt. However, a comparison of the diagrams in Figs. 2 and 3 demonstrates that the attack was less extensive than in the case of the gamma matrix system. Fig. 4 shows the morphology of the corrosion scale corresponding to curve (b) in Fig. 3, consisting mainly of Ni_3S_2 in all probability molten at temperature.

The above results indicate that in environmental conditions leading to high sulfur potentials and in the presence of molten films of sodium sulfate both the gamma matrix and the gamma-prime phase show scarce resistance to corrosion, mainly because of very rapid formation of the liquid nickel-nickel sulfide eutectic.

Oxidizing Conditions

A different situation occurs when gamma matrix and gamma-prime are corroded in oxidizing conditions. Fig. 5 shows the weight gain curve for a specimen of Ni-20Cr coated with 10 mg/cm^2 of sodium sulfate and exposed to oxygen at 900°C for about 6 days. The initial weight gain of the specimen amounted to less than 1 mg/cm^2 within the first day, after which the rate of evaporation of sodium sulfate became higher than that of weight gain and the specimen started losing weight. These results agree qualitatively with those of Goebel at al (3) and those of Hardt et al (17) for Ni-Cr alloys of similar composition. The specimen cross section is shown in Fig. 6. The scale was found to consist of an outer layer of NiO and an inner layer of Cr$_2$O$_3$. Internal precipitates of chromium sulfide can still be detected within the alloy. In this case, however, the scale offered a considerable resistance to corrosive attack, most probably because at low sulfur potentials relatively little sulfur diffuses through the compact scale, and at the same time the rate of dissolution of NiO and Cr$_2$O$_3$ in the sodium sulfate melt is very slow.

A much larger rate of attack was instead noticed when a specimen of nominal gamma-prime was coated with sodium sulfate and exposed to oxygen at 900°C. Fig. 7 shows three weight gain curves for specimens of gamma-prime coated with different amounts of sodium sulfate. In all cases an initial stage of rapid attack was noticed, the extent of which was roughly proportional to the amount of sodium sulfate coating. In a subsequent stage the curves tend to taper off. Fig. 8 shows the scale grown on one of the specimens. The corrosion product was found to consist mainly of porous NiO, together with particles of α-Al$_2$O$_3$. The scarce resistance to hot corrosion in oxidizing conditions of the gamma-prime phase is probably due to the initial formation of a discontinuous layer of Al$_2$O$_3$ at its surface. If this layer is dissolved by the film of molten sodium sulfate the growth of a porous layer of NiO is favored. This porous scale progressively separates the sodium sulfate film from the metal; consequently, the slope of the weight gain curves progressively decreases. Crucible tests have indeed indicated that exposure of specimens of gamma-prime to excess sodium sulfate at 900°C in air results in their total destruction after only two hours. It can be then concluded that in purely oxidizing conditions the gamma matrix offers excellent resistance to hot corrosion, while the gamma-prime appears to be a "weak link" in the overall hot corrosion process of a superalloy.

The System Gamma + Gamma-Prime

Experiments were also carried out with a ternary alloy of composition (wt.%) Ni-10.4Cr-13.5Al, to simulate a system in which at high temperature the two major phases gamma and gamma-prime coexist. Specimens of this ternary alloy were exposed to reducing and oxidizing environments, as described previously for the binary Ni-Cr and Ni-Al alloys.

Fig. 9 shows the dramatic difference between the corrosive attack in the absence and in the presence of sodium sulfate coatings. The top micrograph shows the relatively little amount of corrosion scale formed on a specimen of Ni-10Cr-13Al alloy pre-oxidized and exposed isothermally to a 10% H_2S-H_2 gas mixture for 8 hours. In this case evidently the oxide layer offered some barrier to the inward diffusion of sulfur, and the attack was confined to a narrow surface layer. On the contrary, when another specimen of the same alloy was pre-oxidized and coated with 2 mg/cm^2 of sodium sulfate, catastrophic attack took place, as demonstrated by the massive and complex corrosion product in the lower micrograph of Fig. 9. In this case the fluxing action of the melt was combined with the presence of high sulfur potentials, which favored the formation of a liquid nickel sulfide phase and the extensive disruption of the alloy surface layer. The attack appears to propagate preferentially at the darker areas in the alloy, of composition corresponding to the gamma-prime. Fig. 10 shows the weight gain curves for specimens of a Ni-10Cr-13Al alloy exposed at 850°C to a 10% H_2S-H_2 gas mixture, for different conditions of the metal surface. Comparing curve (a) in Fig. 10 with the curves in Fig. 2 shows that addition of aluminum to a binary Ni-Cr alloy delays considerably catastrophic attack, probably because of initial formation of a protective barrier of oxides and sulfides of aluminum and chromium. Subsequent depletion of the alloy in these elements favors the formation of the liquid $Ni-Ni_3S_2$ eutectic, and the reaction becomes much faster. The influence of a protective oxide in delaying sulfidation is also shown by curve (c) in Fig. 10, corresponding to a specimen pre-oxidized prior to sulfidation with the H_2S-H_2 mixture, but not exposed to any fluxing action of sodium sulfate. Curves (b) and (d) show instead that removal of protective oxides by the molten sodium sulfate coating originates catastrophic attack soon after the reaction is started.

When the same Ni-10Cr-13Al alloy was exposed to oxidizing environments in the presence of sodium sulfate, a much larger incubation period appeared to precede the onset of accelerated attack. Fig. 11 shows the weight gain curves for two specimens of Ni-10Cr-13Al pre-oxidized, coated with 10 mg/cm^2 of sodium sulfate and exposed to oxygen at 900°C. In this case the oxide layer formed on the alloy was found to consist of a mixture of Ni-Cr and Ni-Al

spinels, as shown by the micrograph in Fig. 12. Again, the rate of dissolution of the oxide scale in the melt was the factor retarding accelerated attack of the alloy. The difference in the duration of the incubation period is probably to be ascribed to non-uniformity of the oxide film thickness due to variations in the surface preparation of the specimen. It is worth noting that in Fig. 12 the attack proceeds internally at localized areas, the composition of which was found to correspond to the gamma-prime phase; a larger amount of sulfur appears to have diffused into the alloy at these areas possibly as a result of a larger density of grain boundaries.

CONCLUSIONS

The hot corrosion behavior of an alloy depends on the alloy chemistry, its microstructure and the composition of the corrosive environment. Because of its inherent complexity, a generalized model for hot corrosion is not yet possible.

The gamma matrix undergoes catastrophic corrosion in environments characterized by high sulfur potentials. At low sulfur potentials, such as those prevailing in a gas turbine environment, the gamma matrix shows excellent resistance to corrosion. On the contrary, the gamma-prime undergoes hot corrosion both in reducing and oxidizing environments. In addition, the gamma-prime is much less resistant than the gamma matrix in oxidizing environments, and can be considered a "weak link" in the overall corrosion process of commercial nickel-base alloys.

Studies of the rate of dissolution in molten sodium sulfate of protective oxides, and of the correlation between alloy microstructure and accelerated attack would provide a better understanding of hot corrosion processes.

ACKNOWLEDGMENT

REFERENCES

1. "Hot Corrosion Problems Associated with Gas Turbines", ASTM Special Technical Publication No. 421 (1967).

2. J. Stringer, "Hot Corrosion in Gas Turbines", MCIC Report No. 72-08, Battelle-Columbus (1972).

3. J.A. Goebel, F.S. Pettit and G.W. Goward, Met. Trans., 4, 261 (1974).

4. N.S. Bornstein and M.A. DeCrescente, Corrosion, 26, 209 (1970).

5. A.M. Beltran and D.A. Shores, "Superalloys", ed. by C.T. Sims and W.C. Hagel, J. Wiley & Sons, P. 317 (1972).

6. D.W. McKee and G. Romeo, Met. Trans., 4, 1877 (1973).

7. A.U. Seybolt, Trans. AIME, 242, 1955 (1968).

8. A.U. Seybolt, "Na_2SO_4-Superalloy Corrosion Mechanism Studies", General Electric Co., Corp. R&D Report No. 70-C-189 (1970).

9. D.W. McKee and G. Romeo, Met. Trans., 5, 1127 (1974).

10. D.W. McKee and G. Romeo, Met. Trans., in press.

11. R.F. Decker and C.T. Sims, ref. 5, p. 33.

12. C.S. Giggins and F.S. Pettit, J. Electrochem. Soc., 118, 1782 (1971).

13. C.J. Bechtold and H.C. Vacher, Trans. AIME, 221, 14 (1961).

14. M. Hansen, "Constitution of Binary Alloys", 2nd ed., p. 119, McGraw Hill, New York (1958).

15. A. Taylor and R.W. Floyd, J. Inst. Metals, 81, 451 (1952-53).

16. G. Romeo and W.W. Smeltzer, J. Electrochem. Soc., 119, 1268 (1972).

17. R.W. Hardt, J.R. Gambino and P.A. Bergman, ref. 1, p. 64.

Ni-35Cr   ⎸50μ⎸

Fig. 1. Ni-35Cr alloy treated at 850°C with a
10%H₂S-H₂ gas mixture for 2½ hours. The scale
consists of an outer layer of nickel sulfide
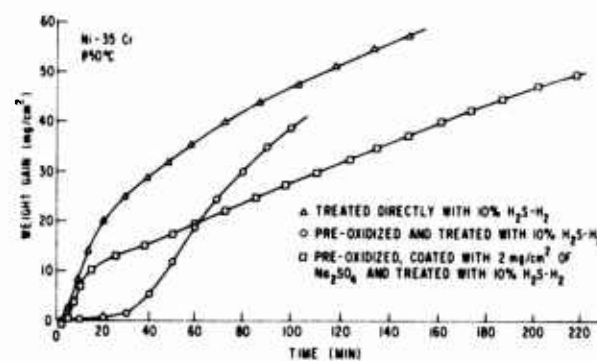which was molten at temperature, and an inner
layer of chromium sulfide.

Fig. 2. Weight gain curves for a Ni-35Cr alloy
exposed at 850°C to a 10%H₂S-H₂ gas mixture after
different treatments.

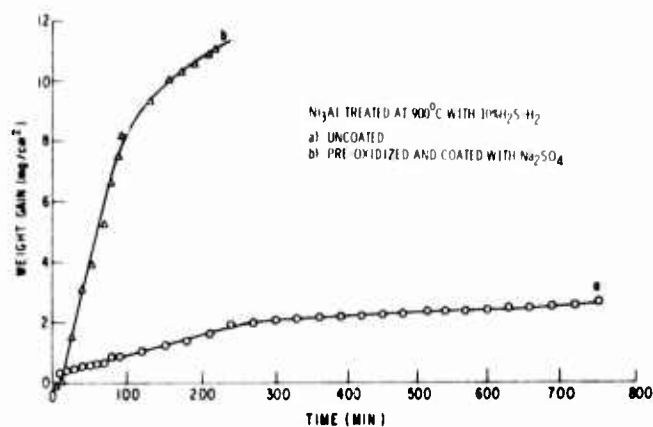427

Fig. 3. Weight gain curves for a Ni-13Al alloy
treated with a 10%H_2S-H_2 gas mixture at 900°C
after different treatments.
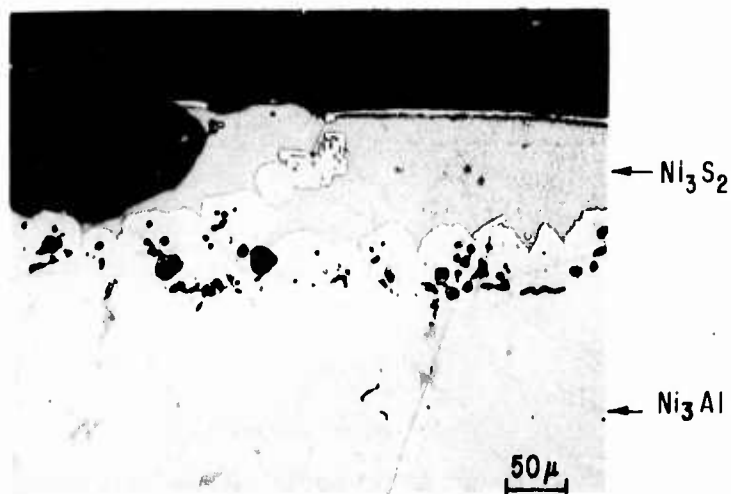
Fig. 4. Scale formed on a Ni-13Al alloy pre-oxidized,
coated with 9 mg/cm^2 of Na_2SO_4 and treated with a
10%H_2S-H_2 gas mixture at 900°C. The portion labeled
as Ni_3S_2 was probably molten at reaction temperature.
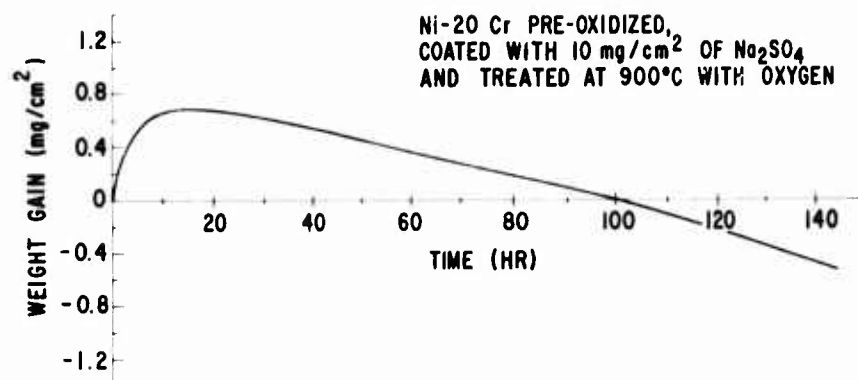
Fig. 5. Weight gain curve for a Ni-20Cr alloy pre-
oxidized, coated with 10 mg/cm^2 of Na$_2$SO$_4$ and
exposed to oxygen at 900°C. The weight loss of
the specimen can be attributed mainly to evaporation
of sodium sulfate.
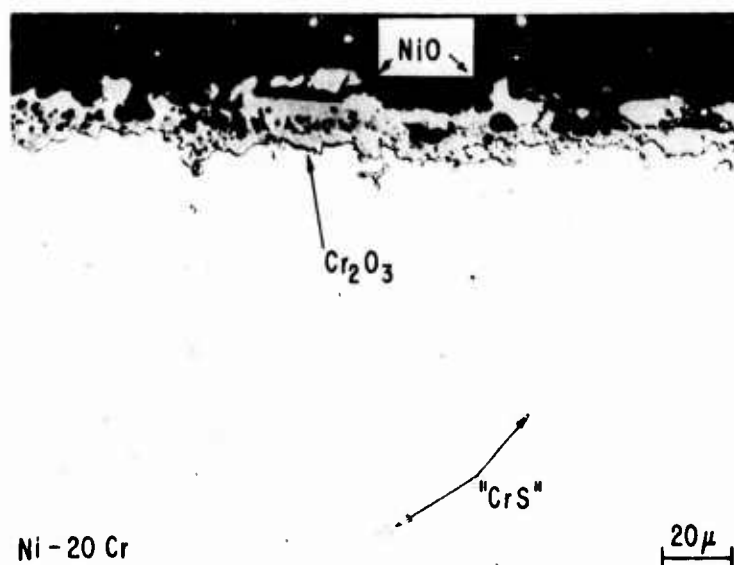
Fig. 6. Duplex oxide scale formed on a Ni-20Cr alloy
pre-oxidized, coated with 10 mg/cm^2 of Na$_2$SO$_4$ and
exposed to oxygen at 900°C for about 6 days. Some
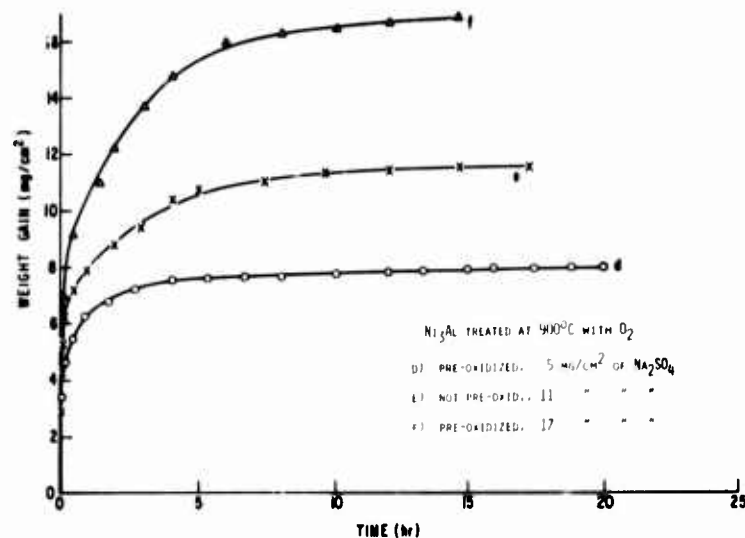particles of chromium sulfide have precipitated
within the alloy.

Fig. 7. Weight gain curves for a Ni-13Al alloy exposed to oxygen at 900°C after different treatments.
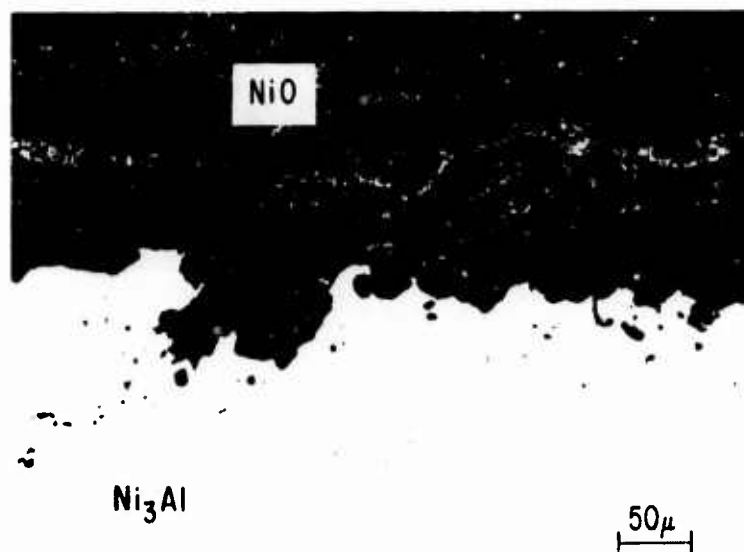

Fig. 8. Cross section of Ni-13Al alloy coated with 11 mg/cm² of Na₂SO₄ and treated with oxygen at 900°C for 18 hours. A small amount of α-Al₂O₃ was detected in the main NiO porous scale.

Copper plate
for scale retention

Thin oxide layer

Chromium sulfide

30μ

Corrosion product

Chromium sulfide
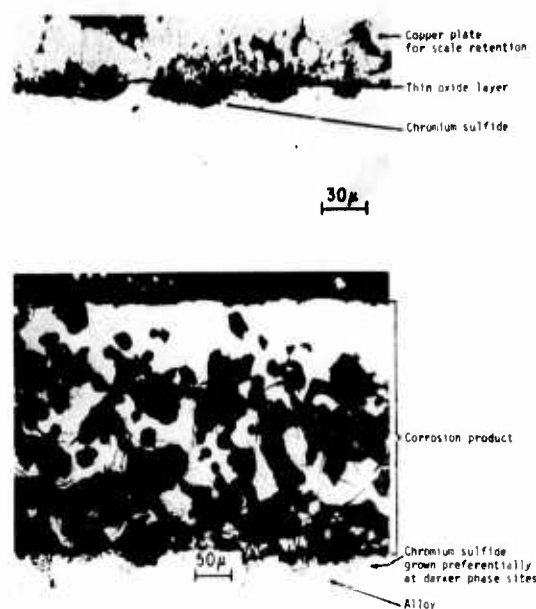grown preferentially
at darker phase sites

Alloy

50μ

Fig. 9. Ni-10.4Cr-13.5Al alloy treated with a 10%H$_2$S-H$_2$
gas mixture at 850° for 8 hours:

Top micrograph: the specimen was pre-oxidized
but not coated with sodium sulfate. A copper
plate was used for retaining the relatively
thin chromium sulfide layer.

Bottom micrograph: coating a pre-oxidized
specimen with sodium sulfate produced deep attack
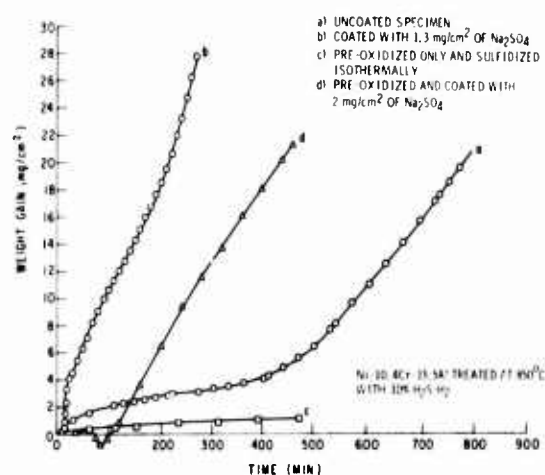and a complex scale morphology.

a) UNCOATED SPECIMEN
b) COATED WITH 1.3 mg/cm^2 OF Na$_2$SO$_4$
c) PRE-OXIDIZED ONLY AND SULFIDIZED
   ISOTHERMALLY
d) PRE-OXIDIZED AND COATED WITH
   2 mg/cm^2 OF Na$_2$SO$_4$

Ni-10.4Cr-13.5Al TREATED AT 850°C
WITH 10% H$_2$S-H$_2$

Fig. 10. Weight gain curves for a Ni-10.4Cr-13.5Al
alloy exposed to a 10%H$_2$S-H$_2$ gas mixture at 850°C
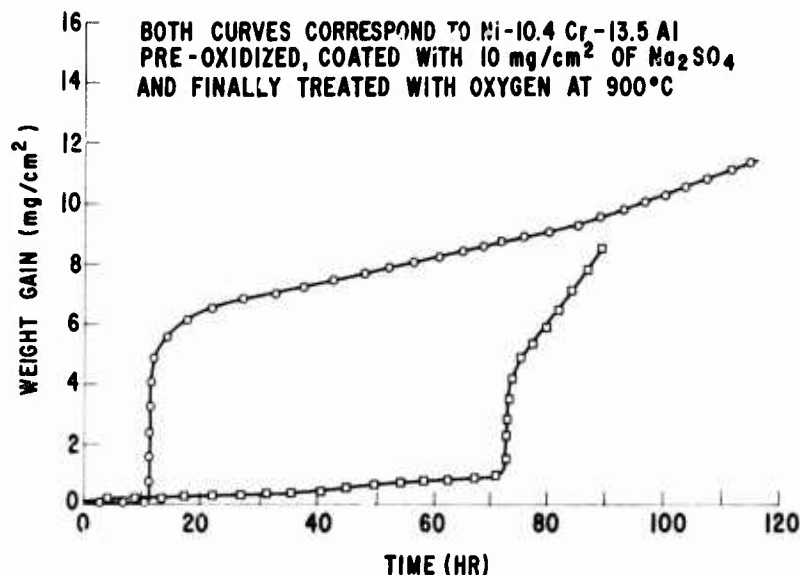after different treatments.

431

Fig. 11. Weight gain curves for two specimens of a
Ni-10.4Cr-13.5Al alloy pre-oxidized, coated with
10 mg/cm² of Na₂SO₄ and treated with oxygen at 900°C.
An incubation period of varying length has preceded
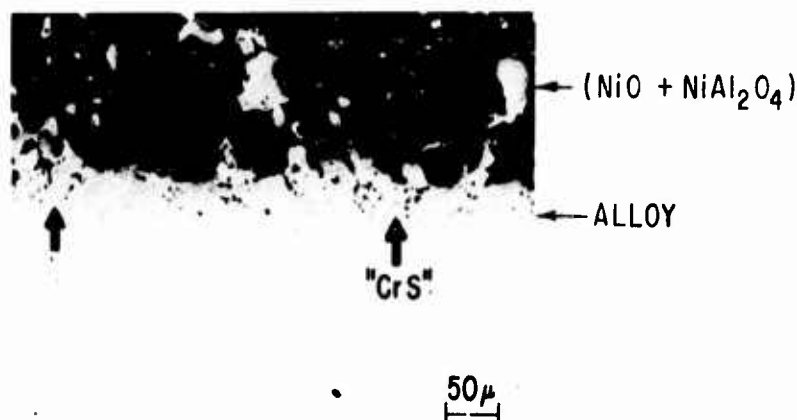in both cases accelerated attack.

Fig. 12. Ni-10.4Cr-13.5Al alloy pre-oxidized, coated
with 10 mg/cm² of Na₂SO₄ and treated with oxygen at
900°C for about 4 days. A thick and porous scale
consisting of NiO and NiAl₂O₄ has grown externally.
The arrows indicate internal precipitates of chromium
sulfide, localized preferentially at the darker phase
within the alloy.

432

ENVIRONMENTAL PROTECTION TO 922 K (1200°F) FOR TITANIUM ALLOYS

BY M. T. GROVES

TRW INC.
MATERIALS TECHNOLOGY
CLEVELAND, OHIO 44117

ABSTRACT

The purpose of this program was to evaluate potential coating systems for protection of titanium alloys from hot-salt stress-corrosion up to temperatures of 755 K (900°F) and from oxidation embrittlement up to temperatures of 922 K (1200°F). Diffusion type coatings containing Si, Al, Cr, Ni or Fe as single coating elements or in various combinations were evaluated for oxidation protection, hot-salt stress-corrosion (HSSC) resistance, effects on tensile and fatigue properties, erosion resistance and ballistic impact resistance on an α + β titanium alloy (Ti-6Al-2Sn-4Zr-2Mo). All of the coatings investigated demonstrated excellent oxidation protectiveness, but none of the coatings provided protection from hot-salt stress-corrosion. Experimental results indicated that both the aluminide and silicide types of coatings actually decreased the HSSC resistance of the substrate alloy. Oxidation exposed coated specimens (922 K (1200°F)) exhibited some degradation in tensile properties compared to unexposed Ti-6-2-4-2. About half of the coated specimens had strengths comparable to the uncoated Ti-6-2-4-2 substrate exposed at 922 K (1200°F) and tensile elongation values that exceeded those of the uncoated substrate. Fatigue properties were degraded by the presence of the coatings. Ballistic impact damage degraded the mechanical properties of the coated specimens. Only two of the coatings completely protected the substrate against erosion resistance at a 20° impingement angle, while none of the coatings were completely protective at an impingement angle of 90°. Tests with a β titanium alloy (Ti-13V-11Cr-3Al) indicated oxidation protectiveness comparable to the α + β alloy, but the thermal cycles employed in coating deposition severely degraded the mechanical properties of the β alloy. It was concluded that the types of coatings which have typically been used for oxidation protection of refractory metals and nickel base superalloys are not suitable for titanium alloys because they increase the susceptibility to hot-salt stress-corrosion and that entirely new coating concepts must be developed for titanium alloy protection in advanced turbine engines.

1.0 INTRODUCTION

Titanium alloys are used extensively for turbine engine compressor components up to about 700-750 K (800-900°F) because of excellent strength-to-weight ratio, fracture toughness and structural stability. These unique properties have been utilized in the manufacture of turbine engine compressor and fan blades, inlet cases, disks and other components. Titanium alloys with a greater strength capability are being developed for use in advanced engines at temperatures to 922 K (1200°F). The use of titanium alloys in some applications may be restricted by erosion and hot-salt stress-corrosion cracking. In addition, as the use temperature of advanced titanium alloys exceeds about 755 K (900°F), another potential problem limiting their long term use may be oxygen contamination. If the full potential of titanium alloys is to be exploited, coating systems must be developed to protect against the damaging influence of the higher temperature turbine engine environment.

In previous work, a variety of coatings have been evaluated on titanium alloys. Coatings that have provided high temperature oxidation protection for titanium alloys in previous work include aluminides[1][2], silicides[2][3], titanium intermetallic compounds (TiC, TiN, TiB and TiNi)[4,5,6], nickel aluminide[2], and diffused coatings of nickel, zinc and chromium[2]. Coatings deposited on titanium alloys that have been reported to exhibit resistance to hot-salt stress-corrosion cracking include nickel plate and an aluminide at 589 K (600°F)[7]; aluminides, silicides, diffused chromium and diffused zinc at 672 K (750°F)[2]; and plasma sprayed aluminum at 728 K (850°F)[8]. Hard chromium plate has provided better dust erosion protection than aluminides, beryllides, borides and nickel oxides[9]. A titanium carbide coating applied by chemical vapor deposition displayed excellent erosion resistance but significantly reduced fatigue strength[10]. Erosion tests on diffusion coatings indicated that nickel and chromium were protective at impingement angles of 20° and 90° while aluminum and silicon were protective only at the 20° impingement angle[2].

The objective of this program was to evaluate aluminides and silicides as potential protective coating systems for titanium alloys. Deposition of aluminide coatings on superalloys and silicide coatings on refractory metals by diffusion techniques are well developed processes. Previous work indicated that diffusion coatings containing aluminum or silicon could provide oxidation and hot-salt

stress-corrosion protection for titanium alloys. In addition, previous work indicated that diffusion coatings containing chromium and nickel provided erosion protection at both high and low impingement angles. Therefore, coatings selected for evaluation included both unmodified and modified variations of aluminides and silicides.

2.0 EXPERIMENTAL PROGRAM

The experimental work was conducted in two phases. In Phase I, ten experimental coating compositions were evaluated for oxidation protection and erosion resistance on Ti-6Al-2Sn-4Zr-2Mo sheet. In Phase II, the five most promising coating systems were further evaluated for fatigue and ballistic impact properties on the Ti-6-2-4-2 sheet and for oxidation protection on Ti-13V-11Cr-3Al sheet. Phase II also included an evaluation of the hot-salt stress-corrosion resistance of the five selected coating systems on two heats of Ti-6-2-4-2 sheet and a heat of Ti-6-2-4-2 bar stock.

2.1 Substrate Materials, Coatings and Test Specimens

Chemical compositions and mill forms of the substrate materials are listed in Table I. The majority of the experimental work was conducted with Ti-6-2-4-2 Heat No. A-1 in the form of sheet. Additional hot-salt stress-corrosion testing was performed on a second heat of Ti-6-2-4-2 sheet B-1. Heat treatments and vendor certified mechanical properties (where available) are listed in Table II. Table III lists the coating source compositions, deposition processes and deposition temperatures for the ten experimental coating systems. The coating elements were Al, Si, Cr, Ni, Mg and Fe which were used either as single coating elements or in various combinations. All of the coatings were diffusion deposited either by pack cementation or slurry slip pack. Some of the coatings were applied in two separate deposition steps (duplex coatings). Silicon, chromium, magnesium and nickel were used in the form of elemental powders, while the remainder of the materials were purchased as alloy powders. Slurry coatings were applied by spraying with suspensions consisting of 100 grams of powder in 300 ml of cellulose nitrate to obtain a bisque weight of approximately 50 mg/cm^2. The green bisques were air dried and fired in a 10^{-2} torr vacuum furnace. The slurry coated specimens were supported by bubbled alumina contained within Inconel retorts during firing. Pack cementation coatings were deposited from packs containing source material plus 1/2 weight percent CrCl$_3$ activator. The packs were also contained

in Inconel retorts and heated in a 10^{-2} torr vacuum. Deposition temperatures ranged from 972 K to 1228 K (1200°F to 1750°F) for times ranging from 2 hours to 15 hours. Coating thicknesses ranged from 5.1μm (0.0002 inch) to 45.7μm (0.0018 inch). Deposition times were adjusted so that two coating thickness levels, designated A and B, were obtained for each of the coating systems. In general, the B levels were approximately twice the A levels.

Mechanical property specimens are shown in Figure 1. Tensile and hot-salt stress-corrosion tests were conducted using the flat tensile specimen shown in Figure 1(a). Hot-salt stress-corrosion tests on bar stock were performed using the tubular specimens shown in Figure 1(b). Mechanical fatigue tests were performed using the flat tensile specimen shown in Figure 1(c). All test specimens were stress relieved by chemical milling in a solution of 3 volume percent hydrofluoric acid, 30 volume percent nitric acid and 67 volume percent water prior to coating or testing. A minimum of 0.0025 cm (0.001 inch) of metal was removed from all surfaces.

2.2   Metallography

Typical microstructures of the coatings in the as-deposited condition on Ti-6-2-4-2 sheet are shown in Figure 2. The microstructures could be classified into one of three categories. Coatings containing large amounts of aluminum consisted of an outer aluminide and an α layer adjacent to the substrate as illustrated by coating No. 1 (Figure 2(a)). Duplex coatings containing a Cr or Fe/Cr pre-coat consisted of an outer coating and a chromium rich layer adjacent to the unaffected substrate as illustrated by coating the Cr + Al-Mg system (Figure 2(b)). Layers adjacent to the unaffected substrate in these coatings probably contained appreciable amounts of the β phase due to the presence of the β stabilizing elements, Fe and Cr. The other type of coating microstructure consisted of a coating layer adjacent to an unaffected substrate. This type of microstructure was obtained for the silicon coating (No. 2) shown in Figure 2(c) and for coatings in which the α and β stabilizing elements apparently offset each other. The microstructure of the Ni-Cr-Al-Si system, shown in Figure 2(d), was typical of the multi-element coating systems in which an apparent balance was obtained between α and β stabilizing elements.

436

2.3   Oxidation Protection

The ten experimental coatings were screened for oxidation protection on Ti-6-2-4-2 sheet (Heat No. A-1)   under 922 K (1200°F) static oxidation exposure conditions.   Coated and uncoated coupons and tensile specimens were exposed for times up to 1000 hours.   Evaluation consisted of weight gain, electron microprobe analyses of exposed coatings and residual tensile properties.

Weight gains were determined by cycling to room temperature at 100 hour intervals.   Cumulative weight gains after 1000 hours of exposure are shown in Figure 3 for uncoated Ti-6-2-4-2 sheet and coated specimens with the A level coating thickness.   (Coating No. 4 (Al-Si) was omitted because its true weight gain could not be established.)   Nearly all coatings provided significant protection from oxidation as reflected by the low weight gains of the coated specimens compared to uncoated specimens.   Particularly outstanding were coatings 1, 3, 5 and 6.   These coatings had cumulative weight gains of 0.05 to 0.075 mg/cm^2 compared to a weight gain of 1.110 mg/cm^2 for uncoated Ti-6-2-4-2 sheet.   After exposure, both the uncoated and coated specimens were semi-quantitatively analyzed for oxygen content using a Phillips electron probe mic analyzer.   The scan areas were at the mid-thickness of the substrate (or uncoated specimens), immediately below the coatings and immediately below the surface of the uncoated specimen. For coatings that contained an α layer in the as-deposited microstructure, the scan area beneath the coating was the α layer.   Coated specimens had equivalent oxygen contents at the mid-thickness of the substrate and the area immediately beneath the coating.   Uncoated specimens had a significantly higher concentration of oxygen near the surface compared to the mid-thickness.   The electron microprobe analyzer indicated that all of the coatings protected the substrate from oxidation at 922 K (1200°F).

Tensile properties of the oxidation-exposed coated specimens are compared to the tensile properties of uncoated specimens in Figures 4 and 5.   The specimens were exposed at 922 K (1200°F) for either 100 or 1000 hours.   Following exposure the specimens were slow rate tensile tested at room temperature (0.125 mm/min. (0.005 in/min.)).   Data are presented for both thickness variations of all ten coatings.   Figure 4 compares the residual tensile properties of the exposed coated specimens with uncoated, unexposed mill annealed Ti-6-2-4-2.   The properties of the coated specimens are presented as a percentage of the properties of

the uncoated material as the baseline for both 100 hour and 1000 hour exposures.
The tensile property which was degraded to the greatest extent was tensile
elongation. Coatings with the best residual tensile elongation were coatings 2,
4 and 5. These coatings had tensile elongation values equivalent to 90-97% of
the baseline after 100 hours of exposure. After 1000 hours of exposure, tensile
elongations of these coatings ranged from about 65-92% of the baseline. For the
majority of the coatings, yield strengths and tensile strengths after 100 hours
of exposure were comparable to those of uncoated, unexposed material and for these
coatings only a small reduction in strength (1-5%) was obtained after 1000 hours
of exposure. Increased coating thickness generally reduced the tensile properties
by a small amount (1-5%). The poorest tensile properties were obtained from the
duplex coatings containing β stabilized substrate/coating interface layers
(coatings 3, 6 and 9).

In Figure 5 the residual tensile properties of the coated-exposed tensile
specimens are compared with the residual tensile properties of similarly exposed
uncoated specimens as the baseline. Elongation values of about half of the
coatings exceeded those of the uncoated material after both 100 and 1000 hours
exposure. This was particularly evident after the 1000 hour exposures. After
this exposure time, coatings 2, 4, 5, 7 and 10 had elongation values ranging from
180 to 280% of the baseline. Again the duplex coatings containing the β stabilized
substrate/coating interface layers (coatings 3, 6 and 9) had the poorest elongation
values amounting to only 5 to 30% of the elongation of the uncoated, exposed
material. About half of the coatings had strengths equivalent or higher than the
uncoated material.

2.4   Dust Erosion Tests

All ten coating systems at the greater coating thickness (B level) were
evaluated for dust erosion resistance using coated and uncoated (mill annealed)
Ti-6-2-4-2 coupons. Erosion tests were conducted using an S.S. White Mini-blast
unit at impingement angles of 20 and 90 degrees. The eroding abrasive used was
27 micron alumina carried through a 0.051 mm (0.019 inch) diameter nozzle at a
5.08 cm (2.0 inch) standoff distance in an argon gas stream under a pressure of
344.5 KN/m^2 (50 psig). An abrasion time of 60 seconds was electronically
controlled. Erosion resistance was determined by the weight lost from a constant
surface area obtained by masking. Details of this evaluation technique are given
elsewhere[11].

Test results are summarized in the bar graphs presented in Figure 6. At an impingement angle of 20°, only coatings 3 and 5 completely protected the substrate; i.e., no substrate was eroded. At an impingement angle of 90°, none of the coatings completely protected the substrate. However, coatings 1, 5, 6, 9 and 10 provided some erosion protection in that less material was eroded from the coated specimens than from the uncoated specimens.

2.5   Fatigue and Ballistic Impact Resistance

Following screening tests of all ten experimental coating systems for oxidation protection and erosion resistance, the five most promising coating systems were selected for further evaluation under fatigue and ballistic impact conditions at the B coating thickness level. Coatings selected for further evaluation included Nos. 1, 2, 5, 8 and 10. Figure 7 compares the fatigue properties of these coatings on Ti-6-2-4-2 sheet with uncoated Ti-6-2-4-2 sheet in various heat treated conditions. Tests were performed at room temperature on a Baldwin-Universal fatigue machine operating at a frequency of 30 Hz. The endurance limit at a maximum of 10^7 cycles was determined in tension-tension utilizing an A ratio (ratio of alternating-to-mean stress) of 0.67. Uncoated specimen heat treated conditions included mill annealed, duplex annealed and a 15 hr/1228 K (1750°F) heat treatment to simulate the most severe coating cycle.

Compared to uncoated material, the coated specimens all had reduced endurance limits. Based on uncoated duplex annealed material, the endurance limit was reduced by 30 to 40%. Based on uncoated mill annealed material or uncoated material heat treated to simulate the coating thermal cycle, the endurance limit was reduced by 25 to 35%.

Ballistic impact resistance of the five selected coatings was evaluated on Ti-6-2-4-2 sheet at the B thickness levels of the coatings. Uncoated mill annealed specimens and the coated specimens were impact damaged at room temperature using a 0.656 gm steel ball fired from a gas operated pellet gun at a standoff distance of 38.1 cm (15 inches). Velocities up to 232 m/sec (760 ft/sec) were employed and specimens were examined at 30X magnification to detect cracking. Results of the ballistic impact tests are presented in Figure 8. Initially, the crack threshold velocity was determined for uncoated and coated specimens. The crack threshold velocity was defined as the minimum velocity at which the coating would

439

crack without rupture of the substrate material. As shown in Figure 8(a), a crack threshold velocity could not be determined for uncoated material. Gross rupture occurred at the highest impact velocity, 232 m/sec (760 ft/sec), employed in the tests. The coatings all had crack threshold velocities lower than 232 m/sec (760 ft/sec). Coating No. 2 had the highest crack threshold velocity, 145 m/sec (475 ft/sec) while coatings 1 and 10 had the lowest crack thresholds, 76 m/sec (248 ft/sec). To determine the effect of impact damage on tensile properties, coated specimens were damaged using an impact velocity that was 10% greater than the crack threshold velocity. The damaged specimens were then exposed at 922 K (1200°F) for 100 hours along with undamaged specimens. Both groups of specimens were tensile tested at room temperature after exposure. Yield and tensile strengths were comparable for the damaged and undamaged specimens. Tensile ductility of the damaged specimens, however, was reduced as indicated in Figure 8(b). The tensile ductility of the damaged specimens is expressed as a percentage of the tensile ductility of the undamaged specimens. The best coatings (Nos. 1 and 5) had tensile elongation reduced by 5 to 10% compared to undamaged coatings.

2.6 β Alloy

The five coatings selected for further evaluation (Nos. 1, 2, 5, 8 and 10) were evaluated for oxidation resistance and tensile properties on the β alloy. Ti-13V-11Cr-3Al coupons and tensile specimens of Ti-13V-11Cr-3Al were coated using the same deposition parameters that were used to obtain the β coating thickness levels on the Ti-6-2-4-2 specimens. Coating thicknesses obtained on Ti-13-11-3 were comparable to those obtained on the Ti-6-2-4-2. The coated coupons and tensile specimens were exposed for 1000 hours at 922 K (1200°F) along with uncoated Ti-13-11-3 coupons. After exposure, the tensile specimens were tested at room temperature using slow strain rates (0.125 mm/min. (0.005 in/min.)). Results of the static oxidation tests and post-exposure tensile tests are presented in Table IV. All five of the coatings were protective with respect to oxidation of the β titanium alloy as evidenced by significantly lower weight gains on the coated specimens. The tensile specimens, however, had almost zero ductility and tensile strengths that ranged between 22 to 48% of the strength of uncoated, unexposed Ti-13-11-3 tensile specimens.

The reduction in tensile properties of the coated specimens was attributed to excessive grain growth occurring during the coating cycles. Examination of

tensile fractures in the coated, exposed specimens showed that excessive grain growth had occurred during the coating thermal cycles and resulted in appreciable amounts of intergranular failure. Typical scanning electron micrographs of the fractures observed for the uncoated and coated specimens are shown in Figure 9. Grain size (as indicated by the fractographs) and amount of intergranular fracture was directly related to the coating thermal cycle. Fractures from Coating No. 2 (coating cycle - 15 hr/1228 K (1750°F)) failed primarily by an intergranular mode as shown in Figure 9(a). The fracture of a coated specimen processed under a less severe thermal cycle (12 hr/1200 K (1700°F)) had approximately equal amounts of intergranular and transgranular failure and a somewhat finer grain size as shown in Figure 9(b). Figure 9(c) shows the transgranular mode of failure exhibited by an uncoated specimen. Although the coatings protected the Ti-13-11-3 substrate from oxidation, it was apparent that the coating thermal cycles seriously degraded the mechanical properties of this alloy.

2.7 Hot-Salt Stress-Corrosion Resistance

Initial hot-salt stress-corrosion (HSSC) tests were conducted on Ti-6-2-4-2 sheet (Heat No. A-1). The five coatings selected for further evaluation were deposited on tensile specimens at the B coating thickness levels. The gage lengths of the specimens were then salted and the specimens were creep exposed at 755 K (900°F) for 100 hours under various loads. Uncoated specimens were also salted and exposed under the same conditions. If the specimens survived the exposure, they were tensile tested at room temperature using slow strain rates. Two criteria were used to determine if hot-salt stress-corrosion had occurred in specimens which survived the creep exposure. First a crack threshold stress was determined. This was defined as the minimum stress at which heat tint cracks could be observed in the tensile fracture under a magnification of 30X. The presence of heat tint cracks indicated that cracking occurred during the high temperature exposure. The second criteria was an embrittlement threshold stress. Once the crack threshold was established for a particular coating, the exposure stress was lowered on successive specimens to determine the minimum creep stress under which embrittlement did not occur. A specimen was considered to be embrittled by the presence of the salt if its residual tensile elongation was less than 80% of the tensile elongation of oxidation exposed specimens.

HSSC results for the initial heat of Ti-6-2-4-2 sheet are presented in Figure 10. Initially, both the uncoated and coated specimens were salted with a

6 mg/cm^2 concentration of NaCl. With this salt concentration, a crack threshold stress could not be determined for uncoated Ti-6-2-4-2. Heat tint cracks were observed as low as 17.2 MN/m^2 (2.5 ksi), the lowest exposure stress used in the testing. Crack threshold stresses for the coating varied from 34.5 MN/m^2 to 68.9 MN/m^2 (5.0 to 10.0 ksi). Embrittlement thresholds for the coated specimens were lower than 17.2 MN/m^2 to 68.9 MN/m^2 (2.5 to 5.0 ksi) the lowest creep exposure stresses used as indicated in Figure 10. Although the coatings increased the crack threshold stresses, embrittlement still occurred at low threshold stresses. At this point, it was thought that the salt concentration (6 mg/cm^2) could be unrealistically high and a 0.2 mg/cm^2 concentration was tested on uncoated material. The crack threshold was increased, but embrittlement was still detected under an exposure stress of 68.9 MN/m^2 (10 ksi) as indicated indicated in Figure 10. From the results of the preceding creep exposure tests, it was apparent that the coatings did not protect the substrate from HSSC. In addition, the Ti-6-2-4-2 sheet material appeared to have abnormally high sensitivity to HSSC compared to Ti-6-2-4-2 bar stock. A threshold embrittlement stress of 447.9 MN/m^2 (65 ksi) has been reported for uncoated Ti-6-2-4-2 bar stock[12]. An additional series of tests was conducted with the Ti-6-2-4-2 sheet in which tensile specimens were salted and exposed at 755 K (900°F) for 100 hours with no applied load. These tests showed that the presence of salt at 755°K (900°F) was sufficient to embrittle the program Ti-6-2-4-2 sheet material. A similar series of tests were performed on a second heat of Ti-6-2-4-2 sheet material (Heat No. B-1). Salted specimens from this second heat, exposed with or without an applied load also exhibited an extreme sensitivity to HSSC.

The extremely high sensitivity of the sheet materials to HSSC embrittlement precluded a judgment as to the effect of the coatings on HSSC. In order to better gage the performance of the coatings, a quantity of Ti-6-2-4-2 bar stock was obtained that had exhibited good HSSC in a previous study[12]. Tubular tensile specimens, previously shown in Figure 1(b), were machined from the bar stock. The five coatings selected for further evaluation were deposited on both the I.D. and O.D. of the specimens using the deposition parameters for producing the B coating thickness level on the sheet stock. A 0.2 mg/cm^2 salt concentration was placed on the gage length (O.D. only) of both coated and uncoated specimens. As before, the specimens were exposed under various creep loads at 755 K (900°F) for 100 hours. Specimens surviving the creep-exposure were then slow rate tensile tested

442

at room temperature. A crack threshold stress and an embrittlement threshold stress were determined as with the HSSC tests on sheet specimens. Following the criteria used by Gray[12], an uncoated specimen was considered embrittled if the residual tensile elongation was less than 15%, and the apparent residual reduction in area (based on O.D. measurements only) was less than 25%. A coated specimen was considered embrittled if the residue tensile elongation was less than 4%, and the apparent residual reduction in area was less than 6%. The results of the HSSC tests on Ti-6-2-4-2 bar stock are presented in Figure 11. Uncoated material had a crack threshold stress between 137.8 MN/m^2 (20 ksi) and 344.5 MN/m^2 (50 ksi) and an embrittlement threshold stress of 103.4 MN/m^2 (15 ksi), a considerable improvement in HSSC resistance over the sheet materials. All of the coatings, however, reduced the HSSC resistance of the substrate. The crack threshold stress for all five of the coatings was 68.9 MN/m^2 (10 ksi) and embrittlement again occurred at low stress levels, 17.2 MN/m^2 to 34.5 MN/m^2 (2.5 to 5.0 ksi). Coating No. 2 had an apparent crack threshold stress of 34.5 MN/m^2 (5.0 ksi). When it was attempted to verify the threshold stress level for this coating, embrittlement was again evidenced in a post-exposure tensile test as indicated by the bar graph.

3.0   SUMMARY OF RESULTS

The following summation can be made from the experimental work performed in this investigation:

1.   All ten experimental coatings protected the substrates from oxidation under 1000 hr/922 K (1200°F) exposure conditions.

2.   Tensile tests of coated Ti-6-2-4-2 specimens oxidation exposed at 922 K (1200°F) indicated that tensile properties, particularly elongation, were degraded with respect to uncoated, unexposed Ti-6-2-4-2.

3.   Tensile properties of coated Ti-6-2-4-2 specimens, oxidation exposed at 922 K (1200°F) compared more favorably to uncoated Ti-6-2-4-2 that was comparably exposed. After 1000 hours of exposure, about half of the coated specimens had strengths equivalent or somewhat higher than uncoated materials and increased ductility over uncoated specimens.

443

4. Erosion test results indicated that only two coatings (3 and 5) completely protected the substrate from erosion at an impingement angle of 20°, while none of the coatings completely protected the substrate from erosion at an impingement angle of 90°.

5. All five of the coatings selected for fatigue testing (coatings 1, 2, 5, 8 and 10) reduced the fatigue properties of Ti-6-2-4-2 sheet.

6. Ballistic impact damage, followed by oxidation exposure, reduced the tensile properties of coatings 1, 2, 5, 8 and 10 on Ti-6-2-4-2.

7. Deposition of the selected coatings (1, 2, 5, 8 and 10) on Ti-13V-11Cr-3Al drastically reduced the tensile properties of this alloy.

8. All of the coatings displayed poor resistance to HSSC. The presence of the coating intensified the attack on the substrate.

4.0 CONCLUSIONS

The present study has shown that the most serious problem associated with the diffusion coatings tested on the program is their poor resistance to HSSC at 755 K (900°F). While good oxidation protection and minimal reduction in tensile properties could be obtained with some of the coatings, the fact that the coatings intensified HSSC would preclude their use in turbine engine environments. The program results indicate that the diffusion coating approach, utilizing elements such as Si, Al and Cr, that has been used successfully for protecting superalloy components, will probably not be useful for protecting titanium alloys from HSSC.

REFERENCES

1. Anon, "The Characteristics and Uses of Aluminum Coatings on Titanium and Titanium Alloys," TML Memo No. 79, October 1956.

2. Nejedlik, J. F.,"Protective Coatings for Titanium Alloy Compressor Blades," TRW Report TM-4580, December 1970.

3. Kluz, S., Kolinowski, C. and Wehrman, R., "Development of Protective Coatings for Titanium Alloys," Watertown Arsenal Report WAL-401-51-22, October 1953.

4. Coatings of High Temperature Materials, H. H. Hauser, Editor, Plenum Press (1966).

5. Latva, J. D., "Selection and Fabrication of Ceramics and Intermetallics," Metal Progress, October 1962.

6. "Structures and Properties of Heat Resistant Metals and Alloys," M. V. Pridantseu, Editor, NASA TTF-557, 1970.

7. Stein, B. A. and Dexter, H. G., "Coatings and Surface Treatments for Longtime Protection of Ti-8Al-1Mo-1V Alloy Sheet from Hot-Salt Stress-Corrosion," NASA TND-4319, March 1968.

8. Schwartz, R., "Development of Improved Corrosion Protection for Long Time Exposure of S-II Stage and/or Hardware," Final Report to Contract NAS7-200, Supplemental Agreement 2049, North American Rockwell Space Division, December 1971

9. Rapp, G. C. and Rosenthal, S. H., "Problems and Solutions for Sand Environment Operation of Helicopter Gear Turbines," ASME Paper 65-WA/Prod-7, 1965.

10. Gulbransen, E. A. and Andrew, K. F., "Kinetics of the Reactions of Titanium with O_2, N_2 and H_2," Transactions AIME, October 1949.

11. Groves, M. T., "Environmental Protection to 922 K (1200^OF) for Titanium Alloys," NASA CR-134537, November 1973.

12. Gray, H. R., "Relative Susceptibility of Titanium Alloys to Hot-Salt Stress-Corrosion," NASA TND-6498.

TABLE I

CHEMICAL COMPOSITION OF TITANIUM ALLOY SUBSTRATE MATERIALS (WEIGHT PERCENT)

Alloy[a]	Vendor	Heat No.	Form	Source of Analysis	Al	Sn	Zr	Mo	V	Cr	Fe	N	C	O	H
6-2-4-2	A	A-1	1.27 mm (0.050") sheet	Vendor[b]	6.3	2.02	4.38	2.03			0.22	0.02	0.044	0.06	0.009
	"	"	" "	TRW[c]	6.5	2.17	4.45	1.99			.12	.002	.016	.03	.0074
6-2-4-2	B	B-1	1.57 mm (0.062") sheet	Vendor[b]	6.3	2.1	3.8	2.1			.07	.007	.02	.129	.0036
6-2-4-2	B	B-2	1.91 cm (0.75") bar	NASA[d]	6.3	2.0	3.8	2.0			.07	.009	.01	.098	.0070
13-11-3	A	A-2	1.27 mm (0.050") sheet	Vendor[b]	3.25				13.8	11.2	.31	.03	.028	.15	.020

NOTES:
(a) 6-2-4-2: Ti-6Al-2Sn-4Zr-2Mo
    13-11-3: Ti-13V-11Cr-3Al

(b) Vendor - Certified Chemical Analysis

(c) TRW - Analysis No. 68551

(d) Literature - NASA TN D-6498 (Reference No. 12)

446

TABLE II

TITANIUM ALLOY HEAT TREATMENTS AND VENDOR CERTIFIED MECHANICAL PROPERTIES

Alloy (a)	Heat No.	Heat Treatment Cycles Studied		Tensile Strength		0.2% Yield Strength		% R.A.	% El.
		Designation	Treatment	(MN/m²)	(ksi)	(MN/m²)	(ksi)		
6-2-4-2	A-1	Mill Anneal	As Received; 1200 K(1700°F), 1/2 hr, A.C.	944	137	881.9	128.0	-	19
		Duplex Anneal	1228 K(1750°F), 1/2 hr, furnace cool plus 1061 K(1450°F), 1/4 hr, furnace cool	-	-	-	-	-	-
		Simulated Coating Cycle	1228 K(1750°F), 15 hrs, furnace cool	-	-	-	-	-	-
6-2-4-2	B-1	Duplex Anneal	1172 K(1650°F), 1/2 hr, A.C. 1061 K(1450°F), 1/4 hr, A.C.	-	-	-	-	-	-
6-2-4-2	B-2	Mill Anneal	As Received; 1172 K(1650°F), 1 hr, A.C.	1120	162	-	-	33	18
13-11-3	A-2	Mill Anneal	As Received; 1089 K(1500°F), 1/2 hr, A.C.	919.8	133.5	915.0	132.8	-	20
"	"	Duplex Anneal	1033 K(1400°F), 1/2 hr, A.C. 755 K(900°F), 48 hrs, A.C.	-	-	-	-	-	-

NOTES: (a) Ti-6-2-4-2 - Ti-6Al-2Sn-4Zr-2Mo
Ti-13-11-3 - Ti-13V-11Cr-3Al

(b) Data from NASA TND-6498 (Reference 12)

TABLE III

EXPERIMENTAL COATING SYSTEMS

Coating No.	System Designation	Source Composition (Weight Percent) and Deposition Method	Deposition Temperature K	Deposition Temperature °F	Time (hr)	Thickness Level	Metallographic Thickness Ti-6-2-4-2 μm	Ti-6-2-4-2 Inx10⁻³	Ti-13-11-3 μm	Ti-13-11-3 Inx10⁻³
1	Al	56Cr-44Al Alloy, Pack Cementation	1200 / 1200	1700 / 1700	4 / 12	A / B	9.7 / 19.1	0.38 / 0.75	11.2 / 19.1	0.44 / 0.75
2	Si	Si Metal, Slurry	1228 / 1228	1700 / 1700	6 / 15	A / B	6.4 / 6.4	0.25 / 0.25	4.8 / 6.4	0.19 / 0.25
3	Duplex Cr Al-Mg	Cr Metal, Slurry 90 (56Cr-44Al Alloy) + 10 Mg, Pack Cementation	1228 / 1200	1750 / 1700	2 / 6	A / A	25.4 / 12.7-25.4	1.0 / 0.5-1.0	-- / --	-- / --
	Duplex Cr Al-Mg	Cr Metal, Slurry 90 (56Cr-44Al Alloy) + 10 Mg, Pack Cementation	1228 / 1200	1750 / 1700	5 / 6	B / B	45.7 / 50.8	1.80 / 2.00	-- / --	-- / --
4	Al-Si	87 Al - 13 Si, Slurry	922 / 922	1200 / 1200	2 / 4	A / B	6.4 / 20.8	0.25 / 0.82	-- / --	-- / --
5	Al-Mg	90 (56Cr-44Al Alloy) + 10 Mg, Pack Cementation	1200 / 1200	1700 / 1700	4 / 12	A / B	12.7 / 19.1	0.50 / 0.75	12.7 / 19.1	0.50 / 0.75
6	Duplex Cr-Fe Al-Mg	(75Cr-25Fe Alloy), Slurry 90 (56Cr-44Al Alloy) + 10 Mg, Pack Cementation	1228 / 1200	1750 / 1700	4 / 6	A / A	9.7 / 9.7	0.38 / 0.38	-- / --	-- / --
	Duplex Cr-Fe Al-Mg	(75Cr-25Fe Alloy), Slurry 90 (56Cr-44Al Alloy) + 10 Mg, Pack Cementation	1228 / 1200	1750 / 1700	10 / 6	B / B	12.7 / 12.7	0.53 / 0.50	-- / --	-- / --

TABLE III (continued)

Coating No.	System Designation	Source Composition (Weight Percent) and Deposition Method	Deposition Temperature		Time (hr)	Thickness Level	Metallographic Thickness			
			K	°F			Ti-6-2-4-2		Ti-13-11-3	
							µm	Inx10⁻³	µm	Inx10⁻³
7	Si-Cr-Al	71Si + 25Cr + 4 (87Al-13Si Alloy), Slurry	1228	1750	4	A	5.1	0.20	-	-
			1228	1750	15	B	12.7	0.50	-	-
8	Ni-Cr-Al-Si	50Ni + 20Cr + 30 (87Al-13Si Alloy), Slurry	1200	1700	3	A	12.7	0.50	6.4	0.25
			1200	1700	12	B	19.1	0.75	12.7	0.50
9	Duplex Cr Al-Si	Cr Metal, Slurry 87Al-13Si Alloy, Slurry	1228	1750	2	A	12.7	0.50	-	-
			922	1200	2	A	19.1	0.75	-	-
	Duplex Cr Al-Si	Cr Metal, Slurry 87Al-13Si Alloy, Slurry	1228	1750	5	B	31.8	1.25	-	-
			922	1200	2	B	33.0	1.30	-	-
10	Ni-Fe-Al-Si	40Ni + 40 (50Fe-50Al Alloy) + 20 (87Al-13Si Alloy), Slurry	1228	1750	3	A	6.4	0.25	6.4	0.25
			1228	1750	10	B	19.1	0.75	15.2	0.60

449

TABLE IV

TOTAL WEIGHT GAINS AND TENSILE TEST RESULTS
FOR UNCOATED AND COATED Ti-13-11-3 ALLOY
EXPOSED AT 922 K (1200°F) FOR 1000 HOURS

Coating	Total Weight Gain (Mg)	U.T.S. (MN/m^2)	U.T.S. (ksi)	.2% Y.S. MN/m^2	.2% Y.S. (ksi)	% Elongation[a]
Uncoated	35	509.1	73.9	-	-	0.5
Uncoated	46	550.5	79.9	-	-	0.5
1B	2	554.6	80.5	-	-	0.3
1B	1	638.7	92.7	-	-	0.4
2B	22	642.8	93.3	-	-	0.4
2B	21	598.7	86.9	-	-	0.2
5B	1	652.5	94.7	-	-	0.3
5B	1	736.5	105.9	-	-	- (b)
8B	7	598.1	86.8	-	-	0
8B	5	564.3	81.9	-	-	0.8
10B	3	663.5	96.3	-	-	0.5
10B	3	575.3	83.5	-	-	0.1
Uncoated[c]	-	1332.5	193.4	1223.0	177.5	2.9

NOTES: (a) 2.54 cm (1 inch) gage length.

(b) Pin hole failure.

(c) Average data for unexposed solution treated and aged Ti-15V-11Cr-3Al.

450
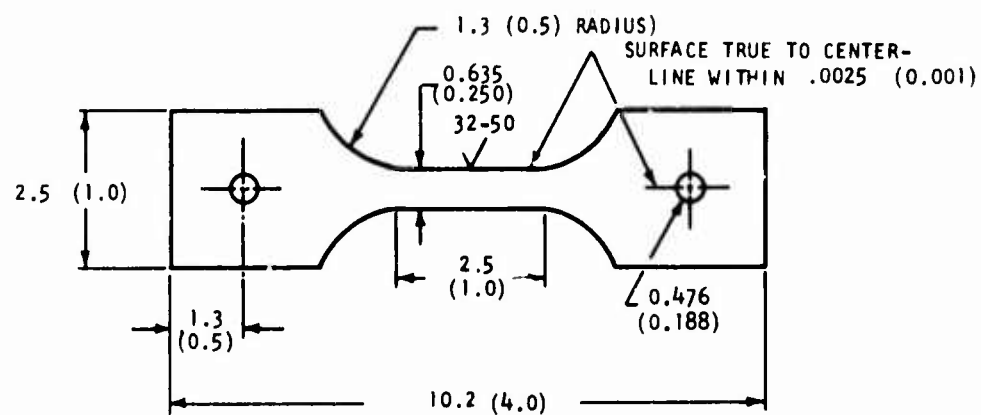
(a) Tensile and HSSC Specimens (Sheet)
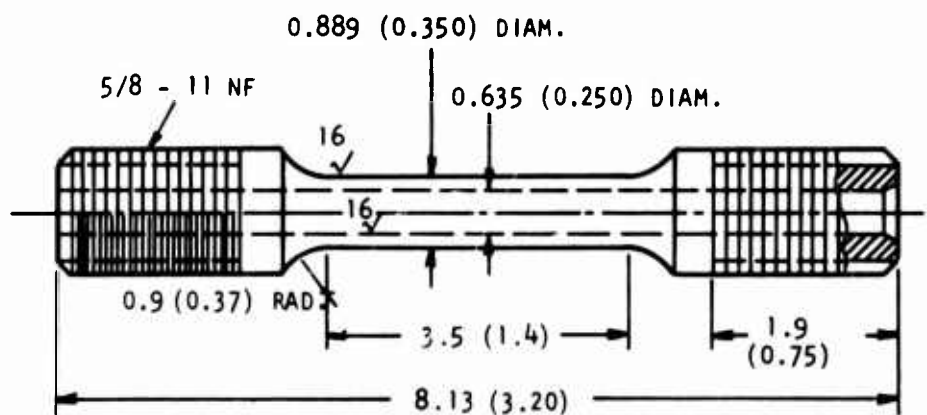
(b) Tubular Specimen (Bar Stock)
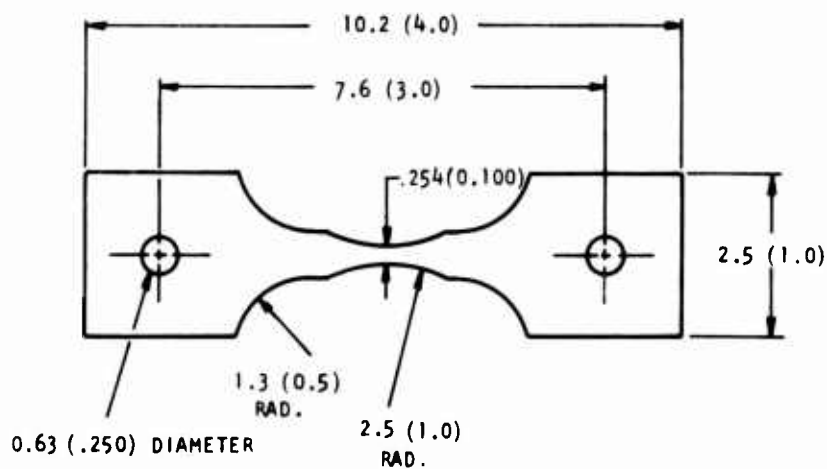
(c) Fatigue Specimen

Figure 1. Mechanical Test Specimens
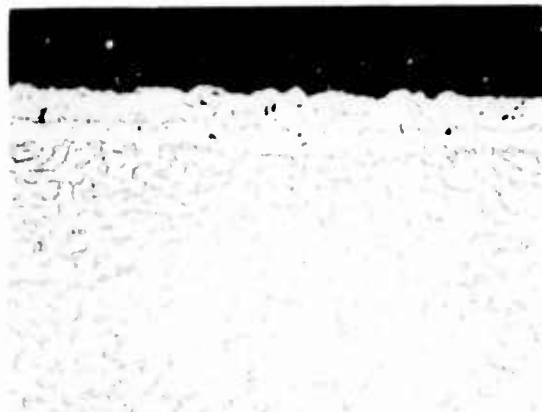
(a) No. 1 - Al

(b) No. 3 - Cr + Al - Mg
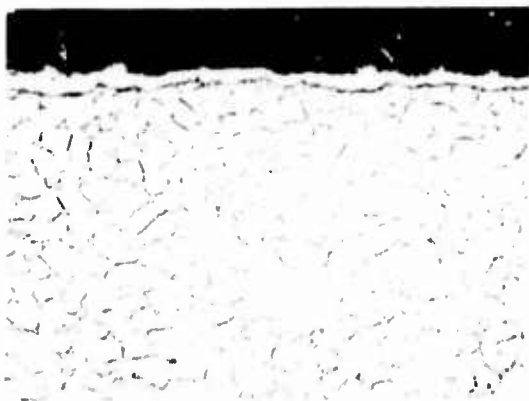
(c) No. 2 - Si
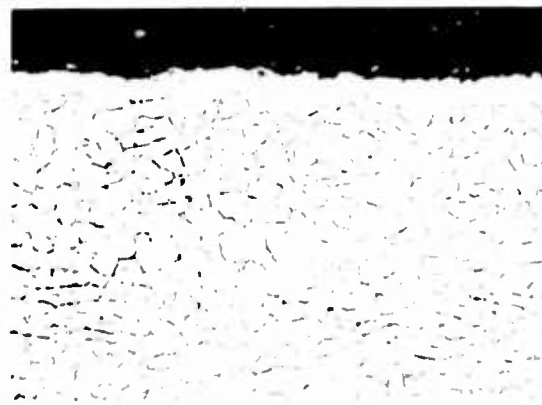
(d) No. 8 - Ni-Cr-Al-Si

Figure 2. Typical As-Deposited Coating Mircostructure on Ti-6-2-4-2 Sheet

(Magnification - 500X
Etchant - 2 v/o HF + 2 v/o HNO_3 + H_2O)

Figure 3. Cumulative Weight Gains of Uncoated and Coated Ti-6-2-4-2 Sheet After 1000 Hr/922 K (1200°F) Oxidation Exposure
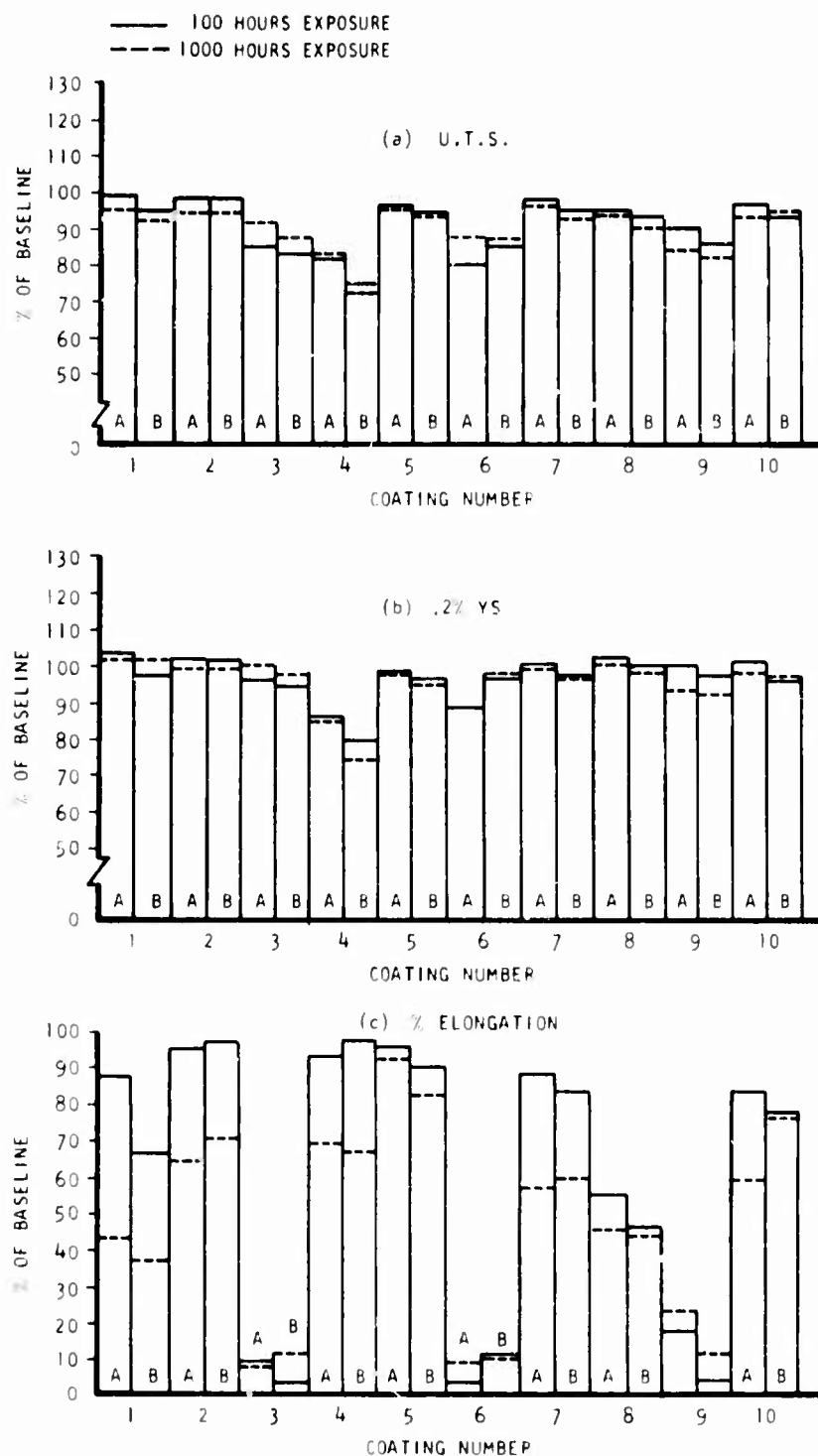
Figure 4. Tensile Properties of Coated Ti-6-2-4-2 After Exposure at 922 K (1200°F) Compared to Uncoated, Unexposed Mill Annealed Ti-6-2-4-2
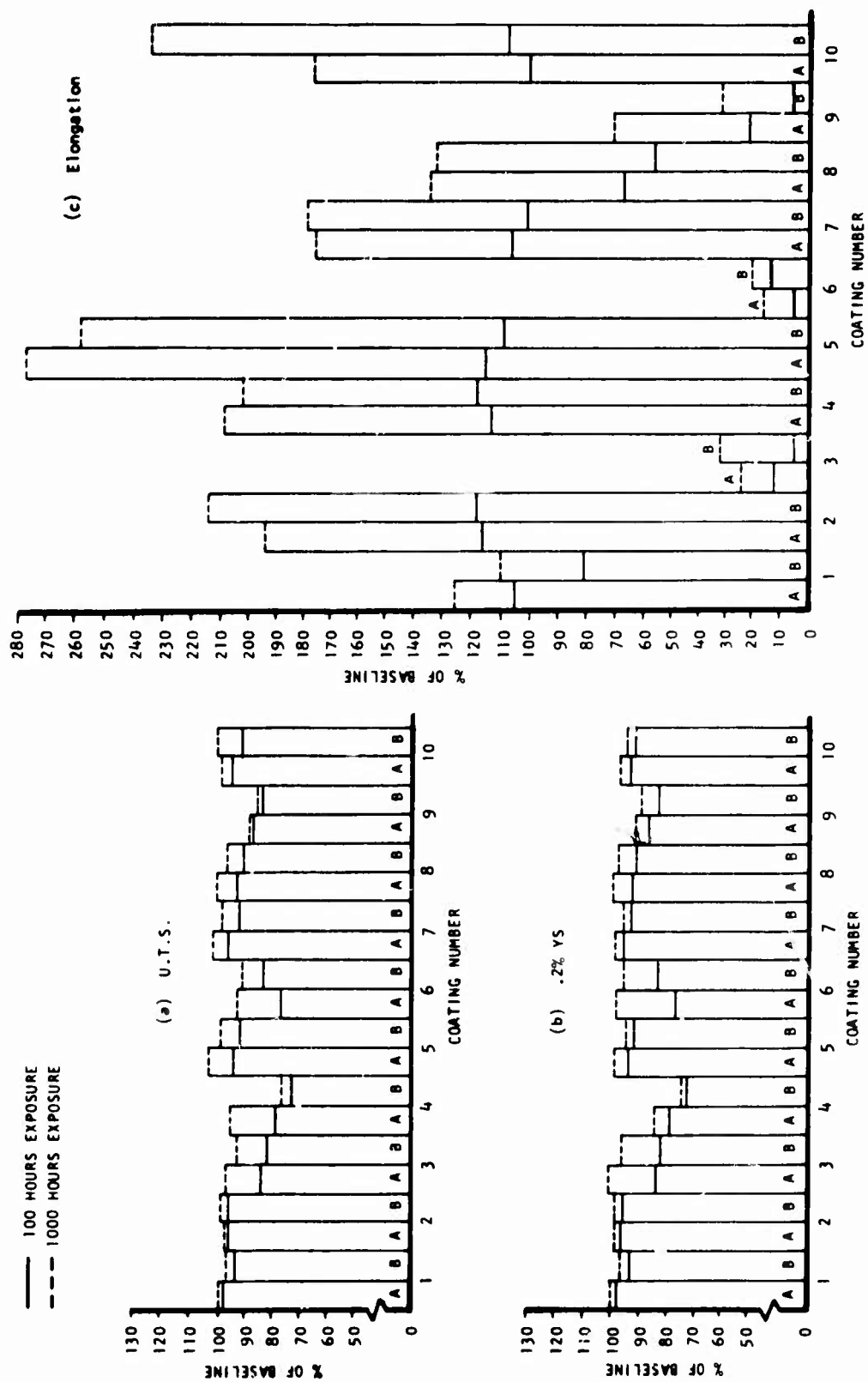
Figure 5. Tensile Properties of Coated Ti-6-2-4-2 After Exposure at 922 K (1200°F) Compared to Uncoated, Exposed, Mill Annealed Ti-6-2-4-2
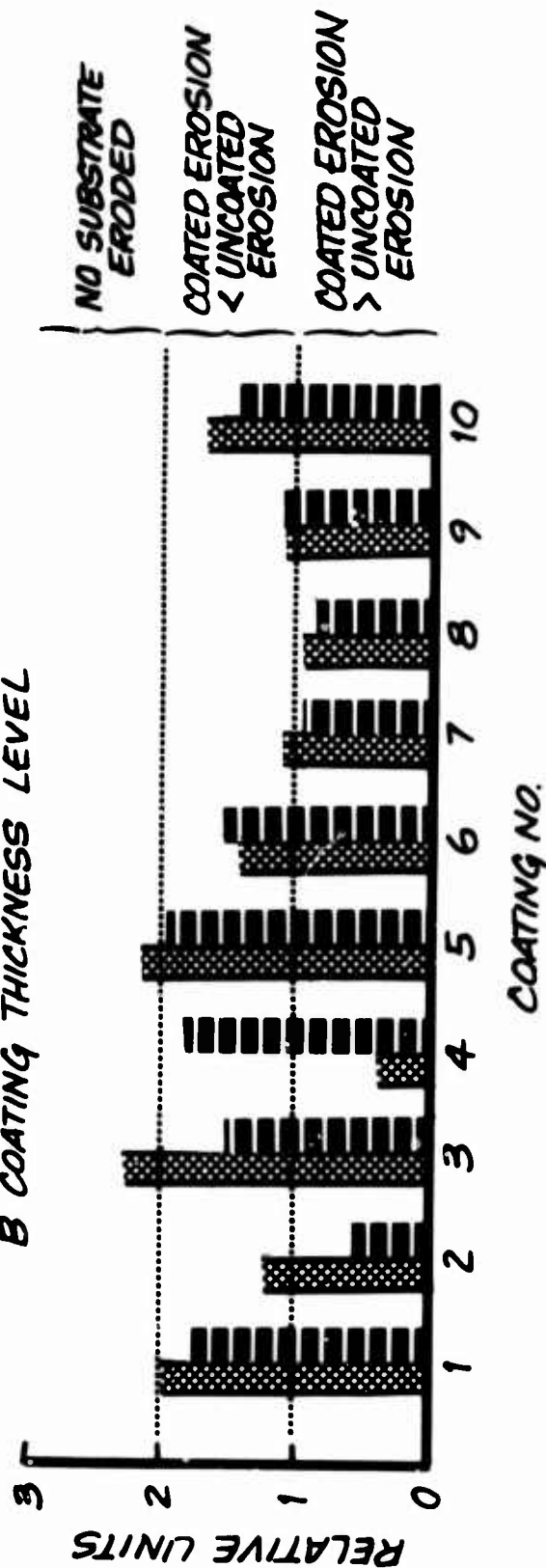
Figure 6. Results of Erosion Tests on Coated Ti-6-2-4-2 Sheet

456
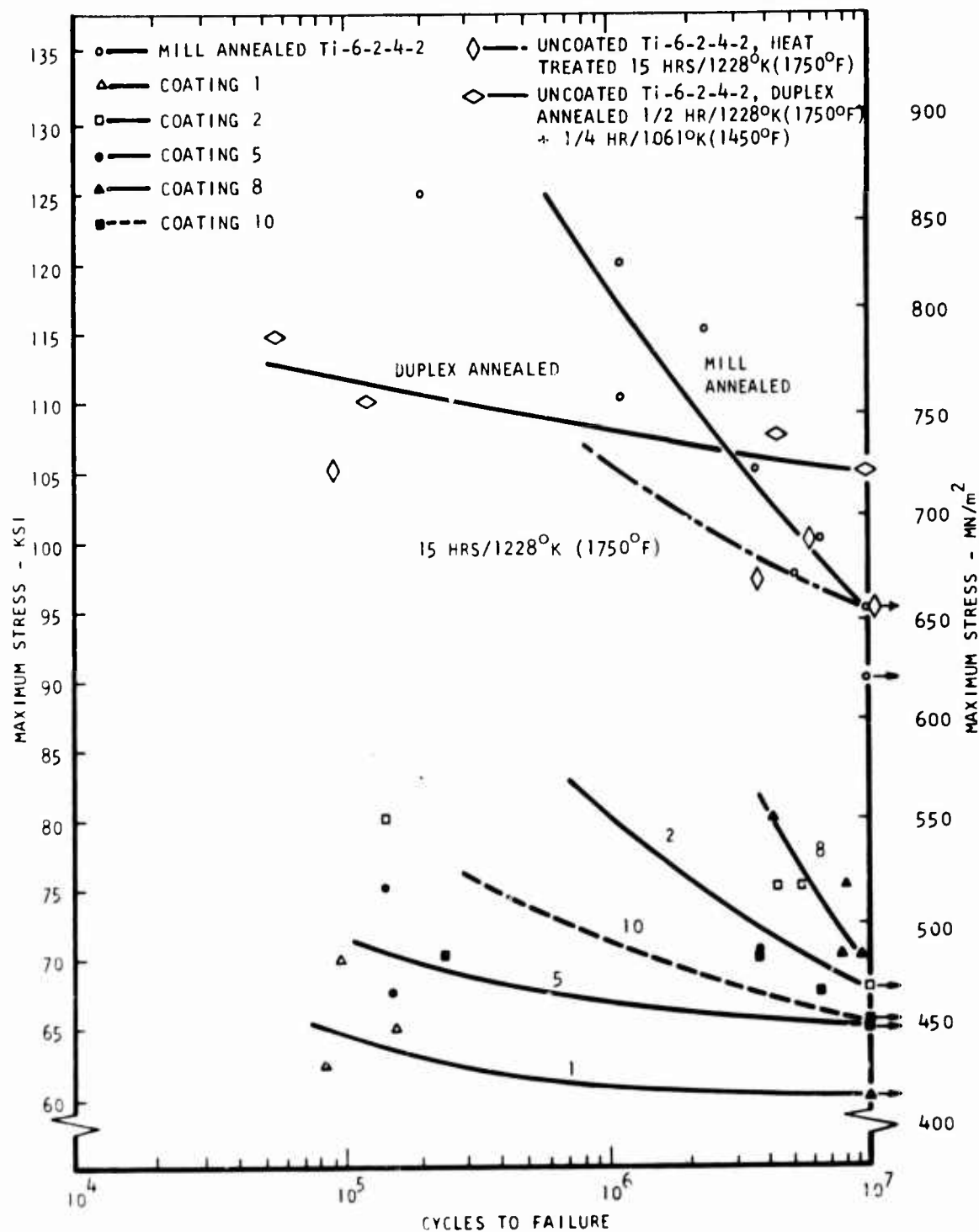
Figure 7.   Fatigue Properties of Coated and Uncoated Ti-6-2-4-2

457
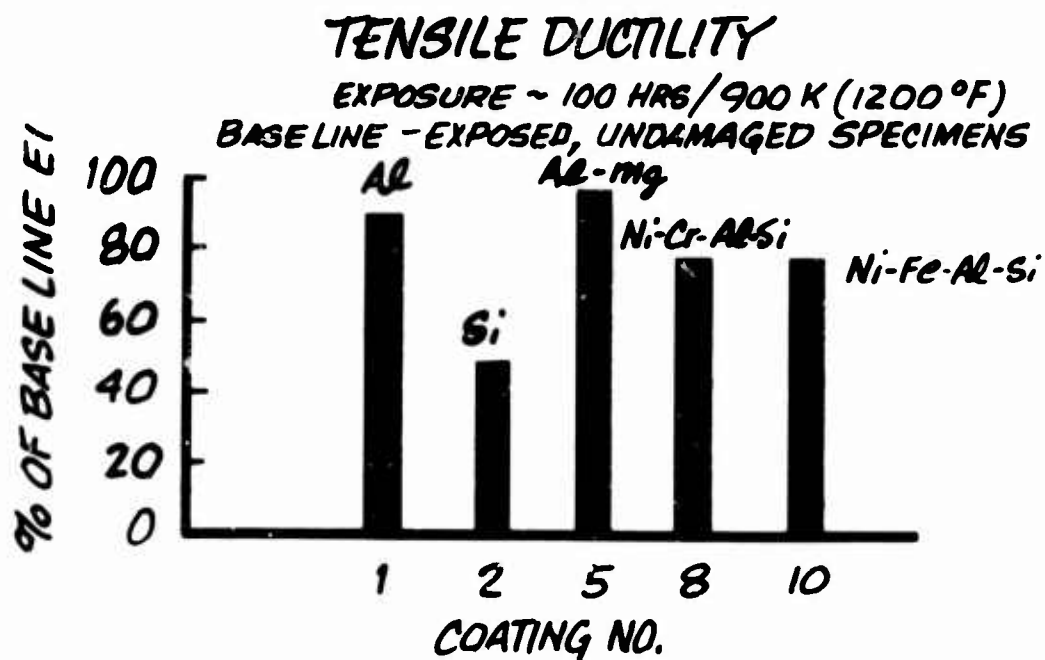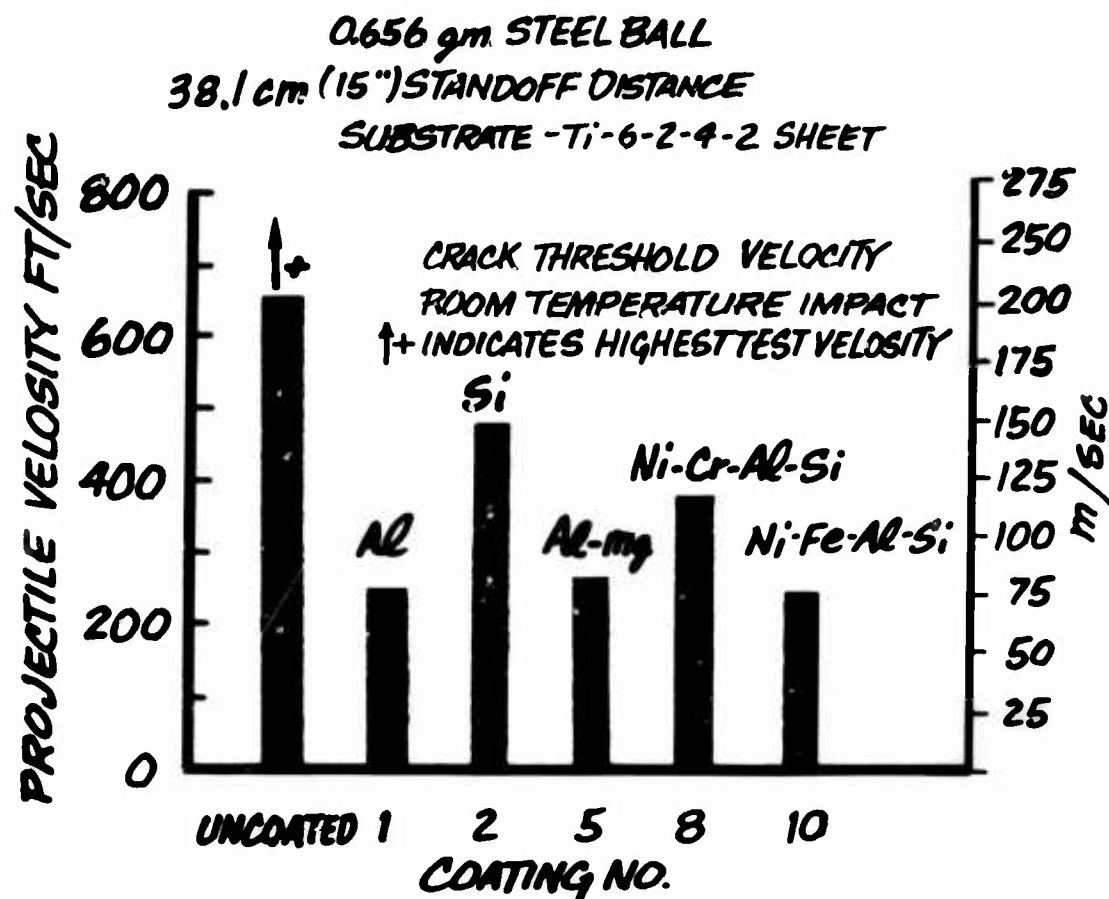
Figure 8. Results of Ballistic Impact Tests
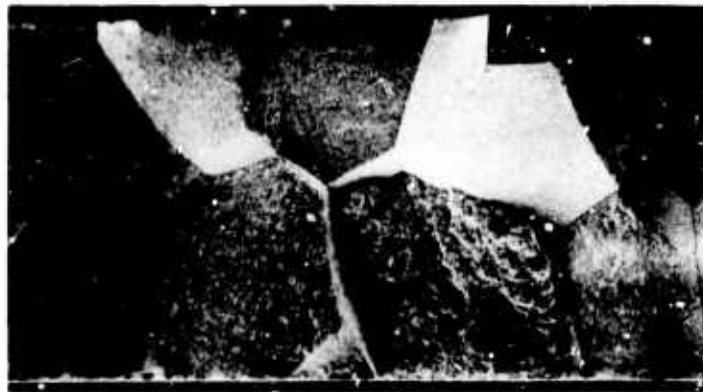
(a) Specimen 2B - Coating Cycle 15 Hr/1228 K (1750°F)

(b) Specimen 1B - Coating Cycle 12 Hr/1200 K (1700°F)
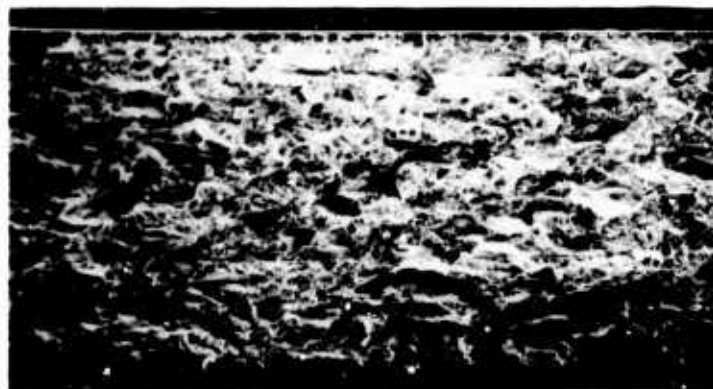
300 μm

(c) Uncoated Tensile Specimen

Figure 9. Scanning Electron Microscope Fractographs of Failures in
Exposed (1000 Hr/922 K (1200°F)) Tensile Specimens

459

Figure 10. Hot-Salt Stress-Corrosion Tests on Ti-6-2-4-2 Sheet

SPECIMEN — TUBULAR TENSILE, ID & OD COATED

EXPOSURE — 0.2 mg/cm² NaCl on OD
100 HR/755 K (900°F) CREEP EXPOSURE

TESTING — POST EXPOSURE TENSILE TESTS
0.125 mm/min (0.005 IN/MIN) CROSS HEAD SPEED

HSSC CRITERIA

CRACK THRESHOLD - HEAT TINT CRACKS AT 30 X
EMBRITTLEMENT THRESHOLD

UNCOATED - < 15.5 % EL, < 25 % APPARENT R.A
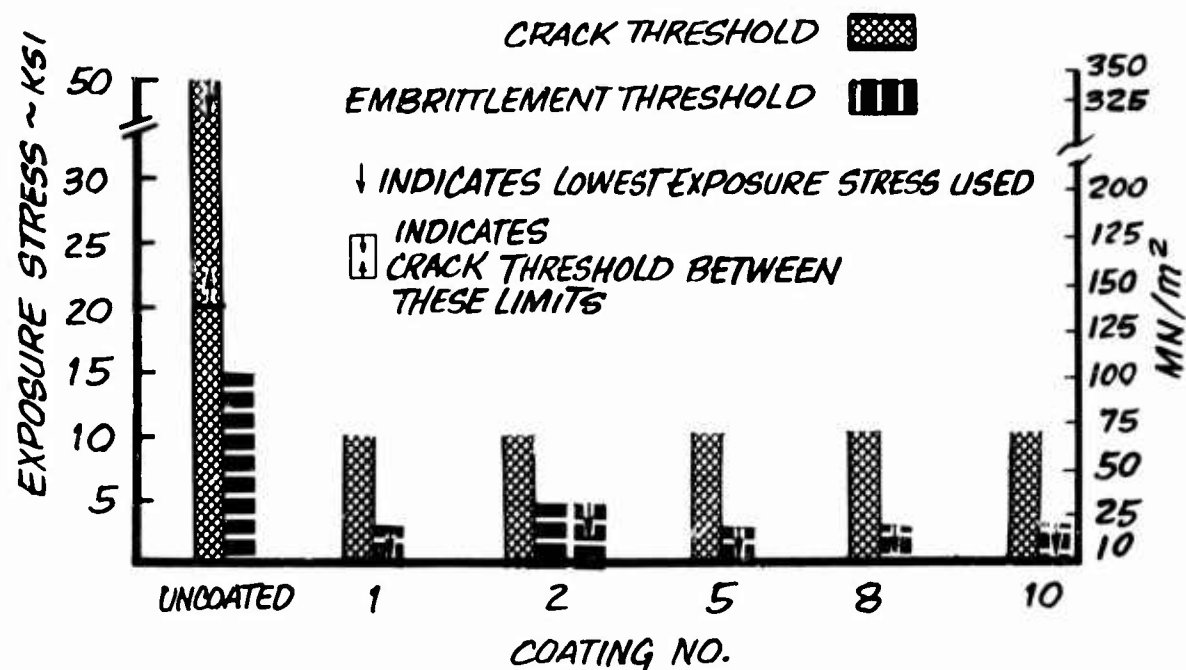COATED - < 4 % EL, < 6 % APPARENT R.A.

Figure 11.   Hot-Salt Stress-Corrosion Tests on Ti-6-2-4-2 Bar Stock

461

CORROSION RESISTANT ANODIC COATINGS FOR TITANIUM

B. A. Manty, J. P. Winfree, S. Bonifazi
Florida Research and Development Center
Pratt & Whitney Aircraft Division
United Aircraft Corporation
West Palm Beach, Florida

ABSTRACT

Extensive efforts have been undertaken with varying degrees of success, to employ both conventional and sophisticated coating systems to titanium alloys. As a class, anodically formed oxide coatings have shown promise in solving both wear and corrosion problems. This paper discusses the development of an anodically-formed coating designed specifically to provide a barrier layer to counteract the severe galling that occurs in bearings when titanium is subjected to medium-to-high intensity rubbing or sliding forces. The coating procedure is described and discussed in some detail including electrolyte compositions and operating conditions. When used in conjunction with a dry film lubricant, the coating serves as a base for lubrication and improves the overall wear life. Other areas of established value include the prevention of both hot salt stress corrosion cracking and galvanic attack of dissimilar metals. All these desirable qualities are provided without reducing either the tensile strength or fatigue properties of the base titanium alloy.

INTRODUCTION

Evolution of the modern gas turbine engine has provided the impetus to use light-weight metals as a substitute for steel. In the continuing effort to reduce weight, and consequently improve aircraft performance, titanium offers especially valuable assistance. The rapid and widespread acceptance of titanium alloys by the aerospace industry has been based on two important factors: strength/weight ratio and corrosion resistance. This acceptance has occurred in spite of shortcomings which, in turn, are responsible for restricting fuller use. The tendency of titanium to gall and seize when used in medium-to-high bearing loads and its susceptibility to stress corrosion cracking have been formidable obstacles. These shortcomings of titanium and its tendency to induce galvanic corrosion of other metals have restricted the full use of its alloys. Pratt & Whitney Aircraft (P&WA) developed a process that ameliorates the aforementioned shortcomings without affecting mechanical properties.

TITANIUM ANODIZING METHODS

General

Anodic coatings have been widely used in the field of reactive metal finishing for some time and are easily applied to titanium and its alloys. In contrast to metals such as aluminum and magnesium where the oxides have a demonstrated value for improving wear resistance and providing corrosion protection, oxides on titanium usually manifest themselves as thin (100-10,000 angstrom) interference-colored films. The coloration results from interference due to light refraction/reflection within the surface oxide and is, therefore, directly proportional to oxide thickness (References 1 and 2).

Anodic oxidation can lead to any of three events on the titanium surface, namely (1) oxygen evolution, (2) metal solution and (3) formation of a metal oxide. Most processes lead to some combination of these three although any one may predominate. Generally, anodic treatment in a halogen-containing electrolyte causes titanium dissolution and oxygen evolution to predominate over the oxide formation. Most other electrolytes, during anodic treatment, form oxides on titanium with little oxygen evolution or metal dissolution.

Since titanium can be anodized in virtually any electrolyte, an abundance of "exotic", and "special" solutions have been reported and/or patented. The effectiveness of the oxide depends on its physical properties, which are in turn dependent on the electrolyte composition controlling both structure and ionic or "space charge" inclusions in the oxide.

Thicker oxides with desirable engineering properties have also been reported; these usually require a more sophisticated process than do the thinner, colored, decorative layers.

P&WA Process

P&WA's titanium anodize is classified as a hard coating process and is based on earlier work of Covington and Millaway (Reference 3). It uses a neutral electrolyte containing sodium ammonium phosphate and half-wave rectification.

Preparation for processing is considerably simpler than that required for anodic treatment of other alloys such as aluminum. All items should be free of sharp burrs before degreasing in alkali or halogenated hydrocarbon. If the part in process contains residual stresses from welding or forming operations, alkali degreasing is used to minimize the chances of stress corrosion cracking. Heavy scale or oxides are removed by vapor blasting or by pickling in a nitric-hydrofluoric acid solution. The former provides a more uniform surface, especially if there are any welds on the part. Glass bead peening can be used before anodizing and is recommended for low-temperature (less than 600°F) applications where maximum fatigue strength is required. Subsequent anodizing does not remove the beneficial compressive stresses resulting in improved fatigue properties.

Stop-off paints and tapes are used to avoid coating select areas; however, the maskants tend to lift, exposing bare surfaces that are subject to a high current surge. Maskants are, therefore, not recommended; whenever possible, the entire part is coated.

The Anodizing Electrolyte, as mentioned earlier, consists of a neutral sodium ammonium phosphate solution. It is prepared by mixing trisodium phosphate with phosphoric acid and ammonium hydroxide:

	Concentration
Trisodium Phosphate	100 g/l
Phosphoric Acid	50 ml/l
Ammonium Hydroxide	70 ml/l
pH	7.0 - 8.0
Operating Temperature	80°F - 130°F

In this system either lead or carbon can be cathode material. Agitation is necessary to dissipate the heat generated during the process and retain the homogeneity of the solution. Electrolyte temperatures below 80°F are not recommended because they make production of thin uniform oxides difficult; operation at temperatures above 130°F results in softer, more porous oxide coatings. Because the suitable temperature range of operation is wide, cooling methods such as coils or heat exchangers are not necessary.

The Processing Tank may be constructed from a wide variety of materials because the electrolyte is not particularly aggressive. The basic requirement is for a sufficiently reinforced tank of suitable size. At the Florida Research and Development Center (FRDC), a Poly Vinyl Chloride (PVC) tank has been used for over three years with satisfactory results.

Processing of parts can be done as summarized on Figure 1. After placing the prepared part into the electrolyte and making electrical connections, the voltage is raised to a predetermined point using a half-wave rectifier similar to that shown in Figure 2. As the voltage is increased, the oxide increases in thickness producing a series of interference colors until a voltage is reached where surface sparking begins. A few volts above this point will produce the desired thickness. The sparking (or surface burning) will continue throughout the coating process and cease only after the titanium is uniformly coated with oxide. The rate at which the voltage is increased is limited only by the current restrictions of the rectifier. The parts are then removed, rinsed, and air dried. When a subsequent treatment - such as a dry film lubricant application - is performed, the surfaces should not be handled before application of the lubricant.

Figure 2 illustrates the approximate shape of potential vs time plots for the rectifier output at various locations along its circuit. During anodizing, the insulating oxide forming on the titanium acts like a capacitor and therefore the waveform approaches that of full wave rectified current. When the DC voltage is measured (V_2), the apparent voltage increases with time because the meter is measuring RMS voltage, which for the same peak voltage becomes greater as full wave rectification is approached. Voltage used for thickness control should therefore be measured with the AC voltmeter (V).

To determine the voltage desired for processing parts, a series of specimens are run at various voltages, and either thickness or weight gain measurements are made. Figure 3 illustrates a typical voltage-vs-thickness and voltage-vs-weight gain plot obtained with this anodizing process. This type of plot should be repeated at regular intervals since electrolyte composition variations change the results.
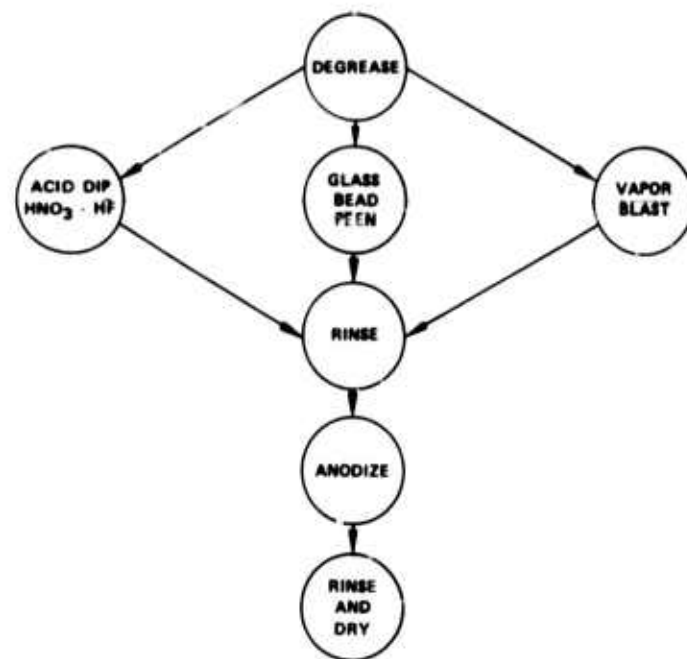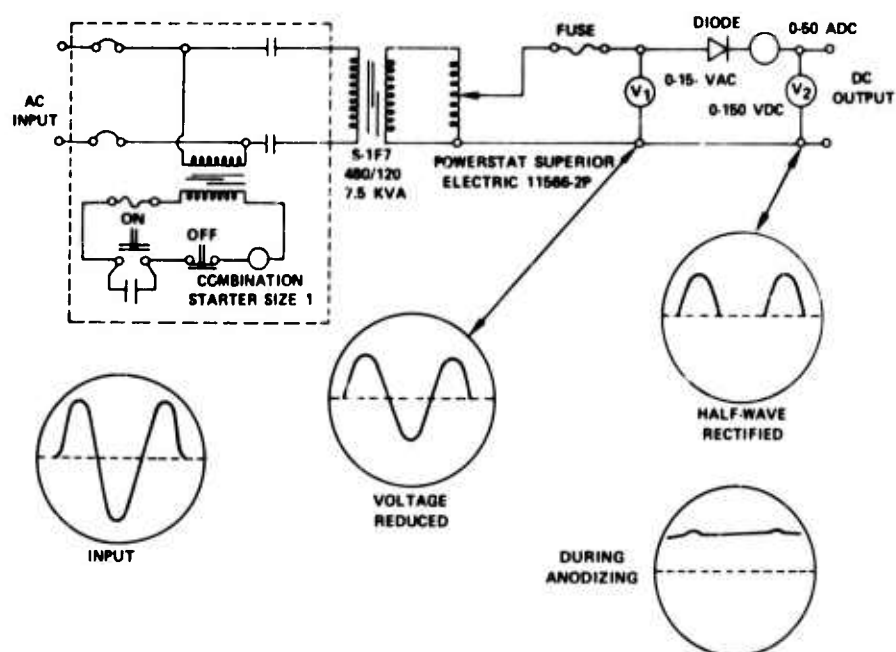
Figure 1. P&WA Anodizing Process
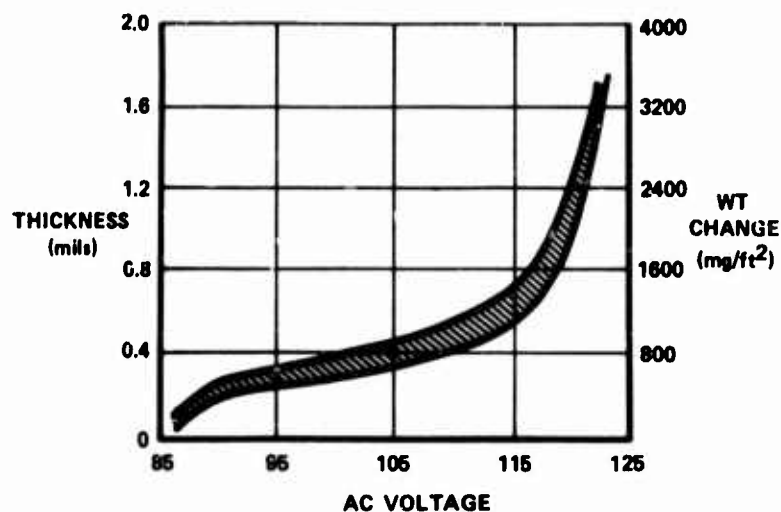

Figure 2. Anodizing Rectifier

466

Figure 3. Effect of Anodizing Voltage on Oxide Thickness
and Weight Gain

Since the "throwing power" of the solution is high, the most complicated part
configurations, including blind holes and ID tubing walls, can be anodized. The main
reason for uniformity in areas remote from the cathode is the insulating nature of the
coating formed together with the high conductivity of the anodizing solution. As the
coating builds up in one area, resistance increases so current is directed to another area
with a thinner oxide. It is therefore impossible to treat a part too long. At the preselected
voltage, anodizing continues only until the coating is complete and then the current ceases.

With continued use, the solution becomes bluish-violet in color; this is attributed to
the formation of $[Ti (H_2O)_6]^{+3}$ ions in solution. This color will not interfere with the
anodizing process; however, a sludge of titanium oxide, which forms in the solution,
should be periodically removed to ensure continued uniform coating.

OXIDE COMPOSITION AND CHARACTERISTICS

Composition

Analyses of these coatings show a high concentration of occluded phosphate. X-ray
fluorescence and chemical analysis show a phosphorous content of 25 percent expressed
as Ti PO_4 (which is probably not the only form present). Infrared analysis has confirmed
the presence of phosphate ions; X-ray diffraction indicates amorphous oxides.

Surface Finish

Final finishes depend on both the original surface finish and the thickness of the oxide
produced. For most applications, a thickness of 0.0002 in. - 0.0003 in. is recommended
and results in a surface finish of 15-30AA (microinches) on surfaces with a 30AA or less
starting finish. Rougher surfaces remain virtually unchanged after anodizing. Thicker
oxides result in a slightly rougher surface (Table 1). Generally, the surfaces take on a
mat appearance with a color of either brown (similar to a cardboard box) for alloys such
as Ti-6Al-4V or gray for alloys such as Ti-8Al-1Mo-1V. Compositional variations causing
the color differences have not been determined, but with experience it is possible to
identify some alloys by the colors produced by anodizing.

Table 1. Effect of Anodizing on Surface Finish (AMS 4928)

Surface Preparation	500 mg/in² Weight Gain**		800 mg/in² Weight Gain**	
	Before	After	Before	After
6 micron Al₂O₃ polish	4AA*	25–30AA	6AA	45AA
Grind on 600 grit paper	7AA	15–20AA	17AA	50AA
Grind on 400 grit paper			18AA	55AA
Grind on 240 grit paper	10AA	20–25AA	15AA	55AA
Grind on 120 grit paper	14AA	15–20AA	27AA	50AA
As machined			40AA	60AA
Vapor blast	16AA	20–30AA		
Grit blast	70AA	55–65AA		

NOTE: *Surface finishes reported as arithmetic average, microinches.

**Refers to weight gain caused by anodizing
500 mg/in² = 0.00025 in.
800 mg/in² = 0.0004 in.

EFFECT OF ANODIZE ON WEAR BEHAVIOR

When titanium is exposed to air it very rapidly becomes coated with a tenacious oxide coating that, with repeated exposures, recurs almost instantaneously. This oxide interferes with many coating processes by presenting a barrier to an intimate bond. It is therefore easier to produce a significant coating by modifying the oxide (by anodizing) than it is to apply overlays or other (i.e., metallic) coatings. This anodize was advanced by both chemical and electrical process development for specific P&WA gas turbine engines. The anodize provides a barrier layer that reduces or eliminates the severe galling that occurs when titanium is subject to rubbing or sliding forces. Moreover, since dry film lubricants containing molybdenum disulfide have been successfully used in many applications, the anodize was developed to provide a good base to augment this type of lubrication.

Pin-on-Disk Wear Test

A pin-on-disk test, similar to that described in ASTM D2716-68T, was used to evaluate the wear life of lubricated titanium with and without anodizing. The wear disk is rotated at some selected velocity while a pin rides on the disk subject to a load (Fn) as shown in Figure 4. Tangential forces are measured using strain gages, and coefficients of friction (tangential load/normal load) are continuously monitored with high and low values recorded during the test until a sharp increase in coefficient occurs (indicating coating failure).

Results of these tests demonstrate that anodizing before lubricating increases the wear life more than 40 percent. Coefficients of friction varied from 0.05-0.15 in systems with molybdenum disulfide type dry film lubricants over the anodic coating. Tests conducted from 80°F-900°F all indicated anodizing improved the wear life.
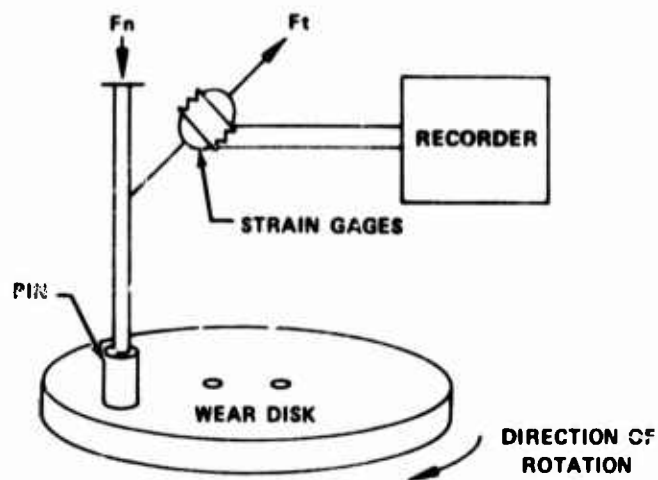
Figure 4.   Pin-on-Disk Wear Test

Other tests conducted at FRDC with threaded connectors demonstrate both the oxide's ability to prevent galling when used alone and its suitability as a base for dry film lubrication.

EFFECT OF ANODIZE ON CORROSION SUSCEPTIBILITY

The overall corrosion resistance of titanium alloys led to their wide use in environments hostile enough to destroy many others in a short time. Its natural resistance to corrosion is attributed to the tenacious oxide, which forms over the surface and protects the metal from further attack. There are, however, two forms of corrosion that gas turbine manufacturers have as a common problem; these forms restrict some aerospace applications.

Among the limitations is hot salt stress corrosion cracking (HSSCC), which was first observed during creep testing of titanium alloys (Reference 4) and extensively dealt with in the past (References 5, 6, 7). Generally, titanium alloys are susceptible to HSSCC at temperatures above 500°F.

The P&WA anodize has been evaluated in HSSCC on numerous commercial alloys by both conventional salted stress rupture and bent beam (with stresses calculated using the method of Haaijer and Loginow, Reference 8) and has been demonstrated to provide a significant improvement in the resistance to cracking (Figure 5) of both Ti-8-1-1 and Ti-6-4. Limited data show that significant improvements can be expected in the stress corrosion resistance of many alloys through this anodizing.

Titanium-induced galvanic corrosion of dissimilar metals is likewise an area of concern. Substantial increases are experienced in the corrosion rates of dissimilar metals, such as aluminum or low alloy steels coupled to titanium alloys (References 9, 10). It was therefore intended to develop the anodizing process to produce a nonconductive oxide barrier. In this way, galvanic currents are reduced as is the accelerated attack. Figure 6 shows the effect of P&WA's anodize on the galvanic attack of a sulfuric acid anodized aluminum C355 block with Ti-6Al-4V connectors threaded into it after salt spray testing per ASTM B117. The massive aluminum oxide production occurring at the Ti/Al interface was eliminated by anodizing the titanium.

In summary, this anodize improves titanium's HSSCC resistance and controls galvanic attack of less noble metals coupled to titanium in a corrosive environment.
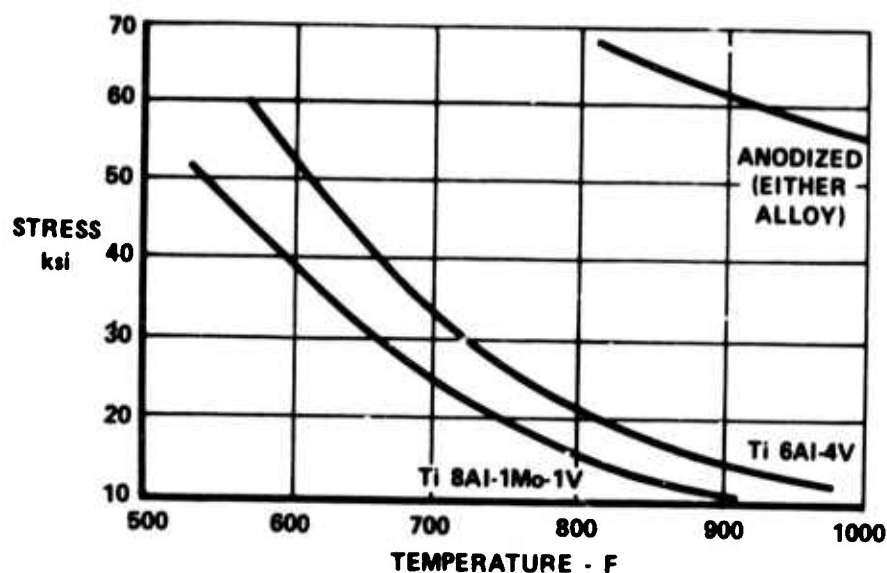

Figure 5. Threshold Stress for Salted Ti-8Al-1Mo-1V and Ti-6Al-4V as Affected by Anodizing
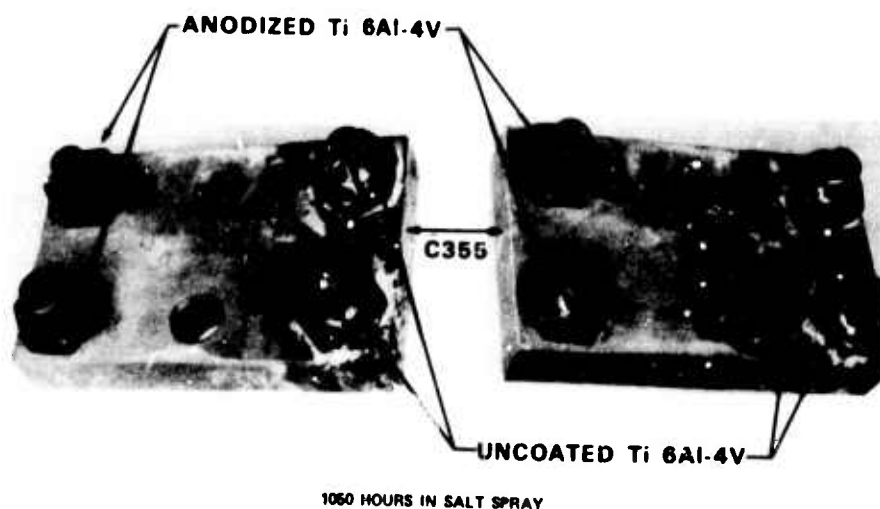

Figure 6. Titanium Induced Galvanic Corrosion of Aluminum

EFFECT OF ANODIZE ON MECHANICAL PROPERTIES

For many applications of coated titanium alloys, it is important that the coating not compromise mechanical properties. Generally, anything applied to the surface will reduce the strength of titanium. One of the development objectives for this anodic coating system was minimal effects on important engineering properties including tensile and fatigue strengths.

Hydrogen Embrittlement

Whenever dealing with electrochemical processing of titanium alloys, the possibility of hydrogen absorption and resultant embrittlement must be considered. In an anodic process, with current "on", the workpiece is protected against hydrogen discharge at the cathode. Further, at an efficiency of less than 100%, oxygen is evolved at the workpiece, providing additional assurance that hydrogen will not cause a problem.

Although hydrogen adsorption/absorption is unlikely during anodizing, some caution is appropriate regarding possible hydrogen entry during preanodizing operations. For example, pickling with nitric-hydrofluoric acid mixtures requires careful control of the acid ratios, otherwise substantial hydrogen pick-up will likely occur (Reference 11). Another source of hydrogen in some anodizing processes is related to the pH of the anodizing electrolyte. When workpieces are in contact with acid electrolytes, without current applied, there is a possibility of hydrogen absorption. With the neutral electrolyte process described in this paper, prolonged immersion, with or without current, will not result in hydrogen pickup.

Therefore, when working with hydrogen-sensitive materials such as titanium, safeguards are required to prevent embrittlement. P&WA's anodizing process provides these safeguards.

Tensile Strength

The effect of anodizing on tensile strength and ductility was investigated using standard tensile specimens. Agreement was good between the yield and ultimate strengths and the ductility for anodized and uncoated specimens. Table 2 summarizes tests conducted at room temperature.

Tests using other titanium alloys and temperatures up to 600°F gave results comparable to those above; i.e., no effect of anodizing on tensile properties.

High Cycle Fatigue

Krouse rotating beam specimens fabricated from Ti-8Al-1Mo-1V were used to determine the effects of anodizing on the high cycle fatigue (HCF) strength. The fatigue limits were determined by loading to a point of alternating stress at which the life exceeded 1.0×10^7 cycles. Anodizing did not reduce the fatigue properties at the elevated temperatures (600°F or 900°F, as shown on Figure 7); however, at room temperature a 5% reduction in strength occurred. Other alloys in both bar and sheet form behave similarly.

Table 2. Tensile Properties of Anodized AMS 4916

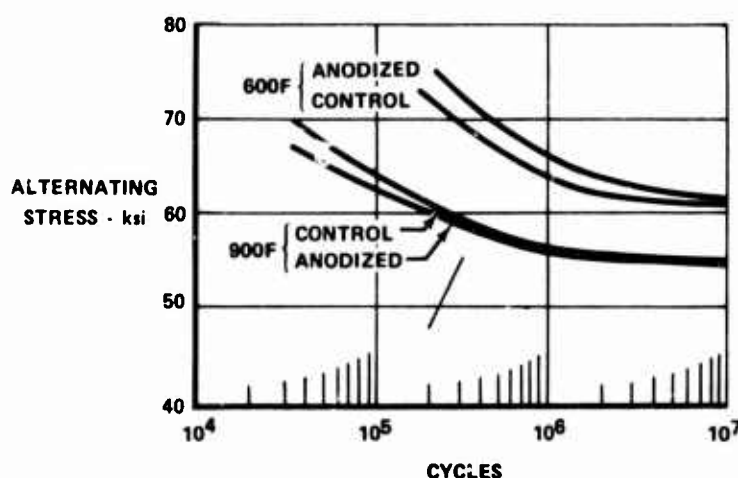| Processing	Tensile Yield psi x 10^3	Tensile Ultimate psi x 10^3	Elongation, Percent
Control 1	133.0	141.0	11.4
Control 2	134.5	144.5	13.0
Control 3	133.8	143.2	12.2
Anodize 4	133.7	143.0	12.0
Anodize 5	135.6	146.0	13.3
Anodize 6	131.1	141.9	13.3

Figure 7. Elevated Temperature High Cycle   FD 82922
Fatigue Strength of Ti-8Al-1Mo-1V

A second HCF test utilizing a constant-stress specimen (Figure 8) in a plate fatigue machine was used to assess effects of anodizing on fatigue properties. The specimens were coated on one side only and tested in reverse bending at 600°F and a vibratory stress of ·65 ksi. There was no significant difference in the cycles to failure of one-side-coated and uncoated specimens. Further, the failures in four of the ten anodized specimens originated on the coated side while six originated on the uncoated side. No failures originated at the specimens' edge (see Table 3).

It must be concluded that anodizing should not have a significant effect on HCF properties. This characteristic enables the use of anodizing in fatigue limited areas where other coatings are not practical. Moreover, HCF testing forms an integral, and important index of conformance to P&WA's anodizing specification.
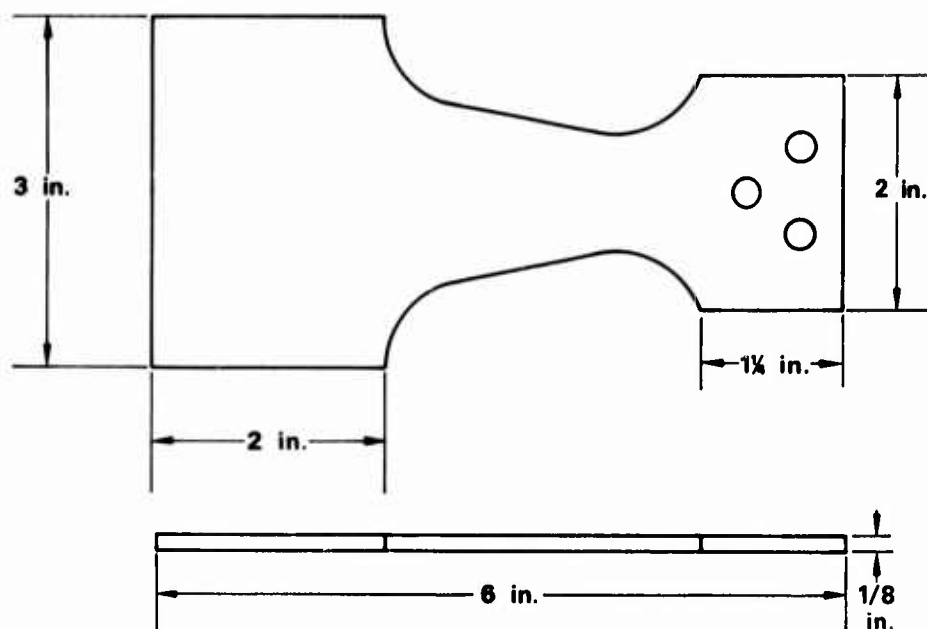
Figure 8. Constant Stress High Cycle Fatigue Specimen   FD 82920

Table 3. Reverse Bending Fatigue Results of Ti-8Al-1Mo-1V
Constant Force Plate Specimens Tested at 600°F With
a Vibratory Stress of ± 65.0 ksi

Specimen Description	Test Orientation	Cycles to Failure	Failure Origin
Uncoated	--	1.3×10^5	Side
Uncoated	--	1.02×10^5	Side
Uncoated	--	1.08×10^5	
Anodized, one side	Coated side up	7.2×10^4	Uncoated side
Anodized, one side	Coated side up	9.35×10^4	Uncoated side
Anodized, one side	Coated side up	1.08×10^5	Coated side
Anodized, one side	Coated side up	1.01×10^5	Coated side
Anodized, one side	Coated side up	5.94×10^4	Uncoated side
Anodized, one side	Coated side down	8.47×10^4	Uncoated side
Anodized, one side	Coated side down	1.13×10^5	Coated side
Anodized, one side	Coated side down	1.5×10^5	Uncoated side
Anodized, one side	Coated side down	8.1×10^4	Coated side
Anodized, one side	Coated side down	1.1×10^5	Uncoated side

473

Low Cycle Fatigue

Cyclic tension-compression tests at 600°F and approximately 3 cpm were conducted on conventional specimens fabricated from Ti-6Al-2Sn-4Zr-6Mo.

The specimens were tested as-machined, after shot-peening, and after anodizing (on both as-machined and shot-peened surfaces). Shot-peening tended to increase the LCF strength of either as-machined or anodized specimens. The increased life is attributed to compressive stresses induced in the surface to a depth which must be significantly greater than the metal involved in anodizing since specimens anodized after peening still demonstrated the improved properties attributed to the compressive stresses. At high alternating stresses, above 120 ksi, anodizing alone (without peening) appeared to reduce the fatigue life, while at stresses below 120 ksi, anodizing alone actually increased the life. These results are summarized in Figure 9.
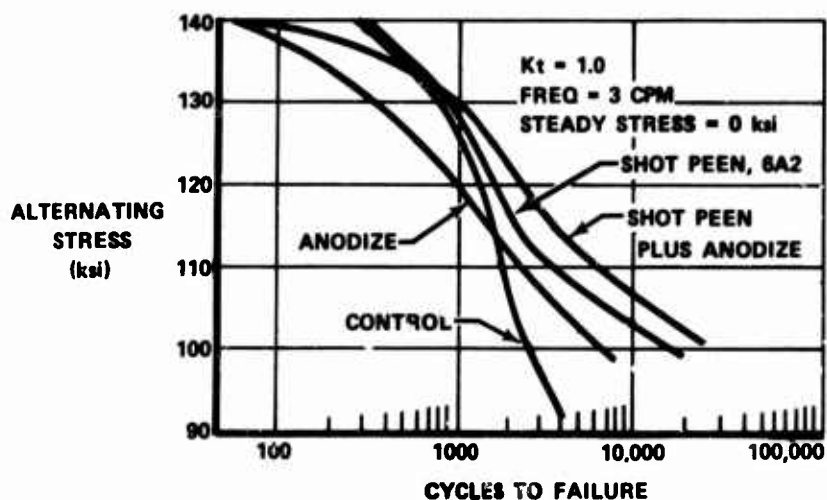
Figure 9. Effects of Anodize and Peening on Low Cycle   FD 82921
Fatigue Properties of Ti-6Al-2Sn-4Zr-6Mo at 600°F

SUMMARY

Anodically controlled oxidation of titanium is used to overcome some of the more important limitations to its use in gas turbine engine environments. Problems in wear and corrosion are significantly ameliorated without adversely affecting mechanical properties; thus anodically controlled oxidation extends the use of titanium alloys to more fully exploit their favorable strength/weight ratios.

The coatings produced do however have definite limitations. They offer no structural strength and may not properly be used to build up the thicknesses of a worn or undersize part. Attempts to build up the thickness to 0.010 in., although these thicknesses are easily achieved, incur significant porosity and nonuniformity. Likewise, erosion resistance of state-of-the-art anodic coatings is poor; they are of little value for gas path components. Since many such parts could use the type of protection supplied by this type coating, further work is in order to improve erosion resistance.

Although high temperature stability of the coating has not been seriously investigated above 900°F, it is suspected that recrystallization of the original amorphous oxide, which occurs above 1000°F, would drastically reduce its protective qualities.

It has now been demonstrated, outside the laboratory, that the coating improves the operational wear life of titanium parts. This coating appears on over 200 different components in P&WA advanced engines. On fasteners, it prevents galling wear both with and without dry film lubrication. Vanes that were previously damaged during force fit assembly are now coated, eliminating that problem. A further application adopted by another aerospace company is the coating's use on a titanium alloy nose gear for an advanced aircraft.

In other applications, the coating offers protection from galvanic corrosion and hot salt stress corrosion. Titanium plumbing connecting with aluminum alloy gearboxes are anodized to reduce galvanic attack of the aluminum. Two years service experience attests to the effectiveness of this preventative measure.

The P&WA anodic hardcoating of titanium represents a further extension of the technology of titanium alloy surface treatment. Properly employed, it permits reliable application of titanium alloys in environments that previously were considered too severe.

REFERENCES

1. A. Vasicek, Optics of Thin Films, North-Holland, Amsterdam (1960).

2. M.F. Sibert, J. Electrochem. Soc. 110, 65 (1963).

3. L. C. Covington, E. E. Milloway, Titanium Metals Corporation of American Project 47-72, September 1958.

4. F. A. Crossley, et. al, "The Determination of the Effects of Elevated Temperatures on the Stress Corrosion Behavior of Structural Materials", WADD Technical Report 60-191, May, 1960.

5. R. Newcomber, et. al, "Elevated Temperature Stress Corrosion Resistance of Titanium Alloys", Corrosion Vol. 21, No. 10, October 1965.

6. H. R. Gray, J. R. Johnston, "Hot Salt Stress-Corrosion of a Titanium Alloy under a Simulated Turbine Engine Compressor Environment", NASA TND-5510, October 1969.

7. E. L. Kochka and V. C. Petersen, "The Salt Corrosion of Titanium Alloys at Elevated Temperature". Contract NOAS 60-6004-C, January 1961.

8. G. Haaljer and A. W. Loginow, "Stress Analysis of Bent-Beam Stress Corrosion Specimen", Corrosion 21, 4, April 1965.

9. B. Manty, J. P. Winfree, S. Bonifazi, "Corrosion Susceptibility Testing of F100/F401 Gas Turbine Engine", Gas Turbine Materials in Marine Environments Conference, July 1974.

10. N. G. Feige, R. L. Kane, 'Service Experienced with Titanium Structures in Marine Service", NACE 26th Annual Conference, March 1970.

11. PFA Bijlmer, "Pickling Titanium in Hydrofluoric-Nitric Acid", Metal Finishing, November 1970.

STRESS CORROSION CRACKING OF URANIUM ALLOYS

W. Czyrklis and M. Levy*

ABSTRACT

The stress corrosion cracking behavior of U-3/4% Ti, and AMMRC uranium alloys 3/4% Quad, 1% Quad and 1% Quint have been studied utilizing a linear elastic fracture mechanics approach. The threshold stress intensities for stress corrosion crack propagation for these alloys have been determined in distilled H_2O and NaCl solutions containing 50 ppm Cl^- and 21,000 ppm Cl^-. All of the alloys studied may be classified as very susceptible to SCC in aqueous solutions since they exhibit SCC in distilled H_2O (<1 ppm Cl^-) and have low K_{Iscc} values in NaCl solutions. Crack extension in all of the alloys in all environments was transgranular and failure occurred by brittle quasi-cleavage fracture in NaCl solution.

*Army Materials & Mechanics Research Center, Watertown, MA   02172.

STRESS CORROSION CRACKING BEHAVIOR OF URANIUM ALLOYS

INTRODUCTION

The superior armor piercing capabilities and ballistic properties of
high density depleted uranium alloys make them prime candidates for artillery
applications involving penetrators and nuclear ammunition. Many of these
alloys, however, are susceptible to stress corrosion cracking (SCC) in a
variety of environments[1-7].

Stress corrosion cracking service failures, in general, result from the
superposition of residual stresses in the system and the applied design
stresses, or frequently from residual stresses alone. Table 1 lists some
of the fabrication processes which leave high residual stresses in an alloy
component. Several of these processes may be applicable to both penetrator
and nuclear shell applications. One example is the XM-673 projectile, where
an important consideration is the resistance of the uranium alloy shell
material to environmentally induced crack-growth in the region of pins
(steel) which are retained by interference fit. A state of residual
tangential tension exists around the pins which in combination with the
effects of an aggressive environment can cause crack propagation during
the period of time between manufacture and firing. Utilizing a linear
elastic fracture mechanics approach, the uranium alloy shell material thres-
hold of resistance to SCC (K_{Iscc}) can be determined.

This study was carried out to determine the critical threshold intensity
for SCC, K_{Iscc}, of several uranium alloys which are candidates for penetrator
and nuclear shell applications. The data reported herein are for alloys
in the as-extruded condition only and will serve as base-line data for
future studies involving the solution treated and aged alloys.

478

EXPERIMENTAL PROCEDURE

Materials

The uranium alloys studied include the 3/4% Ti, 3/4% Quad, 1% Quad, and the 1% Quint compositions. These alloys were in the as-extruded condition and their chemical analyses and mechanical properties are listed in Tables 2 and 3, respectively. It should be noted that the 1% Quint alloy had the highest strength while the 3/4 Quad alloy had the highest elongation and reduction in area (ductility). The 3/4% Ti alloy had the lowest strength and had relatively low ductility.

Microstructures of the alloys are shown in Figure 1 (a, b, c, d). The 3/4 Ti alloy (a) contains some martensite which is due to the high M_s temperature, even though it is air cooled from a high extrusion temperature. Although the alloy is primarily alpha uranium, some beta uranium (identified by x-ray diffraction) is present because of slow cooling through the two-phase region. The black specks are probably U_2Ti intermetallic. The structure for the 3/4% Quad alloy (b) is primarily alpha and shows large recrystallized grains which probably were prior gamma grains. A second light etching phase is present at the grain boundaries. Another phase appears to be finely distributed throughout the grains and inclusions of varying shape are also present. The microstructure of the 1% Quad alloy (c) is similar to that of the 3/4% Quad alloy but also shows evidence of banding. The 1% Quint alloy structure (d) is again primarily alpha uranium and shows late recrystallized equiaxed grains. A second dark etching phase appears to outline some of the grains in the direction of banding. Another phase or precipitate is distributed throughout the grains and both inclusions and larger scale inhomogeneities are evident.

The environments used were distilled H_2O (contained <1 ppm Cl^-) and 3.5% NaCl solution (>21,000 ppm Cl^-). A limited number of SCC tests were carried out in solutions containing 50 ppm Cl^- in order to determine the effect of Cl^- concentration. Reagent grade chemicals and distilled H_2O were used to prepare the solutions.

Specimens and Test Procedure

The stress corrosion specimens (see Figure 2) which were single-edge notch specimens (6.0" x 0.35" x 0.35") were fabricated from 5/8" diameter extrusions and are designated LR, that is, the specimens were cut with the long dimension parallel to the direction of maximum grain flow and notched so that crack growth and fracture will occur in the radial direction.

The test uses a precracked bar stressed as a cantilever beam. A sharp notch is machined across the rectangular bar specimen at mid-length, and is sharpened by fatiguing. The specimen is held in a rack horizontally (as shown in Figure 3) with the precracked central portion surrounded by a plastic bottle which contains the environment. One end of the specimen is clamped to the mast of the rack and the other end to an arm from which weights are suspended. On evaluating the alloy, the specimen is first stressed in air at increasing loads until it fractures. The data are reduced to stress intensity using the Kies equation (shown in Figure 2). Having established the stress intensity for "dry" conditions, K_{Ic}, a specimen is similarly tested in distilled H_2O and NaCl solutions at a somewhat lower stress intensity. If the specimen did not fail within an hour, the stress intensity was increased by approximately 3% each succeeding hour until failure occurred and the time required for rupture noted. Additional specimens were stressed at lower stress intensities

for 12-24 hours to give a more valid value for K_{Iscc} which was determined from a plot of stress intensity versus time to failure. K_{Iscc} is the threshold stress intensity value for the onset of cracking.

Fractured surfaces were replicated by the plastic carbon technique and examined by electron microscopy. Chromium was used as a replica-shadowing material.

RESULTS AND DISCUSSION

K_{Iscc} Determination

Figure 4 contains plots of critical stress intensity versus time-to-failure for the alloys tested in distilled H_2O (<1 ppm Cl^-). The data show that K_{Iscc} is 40 ksi $\sqrt{in.}$ for the 3/4 Quad alloy, 28 ksi $\sqrt{in.}$ for the 1% Quad alloy, 21 ksi $\sqrt{in.}$ for the 3/4 Ti alloy, and 9 ksi $\sqrt{in.}$ for the 1% Quint alloy. The "dry air" values are 47 ksi $\sqrt{in.}$, 32 ksi $\sqrt{in.}$, 24 ksi $\sqrt{in.}$, and 20 ksi $\sqrt{in.}$ respectively. For the test duration time of 12-24 hours that was employed, the alloys showed relatively little susceptibility to SCC in distilled H_2O, except for the 1% Quint composition which exhibited greater susceptibility. Figure 5 shows similar plots for the alloys in a 3.5% NaCl environment (>21,000 ppm Cl^-). The K_{Iscc} values obtained, i.e., 15 ksi $\sqrt{in.}$ for the 3/4 Ti alloy, 12 ksi $\sqrt{in.}$ for the 3/4 Quad alloy, 7 ksi $\sqrt{in.}$ for the 1% Quad alloy, and 5 ksi $\sqrt{in.}$ for the 1% Quint alloy, indicate that all the alloys are very susceptible to SCC in this environment.

Additional tests were carried out with the 1% Quad and 1% Quint alloys in a NaCl solution containing only 50 ppm Cl^-. Threshold values similar to those found in the 3.5% NaCl environment (>21,000 ppm Cl^-) were obtained (see Figure 6) indicating that the lower chloride concentration did not

significantly affect (reduce) the susceptibility of these two alloys to

SCC in NaCl. Figure 6 also shows that the susceptibility of the 1% Quint

alloy to SCC in a NaCl solution containing 50 ppm Cl^- can be markedly reduced

by adding 0.1M sodium nitrate to the solution. Electrochemical studies

of unstressed specimens have shown that the uranium alloys studied cannot

be anodically passivated in NaCl solutions containing 50 ppm Cl^- or greater

and pitting of the alloys occurs[8]. However, the addition of 0.1M sodium

nitrate shifts the corrosion potential in the more noble direction, stifles

the anodic reaction and prevents pitting at potentials up to +0.6V vs SCE.

The $NaNO_3$ also provides an inhibiting effect in the stress corrosion tests

since the compound reduces the susceptibility of the alloy, that is, it

increases the K_{Iscc} from 5 to 16 ksi $\sqrt{in.}$ which approaches the air value

of 20 ksi $\sqrt{in.}$

A summary of all the results obtained are shown in Table 4 along with

the ASTM recommended minimum thickness requirement. It should be noted

that the specimen geometry for the alloys studied meets all the criteria

for plane-strain conditions according to ASTM Specification E399-72 "Plane-

Strain Fracture Toughness of Metallic Materials" except for the "dry air"

value obtained for the 3/4% Quad alloy.

Fractography

Figures 7 through 10 are high magnification replica fractographs for

each alloy showing the effect of environment on the fracture mode. Figure

7 shows that the predominant mode of failure for the U-3/4 Ti alloy in air,

distilled H_2O and 3.5% NaCl solution is transgranular quasi-cleavage. The

cleavage planes are broken up into small facets with coarse and ill-defined

river markings and the facets are joined by highly distorted regions. The fractograph for the 3/4 Quad alloy, Figure 8, shows that the fracture mode in air is transgranular plastic fracture, normal mode. Note the round and equiaxed dimples. In distilled H_2O there is a dual-structured topography in the slow growth region. Areas of quasi-cleavage and ductile dimple fracture are observed. In the slow growth (SCC) region the predominant failure mode in 3.5% NaCl is quasi-cleavage.

Figure 9 shows that the fracture mode for the 1% Quad alloy in air is mixed quasi-cleavage and dimple rupture. A similarly structured topography was observed in the slow growth region of the alloy in the distilled H_2O environment, while quasi-cleavage was the failure mode in 3.5% NaCl solution. Dimple rupture is the mode for the 1% Quint alloy in air, Figure 10. Note that the dimples are smaller than those observed in the 3/4 Quad alloy indicating that the Quint alloy is less ductile (see RA values in Table 3). In distilled H_2O the fracture consisted of a mixed quasi-cleavage and dimple rupture slow growth mode. The addition of chloride ion (50 ppm and 21,000 ppm) to the distilled H_2O resulted in pure quasi-cleavage fracture while the addition of an inhibitor, $NaNO_3$, to the chloride solution (50 ppm Cl^-) produced the dual mode quasi-cleavage and dimple rupture topography observed in distilled H_2O. A summary of the influence of environment on the fracture behavior of the uranium alloys is contained in Table 5.

Magnani[7] has tested U-0.5% Ti alloy in air and in 50 ppm Cl^- solution and has reported that the K_{Iscc} value in air was 25-30 ksi $\sqrt{in.}$ and 22 ksi $\sqrt{in.}$ in the chloride solution. The alloy was in the metastable condition obtained by quenching from the gamma region. The stress corrosion fracture

mode in both the air and the chloride environment was transgranular. Our
data for the U-3/4% Ti alloy is quite similar although the Ti content is
.20% greater. Magnani[7] observed that the relative susceptibility to
intergranular cracking decreases as the alloy content decreases. It appears
from his work that intergranular cracking is observed when the alloy content
is 4-1/2% or greater while at lower alloy content the transgranular mode
is operative. Our work reported herein supports this observation insofar
as all of the alloys tested had alloy contents less than 4.0% and the
stress corrosion cracking failure mode was transgranular in all cases.

Critical Flaw Depth

In Figure 11, the stress corrosion cracking threshold K_{Iscc} in air and
aqueous environments is plotted as a function of yield strength to give an
analysis of the relative merit of various alloy compositions[9]. The data
in this figure can be related to critical flaw sizes for propagation of a
stress corrosion crack by the Irwin equation, which gives the crack tip
stress intensity for a surface flaw of arbitrary geometry:

$$K^2 = \frac{1.2\pi\sigma^2 a}{Q^2 - 0.212(\frac{\sigma}{\sigma_y})^2} \tag{1}$$

where a is the depth of the crack, σ is the applied stress, σ_y is the yield
stress, and Q is a shape factor for the crack. By assuming a ratio of
applied stress to yield stress, the minimum critical flaw depth to propagate
a stress corrosion crack can be expressed in terms of the materials properties
K_{Iscc} and σ_y. The straight lines representing flaw depths plotted in Figure
11 are based on the assumption of a long thin crack ($Q^2 = 1$), and $\sigma = \sigma_y$,
for which equation (1) becomes:

$$a_{cr} = 0.2 \left(\frac{K_{Iscc}}{\sigma_y} \right)^2 \qquad\qquad (2)$$

The assumption $\sigma/\sigma_y = 1$ represents the most conservative case. In applications where the applied stress derives solely from residual or fit-up stresses, σ/σ_y ratios on the order of 0.25 to 0.50 are probably more realistic. In that case the critical flaw depths shown in Figure 11 would be 20 times and 5 times larger than those computed from equation (2), respectively. The significance of this figure is that if one has a flaw size represented by one of the lines, an alloy whose K_{Iscc} falls above that line should be utilized if SCC is to be avoided.

For the "worst case", ($\sigma = \sigma_y$), the K_{Iscc} data which have been plotted in Figure 11 show that none of the alloys studied can tolerate a flaw as deep as.0.050" in any of the environments if the operative stress equals the yield strength. The critical flaw size for the 3/4 Ti alloy appears to be 0.010" in both air and H_2O. The alloy can tolerate a flaw as deep as 0.001" in 3.5% NaCl solution. The 3/4% Quad alloy can readily tolerate a flaw 0.010" deep in air and in H_2O. In 3.5% NaCl solution the tolerable crack depth is 0.001". Flaws as deep as 0.001" can be tolerated by the 1% Quad alloy in both air and H_2O, but in NaCl solutions, the crack depth tolerance is reduced to 0.0001". The 1% Quint alloy, which is the most susceptible alloy, can tolerate a flaw as deep as 0.0001" in most environmosts. Based on crack depth tolerances the alloys can be listed in the following order of decreasing merit: 3/4 Quad alloy, 3/4 Ti alloy, 1% Quad alloy, and 1% Quint alloy. For a lower ratio of σ/σ_y, the magnitudes of the crack depth tolerances would increase, but the order of merit ranking would remain the same.

CONCLUSIONS

1. In relative terms all the alloys studied may be classified as very susceptible to SCC in aqueous solutions since they exhibit SCC in distilled H_2O and have low K_{Iscc} values in NaCl solution.

2. The alloys can be ranked in the following order of decreasing merit incorporating both the SCC resistance K_{Iscc} and the contribution which yield strength levels can make to SCC failure: 3/4% Quad alloy, 3/4% Ti alloy, 1% Quad alloy, and 1% Quint alloy.

3. Sodium chloride provides an extremely aggressive environment for SCC of uranium alloys, even at a concentration of 50 ppm Cl^-.

4. The SCC resistance of the most susceptible alloy, the 1% Quint, can be significantly improved by adding sodium nitrate to the chloride solution.

5. Fractographic analysis of the stress corroded specimens showed that crack extension in all of the alloys in all environments was transgranular. The 3/4% Ti alloy failed by brittle quasi-cleavage fracture in air, distilled H_2O and NaCl solution. The AMMRC Quad and Quint alloys exhibited fractographic ductile characteristics in air (dimple rupture). The distilled H_2O environment produced a mixed brittle and ductile topography while NaCl solution produced only brittle characteristics in these alloys.

FUTURE WORK

Similar studies will be carried out with these alloys in the solution treated and aged condition. Applied anodic and cathodic potential as well as hydrogen permeation experiments will also be carried out in order to elucidate the SCC mechanism or mechanisms which may be operative.

REFERENCES

1. C.A.W. Peterson, "A Stress Cracking Study of a Gamma Extruded U-8 wt % Mo-0.05 wt % Ti Alloy", UCRL-14132 (1965) April.

2. G.A. Whitlow, "Stress Corrosion of Uranium Alloys", AWRE-0-49/66 (1966) July.

3. N.J. Magnani and H. Romero, "Environmental Cracking of Mulberry", Sandia Corp., SC-TM-69-253, April 1969.

4. N.J. Magnani, "Stress Corrosion Cracking of Uranium Alloys", presented at NACE Spring 1970 Meeting.

5. N.J. Magnani, "Stress Corrosion of Mulberry", Corrosion, 26, 406 (1970).

6. J. Greenspan and R. Fitzpatrick, "Delayed Cracking and Corrosion Resistance of Some Uranium Alloys", AMMRC Interim Report PDD-1, 24 September 1969.

7. N.J. Magnani, "The Effects of the Environment on the Cracking Behavior of Selected Uranium Alloys", presented at the NACE 1972 Meeting.

8. Unpublished data of M. Levy and C.V. Zabielski, AMMRC.

9. B.F. Brown, Editor, "Stress Corrosion Cracking in High Strength Steels and in Titanium and Aluminum Alloys", Naval Research Laboratory, Washington, D.C., 1972, p. 10-12.

Table 1

Fabrication Processes Which Leave High Residual Stresses

Welding

Spinning

Punching

Deep Drawing

Riveting

*Overtorquing Threaded Joints (Particularly Tapered Threads)

*Overtorquing Nut, Bolt and Capscrew Connections

*Inserting Over-size and Dissimilar Metal Bushings into Fittings

Pull-up in the Case of Mismatched Rivets or Holes

Caulking of Riveted Joints to Prevent Leaks

*Improper Heat Treatments

*Most Applicable to Our Applications

Table 2

Chemical Analysis of Uranium Alloys

Alloy	ppm by wt				wt %				
	C	H	O	N	Mo	Nb	Zr	Ti	V
3/4% Ti	<10	2.4	20	7	-	-	-	0.70	-
3/4% Quad	50	1.6	40	54	0.73	0.74	0.70	0.49	-
1% Quad	22	4.4	74	-	1.03	1.04	0.98	0.62	-
1% Quint	59	-	-	23	1.00	1.00	0.94	0.47	0.57

Table 3

Mechanical Properties of Uranium Alloys

Alloy	UTS ksi	0.2YS ksi	Elong %	R.A. %	Hard Rc
3/4% Ti	161.6	88	4.5	4.6	32
3/4% Quad	200	111.5	16.5	25.4	41
1% Quad	234	170	8.0	20.5	47
1% Quint	281.4	236	3.5	4.6	52

Table 4

Summary of Uranium SCC Results

Environment	3/4% Ti 161.6 UTS 88 YS		3/4% Quad 200 UTS 111.5 YS		1% Quad 234 UTS 170 YS		1% Quint 281.4 UTS 236 YS	
	K ksi$\sqrt{in.}$	min. thick*	K ksi$\sqrt{in.}$	min. thick*	K ksi$\sqrt{in.}$	min. thick*	K ksi$\sqrt{in.}$	min. thick*
Air	24	0.015	47	0.44	32	0.089	20	0.018
H_2O	21	0.011	40	0.32	28	0.068	9	0.004
3.5% NaCl	15	0.006	12	0.029	7	0.004	5	0.001
50 ppm Cl$^-$	-	-	-	-	9	0.007	5	0.001
50 ppm Cl$^-$ +0.1M NaNO$_3$	-	-	-	-	-	-	16	0.011

*Note: ASTM Minimum Thickness $= 2.5 \left(\frac{K}{\sigma y}\right)^2$

Table 5

Summary of the Influence of Environment
on the Fracture Behavior of Uranium Alloys

Type of Fracture
Influence of Environment

Alloy	Air	H_2O	50 ppm Cl^-	21,000 ppm Cl^-	50 ppm Cl^- + $NaNO_3$
3/4% Ti	quasi-cleavage	quasi-cleavage		quasi-cleavage	
3/4% Quad	plastic fracture, normal mode (ductile dimple)	quasi-cleavage plus ductile dimple		quasi-cleavage	
1% Quad	cleavage facets plus dimples	cleavage facets plus dimples		quasi-cleavage	
1% Quint	normal plastic fracture. smaller dimples than Quads	quasi-cleavage some dimples	quasi-cleavage	more cleavage-like	cleavage plus ductile dimple

A. 3/4% Ti ALLOY

B. 3/4% QUAD ALLOY

C. 1% QUAD ALLOY
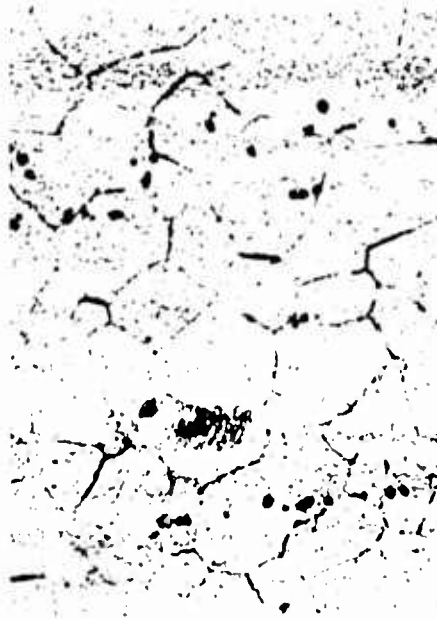
D. 1% QUINT ALLOY

Figure 1. PHOTOMICROGRAPHS OF AS-EXTRUDED URANIUM ALLOYS. MAG. 500X

ARMY MATERIALS AND MECHANICS RESEARCH CENTER

$$K = \frac{4.12\,(a^{-3} - a^3)^{1/2}\,M}{BW^{3/2}}$$
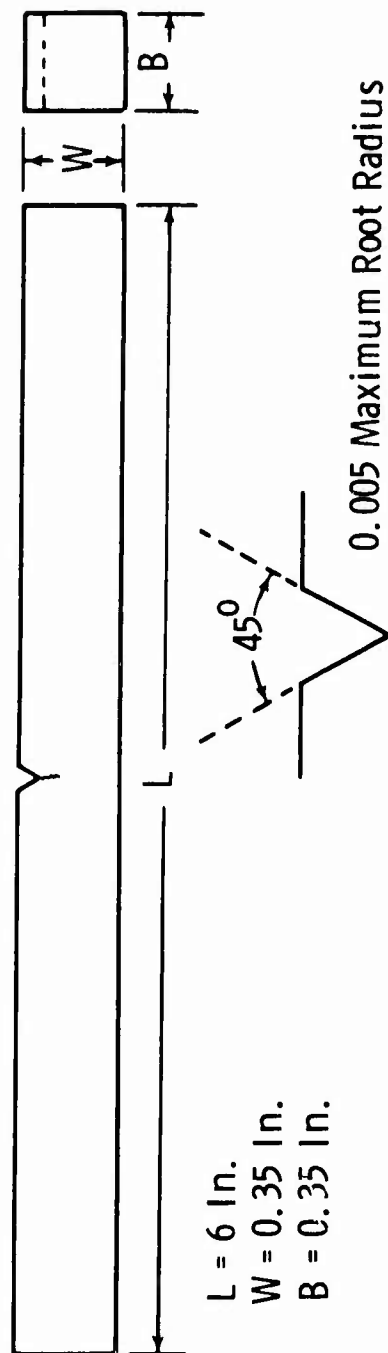
where $a = 1 - a/W$,

a = crack length + notch depth

L = 6 In.
W = 0.35 In.
B = 0.35 In.

45°

0.005 Maximum Root Radius

M = Moment
B = Thickness
W = Width

Figure 2. SPECIMEN GEOMETRY AND EQUATION FOR K VALUES

ARMY MATERIALS AND MECHANICS RESEARCH CENTER
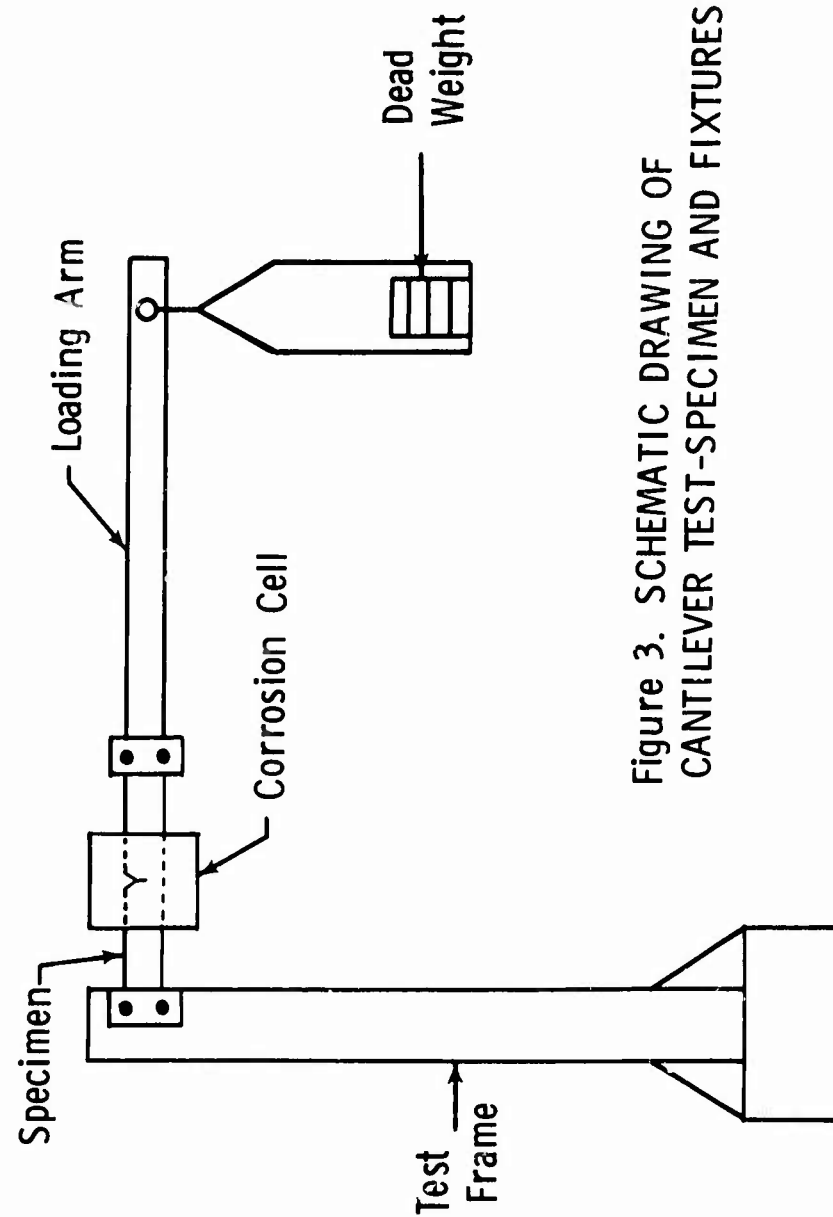
Figure 3. SCHEMATIC DRAWING OF CANTILEVER TEST-SPECIMEN AND FIXTURES

ARMY MATERIALS AND MECHANICS RESEARCH CENTER

495
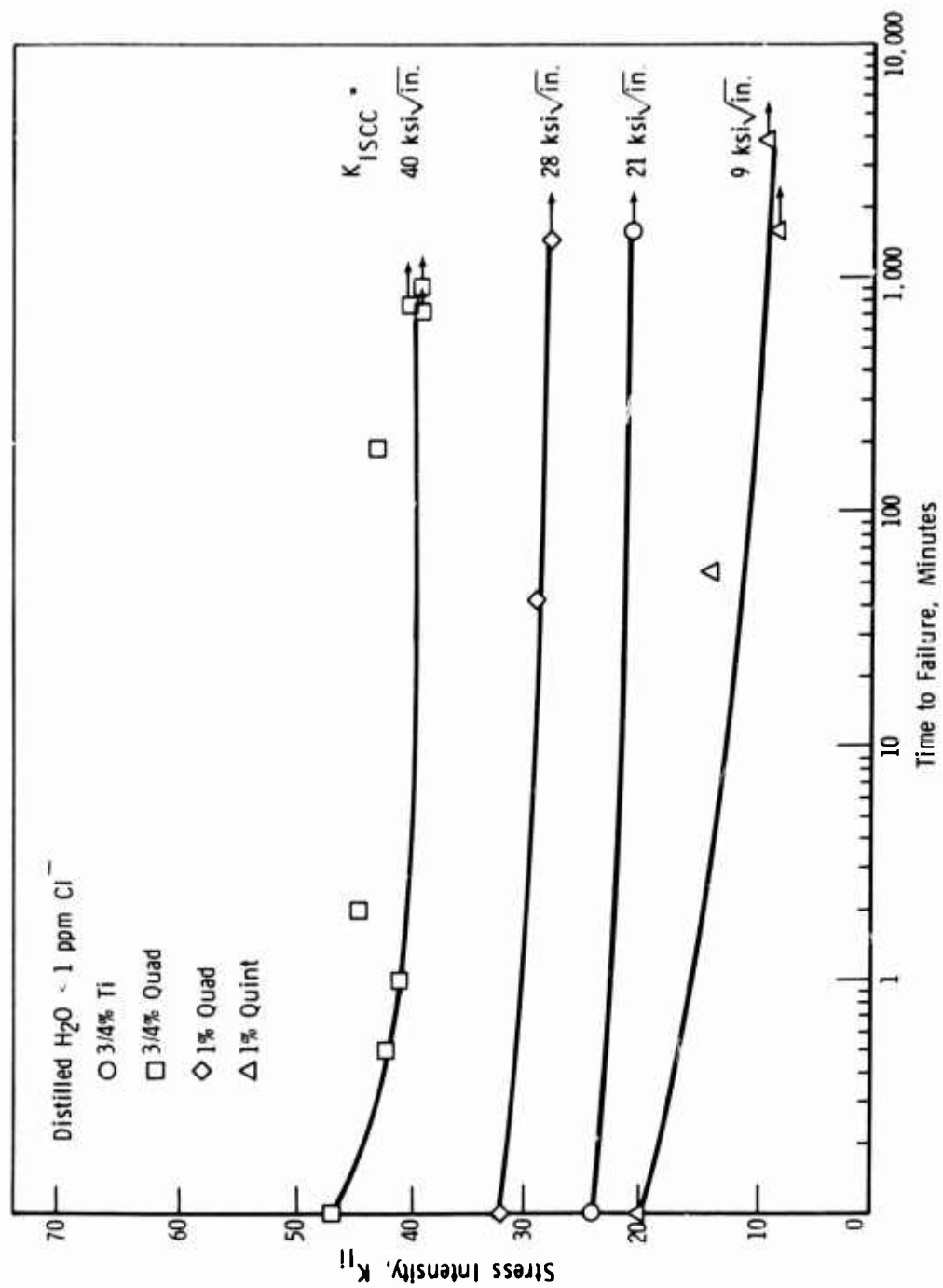
Figure 4. STRESS-CORROSION CRACKING BEHAVIOR OF URANIUM ALLOYS
IN DISTILLED WATER

ARMY MATERIALS AND MECHANICS RESEARCH CENTER
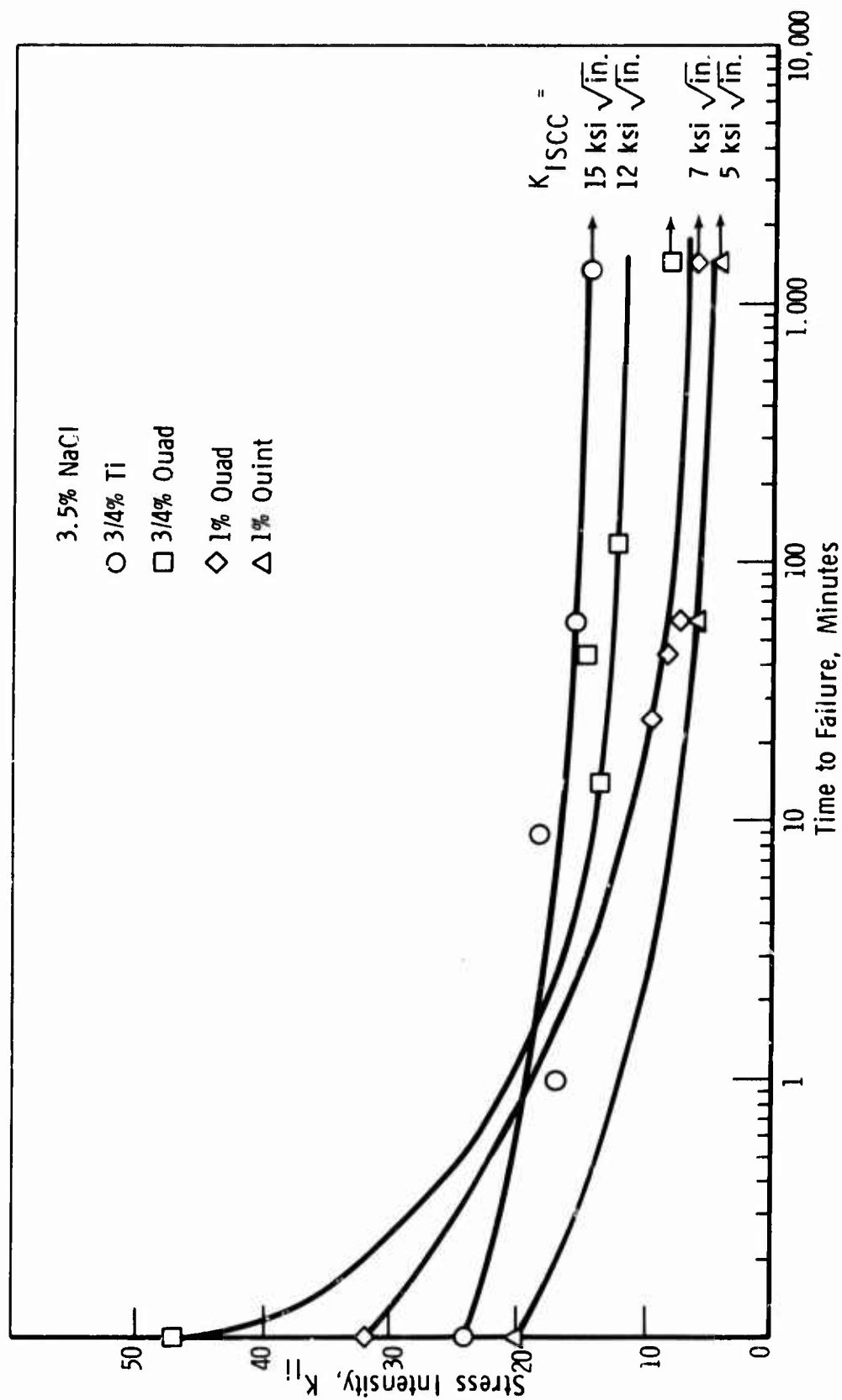
Figure 5. STRESS-CORROSION CRACKING BEHAVIOR OF URANIUM ALLOYS IN 3.5% SODIUM CHLORIDE
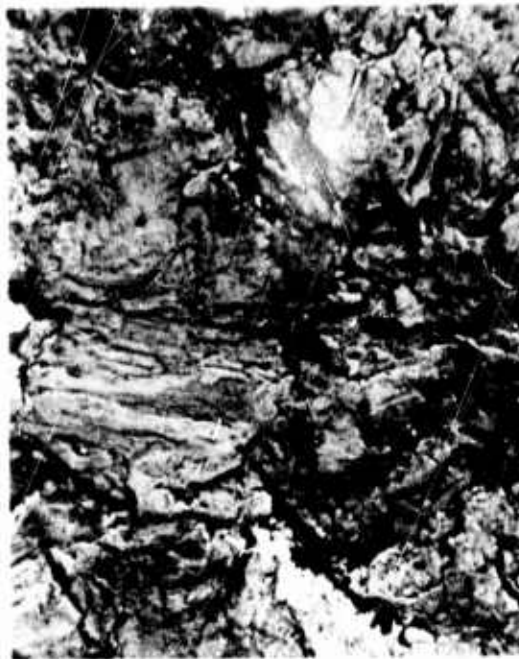
ARMY MATERIALS AND MECHANICS RESEARCH CENTER

497
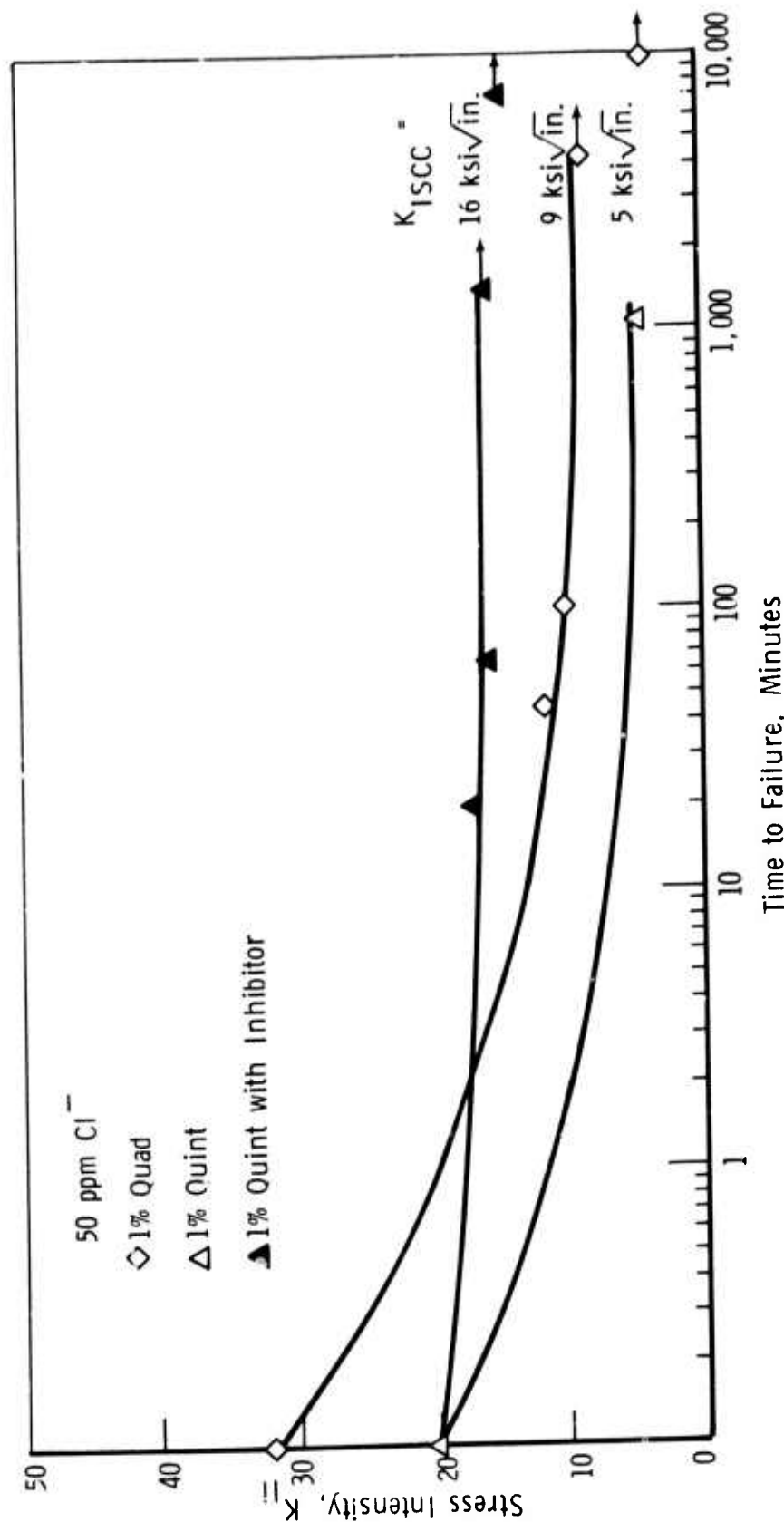
Figure 6. STRESS-CORROSION CRACKING BEHAVIOR OF THE 1% QUAD AND 1% QUINT ALLOYS IN SODIUM CHLORIDE SOLUTION CONTAINING 50 PPM CHLORIDE; EFFECT OF SODIUM NITRATE ADDITION

ARMY MATERIALS AND MECHANICS RESEARCH CENTER

3/4% Ti ALLOY

A. AIR - Mag. 2,800X

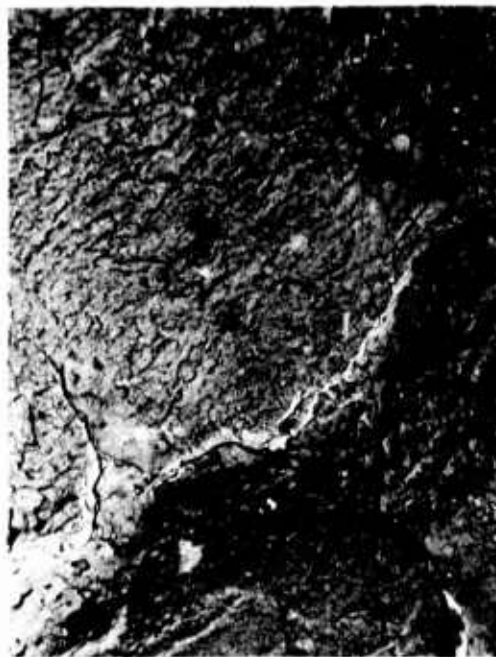B. H$_2$O - Mag. 2,800X

C. 3.5% NaCl - Mag. 2,500X

Figure 7. ELECTRON FRACTOGRAPHS OF THE 3/4% Ti ALLOY SHOWING FRACTURE IN (A) AIR, (B) H$_2$O, AND (C) 3.5% NaCl

ARMY MATERIALS AND MECHANICS RESEARCH CENTER

A. AIR - Mag. 2,800X

B. H_2O - Mag. 2,800X

C. 3.5% NaCl - Mag. 3,000X

Figure 8. ELECTRON FRACTOGRAPHS OF THE 3/4% QUAD ALLOY SHOWING FRACTURE IN (A) AIR, (B) H_2O, AND (C) 3.5% NaCl

ARMY MATERIALS AND MECHANICS RESEARCH CENTER

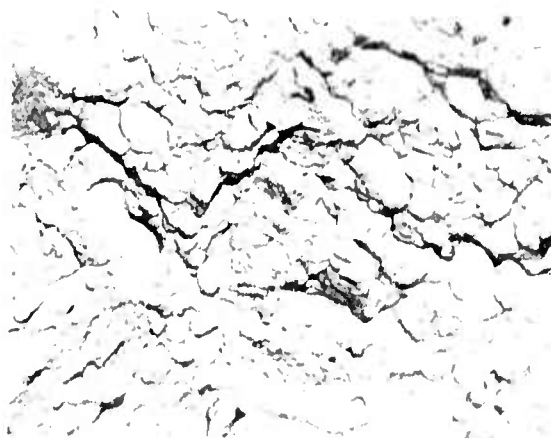A. AIR - Mag. 2,900X

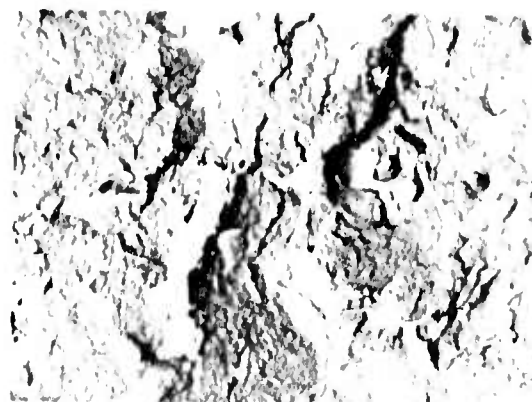B. H_2O - Mag. 2,800X

C. 3.5% NaCl - Mag. 2,500X

Figure 9. ELECTRON FRACTOGRAPHS OF THE 1% QUAD ALLOY SHOWING FRACTURE IN (A) AIR, (B) H_2O, AND (C) 3.5% NaCl

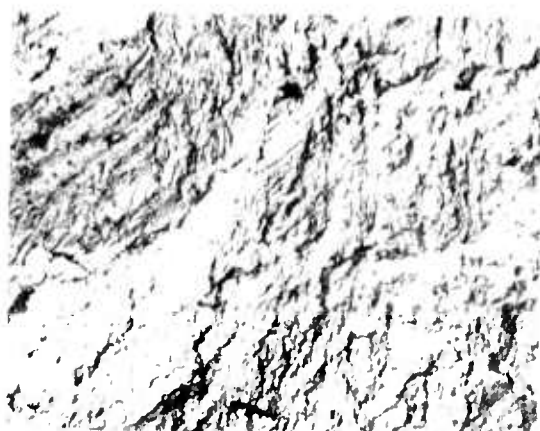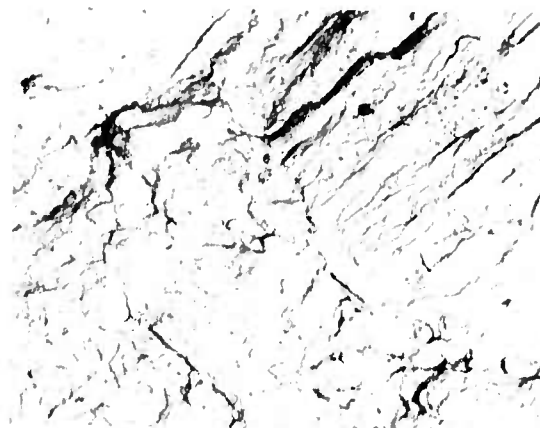ARMY MATERIALS AND MECHANICS RESEARCH CENTER
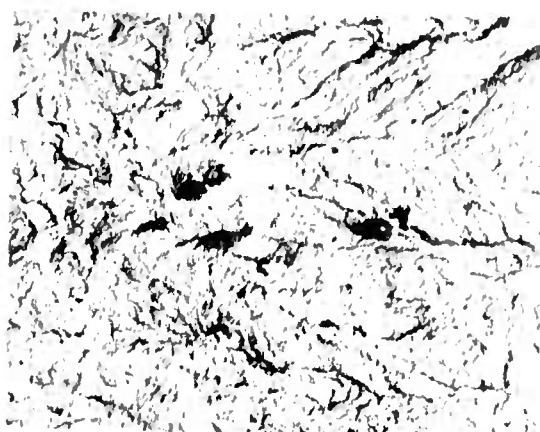
A. AIR - Mag. 2,500X

B. H_2O - Mag. 3,800X

C. 50 PPM Cl - Mag. 3,000X

D. 50 PPM Cl + 0.1% $NaNo_3$ -
Mag. 3,500X

E. 3.5% NaCl - Mag. 3,800X

Figure 10. ELECTRON FRACTOGRAPHS
OF THE 1% QUINT ALLOY SHOWING
FRACTURE IN (A) AIR, (B) H_2O,
(C) 50 PPM CHLORIDE, (D) 50 PPM
CHLORIDE PLUS 0.1 M SODIUM
NITRATE, AND (E) 3.5% NaCl
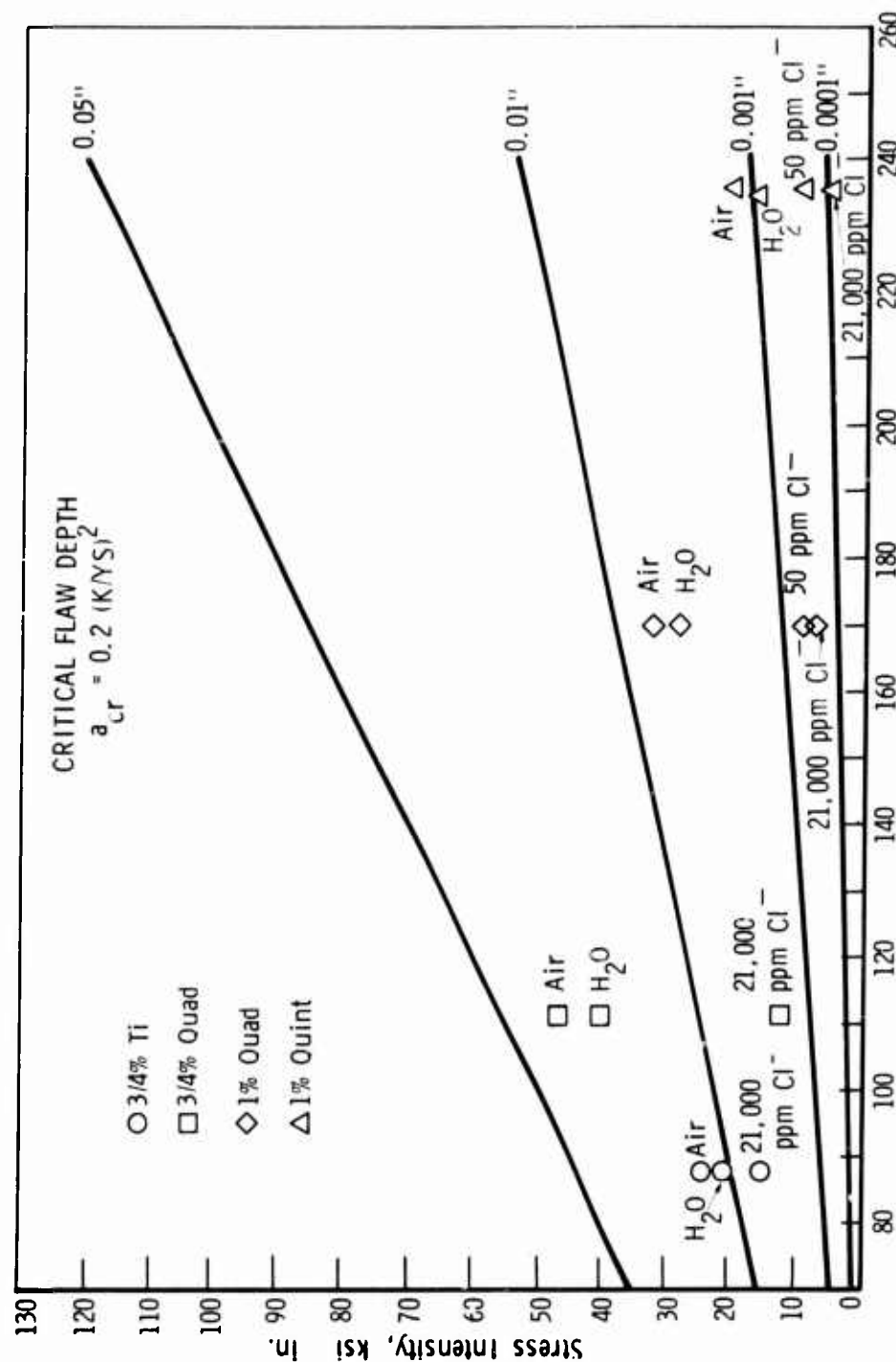
ARMY MATERIALS AND MECHANICS RESEARCH CENTER

Figure 11. K_{ISCC} FOR URANIUM ALLOYS IN AIR, DISTILLED WATER, AND 3.5% SODIUM CHLORIDE, SHOWN AS A FUNCTION OF YIELD STRENGTH. EQUATION (2) IS PLOTTED FOR FOUR VALUES OF CRACK SIZE.

ARMY MATERIALS AND MECHANICS RESEARCH CENTER

19-066-813/AMC-73

Hot-Salt Stress-Corrosion Cracking
of Titanium Alloys:
An Improved Model for the Mechanism
by
J. R. Myers and J. A. Hall
Metals and Ceramic Division
Air Force Materials Laboratory
Wright-Patterson AFB, Ohio

Introduction

Various titanium-alloy components in the compressor sections of modern
aircraft-gas-turbine engines are subjected to stresses, temperatures, and en-
vironmental conditions which cause hot-salt stress-corrosion cracking (HSSCC)
in laboratory testing. Ironically, no definitely-identified failures of this
type have ever occurred in service.

First observed in 1955 during the creep testing of perspiration contam-
inated specimens, (1) the hot-salt stress-corrosion cracking of titanium
alloys has been extensively studied. (2-42) This research has permitted many
general statements to be made regarding the environmentally-induced delayed-
failure process.

Numerous models have been proposed to describe the mechanism by which
this laboratory-observed phenomenon occurs. (19,30,31,33,41) Unfortunately,
none of these models can be completely rationalized in terms of the general
knowledge which presently exists on corrosion theory and hot-salt stress-
corrosion cracking. This is understandable because several of the models were
proposed prematurely; subsequent research revealed important factors which had
not been considered by the earlier investigators. Other models are considered
to be inadequate because they were either based upon hypothesis, or they
failed to completely describe the electrochemistry involved.

It is the purpose of this paper to present an improved model for the hot-
salt stress-corrosion cracking of titanium alloys. This explanation of the
mechanism is based upon data and verified observations which have been reported
in the literature. Basically, it will be shown that corrosion-produced hydrogen
is responsible for the premature failure which can occur when tensile-stressed
titanium alloys are exposed to hot-salt environments.

General Statements on HSSC

In many respects, the HSSCC of titanium alloys is similar to the environ-
mentally-induced-delayed-failure which has been observed for other materials.
Surface tensile stresses and a susceptible environment are required if crack-
ing is to occur. Unalloyed titanium is not susceptible to the deleterious
phenomenon. It is also known that the time-to-failure decreases as the tensile
stress increases, the time-to-failure can be significantly extended by small
cathodic currents, a minimum or threshold stress is required, an incubation
period precedes crack initiation, and the cracks propagate primarily intergran-
ularly.

Other factors which must be considered in the development of a HSSCC mech-
anism are more specifically related to titanium alloys.

HSSCC can be expected to occur when titanium alloys are exposed to certain chloride-containing environments over the temperature range of about 425 to 950°F (220 to 510°C).* The thermal environment must be continuously maintained. Otherwise, cracking may not occur in a reasonable time period. Certain thermal cycles which allow the specimens to be periodically exposed at ambient temperatures mitigate HSSCC. (20,39) Cracking does not occur at temperatures above about 950°F (510°C) because titanium alloys are creep limited; further, rapid general corrosion occurs at these elevated temperatures. Cracking probably has not been observed at temperatures below about 425°F (220°C) because of the extremely long incubation periods which would be required for cracking; further, thermal energy is required for pyrohydrolysis of titanium chloride.

Oxygen (8,11,19,26,33,41) and at least a small amount of moisture (5,19,26,33) are required for HSSCC. The water could come from the atmosphere or fluid inclusions (30) retained in the salt.

It is also known that very small concentrations of salt deposits (0.05 to 2 mg/in^2) can cause HSSCC.(19) Concentrations of this magnitude and greater exist on the compressor components of aircraft-gas-turbine engines.(7)

The final environmental factor which must be considered is the presence of sodium hydroxide. When sufficient quantities of sodium hydroxide are available, the HSSCC phenomenon appears to be inhibited. (11,33)

Compressive stresses on the surface tend to mitigate the corrosion process. (5,20) It is also known that the presence of fatigue pre-cracks do not decrease the cracking time-to-failure. (3,19,36)

Earlier investigators have presented evidence to show that titanium chloride (26,37) and titanium hydroxide (or titanium oxide)(11,37) are involved in the corrosion process. Hydrogen, however, is the important end product of the electrochemical process. Hydrogen diffuses into the titanium alloy prior to cracking (17,18,21); very high localized concentrations of hydrogen are known to exist near the cracks when HSSCC does occur.(17,18,33) The embrittlement which is induced before cracking can be reduced/eliminated by vacuum annealing. (6,12)

Although it cannot be firmly established whether hydrogen** or a titanium hydride (14,20) is involved, the species present is not considered to be important. The important fact is that dissolved hydrogen must be present in sufficient quantities if cracking is to occur.

Proposed Model for HSSCC

Using the documented observations which have been described, it is reasonable to believe that an improved model for HSSCC can be proposed.

The hot titanium-alloy surface is covered with salt deposits and an adsorbed moisture film; oxygen exists in and in-contact-with this electrolyte (Figure 1A). Being a boundary layer film, the aggressive environment would not be removed by high velocity gases which might pass over it. This is consistent

*Although other halides reportedly can cause HSSCC (30), it will be assumed that chloride is the aggressive ion for this discussion.

**Embrittlement could be caused by the interaction of hydrogen with dislocations or grain boundaries in such a manner as to inhibit stress-relieving slip and facilitate crack nucleation.

with the observation that salt deposits exist on gas-turbine-engine compressor components. (7) Laboratory testing has also shown that increasing gas velocities have little, if any, effect on the HSSCC time-to-failure. (5,19,20,37)

Pitting corrosion occurs under salt deposits on the alloy surface where the passive film has failed and cannot be repaired because of the high-chloride concentration (Figure 1C).(44) Localized breakdown of the passive film would tend to be facilitated by the presence of a surface tensile stress. This is a logical analysis because it is well established that passive films on an unstressed metal surface are continuously breaking down and being repaired on a microscopic scale. (45) (It is also possible that the salt deposit itself may locally destroy the passive film.) Pitting in the low-oxygen content electrolyte under the salt deposit would occur according to the anodic reaction: $Ti \longrightarrow Ti^n + ne$, where $n = 2, 3,$ or 4 (Figure 2).

The cathodic reaction which would occur in the higher-oxygen-content electrolyte adjacent to the salt deposit would be the reduction of oxygen, according to the reaction: $O_2 + 2H_2O + 4e \longrightarrow 4OH^-$. Analysis of this reaction and appreciation for the Guldberg Waage Law of Mass Action show why oxygen and moisture are required if corrosion of the titanium alloy is to occur. It also shows why increasing the hydroxide-ion content of the electrolyte (e.g., by adding sodium hydroxide) stifles the HSSCC process.

After the pit has formed, electrolyte would fill this void by capillary action. A net positive charge would develop in the pit electrolyte because of the anodic dissolution of titanium. This charge would be neutralized by the diffusion of chloride ions into the pit. Any oxygen in the pit would rapidly be consumed; further, the concentrated solution in the pit wouldn't tolerate the presence of oxygen. The oxygen content of the pit electrolyte would rapidly approach zero. In the pit, titanium ions would react with the chlorides to form titanium chloride (e.g., $TiCl_2$). This is consistent with the observation that titanium chloride has been detected as a corrosion product during HSSCC.(26,37)

Pyrohydrolysis (9,33) of the titanium chloride ($TiCl_n$) in the pit would occur according to the general reaction: $TiCl_n + nH_2O \xrightarrow{\Delta} Ti(OH)_n + nH^+ + nCl^-$. More specifically, one reaction could be: $TiCl_2 + 2H_2O \xrightarrow{\Delta} TiO_2 + 4H^+ + 2Cl^-$. The hydrogen-ion concentration in the pit would increase and permit a secondary cathodic reaction, the reduction of hydrogen ions within the pit, to occur: $H^+ + e \longrightarrow H$. This is the source of the monatomic hydrogen required for the cracking process.

Hydrogen formed at these secondary-cathodic sites within the pit would readily diffuse into the titanium alloy. The hydrogen would concentrate in the immediate vicinity of the tensile stresses which exist in the titanium alloy at the base of the corrosion pit (Figure 1D). Providing the tensile stresses and temperature are maintained for a sufficiently long time period, this localized-hydrogen content could easily exceed 1000 ppm (23). As the localized hydrogen content increases, the fracture toughness of this region would be markedly decreased. Eventually, the stress-intensity factor at the base of the corrosion pit would exceed the fracture toughness of the hydrogen-concentrated region. A crack would then propagate through the concentrated-hydrogen region (Figure 1E). Cracking would stop as soon as the crack tip came in contact with a region sufficiently lower in hydrogen than that required for crack propagation. At the crack tip, however, additional hydrogen would be generated; this would ultimately reduce the fracture toughness of a second region and permit additional crack propagation. This sequence of events would be repeated until the remaining sound metal could no longer support the applied load. Failure of the specimen by rapid crack propagation associated
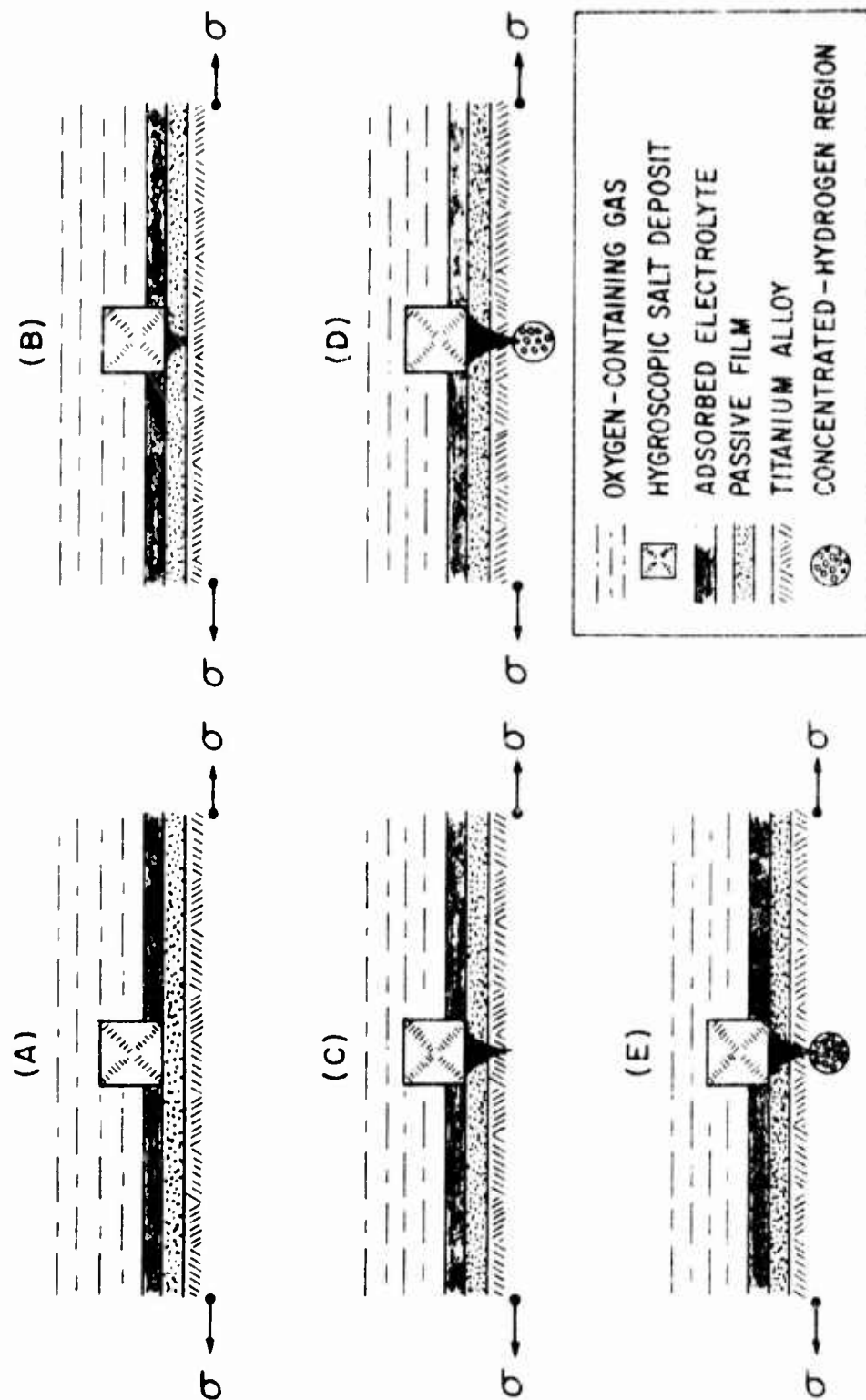
Figure 1 - Sequence of events in HSSCC: (A) Salt deposit on passive titanium alloy; (B) localized passive-film failure under salt deposit; (C) pitting corrosion at break in passive film; (D) concentration of hydrogen in titanium alloy at base of pit; and (E) crack propagation through region concentrated in hydrogen.

Legend:
- OXYGEN-CONTAINING GAS
- HYGROSCOPIC SALT DEPOSIT
- ADSORBED ELECTROLYTE
- PASSIVE FILM
- TITANIUM ALLOY
- CONCENTRATED-HYDROGEN REGION

Figure 2 - Detailed view of Figure 1b showing electrochemistry of USSCC.

with the instantaneous release of stored elastic energy would then occur.

Once the crack had been initiated, it is also reasonable to believe that each subsequent crack increment would occur more rapidly because a lower-hydrogen content would be required to achieve the critical stress-intensity factor.

The model described is consistent with all observations which have been verified on the HSSCC of titanium alloys. It also can be used to explain why failures probably have not been observed in service. Time is required for pit initiation and diffusion of hydrogen into the titanium alloy. Unless sufficient localized hydrogen diffuses into the substrate, the stress-intensity factor at the base of the corrosion pit will never exceed the fracture toughness of the hydrogen-affected region; the crack cannot be incubated. Further, if the stress is relaxed prior to crack initiation, the hydrogen would diffuse from the localized region of high tensile stress which exists at the base of the corrosion pit.

Unless titanium-alloy components in an aircraft-gas-turbine engine are operated at high tensile stresses for sufficiently-long time periods, the localized hydrogen content will never exceed the critical value required for crack initiation. Typical aircraft operations are of relatively short duration; they do not exceed the time required for crack initiation. Fortunately, also, the hydrogen damage is not cumulative. Each flight requires that the localized hydrogen region (necessary for cracking) be re-established.

References

1. G. W. Bauer, "Elevated Temperature Stability of Commercial Titanium Alloys", paper presented at Physical Metallurgy Symposium, Watertown Arsenal, September 1955.

2. W. K. Boyd and F. W. Fink, "The Phenomenon of Hot-Salt Stress-Corrosion Cracking of Titanium Alloys", NASA CR-117, October 1964.

3. R. Newcomer, H. C. Tourkakis, and H. C. Turner, "Elevated Temperature Stress Corrosion Resistance of Titanium Alloys", Corrosion, Vol. 21, pp. 307-315 (1965).

4. G. Sanderson and J. C. Scully, "The Hot Salt Cracking of Ti Alloys", Corrosion Science, Vol. 8, pp. 771-777 (1968).

5. H. R. Gray and J. R. Johnston, "Hot-Salt Stress-Corrosion of a Titanium Alloy Under a Simulated Turbine-Engine Compressor Environment", NASA TN D-5510, 1969.

6. H. R. Gray, "Hot-Salt Stress-Corrosion of Titanium Alloys: Generation of Hydrogen and Its Embrittling Effect", NASA TN D-5000, 1969.

7. R. L. Ashbrook, "A Survey of Salt Deposits in Compressors of Flight Gas Turbine Engines", NASA TN D-4999, 1969.

8. W. K. Boyd, "Stress Corrosion Cracking of Titanium and Its Alloys", Fundamental Aspects of Stress Corrosion Cracking (NACE, Houston), pp. 593-602 (1969).

9. S. P. Rideout, R. S. Ondrejcin, M. R. Louthan, Jr., and D. E. Rawl, "The Role of Moisture and Hydrogen in Hot-Salt Cracking of Titanium Alloys", Fundamental Aspects of Stress Corrosion Cracking (NACE, Houston), pp. 650-661 (1969).

10. R. E. Adams and E. von Tiesenhausen, "Study of Stress Corrosion Cracking of Commercial Titanium Alloys", Fundamental Aspects of Stress Corrosion Cracking (NACE, Houston), pp. 691-700 (1969).

11. H. L. Logan, "Studies of Hot Salt Cracking of the Titanium 8% Al - 1% Mo - 1% V Alloy", Fundamental Aspects of Stress Corrosion Cracking (NACE, Houston), pp. 662-672 (1969).

12. H. R. Gray, "Hot Salt Stress Corrosion of a Titanium Alloy: Generation of Hydrogen and Its Embrittling Effect", Corrosion, Vol. 25, pp. 337-341 (1969).

13. J. D. Boyd, P. J. Moreland, W. K. Boyd, R. A. Wood, D. N. Williams, and R. I. Jaffee, "The Effect of Composition on the Mechanism of Stress-Corrosion Cracking of Titanium Alloys in N_2O_4 and Aqueous and Hot-Salt Environments", NASA CR-1525, 1970.

14. R. S. Ondrejcin, "Hydrogen in Hot-Salt Stress Corrosion Cracking of Titanium-Aluminum Alloys", Metallurgical Transactions, Vol. 1, pp. 3031-3036 (1970).

15. H. R. Gray, "Hot-Salt Stress-Corrosion of Titanium Alloys", NASA SP-227, 1970.

16. H. R. Gray, "Relative Susceptibility of Titanium Alloys to Hot-Salt Stress Corrosion", NASA TN D-6498, 1971.

17. H. R. Gray, "Effect of Initial Hydrogen Content of a Titanium Alloy on Susceptibility to Hot-Salt Stress-Corrosion", NASA TM X-2404, November 1971.

18. H. R. Gray, "Role of Hydrogen in Hot-Salt Stress-Corrosion of a Titanium Alloy", NASA TN D-6188, February 1971.

19. V. C. Peterson, "Hot-Salt Stress-Corrosion of Titanium", Journal of Metals, Vol. 23, pp. 40-47, 1971 (April).

20. H. R. Gray, "Hot-Salt Stress-Corrosion of Titanium Alloys as Related to Turbine Engine Operation", NASA TM X-68015, 1972.

21. H. R. Gray, "Ion and Laser Microprobes Applied to the Measurement of Corrosion Produced Hydrogen on a Microscopic Scale", Corrosion, Vol. 28, pp. 47-54 (1972).

22. M. W. Mahoney and N. E. Paton, "The Effect of Oxide Thickness on the Hot Salt Stress Corrosion Susceptibility of Ti-6 Al-4V", Corrosion, Vol. 28, pp. 374-377 (1972).

23. H. R. Gray, "Effect of Initial Hydrogen Content of a Titanium Alloy on Susceptibility to Hot Salt Stress Corrosion", Corrosion, Vol. 28, pp. 186-188 (1972).

24. H. R. Gray, "Effects of Hot-Salt Stress Corrosion on Titanium Alloys", Metals Engineering Quarterly, Vol. 12, pp. 10-17, 1972 (November).

25. A. K. Wong and M. Levy, "Hot Salt Stress Corrosion of Titanium Alloys in an Adjustable Deflection, Multi-Specimen Bent Beam Test Apparatus", AMMRC TR 73-10, March 1973.

26. A. J. Hatch, H. W. Rosenberg, and E. F. Erbin, "Effects of Environment on Cracking in Titanium Alloys", Stress-Corrosion Cracking of Titanium, Am. Soc. Testing Mater., Spec. Tech. Publ. No. 397, 1966, pp. 122-136.

27. V. C. Petersen and H. B. Bomberger, "The Mechanism of Salt Attack of Titanium Alloys", Stress-Corrosion Cracking of Titanium, Am. Soc. Testing Mater., Spec. Tech. Publ. No. 397, 1966, pp. 80-94.

28. R. L. Kirchner and E. J. Ripling, "The Diffusion of Corrosion Products in Hot-Salt Stress Corrosion Cracking of Titanium", Stress-Corrosion Cracking of Titanium, Am. Soc. Testing Mater., Spec. Tech. Publ. No. 397, 1966, pp. 230-245.

29. H. R. Gray, "Hot-Salt Stress-Corrosion of Titanium Alloys as Related to Turbine Engine Operation", Titanium Science and Technology (Plenum Press, New York), pp. 2627-2638 (1973).

30. S. P. Rideout, M. R. Louthan, Jr., and C. L. Selby, "Basic Mechanism of Stress-Corrosion Cracking of Titanium", Stress-Corrosion Cracking of Titanium, Am. Soc. Testing Mater., Spec. Tech. Publ. No. 397, 1966, pp. 137-151.

31. R. G. Lingwall and E. J. Ripling, "Elevated Temperature Stress Corrosion of High Strength Sheet Materials in the Presence of Stress Concentrators", NASA CR-88979, August 1967.

32. H. L. Logan, "The Mechanisms of Stress Corrosion of the Titanium Alloy Ti-8-1-1 Exposed to Salt Environments at Elevated Temperatures", National Bureau of Standards Report No. 9468 (NASA CR-82511, May 1964).

33. M. Garfinkle, "An Electrochemical Model for Hot-Salt Stress-Corrosion of Titanium Alloys", NASA TN D-6779, April 1972.

34. H. R. Gray and J. R. Johnston, "Hot-Salt Stress Corrosion of A Titanium Alloy in a Dynamic Air Environment", Metallurgical Transactions, Vol. 1, pp. 3101-3105 (1970).

35. D. E. Piper and D. N. Fager, "The Relative Stress-Corrosion Susceptibility of Titanium Alloys in the Presence of Hot Salt", Stress-Corrosion Cracking of Titanium, Am. Soc. Testing Mater., Spec. Tech. Publ. No. 397, 1966, pp. 31-52.

36. R. V. Turley and C. H. Avery, "Elevated-Temperature Static and Dynamic Sea-Salt Stress Cracking of Titanium Alloys", Stress-Corrosion Cracking of Titanium, Am. Soc. Testing Mater., Spec. Tech. Publ. No. 397, 1966, pp. 1-30.

37. G. J. Heimerl, D. N. Braski, D. M. Royster, and H. B. Dexter, "Salt Stress Corrosion of Ti-8Al-1Mo-1V Alloy Sheet at Elevated Temperatures", Stress-Corrosion Cracking of Titanium, Am. Soc. Testing Mater., Spec. Tech. Publ. No. 397, 1966, pp. 194-214.

38. E. L. Kochka and V. C. Petersen, "The Salt Corrosion of Titanium Alloys at Elevated Temperatures", Final Technical Report, Contract No. NOas 60-6004-c, AD-255871, 15 January 1961.

39. L. H. Stone and A. H. Freedman, "Cyclic Hot-Salt Stress Corrosion of Titanium Alloys", AFML-TR-67-289, AD-825239, September 1967.

40. N. J. Donachie, Jr., W. P. Danesi, and A. A. Pinkowish, "Effects of Salt Atmosphere on Crack Sensitivity of Commercial Titanium Alloys at 600 to 900°F", Stress-Corrosion Cracking of Titanium, Am. Soc. Testing Mater., Spec. Tech. Publ. No. 397, 1966, pp. 179-193.

41. H. L. Logan, M. J. McBee, C. J. Bechtoldt, B. T. Sanderson, and G. M. Ugiansky, "Chemical and Physical Mechanisms of Salt Stress-Corrosion Cracking in the Titanium 8-1-1 Alloy", Stress-Corrosion Cracking of Titanium, Am. Soc. Testing Mater., Spec. Tech. Publ. No. 397, 1966, pp. 215-229.

42. R. F. Simenz, J. M. Van Orden, and G. G. Wald, "Environmental Effects Studies in Selected Titanium Alloys", Stress-Corrosion Cracking of Titanium, Am. Soc. Testing Mater., Spec. Tech. Publ. No. 397, 1966, pp. 53-79.

43. G. Martin, "Investigation of Long-Term Exposure Effects Under Stress of Two Titanium Structural Alloys", Stress-Corrosion Cracking of Titanium, Am. Soc. Testing Mater., Spec. Tech. Publ. No. 397, 1966, pp. 95-121.

44. J. M. Kolotyrkin, "Pitting Corrosion of Metals", Corrosion, Vol. 19, pp. 261t-268t (1963).

45. H. H. Uhlig, Corrosion and Corrosion Control, p. 63, John Wiley and Sons Inc., New York, 1963.

CORROSION RESISTANCE OF ALCLAD 7050 SHEET

S. J. Ketcham

Naval Air Development Center
Warminster, Pennsylvania 18974

ABSTRACT

The corrosion resistance of laboratory produced Alclad 7050 sheet has been determined in a NaCl-SO_2 environment. The cladding itself has good corrosion properties and effectively protects the core from attack. Surface treatments such as chromate conversion coatings and anodizing retard the rate of sacrificial attack of the cladding.

INTRODUCTION

Under a Naval Air Systems Command contract (1), Alcoa Technical Center developed a cladding for 7050 sheet that would sacrificially protect the core without appreciably reducing mechanical properties. The Naval Air Development Center was tasked to determine the corrosion resistance of the clad 7050 sheet in the salt-sulfur environment in which carrier based naval aircraft operate. Protection provided by chromating and anodizing was also determined.

EXPERIMENTAL PROCEDURE

Material

The Alcoa Technical Center furnished three sheets of Alclad 7050-T76, 0.180 in. x 12 in. x 36 in. (Lot No. S-412843). These sheets were produced in the Alcoa laboratories. Nominal compositions of the 7050 core and the cladding are as follows:

P E R C E N T A G E

	Zn	Mg	Cu	Zr	Si	Fe	Ti	Cr	Mn
Core	6.0	2.3	2.5	0.1	0.12*	0.15*	0.06*	0.04*	0.10*
Cladding	5.0	1.1	0.03*	0.1	0.10*	0.08*	0.03*	0.00	0.10*

* maximum limit

The thickness of the cladding was measured microscopically and averaged 3.5 to 5.0 mils on a side.

Corrosion Tests

Triplicate panels 3 in. x 10 in. x .087 in. were used for the corrosion tests. Exposure times in the salt-SO_2 salt fog cabinet were 4, 6, and 8 weeks. Operating conditions for this test are:

> 5% Salt Solution - pH 6.5-7.2
> Tower Temperature - 115°F $\pm$ 2
> Cabinet Temperature - 95°F $\pm$ 2
> SO_2 gas injection - 1 hour/6 hour cycle at a flow
> rate of 25 cc/min.

Stepped panels were machined to expose the core at the T/4 and T/2 planes (one quarter through the thickness and the midplane) in addition to the as clad surface

to ascertain corrosion behavior throughout the thickness of the sheet. A flap brush was used to remove the machining marks.

Panels were exposed as received, also chromated with a MIL-C-81706 chemical film or anodized with MIL-A-8625 coatings, both Type I and II, followed by a dichromate seal. Some of the panels had crosses of three widths, 1/16, 1/8 and 1/4 in. machined through the cladding to expose the core. This was done to ascertain the degree of sacrificial protection afforded by the cladding to the core, including its throwing power.

RESULTS AND DISCUSSION

The as received clad surface had a very mottled appearance over large areas of the sheets. The Alcoa Technical Center was contacted as to whether the material should be tested as received or whether the surface should be abraded with nylon pads or a flap brush to remove the scale. It was recommended that the material be tested as received.

This mottled appearance was not removed by the non-etch alkaline cleaning or de-oxidizing solutions and influenced the visual quality of the subsequent chromate coating. The anodized coatings, as far as appearance was concerned, were not so affected.

Figure 1 shows the appearance of the as-received surface after 4, 6 and 8 weeks exposure in salt spray. The cladding proved to be very effective in protecting the core. The cladding itself underwent general, uniform pitting attack.

The corrosion behavior of the cladding is seen more clearly at higher magnification. Figure 2 is a cross section of the as received sheet. Figures 3, 4 and 5 are photomicrographs taken of panels exposed to salt spray which were cross-sectioned through the 1/16 in. wide scribe. After 4 weeks, the cladding thickness has been reduced at least 50%. After 6 weeks there is further reduction and at 8 weeks no cladding is evident.

An 8-week specimen was also sectioned at the 1/8 and 1/4 in. scribes to determine throwing power of the cladding. There was no attack in the 1/8 in. scribe and only one small area in the 1/4 in. scribe.

Figure 6 shows the appearance of the stepped panels after 4 weeks salt spray. After 2 weeks the core surfaces were showing severe pitting attack and some exfoliation which worsened with time (Figure 7). The cladding alloy has better corrosion resistance than the core alloy (when cladding is not providing sacrificial protection to core).

Chromated and anodized panels are shown in Figures 8, 9 and 10 after exposure times of 4, 6 and 8 weeks, respectively. The coatings performed as expected, the chromate conversion coating showing the most attack, the Type II anodize the least.

Again, the photomicrographs provide more quantitative evaluation of the protection afforded to the cladding by surface treatments. Figures 11, 12 and 13 are cross-sections through treated panels exposed for 8 weeks in the NaCl-SO$_2$ cabinet. These should be compared with Figure 5 of an untreated panel after 8 weeks when

the cladding has been totally consumed. All three treatments protected the cladding to some extent, the cladding showing approximately at 50% reduction in the same period.

Figures 14, 15 and 16 show the corrosion resistance of the various treatments after 4, 6 and 8 weeks respectively. The sulfuric acid anodized/dichromate sealed treatment in itself has the best corrosion resistance.

Paint films were not included in this study since their performance over the above surface treatments was comprehensively presented in a previous publication (2). If sufface treated Alclad 7050 is to be painted with a MIL-P-22750 inhibited epoxy primer and a topcoat, the MIL-C-81706 chromate provides better paint adhesion than the anodized coatings.

CONCLUSIONS

1. Laboratory produced Alclad 7050 sheet has good corrosion resistance and adequately protects the core from attack in a salt+SO_2 environment.

2. The use of surface treatments, either a MIL-C-81706 chromate conversion or MIL-A-8625, Type I and II, anodized coatings (dichromate sealed) retards the rate of sacrificial attack of the cladding.

3. For applications where a paint system is to be used, the MIL-C-81706 chromate treatment provides the best paint adhesion.

4. For applications where paint systems will not be used, a MIL-A-8625, Type II/ dichromate sealed coating provides the most corrosion protection to the cladding.

REFERENCES

(1) NAVAIRSYSCOM Contract No. N00019-72-C-0146

(2) S. Brown, I. Shaffer, "Optimum Corrosion Protective Finishing Systems for Aluminum Alloys Used in Naval Aircraft", Proceedings of 1972 Tri-Service Conference on Corrosion, MCIC-73-19 of Dec. 1973.
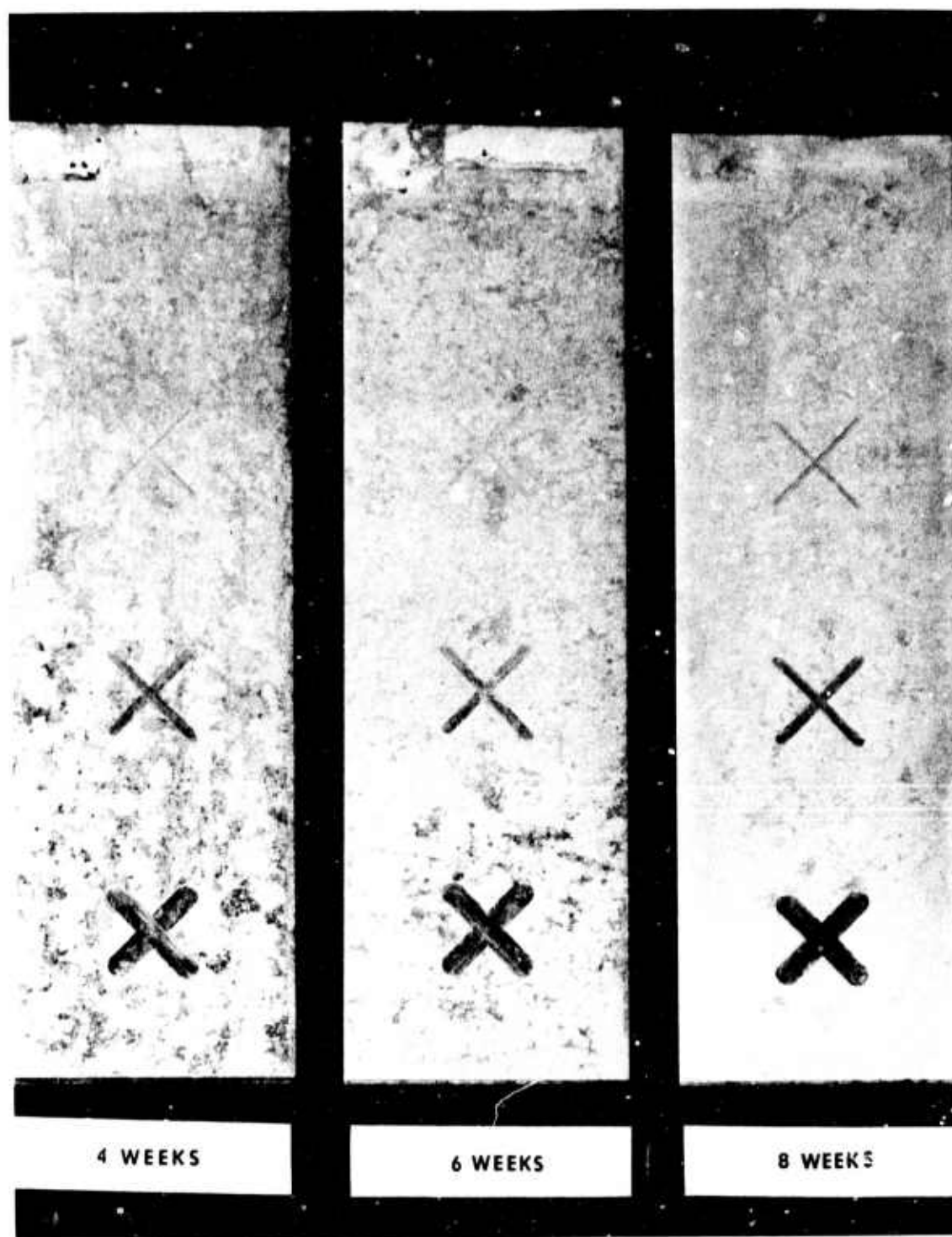
Figure 1. Alclad 7050 with no surface treatments after various times in
NaCl-SO$_2$ salt spray (corrosion products removed).

Cladding

Core

Figure 2.   Cross section through Alclad 7050 (S No. 412843)
.187 in. thick - Keller's etch - 100X

Cladding

Core

Figure 3. Cross-section through 1/16 in. scribe on clad 7050 after 4 weeks.
Cladding thickness reduced by 50%

Cladding

Core

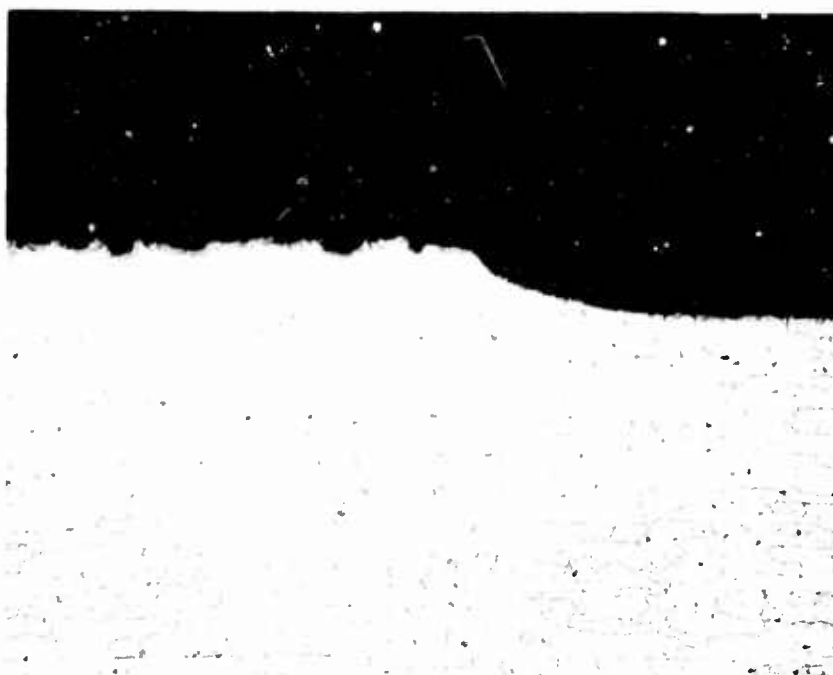Figure 4. Cross-section through 1/16 in. scribe on clad 7050 after 6 weeks

Figure 5. Cross-section through 1/16 in. scribe on clad 7050 after 8 weeks. No cladding evident.

Keller's etch - 112X

As
clad
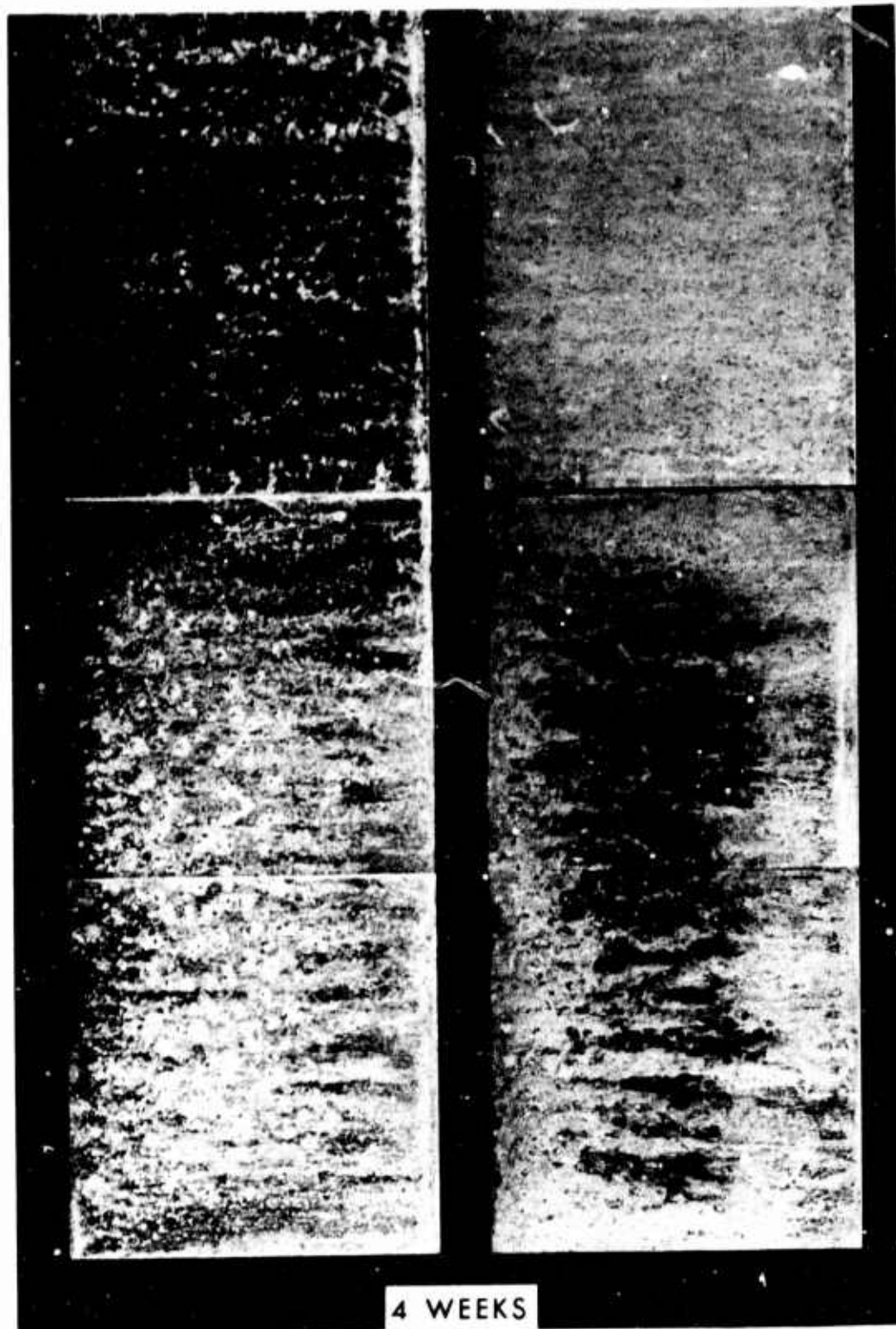surface

T/4
plane

T/2
plane
(midplane)

4 WEEKS

Figure 6. Stepped panel with as received surface, and the T/4 and T/2 planes
exposed to NaCl-SO$_2$ salt spray for 4 weeks. Panel on the right has
had corrosion products removed in chromic-phosphoric acid solution.

523

Figure 7. Exfoliation attack at midplane of Alclad 7050 sheet after 4 weeks in NaCl-SO$_2$ salt spray - 100X

MIL-C-81706

MIL-A-8625
Type I
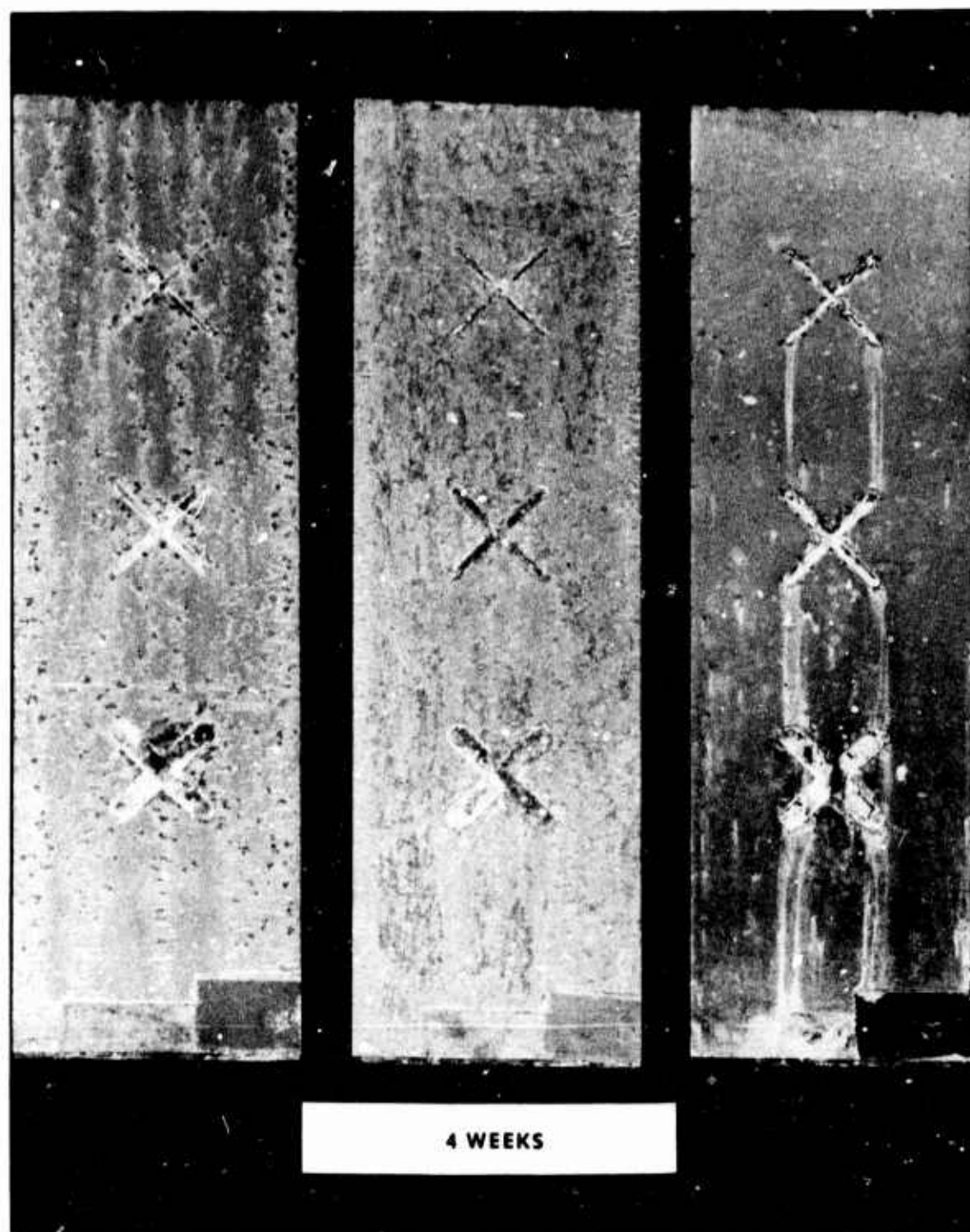Dichromate Seal

MIL-A-8625
Type II
Dichromate Seal

4 WEEKS

Figure 8. 4 weeks in NaCl-SO$_2$ salt spray

Figure 9. 6 weeks in NaCl-SO$_2$ salt spray

MIL-C-81706   MIL-A-8625 Type I Dichromate Seal   MIL-A-8625 Type II Dichromate Seal

8 WEEKS

Figure 10.   8 weeks in NaCl-SO$_2$ salt spray

Figure 11.
MIL-C-81706

Cladding

Core

Figure 12.
MIL-A-8625
Type I,
dichromate
seal

Cladding

Core

Figure 13.
MIL-A-8625
Type II,
dichromate
seal

Cladding

Core

8 weeks in NaCl-SO$_2$ salt spray
Keller's etch - 100X

528

MIL-C-81706

MIL-A-8625
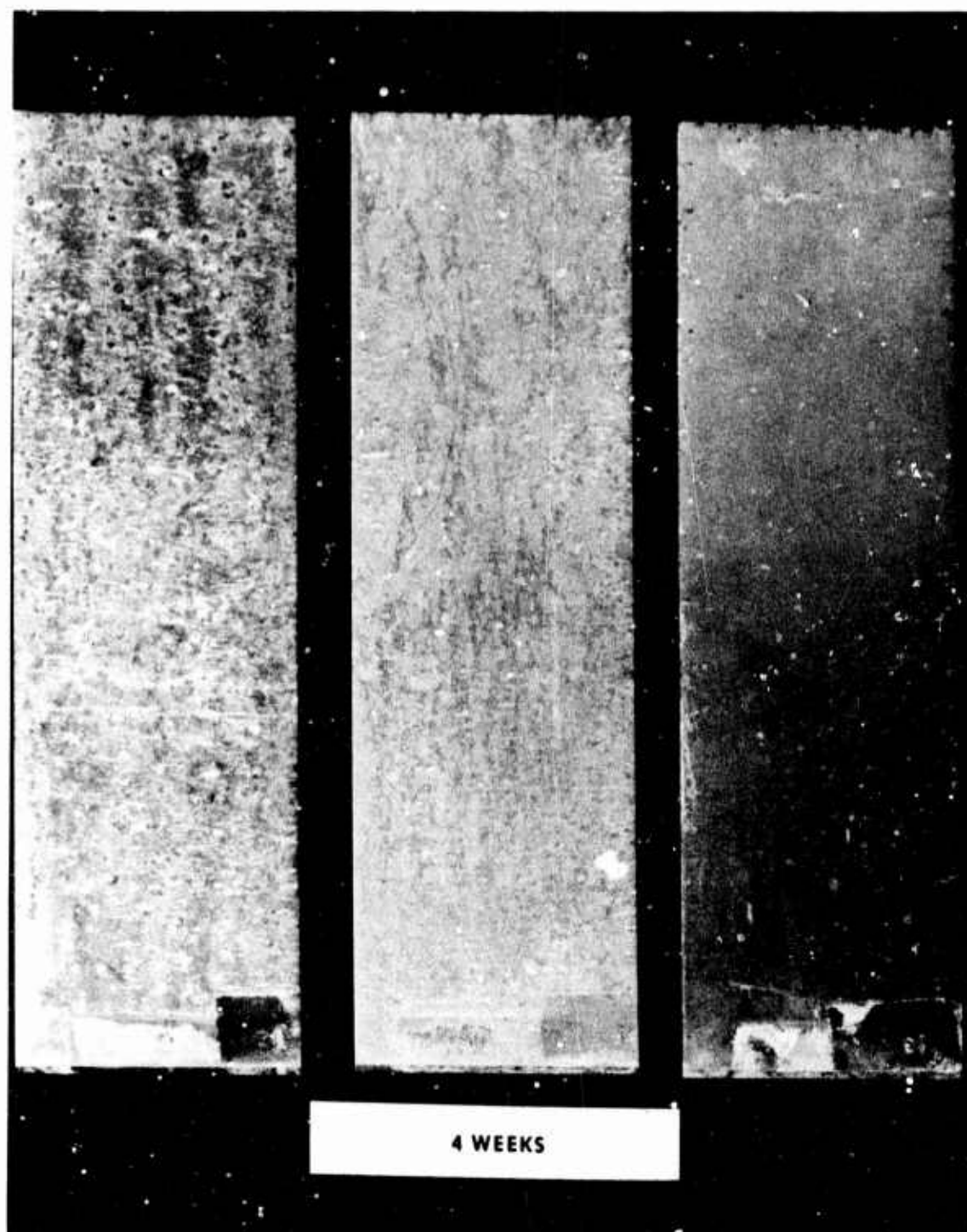Type I
Dichromate Seal

MIL-A-8625
Type II
Dichromate Seal

4 WEEKS

Figure 14.   4 weeks in NaCl-SO$_2$ salt spray

MIL-A-81706   MIL-A-8625 Type I Dichromate Seal   MIL-A-8625 Type II Dichromate Seal

6 WEEKS

Figure 15.   6 weeks in NaCl-SO$_2$ salt spray.

530

MIL-C-81706   MIL-A-8625   MIL-A-8625
                     Type I   Type II
                     Dichromate Seal   Dichromate Seal

8 WEEKS

Figure 16.   8 weeks in NaCl-SO$_2$ salt spray

531